Journal of Turbomachinery

Published Quarterly by ASME

VOLUME 127 • NUMBER 2 • APRIL 2005

TECHNICAL PAPERS

241 **High Frequency Surface Heat Flux Imaging of Bypass Transition** (2004-GT-54162)
Richard J. Anthony, Terry V. Jones, and John E. LaGraff

251 **Measured Adiabatic Effectiveness and Heat Transfer for Blowing From the Tip of a Turbine Blade** (2004-GT-53250)
J. R. Christophel, E. Couch, K. A. Thole, and F. J. Cunha

263 **Large Eddy Simulation of Flow and Heat Transfer in a Channel Roughened by Square or Semicircle Ribs** (2004-GT-53401)
Joon Ahn, Haecheon Choi, and Joon Sik Lee

270 **Cooling the Tip of a Turbine Blade Using Pressure Side Holes—Part I: Adibatic Effectiveness Measurements** (2004-GT-53251)
J. R. Christophel, K. A. Thole, and F. J. Cunha

278 **Cooling the Tip of a Turbine Blade Using Pressure Side Holes—Part II: Heat Transfer Measurements** (2004-GT-53254)
J. R. Christophel, K. A. Thole, and F. J. Cunha

287 **Parametric Effects on Heat Transfer of Impingement on Dimpled Surface** (2004-GT-53142)
Koonlaya Kanokjaruvijit and Ricardo F. Martinez-Botas

297 **Adiabatic Effectiveness Measurements of Endwall Film-Cooling for a First-Stage Vane** (2004-GT-53326)
D. G. Knost and K. A. Thole

306 **Flow and Heat Transfer in an Internally Ribbed Duct With Rotation: An Assessment of Large Eddy Simulations and Unsteady Reynolds-Averaged Navier-Stokes Simulations**
A. K. Saha and Sumanta Acharya

321 **Nusselt Numbers and Flow Structure on and Above a Shallow Dimpled Surface Within a Channel Including Effects of Inlet Turbulence Intensity Level** (2004-GT-54231)
P. M. Ligrani, N. K. Burgess, and S. Y. Won

331 **Three-Dimensional Separations in Axial Compressors** (2004-GT-53617)
Semiu A. Gbadebo, Nicholas A. Cumpsty, and Tom P. Hynes

340 **Experimental Investigation of a Transonic Aspirated Compressor** (2002-GT-30370)
Brian J. Schuler, Jack L. Kerrebrock, and Ali Merchant

349 **On the Use of Atmospheric Boundary Conditions for Axial-Flow Compressor Stall Simulations**
M. Vahdati, A. I. Sayma, C. Freeman, and M. Imregun

352 **Active Control of Tip Clearance Flow in Axial Compressors** (2003-GT-38661)
Jin Woo Bae, Kenneth S. Breuer, and Choon S. Tan

363 **Numerical Study of Unsteady Flow in a Centrifugal Pump** (2004-GT-54099)
Kitano Majidi

372 **Thermoacoustic Modeling of a Gas Turbine Combustor Equipped With Acoustic Dampers** (2004-GT-53977)
Valter Bellucci, Bruno Schuermans, Dariusz Nowak, Peter Flohr, and Christian Oliver Paschereit

(Contents continued on inside back cover)

This journal is printed on acid-free paper, which exceeds the ANSI Z39.48-1992 specification for permanence of paper and library materials. ∞™
♲ **85% recycled content, including 10% post-consumer fibers.**

Transactions of the ASME, Journal of Turbomachinery (ISSN 0889-504X) is published quarterly (Jan., Apr., July, Oct.) by The American Society of Mechanical Engineers, Three Park Avenue, New York, NY 10016. Periodicals postage paid at New York, NY and additional mailing offices. POSTMASTER: Send address changes to Transactions of the ASME, Journal of Turbomachinery, c/o THE AMERICAN SOCIETY OF MECHANICAL ENGINEERS, 22 Law Drive, Box 2300, Fairfield, NJ 07007-2300. **CHANGES OF ADDRESS** must be received at Society headquarters seven weeks before they are to be effective. Please send old label and new address.

Canadian Goods & Services Tax Registration #126148048

(**Contents continued**)

Journal of Turbomachinery **Volume 127, Number 2** **APRIL 2005**

380 **Experimentally Verified Numerical Optimization of a Three-Dimensional Parametrized Turbine Vane With Nonaxisymmetric End Walls** (2003-GT-38624)
Marc G. Nagel and Ralf-D. Baier

388 **The Unsteady Development of a Turbulent Wake Through a Downstream Low-Pressure Turbine Blade Passage** (2004-GT-53061)
R. D. Stieger and H. P. Hodson

395 **An Implicit Fluctuation Splitting Scheme for Turbomachinery Flows**
A. Bonfiglioli, P. De Palma, G. Pascazio, and M. Napolitano

402 **Modeling Transition in Separated and Attached Boundary Layers** (2004-GT-53664)
Stephen K. Roberts and Metin I. Yaras

412 **Nonsynchronous Vibration (NSV) due to a Flow-Induced Aerodynamic Instability in a Composite Fan Stator** (2004-GT-53492)
A. J. Sanders

ANNOUNCEMENTS AND SPECIAL NOTES

422 **Information for Authors**

The ASME Journal of Turbomachinery is abstracted and indexed in the following:

Aluminum Industry Abstracts, Aquatic Science and Fisheries Abstracts, Ceramics Abstracts, Chemical Abstracts, Civil Engineering Abstracts, Compendex (The electronic equivalent of Engineering Index), Corrosion Abstracts, Current Contents, Ei EncompassLit, Electronics & Communications Abstracts, Energy Information Abstracts, Engineered Materials Abstracts, Engineering Index, Environmental Science and Pollution Management, Excerpta Medica, Fluidex, Fuel and Energy Abstracts, INSPEC, Index to Scientific Reviews, Materials Science Citation Index, Mechanical & Transportation Engineering Abstracts, Mechanical Engineering Abstracts, METADEX (The electronic equivalent of Metals Abstracts and Alloys Index), Metals Abstracts, Oceanic Abstracts, Pollution Abstracts, Referativnyi Zhurnal, Shock & Vibration Digest, Steels Alert

Richard J. Anthony
AFRL Propulsion Directorate,
Wright-Patterson, AFB, OH 45433
e-mail: richard.anthony@wpafb.af.mil

Terry V. Jones
Department of Engineering Science,
University of Oxford,
Oxford, UK
e-mail: terry.jones@eng.ox.ac.uk

John E. LaGraff
Department of Mechanical, Aerospace, and
Manufacturing Engineering,
Syracuse University,
Syracuse NY 13201
e-mail: jlagraff@syr.edu

High Frequency Surface Heat Flux Imaging of Bypass Transition

A high-frequency surface heat flux imaging technique was used to investigate bypass transition induced by freestream turbulence. Fundamental experiments were carried out at the University of Oxford using high-density thin film arrays on a flat plate wind tunnel model. Bypass transition was induced by grid-generated turbulence with varying intensities of 2.3%, 4.2%, and 17% with a fixed integral length scale of approximately 12 mm. Unique high resolution temporal heat flux images are shown which detail significant differences between unsteady surface heat flux events induced by freestream turbulence and the classical Emmons-type spots which many turbomachinery transition models are based on. The temporal imaging technique presented allows study of unsteady surface heat transfer in detail, and helps elucidate the complex nature of transition in the high-disturbance environment of turbomachinery. [DOI: 10.1115/1.1860379]

1 Introduction

Gas turbine engineers must design turbine blades capable of operating in freestream temperatures well above the maximum allowable temperature of the lade material. In this situation, knowledge of the unsteady surface heat flux characteristics of the boundary layer can be critical [1]. Note some axial flow turbines can have approximately 700 individual blades, each one developing its own boundary layer that undergoes laminar-turbulent transition. In some cases, up to 50% of a blade chord length may be transitional [2].

Many predictive heat transfer codes attempt to model boundary layer transition based on the generation, propagation, and coalescence of turbulent "spots" in a laminar boundary layer. Most experimental studies of turbulent spot characteristics in the past have been performed in relatively low disturbance environments using artificially triggered spots. In more practical engineering flows, however, boundary layer transition is often affected by many flow disturbances. This is especially true for flow through turbines. Figure 1 is a sketch of some of the disturbances affecting the boundary layer over a turbine blade. These include freestream turbulence, wakes from upstream blade rows, and variable pressure gradients, all of which alter transition and heat flux to the blade. Understanding how each affect the blade boundary layer is very important for those trying to model heat transfer in turbines. Before such complex effects can be modeled, though, greater insight into the physics of turbulence-induced transitional heat transfer is needed.

Transitional heat transfer predictions based on simple spot models often assume classical Emmons spots form at a certain streamwise location based on a critical Reynolds number and then spread downstream with a self-similar triangular shape. This behavior can be witnessed in a low disturbance environment where turbulent spots are allowed to grow into a mature, fully-developed patch of turbulence along the surface. Transition in most real engineering flows, however, particularly in gas turbine engines, occurs differently.

2 Background

Efforts in boundary layer transition research have traditionally focused on the growth of natural laminar boundary layer instabilities and their subsequent breakdown into turbulence [3,4]. In this process, primary laminar instability appears at a critical local Reynolds number taking the form of two-dimensional Tollmien–Schlichting ($T-S$) waves. The $T-S$ waves grow slowly, but exponentially, as they propagate downstream. They soon develop spanwise distortions, become nonlinear, and rapidly breakdown into turbulent spots. The turbulent spots, in turn, cause a substantial rise in local surface shear stress and increase the local surface heat transfer rate. The turbulent spots spread and convect along the surface coalescing into a fully turbulent boundary layer (see Fig. 2). For many years, this path to transition has been the most recognized and studied, aided in part by its early explanation by linear stability theory [3]. In reality, this type of transition is usually limited to relatively low disturbance environments, where surface and freestream perturbations have a minimal influence.

In most practical engineering flows, however, small disturbances often cause the boundary layer to bypass the relatively slow development of $T-S$ waves and cause transition to occur sooner at a significantly lower Reynolds numbers. The term "bypass transition" was originally coined by Morkovin [5] to describe flows that bypassed the 'regular' transition modes then explained by linear stability theory.

Experimental research in the field of turbomachinery aerodynamics has searched for empirical correlations to help predict transitional surface heat flux under freestream turbulence. Experiments by Abu-Ghannam and Shaw [6], Narasimha [7], Mayle [2], and Fraser [8] attempt to correlate turbulent spot onset location, and spot generation rate, with the freestream turbulence intensity Tu. The earliest attempt to correlate spot generation rate with freestream turbulence was made by Emmons and Bryson [9]. Experiments show increasing freestream turbulence intensity moves the transition onset location further upstream, thus increasing the overall heat transfer to the surface.

Kittichaikarn, Ireland, Zhong, and Hodson [10] obtained surface heat flux images of turbulent spots generated by a bar wake using liquid crystals in a water channel experiment. Their images show irregular shaped spots with a streaky surface heat flux footprint. Flow visualization experiments by Matsubara, Alfredsson, and Westin [11] show grid generated freestream turbulence develops unsteady streaky structures within the boundary layer with high and low streamwise velocity. They state the longitudinal streaky structures create large amplitude, low frequency fluctuations inside the boundary layer.

Direct numerical simulations by Jacobs and Durbin [12] show low frequency perturbations are amplified and elongated in the streamwise direction by the shear. They argue these streaks are an implicit property of the boundary layer under moderate levels of

---

Contributed by the International Gas Turbine Institute (IGTI) of THE AMERICAN SOCIETY OF MECHANICAL ENGINEERS for publication in the ASME JOURNAL OF TURBOMACHINERY. Paper presented at the International Gas Turbine and Aeroengine Congress and Exhibition, Vienna, Austria, June 13–17, 2004, Paper No. 2004-GT-54162. Manuscript received by IGTI, October 1, 2003; final revision,March 1, 2004. IGTI Review Chair: A. J. Strazisar.

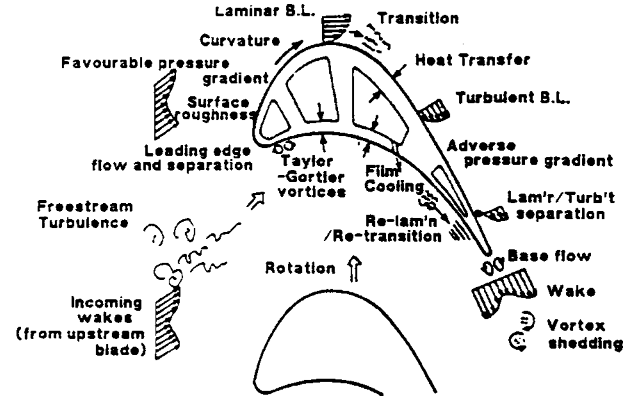

Fig. 1 2D disturbances affecting turbine blade boundary layers. (Sketch by Coupland [28].)

freestream turbulence, and that they are instantaneous manifestations of what has been termed the "Klebanoff modes" described by Kendall [13].

In a review of analytical approaches, Schmid and Henningson [14] offer a re-examination of classical linear stability theory, describing how transient algebraic growth mechanisms bypass the T–S route and develop vortices aligned in the streamwise direction.

The question remains, "Exactly how does elevated freestream turbulence affect the unsteady surface heat flux characteristics of turbine boundary layers?" It is difficult to see or measure boundary layer transition, especially in the complex environment of a gas turbine engine. Capturing turbulent spot detail in a high speed transitional boundary layer requires resolution of very small, and very fast, surface heat flux events. The ability to visualize surface heat flux under a high-speed transitioning boundary layer is of great value to those wishing to understand, or model complex transitional heat transfer. This experimental study attempts to characterize the structure of unsteady surface heat flux under varying levels of freestream turbulence using a temporal heat flux imaging technique.

3 Instrumentation

High frequency temporal heat flux images are acquired using high density thin film gauge arrays developed at the University of Oxford particularly for this research. The arrays of flexible thin film gauges are capable of high frequency (200 kHz), high spatial resolution (0.2 mm spacing) surface heat flux measurements. A drawing of the thin flexible sheet of sensors used in the flat-plate experiment is shown in Fig. 3. The sensor layout includes fifteen different arrays with 233 total thin film heat flux sensors. The films are made of platinum and have a temperature sensitive resistance. Sensors within a single array are arranged in series and supplied with a constant current I_s. The change in film resistance is monitored by measuring the differential voltage drop across each gauge. Surface temperature is given by

$$T = \frac{v_f}{\alpha_R V_0}, \tag{1}$$

where V_0 is the dc voltage across the film at T_0, and α_R is the temperature coefficient of resistance for the thin film which is determined by calibration.

Low noise differential amplifiers are used to obtain the temperature signal from each sensor in the array. Custom built electronics include a pre-emphasis filter to boost the low sensitivity of the thin film at high frequencies, followed by an adjustable anti-alias filter for proper A/D conversion. An efficient digital filtering technique is then used to convert the recorded surface temperature into heat flux. Experiments are set-up for transient, one-

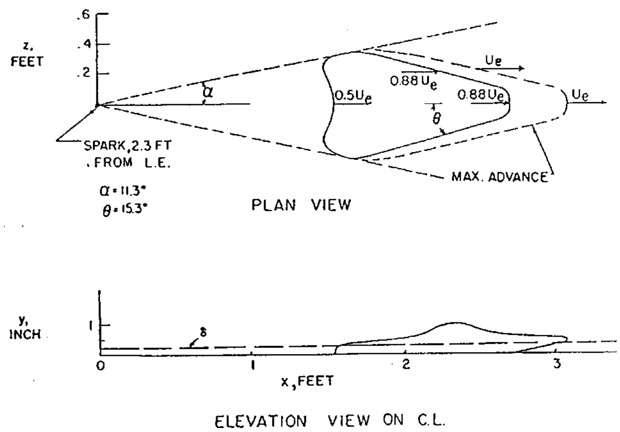

Fig. 2 How do turbulent spot characteristics in a high disturbance environment differ from the classical Emmon's type spot? (Sketch by Schubauer and Klebanoff [29].)

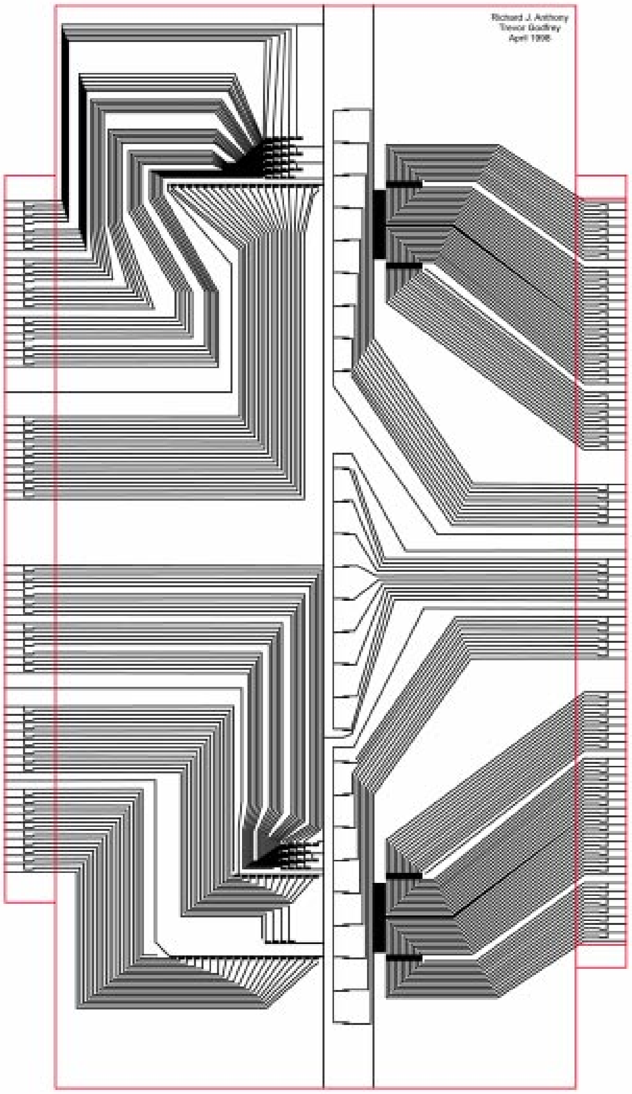

Fig. 3 Platinum gauge layout for flat plate model having 15 different thin film gauge arrays with 233 total thin film sensors. (Instrumented surface is 332 mm×150 mm.)

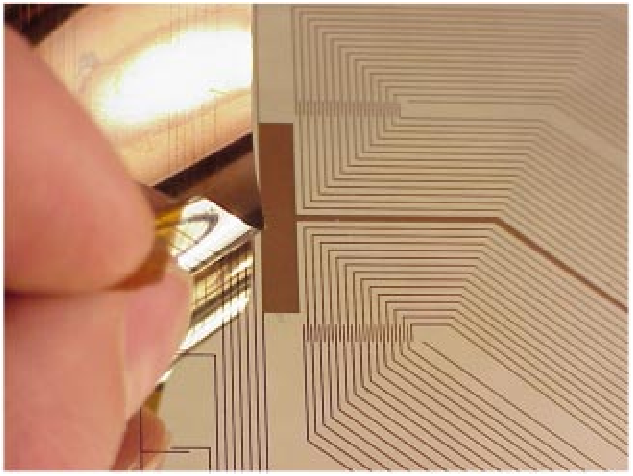

Fig. 4 The platinum arrays are sputtered onto a thin flexible sheet that is laid over the model surface

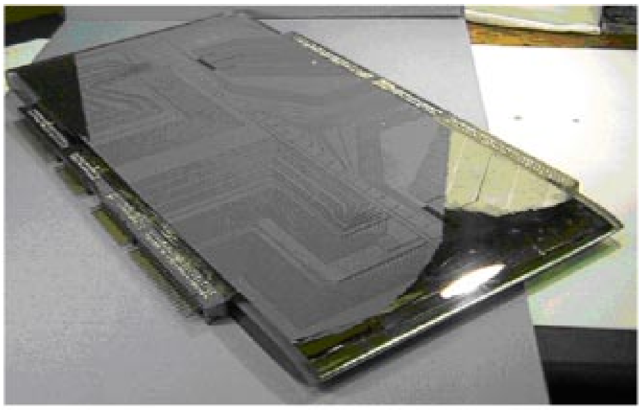

Fig. 5 Completed perspex flat plate model with platinum sensor surface and gold-plated pin-out connections

dimensional heat conduction into a semi-infinite solid. For details, the reader is referred to a full explanation of the thin film array instrumentation and signal processing given in Anthony, Oldfield, Jones, and LaGraff [15].

The recorded surface temperature fluctuation is converted to heat flux through equations governing the unsteady heat conduction into a semi-infinite substrate. The time-varying heat transfer rate q is given in frequency space by Eq. (2).

$$q = (\sqrt{\rho c k}\sqrt{\mathrm{j}\omega})T \tag{2}$$

where ρck is the product of the density, specific heat, and thermal conductivity of the substrate material. Techniques for the transformation in Eq. (2) are described by Schultz and Jones [16].

Specialized Matlab code developed by Oldfield (2000) approximates the continuous $\sqrt{\mathrm{j}\omega}$ frequency characteristic required by Eq. (2) with a digital filter having multiple, alternate, real poles, and zeros spaced evenly on a logarithmic frequency scale. In the Laplace domain, the transfer function is represented by

$$H(s) = \frac{q(s)}{T(s)} = A\frac{(s-z_1)(s-z_2)\cdots(s-z_{2n})}{(s-p_1)(s-p_2)\cdots(s-p_{2n})}. \tag{3}$$

These cascaded filters give a "staircase" frequency characteristic that is a good approximation to the $\sqrt{\mathrm{j}\omega}$ response required. A typical 12 zero, 12 pole filter designed for a 400 kHz sampling rate has a frequency response accurate to better than 1% over the range 0.02 Hz to 80 kHz. The time response to a $T \sim \sqrt{t}$ input (this should ideally give a step output) is accurate to better than 1% over the time range 10 μs to 1.0 s.

The platinum thin film arrays are magnetron-sputtered onto a thin flexible sheet of polyimide that is 50 microns thick (see Figs. 4 and 5). The flexible sheet of sensors can then be adhered to test surfaces, including turbine test blades, to obtain high frequency, high spatial resolution surface heat flux data. In the first demonstration, the films are mounted to a simple flat plate model (Fig. 5). Perspex was chosen for the plate material because its thermal product nearly matches that of the polyimide thin film substrate, thus allowing a single-layer semi-infinite heat transfer analysis to be made. A magnified section of the platinum film layout used in this experiment is shown in Fig. 6. The photo includes two high density arrays on the right aligned in the spanwise direction, perpendicular to the flow. The magnified view of one array in Fig. 6 shows how current enters the array at the left, cascades through all the gauges, and leaves to the right. The platinum leads in Fig. 6 are shown dark, and the substrate is light. Voltage taps are taken off the ends of each film and passed through differential amplifiers. Closely spaced sensors like these can be used to form temporal "images" of the surface heat flux events crossing the span of the array. While other techniques offer greater spatial resolution (liquid crystals, pressure or temperature sensitive paints), the thin films are valuable in their sensitivity, accuracy, and speed. With electronics designed for a bandwidth up to 400 kHz, they can image unsteady boundary layer heat flux structures in a Mach 2 freestream.

Figure 7 shows an example of transitional surface heat flux signals taken from an array of sensors aligned in the streamwise direction down the center of the plate. Turbulent spots appear causing an instantaneous rise in surface heat flux and then grow and convect downstream. Signals from an array of films can be combined into an image in the $x-t$ plane (Fig. 8) showing the appearance and growth of naturally-occurring turbulent spots. Figure 9 is a temporal heat flux image in the $z-t$ plane taken from a wide, low resolution (2 mm), array aligned in the spanwise direction. Images in the $z-t$ plane provide a 2D time history of the surface heat flux events crossing over the array. This example was taken without the turbulence generating bar grid installed and freestream turbulence intensity $<0.5\%$. This will be compared and contrasted with transitional heat flux images taken under turbulence intensities above 1.0% later in the paper.

The images are simply a color-scaled plot of the individual heat transfer signals from an array of evenly spaced surface sensors. Each line of horizontal pixels in the image is formed by an individual sensor's heat flux time series. The $z-t$ images are typically plotted as a nondimensional Nusselt number $\mathrm{Nu}_x = hx/k$, where the instantaneous heat transfer coefficient h is calculated from the

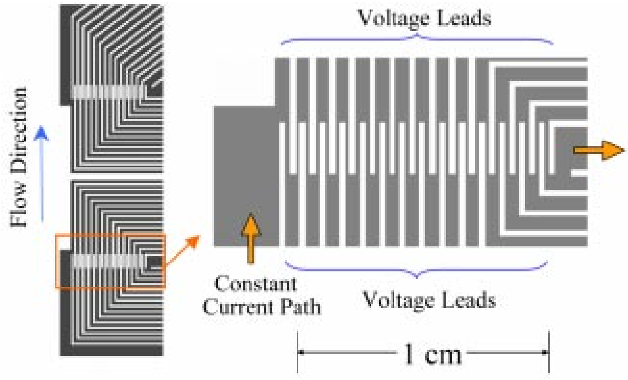

Fig. 6 Magnified image of two high density platinum thin film arrays aligned in the spanwise direction (perpendicular to the flow). Each array consists of 27 sensors. Note the platinum is shown dark and the substrate is shown light in this figure.

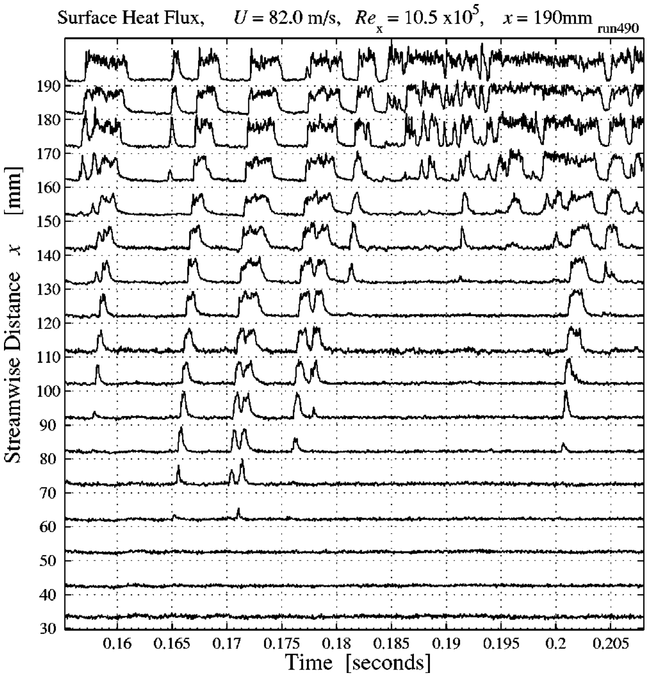

Fig. 7 Turbulent spot heat flux traces measured along streamwise arrays #5 and #6. Intermittent turbulent spots can be tracked as they convect downstream.

instantaneous heat flux signal q and recorded temperature difference $(T_\infty - T_s)$. The dark-to-light color scale of each image typically ranges from the minimum to maximum Nusselt number measured within the time window. In the $x-t$ plots, the color is typically scaled from the fully laminar level to the fully turbulent level at each downstream sensor location.

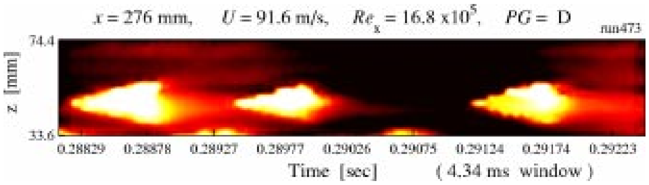

Fig. 9 Example surface heat flux image in the *z–t* plane recorded from a wide, low resolution array at the rear of the plate

Spanwise heat flux images will be presented throughout this paper, and the following should be made clear. First, note this is not a true spatial image of an entire turbulent spot; but only the surface heat flux footprint. The actual spot leading edge is above the surface and thus further downstream.

Second, note that spots in a $z-t$ image appear pointed to the left, because the leading edge crosses the array at an earlier time than the trailing edge. Third, the duration or width of each $z-t$ image is scaled by a constant fraction of the local freestream velocity, 0.65, which is the mean fractional propagation rate of turbulent spots determined experimentally. The scaling keeps the aspect ratio of the turbulent structures within each image constant, regardless of flow speed.

The labels above the figure are distance from the leading edge, mean flow velocity, and local Reynolds number for the run. The value of freestream turbulence intensity Tu is labeled with images taken with the bar grid in place. The Blasius flat plate solution may be used [3] to calculate the local boundary layer thickness for each run, $\theta = 0.664x\,\mathrm{Re}_x^{-1/2}$. Example measurement uncertainties for a typical run are shown in Table 1. Uncertainty of the freestream turbulence measurements is given in Table 2.

4 Experimental Set-Up

Experiments were run in the Oxford 150 mm × 150 mm suction tunnel. The tunnel is powered by four axial-flow fans at the rear

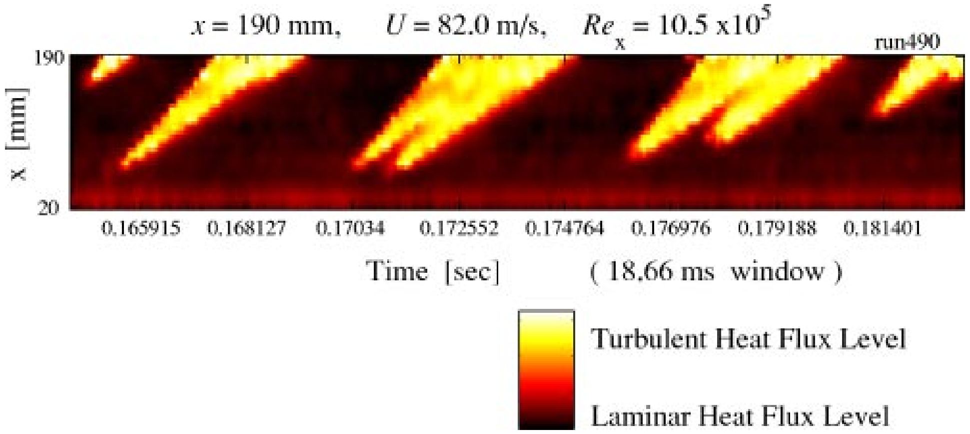

Fig. 8 Surface heat flux image in the *x–t* plane showing turbulent spots appearing and growing as they convect down the model surface

Table 1 Measurement uncertainties for a typical run (run 249)

Variable	Symbol	Nominal value	Standard uncertainty u	Expanded uncertainty 95% Confidence interval ($\pm 2u$)
Distance from leading edge	x	65 mm	0.5 mm	1 mm
Flow velocity	U	48.0 m/s	1.15 m/s	2.3 m/s
Local Reynolds number	Re_x	2.09E+05	5.03E+03	1.01E+04
Local Nusselt Number	Nu_x	185	9.5	19

Table 2 Grid turbulence parameters

Grid	Distance upstream of LE	Bar diameter	No. of bars	Predicted Tu% at hot wire	Measured Tu% at hot wire	Predicted length scale Λ_x at hot wire	Measured length scale Λ_x at hot wire
A	560 mm	4 mm	15	2.3%	(2.3±0.1)%	9.7 mm	(12±3) mm
B	370 mm	6 mm	10	3.9%	(4.2±0.3)%	9.8 mm	(11±4) mm
C	140 mm	15 mm	4	14%	(17.0±2.0)%	10.1 mm	(13±3) mm

that draw air through the forward inlet and test section. Variable freestream velocities up to Mach 0.43, or approximately 145 m/s, can be generated through the 150 mm×150 mm test section. In this study, transient, short-duration flow experiments are run using a fast-acting bypass flap. Heat transfer is driven by a typical temperature difference of 30°C (54°F) between the preheated flat plate and cooler ambient freestream. A traversing hot-wire probe was mounted above the plate to measure instantaneous velocity at various locations above the model (see Fig. 10).

Nearly isotropic turbulence was generated using upstream bar grids based on the correlations by Roach [17]. These equations correlate freestream turbulence intensity Tu and integral length scale Λ_x to bar diameter d and distance downstream from the grid x.

$$\text{Turbulence Intensity}\quad \mathrm{Tu} = 0.8\frac{x^{-5/7}}{d} \tag{4}$$

$$\text{Integral Length Scale}\quad \Lambda_x = 0.2\sqrt{xd} \tag{5}$$

Standard bar diameters of 4 mm, 6 mm, and 15 mm were used to generate three different turbulence levels (see Fig. 11). Grid solidity was held constant at 40% in each case. Grid location was also chosen carefully within the geometrical limitations of the tunnel to maintain an approximately constant turbulent length scale of ~12 mm at the leading edge for each case.

Instantaneous freestream velocity was measured using a standard constant-temperature hot-wire anemometer. A Dantec Dynamics 55P15 miniature wire boundary layer probe with a single 5 μm diameter, 1.25 mm long, platinum-plated tungsten wire was used. A Dantec 55 M series hot wire anemometer held the wire temperature constant and provided an output voltage dependent on the flow velocity.

The anemometer output passed through a 25 kHz antialias filter into two separate amplifier channels. The signal was split into a dc component and an amplified ac component and digitized on two separate channels. The first channel recorded the overall rise in tunnel velocity, while the other used the full A/D resolution to digitize the fluctuating component of the signal. This reduced digitization error and provided higher integrity velocity fluctuation data.

The hot wire was calibrated in the tunnel along with pitot pressure transducers at both the beginning and end of each test series. The tunnel was run at full speed with data recorded as each fan was gradually switched off. This allowed the hot wire anemometer voltage and dynamic pressure to be recorded over the full range of tunnel speeds. User-written Matlab software automates the calibration task and provides the instantaneous freestream velocity data.

5 Results and Discussion

This section presents measurements of naturally-occurring turbulent spot heat flux under freestream turbulence. Figure 12 is a comparison of surface heat flux footprints between conventional turbulent spots measured in a low disturbance flow (top two images) and turbulent spots measured under moderate freestream turbulence (bottom three images). Spots generated under freestream turbulence form much further upstream at lower Reynolds numbers. They originate close to the leading edge, where the boundary layer is thinner, and are therefore much smaller in size. The two images in the top of the figure were taken from a larger, lower resolution (2 mm) thin film array located towards the back of the plate. The resolution of the large arrays is too coarse to reveal internal spot structures, but reveals the overall surface heat flux footprint of conventional spots. The bottom images were taken from higher resolution (0.2 mm) arrays located close to the leading edge where turbulence-induced bypass transition occurs. These higher resolution arrays, similar to Fig. 6, are able to resolve greater spanwise heat flux detail.

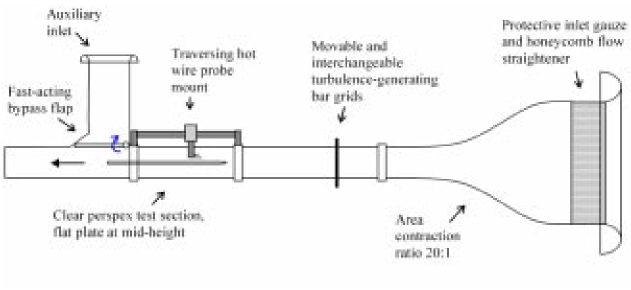

Fig. 10 Test section and inlet of the Oxford 150 mm ×150 mm suction tunnel with transient flow bypass flap

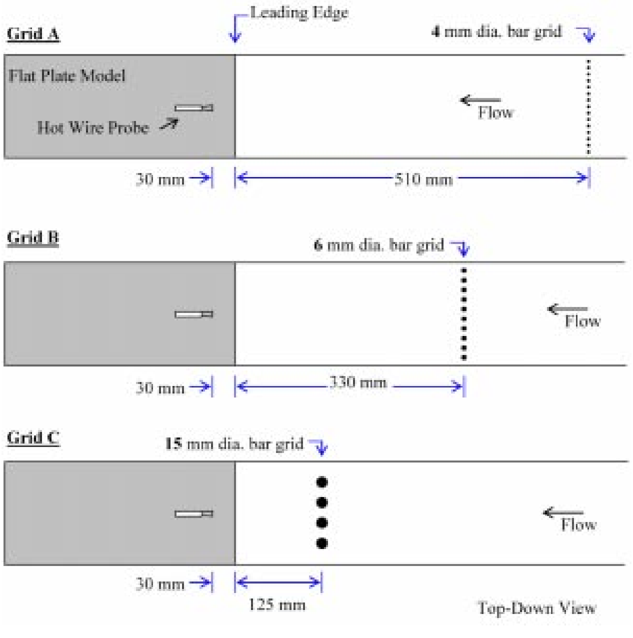

Fig. 11 Bar grid arrangement for three different turbulence intensities at constant integral length scale

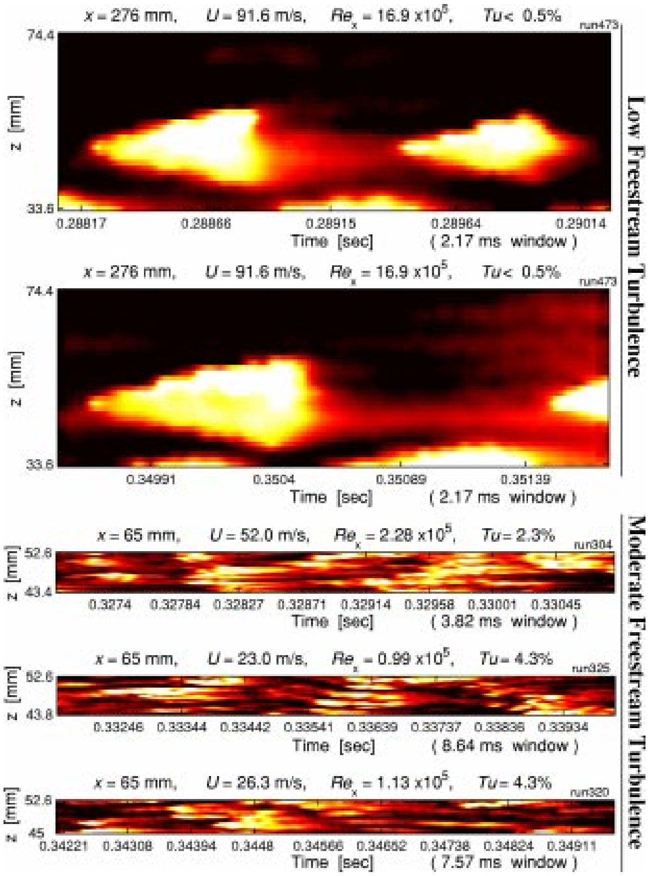

Fig. 12 Surface heat flux footprints of large, mature turbulent spots in a low disturbance environment (top two images) compared with turbulent spot heat flux under moderate freestream turbulence (bottom three images). Turbulence-induced bypass spots appear at much lower Reynolds number and are very streaky in nature.

Turbulence-induced spots appear at Reynolds numbers well below the critical value predicted by classical linear stability theory. Spots formed at such lower Reynolds number do not initially spread as fast as classical Emmons type spots formed via T–S wave breakdown. The initial surface heat flux footprints appear more like fast moving streaks than spreading arrowheads. Eventually additional heat flux streaks appear adjacent to the initial streak as they grow into irregular shaped patches of turbulent heat flux.

One observation from these images is that turbulent spots appear to be made up of individual vortices near the surface that are elongated in the streamwise direction. The streak spacing is about $2-3\delta$. This is not discernible from ensemble-averaged spot measurements in the past. Instantaneous measurements of individual, naturally-occurring turbulent spots in a high-speed airflow with *spanwise* detail are unique, and can help reveal the turbulent structures that make up the base of the spot.

Under moderate freestream turbulence conditions, spots have a more irregular, asymmetrical shape. Examples are shown in Figs. 13 and 14. Figure 13 shows the effect of increasing the local Reynolds number Re_x at fixed freestream turbulence intensity. These measurements were taken at the same streamwise location ($x=6.5$ mm) at three different freestream velocities. The freestream turbulence intensity Tu is constant (2.3%) in each case. As one would expect, increasing Reynolds number increases the turbulent intermittency of the boundary layer, significantly increasing overall heat flux through the surface. This figure shows streaky turbulent events growing and merging into a fully turbulent boundary layer under moderate freestream turbulence.

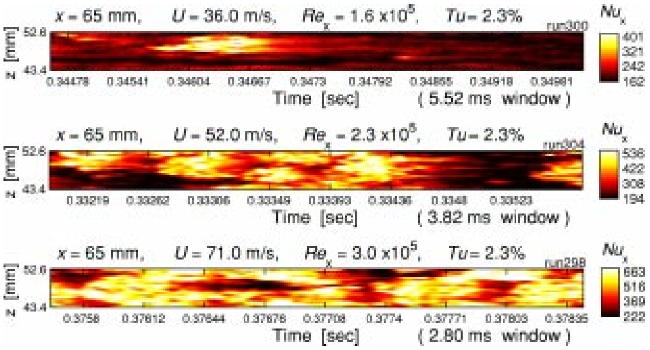

Fig. 13 Increasing local Reynolds number within the transition region under fixed freestream turbulence intensity Tu =2.3% (grid A). As Reynolds number increases, streaky turbulent patches merge and coalesce into a fully turbulent boundary layer.

Under low disturbance, straight parallel flow, the mechanisms of turbulent spot growth form a symmetrical swept back arrowhead shape pointed in the downstream direction. Though this shape rarely has time to develop under freestream turbulence, Fig.

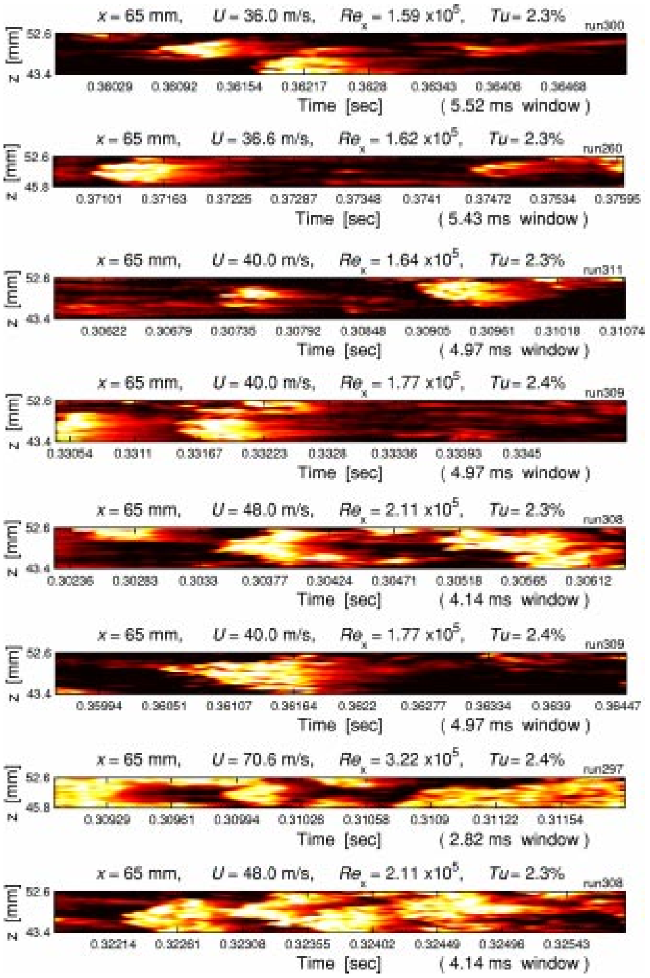

Fig. 14 Unusual examples of spots with an apparent arrowhead shape under 2% turbulence intensity. Most spots seen under moderate freestream turbulence have a rather irregular asymmetrical shape.

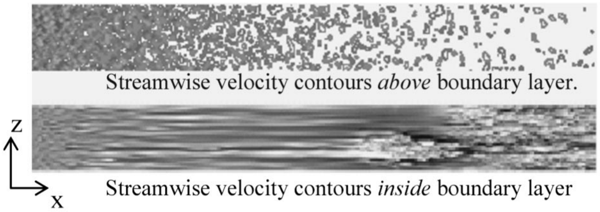

Fig. 15 The numerical simulation by Jacobs and Durbin [12] shows the streaky nature of bypass transition under freestream turbulence. Note when comparing; this is a spatial image in the x–z plane, with flow from left to right, as opposed to a temporal heat flux image in the z–t plane where spots are pointed right to left.

14 presents a collection of young arrowhead spot shapes seen at the lower turbulence level of 2.3%. Again, the spots appear to be made up of individual heat flux streaks aligned in the streamwise direction. The gradually decaying heat flux at the tail of the spot is characteristic of the calmed region.

Note the images presented in this paper are only very short time segments of a few selected runs. Space is limited to show full length images for each condition. Analyzing the full time history for a run allows one to better appreciate the diversity of shapes and sizes of individual heat flux signatures that appear under freestream turbulence, and how they merge to form the fully turbulent boundary layer. Examples in this paper point out some of the key characteristics that are seen throughout the data.

5.1 Comparison to Direct Numerical Simulation. Compelling similarity is found between these measurements and the direct numerical simulation of bypass transition by Jacobs and Durbin [12]. For comparison, a turbulent spot from their simulation is shown in Fig. 15. The image shows streaky structures appearing in the laminar flow just after the leading edge and a turbulent spot moving from left to right. The two horizontal sections show contours of streamwise velocity just above ($y \approx \delta$) and inside ($y \approx \delta/3$) the boundary layer, where δ is the 99% thickness at $\mathrm{Re}_\theta = 250$ ($\mathrm{Re}_\theta = 107$ at the inflow). Note this is a spatial image of velocity fluctuations in the $x-z$ plane as opposed to surface heat flux in the $z-t$ plane. The simulation captures the streaky nature of bypass transition and agrees well with the heat flux data collected from this study.

A significant advantage of DNS is the ability to trace backwards through a solution and investigate how individual spots originated from freestream disturbances. Jacobs and Durbin [12] suggest these spots are induced by low frequency freestream perturbations that initiate breakdown from the top of the boundary layer. In a previous numerical simulation of wake-induced transition, Wu et al. [18] propose that turbulence-induced spots would actually develop a backwards arrowhead shape pointing upstream. No evidence of backwards arrowheads was seen in the surface heat flux data from these experiments. Although the shape of the spots above the surface was not measured in the present study, the turbulent surface heat flux almost always appears pointed in the downstream direction, if any. In reality, symmetrical arrowhead spots are rarely seen under moderate freestream turbulence. In these conditions, many turbulent streaks quickly appear and coalesce before discrete patches are allowed to develop into the classical arrowhead shape.

5.2 Spanwise Turbulence Growth. Figure 16 shows regular symmetrical arrowhead-shaped heat flux events do not always appear under freestream turbulence. Nearly all the patches of turbulent heat flux, however, do develop a characteristically swept-back leading edge and trailing calm region as they convect downstream. The leading edge angle scales approximately with freestream velocity and is fairly consistent throughout the data. The swept leading edge angle is pointed out in the figure.

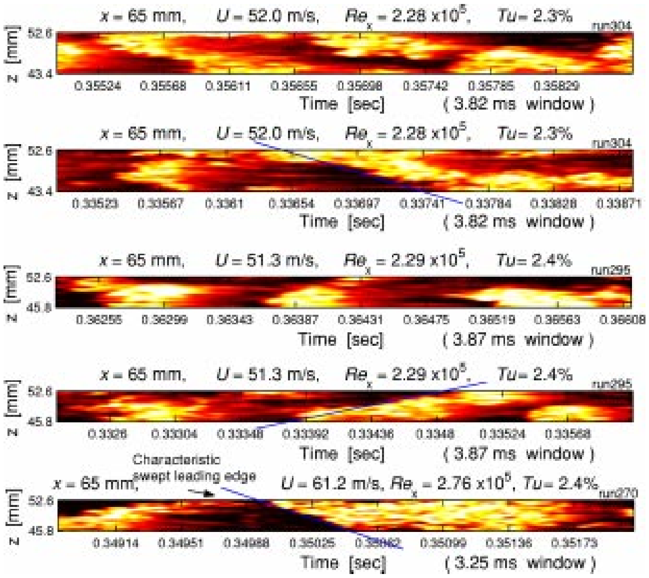

Fig. 16 Irregular "nonarrowhead" spot shapes usually appear in the bypass transitional boundary layer. The swept-back spot leading edge angle, however, is fairly consistent and scales approximately with freestream velocity.

Surface heat transfer footprints show the base of the turbulent spot is made up of a growing number of elongated streamwise structures. This information was often smeared out in past studies by ensemble averaging, or simply not seen due to a lack of spanwise resolution. After reviewing multiple images from these tests, it is clear the original turbulent streak does not spread, but rather, new adjacent streamwise heat flux streaks appear. This growing patch of turbulent heat flux streaks then typically develops a swept-back leading edge.

The mechanism responsible for the spanwise growth of turbulence may be explained by the observations of Acarlar and Smith [19], who witnessed asymmetrical hairpin vortices inducing adjacent secondary streamwise vortices near the surface of a growing spot. Heat flux results from the present study found no evidence of $T-S$ type waves following the spot edges as detected by Wygnanski, Haritonidis, and Kaplan [20]. Bypass transition in these experiments occurs at relatively low Reynolds number, before $T-S$ type instabilities would be expected to take effect.

5.3 Streamwise Turbulence Growth and Development. An example of data from an array of thin films aligned in the downstream direction is shown in Fig. 17. The data are taken at a much lower speed than the previous $z-t$ images in order to view a longer transition region across the model. Turbulent spots originate near the front of the plate and then travel downstream. Increasing the freestream turbulence intensity moves transition on-

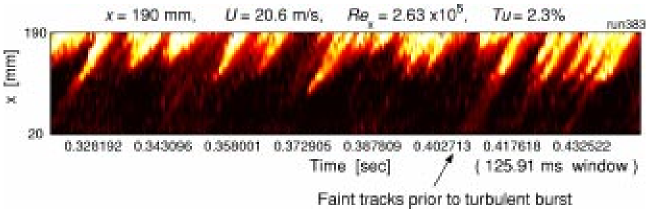

Fig. 17 Turbulence-induced spots in the x–t plane. Faint tracks of enhanced heat flux are seen upstream of the jump to turbulent heat flux.

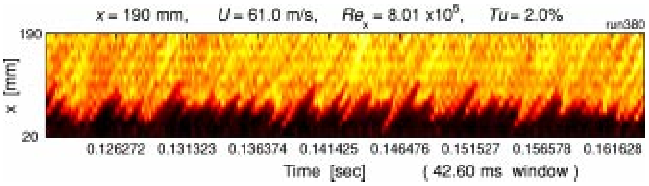

Fig. 18 *x–t* image of turbulence-induced bypass transition at higher Reynolds number. Initial spot structures can be tracked through the turbulent boundary layer downstream.

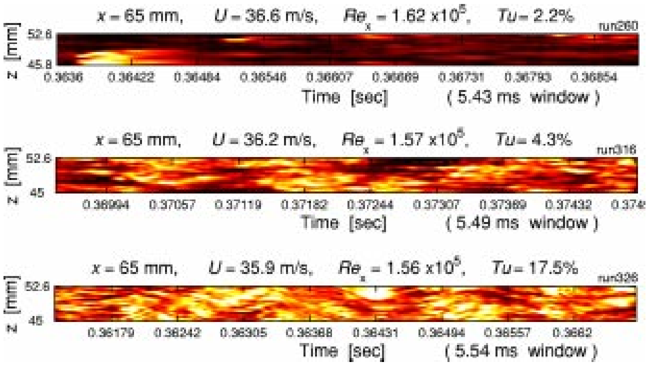

Fig. 19 Effect of increasing freestream turbulence intensity at a set local Reynolds number of 1.6×10^5 and fixed integral length scale of approximately 12 mm

set closer to the leading edge.

One discovery in these $x-t$ plots is the faint tracks of enhanced heat flux occasionally seen upstream, preceding the initial jump in turbulent heat flux. This enhanced unsteady surface heat flux prior to the turbulent jump is not seen in the tests without freestream turbulence. The low-level events preceding the jump in heat flux travel at $0.63(\pm0.07)^*U$. The faint tracks in the $x-t$ image, and the low level heat flux streaks seen in the laminar region of the $z-t$ images, may help explain the Klebanoff modes defined by Kendall, [13] which are noted to appear at Tu > 0.7%. Jacobs and Durbin [12] make a similar observation in their DNS, suggesting the Klebanoff modes in the past were just an ensemble-averaged view of the instantaneous streaks observed under turbulence-induced transition. These measurements provide detailed experimental evidence of their effect on surface heat flux.

A second characteristic of turbulence-induced spots is their reduced initial spread rate. The turbulent heat flux tracks are very slender at first, showing a small difference between the velocity of the turbulent heat flux leading edge and the trailing edge. Classical studies of fully-developed spots show the spot trailing edge clearly moves slower than the leading edge. Sankaran, Sokolov, and Antonia [21] determined that the streamwise growth of the spot was directly related to the number of eddies present. The addition of more eddies at the rear causes the trailing edge of a mature spot to travel at a lower speed. Turbulence-induced spots do not initially grow as fast in the streamwise direction because they appear at low Reynolds number where the surrounding boundary layer is relatively stable, and new secondary vortices do not form as readily.

A third observation is that turbulent spot structure can be tracked up into the fully turbulent region of the boundary layer in the $x-t$ images. This can be seen in Fig. 18. The present data show intense heat flux events during bypass transition can be tracked for a considerable distance through the fully turbulent boundary layer, traveling at a velocity between $0.55U$ and $0.85U$.

5.4 Effect of Increasing Turbulence Intensity. The effect on transitional heat flux of increasing freestream turbulence intensity, at a fixed local Reynolds number, is shown in Fig. 19. The $z-t$ images are from a high density thin film array located at $x = 65$ mm from the leading edge. The images clearly show that increasing freestream turbulence intensity increases the number and complexity of turbulent spots seen at a given Reynolds number. The streaky nature of transitional heat flux events under freestream turbulence is evident. Individual spots are difficult to discern at Tu > 4% since so many turbulent heat flux streaks appear and quickly coalesce.

Spot generation and development appears significantly different under the highest freestream turbulence case (Tu > 17%, Grid C). Figure 20 shows a number of $z-t$ images taken from a dense array 65 mm downstream from the leading edge under Tu = 17.5%. The surface heat flux in this case has a more wavy structure not seen at lower Tu. Images in the $x-t$ plane show transition occurs very soon, before the first sensor at $x = 20$ mm from the leading edge. The structures within the boundary layer show unsteady spanwise movement as they are continually forced by the large freestream eddies above. They travel at a fraction of the streamwise velocity, between $0.55U$ and $0.88U$, similar to regular turbulent spots. These undulating turbulent structures moving *within* the boundary layer, continually forced by the large freestream eddies above, are what directly determine the elevated surface heat transfer under high freestream turbulence. It is not simply due to the penetration of the freestream eddies themselves. Freestream eddies by definition travel at the freestream velocity, but here, the unsteady coherent structures on the surface are tracked moving downstream at a fraction of the freestream velocity, and therefore must be separate, slower moving structures within the boundary layer.

It is possible the large freestream eddies at such high turbulence intensities force localized 3D crossflow effects within the boundary layer. The strong effect of crossflow on unsteady surface heat flux is further investigated in Anthony, Jones, and LaGraff [22]. There it was found a slight spanwise acceleration of the flow across the surface produces an unsteady pattern of traveling heat flux waves at the surface. It would be valuable to investigate the

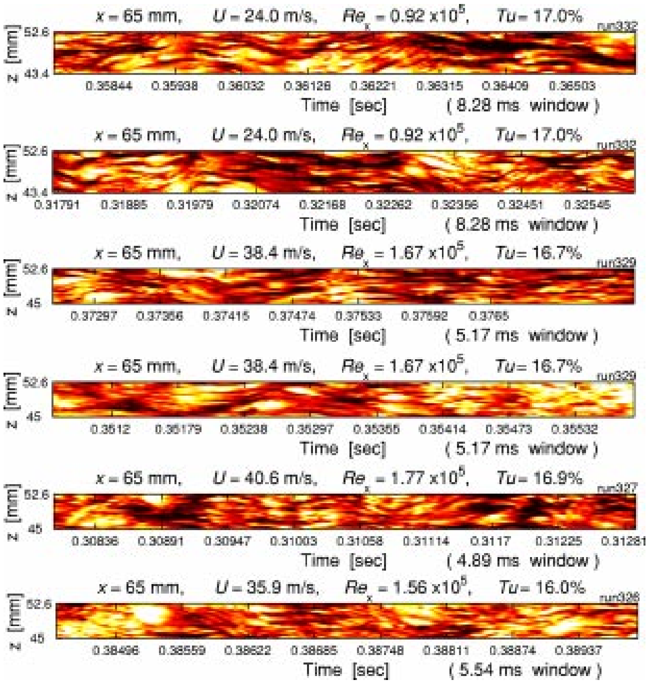

Fig. 20 Wavy transitional heat flux structures under strong freestream turbulence intensity (Tu = 17.5%, grid C). The color scale has been adjusted to bring out the detail of the turbulent heat flux structure.

effect of large freestream eddies further, perhaps with simultaneous time-resolved surface and PIV measurements. Sabatino and Smith [23] have used this dual measurement technique for conventional turbulent spots in a low disturbance flow.

Results are shown with varying levels of freestream turbulence intensity, but several researchers have also noted an effect of turbulence length scale [24–26]. Another complete series of experiments using three additional grid configurations was performed to isolate the effect of varying turbulent length scale at fixed turbulence intensity. The range of length scales tested proved too small to see any considerable difference, and the data has not been presented. The small range of length scales at fixed Tu was limited by the geometrical limitations of the tunnel.

It is difficult for correlations based solely on Tu to take into account all the disturbance characteristics present between simple wind tunnel tests and a real turbine environment. In fact, Morkovin [27] states, "there is no single Tu number that can characterize the turbulent field as a guide to the onset of transition. There are too many parameters and subtle nonlinearities (many not even recorded) to make possible any kind of credible statistical base for such prediction codes to be trustworthy." The authors agree that turbulence intensity alone is not enough to characterize the freestream, and that turbulent length scale must also be taken into account when making predictions. More work is needed to understand the receptivity of freestream disturbances into the boundary layer. A question that remains is how to properly quantify the freestream disturbance environment in a real turbine. Are freestream turbulence intensity, length scale, and/or spectra all that are needed? Measuring the unsteady turbine inlet boundary conditions in a real engine is a challenge that could require greater cooperation between industry and academia.

6 Conclusion

This study investigates the characteristics of unsteady surface heat flux under varying levels of freestream turbulence using a high frequency, temporal heat flux imaging technique. Detailed surface measurements show turbulent spots and the resulting unsteady surface heat flux appears quite differently than turbulent spot models currently predict.

Results show, under moderate freestream turbulence (Tu $>0.7\%$), enhanced heat flux streaks first appear elongated in the streamwise direction and originating near the leading edge. These are followed by a distributed breakdown into streaky, subcritical turbulent spots at low Reynolds number. The unique measurements show the diverse size and shape of turbulence-induced spots in a high-speed airflow.

Under strong freestream fluctuations (Tu$>0.7\%$), temporal heat flux images show structures traveling within the boundary layer at a fraction of the freestream velocity with unsteady spanwise motion. Images suggest strong spanwise fluctuations in the freestream may force local, unsteady crossflow effects within the boundary layer. This inference, though, requires a more focused study. The behavior differs markedly from conventional models based on the classical Emmons-type spot. The temporal imaging technique presented allows study of unsteady surface heat transfer in detail, and helps elucidate the complex nature of transition in the high-disturbance environment of turbomachinery.

Acknowledgments

The analog and digital signal processing techniques for the arrays were developed with Dr. M.L.G. Oldfield, University of Oxford. Support for this work was provided by the United States Air Force Office of Scientific Research Grant No. F49620-97-1-0524, technical monitor Dr. Thomas J. Beutner. The views and conclusions contained herein are those of the authors and should not be interpreted as necessarily representing the official policies or endorsements, either expressed or implied, of the Air Force Office of Scientific Research or the U.S. Government.

Nomenclature

c = specific heat (kJ/kg K)
d = bar diameter (m)
h = convective heat transfer coefficient ($\mathrm{W/m^2\,K}$)
I_s = constant current supplied by source (A)
k = thermal conductivity (W/m K)
q = heat flux ($\mathrm{W/m^2}$)
Nu_x = local Nusselt Number (hx/k)
R = resistance (Ω)
R_0 = resistance at T_0 (Ω)
Re_x = local Reynolds number (Ux/υ)
Re_θ = Reynolds number based on momentum thickness
s = Laplace transform variable
T = temperature (K)
Tu = turbulence intensity level $\mathrm{Tu}=\sqrt{\overline{u'^2}}/U$ (×100 for %)
T_0 = reference temperature (K)
t = time (s)
U = mean freestream velocity (m/s)
u = instantaneous freestream velocity (m/s)
u' = fluctuating component of velocity (m/s) ($u'=u-U$)
V = voltage (V)
V_0 = voltage across film at T_0 (V)
ν_f = voltage across thin film element (V)
x = streamwise coordinate from leading edge (m)
z = spanwise coordinate from sidewall (m)
α_R = temperature coefficient of resistance (1/K)
δ = boundary layer thickness (m)
γ = intermittency
Λ_x = turbulence integral length scale (m)
ρ = density ($\mathrm{kg/m^3}$)
θ = boundary layer momentum thickness (m)
ν = dynamic viscosity ($\mathrm{m^2/s}$)
ω = angular frequency (rad/s)

References

[1] Dunn, M. G., 2001, "Convective Heat Transfer and Aerodynamics in Axial Flow Turbines," ASME Paper No. 2001-GT-0506.
[2] Mayle, R. E., 1991, "The Role of Laminar-Turbulent Transition in Gas Turbine Engines," ASME J. Turbomach., **113**, pp. 509–537.
[3] Schlichting, H., 2000, *Boundary Layers*, 9th ed., McGraw–Hill, New York.
[4] White, F. M., 1974, *Viscous Fluid Flow*, 1st ed., McGraw-Hill, New York.
[5] Morkovin, M. V., 1993, "Bypass—Transition Research: Issues and Philosophy," *Instabilities and Turbulence in Engineering Flows*, D. E. Ashpis, T. B. Gatski, R. Hirsch, eds., Kluwer Academic, Dordrecht, 1993, pp. 3–30.
[6] Abu Ghannam, B. J., and Shaw, R., 1980, "Natural Transition of Boundary Layers—The Effects of Turbulence, Pressure Gradient, and Flow History," J. Mech. Eng. Sci., **22**, pp. 213–228.
[7] Narasimha, R., 1985, "The Laminar-Turbulent Transition Zone in the Boundary Layer," Prog. Aerosp. Sci., **22**, pp. 29–80.
[8] Fraser, C. J., Higazy, M. G., and Milne, J. S., 1994, "End-Stage Boundary Layer Transition Models for Engineering Calculations," Proc. Inst. Mech. Eng., IMechE, 208, pp. 47–60.
[9] Emmons, H. W., 1951, "The Laminar-Turbulent Transition in a Boundary Layer—Part 1," J. Aeronaut. Sci., **18**, pp. 490–498.
[10] Kittichaikarn, C., Ireland, P. T., Zhong, S., and Hodson, H. P., 1999, "An Investigation on the Onset of Wake-Induced Transition and Turbulent Spot Production Rate Using Thermochromic Liquid Crystals," ASME Paper No. 99-GT-126.
[11] Matsubara, M., Alfredsson, P. H., and Westin, K. J. A., 1998, "Boundary Layer Transition at High Levels of Free Stream Turbulence," ASME Paper No. 98-GT-248.
[12] Jacobs, R. G., and Durbin, P. A., 2001, "Simulations of Bypass Transition," J. Fluid Mech., **428**, pp. 185–212.
[13] Kendall, J. M., 1985, "Experimental Study of Disturbances Produced in a Pre-Transitional Laminar Boundary Layer by Weak Freestream Turbulence," AIAA Paper No. 85-1695.
[14] Schmid, P. J., and Henningson, D. S., 2001, "Stability and Transition in Shear Flows," *Applied Mathematical Sciences*, Springer-Verlag, Berlin, Vol. 142.
[15] Anthony, R. J., Jones, T. V., and LaGraff, J. E, 2004, "Unsteady Surface Heat Flux Under a Three-Dimensional Crossflow Boundary Layer," AIAA Paper No. 2004-1344.

[16] Schultz, D. L., and Jones, T. V., 1973, “Heat Transfer Measurements in Short-Duration Hypersonic Facilities,” AGARD AG-165.

[17] Roach, P. E., 1987, “The Generation of Nearly Isotropic Turbulence by Means of Grids,” Int. J. Heat Fluid Flow, **8**,(2) 82

[18] Wu, X., Jacobs, R. G., Hunt, J. C. R., and Durbin, P. A., 1999, “Simulation of Boundary Layer Transition Induced by Periodically Passing Wakes,” J. Fluid Mech., **398**, pp. 109–153.

[19] Acarlar, M. S. and Smith, C. R., 1987, “A Study of Hairpin Vortices in a Laminar Boundary Layer. Part 2. Hairpin Vortices Generated by Fluid Injection,” J. Fluid Mech., **175**, pp. 43–83.

[20] Wygnanski, I., Haritonidis, J. E., and Kaplan, R. E., 1979, “On a Tollmien-Schlichting Wave Packet Produced by a Turbulent Spot,” J. Fluid Mech., **92**, p. 505.

[21] Sankaran, R., Sokolov, M., and Antonia, R. A., 1988, “Substructures in a Turbulent Spot,” J. Fluid Mech., **197**, pp. 389–414.

[22] Anthony, R. J., Oldfield, M. L. G., Jones, T. V., and LaGraff, J. E, 1999, “Development of High Density Arrays of Thin Film Heat Transfer Gauges,” *Proceedings of the 5th ASME/JSME Thermal Engineering Joint Conference*, San Diego, CA, Paper No. AJTE99-6159.

[23] Sabatino, D. and Smith, C. R., 2002, “Simultaneous Velocity-Surface Heat Transfer Behavior of Turbulent Spots,” Exp. Fluids, **33**, pp. 13–21.

[24] Moss, R. W., 1992, “The Effects of Turbulence Length Scale on Heat Transfer,” Ph.D. Thesis, Department of Engineering Science, University of Oxford, Report No. OUEL 1924/92.

[25] Dullenkopf, K., and Mayle, R. E., 1995, “An Account of Free-Stream-Turbulence Length Scale on Laminar Heat Transfer,” ASME J. Turbomach., **117**, pp. 401–406.

[26] Schook, R., de Lange, H. C., and van Steenhoven, A. A., 1998, “Effects of Compressibility and Turbulence Level on Bypass Transition,” ASME Paper No. 98-GT-286.

[27] Morkovin, M. V., 1969, “On the Many Faces of Transition,” *Viscous Drag Reduction*, C. Wells, ed., Plenum, New York, pp. 1–31.

[28] Coupland, J., 1995, “Transition Modelling for Turbomachinery Flows,” *European Research Community On Flow Turbulence And Combustion (ERCOFTAC) Bulletin*, Iss. 24, March 1995, pp. 5–8.

[29] Schubauer, G. B., and Klebanoff, P. S., 1955, “Contributions on the Mechanics of Boundary Layer Transition,” NASA TN-3489.

Measured Adiabatic Effectiveness and Heat Transfer for Blowing From the Tip of a Turbine Blade

J. R. Christophel

E. Couch

K. A. Thole

Mechanical Engineering Department,
Virginia Polytechnic Institute and State University,
Blacksburg, VA 24061

F. J. Cunha

Turbine Durability,
Pratt & Whitney Aircraft Company,
United Technologies Corporation,
East Hartford, CT 06108

The clearance gap between the tip of a turbine blade and the shroud has an inherent leakage flow from the pressure side to the suction side of the blade. This leakage flow of combustion gas and air mixtures leads to severe heat transfer rates on the blade tip of the high-pressure turbine. As the thermal load to the blade increases, blade alloy oxidation and erosion rates increase thereby adversely affecting component life. The subject of this paper is the cooling effectiveness levels and heat transfer coefficients that result from blowing through two holes placed in the forward region of a blade tip. These holes are referred to as dirt purge holes and are generally required for manufacturing purposes and expelling dirt from the coolant flow when operating in sandy environments. Experiments were performed in a linear blade cascade for two tip-gap heights over a range of blowing ratios. Results indicated that the cooling effectiveness was highly dependent on the tip-gap clearance with better cooling achieved at smaller clearances. Also, heat transfer was found to increase with blowing. In considering an overall benefit of cooling from the dirt purge blowing, a large benefit was realized for a smaller tip gap as compared with a larger tip gap. [DOI: 10.1115/1.1811095]

Introduction

The performance of a turbine engine is a strong function of the maximum gas temperature at the rotor inlet. Because turbine airfoils are exposed to hot gas exiting the combustion chamber(s), the materials and cooling methods are of critical importance. Turbine blade designers concentrate heavily on finding better cooling schemes to increase the overall operation life of all turbine airfoils, namely, the high-pressure turbine blades. The clearance between the blade tip and the associated shroud, also known as the blade outer air seal, provides a flow path across the tip that leads to aerodynamic losses and high heat transfer rates along the blade tip. The flow within this clearance gap is driven by a pressure differential between the pressure and suction sides of the blade, but is also affected by the viscous forces as the fluid passes through the gap.

From an operational point of view, engine removals from service are primarily dictated by the spent exhaust gas temperature (EGT) margin caused by deterioration of the high-pressure turbine components. Increased clearance gaps accelerate effects of low-cycle thermal-mechanical fatigue, oxidation, and erosion as a result of increased temperatures in the turbine and decreased EGT margin. In general, tip clearances for large commercial engines are of the order of 0.25 mm, which can reduce the specific fuel consumption by 1% and EGT by 10°C [1]. Improving the blade tip durability can, therefore, produce fuel and maintenance savings over hundreds of millions of dollars per year [1].

The work presented in this paper is on a realistic design for a turbine blade tip consisting of a flat tip, with the exception of a small cavity in which two dirt holes are placed. The location of these holes is a direct consequence of the internal cooling passages within the blade. The purge hole cavity extends only over a small area in the front portion of the blade tip. The function of the dirt purge holes includes the following: (i) purge holes allow centrifugal forces to expel any dirt ingested by the compressor into the turbine rather than clogging the smaller diameter film cooling holes and (ii) purge holes provide a way to support the ceramic core during the lost-wax investment casting of the blade manufacturing process. The dirt purge cavity is present to insure that the purge holes remain open during eventual blade rubbing.

This paper details the film cooling and heat transfer associated with blowing from the dirt purge holes along the tip of a turbine blade. Measurements of adiabatic effectiveness and heat transfer coefficients are studied while varying the tip clearance and mass flux (blowing) ratios.

Relevant Past Studies

The work presented in this paper is concerned with the effects of injecting coolant from the tip of a turbine blade, where the experiments were completed for a stationary, linear cascade. As such, it is important to consider the relevance of past studies to evaluate the effects of the relative motion between the blade tip and outer shroud. It is also relevant to consider tests where tip blowing has been investigated.

Regarding the effects of blade rotation, the first work to address the flow field effects was that of Morphis and Bindon [2] who found that their static-pressure measurements across the blade tip in an annular turbine cascade were not affected by the relative motion at the tip. They concluded that the basic nature of the flow structures remained unchanged with and without relative motion. In contrast, the studies by Tallman and Lakshminarayana [3] and Yaras and Sjölander [4] showed that the leakage flow through the gap was reduced along with the leakage vortex in the case of a moving wall relative to a fixed wall. They attributed this difference to the passage vortex being convected toward the suction surface by the moving wall and postulated that the passage vortex position can alter the driving pressure through the tip gap.

Although there are apparent effects of a moving wall on some of the reported flow field studies, tip heat transfer studies generally indicate relatively minor to nonexistent effects of a moving wall. The reason for this relatively minor effect was first hypothesized by Mayle and Metzger [5], who evaluated the effects of relative motion on the heat transfer in a simple pressure-driven duct flow. They derived and also showed experimentally that for a flow-path length with less than 20 times the clearance gap, the flow can be considered as a developing duct flow. As such, the

---

Contributed by the International Gas Turbine Institute (IGTI) of THE AMERICAN SOCIETY OF MECHANICAL ENGINEERS for publication in the ASME JOURNAL OF TURBOMACHINERY. Paper presented at the International Gas Turbine and Aeroengine Congress and Exhibition, Vienna, Austria, June 13–17, 2004, Paper No. 2004-GT-53250. Manuscript received by IGTI, October 1, 2003; final revision, March 1, 2004. IGTI Review Chair: A. J. Strazisar.

boundary layers on each surface do not merge and, therefore, the effect of the relative wall (shroud) movement is inconsequential. This range is relevant to the assessment given that the length of the flow path along the blade tip relative to the clearance gap ranges between 2.5 near the trailing edge for the smallest gap to 25 near the leading edge (thickest part of the airfoil) for the largest gap. Lending further credibility to the hypothesis of Mayle and Metzger are the works of Chyu et al. [6] with a shroud surface moving over a simple rectangular cavity and Srinivasan and Goldstein [7] with a moving wall over a turbine blade. In particular, the work of Srinivasan and Goldstein showed only small effects of the wall motion on their measured Sherwood numbers (heat-mass transfer analogy) in the leading-edge region where the path length-to-clearance gap was larger (30) than the criterion stated by Mayle and Metzger (20) for the smallest clearance gap that they studied. For the largest gap in their study, they saw no noticeable effect of the wall motion.

The only reported tip-blowing studies were those completed by Kim and Metzger [8] and Kim et al. [9], who used a two-dimensional channel with a number of different injection geometries, and by Kwak and Han [10,11], Acharya et al. [12], and Hohlfeld et al. [13], who all used blade geometries. Four tip-blowing geometries were investigated by Kim et al. [9], which included the following: discrete slots located along the blade tip, round holes located along the blade tip, angled slots positioned along the pressure side, and round holes located within a cavity of a squealer tip. For a given coolant flow, the best cooling performance was obtained using the discrete slot configuration whereby an optimum blowing ratio was discerned. In general, Kim et al. reported higher effectiveness accompanied by higher heat transfer coefficients with higher injection rates. Kwak and Han [10,11] reported measurements for varying tip gaps with cooling holes placed along the pressure surface at a 30 deg breakout angle, relative to the pressure surface, and on the tip surface for an unshrouded [10] and shrouded [11] tip. For the unshrouded (flat) tip, Kwak and Han found that increases in the heat transfer coefficients and adiabatic effectiveness occurred with increased coolant injection and increased gap heights. This is in contrast to the work presented by Kim et al. [9], who identified an optimum blowing ratio. For the shrouded tip, Kwak and Han indicated a benefit of having a shroud in that there was a reduction of the heat transfer coefficients and an increase in adiabatic effectiveness levels when compared to the flat tip.

Heat transfer measurements on flat tips with no cooling have been presented by many authors, including Bunker et al. [14], Kwak and Han [10], and Jin and Goldstein [15]. These studies have shown there to be a region of low heat transfer located near the thickest portion of the blade. Morphis and Bindon [2] and Bindon [16] have also shown there to be a separated region followed by a reattachment with high heat transfer coefficients along the pressure side of the blade tip in the entry region [14].

Table 1 Geometry for the blade tip model

Parameter	Scaled model
Scaling factor	12×
Axial chord, B_x (% Span)	63
True chord, C (% Span)	96.3
Pitch, P (% Span)	78
Re	2.1×10^5
Inlet angle, θ	16.5 deg
Coolant to mainstream ΔT	25 deg
Small tip gap, h (% span)	0.545
Large tip gap, H (% span)	1.635

There have also been only a relatively few computational predictions for a tip gap with blowing, including those by Acharya et al. [12] and Hohlfeld et al. [13]. Acharya et al. found that film-coolant injection lowered the local pressure ratio and altered the nature of the leakage vortex. High film-cooling effectiveness and low heat transfer coefficients were predicted along the coolant trajectory. Both studies indicated that for the smallest tip gap, the coolant impinged directly on the shroud; but as the gap size increased, predictions indicated that the coolant jets were unable to impinge upon the shroud.

In summary, only one experimental study has addressed blowing in the tip gap of a turbine blade. The objectives of the work presented in this paper are to present the benefits of film-cooling of a blade tip using coolant exhausted from dirt purge holes. In particular, both the effectiveness levels and heat transfer coefficients were measured and combined using a net heat flux reduction to evaluate the benefits.

Experimental Facility and Methodology

The experiments were conducted in a large-scale, low-speed, closed-loop wind tunnel that provided matched-engine Reynolds number conditions. The flow conditions and relevant geometry are summarized in Table 1 with a diagram of the wind tunnel and test section shown in Figs. 1 and 2. Results reported in this paper include adiabatic wall temperature measurements and heat transfer coefficients along the tip.

The wind tunnel, shown in Fig. 1, includes a 50 Hp fan that drives the flow through a primary heat exchanger to obtain a uniform temperature profile. The flow is divided into three passages. The main passage, located in the center, has a heater used to achieve a hot mainstream gas, while the flow in the two outer passages provided a single row of normal jets used to generate an inlet turbulence level to the cascade of 10% and an integral length

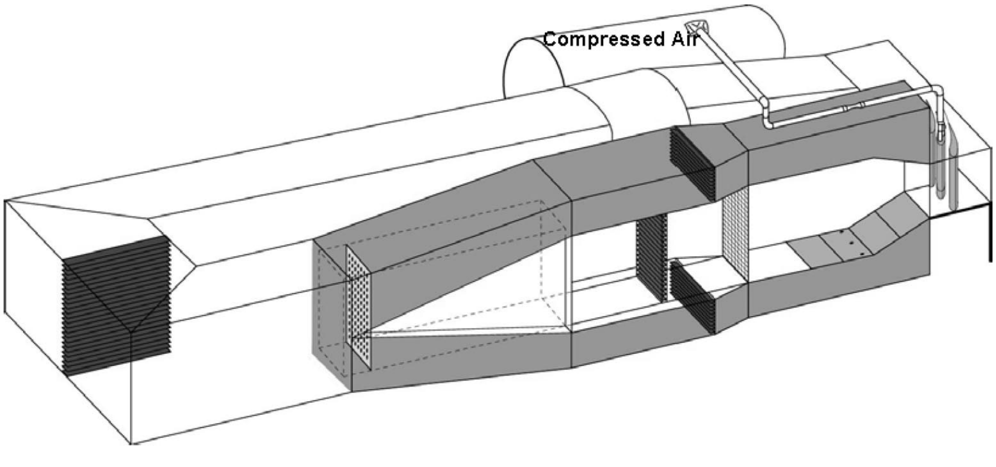

Fig. 1 Schematic of the wind tunnel facility used for the testing of the blade tips

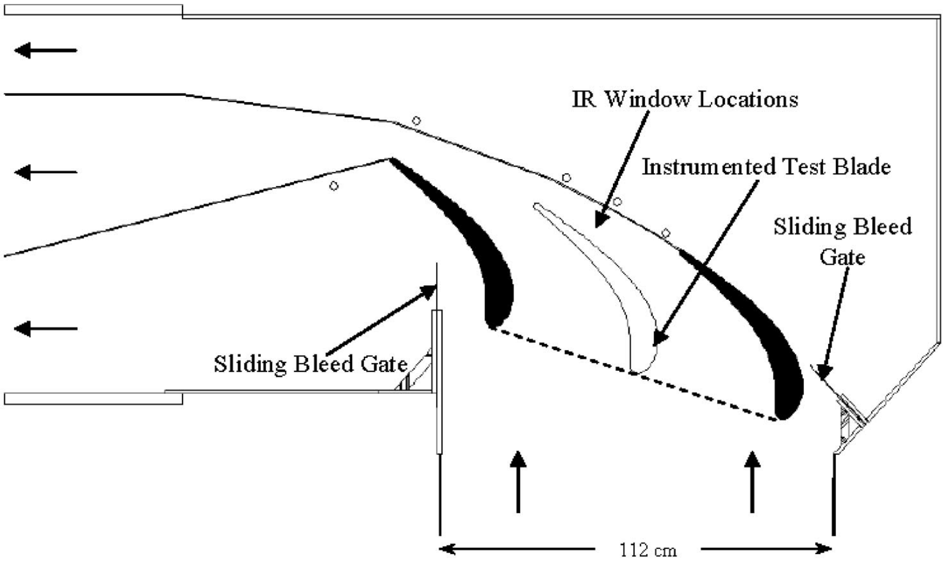

Fig. 2 The corner test section of the wind tunnel housed three blades that formed two full passages

scale of 11 cm. To quantify the integral time scale, velocity fluctuations were measured using a hot-wire anemometer. These jets were unheated (due to a facility constraint) and were injected one chord upstream of the blade. The mass flow of the injected jets represented 4.3% of the core mass flow and had a momentum flux ratio of 8. Because of the high turbulence generated, the thermal field entering the cascade was quite uniform.

The main features of the linear cascade test section, shown in Fig. 2, were an instrumented center blade, two outer blades, sidewall bleeds, and adjustable tailboards. These components were required to ensure periodic flow conditions. Coolant flow for the blade tip was provided to a plenum inside the center blade from an independent pressurized air supply. The pressure drop across a venturi meter was used to quantify the coolant flow rate, while the incoming velocity to the test section was measured with a pitot probe at several locations across the blade pitch.

Figure 3 shows the details of the plenum for the blade tip, the dirt purge cavity, and the dirt purge holes. The removable portion of the tip was 28% of the span (total span was 55 cm) and was specifically molded to allow for a number of different tip geometries to be studied. A two-part foam mixture that exothermically expanded was used to mold the blade tip. The thermal conductivity of this foam was quite low at 0.036–0.043 W/mK and was dependent on the foam properties after expansion, thereby allowing for an adiabatic surface on the blade tip. Only the foam surface (no heater) was present during the adiabatic effectiveness tests.

For the adiabatic effectiveness tests, the experiments were conducted such that the coolant was nominally 25°C lower than the mainstream. Thermal equilibrium required about 4 hr for each test. For the heat transfer measurements, separate experiments were performed with a constant heat flux surface installed on the tip surface. For these tests, the coolant and mainstream temperatures were typically kept to within 0.15°C of one another. Two separate heaters were necessary because of the dirt purge cavity on the tip. The dirt purge cavity was heated with one strip of Inconel that was 0.051 mm thick and had a surface area of 17.3 cm^2. The main heater covered an area of 261.2 cm^2 and consisted of a serpentine Inconel circuit. As shown in Fig. 4, the circuit consisted of the Inconel sandwiched between insulating Kapton and then covered with a very thin (0.013 mm) layer of copper on both sides. Both heaters were attached to a foam blade tip using double-sided tape that was 0.64 mm thick. The nominal heat flux for both heaters was set to 3700 W/m^2, which provided a maximum temperature difference between the mainstream and blade surface of 28°C. The two heaters were controlled independently to within 0.67% of one another during all tests. The current supplied to each heater was known by placing a precision resistor ($R = 1.0\Omega \pm 0.1\%$) in each circuit and measuring the voltage drop across each resistor with a digital multimeter. The heater power was then determined from the supplied current and known heater resistance.

Equation (1) was used when calculating the heat transfer coefficients,

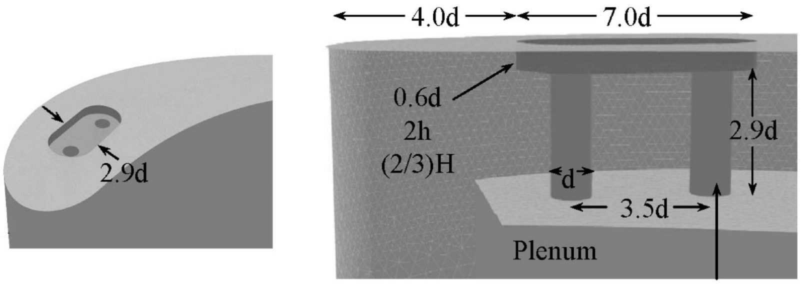

Fig. 3 The blade tip included a plenum that supplied coolant to the dirt purge holes

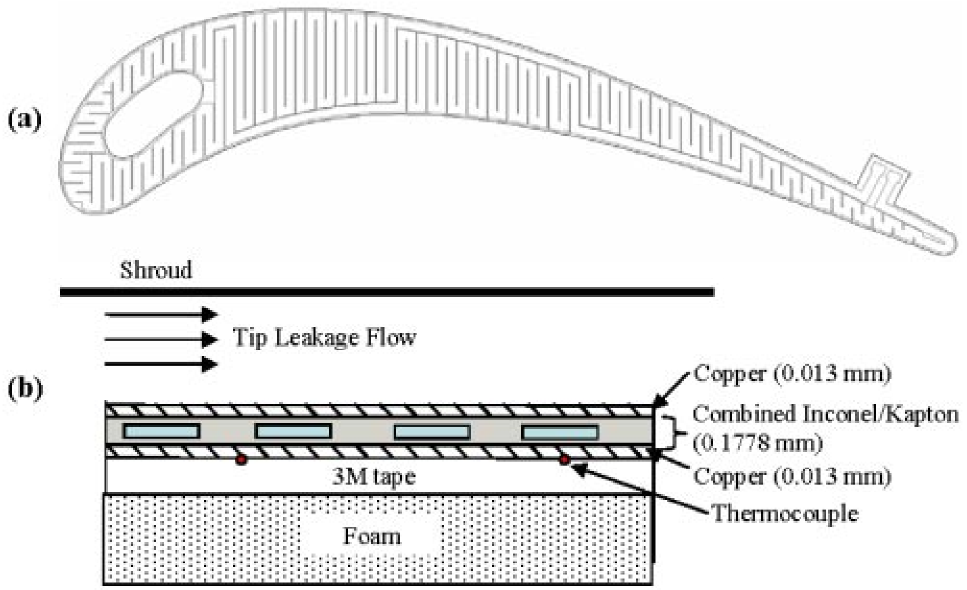

Fig. 4 Main tip heat transfer surface showing (*a*) serpentine passages and (*b*) detail of main tip heater as placed on the blade surface

$$h=(q''_{\mathrm{tot}}-q''_r)/(T_w-T_\infty) \quad (1)$$

In this equation, q''_{tot} represents the total heat flux output from the resistive heaters and q''_r represents the energy lost to radiation. Typically, radiation losses were less than 2% with the maximum for all cases being 3.4%. Conduction losses were found to be negligible because the heaters were placed on the low-thermal conductivity foam.

For the surface-temperature measurements along the tip, an infrared (IR) camera was used to take four separate images that were then assembled to provide the entire surface temperatures of the tip. The image locations are shown by the boxes in Fig. 2. The IR camera was positioned to look directly at the blade tip and required the use of a zinc selenide window placed along the outer shroud that permitted 8–12 micron wavelengths to pass through. Each of the four IR camera images covered an area that was 21.3 cm by 16 cm with the area being divided into 320 by 240 pixel locations. The camera was located approximately 55 cm from the tip, resulting in a spatial resolution of 0.63 mm, which is over 16 times smaller than the dirt purge hole diameter. At each viewing location five images were acquired and averaged at each pixel location to give an overall image of the tip.

The calibration process for the camera involved direct comparisons of the infrared radiation collected by the camera with measured surface temperatures, using either thermocouple strips placed on the tip surface (for the adiabatic effectiveness measurements) or thermocouple beads placed underneath the heater (for the heat transfer measurements). For both experiments, thermocouples were placed on the blade surface using a bonding agent with a high thermal conductivity of 1.6 W/mK. For the thermocouples placed underneath the main tip heater, a 2°C temperature adjustment was applied during calibration to account for the thermal resistivity of the heater at the nominal $q''=3700\ \mathrm{W/m^2}$. The thermal resistance of the Inconel heater in the dirt purge cavity was found to be negligible, and no correction was needed for this area of the blade tip. After the experiments were completed, the infrared images were processed, where adjustments of the surface emissivity and background temperature (irradiation) were made until the image and thermocouple temperatures matched. This process resulted in an agreement between all of the thermocouples and infrared temperatures to within ±1.0°C ($\Delta\eta=\pm0.04$). A check on the calibration process is that the four individual images matched up well to form one entire blade contour without any discontinuities in measured values between images.

Static-pressure taps were located near the midspan of the central blade, and tufts were located near the stagnation locations of all the blades to ensure periodic flow through the passages was achieved. The measured static-pressure distribution around the center blade was compared with an inviscid CFD simulation using periodic boundary conditions, as shown in Fig. 5. This pressure loading is representative of a modern, high-pressure turbine blade.

Overall uncertainties were calculated for nondimensional temperature and heat transfer (η and Nu values) according to the partial derivative method described in Moffat [17]. The total uncertainty of all measurements was calculated as the root of the sum of the squares of the precision uncertainty and the bias uncertainty.

The precision uncertainty for measurements made with the in-

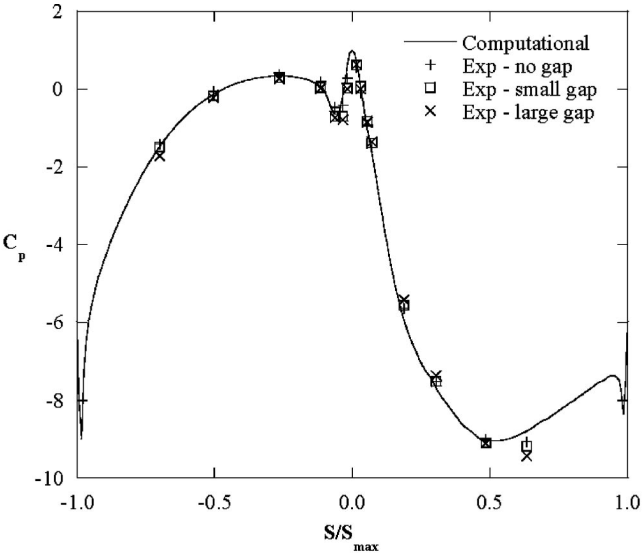

Fig. 5 Measured and predicted static pressures at the blade midspan

Table 2 Matrix of experiments and blowing ratios

Coolant flow (% total flow)	Tip gap	Holes 1 and 2 Global M	Holes 1 and 2 Global I	Hole 1 Local M	Hole 1 Local I	Hole 2 Local M	Hole 2 Local I
0.10	small, large	1.4	3.6	1.9	6.6	1.1	2.1
0.19	small, large	2.7	13.0	3.6	23.7	2.0	7.5
0.29	small, large	4.1	30.3	5.5	55.3	3.1	17.4
0.38	small, large	5.3	52.0	7.2	94.9	4.1	29.9

frared camera was determined through an analysis of five calibrated images taken in succession on one portion of the tip at constant conditions. The precision uncertainty was calculated to be 0.31°C, which is the standard deviation of the five readings based on a 95% confidence interval. The camera manufacturer reported the bias uncertainty as 2.0% of the full scale. The largest scale used in this study was 20°C though some images could be captured on a 10°C range. A bias error of ±1°C was considered for the camera calibration. The thermocouples measuring the freestream and coolant temperatures were reported by the manufacturer to read within ±0.2°C. The total uncertainty in effectiveness was found to be $\delta\eta=\pm0.046$ at $\eta=1$ and $\delta\eta=\pm0.046$ at $\eta=0.2$. The total uncertainty in heat transfer measurements was 6% at $\mathrm{Nu}_{Dh}=45$ and 10.5% at $\mathrm{Nu}_{Dh}=55.7$. Note that the uncertainty is higher in the immediate vicinity of the dirt purge holes where the heat flux is not uniform. The nonuniformity of the heat flux does not affect the ratios of the heat transfer coefficients with and without blowing, however, because this effect is canceled.

Experimental Test Cases

This series of experiments focused on investigating the effect of tip gap height and blowing ratio as indicated in Table 2. With regard to the tip gap height, two different gaps relative to the span were investigated, including gaps that were 0.54% (*h*) and 1.63% (*H*) of the span. Through the remainder of this paper these two tip gaps will be referred to as small and large tip gaps. With regard to the blowing from the dirt purge holes, cases at each tip gap height were measured with a coolant flow rate that ranged from 0.10% to 0.38% of the primary core flow. Note that these flow rate ranges were chosen to simulate engine conditions. A baseline case was also considered for heat transfer measurements that had the dirt purge cavity present, but no holes. Measurements were performed at both gap heights for the baseline case.

The global and local ratios of mass and momentum fluxes were calculated for the blowing cases and are also given in Table 2. The global mass and momentum flux ratios were based on the incident inlet velocity to the blade passage, while the local mass and momentum flux ratios were based on the local tip flow conditions for each of the two dirt purge holes. To compute the local external velocity for the dirt purge hole exits, the local static pressure for the dirt purge holes was taken as the average of the predicted static pressures for the pressure and suction surfaces at the 95% blade span location. The blade locations of these pressures were at 2% and 5% of the total surface distance measured from the stagnation location for dirt purge holes 1 and 2, respectively. The coolant velocity was calculated directly from measured coolant flow rates. As seen in Table 2, the local blowing (and momentum) ratio for hole 1, which is the hole closest to the leading edge, is significantly higher than hole 2 due to the lower local velocity present at the hole 1 location.

Adiabatic Effectiveness Results

The dirt purge holes serve the functional purpose of expelling dirt from the blade that might otherwise block smaller film-cooling holes. Any cooling from the dirt purge holes is of potential benefit for cooling the leading-edge region. The cooling effects of the dirt purge jets are presented as adiabatic effectiveness levels that were measured only in the leading-edge half of the blade. No coolant from the dirt purge holes was measured along the downstream portion of the blade tip, and as such, only the front portions of the tip were measured.

Figure 6 presents the measured adiabatic effectiveness contours for the small tip gap case at four different blowing ratios, ranging from 0.10% to 0.38% (percents based on passage flow). At the lowest blowing ratio, the dirt purge holes cool only a portion of the tip downstream of the holes. There is very little cooling measured within the dirt purge cavity. There is a dramatic increase in the measured adiabatic effectiveness levels as the coolant flow is increased for the small tip gap. The maximum effectiveness for the lowest blowing ratio was 0.86 while a maximum value of $\eta=1.0$ was reached for the 0.19%, 0.29%, and 0.38% blowing ratios. For coolant injection greater than the 0.19% case, a completely cooled region was measured to extend from the pressure side of the tip to the suction side. Interestingly, the coolant is also present upstream of the dirt purge holes such that at the highest blowing ratio, the coolant extended to the leading edge of the tip. This is because the coolant exiting the dirt purge holes impacted the shroud and then propagated outward in all directions. These very high effectiveness levels in the leading-edge region indicate a saturation of the coolant within the tip gap. In general, this is consistent with field-run hardware where this portion of the airfoil has little evidence of tip oxidation.

Figure 7 presents the measurements of adiabatic effectiveness contours for the large tip gap. Results indicate a significantly reduced benefit of the coolant exiting the dirt purge holes as compared to the small tip gap. As the coolant is increased, the experiments show a much broader cool region downstream of the cavity. This spreading of the coolant for the higher blowing ratio cases is caused by an impingement of the jets onto the shroud. At the

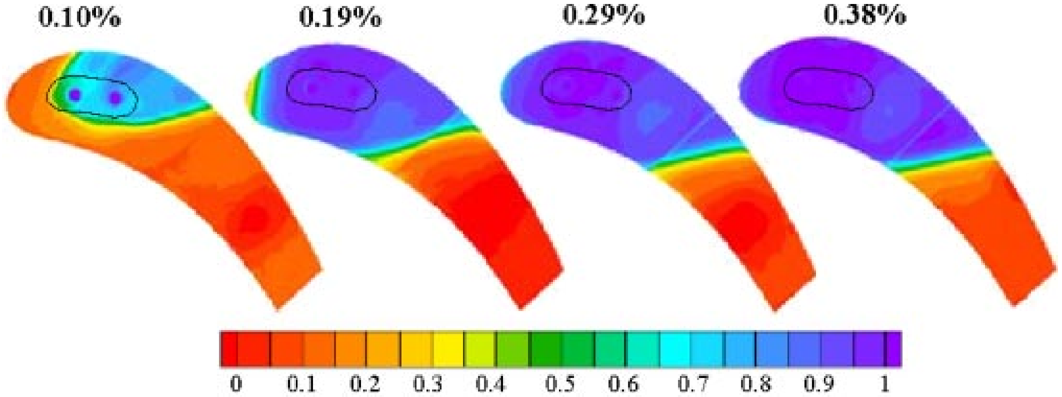

Fig. 6 Adiabatic effectiveness contours taken along the tip with dirt purge blowing for the small tip gap

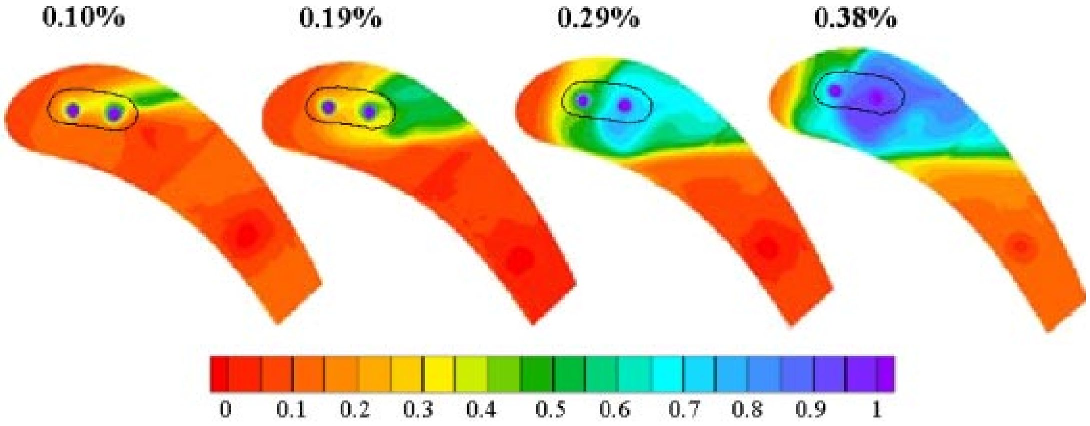

Fig. 7 Adiabatic effectiveness contours taken along the tip with dirt purge blowing for the large tip gap

0.38% coolant injection, there is coolant present with the dirt purge cavity and upstream of the cavity. This is more similar to the small tip gap where coolant is filling the entire gap.

The camber line of the blade is used to compare data and is defined in Fig. 8. This line extends through the midsection of the blade. Effectiveness data were taken along the camber line of the blade, shown in Fig. 9, to further illustrate the differences between the cases tested. The vertical lines on both plots indicate the location of the dirt purge holes. For the small tip gap shown in Fig. 9(*a*) the 0.10% case has significantly lower effectiveness values than the other coolant levels. For the 0.19%, 0.29%, and 0.38% cases, there is hardly any difference in peak values between the cases, but there is increased spreading in the leading-edge region with increased blowing. Also, at the higher blowing ratios, the camber line shows that the adiabatic effectiveness reaches a value of one almost all the way to the stagnation point $(x/C=0)$. For the large tip gap shown in Fig. 9(*b*) the effectiveness steadily increases with each blowing case, as was discussed for the contour levels. Both the peak values and spreading in the leading edge are increased with each increase in blowing rate. However, there appears to be no benefit of nearly doubling the coolant flow from 0.10% to 0.19% at the large tip gap until downstream of the second hole after which there is more spreading of the coolant for the higher coolant flow. Also, the overall effectiveness levels are lower at the large tip gap relative to the small tip gap.

For all cases shown in Figs. 9(*a*) and 9(*b*), the results indicate η values that are above zero outside of the region affected by the dirt purge blowing. The reason for this nonzero effectiveness level is due to a thermal boundary layer effect. As was discussed in the experimental section of this paper, the heaters for the main gas path are located significantly upstream of the test section. As the flow progresses through the contraction of just upstream of the test section, the flow near the wall is slightly cooler than the midspan temperature, resulting in nonzero effectiveness levels.

All of the adiabatic effectiveness measurements for dirt purge cases are summarized by considering an area average that was calculated for a region defined from the leading edge to a location along the pressure side of $s/C=0.3$. A line drawn normal to the pressure side extending to the suction side defines the area. These area averages, which represent effectiveness averages over 46% of the total blade tip area, are shown in Fig. 10. Overall there is a dramatic difference between the small tip gap and the large tip gap at each blowing ratio. The small tip gap shows the average effectiveness increases with blowing ratio, but is leveling off at the higher injection levels. The area averages for the large tip gap case show that the effectiveness only slightly increases when the blowing ratio is increased from 0.10% to 0.19% with larger increases being measured beyond 0.19% injection levels.

Heat Transfer Results

As discussed, separate experiments were performed to measure heat transfer for baseline cases with no blowing and for the blowing cases at both tip gap heights. These measurements were completed using a constant heat flux boundary condition on the tip surface. Baseline studies with no blowing were used to validate the current experiments with previous ones by comparing with a fully developed channel flow correlation. The heat transfer for the blowing cases was normalized by the baseline cases to provide the heat transfer augmentation associated with each blowing case considered. Also, the results from the adiabatic effectiveness experiments were combined with these heat transfer measurements to quantify the overall blade thermal loading for each of the blowing cases.

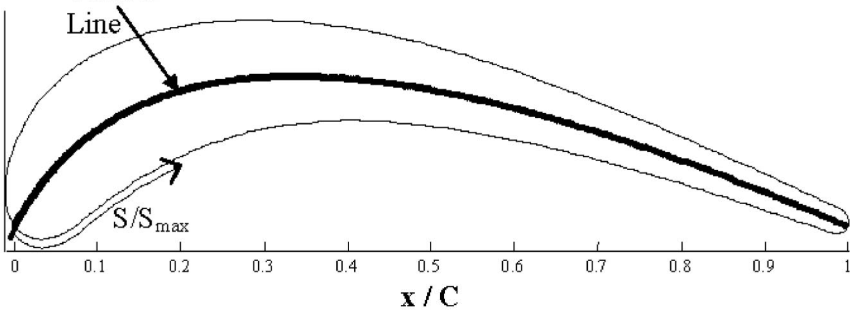

Fig. 8 Definition of the blade camber line

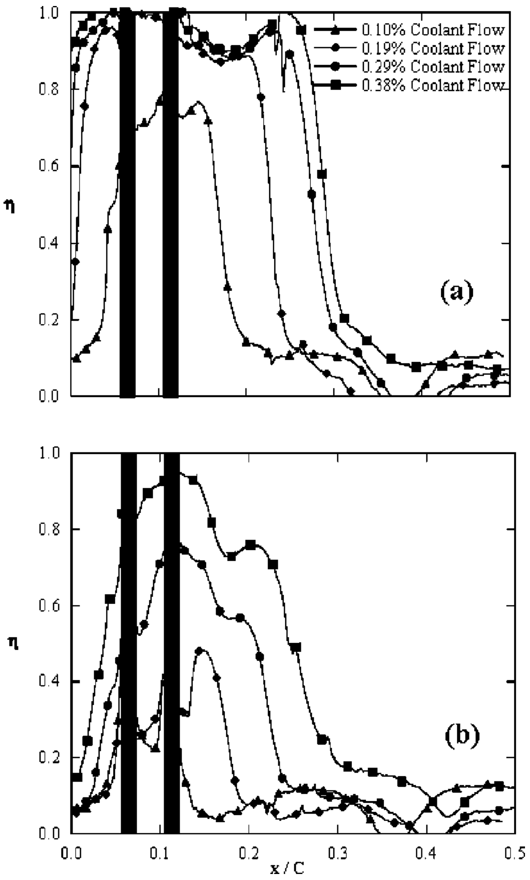

Fig. 9 Effectiveness taken along the blade camber line for the (*a*) small and (*b*) large tip gaps

Baseline Cases—No Blowing. Previous studies have compared flow in a turbine blade tip gap to that of a fully developed channel flow correlation for turbulent flow in a duct. The correlation that was used for comparison was developed by Gnielinski [18]. Gnielinski's correlation is given in Eq. (2) and has been reported in the literature to provide accuracy to within 6% as reported by Kakaç et al. [19] for a large Reynolds number range ($10^4 < \mathrm{Re} < 10^6$).

$$\mathrm{Nu}_{fd} = 0.0214(\mathrm{Re}^{0.8} - 100)\mathrm{Pr}^{0.4} \tag{2}$$

Mayle and Metzger [5] furthered this correlation for a tip gap by adding an augmentation factor to account for the overwhelming entry-region effects of thin blade tips. This augmentation factor, which was taken from Kays and Crawford [20], allows blade designers to relate overall blade tip heat transfer (for a given blade thickness and tip gap) to an overall heat transfer expected in a fully developed channel as shown in Eq. (3). Equation (3), as pointed out by Mayle and Metzger [5], accounts for the fact that only one side of the channel (blade tip) was heated.

$$\mathrm{Nu}/\mathrm{Nu}_{fd} = 1 + \frac{3}{L_t/D_h} \tag{3}$$

Comparisons have been made to the data of Jin and Goldstein [15] and Bunker et al. [14] that confirm this augmentation factor approach. Although Mayle and Metzger [5] first noted the augmentation factor, their data have not been included in this comparison because only experiments performed on airfoil shapes were considered. This is because the plotting variables were based on blade exit velocity, of which there is no equivalent in the Mayle and Metzger tests. Figure 11 shows Nusselt number values based on the hydraulic diameter of the tip gap (2h or 2H) plotted as a function of the blade Reynolds number based on the exit velocity and hydraulic diameter. The Gnielinski correlation has been plotted for several L_T/D_h ratios as shown on the plot. Note that L_T represents the maximum thickness of the blade. As known for turbulent channel flow, fully developed conditions generally occur for $L/D_h > 20$ [20]. The correlations given in Fig. 11 indicate similar trends to the experimental data despite very different blade shapes with the largest outliers occurring at the lowest blade Reynolds numbers (not tip gap Reynolds number). It should be noted that the L_T/D_h ratios are based on the maximum blade thickness, and the Nusselt numbers are the average values calculated for the tip surface. Therefore, this ratio is not a perfect representation of a blade profile. More experiments should be performed to further verify this trend.

The baseline results are presented as contour plots of Nusselt number (based on chord) in Fig. 12. Note that the chord rather than hydraulic diameter was used for these contour plots to illustrate the differences in the heat transfer coefficients along the blade tip for both tip gaps. Also, it is important to recognize that the heat flux is not uniform in the immediate vicinity of the dirt purge holes. Results at both gap heights show similar trends, however, the large tip gap shows higher Nusselt numbers at the blade trailing edge relative to the small tip gap. This increase in heat transfer at the larger tip gap trailing edge is a result of the increased entry region effect relative to the small tip gap. With smaller L/D_h values (for the large tip gap), the entry region is expected to have a greater effect, as mentioned at the beginning of this section. For the large tip gap, the L/D_h is as low as 1 across the trailing edge of the tip surface, whereas for the small tip gap the L/D_h is 3.5.

The area-averaged Nusselt numbers are given for each case to quantify the increase in heat transfer with gap height. For these cases, the Nusselt number at the large tip gap is 3.2 times that of the small tip gap when based on the exit velocity and hydraulic diameter. By using Reynolds number scaling for a turbulent channel flow, the large tip gap is expected to have 2.4 times the heat transfer of the small tip gap. This larger than expected increase results from the overwhelming entry region effects, which serve to greatly increase the tip heat transfer.

As shown in Fig. 12, there are regions of low heat transfer immediately downstream of the dirt purge cavity for both tip gap heights. This is near the thickest portion of the blade and represents the area of lowest heat transfer on the blade tip. This region

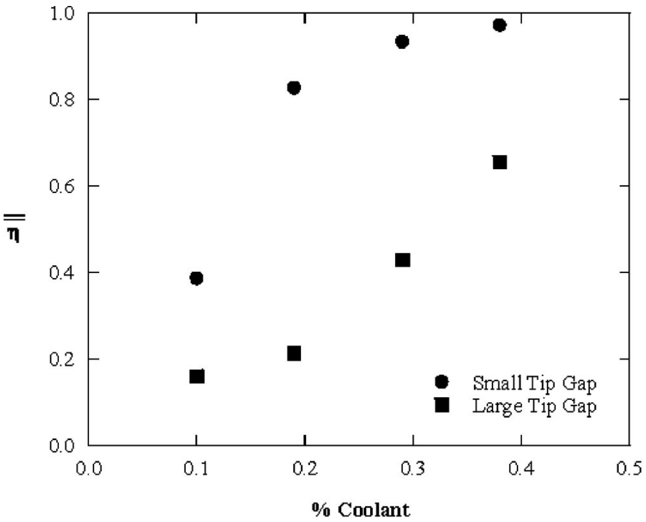

Fig. 10 Area-averaged effectiveness of the tip at various coolant blowing levels

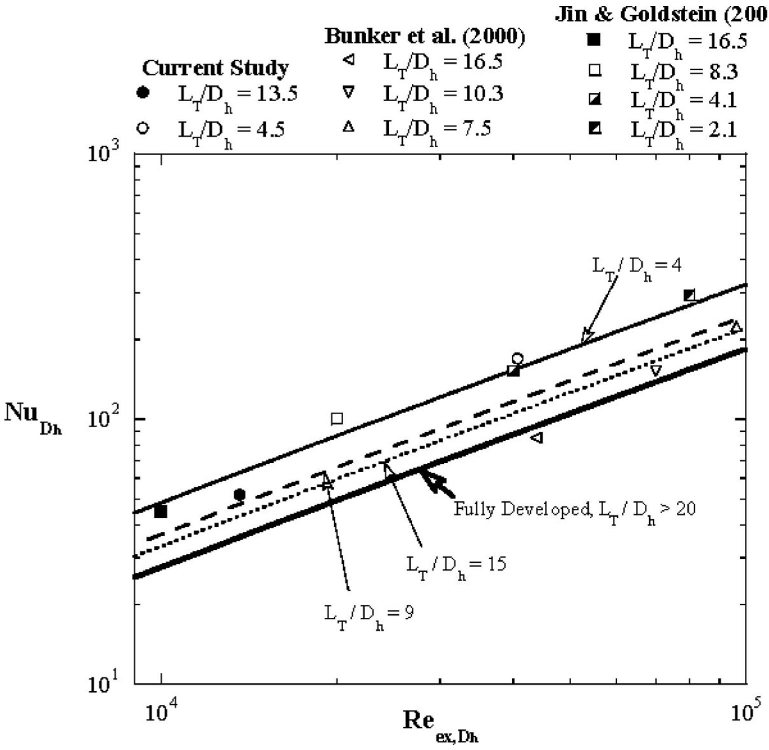

Fig. 11 Comparison of experimental data to a fully developed correlation

was first pointed out by Bunker et al. [14] and has been confirmed by other authors. Within the dirt purge cavity, there are high heat transfer coefficients resulting from low velocity flow recirculation in the cavity. Overall, the leading-edge region experiences relatively low heat transfer outside of the dirt purge cavity relative to the trailing edge.

Also seen on these contour plots are regions of high heat transfer along the pressure side that begin around $S/S_{\max}=0.1$ and extend until the trailing edge. These regions of high heat transfer have been noted by Morphis and Bindon [2] and Bindon [16] to be the separation-reattachment region that forms along the pressure side due to mainstream and leakage flow interaction. This region occurs within the entry region, is more dominant at the large tip gap than at the small tip gap, and extends over a large region of the tip for the large tip gap.

Heat Transfer Augmentation With Blowing. By comparing the heat transfer with blowing to that of the baseline cases, the augmentation associated with tip blowing can be studied. The camber line plots for the dirt purge blowing are shown in Figs. 13(*a*) and 13(*b*) for the small and large tip gaps, respectively. For both tip gaps, the heat transfer is increased with blowing for the

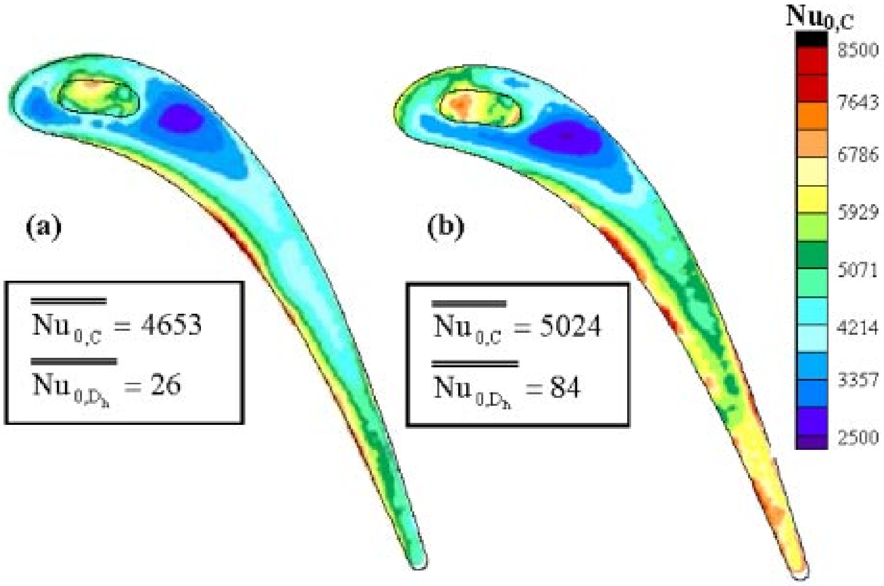

Fig. 12 Baseline Nusselt number contour plots for the (*a*) small and (*b*) large tip gap heights

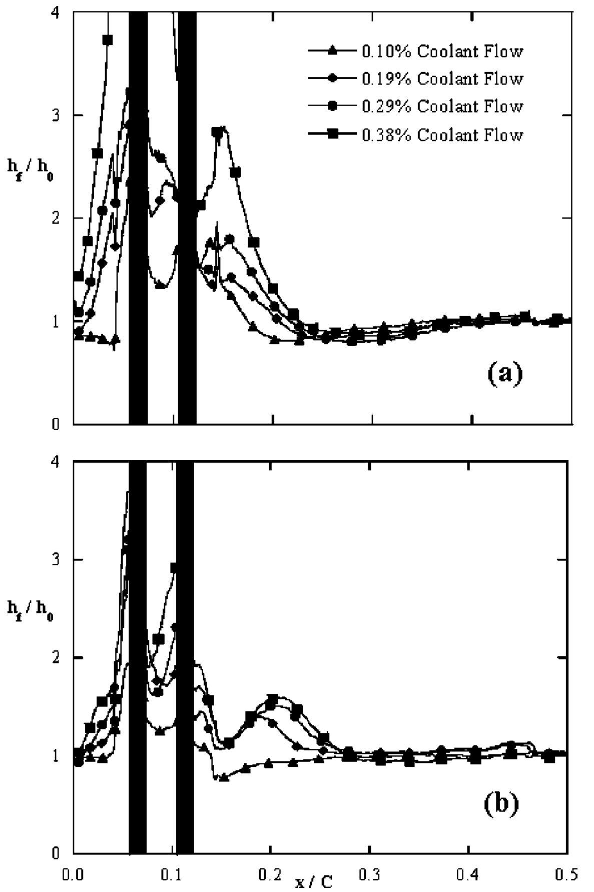

Fig. 13 Camber line data for h_f/h_0 for the (*a*) small and (*b*) large tip gaps

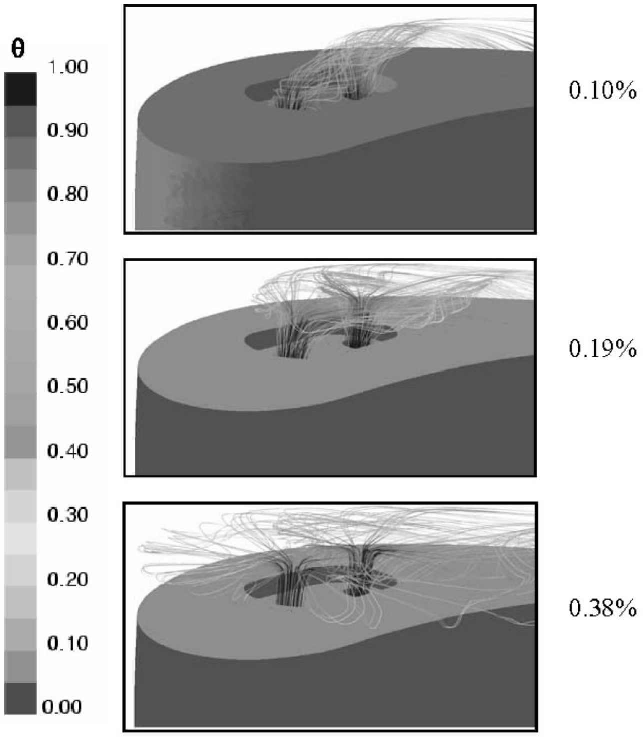

Fig. 14 CFD predictions of dirt purge streamlines for the large tip gap [21]

region of $0<x/C<0.25$. Beyond $x/C=0.3$, there is no difference between any of the cases because the dirt purge blowing does not affect heat transfer in this area. In comparing Fig. 13 with Fig. 9, there are striking differences between the two data sets. The film-cooling effectiveness (Fig. 9) extends further down the blade than does the heat transfer augmentation. For the small tip gap, the film cooling remains near $\eta=1$ out to $x/C=0.25$ for the highest blowing ratio, whereas the heat transfer augmentation is at a value of one at that location. This shows that for the small tip gap, the dirt purge holes are impinging upon the shroud and effectively spreading coolant flow while the heat transfer increase is localized around the hole exits. For the large tip gap, there are localized peaks of film effectiveness for each of the three highest blowing ratios located at $x/C=0.15$ for the 0.19% case, and near $x/C=0.2$ for the 0.29% and 0.38% cases. These peaks of adiabatic effectiveness correspond to peaks of heat transfer. At the 0.29% and 0.38% cases, the peaks are located at the same position, suggesting that the coolant flow has impinged upon the shroud and returned back to the tip. For the 0.19% case, however, the peaks are not colocated. Instead, the peak in heat transfer is located downstream of the peak in film effectiveness. This suggests that at this particular blowing ratio, the dirt purge jet is causing flow vortices to form near the jet that do not cause high film effectiveness, but do increase the heat transfer.

CFD results by Hohlfeld [21] predicted these voritices. Coolant-flow streamlines for the large tip gap are shown in Fig. 14. At the highest blowing ratio (0.38%), the coolant is spread in all directions after hitting the shroud. At the 0.19% case, the first dirt purge hole is split by the second hole such that part of the flow rolls into a vortex around the right side of the second hole jet. This vortex extends the full gap height and is what causes the peak in heat transfer to be located further downstream than the peak in film effectiveness for this case. The 0.10% case is shown to verify that there are no vortices at this case, but rather flow exiting the holes and immediately flowing out of the gap region.

Peaks of heat transfer are seen immediately around both of the dirt purge holes in Fig. 13. The reason for this is that the holes cut out of the foil heater had high current gradients very near to the holes, resulting in high heat transfer coefficients.

Area averages of the heat transfer augmentation for both tip gaps are shown in Fig. 15. Again, these averages are over the forward 46% of the blade tip area, so that only the area affected by the blowing is considered. These results show there to be the same heat transfer augmentation for the lowest blowing ratios at

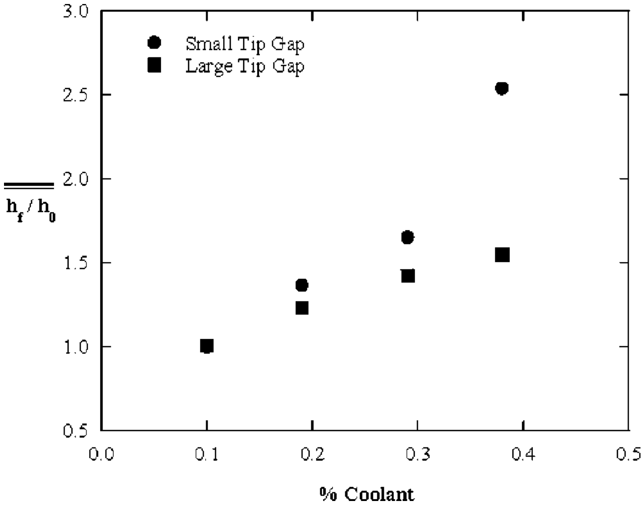

Fig. 15 Area-averaged heat transfer augmentation for the small and large tip gaps

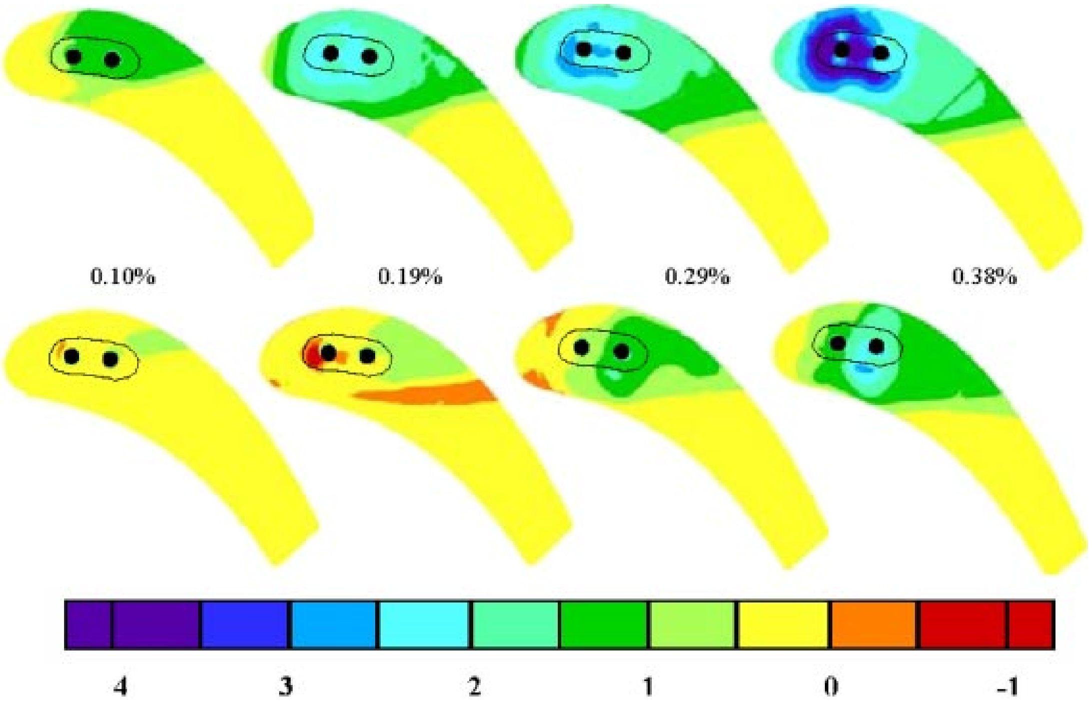

Fig. 16 Contour plots of NHFR for the small (top) and large (bottom) gap heights at all blowing ratios

both tip gaps. As the blowing ratio increases, however, the small tip gap shows increasingly higher augmentation than the large tip gap. This higher augmentation is because of the influence of the three-dimensional vortices formed as the jets exit the dirt purge holes. As was discussed in the adiabatic results section, flow from the dirt purge holes for the small tip gap can flood the leading-edge gap region, causing very good cooling over most of the leading edge. At the large tip gap, the flow is blowing off the tip surface and impinging on the shroud. Because of this, the augmentation is higher at the small tip gap than at the large tip gap for the same blowing ratio.

Net Heat Flux Reduction. Combining the heat transfer measurements with the film effectiveness measurements can give the overall cooling benefit in the form of a net heat flux reduction (NHFR). Shown in Eq. (4), NHFR is an established method of evaluating the overall effect of a cooling scheme on a surface [22],

$$\mathrm{NHFR}=1-(h_f/h_0)[1-\eta\cdot\theta)] \tag{4}$$

All variables have been measured experimentally except for θ, which was assumed to be 1.6 based on previous literature [22]. This value corresponds to a cooling effectiveness of 62.5%. As this equation shows, when high heat transfer augmentation is not accompanied by high film cooling, the NHFR can become negative. A negative NHFR means that there is an increased heat load to the blade surface, which is undesirable.

The NHFR values were calculated locally for each case and are shown in Fig. 16. The NHFR is always higher at the small tip gap relative to the large tip gap. This can be attributed to the much higher film-cooling effectiveness and only slightly higher heat transfer augmentation of the small tip gap relative to the large tip gap. At the small tip gap, the NHFR always increases with blowing. For the large tip gap, the area downstream of the dirt purge cavity shows increased NHFR values with increased blowing, however, for the entire leading-edge region, the 0.19% case appears to be lower than the 0.10% case. This is because of the slightly negative NHFR downstream of the second dirt purge hole. This region is caused by the vortices created by the dirt purge blowing, which are not seen in any of the other cases, as was previously discussed.

NHFR values along the camber line are shown in Fig. 17 for the small and large tip gaps. For the small tip gap [Fig. 17(*a*)], there is increased spreading of the NHFR in the region $0<x/C<0.3$ as blowing increases. The highest blowing case (0.38%) shows a large spike at the first dirt purge hole. This is caused by high heat transfer immediately surrounding the dirt purge hole, where the uncertainly is higher due to nonuniform heat flux, as discussed previously. For the large tip gap, there is generally increased NHFR with increased blowing with the exception of the region around $x/C=0.2$. Around this area, the 0.19% case actually shows lower NHFR than the 0.10% case due to the decreased film effectiveness.

Area averages of the NHFR values were calculated for the forward part of the blade. The results, shown in Fig. 18, indicate the NHFR is always higher for the small tip gap. For the small tip gap, the NHFR levels increase nearly linearly with blowing ratio. For the large tip gap, however, the lowest blowing ratio shows higher NHFR values than the 0.19% case, although increases in blowing ratio result in increased NHFR.

Conclusions

Intended to prevent dirt and dust particles from clogging smaller film-cooling holes, dirt purge holes can provide significant cooling to the leading edge of a blade tip. Note that in an engine design, the entry corner and trailing-edge regions also need to be cooled. The dirt purge jets provided a significant amount of cooling for the leading-edge area, particularly for the small tip gap. From the contours and profiles on the tip for the small gap case, it was apparent that there was an overcooling of the leading-edge area for coolant injections that were greater than 0.19% of the main passage flow. Increased blowing resulted in a larger cooling benefit for the large tip gap as compared to the small tip gap, although the small tip gap always showed higher overall effectiveness for the same blowing ratio. For the large tip gap, which is most likely to occur for operating engine conditions, the lower

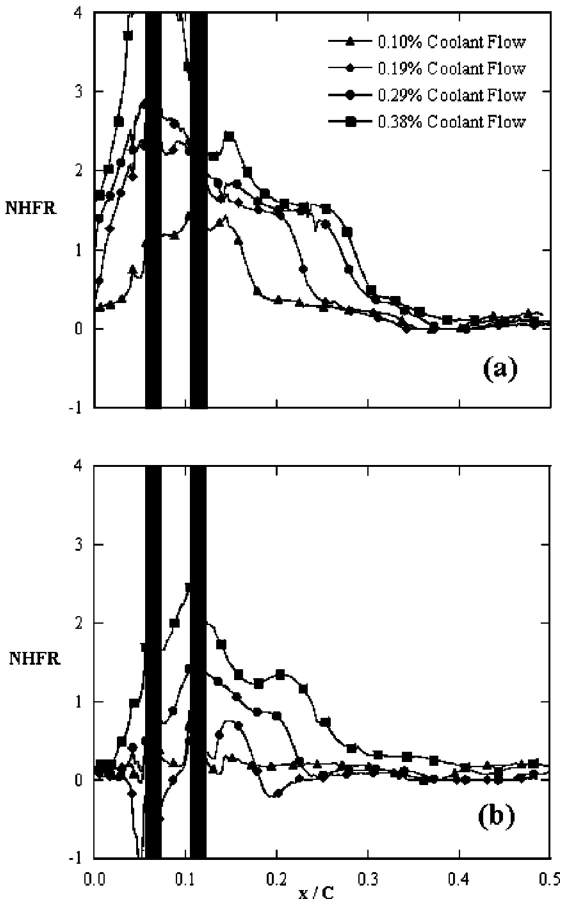

Fig. 17 NHFR taken along the Camber line for the (*a*) small and (*b*) large gap heights

coolant injection rates of 0.10% and 0.19% of the passage flow, the coolant was only effective within the dirt purge cavity and just downstream of the cavity. As the coolant injection was increased to 0.29% and 0.38% for the large tip gap, cooling was evident within, upstream, and downstream of the purge cavity.

Heat transfer measurements indicate that heat transfer augmentation with blowing is increased with higher blowing ratios for both gap heights tested. Also, the augmentation seen for the small tip gap tends to be higher than that of the large tip gap. By combining the adiabatic effectiveness and heat transfer measurements, the large tip gap experienced less benefit than the small tip gap of the dirt purge cooling. For the large tip gap, the NHFR decreased from the 0.10% case to the 0.19% case, but increased with subsequent blowing ratios. Overall, the measurements indicate that better NHFR from the dirt purge holes can be achieved for a small tip gap as compared to a large tip gap.

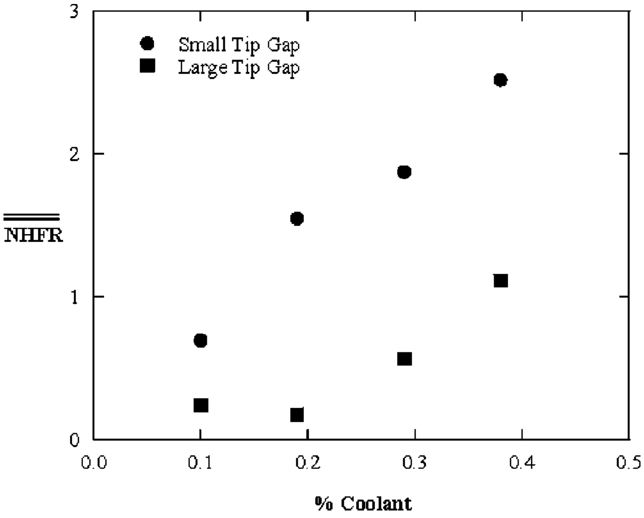

Fig. 18 Area-averaged NHFR for both gap heights

Acknowledgment

The authors gratefully acknowledge United Technologies—Pratt and Whitney for its support of this work.

Nomenclature

B_x = axial chord
C = true chord of blade
C_p = pressure coefficient, $C_p=(p-p_{in})/(\rho U_{in}^2/2)$
d = hole diameter of the dirt purge
D_h = hydraulic diameter, always used as 2h or 2H
h = small tip gap height
H = large tip gap height
h_f = film heat transfer coefficient
h_0 = blade heat transfer coefficient with no blowing
k = thermal conductivity
I = local $(\rho_c U_c^2/\rho_\infty U_\infty^2)$ or global $(\rho_c U_c^2/\rho_{in} U_{in}^2)$ momentum flux ratio
L = local thickness of blade
$L_{\max}$ = max local thickness of blade
L_T = max thickness of blade overall
$\dot{m}$ = mass flowrate
M = local $(\rho_c U_c/\rho_\infty U_\infty)$ or global $(\rho_c U_c/\rho_{in} U_{in})$ mass flux ratio
NHFR = net heat flux reduction, see Eq. (4)
Nu_{Dh} = Nusselt number based on hydraulic diameter, $h(D_h)/k$
Nu_{fd} = Nusselt number at fully developed condition based on hydraulic diameter, $h(D_h)/k$, see Eq. 2
$\mathrm{Nu}_{0,C}$ = baseline Nusselt number based on chord, $h(C)/K$
$\mathrm{Nu}_{0,Dh}$ = baseline Nusselt number based on hydraulic diameter, $h(D_h)/k$
P = blade pitch
P_o, p = total and static pressures
Pr = Prandtl number
q''_{tot} = heat flux supplied to tip surface heater
q''_r = heat flux loss due to radiation
R = resistance in Ω.
Re_{in} = inlet Reynolds number, $U_{in}(C)/\nu$
Re_{Dh} = Reynolds number based on local velocity and hydraulic diameter, $U_{local}(D_h)/\nu$
$\mathrm{Re}_{ex,Dh}$ = Reynolds number based on exit velocity and hydraulic diameter, $U_{ex}(D_h)/\nu$
Re = Reynolds number
S = surface distance along blade
T = temperature
U_{local} = local velocity on tip gap
U_{ex} = exit velocity (at blade trailing edge)
U_{in} = inlet velocity (1 chord upstream)
x = distance along blade chord

Greek

η = adiabatic effectiveness, $\eta=(T_{in}-T_{aw})/(T_{in}-T_c)$
Δ = denotes a difference in value
ρ = density
ν = kinematic viscosity
ε = emissivity of tip heater surface, always set to 0.93.
θ = dimensionless temperature ration, $(T_\infty-T_c)/(T_\infty-T_w)$, always set to 1.6.
θ_1 = dimensionless thermal field, $(T_\infty-T)/(T_\infty-T_c)$

Subscripts

$ave,—$ = pitchwise average at a given axial location
$ave,═$ = area average
aw = adiabatic wall
c = coolant conditions
in = inlet value at 1C upstream of blade
ms = value at blade midspan
∞ = local inviscid value
w = wall temperature with heat transfer surface
b = background temperature for surface radiation

References

[1] Lattime, S. B., and Steinetz, B. M., 2002, ‘‘Turbine Engine Clearance Control Systems: Current Practices and Future Directions,’’ NASA TM 2002-211794.

[2] Morphis, G., and Bindon, J. P., 1988, ‘‘The Effects of Relative Motioin, Blade Edge Radius and Gap Size on the Blade Tip Pressure Distribution in an Annular Turbine Cascade With Clearance,’’ ASME Paper No. 88-GT-256.

[3] Tallman, J., and Lakshmiarayana, B., 2001, ‘‘Numerical Simulation of Tip Leakage Flows in Axial Flow Turbines, With Emphasis on Flow Physics: Part II—Effect of Outer Casing Relative Motion,’’ ASME J. Turbomach., **123**, pp. 324–333.

[4] Yaras, M. I., and Sjölander, S. A., 1992, ‘‘Effects of Simulated Rotation on Tip Leakage in a Planar Cascade of Turbine Blades: Part I Tip Gap Flow,’’ ASME J. Turbomach., **114**, pp. 652–659.

[5] Mayle, R. E., and Metzger, D. E., 1982, ‘‘Heat Transfer at the Tip of an Unshrouded Turbine Blade,’’ *Proc. of 7th Int. Heat Transfer Conf.*, Vol. 3, ASME, New York, pp. 87–92.

[6] Chyu, M. K., Moon, H. H., and Metzger, D. E., 1989, ‘‘Heat Transfer in the Tip Region of Grooved Turbine Blades,’’ ASME J. Turbomach., **111**, pp. 131–138.

[7] Srinivasan, V., and Goldstein, R. J., 2003, ‘‘Effect of Endwall Motion on Blade Tip Heat Transfer,’’ ASME J. Turbomach., **125**, pp. 267–273.

[8] Kim, Y. W., and Metzger, D. E., 1995, ‘‘Heat Transfer and Effectiveness on Film Cooled Turbine Blade Tip Models,’’ ASME J. Turbomach., **117**, pp. 12–21.

[9] Kim, Y. W., Downs, J. P., Soechting, F. O., Abdel-Messeh, W., Steuber, G., and Tanrikut, S., 1995, ‘‘A Summary of the Cooled Turbine Blade Tip Heat Transfer and Film Effectiveness Investigations Performed by Dr. D. E. Metzger,’’ ASME J. Turbomach., **117**, pp. 1–11.

[10] Kwak, J. S., and Han, J. C., 2002, ‘‘Heat Transfer Coefficient and Film-Cooling Effectiveness on a Gas Turbine Blade Tip,’’ ASME Paper No. GT-2002-30194.

[11] Kwak, J. S., and Han, J. C., 2002, ‘‘Heat Transfer Coefficient and Film-Cooling Effectiveness on a Squealer Tip of a Gas Turbine Blade Tip,’’ ASME Paper No. GT-2002-30555.

[12] Acharya, S., Yang, H., Ekkad, S. V., Prakash, C., and Bunker, R., 2002, ‘‘Numerical Simulation of Film Cooling Holes On the Tip of a Gas Turbine Blade,’’ ASME Paper No. GT-2002-30553.

[13] Hohlfeld, E. M., Christophel, J. R., Couch, E. L., and Thole, K. A., 2003, ‘‘Predictions of Cooling From Dirt Purge Holes Along the Tip of a Turbine Blade,’’ ASME Paper No. GT2003-38251.

[14] Bunker, R. S., Bailey, J. C., and Ameri, A. A., 2000, ‘‘Heat Transfer and Flow on the First-Stage Blade Tip of a Power Generation Gas Turbine: Part 1—Experimental Results,’’ ASME J. Turbomach., **122**, pp. 263–271.

[15] Jin, P., and Goldstein, R. J., 2003, ‘‘Local Mass/Heat Transfer on a Turbine Blade Tip,’’ Int. J. Rotating Mach., **9**(2), pp. 981–995.

[16] Bindon, J. P., 1989, ‘‘The Measurement and Formation of Tip Clearance Loss,’’ ASME J. Turbomach., **111**, pp. 257–263.

[17] Moffat, R. J., 1988, ‘‘Describing the Uncertainties in Experimental Results,’’ Exp. Therm. Fluid Sci., **1**, pp. 3–17.

[18] Gnielinski, V., 1976, ‘‘New Equations for Heat and Mass Transfer in Turbulent Pipe and Channel Flow,’’ Int. Chem. Eng., **16**, pp. 359–368.

[19] Kakaç, S., Shah, R. K., and Aung, W., 1987, *Handbook of Single-Phase Convective Heat Transfer*, Wiley, New York, pp. 34–35.

[20] Kays, W. M., and Crawford, M. E., 1980, *Convective Heat and Mass Transfer*, Second Edition, McGraw-Hill, New York, pp. 269–270.

[21] Hohlfeld, E. H., 2003, ‘‘Film Cooling Predictions Along the Tip and Platform of a Turbine Blade,’’ Master’s thesis, Virginia Polytechnic Institute and State University, Blacksburg, VA.

[22] Sen, B., Schmidt, D. L., and Bogard, D. G., 1994, ‘‘Film Cooling With Compound Angle Holes: Heat Transfer,’’ ASME Paper No. 94-GT-311.

Large Eddy Simulation of Flow and Heat Transfer in a Channel Roughened by Square or Semicircle Ribs

Joon Ahn

Haecheon Choi

Joon Sik Lee

School of Mechanical and Aerospace Engineering,
Seoul National University,
Seoul 151-744, Korea

The internal cooling passage of a gas turbine blade has been modeled as a ribbed channel. In the present study, we consider two different rib geometries, i.e., square and semicircle ribs, in order to investigate their thermal and aerodynamic performance. Large eddy simulations (LESs) of turbulent flow in a ribbed channel with a dynamic subgrid-scale model are performed. In our simulation, the no-slip and no-jump conditions on the rib surface are satisfied in the Cartesian coordinates using an immersed boundary method. In order to validate the simulation results, an experimental study is also conducted, where the velocity and temperature fields are measured using a hot wire and a thermocouple, respectively, and the surface heat transfer is measured using the thermochromic liquid crystal. LES predicts the detailed flow and thermal features, such as the turbulence intensity around the ribs and the local heat transfer distribution between the ribs, which have not been captured by simulations using turbulence models. By investigating the instantaneous flow and thermal fields, we propose the mechanisms responsible for the local heat transfer distribution between the ribs, i.e., the entrainment of the cold fluid by vortical motions and the impingement of the entrained cold fluid on the ribs. We also discuss the local variation of the heat transfer with respect to the rib geometry in connection with flow separation and turbulent kinetic energy. The total drag and heat transfer are calculated and compared between the square and semicircle ribs, showing that two ribs produce nearly the same heat transfer, but the semicircle one yields lower drag than the square one. [DOI: 10.1115/1.1811098]

Introduction

The cycle efficiency of a gas turbine can be enhanced through raising its inlet temperature. However, there is a limitation in increasing the inlet temperature due to the material problem. Accordingly, blades subject to high temperature are manufactured to have internal cooling passages equipped with ribs [1]. Therefore, the pressure drop and heat transfer characteristics inside the cooling passage have been investigated for better design of a gas turbine blade.

One of the important factors determining the flow and heat transfer characteristic is the geometry. Among the geometric parameters affecting the heat transfer characteristics, the ratios of the rib height to channel height $(=e/H)$ and the rib pitch to height $(=p/e)$ are important ones. In general, the increase in the rib height increases the heat transfer, but raises the pressure drop. The optimum e/H is known to be around 0.1 [2]. There also exists an optimum pitch, since the pitch should be longer than the recirculation zone formed behind the rib. The ratio of the rib pitch to height recommended is about 10 for the Reynolds number range of interest [2]. Since the optimum values of the aforementioned geometric parameters are well established through the extensive experimental data, we pay our attention to the cross-sectional geometry of the rib in the present study.

Heat transfer in a ribbed channel is locally deteriorated immediately behind the ribs. The recirculation zone caused by flow separation is responsible for the low level of heat transfer. Attempts have been made to alleviate this problem by changing the geometry of rib cross section. For instance, a round cross section is likely to reduce the size of the recirculation zone and relieve the pressure drop. The ribs can be also rounded due to improper manufacturing or wear during the operation. Hence, we need to investigate whether a rounded rib, indeed, produces a better performance or not.

Cho et al. [3] reported by measuring the local heat transfer along the wall between ribs that the semicircle rib shows higher heat transfer rate than the conventional square rib. On the other hand, Liou and Hwang [4] showed that the semicircle rib results in a lower heat transfer rate than the square one. Taslim and Korotky [5] pointed out that a rounded rib corner deteriorates the heat transfer performance of the rib. As is clear from these experimental results, the effect of the rib cross-sectional shape on the heat transfer characteristics is still unclear and thus should be investigated further.

Most of the earlier computational studies on the ribbed channel have been restricted to RANS (Reynolds Averaged Navier-Stokes Simulation). Although it predicts the mean flow field fairly well, the standard k-ε model fails to capture the sharp peak in the turbulence intensity profile observed near the rib. It also underpredicts the heat transfer rate and does not capture the high heat transfer rate ahead of the rib. Acharya et al. [6] indicated the reason for this failure of the standard k-ε model twofold: first, the large-scale motion is not properly reflected in the k-ε model, and second, the introduction of the wall function may cause the discrepancy in the heat transfer.

Recently large eddy simulation (LES) has been performed for flow and heat transfer inside the ribbed channel. Ciafalo and Collins [7] performed LES and captured the high heat transfer region in front of the rib. Near the wall, however, their result overestimated the streamwise velocity, temperature drop, and streak spacing due to the lack of resolution. More recently, Murata and Mo-

---

Contributed by the International Gas Turbine Institute (IGTI) of THE AMERICAN SOCIETY OF MECHANICAL ENGINEERS for publication in the ASME JOURNAL OF TURBOMACHINERY. Paper presented at the International Gas Turbine and Aeroengine Congress and Exhibition, Vienna, Austria, June 13–17, 2004, Paper No. 2004-GT-53401. Manuscript received by IGTI, October 1, 2003; final revision, March 1, 2004. IGTI Review Chair: A. J. Strazisar.

Table 1 Flow and geometric parameters

	Present (LES)	Present (Experiment)	Cho et al. [3]	Liou and Hwang [4]
Re	30,000	30,000	30,000	13,000
p/e	10	10	10	10
AR	∞	8	2	4
e/H	0.1	0.1	0.1	0.13

chizuki [8] performed LES using the dynamic subgrid-scale model [9,10], but their simulation was performed at the Reynolds number roughly 10 times lower than that of a real gas turbine blade.

In the present study, we perform LES for two different rib cross-sectional geometries, i.e., square and semicircle. Other geometric parameters, such as the blockage ratio and pitch, are fixed to be similar to the values typically found in a gas turbine blade (see Table 1). We also conduct an experimental study to validate the simulation. First, we compare the time-averaged results from LES with those from the present and past experiments to verify that LES accurately predicts the flow and heat transfer characteristics. Second, we investigate the instantaneous thermal and flow fields to draw a mechanism responsible for the local heat transfer distribution. Finally, we compare the thermal performances from the two cross-sectional geometries.

Computational and Experimental Setup

Numerical Method. The governing equations for LES are the grid-filtered continuity, Navier-Stokes, and energy equations for incompressible flow and heat transfer,

$$\frac{\partial \overline{u_i}}{\partial x_i} - m = 0 \tag{1}$$

$$\frac{\partial \overline{u_i}}{\partial t} + \frac{\partial}{\partial x_j}\overline{u_i}\,\overline{u_j} = -\frac{\partial \overline{p}}{\partial x_i} + \frac{1}{\mathrm{Re}}\frac{\partial^2 \overline{u_i}}{\partial x_j \partial x_j} - \frac{\partial \tau_{ij}}{\partial x_j} + f_i \tag{2}$$

$$\frac{\partial \overline{T}}{\partial t} + \frac{\partial}{\partial x_j}\overline{T}\,\overline{u_j} = \frac{1}{\mathrm{Re}\,\mathrm{Pr}}\frac{\partial^2 \overline{T}}{\partial x_j \partial x_j} - \frac{\partial q_j}{\partial x_j} + \Phi \tag{3}$$

In the above equations, an overbar represents a grid-filtered value, τ_{ij} is the subgrid-scale stress and q_j is the subgrid-scale heat flux. Here, τ_{ij} and q_j are the terms to accommodate unresolved small-scale motion modeled with a dynamic subgrid-scale model [9,10,11]. The periodic boundary condition is applied in the streamwise (x) and spanwise (z) directions, and no-slip and no-jump conditions are applied on the channel wall. The no-slip and no-jump conditions on the rib surface are applied in Cartesian coordinates using an immersed boundary method. In this method, the momentum forcing f_i and heat source/sink Φ are provided to satisfy the no-slip and no-jump conditions at the rib surface, respectively. A mass source/sink m is given to satisfy the continuity for the cell containing the immersed boundary. The numerical details are found in Kim et al. [12] and Kim and Choi [13].

The numerical method used consists of a semi-implicit fractional step method and the second-order central difference scheme in space. The periodic boundary condition is justified using a sufficiently large computational domain. In order to decide the streamwise domain size, we conducted simulations with two different computational domain sizes, respectively, containing three pairs of ribs and one pair of ribs (see Fig. 1(a) for pairs of three ribs). They resulted in nearly the same time-averaged values of flow and heat transfer quantities. Therefore, below we present results from the simulation with a streamwise computational domain size containing only one pair of ribs. The spanwise domain size is set to be 2.5π times the rib height; the two-point correlation at the separation distance of half the domain size shows zero falloff. The information about the grid system is summarized in Table 2. Grids are clustered near the wall and around the rib surface in the streamwise and wall-normal directions. Uniform grids are used in the spanwise direction. The simulations are carried out for 10,000 time steps to reach a fully developed flow. After the initial 10,000 steps, an additional 10,000 time steps ($tU_b/D_h = 5$) are performed to obtain the statistics.

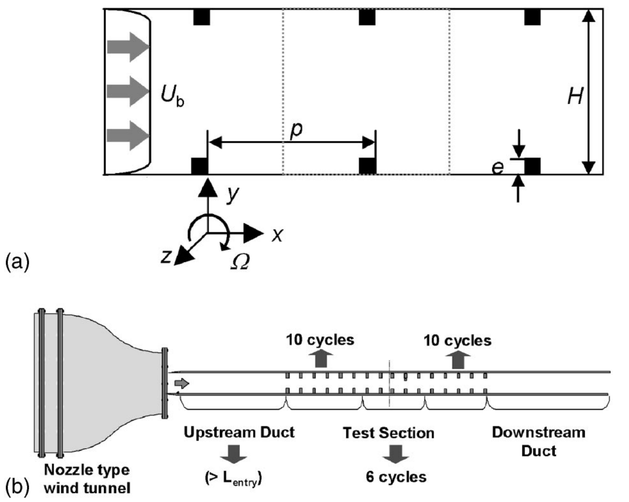

Fig. 1 Computational domain and experimental setup: (*a*) computational domain; (*b*) schematic of experimental setup

Experimental Apparatus. Our experimental setup is designed to form a fully developed ribbed-duct flow as shown in Fig. 1(b). A wind tunnel is used to supply the flow to the channel at the bulk speed ($= U_b$) of 5 m/s. Its cross-sectional area is 0.4 m×0.05 m, with which the bulk Reynolds number is Re $= 30{,}000$. The Prandtl number is Pr$= 0.71$. The duct, which is made of polycarbonate, is composed of the upstream, ribbed, and downstream ducts. The upstream duct is installed to introduce a fully developed channel flow to the ribbed duct. Data are acquired in the middle of the ribbed duct. There are more than 10 ribs upstream of the measuring point in order to secure fully developed flow at the test section. Additional 10 ribs and downstream duct are installed after the test section to exclude any effect from the duct exit.

The streamwise velocity and turbulence intensity are measured using an I-type hot wire anemometry. The temperature profiles are also measured at several streamwise locations using a T-type thermocouple. Because the local distribution of the heat transfer rate is an important property to validate the simulation, we measure it using TLC (thermochromic liquid crystal) with high spatial resolution.

The heat transfer coefficient ($= h$) in a channel flow is defined as

$$q'' = h(T_w - T_b) \tag{4}$$

A gold-coated film is used to supply uniform heat flux, whose value ($= q''$) is measured through a power meter. The heating film is attached on the 12.7 mm thick polycarbonate test section.

Table 2 Computational parameters

	Square	Semicircle
Grid number	128×128×48	128×160×48
Δx	0.015∼0.231 e	0.015∼0.193 e
Δy	0.014∼0.261 e	0.015∼0.195 e
Δz	0.164 e	0.164 e
$\Delta t\ U_b/D_h$	0.0005	0.0005
CFL$_{\max}$	0.7	0.7

Formed polystyrene of 50 mm thickness is used beneath as an insulator. The bulk temperature (T_b) is evaluated as a function of the streamwise location. The wall temperature (T_w) is measured using TLC with a hue capturing technique in a steady state. The liquid crystal has a color changing temperature range from 25°C to 45°C. With the wide bandwidth of the TLC, entire temperature distribution is captured from a single image.

The uncertainty is evaluated on 20 to 1 odds (95% confidence level). All the uncertainty values are evaluated based on single-sample experiments proposed by Kline and McClintock [14]. The uncertainty of the dimensionless temperature Θ is estimated at $\Theta = 0.5$, and its value is 14.5%. The uncertainty of the heat transfer coefficient (h) is 13.0% at its typical value of 100 W/m^2 K.

Results and Discussion

Time-Averaged Quantities. Time-averaged streamlines for both the square and semicircle rib cases show three characteristic recirculation bubbles between ribs (Fig. 2): main recirculation bubble behind the rib, a secondary one near the backward-facing corner, and a bubble in front of the forward-facing corner. However, last two bubbles are significantly weakened for the semicircle rib case. The reattachment locations are $x/e \approx 4.5$ for both cases. For the square rib case, a separation bubble is observed also on the top of the rib.

The time-averaged streamwise velocity profiles at three different streamwise locations from LES show good agreement with the present experimental data for both cases (Fig. 3). The mean velocity profiles follow the experimental data very well, down to the rib height ($y/e = 1$). Especially, the agreement at $x/e = 0.5$ is of great interest because the flow has not been well predicted from RANS [6]. Figure 4 shows the turbulence intensity profiles, which agree well with the experimental data. Especially, at $x/e = 0.5$, the peak in the turbulence intensity formed around the rib height is successfully captured by LES. An excellent agreement is also found for the time-averaged temperature (see Fig. 5).

Liou et al. [15] reported that the behavior of heat transfer is closely related to the turbulent kinetic energy (k). Maximum turbulent kinetic energy occurs right above the rib for the square rib, while it is observed at $x/e \approx 3$ for the semicircle rib (see Fig. 6). For both cases, a band of high turbulent kinetic energy is formed around the rib height. A relatively high turbulent kinetic energy is also observed near the forward-facing side of the rib. On the other hand, the turbulent kinetic energy is low, right behind the rib, where the heat transfer is not active.

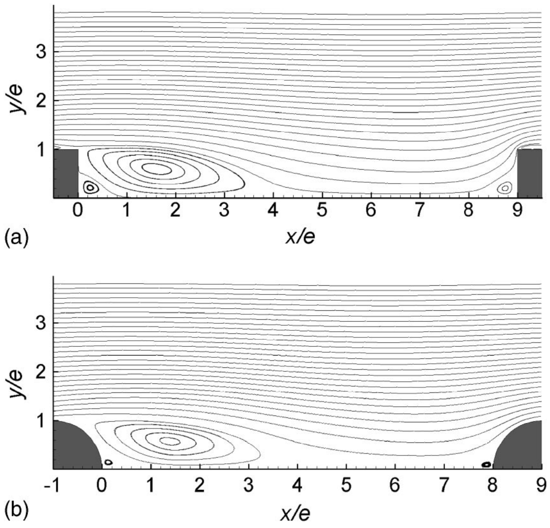

Fig. 2 Time-averaged streamlines from LES: (*a*) square rib; (*b*) semicircle rib

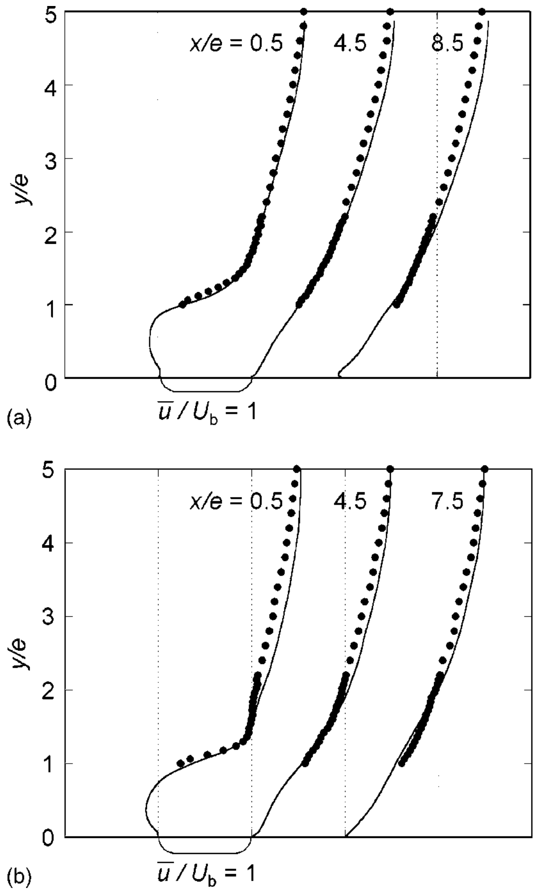

Fig. 3 Time-averaged streamwise velocity profiles: (*a*) square rib; (*b*) semicircle rib. —, LES (present); ●, experiment (present)

Local Heat Transfer Between Ribs. Figure 7 shows the Nusselt number distributions between the ribs, normalized by the well-known Dittus-Boelter correlation for fully developed turbulent pipe flow. For the square rib (Fig. 7(*a*)), the agreement between Nusselt numbers from the present experiment and LES is not as good as that between the mean temperatures, whereas the result from the present LES agrees well with those by other experimental results. The Nusselt number in Fig. 7(*a*) shows two sharp peaks near backward-facing and forward-facing corners and one broad peak near $x/e \approx 3.5$, which is about one rib height (e) ahead of the reattachment point.

For the semicircle rib (Fig. 7(*b*)), the Nusselt number distribution between ribs is similar to that for the square rib because the flow structures for both cases are characterized as the three vortices shown in Fig. 2. However, the local maxima near the backward- and forward-facing corners for the semicircle rib are not as sharp as those for the square rib, which is expected from Fig. 2 in that the recirculation bubbles in the corners are much smaller and weaker for the first than for the latter. The heat transfer rate on the channel wall ($\overline{\mathrm{Nu}}_t$) is slightly larger with the semicircle rib than with the square rib (see Table 3). Especially, the semicircle rib improves heat transfer right behind the rib. Compared to other data sets, the result from Liou and Hwang [4] shows a low heat transfer rate for the semicircle rib case. Judging from the parameters summarized in Table 1, the performance of the semicircle rib seems to be quite sensitive to the Reynolds number.

The instantaneous flow and thermal fields from LES are investigated to explain the mechanisms responsible for the local heat transfer variation. Figure 8 shows the instantaneous velocity vec-

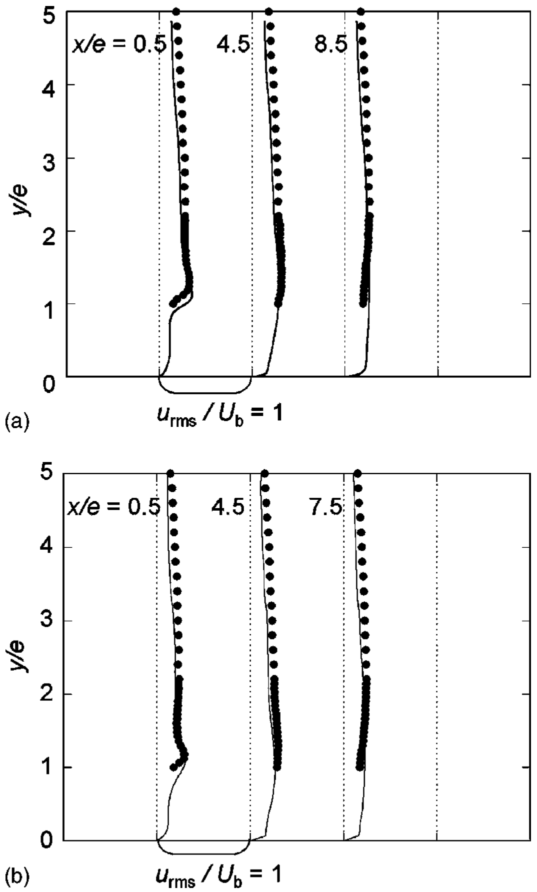

Fig. 4 Root-mean-square streamwise velocity fluctuation profiles: (*a*) square rib; (*b*) semicircle rib. —, LES (present); ●, experiment (present)

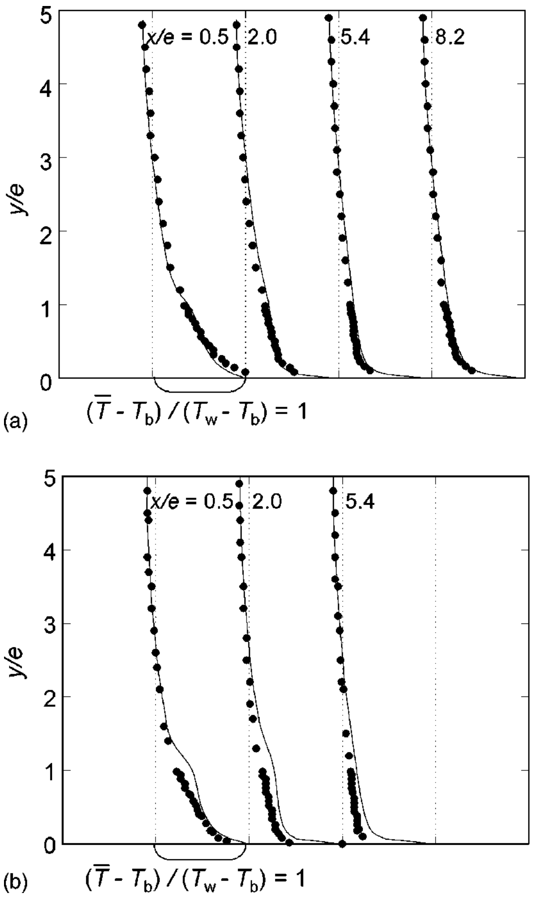

Fig. 5 Time-averaged temperature profiles: (*a*) square rib; (*b*) semicircle rib. —, LES (present); ●, experiment (present)

tors together with the temperature contours. Many vortices, which are identified using a vortex identification technique [16] and marked as white circles, appear near the wall. By observing the velocity vectors and temperature contours at the same time, one may notice in Fig. 8(*a*) that the cold fluid (bright gray) is entrained toward the wall due to downwash motion induced by the vortices, which enhances the heat transfer on the wall. From this observation, we may be able to answer the question why the maximum value of the local heat transfer appears in front of the reattachment point (see Fig. 7). The reattachment point is only a statistical one where the time-averaged streamwise velocity gradient is zero at the wall. Because the vortices near the wall entrain the cold core flow and the clockwise vortices are prevalent, the entrained cold fluid tends to move backward underneath the vortices. This relocates the peak of the time-averaged Nusselt number upstream of the reattachment point. Like in the case of the square rib, vortices entrain the cold core flow to enhance the heat transfer. As is clear, the semicircle rib also enhances the heat transfer with the mechanism similar to that by the square rib.

Another important phenomenon is the existence of sharp peak in the Nusselt number in front of the rib (Fig. 7). The instantaneous flow and thermal fields in the *xz* plane at $y/e = 0.06$ are shown in Fig. 9 to explain the sharp peak of $\overline{\mathrm{Nu}}$. As shown, the velocity and temperature vary significantly in the spanwise direction. Many instantaneous backward motions are also found, which indicates active vortical motions near the wall. The low-temperature (bright gray) patches are formed by the entrainment and are elongated in the streamwise direction before they meet the front surface of rib. When they reach the front surface of the rib, they impinge on the rib and move in the spanwise direction. This impinging motion is observed for both cases, but is weaker for the semicircle rib than for the square rib.

Heat Transfer on the Rib. While numerous measurements have reported the heat transfer on the wall between ribs, there are few data concerning the heat transfer on the rib surface [17]. The

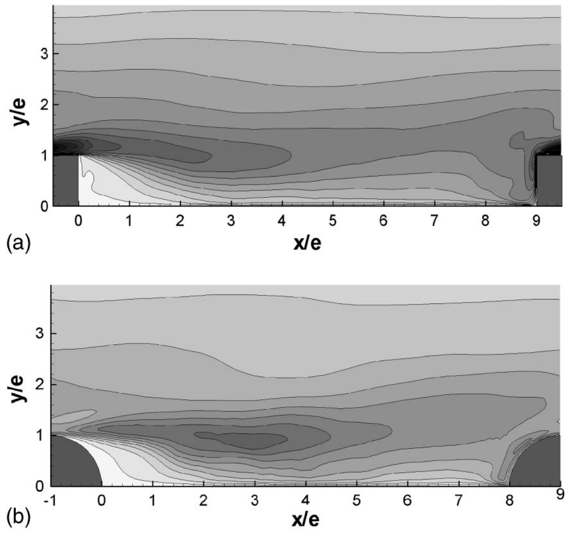

Fig. 6 Contours of the turbulent kinetic energy from LES: (*a*) square rib; (*b*) semicircle rib

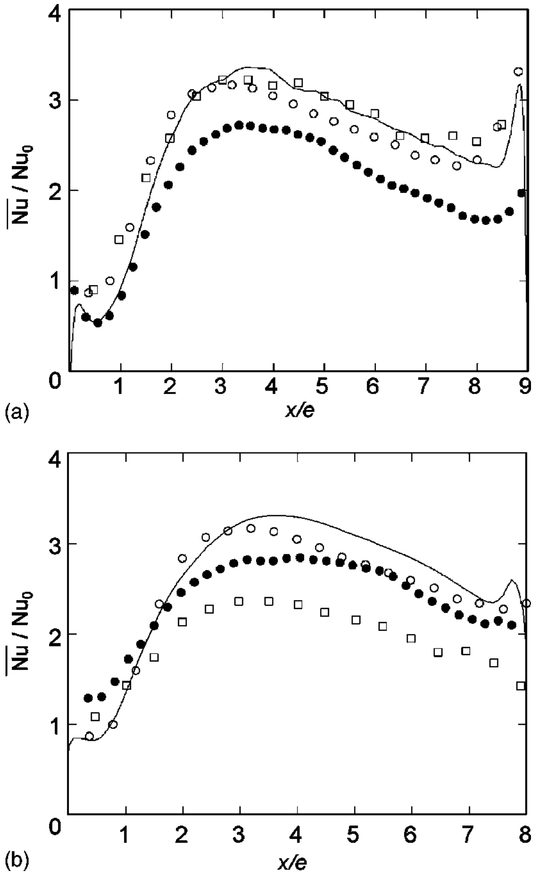

Fig. 7 Time-averaged Nusselt number between ribs: (*a*) square rib; (*b*) semicircle rib. —, LES (present); ●, experiment (present); ○, Cho et al. [3]; □, Liou and Hwang [4]

heat transfer coefficient on the rib surface is thought to be high, and a considerable amount of heat might be transferred from the rib surface. For the present square rib, 24% of heat is ideally transferred to the fluid from the rib. Figure 10 shows the local variation of Nusselt number along the rib surface for both cases. Here, the coordinate ξ is defined along the rib surface ($\xi = 0$ corresponds to the forward-facing corner of the rib). For the square rib (Fig. 10(*a*)), the rate of heat transfer sharply decreases around the two edges of the rib ($\xi/e = 1$ and 2). This sharp decrease in $\overline{\text{Nu}}$ is due to the flow separation at the edges (see Fig. 2(*a*)). The prediction of $\overline{\text{Nu}}$ by LES shows a fair agreement with the measurement data by Liou and Hwang [4], considering different Reynolds numbers investigated.

For the semicircle rib (Fig. 10(*b*)), the heat transfer increases from the forward-facing corner to the point rotated by 70 deg along the surface of the semicircle and then decreases. Unlike for the square rib, the flow separates at the backward-facing side of the semicircle rib (Fig. 2(*b*)). Therefore, the peak in the Nusselt number does not occur near the separation point, but occurs at the forward-facing side of the rib. Although the result by LES does not agree well with the experiment by Liou and Hwang [4], both data show the maximum Nusselt number on the forward-facing side of the rib. The maximum heat transfer on the semicircle rib seems to be related to the high turbulent kinetic energy observed in front of the rib (Fig. 6(*b*)).

Table 3 Rib performance

	Square	Semicircle
$\overline{\text{Nu}}_t/\text{Nu}_0$	2.49	2.56
Q/Q_0	3.29	3.28
f/f_0	11.4	9.97
$(Q/Q_0)/(f/f_0)^{1/3}$	1.46	1.52

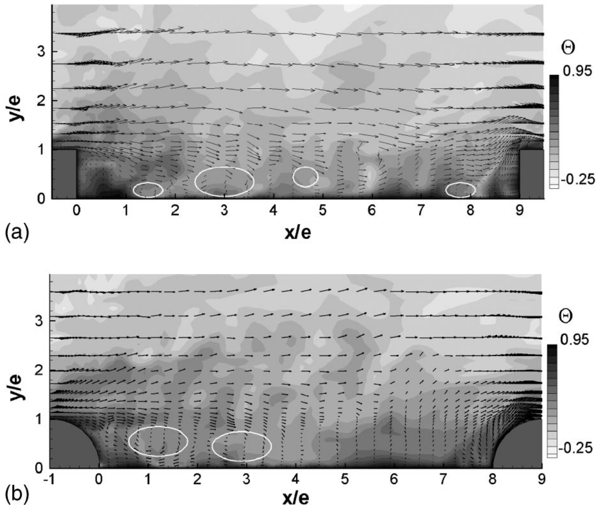

Fig. 8 Instantaneous velocity vectors and temperature contours in an *xy* plane (LES): (*a*) square rib; (*b*) semicircle rib

Many previous studies have evaluated the thermal performance based on the heat transfer on the wall between the ribs [3]. However, a more accurate comparison of the performance may be

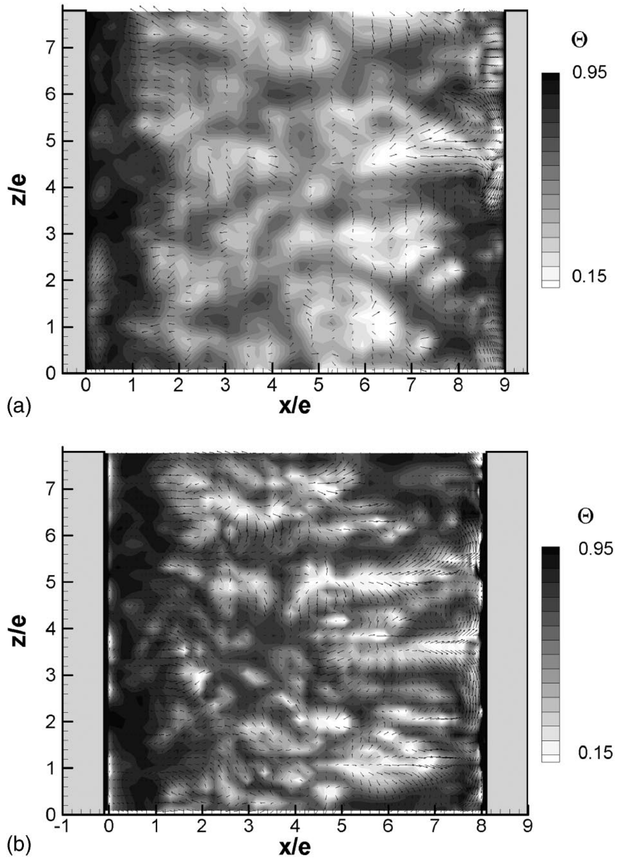

Fig. 9 Instantaneous velocity vectors and temperature contours in the *xz* plane at $y/e = 0.06$ (LES): (*a*) square rib; (*b*) semicircle rib

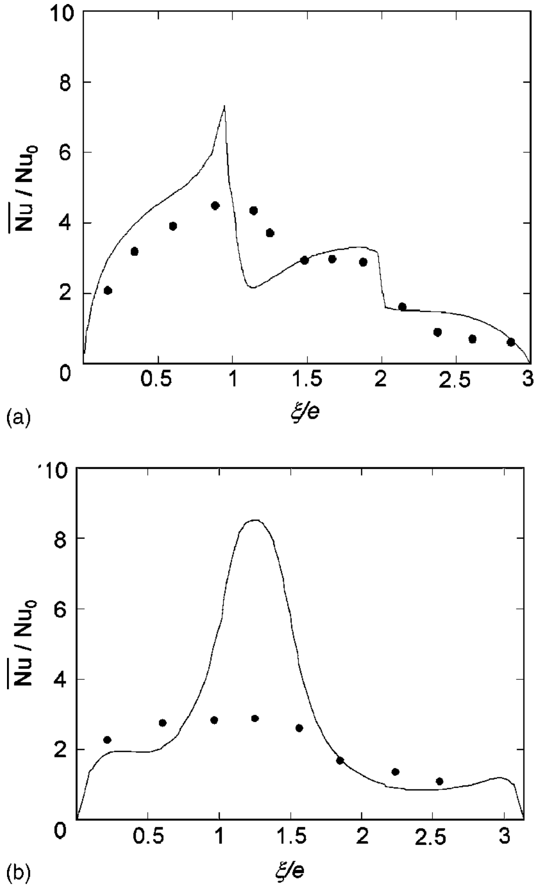

Fig. 10 Time-averaged Nusselt number on the rib surface: (*a*) square rib; (*b*) semicircle rib. —, LES (present); ●, Liou and Hwang [4]

achieved when the heat transfer from the rib surface is included. Therefore, we evaluated the total amount of the heat transfer as

$$\frac{Q}{Q_0}=\frac{\int \mathrm{Nu}\,ds}{\mathrm{Nu}_0 p} \tag{5}$$

The results, including the normalized friction factor, are summarized in Table 3. The semicircle cross section gives a better performance between the ribs, but the total amount of heat transfer is almost the same as that of the square rib. On the other hand, the increase in the pressure drop is smaller for the semicircle rib than for the square rib, and thus the thermal performance $[=(Q/Q_0)/(f/f_0)^{1/3}]$ becomes 5% higher than that for the square rib.

Conclusions

The flow and heat transfer in a channel roughened by square or semicircle ribs were investigated using the large eddy simulation (LES) technique. Comparing the time-averaged data from LES with the experimental data, LES was found to predict the flow and heat transfer characteristics very well. From the instantaneous fields, it was shown that the local peaks in the heat transfer rate along the wall are caused by the entrainment of the cold fluid by the vortical motions and the impingement of the entrained cold fluid on the ribs. Finally, the total amount of heat transfer by the semicircle rib was nearly the same as that by the square rib. Considering the penalty of the pressure drop caused by the rib, the semicircle rib provides a better thermal performance by 5% at the flow conditions investigated than the square rib.

Acknowledgments

The authors acknowledge the support from the Micro Thermal System Research Center and the Creative Research Initiative of the Korea Ministry of Science and Technology.

Nomenclature

AR = aspect ratio of the channel, $AR=W/H$
CFL = Courant-Friedrichs-Lewy number
D_h = hydraulic diameter of the channel
e = rib height
f = friction factor, $f=-(dp/dx)D_h/\rho U_b^2/2$
f_i = momentum forcing
H = channel height
h = heat transfer coefficient
k = thermal conductivity or turbulent kinetic energy, $k=1/2(\overline{u'^2}+\overline{v'^2}+\overline{w'^2})$
m = mass source/sink
Nu = Nusselt number, $\mathrm{Nu}=hD_h/k$
$\overline{\mathrm{Nu}}_t$ = Nusselt number averaged over the channel wall between the ribs
p = rib to rib pitch or pressure
Pr = Prandtl number, $\mathrm{Pr}=\nu/\alpha$
Q = total heat transfer rate
q'' = heat flux
q_j = subgrid-scale heat flux, $q_j=\overline{Tu}_j-\overline{T}\overline{u}_j$
Re = bulk Reynolds number, $\mathrm{Re}=U_bD_h/\nu$
s = coordinate along the solid surface
T = temperature
T_b = bulk temperature
Δt = computational time step
U_b = bulk velocity
u, v, w = streamwise, wall-normal, and spanwise velocity components
W = channel width in the spanwise direction
x, y, z = Cartesian coordinates in the streamwise, wall-normal and spanwise directions $(=x_1,x_2,x_3)$
$\Delta x, \Delta y, \Delta z$ = grid spacings in x, y, z directions

Greek Symbols

Φ = heat source/sink
θ = non-dimensional temperature, $\theta=(\overline{T}-T_b)/(T_w-T_b)$
τ_{ij} = subgrid-scale stress, $\tau_{ij}=\overline{u_iu_j}-\overline{u}_i\overline{u}_j$
ξ = coordinate fitted with the rib surface

Subscripts

0 = value of a fully developed turbulent flow in a smooth pipe
b = bulk
rms = root-mean-square value
w = wall

Superscipt

— = time-averaged value or grid-filtered value
$'$ = fluctuations

References

[1] Lakshminarayana, B., 1996, *Fluid Dynamics and Heat Transfer of Turbomachinery*, Wiley, New York, pp. 315–322.
[2] Han, J. C., 1984, "Heat Transfer and Friction in Channels With Two Opposite Rib Roughened Walls," ASME J. Heat Transfer, **106**, pp. 774–781.
[3] Cho, H. H., Wu, S. J., and Kim, W. S., 1998, "A Study on Heat Transfer Characteristics in a Rib-Roughened Rectangular Duct," *Proc. of 11th Int. Symp. on Transport Phenomena*, Hsinchu, Taiwan, pp. 364–369.
[4] Liou, T.-M., and Hwang, J.-J., 1993, "Effect of Ridge Shapes on Turbulent Heat Transfer and Friction in a Rectangular Channel," Int. J. Heat Mass Transfer, **36**(4), pp. 931–940.
[5] Taslim, M. E., and Korotky, G. J., 1998, "Low-Aspect-Ratio Rib Heat Transfer Coefficient Measurements in a Square Channel," ASME J. Turbomach., **120**, pp. 831–838.
[6] Acharya, S., Dutta, S., Myrum, T., and Baker, R. S., 1993, "Periodically De-

veloped Flow and Heat Transfer in a Ribbed Duct,'' Int. J. Heat Mass Transfer, **36**, pp. 2069–2082.

[7] Ciafalo, M., and Collins, M. W., 1992, ''Large Eddy Simulation of Turbulent Flow and Heat Transfer in Plane and Rib-Roughened Channels,'' Int. J. Numer. Methods Fluids, **15**, pp. 453–489.

[8] Murata, A., and Mochizuki, S., 2000, ''Large Eddy Simulation With a Dynamic Subgrid-Scale Model of Turbulent Heat Transfer in an Orthogonally Rotating Rectangular Duct With Transverse Rib Turbulators,'' Int. J. Heat Mass Transfer, **43**, pp. 1243–1259.

[9] Germano, M., Piomelli, U., Moin, P., and Cabot, W., 1991, ''A Dynamic Subgrid-Scale Eddy Viscosity Model,'' Phys. Fluids A, **3**(7), pp. 1760–1765.

[10] Lilly, D. K., 1992, ''A Proposed Modification of the Germano Subgrid-Scale Closure Model,'' Phys. Fluids A, **4**, pp. 633–635.

[11] Cabot, W. and Moin, P., 1993, ''Large Eddy Simulation of Scalar Transport With the Dynamic Subgrid-Scale Model,'' *Large Eddy Simulation of Complex Engineering and Geophysical Flows*, Cambridge Univ. Press, Cambridge, England, pp. 141–158.

[12] Kim, J., Kim, D., and Choi, H., 2001, ''An Immersed-Boundary Finite-Volume Method for Simulations of Flow in Complex Geometries,'' J. Comput. Phys., **171**, pp. 132–150.

[13] Kim, J., and Choi, H., 2004, ''An Immersed-Boundary Finite-Volume Method for Simulations of Heat Transfer in Complex Geometries,'' KSME Int. J., **18**(6), pp. 1026–1035.

[14] Kline, J. S., and McClintock, F. A., 1953, ''Describing Uncertainties in Single Sample Experiments,'' Mech. Eng. (Am. Soc. Mech. Eng.), **75**, pp. 3–8.

[15] Liou, T.-M., Yang, C.-P., and Lee, H.-L., 1997, ''LDV Measurements of Spatially Periodic Flow Over a Detached Solid-Rib Array,'' ASME J. Fluids Eng., **119**, pp. 383–389.

[16] Tanaka, M., and Kida, S., 1993, ''Characterization of Vortex Tubes and Sheets,'' Phys. Fluids A, **5**, pp. 2079–2082.

[17] Srinivasan, V., Simon, T. W., and Goldstein, R. J., 2001, ''Synopsis,'' *Heat Transfer in Gas Turbine Systems*, R. J., Goldstein, ed., The New York Academy of Science, New York, pp. 1–10.

Cooling the Tip of a Turbine Blade Using Pressure Side Holes—Part I: Adiabatic Effectiveness Measurements

J. R. Christophel

K. A. Thole

Mechanical Engineering Department,
Virginia Polytechnic Institute and State University,
Blacksburg, Virginia 24061

F. J. Cunha

Pratt & Whitney,
United Technologies Corporation,
East Hartford, Connecticut 06108

Durability of turbine blade tips has been and continues to be challenging, particularly since increasing turbine inlet temperatures is the driver for improving turbine engine performance. As a result, cooling methods along the blade tip are crucial. Film-cooling is one typically used cooling method whereby coolant is supplied through holes placed along the pressure side of a blade. The subject of this paper is to evaluate the adiabatic effectiveness levels that occur on the blade tip through blowing coolant from holes placed near the tip of a blade along the pressure side. A range of blowing ratios was studied whereby coolant was injected from holes placed along the pressure side tip of a large-scale blade model. Also present were dirt purge holes on the blade tip, which is part of a commonly used blade design to expel any large particles present in the coolant stream. Experiments were conducted in a linear cascade with a scaled-up turbine blade whereby the Reynolds number of the engine was matched. This paper, which is Part 1 of a two part series, compares adiabatic effectiveness levels measured along a blade tip, while Part 2 combines measured heat transfer coefficients with the adiabatic effectiveness levels to assess the overall cooling benefit of pressure side blowing near a blade tip. The results show much better cooling can be achieved for a small tip gap compared with a large tip gap with different flow phenomena occurring for each tip gap setting.

[DOI: 10.1115/1.1812320]

Introduction

The performance of a turbine engine is a strong function of the maximum gas temperature at the rotor inlet. Because turbine airfoils are exposed to hot gas exiting the combustion chambers, the materials and cooling methods are of critical importance. Turbine blade designers concentrate heavily on finding better cooling schemes to increase the overall operational life of all turbine airfoils, namely the high pressure turbine blades. The clearance between the blade tip and the associated shroud, also known as the blade outer air seal, provides a flow path across the tip that leads to aerodynamic losses and high heat transfer rates along the blade tip. The flow within this clearance gap is driven by a pressure differential between the pressure and suction side of the blade, but is also affected by the viscous forces as the fluid comes into contact with the walls of the gap.

The goal of the work presented in this paper is to assess a cooling hole arrangement whereby holes are placed near the tip of a blade along the pressure side. Note that holes are also located on the tip, which are dirt purge holes that are required to expel dirt from the coolant stream. Comparisons of performance were made for a range of coolant flows at two different tip gap settings. The comparisons made in this paper (Part I) have been made through measurements of the adiabatic effectiveness along the turbine blade tip. A companion paper, Part II [1], provides a full heat transfer analysis including the overall benefit of film-cooling on the tip.

Relevant Past Studies

One method for improving the thermal environment along the blade tip is to inject coolant into the tip region. In a review paper on tip heat transfer, Bunker [2] states that for a blade tip there has been very little film-cooling research reported in the literature even though film-cooling is widely used. Blowing from the tip has been considered by Kim and Metzger [3], Kim et al. [4], Kwak and Han [5,6], Acharya et al. [7] and Hohlfeld et al. [8].

Kim et al. [4] present a summary of the experimental work that D. Metzger performed on tip blowing. In addition to concluding that there is only a weak effect of the relative motion between a simulated blade and shroud on tip heat transfer coefficient, they stated that there is a strong dependency of adiabatic effectiveness on the shape of the hole and injection locations. Note that a more recent study by Srinivasan and Goldstein [9], who used an actual airfoil, also indicated a negligible effect of the relative motion between the tip and shroud on tip heat transfer coefficients with the exception being near the leading edge region. Four hole configurations were discussed by Kim et al. [4] that included the following: discrete slots located along the blade tip, round holes located along the blade tip, angled slots positioned along the pressure side, and round holes located within the cavity of a squealer tip. The studies reported by Kim et al. were performed in a channel that simulated a tip gap, whereby no blade with its associated flow field was simulated. In comparing the discrete slots to the holes, their data indicated a substantial increase in adiabatic effectiveness using the discrete slots for all blowing ratios tested. Injection from the pressure side holes provided cooling levels of similar magnitude to the holes placed on the tip. Kim et al. also reported that an increase in coolant mass flow for the discrete slots and pressure side flared holes generally yielded improved cooling to a given mass flux ratio beyond which increased coolant yielded decreased cooling effectiveness.

Kwak and Han [5,6] reported measurements for varying tip gaps with cooling holes placed along the pressure surface at a 30°

Contributed by the International Gas Turbine Institute (IGTI) of THE AMERICAN SOCIETY OF MECHANICAL ENGINEERS for publication in the ASME JOURNAL OF TURBOMACHINERY. Paper presented at the International Gas Turbine and Aeroengine Congress and Exhibition, Vienna, Austria, June 13–17, 2004, Paper No. 2004-GT-53251. Manuscript received by IGTI, October 1, 2003; final revision, March 1, 2004. IGTI Review Chair: A. J. Strazisar.

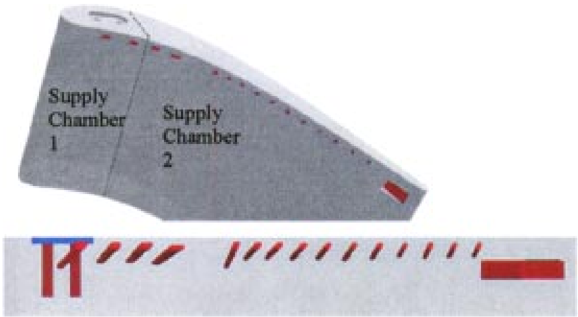

Fig. 1 Schematic showing the approximate hole placement for the tip model

breakout angle and on the tip surface at a 90 deg angle for a flat and a squealer tip geometry. They found a substantial improvement in effectiveness with the addition of a squealer tip. The coolant circulated within the squealer tip providing a better distribution of the coolant along much of the tip compared with no squealer cases. Only along parts of the suction side was the adiabatic effectiveness poor. They found that for the flat tip, good cooling was provided to the trailing edge resulting from the accumulation of coolant that exited in this area. Their results also indicated that more coolant resulted in improved effectiveness.

One of the recent computational studies by Ameri [10] indicated that a sharp edge along the pressure side (with no blowing) was more effective in reducing the tip leakage flow relative to an rounded edge. Predictions for varying tip gap sizes by Acharya et al. [8] indicated that film-cooling injection lowered the local pressure ratio and altered the nature of the leakage vortex. High film-adiabatic effectiveness and low heat transfer coefficients were predicted along the coolant trajectory with the lateral spreading of the coolant jets being quite small for all cases. With an increased tip gap the coolant was able to provide better downstream effectiveness through increased mixing. For the smallest tip gap, the coolant was shown to impinge directly on the surface of the shroud leading to high film effectiveness at the impingement point. As the gap size increased, their predictions indicated that the coolant jets were unable to penetrate to the shroud. Computational results by Hohlfeld et al. [8] indicated that as the blowing ratio is increased for a large tip gap, the tip cooling increased only slightly while the cooling to the shroud increased significantly.

In summary, there are only a limited number of studies that have addressed blowing in the tip gap region. None of these studies compared effectiveness levels for different blowing ratios from cooling holes placed along the pressure side of an actual blade geometry.

Description of Cooling Hole Configuration

Figure 1 is a schematic showing the approximate cooling hole placement along the pressure side of the turbine blade. For proprietary reasons the exact hole locations and orientations are not given. This geometry had a dirt purge cavity that was recessed two small gap heights ($2h$) and 0.67 large gap heights ($0.67H$) from the tip surface. Within this cavity were two dirt purge holes, which have been described in detail by Hohlfeld et al. [8]. In addition to the dirt purge holes, the tip geometry had 15 pressure side holes placed close to the tip surface. The four film-cooling holes just downstream of the stagnation were slightly expanded in the axial direction and had a metering hole diameter of $0.56D$, where D is the diameter of the dirt purge holes, and the remainder of the holes had no expansion with a metering hole diameter of $0.4D$. There was also a slot at the trailing edge called the trailing edge flag (TEF). Table 1 further summarizes the hole geometry in this study.

Table 1 Description of hole model

Parameter	
No. of cooling holes	15
Coolant flow area (dirt purge, cooling holes, andTEF) (cm^2)	5.15
Hole metering area/Coolant flow area	0.51
Dirt purge flow area/Coolant flow area	0.33
TEF flow area/Coolant flow area	0.16

To ensure good control on the blowing ratios through the holes, which will be further discussed in the next section, a dividing wall was placed within the blade cavity to allow for two different supplies inside the blade. The tip model had the separating wall placed after the second cooling hole downstream of the stagnation location. These two different supply cavities are also illustrated in Fig. 1. Each cavity was supplied by a separate coolant flow source such that independent control of the coolant flow rates could be achieved. The placement of the supply cavities was based on best matching to the local blowing ratios of the engine.

Outlines of the holes were made from stereo lithography (SLA) to allow for a good replication of the hole geometry. Because the SLA material does not have a sufficiently low thermal conductivity, the models were designed to have foam molded around the holes and supply chambers. After the SLA model of the hole outlines were made, the SLA model was placed inside a mold of the blade geometry. A polyurethane foam compound, with a thermal conductivity of 0.04 $\text{W/m}^2\,\text{K}$, was poured in the blade mold and then allowed to expand and harden. The combined SLA holes and foam blade were then removed from the mold, attached as the tip to an SLA blade, and then placed in the wind tunnel for testing. The molded tip model extended 28% of the blade span. Pictures of the combined SLA hole model and foam blade for the holes are shown in Fig. 2.

Experimental Facilities

The experimental facility for this work consisted of a large-scale, low-speed, closed-loop wind tunnel providing an inlet velocity to the test section of 12 m/s to match engine Reynolds number conditions for a 12× blade model. The blade geometry and flow conditions are summarized in Table 2 with a diagram of the wind tunnel and test section shown in Figs. 3(*a*) and 3(*b*). Starting at the fan, flow passed through a primary heat exchanger to obtain a uniform temperature profile before being divided into three passages. The main passage, located in the center, has a heater that was used to achieve hot mainstream gas, while flow to the two auxiliary passages was used to supply a single row of high momentum jets used to generate a high turbulence level to the cascade. The inlet turbulence level, measured one chord upstream, was 10% and the length scale was 11 cm. Flow entered the test section, consisting of the blade model as shown in Fig. 3(*b*). An independent compressed air supply provided the coolant flow to the two cavities, which was ultimately injected through cooling holes placed in the blade tip.

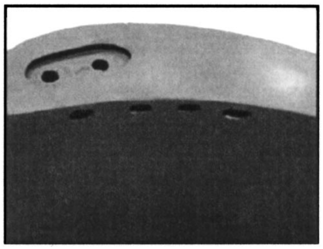

Fig. 2 Photo of SLA/foam model for the dirt purge and cooling holes

Table 2 Blade geometry and flow conditions

Parameter	Wind tunnel settings
Scaling factor	12×
Axial chord/True chord	0.66
Pitch/True chord	0.81
Span/True chord	1.03
Re_{in}	2.1×10^5
Inlet Angle, θ	16.5 deg
Coolant to Mainstream ΔT (°C)	25
Small tip gap/Span (%)	0.54
Large tip gap/Span (%)	1.63

The blade test section consisted of a two passage linear cascade as shown in Fig. 3(*b*). Velocity measurements were taken approximately one chord upstream at a number of pitch-wise locations to verify a uniform incoming velocity field. Static pressure taps were located near the mid-span of the central blade to compare the pressure distribution around the blade to that of an inviscid CFD prediction with periodic boundary conditions. Matching the pressure distribution around the blade ensured equal flow distribution between each of the respective flow passages, and ensured the correct driving pressures across the tip gap. The nondimensional pressure distributions for the central blade are shown in Fig. 4 for representative large and small tip gap settings. Also shown on this graph is the placement of the supply chambers separating the front and back set of holes as well as the stagnation location ($S/S_{max}=0$). Negative values of S/S_{max} are on the pressure side.

Because coolant was supplied to two independently controlled plenums, which also included the supplies for the dirt purge holes and TEF, a number of experiments were conducted to deduce a discharge coefficient for each cooling component to ensure correct cooling flows were ultimately set. The tip had four cooling components: (i) front plenum film-cooling holes, (ii) dirt purge holes, (iii) back plenum film-cooling holes, and (iv) TEF. The discharge coefficients were found by isolating each component while the other three components were sealed. By measuring the supply chamber pressure, the calculated flow rate could be compared to that of the measured flow rate using a venturi flow meter.

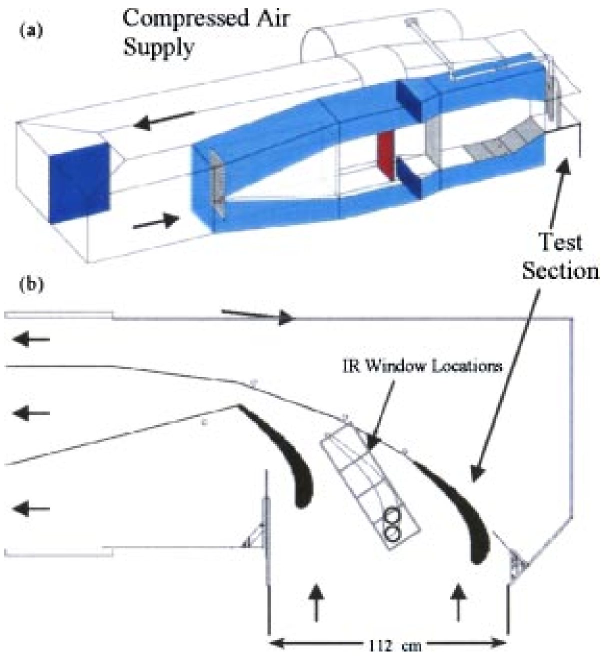

Fig. 3 Schematic of (*a*) wind tunnel facility and (*b*) test section for the blade tips

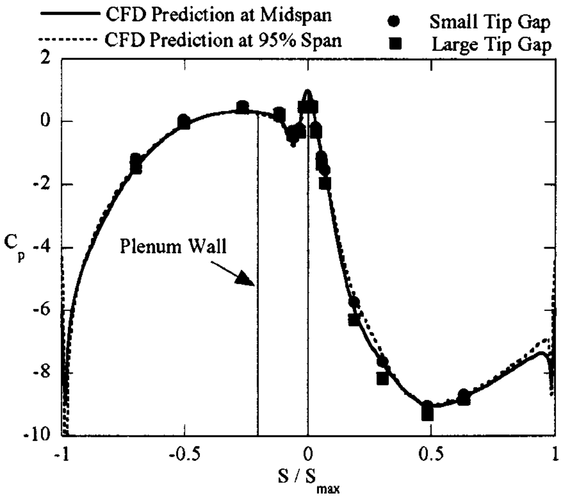

Fig. 4 Predicted and measured static pressure distributions for the large and small tip gap cases

The measured discharge coefficients for the cooling holes are shown in Fig. 5. The front and back holes of the tip model approached nominally the same value ($C_d=0.64$), which is expected because the hole geometries were very similar. As a check on the accuracy of using the previously described method for setting the coolant flows, a comparison was made between the total coolant flow to the entire tip measured using the venturi flow meter and that calculated using the measured pressures combined with the discharge coefficients. The coolant mass balance was within 2.8% for all experimental cases.

Several parameters were considered when comparing the low speed wind tunnel tests to that of an actual engine. A matrix of tests was designed to assess the effects of the blowing ratio, momentum flux ratio, and tip gap setting. The flow split for each of the cases is given in Table 3. For the blowing ratios given for the holes, local values of the external velocity and mass flux through the hole were used. To compute the local external velocity at each hole exit, the predicted static pressure at the 95% span location of the blade (also shown on Fig. 4) was used at each hole location. The coolant velocity through the holes was based on the velocity at the metering area of the hole. The local blowing ratios that were tested are shown in Fig. 6. The density ratio of the jet to mainstream used during testing was 1.08.

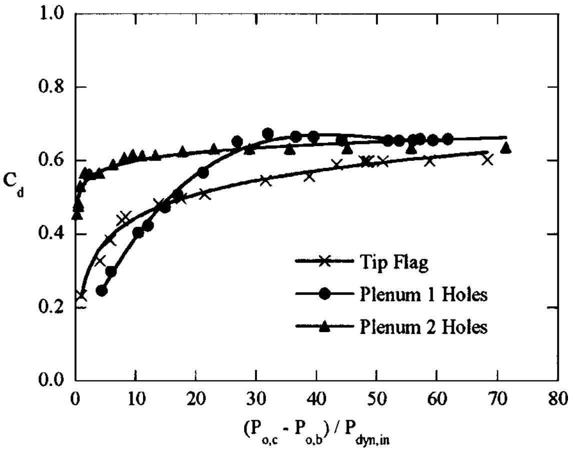

Fig. 5 Discharge coefficients that were measured for the cooling holes, dirt purge holes, and TEF

Table 3 Matrix of experiments

Gap. setting	Total coolant flow (% passage)	Flow split plenums 1/2 (% coolant)
Small, Large	0.47	58/42
Small, Large	0.58	59/41
Small, Large	0.68	59/41
Small, Large	1.0	51/49
Small no dirt purge flow	0.07	100/0

The four nominal total coolant flow rates were 0.47%, 0.58%, 0.68%, and 1.0%. These percentages are given relative to the mainstream passage flow through the blades. In Fig. 6, the blowing ratios are shown for the small tip gap. There was no difference in the blowing ratios with gap height. Figure 7 provides the percentage difference between the CFD predicted and measured distribution of coolant for the 0.68% cooling flow case through each of the film holes, the dirt purge holes, and TEF. Note that the 0.68% refers to the total coolant flow relative to the total blade passage flow. There was good agreement between the individual flow rates for each hole as predicted by CFD and calculated experimentally using the discharge coefficients and measured pressures. The comparisons indicated that the largest difference was 0.45%, which occurred for the fourth cooling hole.

Experimental Methodology. Investigation of the hole geometries required obtaining surface temperatures on the foam model, representing the adiabatic surface temperatures along the tip. Typical operating conditions consisted of a temperature differential between the coolant flow and hot mainstream by approximately 25°C. The mainstream and coolant supply chamber temperatures were measured during the experiments with type E thermocouples. The coolant temperatures were measured inside the two plenums. Each test required the wind tunnel and tip models to reach a thermal equilibrium, which required approximately 4 h. Temperatures and flows were monitored during this time to ensure equilibrium conditions. The tip gaps were set by raising or lowering the blade using a threaded rod to the gap setting. This technique required the use of a precisely machined plate placed under the tip to ensure the correct gap.

The tip surface temperatures were obtained using an Inframetrics P20 infrared (IR) camera. The images were processed with Thermacam Researcher 2002® and an in-house MATLAB code. As shown by the boxes in Fig. 3(*b*), four IR images were acquired through the zinc selenide windows placed in the shroud surface to cover the entire blade, which transmitted the radiation. Each image covered an area that was 21.3 cm by 16 cm and contained 320 by 240 pixels. The camera was located approximately 55 cm from the tip and resulted in a spatial resolution of 0.63 mm. For every test, each of the four images was taken five times and the averaged radiation values were used.

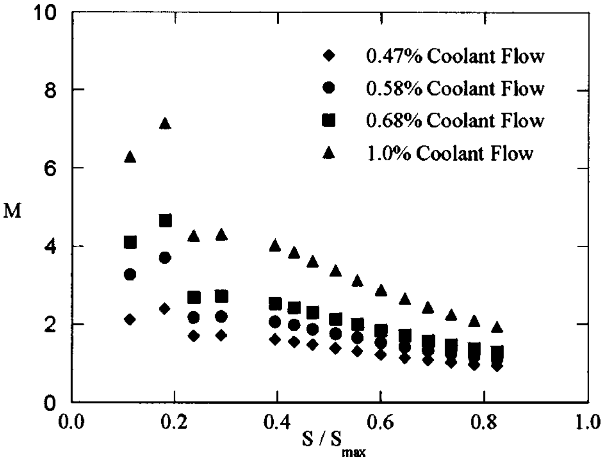

Fig. 6 Local mass flux ratios for each of cooling holes placed on the pressure side of the blade

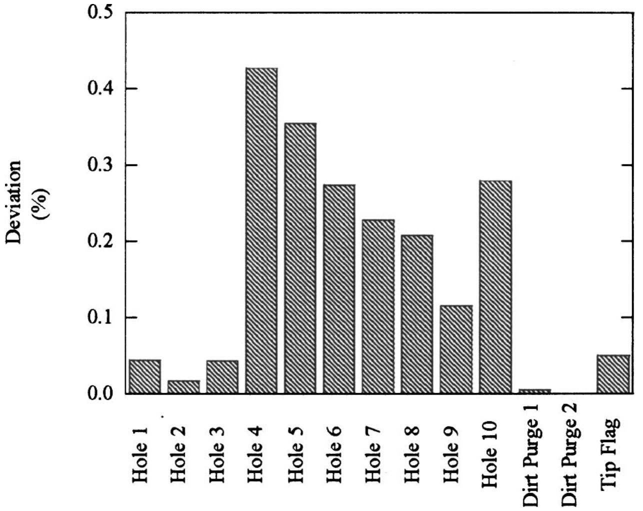

Fig. 7 Percent difference between computational and experimental flow rates at 0.68% coolant flow

The calibration process for the camera required direct comparisons of measured surface temperatures, using thermocouple strips placed on the tip surface, with the infrared radiation collected by the camera. Thermocouple strips were used to ensure accurate surface temperatures were measured. These strips were placed on the blade tip using a thermally conducting bonding agent. After the experiments were completed, the infrared image was processed whereby the emissivity and background temperature of the infrared pixels nearby the surface thermocouple were adjusted to ensure agreement between the measured temperatures. Each of the four images was processed in a similar manner whereby six thermocouples were ultimately used to ensure all four images were accurately calibrated. An emissivity of 0.83 was used for all the images while the background temperatures were adjusted to ensure a calibrated image. This process resulted in an agreement between all of the thermocouples and infrared temperatures to within 1.0°C, thereby giving a difference in effectiveness of η of ± 0.04.

Overall uncertainties were calculated for nondimensional adiabatic effectiveness levels (η) according to the partial derivative method described in Moffat [11]. The total uncertainty of all measurements was calculated as the root of the sum of the squares of the precision uncertainty and the bias uncertainty. The precision uncertainty for measurements made with the infrared camera was determined through an analysis of five calibrated images taken in succession on one portion of the tip at constant conditions. The precision uncertainty was calculated to be 0.31°C, which is the standard deviation of the five readings based on a 95% confidence interval. The camera manufacturer reported the bias uncertainty as 2.0% of the full scale. The largest scale used in this study was 20°C though some images could be captured on a 10°C range. The thermocouples measuring the free-stream and coolant temperatures were reported by the manufacturer to read within ±0.2°C. The total uncertainty in effectiveness was found to be $\partial\eta = \pm 0.046$ at $\eta = 1$ and $\partial\eta = \pm 0.046$ at $\eta = 0.2$.

Computational Methodology. To better understand the effects of these hole shapes, computational fluid dynamics (CFD) simulations were also performed. A commercially available CFD code, Fluent 6.0 [12], was used to perform all simulations. Fluent is a pressure-based flow solver that can be used with structured or unstructured grids. An unstructured grid was used for the study presented in this paper. Solutions were obtained by numerically solving the Navier–Stokes and energy equation through a control volume technique. All geometric construction and meshing were performed with GAMBIT. To ensure a high quality mesh, the flow passage was divided into multiple volumes, which allowed for more control during meshing. The tip gap region was of primary concern and was composed entirely of hexahedral cells with an aspect ratio smaller than three.

Computations were performed on a single turbine blade exposed to periodic conditions along all boundaries in the pitch direction. Inlet conditions to the model were set as a uniform inlet velocity at approximately one chord upstream of the blade. An inlet mass flow boundary condition was imposed for the coolant at the plenum entrance for the cooling holes. The mesh contained approximately 20 grid points across the hole exit. Mainstream flow angles were set to those of the experiments as well as the scaled values for the engine while the turbulence levels and mixing length were set to 1% and 0.1 m, respectively. Computations were also performed with an inlet turbulence level of 10%, but no noticeable differences were predicted between the 1% and 10% inlet turbulence cases. All other experimental conditions were matched in the simulations including the temperature levels and flow rates.

To allow for reasonable computational times, all computations were performed using the RNG k-ε turbulence model with nonequilibrium wall functions whereby the near-wall region was resolved to y^+ values ranging between 30 and 60. Mesh insensitivity was confirmed through several grid adaptions based on viscous wall values, velocity gradients, and temperature gradients. Typical mesh sizes were composed of 1.8 million cells with 50% of the cells in and around the tip gap region. After adapting from a mesh of 1.7×10^6 to 2.2×10^6, the pitchwise-averaged effectiveness predictions on the tip were found to vary by only $\delta\eta=\pm0.007$ at a level of $\eta=0.40$. Typical computations required 1200 iterations for convergence.

Experimental Results for a Range of Blowing Ratios

Contour plots of local adiabatic effectiveness levels are given in this section to show the cooling trends for the two tip gaps for a range of cooling flow conditions. Adiabatic effectiveness levels of one note that the local wall temperature is at the coolant temperature while levels of zero refer to the hot gas temperature. To quantify the differences, data have been compared along various lines across the tip. These comparisons were made along different trajectory lines of the cooling jets (lines 1 and 2) and between the cooling jets (line 3) near the middle of the blade tip. Lines 1 and 2, referred to as line data, have been identified as locations having maximum effectiveness levels while line 3 is between two jet trajectories in the mid-chord region. A third comparison was made along the blade camber line as shown in the illustration of Fig. 8.

Comparisons for the Small Tip Gap. Figure 9 shows the measured adiabatic effectiveness levels along the blade tip for the small tip gap. Note that the exit of one hole location in the mid-chord region is indicated by a black dot along the pressure side. For proprietary reasons not all hole locations are disclosed. As will be discussed later in this text, the location of the cooling hole and the maximum effectiveness levels are not collocated. Although the results are only shown for one cooling hole, this result is representative of all cooling holes. For all cases shown in Fig. 9, the entire leading edge region is nearly completely cooled by the dirt purge holes. This leading edge area shows essentially no change as this entire region is saturated by coolant.

As the blowing ratio is increased for the small tip gap, Fig. 9 shows that there is relatively little increase in effectiveness or in coolant spreading. The effectiveness levels indicate a streaky nature, which is caused by the high momentum jets exiting the cooling holes. As will be discussed later in the text, while the effectiveness contours indicate little improvement in the global cooling characteristics along the blade tip with increased coolant flow, peak effectiveness levels along jet trajectories do increase with increased coolant flow.

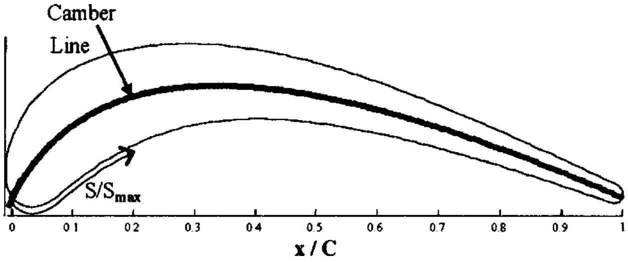

Fig. 8 Location and description of line data taken along blade tip

For the lowest coolant flow (0.47%) case, the effectiveness levels at the trailing edge show that the trailing edge is actually cooler at the lowest coolant flow. The higher effectiveness for the lower coolant flow is because the momentum flux ratios of these jets exiting the trailing edge holes are low, as indicated in Fig. 6 for the 0.47% cooling flow case, resulting in a cooler gap flow along the tip of the blade. This phenomena can be better understood by comparing the hole exit location to the jet trajectory. The upstream cooling hole jets are being swept downstream of the hole exit before entering the tip region. The reason for this is twofold: first, the cooling jets have a high enough momentum to overcome the driving pressure across the tip gap and, second, the jet injection angle forces the jets to follow the pressure side of the blade.

Computations were performed for the small tip gap for a total coolant flow of 0.58% to verify these flow patterns. Path lines exiting the holes are given in Fig. 10. In the mid-chord region, jets appear to be swept downstream before being carried over the tip. The predictions also indicate several jet trajectories where the coolant remains along the pressure side of the blade for most of the blade before entering into the downstream gap region. The holes in the leading edge have the highest blowing ratio, relative

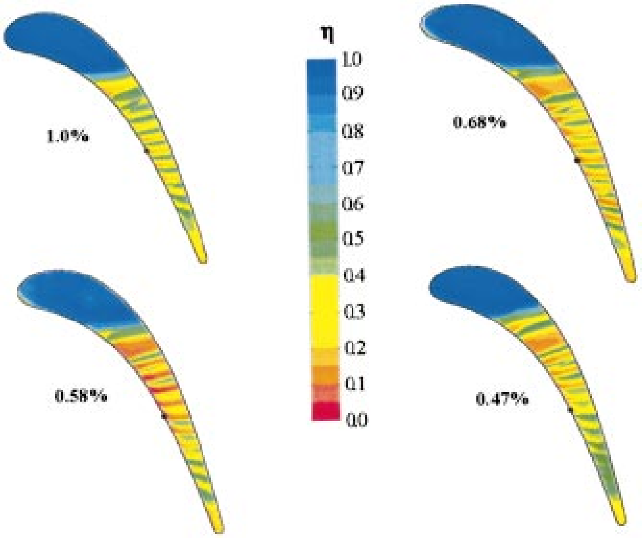

Fig. 9 Measured adiabatic effectiveness levels on the tip for the small tip gap

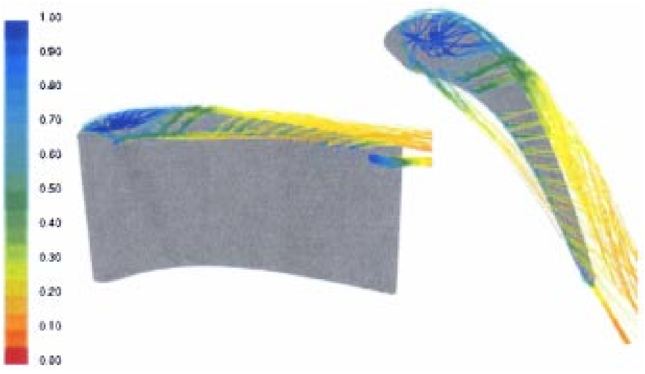

Fig. 10 Predicted path lines for the 0.58% coolant flow at the small tip gap

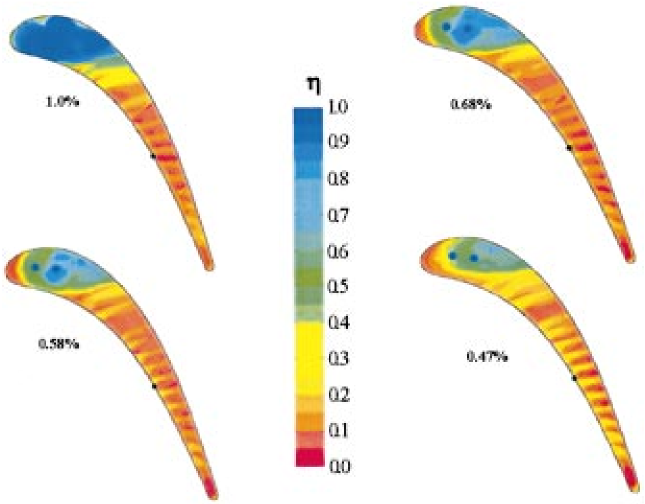

Fig. 12 Measured adiabatic effectiveness levels for the large tip gap

to the rest of the blade, so the prediction of jets following the blade pressure side rather than entering into the tip gap is expected.

Camber line comparisons for the small tip gap are shown in Fig. 11. Note that the distance x is shown as the abscissa of the graph illustrated in Fig. 8. For the same total coolant flow rate, the dirt purge flow dominates to $x/C=0.3-0.4$. For $x/C>0.6$, the effectiveness levels show relatively similar levels for both coolant flows with peaks and valleys ranging between 0.5 and 0.3. It is also interesting to note that the peak effectiveness levels for the two coolant flow conditions do not coincide. The peak for the 1% coolant flow occurs downstream of that for the 0.58% coolant flow. This is consistent with the jets having the higher blowing ratios being swept further downstream before entering the tip gap.

Comparisons for the Large Tip Gap. For the large tip gap results, shown in Fig. 12, the effectiveness levels are much lower than for the small tip gap (Fig. 9). The largest difference relative to coolant flow rates is near the dirt purge holes with better effectiveness levels at higher coolant flow levels. In particular, the largest improvement occurs for the 1% coolant flow condition with nearly perfect cooling of the entire leading edge.

In the mid-chord region, however, the results indicate a worse performance, as shown in Fig. 12, as the coolant flow is increased from of 0.47% to 1%. The reason for the worse performance at high blowing ratios is because the high momentum cooling jets are impinging upon the shroud and are not effective in cooling the blade tip, but are most likely effective in cooling the outer shroud. As the coolant levels are increased, the jet penetration above the blade tip severely reduces the cooling capabilities of the jet along the tip. The hole locations given on these contour plots show the same results as seen with the small tip gap in that the peak effectiveness levels are located downstream of the injection location.

The camber line data for the large tip gap, shown in Fig. 13, indicate no cooling benefit beyond $x/C=0.4$ as the coolant is increased from 0.58% to 1%. In fact, the average appears to be similar for the two blowing cases with the exception that the 0.58% case has higher peaks and valleys than the 1% case. Similar to that of the small tip gap, the peaks in effectiveness are located further downstream for the 1% case relative to the 0.58% case.

Comparisons of Individual Holes. Figures 14(*a*)–(*c*) show line data of the effectiveness levels at blowing ratios of 0.58% and 1.0%. Note that the distance along the tip (L) was normalized with the maximum distance along the tip ($L_{\max}$). Recall lines 1 and 2 are pathlines along the maximum effectiveness levels while line 3 is mid-way between pathlines of maximum effectiveness levels.

For each of the three positions shown in Figs. 14(*a*)–(*c*), the adiabatic effectiveness always increases with coolant flows for the small tip gap. These results indicate that the cooling potential is higher with higher coolant flows for the small tip gap. Even though the momentum flux ratios of the jets increase for increased coolant flow levels, the tip gap is small enough that coolant is forced to also be present along the blade tip.

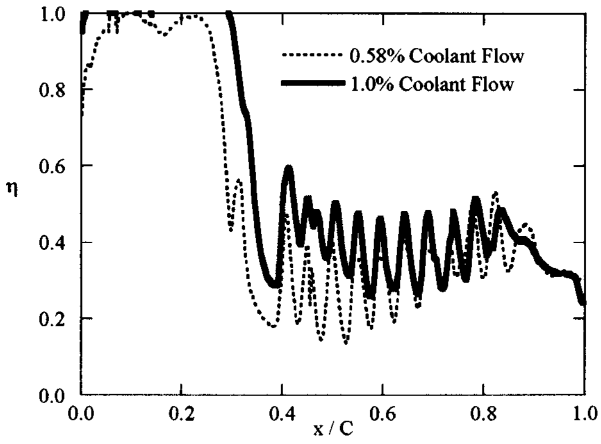

Fig. 11 Data taken along the camber line for the small tip gap at two blowing ratios

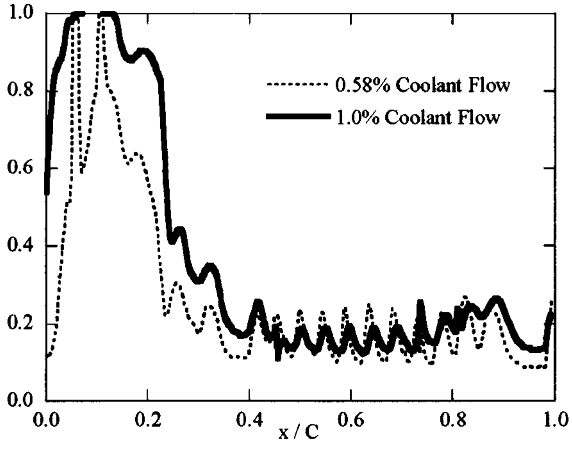

Fig. 13 Data taken along the camber line for the large tip gap

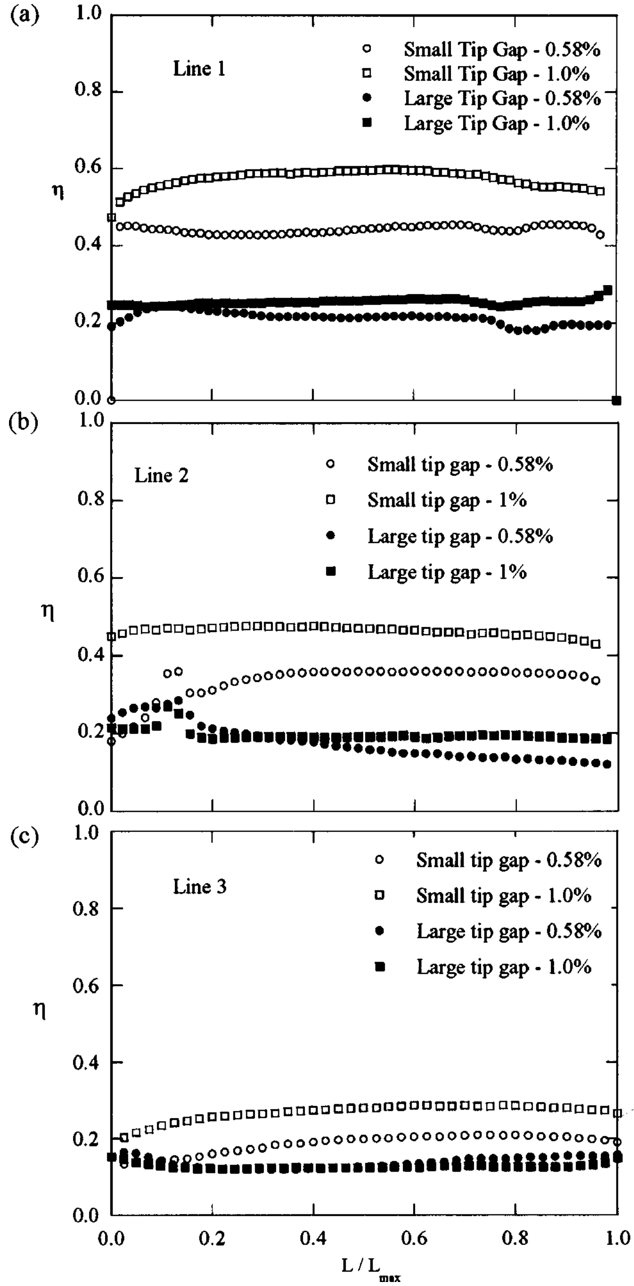

Fig. 14 (*a*)–(*c*) Line data for the different cases

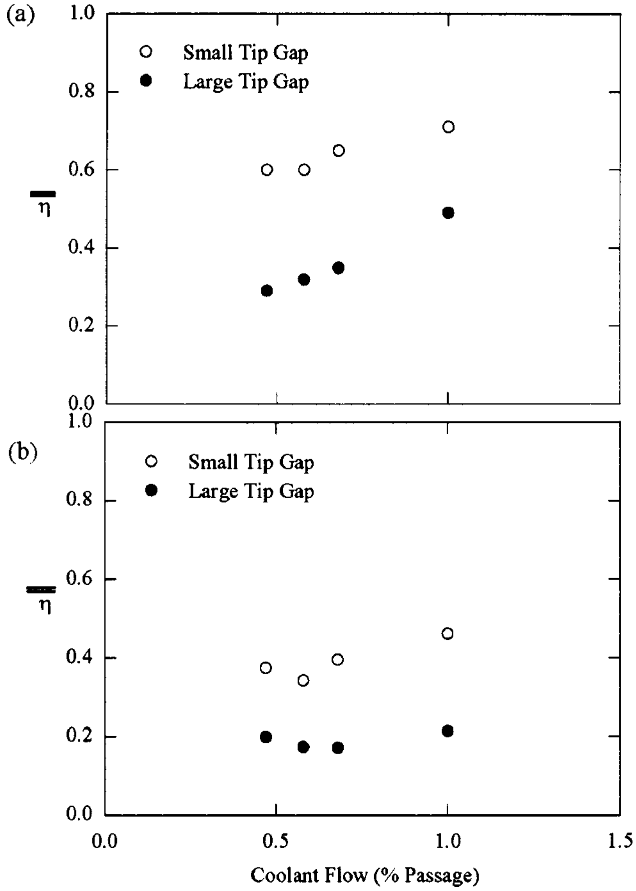

Fig. 15 Area-averages for (*a*) the entire blade tip and (*b*) the downstream 70% of blade

For the large tip gap, however, the same trend is not true as shown by Figs. 14(*a*)–(*c*). There are actually some segments of the blade where the effectiveness is higher with a lower blowing ratio, especially near the pressure side ($L/L_{\max}<0.2$). The reason for this is because at the lower blowing ratios the coolant remains more attached to the blade tip. At higher blowing ratios, the coolant becomes separated from the blade tip and instead cools the outer shroud. Figure 14(*c*) shows data taken between two coolant trajectories. There is essentially no difference with increased blowing for the large tip gap, but a slight increase for the small tip gap because coolant fills the small gap region.

Area-averaged film effectiveness results were calculated using two different areas to make overall conclusions about the testing performed, as shown in Figs. 15(*a*) and 15(*b*). Figure 15(*a*) shows area-averaged effectiveness values for the entire tip while Fig. 15(*b*) shows area-averaged effectiveness values for the downstream 70% of the blade tip to better illustrate the performance of the cooling holes alone (without the effect of the dirt purge holes). Figure 15(*a*) indicates a relatively constant increase in area-averaged effectiveness with coolant flow increase for the large tip gap, but little increase in effectiveness for the small tip gap. The reason for this is because of the increase in effectiveness occurring near the dirt purge holes for the large tip gap. Recall that for the small tip gap, the coolant nearly saturated the leading edge region for all blowing ratios considered. Figure 15(*a*) also shows the overall trend that higher effectiveness levels occur for the smaller tip gap relative to the large tip gap.

Since much of the blade is dominated by dirt purge cooling, a better comparison on the effects of blowing from the pressure side holes can be made by considering the downstream 70% of the blade, as shown in Fig. 15(*b*). While the small tip gap shows a slight decrease with an increase in coolant flow for the first two conditions, beyond that there is an increase in effectiveness with increased coolant flow. For the large tip gap, the area averages indicate a slight decrease with increased coolant flow, which is then followed by only a slight increase in area-averaged effectiveness with values for the 0.47% and 1% coolant flows being at nearly the same level.

Leading Edge Blowing With no Dirt Purge Blowing. Because the dirt purge blowing overwhelms a large portion of the leading edge region, an additional test was conducted whereby coolant from only the film-cooling holes was exhausted in the leading edge (no dirt purge blowing). This case is also relevant from an engine operational standpoint whereby the dirt purge holes may be closed due to rubbing on the shroud. The coolant flow for this case was set to be the coolant exhaust that resulted for the 0.68% case subtracting out the dirt purge, tip flag, and back supply chamber cooling. This resulted in a total coolant flow of

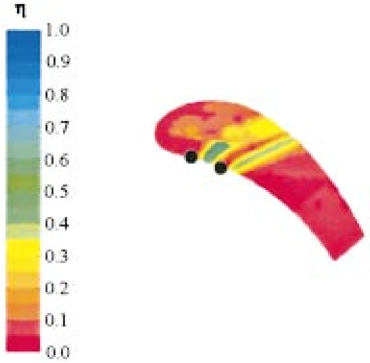

Fig. 16 Effectiveness contours with no dirt purge blowing with 0.07% coolant flow for the large tip gap

0.07% being injected from the first two holes. Figure 16 shows the measured results of this test for a small tip gap. Note that while the dirt purge holes were not flowing, the cavity was still present. The results for this test indicate that the coolant is being brought into the dirt purge cavity and then mixed with hot mainstream fluid before exiting at a much higher temperature. The hole locations indicate that in the leading edge region, without dirt purge blowing, the coolant is swept significantly further downstream of their respective hole exits.

Conclusions

The conclusions reached from these tests indicate that the performance of cooling holes placed along the pressure side tip was better for a small tip gap than for a large tip gap. Disregarding the area cooled by the dirt purge holes, for a small tip gap the cooling holes provided relatively good coverage. For all of the cases considered, the cooling pattern was quite streaky in nature, indicating very little spreading of the jets.

As the blowing ratio was increased for the small tip gap, there was an increase in the local effectiveness levels resulting in higher maxima and minima of effectiveness along the middle of the blade. The small tip gap results also indicated that the coolant was swept further downstream of the hole along the pressure side of the blade prior to entering the tip gap for higher coolant flows, particularly those holes in the leading edge region. In fact, computational predictions and measured effectiveness levels for the low coolant flows indicated that the jets exited into the pressure side passage following the pressure side of the blade until the trailing edge of the blade at which point the coolant entered the tip gap. Although the local momentum flux ratio of the jets increased with increased coolant flow, the coolant still appeared to cool the blade tip, which was different from that of the large tip gap.

For the large tip gap, the data indicated that the adiabatic effectiveness levels decreased, or remained relatively constant, as the coolant flow was increased. As the coolant flow was increased the jets most likely impacted and cooled the outer shroud of the large tip gap rather than the blade tip. The distance between the blade tip and outer shroud were far enough apart that there was little cooling benefit to the blade. These results indicate the importance not only from an aerodynamic loss standpoint but also a thermal standpoint of keeping the tip gap small.

Acknowledgments

The authors gratefully acknowledge United Technologies–Pratt and Whitney for their support of this work.

Nomenclature

C = true chord of blade
C_d = discharge coefficient, $C_d = \dot{m}/(\rho A \sqrt{(2/\rho)(P_{0,c} - p_e)})$
C_p = pressure coefficient, $C_p = (p - p_{in})/(\rho U_{in}^2/2)$
D = dirt purge hole diameter
D_h = hydraulic diameter, set as twice the gap height
h, H = small and large gap distances
L = distance along the path line across the tip
M = mass flux ratio
P_o, p = total and static pressures
$\mathrm{Re}_{\mathrm{in}}$ = Reynolds number defined as $\mathrm{Re}_{\mathrm{in}} = CU_{in}/\nu$
S = distance along blade pressure side from stagnation
T = temperature
U = measured air velocity
x = distance along the blade chord

Greek

Δ = denotes a differential
η = adiabatic effectiveness, $\eta = (T_{\mathrm{in}} - T_{\mathrm{aw}})/(T_{\mathrm{in}} - T_c)$
ρ = density
ν = kinematic viscosity

Subscripts

aw = adiabatic wall
b = blade
c = coolant conditions
dyn = dynamic
in, e = value at 1C upstream of blade, exit
max = denotes maximum value

References

[1] Christophel, J., Thole, K. A., and Cunha, F., 2005, "Cooling the Tip of a Turbine Blade Using Pressure Side Holes—Part II: Heat Transfer Measurements," ASME J. Turbomach. **127**, pp. 278–286.
[2] Bunker, R. S., 2000, "A Review of Turbine Blade Tip Heat Transfer," Turbine 2000 Symposium on Heat Transfer in Gas Turbine Systems, Cesme, Turkey.
[3] Kim, Y. W., and Metzger, D. E., 1995, "Heat Transfer and Effectiveness on Film Cooled Turbine Blade Tip Models," ASME J. Turbomach., **117**, pp. 12–21.
[4] Kim, Y. W., Downs, J. P., Soechting, F. O., Abdel-Messeh, W., Steuber, G., and Tanrikut, S., 1995, "A Summary of the Cooled Turbine Blade Tip Heat Transfer and Film Effectiveness Investigations Performed by Dr. D. E. Metzger," ASME J. Turbomach., **117**, pp. 1–11.
[5] Kwak, J. S., and Han, J. C., 2002, "Heat Transfer Coefficient and Film-Cooling Effectiveness on a Gas Turbine Blade Tip," GT2002-30194.
[6] Kwak, J. S., and Han, J. C., 2002, "Heat Transfer Coefficient and Film-Cooling Effectiveness on the Squealer Tip of a Gas Turbine Blade," GT2002-30555.
[7] Acharya, S., Yang, H., Ekkad, S. V., Prakash, C., and Bunker, R., 2002, "Numerical Simulation of Film Cooling Holes on the Tip of a Gas Turbine Blade," GT-2002-30553.
[8] Hohlfeld, E. M., Christophel, J. R., Couch, E. L., and Thole, K. A., 2003, "Predictions of Cooling From Dirt Purge Holes Along the Tip of a Turbine Blade," GT2003-38251.
[9] Srinivasan, V., and Goldstein, R. J., 2003, "Effect of Endwall Motion on Blade Tip Heat Transfer," ASME J. Turbomach., **125**, pp. 267–273.
[10] Ameri, A. A., 2001, "Heat Transfer and Flow on the Blade Tip of a Gas Turbine Equipped With a Mean-Camberline Strip," 2001-GT-0156.
[11] Moffat, R. J., 1988, "Describing the Uncertainties in Experimental Results," Exp. Therm. Fluid Sci., **1**, pp. 3–17.
[12] Fluent Inc., Fluent User's Guide, Version 6.0, 2002 (Fluent Inc., New Hampshire).

Cooling the Tip of a Turbine Blade Using Pressure Side Holes—Part II: Heat Transfer Measurements

J. R. Christophel

K. A. Thole

Mechanical Engineering Department,
Virginia Polytechnic Institute and State University,
Blacksburg, VA 24061

F. J. Cunha

Pratt & Whitney,
United Technologies Corporation,
East Hartford, CT 06108

The clearance gap between a turbine blade tip and its associated shroud allows leakage flow across the tip from the pressure side to the suction side of the blade. Understanding how this leakage flow affects heat transfer is critical in extending the durability of a blade tip, which is subjected to effects of oxidation and erosion. This paper is the second of a two-part series that discusses the augmentation of tip heat transfer coefficients as a result of blowing from film-cooling holes placed along the pressure side of a blade and from dirt purge holes placed on the tip. For the experimental investigation, three scaled-up blades were used to form a two-passage, linear cascade in a low-speed wind tunnel. The rig was designed to simulate different tip gap sizes and film-coolant flow rates. Heat transfer coefficients were quantified by using a constant heat flux surface placed along the blade tip. Results indicate that increased film-coolant injection leads to increased augmentation levels of tip heat transfer coefficients, particularly at the entrance region to the gap. Despite increased heat transfer coefficients, an overall net heat flux reduction to the blade tip results from pressure-side cooling because of the increased adiabatic effectiveness levels. The area-averaged results of the net heat flux reduction for the tip indicate that there is (i) little dependence on coolant flows and (ii) more cooling benefit for a small tip gap relative to that of a large tip gap. [DOI: 10.1115/1.1811096]

Introduction

Technical advancements in the gas turbine industry require higher turbine rotor inlet temperatures to allow for more efficient operation and engine performance. Inlet temperatures to the rotor are, however, the limiting design criteria because these temperatures, in turn, decrease component life for the same material and cooling technology. Gas turbine airfoils are typically cooled using both convective and film cooling. Film cooling is a method whereby cooler compressor fluid is injected through film holes in the blade surface. This type of protection is important for a turbine blade tip where the heat transfer coefficients can be over two times greater than those on the pressure side of the blade [1]. As such, film-cooling holes can be placed on the pressure side of a turbine blade near the tip region. Because of the pressure-driven flow over the tip, the coolant from these holes sweeps over the tip through the gap clearance thereby providing coolant along the blade tip.

The purpose of this study was twofold. The first part examined the heat transfer on a flat blade tip without cooling to verify fundamental trends. The second part examined the heat transfer coefficients for two different tip gap settings and a range of coolant flows for blowing through combined pressure-side and dirt purge holes. The results from this study were combined with adiabatic effectiveness results from Part I [2] to evaluate the overall benefit of the tip cooling.

Past Relevant Studies

As early as 1982, Mayle and Metzger [3] showed that the tip leakage flow is composed primarily of mainstream passage fluid. Other researchers showed a separation bubble formation along the tip pressure side, which was confirmed by Morphis and Bindon [4]. Bindon [5] went on to show that this separation bubble dominates the gap flow characteristics and associated pressure losses. In his recent review of turbine blade tip heat transfer, Bunker [6] noted that this separation bubble causes a heat transfer enhancement factor of two to three times above that occurring at the tip camber line of an airfoil.

In an effort to reduce the tip leakage flow, many studies have been performed on blade tips with a squealer geometry. This geometry has been shown to significantly reduce the blade tip heat transfer; however, the trends seen on a flat tip are much different from a tip with a squealer cavity. Bunker et al. [7], using a recessed shroud, showed the first experimental heat transfer results on a flat blade tip. His research showed there to be a small area of low heat transfer located near the thickest part of the blade. This low region has been confirmed by many authors, including Kwak and Han [1] and Jin and Goldstein [8]. Kwak and Han [1] also noted that the area of low heat transfer tends to be smaller and pushed downstream at increased gaps.

Azad et al. [9], Teng et al. [10], Kwak and Han [11], and Jin and Goldstein [8] have all shown that the blade tip heat transfer increases with increasing tip gap height. This increase can be explained by the fact that larger gap heights reduce the path length to hydraulic diameter ratio (L/D_h), thereby causing more of the tip surface to be affected by the entry region effects for larger gap heights. For a flat tip with no blowing, Jin and Goldstein [8] showed that the average heat transfer increases along the blade toward the trailing edge. This increase was confirmed by Saxena et al. [12] who showed that the heat transfer along the blade camber line increased toward the trailing edge. One of the recent computational studies by Ameri [13] indicated that a sharp edge along the pressure side (with no blowing) was more effective in reducing the tip leakage flow relative to a rounded edge.

There have been relatively few studies with blowing over a blade tip surface. Kim and Metzger [14] and Kim et al. [15] measured the heat transfer coefficients along a channel representing a blade tip with various film-cooling injection geometries. They showed that injection always led to increases in heat transfer over no injection over most of their surface simulating a blade tip (except their round hole injection, which showed no change). Kwak and Han [11] used an airfoil shape with both tip and pressure-side

---

Contributed by the International Gas Turbine Institute (IGTI) of THE AMERICAN SOCIETY OF MECHANICAL ENGINEERS for publication in the ASME JOURNAL OF TURBOMACHINERY. Paper presented at the International Gas Turbine and Aeroengine Congress and Exhibition, Vienna, Austria, June 13–17, 2004, Paper No. 2004-GT-53254. Manuscript received by IGTI, October 1, 2003; final revision, March 1, 2004. IGTI Review Chair: A. J. Strazisar.

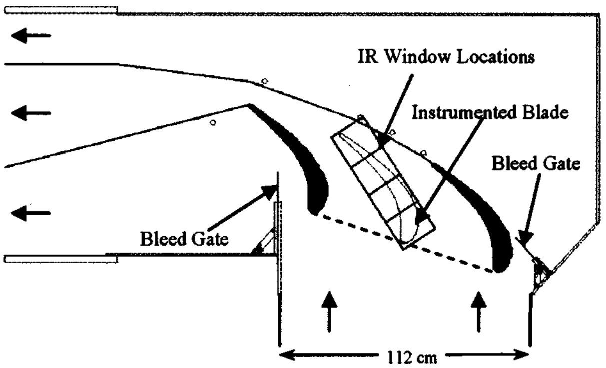

Fig. 1 Test section viewed from top showing adjustment capabilities and infrared windows

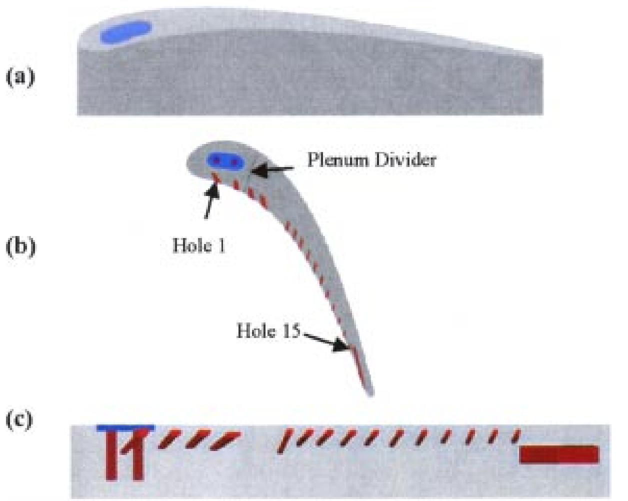

Fig. 2 Tip geometries tested: (*a*) the baseline geometry (filled-in dirt purge holes) and (*b*),(*c*) approximate hole geometry with the dirt purge holes

injection. Their results indicated a decrease in heat transfer coefficients with increased blowing between the pressure-side edge and camber line.

Generally, tip heat transfer studies without injection have all shown that increasing the tip gap increases heat transfer. Also, regions of low heat transfer are expected near the thickest portions of the blade. When coolant injection is introduced, however, the results are still unclear. This study will assess the effects of blowing ratio and tip gap height on tip heat transfer when blowing is present near the pressure-side tip combined with dirt purge holes.

Experimental Facility and Instrumentation

The experiments in this study were performed in a large-scale, low-speed, closed-loop wind-tunnel facility that provided matched-engine Reynolds number conditions, as described in Part 1 [2]. The test section was attached downstream of a contraction section that used a row of high-momentum normal jets to provide a turbulence level of 10% and length scale of 11 cm at the blade entrance. The linear cascade test section, shown in Fig. 1, consisted of an instrumented center blade and two outer blades with tailboards. The tailboards and the bleed gates allowed for flow control around the center blade, insuring flow periodicity. Static pressure measurements were taken at the blade midspan to ensure flow periodicity.

Coolant flow used for the tip-blowing experiments was supplied by an in-house compressor and was controlled by using a series of valves before exiting through the blade tip cooling holes. The overall coolant flow rate was known by measuring the pressure drop across a venturi nozzle. Discharge coefficients, which had previously been measured, allowed for the estimation of flow rate through each individual hole by way of pressure measurements [2]. The total coolant flow could then be calculated by summing each of the individual flows. This calculation for each hole was summed and compared to the total coolant flow measured by the venturi nozzle. In general, the two flows were within 2.8%. The two tips that were tested, shown in Fig. 2, are referred to as the baseline (Fig. 2(*a*)) and cooling hole (Figs. 2(*b*) and 2(*c*)) models. Both blades had a dirt purge cavity that was recessed 2h (0.67H) from the tip surface. The baseline geometry had no holes present on the pressure side or within the dirt purge cavity and, therefore, no film cooling. The cooling-hole model had tip holes placed on the pressure-side surface of the blade in addition to two holes within the dirt purge cavity, which have been described in detail by Hohlfeld et al. [16]. The purpose of the dirt purge holes is to allow for blade manufacturing and to expel dirt particles so as not to plug smaller diameter film-cooling holes.

In addition to the dirt purge holes, the four film-cooling holes just downstream of the stagnation were expanded in the axial direction and had a metering hole diameter of 0.56 D whereas the remainder of the holes had no expansion and a metering hole diameter of 0.41 D. The tip model also contained a slot at the trailing edge denoted as the trailing edge flag (TEF).

Testing conditions and blade parameters are given in Table 1. The small *h* and large *H* tip gap settings considered were 0.54% and 1.63% of full blade span, respectively. All heat transfer coefficient tests were conducted at a density ratio of one, such that the coolant and mainstream temperatures were kept to within 0.15°C. For the baseline geometry, experiments were conducted at both the small and large tip gap settings with no blowing present. For the cooling-hole geometry, experiments were conducted at both tip gap settings and at overall coolant flow rates of 0.58% and 1% of the total passage flow. The total passage flow was calculated based on the inlet mainstream velocity, blade span, and pitch. The local blowing ratios are reported in Part I [2].

For making the heat transfer measurements, foil heaters were used to supply a constant heat flux at the tip surface. Two separate heaters were necessary that included one for the blade tip surface and the other for the dirt purge cavity on the tip. The dirt purge cavity was heated with one strip of Inconel that was 0.051 mm thick and had a surface area of 17.3 cm^2. The main heater covered an area of 261.2 cm^2 and consisted of a serpentine Inconel circuit. The circuit, shown in Fig. 3, used Inconel sandwiched between insulating Kapton and then covered with a very thin (0.013 mm) layer of copper on both sides. Both heaters were attached to a foam blade tip using double-sided tape that was 0.64 mm thick. The nominal heat flux for both heaters was set to 3700 $\mathrm{W/m^2}$, which provided a maximum temperature difference between the mainstream and blade surface of 28°C. The two heaters were controlled independently with a variac to within 0.67% of one an-

Table 1 Testing Conditions and Blade Parameters

Parameter	Wind tunnel settings
Scaling Factor	12×
Axial chord/true chord	0.66
Pitch/true chord	0.81
Span/true chord	1.03
Re_{in}	2.1×10^5
Inlet angle, θ	16.5 deg
T_∞(°C)	21
Small tip gap/span (%)	0.54
Large tip gap/span (%)	1.63

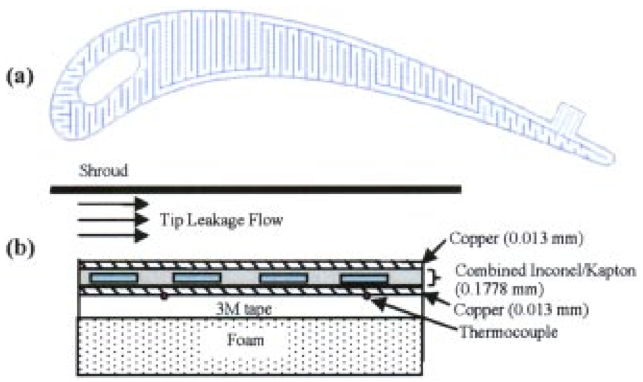

Fig. 3 **Main tip heat transfer surface showing (*a*) serpentine passages and (*b*) detail of main tip heater as placed on the blade surface**

other during all tests. The current supplied to each heater was known by placing a precision resistor ($R = 1\,\Omega \pm 0.1\%$) in each circuit and measuring the voltage drop across each resistor with a digital multimeter. The heater power was then determined from the supplied current and known heater resistance.

Equation (1) was used when calculating the heat transfer results to account for radiation losses,

$$h = (q''_{\text{tot}} - q''_r)/(T_w - T_\infty) \tag{1}$$

In this equation, q''_{tot} represents the total heat flux output from the resistive heaters and q''_r represents the energy lost to radiation. Typically, radiation losses were less than 2% with the maximum for all cases being 3.4%. Conduction losses were found to be negligible because the heaters were placed on low-thermal-conductivity foam.

The surface temperatures on the tip (T_w) were obtained using an Inframetrics P20 infrared (IR) camera. The images were processed with Thermacam Researcher 2002® and using an in-house MATLAB code. Four IR images were acquired through the zinc selenide windows placed in the shroud surface to cover the entire blade, as shown in Fig. 1. Each image covered an area that was 21.3 cm by 16 cm and contained 320 by 240 pixels. The camera was located approximately 55 cm from the tip, resulting in a spatial resolution of 0.63 mm. For every test, each of the four images was taken five times, and the average of these five images was used.

Each image was calibrated using thermocouples placed underneath the heater. These thermocouples were held in place with a highly thermal conductive adhesive ($k = 1.6$ W/mK). This ensured that the thermocouple would read the surface temperature of the heater. This surface temperature was calculated to be 2°C less than the outer test copper surface for $q'' = 3700\ \text{W/m}^2$ due to the Kapton thermal resistance. This temperature difference was accounted for in the calibration process. The thermal resistance of the Inconel heater in the dirt purge cavity was found to be negligible, and no correction was needed for this area of the blade tip. The IR images were calibrated to a total of six thermocouples by adjusting the background temperature (T_b) and surface emissivity (ε). The emissivity is a surface property, which was set to 0.93 for all cases as a result of the heaters being painted with flat black paint. During the calibration process, all IR images were matched to the thermocouples to within 1.0°C. A check on the calibration process is that the four individual images matched up well to form one entire blade contour without any noticeable discontinuities in measured values between images.

Overall uncertainties were calculated for high and low values of heat transfer coefficients and Nusselt numbers according to the partial derivative method described in Moffat [17]. The total uncertainty of any measurement was calculated as the root of the sum of the squares of the precision and bias uncertainties. Based on a 95% confidence interval, the IR camera precision uncertainty was calculated to be 0.06°C. The manufacturers reported bias uncertainty is 2.0% full scale, where typical ranges were set to 20°C. The thermocouples used to determine mainstream and coolant temperatures had a reported bias uncertainty of ±0.2°C, and the precision uncertainty was determined to be ±0.1°C from repeated measurements. The total uncertainty in heat transfer measurements was 6% at $\text{Nu}_{Dh} = 45$ and 10.5% at $\text{Nu}_{Dh} = 55.7$.

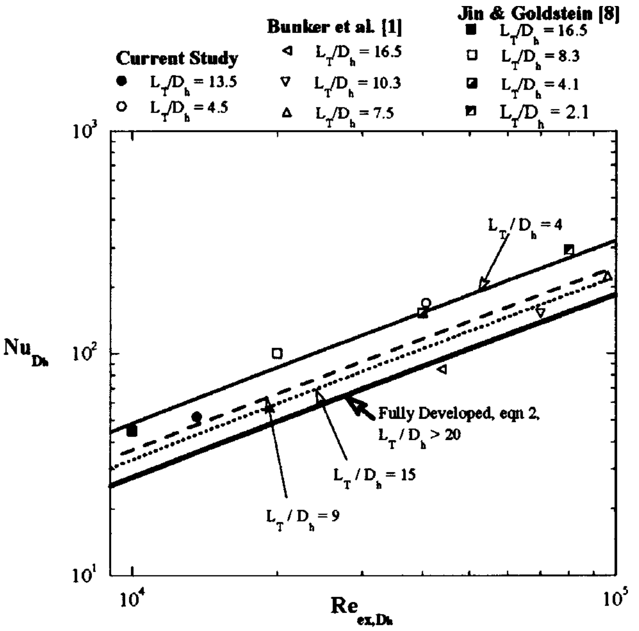

Fig. 4 **Comparison of experimental data to a fully developed correlation**

Tip Heat Transfer Coefficients

Previous studies have compared flow in a turbine blade tip gap region to that of a fully developed channel flow correlation for turbulent flow in a duct. The correlation that was used for comparison in our paper was developed by Gnielinski [18]. Gnielinski's correlation is given in Eq. (2) and has been reported in the literature to provide accuracy to within 6% as reported by Kakaç et al. [19] for a large Reynolds number range ($10^4 < \text{Re} < 10^6$).

$$\text{Nu}_{fd} = hD_h/k = 0.0214(\text{Re}^{0.8} - 100)\text{Pr}^{0.4} \tag{2}$$

Mayle and Metzger [3] furthered this correlation for a tip gap by adding an augmentation factor to account for the overwhelming entry region effects of thin blade tips. This augmentation factor, which was taken from Kays and Crawford [20], allows blade designers to relate overall blade tip heat transfer (for a given blade thickness and tip gap) to an overall heat transfer expected in a fully developed channel. Using data collected in this study, comparisons have been made to the data of Jin and Goldstein [8] and Bunker et al. [7] that confirm this augmentation factor approach. Although Mayle and Metzger [3] first noted the augmentation factor, their data have not been included in this comparison because only experiments performed on airfoil shapes were considered.

Figure 4 shows Nusselt number values based on the hydraulic diameter of the tip gap (2h or 2H) plotted as a function of the blade Reynolds number based on the exit velocity and hydraulic diameter. The Gnielinski correlation has been plotted for several L_T/D_h ratios as shown on the plot. Note that L_T represents the maximum thickness of the blade. As known for the turbulent channel flow, fully developed conditions generally occur for $L/D_h > 20$ [20]. There is fairly good agreement between experi-

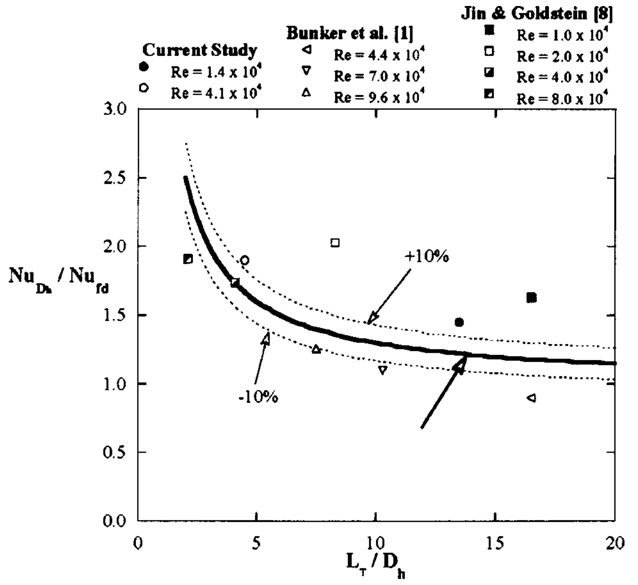

Fig. 5 Comparison of experimental data to the proposed augmentation factor

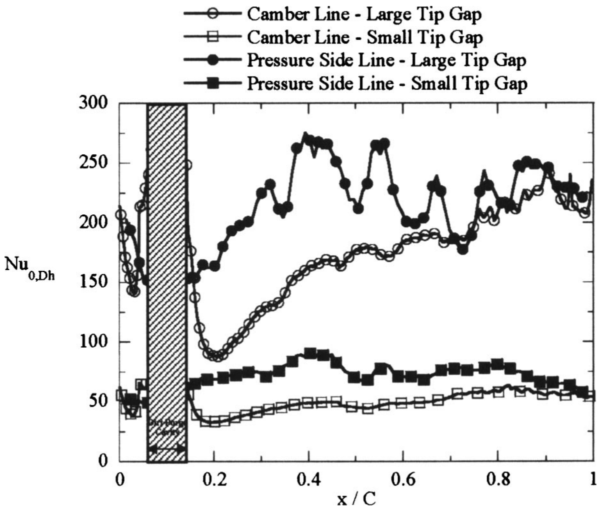

Fig. 7 Nusselt number line plots for the baseline

mental data and the appropriate correlations. It should be noted that the L_T/D_h ratios are based on the maximum blade thickness, and the Nusselt numbers are the average values calculated for the tip surface. Therefore, this ratio is not a perfect representation of a blade profile, but works reasonably well for the area-averaged values shown here.

Figure 5 shows the same experimental data points, plotted as a ratio of the Nusselt number normalized by the fully developed correlation. The solid line represents the augmentation factor given by Kays and Crawford [20]. Most of the data points fall close to the line, with the exception of two Jin and Goldstein points: $\mathrm{Re}=1.0\times 10^4$ and $\mathrm{Re}=2.0\times 10^4$. These data points, however, are at low Reynolds numbers, which has been shown to greatly affect the heat transfer. Mayle and Metzger [3] showed that low Reynolds numbers can cause an increase of 20–30% above of the expected augmentation factors used in Fig. 5. More experiments should be performed to further verify this trend.

Baseline Results (No Blowing). The baseline results with no blowing are presented as contour plots of Nusselt number in Fig. 6. Note that the chord rather than hydraulic diameter was used for these contour plots to illustrate the differences in the heat transfer coefficients along the blade tip for both tip gaps. Results at both gap heights show similar trends, however. The large tip gap shows higher Nusselt numbers at the blade trailing edge relative to the small tip gap. This increase in heat transfer at the larger tip gap trailing edge is a result of the increased entry region effect relative to the small tip gap. With smaller L/D_h values (for the large tip gap), the entry region is expected to have a greater effect, as mentioned at the beginning of this section. For the large tip gap, the L/D_h is as low as 1 across the trailing edge of the tip surface, whereas for the small tip gap, the L/D_h is 3.5.

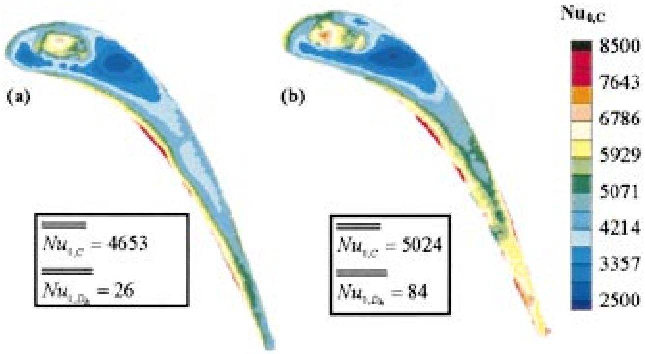

Fig. 6 Baseline Nusselt number contour plots for the (*a*) small and (*b*) large tip gap

The area-averaged Nusselt numbers are given for each case to quantify the increase in heat transfer with gap height. For these cases, the Nusselt number at the large tip gap is 3.2 times that of the small tip gap when based on the exit velocity and hydraulic diameter. By using Reynolds number scaling, the large tip gap is expected to have 2.4 times the heat transfer of the small tip gap. This larger-than-expected increase results from the overwhelming entry-region effect, which serves to greatly increase tip heat transfer coefficients.

As shown in Fig. 6, there are regions of low heat transfer immediately downstream of the dirt purge cavity for both tip gap heights. This is near the thickest portion of the blade and represents the area of lowest heat transfer on the blade tip. This region was first pointed out by Bunker [6] and has been confirmed by other authors. Within the dirt purge cavity, there are high heat transfer coefficients resulting from low velocity flow recirculation in the cavity. Overall, the leading-edge region experiences relatively low heat transfer outside of the dirt purge cavity in comparison to the trailing edge.

Also seen on these contour plots are regions of high heat transfer coefficients along the pressure side that begin around the leading edge at $S/S_{\max}=0.1$ and extend until the trailing edge. These regions of high heat transfer have been noted by Morphis and Bindon [4], Bindon [5], and Teng et al. [10] to be the separation region that forms along the pressure side due to mainstream and leakage flow interaction. This region occurs within the entry region and is more dominant at the large tip gap than at the small tip gap, and extends over a large region of the tip for the large tip gap. To further study the effects of this entry region, line plots have been made that compare Nusselt numbers at the pressure side of the tip to those of the blade camber line in Fig. 7. Note that Nusselt numbers displayed from this point forward in the paper are given based on the hydraulic diameter D_h. Shown in Fig. 7, these line plots show similar trends at both tip gaps.

For the blade camber line data shown in Fig. 7, there are very low values for both tip gaps immediately downstream of the dirt

Table 2 Positions for Line Plots

	Large tip gap		Small tip gap	
	Re_{Dh}	L/D_h	Re_{Dh}	L/D_h
Line 0	4.4×10^4	4.0	1.5×10^4	11.9
Line 1	4.7×10^4	4.0	1.6×10^4	12.1
Line 2	4.5×10^4	2.9	1.5×10^4	8.7
Line 3	4.4×10^4	2.7	1.5×10^4	8.1

purge cavity. Downstream of this area of low heat transfer, the camber line data increase as the blade becomes thinner. The pressure-side data begin to increase at about $x/C=0.15$ as the separation bubble begins to form. Nusselt numbers increase until $x/C=0.4$, where the maximum Nusselt numbers are reached for both tip gaps. Downstream of this location, the pressure-side data remain relatively constant with oscillating levels. These oscillations, seen especially at the large tip gap, suggest localized effects in the separation bubble most likely due to the sensitivity of the separation region to any imperfections at the corner of the blade tip. This separation region was also computationally predicted by Hohlfeld et al. [16]. At the very trailing edge of the blade, the camber and pressure-side lines become equal for the same gap height. This is because the tip is so thin that the entry region dominates the entire tip passage. In general, the pressure side of the blade tip experiences relatively high heat transfer and, as such, justifies the idea of adding pressure-side film-cooling holes.

To compare the baseline results to the turbulent channel flow correlation in Eq. (2), data have been taken along various lines across the tip. For each line to be compared to channel flow, the local inviscid velocity was used to calculate the Reynolds number. This velocity was found from the local pressure difference as predicted at the 95% blade span. The Reynolds number based on local velocity and D_h are given in Table 2 along with the L/D_h at each position. Line 0 is only of interest to the baseline cases because, when blowing is present, this area is affected by the dirt purge holes. Lines 1 and 2 were identified in Part 1 of this paper [2] as the locations having the maximum effectiveness levels while line 3 is between two jet trajectories. Figure 8 shows lines 0, at $S/S_{\max}=0.28$ for the baseline cases (no blowing). Note that for this plot, $L_{\max}$ is the maximum local blade thickness at each line location, and L is the distance along that line. Figure 8 shows that within the range of uncertainty, flow at both gap heights becomes fully developed at line 0. At line 3, the measured heat transfer is higher than the correlation. This is due to $L/D_h \leqslant 20$ at the trailing edge of the blade reflecting the influence of the entry region.

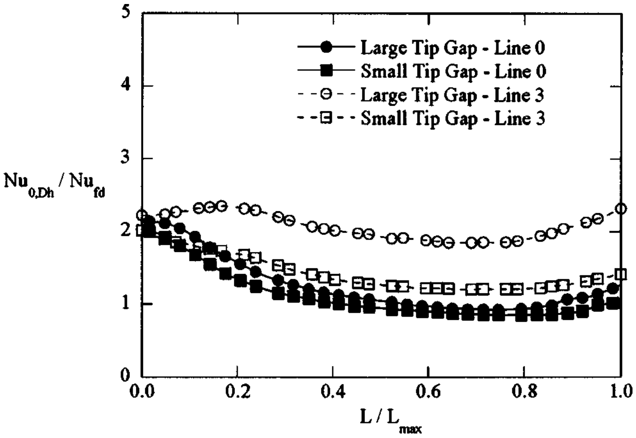

Fig. 8 Line plots at lines 0 and 3 for baseline cases

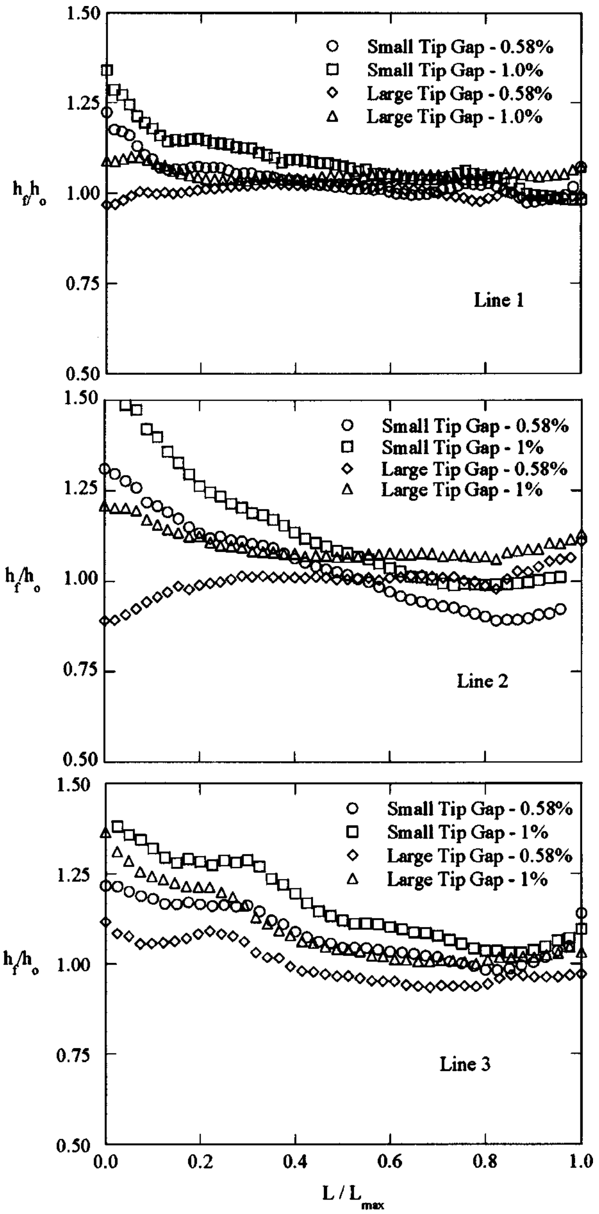

Fig. 9 (*a*)–(*c*) Line plots for the cooling holes at positions 1, 2, and 3

Film-Cooling Hole Results. The heat transfer measurements on the blade tip with blowing from pressure-side holes were compared to the baseline with no blowing. For this comparison, a h_f/h_0 ratio greater than one means that there is increased heat transfer with blowing, and a ratio less than one means that the heat transfer is reduced when blowing is present. Two lines were chosen to follow the peak effectiveness locations of separate film-cooling holes (lines 1 and 2), and a third line was chosen to follow in between two film-cooling holes (line 3).

Figures 9(*a*)–9(*c*) shows the comparison lines for the tip results with blowing. Blowing causes severe increases in heat transfer up to one hydraulic diameter into the large tip gap and up to five hydraulic diameters along the small tip gap. While the enhancement is not as pronounced for the remainder of the gap length, there is still an effect of blowing as h_f/h_0 values are generally above 1.

Based on the results shown in Figs. 9(*a*)–9(*c*) flow models can be described for the pressure side blowing. For the large tip gap, the flow separates from the blade pressure side and impinges upon

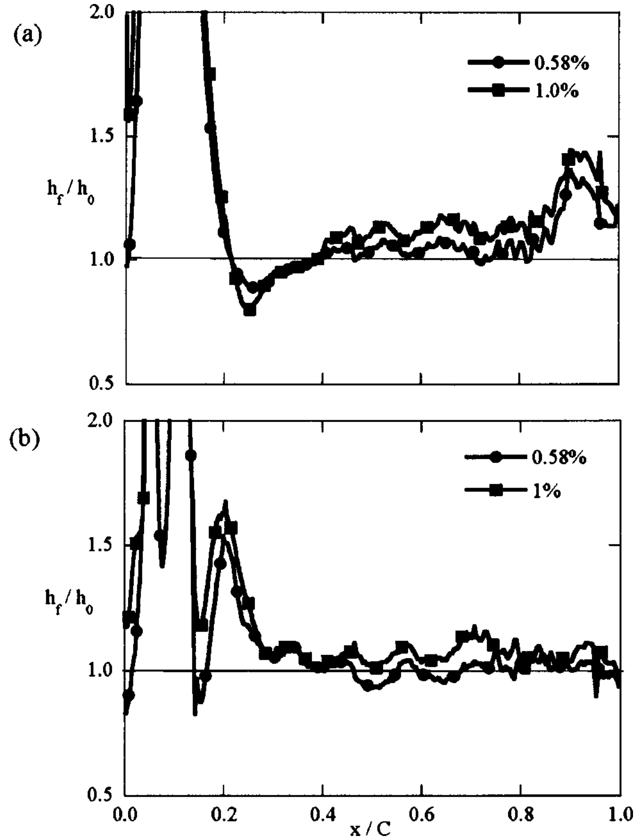

Fig. 10 Heat transfer augmentation at the camber line for the (*a*) small and (*b*) large tip gaps

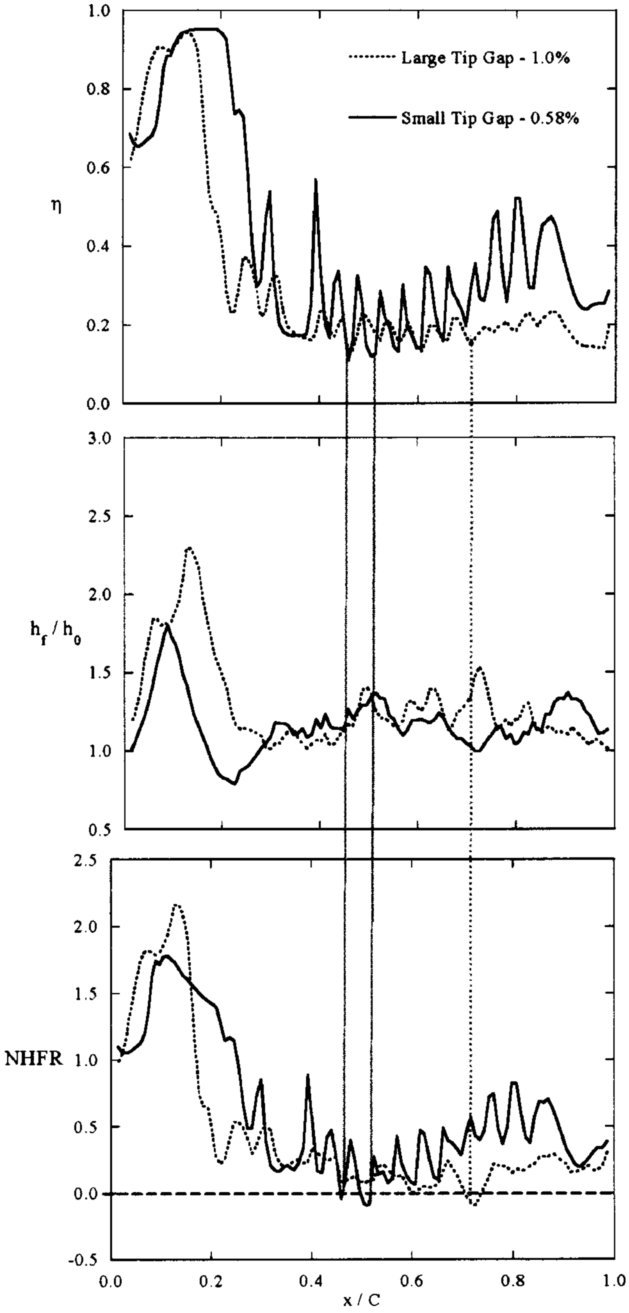

Fig. 12 Pressure side plots of NHFR for the small tip gap

the shroud. The separation region is enhanced by the high momentum flow from the holes thereby causing high augmentations of the heat transfer coefficients. For the small tip gap, the coolant jet fills in the separated region.

Data taken along the camber line are shown in Figs. 10(*a*)–(*b*) for the small and large tip gaps, respectively. Heat transfer augmentation within the dirt purge cavity is very high. Immediately after the dirt purge cavity between $0.2<x/C<0.3$, the large tip gap has a higher h_f/h_0 than the small tip gap. This is most likely due to vortices that are created by the dirt purge holes in the case of the large tip gap. Higher heat transfer augmentations occur on the downstream side of the second dirt purge hole, which is where the lowest heat transfer occurs for the baseline case. This combination results in high augmentation values at this location for the large gap.

At the small tip gap (Fig. 10(*a*)) augmentations decrease to below 1 around $x/C=0.2$. From $x/C=0.3$ to 1, the augmentations show a continued increase along the blade tip at the small tip gap. The increased heat transfer augmentation may likely be due to an increase in the size of the separation region along the pressure side of the tip. The results indicate that there is always an increase in the heat transfer augmentation with increased blowing. Kim et al. [15] showed that with a shaped hole, the heat transfer increases as much as 13% with a 60% increase in coolant flow. Results from this test show about an 8% increase in heat transfer for a 75% increase in coolant flow. The lower augmentations may be attributed to the compound injection angle and the cylindrical hole shape of these tests as compared to Kim et al.

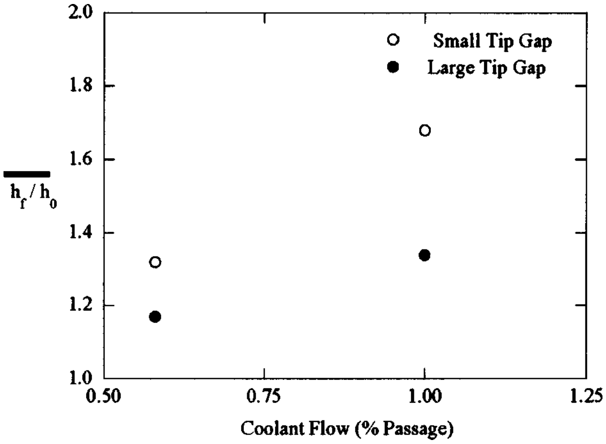

Fig. 11 Area-averaged heat transfer augmentation for the entire blade tip

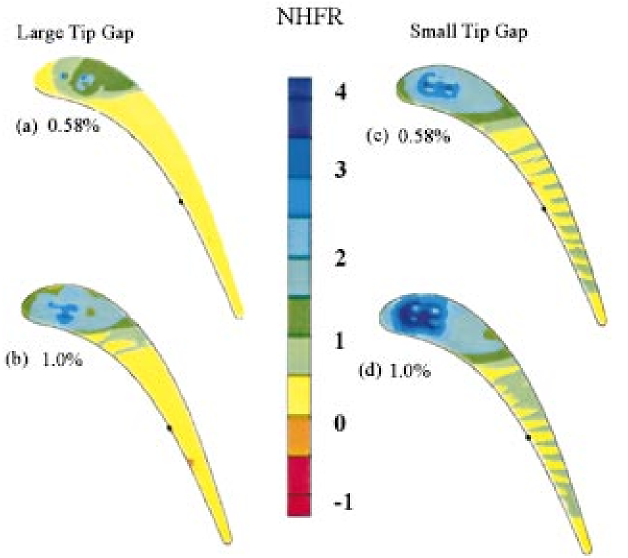

Fig. 13 NHFR for all cases at 0.58% and 1% coolant flow

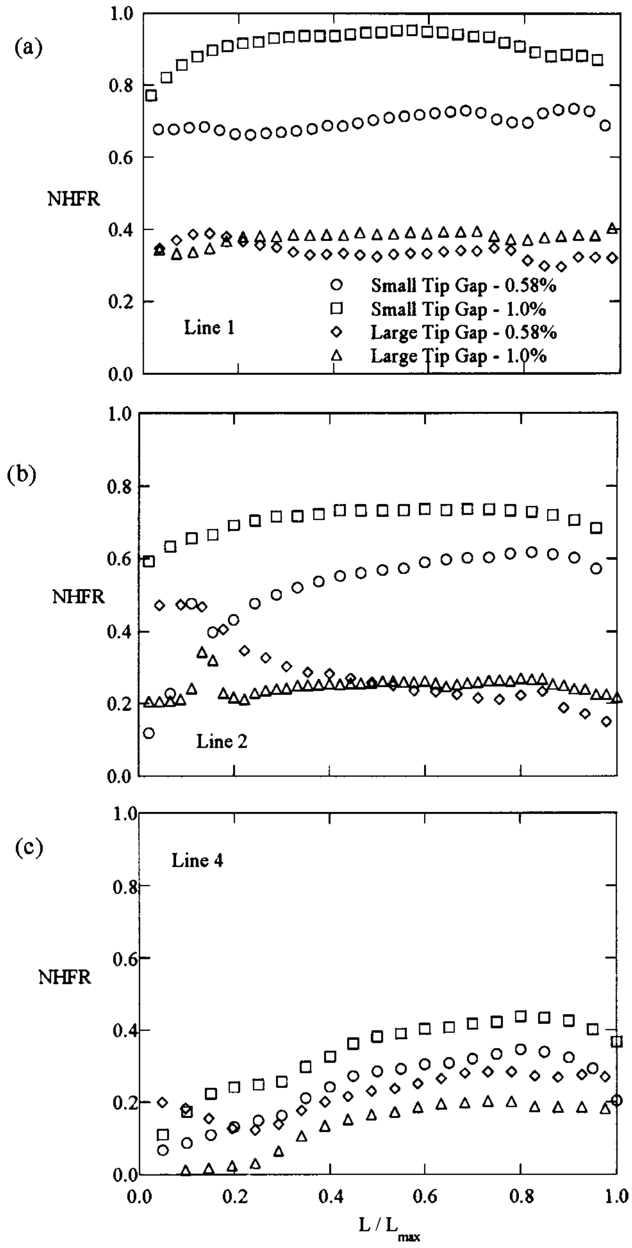

Fig. 14 (*a*)–(*c*) Individual line plots of NHFR at different locations along the blade tip

For the large tip gap (Fig. 10(*b*)), the heat transfer ratio plot shows increased heat transfer augmentation with increased blowing. The area averages in Fig. 11 indicate the rise in the overall heat transfer coefficients as a result of blowing. There appears to be a larger difference between the small and large tip gaps at the higher coolant flow conditions. Overall augmentations for the small tip are larger than for the large tip gap at both blowing ratios.

Net Heat Flux Reduction. Combining the heat transfer measurements of this paper with the film effectiveness measurements of Part I [2], the overall cooling benefit is summarized in the net heat flux reduction (NHFR). Shown in Eq. (3), NHFR is an established method of evaluating the overall effect of a cooling scheme on a surface [21],

$$\mathrm{NHFR}=1-h_f/h_0(1-\eta\cdot\theta) \tag{3}$$

In this equation, all variables have been measured experimentally except for θ. A constant value of 1.6, which corresponds to a cooling effectiveness of 62.5% (inverse of 1.6), was used for this paper and was based on the previous literature [21]. As this equation shows, when high heat transfer augmentation is not accompanied by high film cooling, the NHFR can become negative. A negative NHFR means that the cooling scheme is actually causing an increased heat load to the blade surface. Figure 12 shows two examples of an increased heat load for the small tip gap at 0.58% and for the large tip gap at 1% coolant flow. Line plots along the pressure side of the tip for η, h_f/h_0, and NHFR are shown. The vertical lines show the locations where NHFR is slightly negative. For the negative values relating to the small tip gap case, the negative NHFR comes from localized low values in η along with high heat transfer. These two locations are between film-cooling holes where the cooling effectiveness is low (because the cooling holes have relatively poor spreading) and heat transfer is high.

The NHFR values were calculated locally for each case and are shown in Fig. 13. Also shown in Fig. 13 is a location for one of the hole exits (black dot). Not all of the hole exits are shown for proprietary reasons. Generally the entire blade tip surface has positive values. Also, the leading edge tends to have high NHFR values resulting from the dirt purge blowing. There are noticeable streaks along the blade that are aligned with the film-cooling trajectories for the small tip gap.

To further study the NHFR along a cooling path, data were taken along the path lines described in Table 2. These results are shown in Fig. 14. Once again, lines 1 and 2 follow the direct path of coolant over the tip, and line 3 lies in between two coolant paths. Increased blowing levels result in increased NHFR values at the small tip gap, but not always at the large tip gap. As has been mentioned in Part 1, the lower coolant flow rates actually allow the jet paths to remain attached to the blade for the large tip gap. This is made evident at line 2. The 0.58% case starts off near NHFR=0.5 and quickly decreases as the low coolant flow is diffused with the main gap flow. For the 1% case, however, there is a constant NHFR ~0.2 across the entire gap width. This agrees with previous suggestions that the jets for the large tip gap separate from the blade and attach to the shroud at higher blowing rates. For line 3, which is in between two hole paths, similar results are seen as on the hole paths, such that at the small tip gap, increased blowing increases the NHFR, whereas at the large tip gap, the opposite is true.

NHFR results taken at the camber line are shown in Fig. 15. The results in Fig. 15(*a*) indicate much higher variation (meaning minimum to maximum differences) between hole locations at the

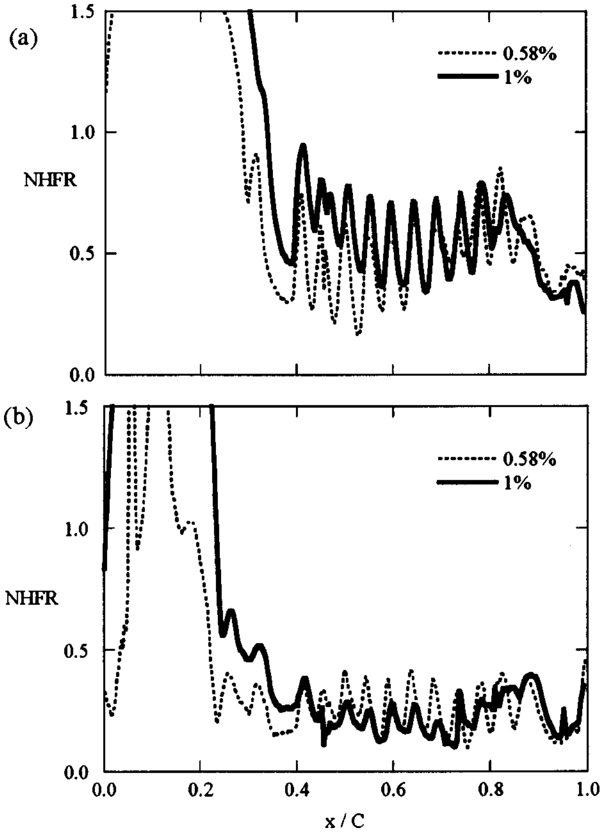

Fig. 15 NHFR levels for camber lines for (*a*) small and (*b*) large tip gap settings

lower blowing ratio than the higher blowing ratio. At the large tip gap (Fig. 15(*b*)) similar trends are seen such that the lower blowing ratio exhibits higher variation between holes than for the higher blowing ratio. Also, increasing the tip gap tends to decrease the NHFR, whereas increased blowing ratio has no noticeable affect on the mean NHFR values.

Area-averaged results of the NHFR are shown in Fig. 16 using both the entire blade tip area and the downstream 70% of the blade tip area. Figure 16 shows increasing NHFR values with increased blowing for the averages over the entire tip surface area. Also, the small tip gap has significantly higher NHFR values than the large tip gap. Because the dirt purge holes dominate the area-averaged results, the NHFR was averaged over the downstream 70% portion of the blade to illustrate the effects blowing and tip gap settings, as shown in Fig. 16. By discounting the dirt purge flow, there is much less dependence on blowing ratio for these results while there is a strong dependence of the tip gap.

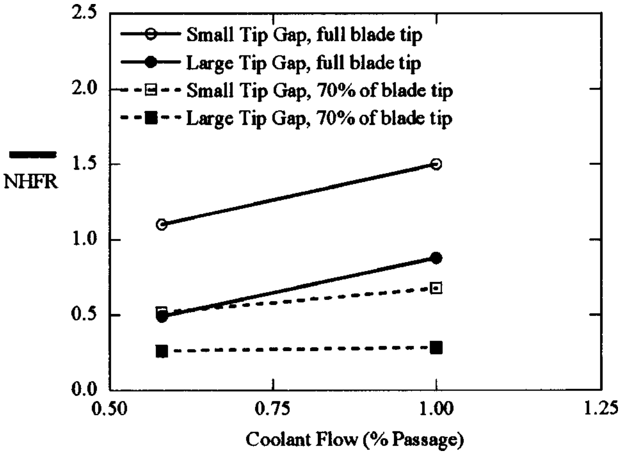

Fig. 16 Area-averaged NHFR for full blade tip and for the downstream 70% of tip

Conclusions

Baseline cases with no blowing at two tip gaps have confirmed that tip heat transfer increases with gap height. This increase can be explained by considering the entry region effect being more dominant for the larger gap distance. Also, a separation region along the pressure side of the tip surface has been indicated by the tip heat transfer measurements. The baseline results showed that there is a small region of low heat transfer, which occurs near the thickest portion of the blade, and tip heat transfer increases toward the trailing edge.

When injecting coolant through pressure-side film-cooling holes, tip heat transfer coefficients are increased above what occurs with no blowing. Increases in the blowing ratio lead to increases in heat transfer on the tip surface. Overall augmentations for the small tip were measured to be larger than for the large tip gap for both blowing ratios.

By evaluating the overall cooling benefit through a net heat flux reduction, the results indicate an overall benefit to the tip by releasing coolant from the pressure-side holes despite increases in the local convective heat transfer coefficients. The area-averaged results for the entire tip indicate relatively little dependence on coolant flow rates and indicate that there is a higher cooling benefit for a small tip gap relative to that of a large tip gap. This higher benefit results from higher adiabatic effectiveness levels.

Acknowledgment

The authors gratefully acknowledge United Technologies–Pratt and Whitney for its support of this work.

Nomenclature

C = true blade chord
D = dirt purge hole diameter
D_h = hydraulic diameter, always used as 2h or 2H
F = augmentation factor for fully developed correlation
h, H = small or large tip gap
h_f = film heat transfer coefficient
h_0 = blade heat transfer coefficient with no blowing
k = thermal conductivity
L = local thickness of blade
$L_{\max}$ = max local thickness of blade
L_T = max thickness of blade overall
NHFR = net heat flux reduction, see Eq. (4)
Nu_{Dh} = Nusselt based on hydraulic diameter, $h(D_h)/k$
Nu_{fd} = Nusselt, fully developed based on hydraulic diameter, $h(D_h)/k$
$\mathrm{Nu}_{0,C}$ = Nusselt based on chord, $h(C)/k$
$\mathrm{Nu}_{0,Dh}$ = Nusselt based on hydraulic diameter, $h(D_h)/k$
Pr = Prandtl number
q''_{tot} = heat flux supplied to tip surface heater
q''_r = heat flux loss due to radiation
R = resistance in Ω.
Re_{in} = Reynolds based on inlet velocity, $U_{in}C/\nu$
Re_{Dh} = Reynolds based on local velocity, $U_{\mathrm{local}}(D_h)/\nu$
$\mathrm{Re}_{ex,Dh}$ = Reynolds based on exit velocity, $U_{ex}(D_h)/\nu$
S = distance from leading edge
$S_{\max}$ = distance from leading to trailing edge
T_w = blade wall temperature
T_∞ = freestream temperature
T_b = background temperature of radiation surface
T_c = coolant temperature
U_{local} = local velocity on tip gap
U_{ex} = exit velocity (at blade trailing edge)

U_{in} = inlet velocity (1 chord upstream)
x = distance along blade chord

Greek

η = film-cooling effectiveness, $(T_{aw}-T_c)/(T_\infty-T_c)$.
ν = fluid dynamic viscosity
ρ = fluid density
ε = emissivity of tip heater surface, always set to 0.93.
θ = dimensionless temperature, $(T_\infty-T_c)/(T_\infty-T_w)$

Superscripts

$=$ = area-averaged value

References

[1] Kwak, J. S., and Han, J. C., 2002, ''Heat Transfer Coefficient on the Squealer Tip and Near Squealer Tip Regions of a Gas Turbine Blade,'' ASME Int. Mech. Eng. Congress and Exposition, ASME Paper No. IMECE 2002-32109.
[2] Christophel, J., Thole, K. A., and Cunha, F., 2005, ''Cooling the Tip of a Turbine Blade Using Pressure Side Holes-Part I: Adiabatic Effectiveness Measurements,'' ASME J. Turbomachinery, **127**, pp. 270–277.
[3] Mayle, R. E., and Metzger, D. E., 1982, ''Heat Transfer at the Tip of an Unshrouded Turbine Blade,'' *Proc. 7th Int. Heat Transfer Conference* **3**, ASME, New York, pp. 87–92.
[4] Morphis, G., and Bindon, J. P., 1988, ''Effect of Relative Motion, Blade Edge Radius and Gap Size on the Blade Tip Pressure Distribution in an Annular Turbine Cascade With Clearance,'' ASME Paper No. 88-GT-256.
[5] Bindon, J. P., 1989, ''The Measurement and Formation of Tip Clearance Loss,'' ASME J. Turbomach., **111**, pp. 257–263.
[6] Bunker, R. S., 2000, ''A Review of Turbine Blade Tip Heat Transfer,'' *Turbine 2000 Symposium on Heat Transfer in Gas Turbine Systems*, Cesme, Turkey.
[7] Bunker, R. S., Bailey, J. C., and Ameri, A. A., 2000, ''Heat Transfer and Flow on the First-Stage Blade Tip of a Power Generation Gas Turbine: Part 1—Experimental Results,'' ASME J. Turbomach., **122**, pp. 263–271.
[8] Jin, P., and Goldstein, R. J., 2003, ''Local Mass/Heat Transfer on a Turbine Blade Tip,'' Int. J. Rotating Mach., **9**(2), pp. 981–995.
[9] Azad, G. S., Han, J. C., and Boyle, R. J., 2000, ''Heat Transfer and Presure Distributions on a Gas Turbine Blade Tip,'' ASME J. Turbomach., **122**, pp. 717–724.
[10] Teng, S., Han, J. C., and Azad, G., 2001, ''Detailed Heat Transfer Coefficient Distributions on a Large-Scale Gas Turbine Blade Tip,'' ASME J. Heat Transfer, **123**, pp. 803–809.
[11] Kwak, J. S., and Han, J. C., 2002, ''Heat Transfer Coefficient and Film-Cooling Effectiveness on a Gas Turbine Blade Tip,'' ASME Turbo Expo, Amsterdam, The Netherlands. Paper No. GT2002-30194.
[12] Saxena, V., Nasir, H., and Ekkad, S. V., 2003, ''Effect of Blade Tip Geometry on Tip Flow and Heat Transfer For a Blade in a Low Speed Cascade,'' ASME Paper No. GT2003-38176.
[13] Ameri, A. A., 2001, ''Heat Transfer and Flow on the Blade Tip of a Gas Turbine Equipped With a Mean-Camberline Strip,'' ASME Paper No. GT2001-0156.
[14] Kim, Y. W., and Metzger, D. E., 1995, ''Heat Transfer and Effectiveness on Film Cooled Turbine Blade Tip Models,'' ASME J. Turbomach., **117**, pp. 12–21.
[15] Kim, Y. W., Downs, J. P., Soechting, F. O., Abdel-Messeh, W., Steuber, G., and Tanrikut, S., 1995, ''A Summary of the Cooled Turbine Blade Tip Heat Transfer and Film Effectiveness Investigations Performed by Dr. D. E. Metzger,'' ASME J. Turbomach., **117**, pp. 1–11.
[16] Hohlfeld, E. M., Christophel, J. R., Couch, E. L., and Thole, K. A., 2003, ''Predictions of Cooling From Dirt Purge Holes Along the Tip of a Turbine Blade,'' ASME Turbo Expo, Atlanta, Georgia. Paper No. GT2003-38251.
[17] Moffat, R. J., 1988, ''Describing the Uncertainties in Experimental Results,'' Exp. Therm. Fluid Sci., **1**, pp. 3–17.
[18] Gnielinski, V., 1976, ''New Equations for Heat and Mass Transfer in Turbulent Pipe and Channel Flow,'' Int. Chem. Eng., **16**, pp. 359–368.
[19] Kakaç, S., Shah, R. K., and Aung, W., 1987, *Handbook of Single-Phase Convective Heat Transfer*, Wiley, New York, pp. 34–35.
[20] Kays, W. M., and Crawford, M. E., 1980, *Convective Heat and Mass Transfer*, Second Edition, McGraw-Hill, New York, pp. 269–270.
[21] Sen, B., Schmidt, D. L., and Bogard, D. G., 1996, ''Film Cooling With Compound Angle Holes: Heat Transfer,'' ASME J. Turbomach., **118**, pp. 800–806.

Parametric Effects on Heat Transfer of Impingement on Dimpled Surface

Koonlaya Kanokjaruvijit

Ricardo F. Martinez-Botas

Department of Mechanical Engineering,
Imperial College London,
Exhibition Road,
South Kensington,
London SW7 2AZ, UK

Jet impingement on a dimpled surface is investigated experimentally for Reynolds numbers in the range 5000–11500, and jet-to-plate spacing from 1 to 12 jet-diameters. These include spatially resolved local Nusselt numbers with impingement both on the dimpled itself and on the flat portion between dimples. Two dimple geometries are considered: hemispherical dimples and double or cusp elliptical dimples. All experiments were carried under maximum crossflow that is the spent air exits along one way. At the narrow jet-to-plate spacing such as $H/D_j=2$, a vigorous recirculation occurred, which prevented the dimpled plate to enhance heat transfer. The effect of impinging jet positions meant that impinging onto dimples generated more and higher energetic vortices, and this led to better heat transfer performance. Cusped elliptical dimples increase the heat transfer compared to a flat plate less than the hemispherical geometry. The influence of dimple depth was also considered, the shallower dimple, $d/D_d=0.15$, improves significantly the heat transfer by 64% compared to that of the flat surface impingement at $H/D_j=4$; this result was 38% higher than that for a deeper dimple of $d/D_d=0.25$. The very significant increase in average heat transfer makes dimple surface impingement a candidate for cooling applications. Detailed pressure measurements will form a second part of this paper, however, plenum pressure measurements are illustrated here as well as a surface pressure measurement on both streamwise and spanwise directions.

[DOI: 10.1115/1.1791292]

Introduction

There have been a number of ideas of complementing jet impingement with other techniques such as initial crossflow, film cooling, ribs and turbulators. Attempts have been made to optimize each method in order to obtain effective heat transfer with low-pressure loss. In order to augment the heat transfer, the boundary layer has to be thinned or be partially broken and restarted.

Regarding the flow passed dimples as a turbulence generator a number of studies have been published. Kesarev and Kozlov [1] studied a flow past a single hemispherical dimple of 150 mm diameter, and explained the phenomenon in terms of a "source" and a "sink." The heat transfer was enhanced by 1.5 times compared to a plane flat circle of the same printed diameter. Afanasyev et al. [2] conducted an investigation on the effect of staggered-dimple density; the greater the density of the dimples on the streamline surface; the greater the deviation of the temperature profile was from the logarithmic law of wall. Moreover, the heat transfer was increased by 30–40% without any significant increase in friction factor. They suggested that the viscous sublayer thickness was slightly decreased due to the concavities of the dimple. Moon et al. [3] studied the heat transfer levels in a staggered-dimple passage using the narrow-band transient liquid crystal method. They stated that the dimpled-passage enhanced heat transfer up to 2.1 times relative to a smooth passage, while the friction factor was twice that of the smooth passage. Mahmood et al. [4] examined the flow past a staggered array of hemispherical dimples. They used the smoke-wire technique to visualize the flow; vortex shedding occurred, and it enhanced heat transfer by 1.85 to 2.89 times that of a flat plate.

Kataoka et al. [5] elucidated the mechanism of impingement on a flat surface, which involved the development of large-scale eddies at the end of the potential core with significant vortex pairing. Turbulent surface renewal was caused by the impingement of these energy containing eddies on the thermal boundary. Gau and Chung [6] considered slot-jet impingement on a semi-cylindrical concave surface, an increase in heat transfer relative to a flat surface was found. In addition, the flow visualization by Cornaro et al. [7] on the concave surface clarified vortex formations both in the radial and axial direction, which were believed to be the reasons of heat transfer improvement. However, at narrow jet-to-plate spacing, a strong jet recirculation was produced.

The current research focuses on impingement heat transfer onto a dimpled surface using the transient wide-band liquid-crystal technique. The influence of Reynolds number, jet-to-plate spacing, impinging jet positions, dimple geometry and depth are examined as well as the technique of calculation of taking into account the dimple areas. Moreover, the detailed heat-transfer inside the dimple cavities is also presented. All overall average results are compared with those of a flat plate impingement. Additionally, plenum and surface pressure measurements are presented.

Experimental Procedure

Figure 1 illustrates a schematic of the experimental apparatus. The measurement technique is based on a transient method; heated air from a fan is passed through a 9-Watt heater, it then flows into a large plenum chamber. The flow is initially by-passed to enable the conditions to be set inside the chamber; a draw is then used to expose the impingement plate to the heated flow. In the working section, three sidewalls were installed in order to constrain the flow in one direction at the exit and thus obtaining the maximum crossflow scheme [8,9]. The target plate was of the dimension 320×320×25.4 mm, and hung beneath the nozzle plate by four adjustable studs. Table 1 summarizes the different configurations in nondimensional terms, as described below.

Two phases of experiments were carried out; the first phase investigated an 8-by-8 array of 10-mm jets impinging on both

---

Contributed by the International Gas Turbine Institute (IGTI) of THE AMERICAN SOCIETY OF MECHANICAL ENGINEERS for publication in the ASME JOURNAL OF TURBOMACHINERY. Paper presented at the International Gas Turbine and Aeroengine Congress and Exhibition, Vienna, Austria, June 13–17, 2004, Paper No. 2004-GT-53142. Manuscript received by IGTI, October 1, 2003; final revision March 1, 2004. IGTI Review Chair: A. J. Strazisar.

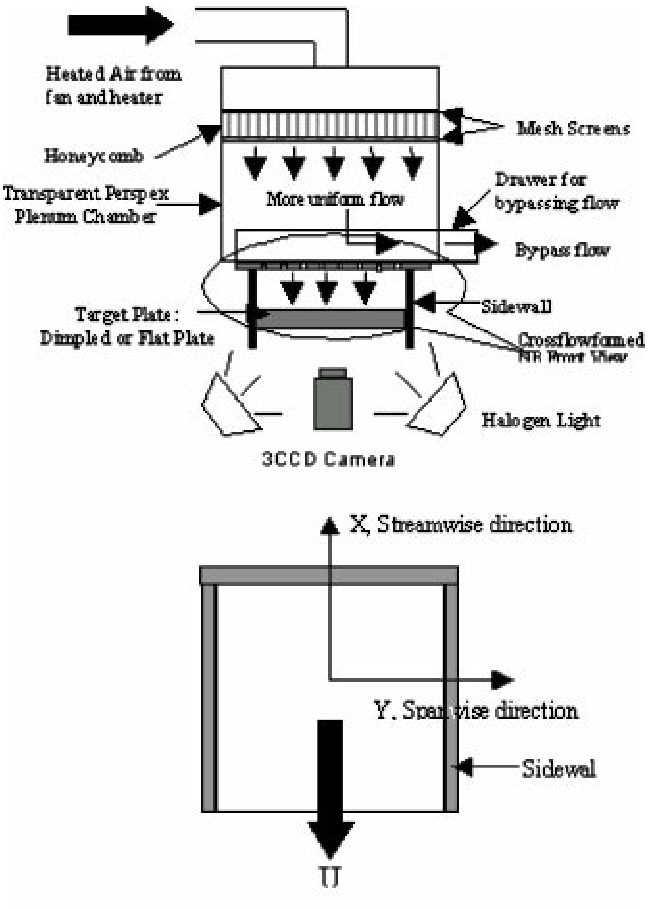

Crossflow schematic and direction

Fig. 1 Schematic of experimental apparatus

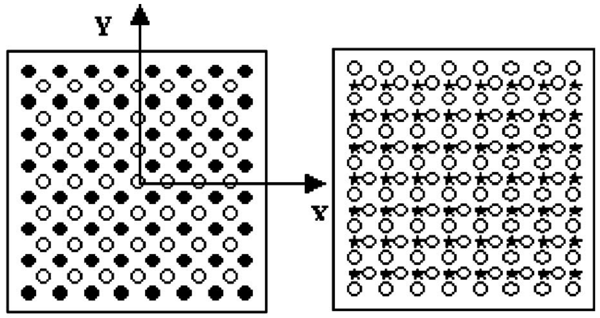

(a) Hemispherical dimples

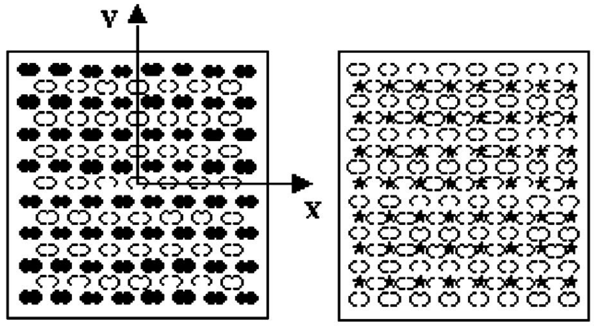

(b) Cusped elliptical dimples

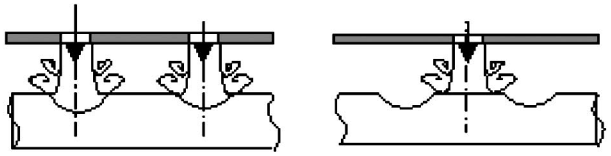

Jet holes aligned with dimples Jet holes aligned with flat portions

(c) Impinging positions

Fig. 2 Dimple plate geometries. In (*a*) and (*b*) the black portions indicate the projection of the jet hole on the plate, the left hand figures are impingement on the dimple itself while the right hand is impingement on the flat portion between dimples. (*c*) shows a schematic diagram of the location of impingement

hemispherical 20-mm diameter dimples and cusped-elliptical dimples. A cusp-elliptical dimple had the same equivalent projected area as the hemispherical geometry. The pitch of the jets and dimples was fixed at 4 diameters of the corresponding geometry. The impinging positions were set to be (i) onto the dimples (shown in Fig. 2 on the left-hand-sided pictures) and (ii) onto flat portions adjacent to dimples (the right-hand-sided pictures in Fig. 2).

In the second phase, the geometrical parameters were designed to be twice as big as those of the first phase: dimple diameter (40 mm), jet diameter (20 mm) and dimple depth (10 mm). The aim was to examine the heat transfer inside the dimple cavities. Two plates were manufactured with two dimple depths of 10 and 6 mm, which corresponded to d/D_d of 0.25 and 0.15, respectively. Figure 2 displays the top views of the two hemispherical dimpled plates. The areas inside the dimples were taken into account in the analysis.

Note that the thickness of the target plates was designed under the assumption of one-dimensional conduction and from the correlation, $z=2\sqrt{\alpha t}$ [10].

Table 1 Test parameters

Phase	D_d/D_j	Re($\times 10^{-3}$)	d/D_d	H/D_j	Impinging onto
1	1.73	5, 8, 11.5	0.25	2, 4, 8, 12	Dimples, Flat
2	2.0	5, 8, 11.5	0.15, 0.25	1, 2, 4, 6, 8	Dimples

Liquid crystals of the temperature range of 35 to 45°C were coated on each Perspex target plate followed by black paint. A 3CCD camera was set up to take a picture from underneath with an off-axis lighting installation. According to Camci et al. [11] and Wang et al. [12], the hue is sensitive to the local light intensity and the illumination angle, hence all the set up was fixed and calibration *in-situ* was achieved. The liquid crystal calibration of the hue value against the temperature was carried out with a calculated uncertainty within $\pm 3\%$. The curve fitting and regression analysis resulted in the fifth order polynomial temperature–hue relationship as per Yuen and Martinez-Botas [13,14]. Each camera image was transferred to a personal computer using a firewire lead, which transferred data directly from the camera to the computer without the usage of a frame grabber. Each experiment was filmed with the noncompression mode in order to receive the data as completely as possible.

Experiments were carried on at Re of 5000, 8000 and 11500. The jet-to-plate spacing was varied at 2, 4, 8 and 12 jet diameters. All tested parameters in this study are exhibited in Table 1. Note that the crossflow was generated only by the spent air after impinging on the target plate.

The transient method was applied throughout the research; hence the well known solution to the 1D unsteady heat conduction

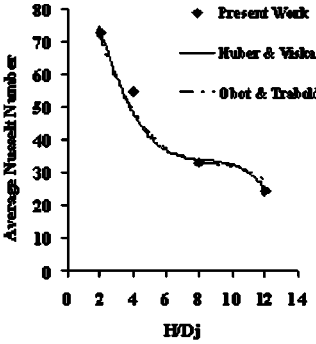

(a) $Re_{Dj} = 11500$

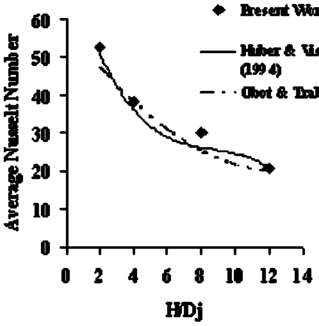

(b) $Re_{Dj} = 8000$

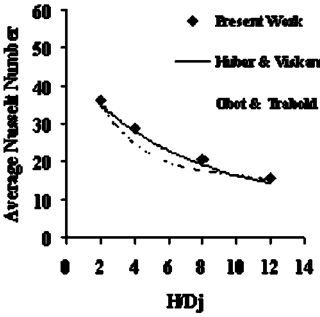

(c) $Re_{Dj} = 5000$

Fig. 3 Overall averaged Nusselt numbers of jet impingement on a flat surface, including results from the literature

equation was used, $\theta = 1 - \exp\beta^2 \operatorname{erfc}\beta$ where $\theta = (T_s - T_i)/(T_m - T_i)$ and $\beta = h\sqrt{t}/\sqrt{\rho c k}$. The bulk temperature was measured inside the plenum chamber.

The experimental uncertainty throughout this study was within $\pm 12.2\%$ based on 95% confidence levels according to Moffat [15]. The highest uncertainty that might happen was the sum of uncertainties of: the temperature measured by the liquid crystals, the initial and the bulk flow temperatures measured by thermocouples, the time frame measurement and the thermal product ($\sqrt{\rho c k}$) for the Perspex substrate. Thermocouples used in this study had the uncertainty of $\pm 0.5°C$, which made the uncertainties of initial and bulk flow temperatures become ± 2.5 and $\pm 1\%$, respectively. The highest uncertainty of time was $\pm 0.67\%$. Finally, the uncertainty of the thermal properties of the Perspex substrate was typically $\pm 5\%$ [16].

In addition to the heat transfer experiments, the pressure loss experiments were carried out by tapping 7 mm holes from the center of the test plate toward one end. In order to achieve the pressure readings across the plate in both directions, the plate was rotated. Three rows of static taps were drilled: through staggered dimples (to the jet holes), inline dimples and flat portions between the staggered and inline rows.

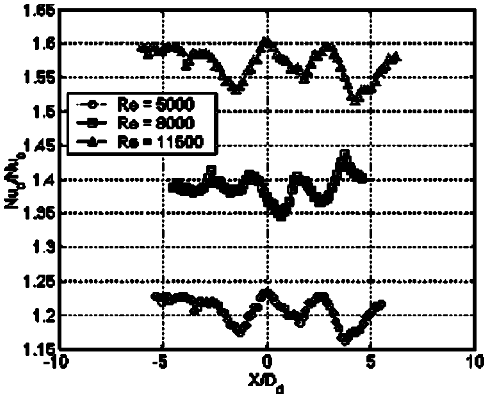

Fig. 4 Normalized streamwise averaged Nusselt numbers at an H/D_j of 8, hemispherical dimples impinging on dimples (Phase 1, Table 1)

Results and Discussions

Overall Average Heat Transfer of Flat Plate (Baseline). Before showing the results of jet impingement on dimples a baseline case on a flat surface was investigated at the same Reynolds numbers. Figure 3 shows the results together with a comparison with published results by Obot and Trabold [17] and Huber and Viskata [18]. Results are presented in the dimensionless form of Nusselt numbers; a good agreement is found. As expected, the heat transfer was higher at the lower jet-to-plate spacing and higher Reynolds number. All experiments were conducted with the three sidewalls (Fig. 1), hence the flow exits in one direction only.

Influence of Reynolds Number. Figure 4 shows the streamwise average of $\mathrm{Nu}_d/\mathrm{Nu}_0$ at different Reynolds numbers at $H/D_j = 8$; the spent air exit direction is from the right to the left (see Fig. 1 for a coordinate system). The highest performance of the dimpled surface was at a Reynolds number of 11500 followed by the 8000 and 5000 cases. In terms of averaged quantities, the heat transfer at Re=11500 was 51% higher than the flat surface, see Fig. 5. For the lower jet-to-plate spacings such as 2 and 4 diameters, the Reynolds number affected the results less than the larger spacings. At H/D_j of 2 for the lower Reynolds number of 5000 and 8000, there was no improvement in heat transfer of the dimpled surface compared to that of the flat surface. However, an 8% increase was found at a higher Reynolds number of 11500. For $H/D_j = 4$, Fig. 5 shows the improvements around 20%. Nonetheless, the Reynolds number was more significantly influenced at higher jet-to-plate spacings of 8 and 12.

The fundamentals of the jet impingement on a flat surface are well established. After jets impinge on a plate they form a cross-

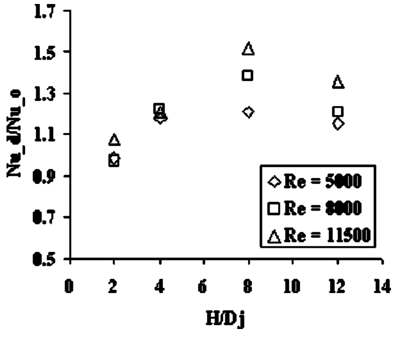

Fig. 5 A comparison of normalized average Nusselt numbers at various jet-to-plate spacings, hemispherical dimples

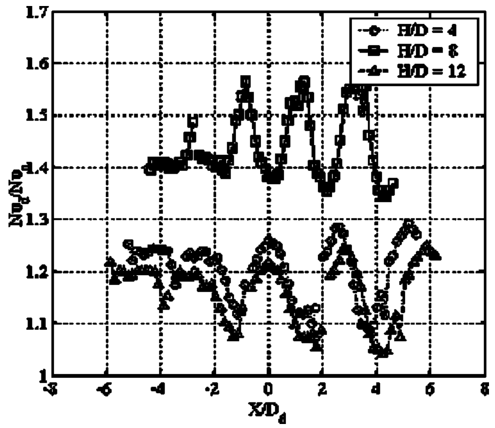

Fig. 6 Normalized streamwise average Nusselt numbers of hemispherical dimples at Re=8000 (Phase 1, Table 1). Note that the crossflow direction is from right to left).

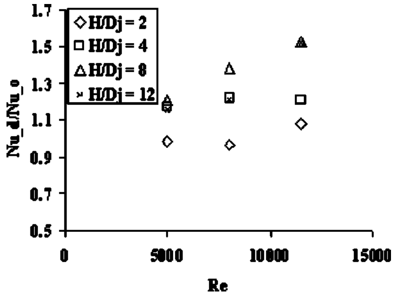

Fig. 7 A comparison of normalized overall average Nusselt numbers at various Reynolds numbers of hemispherical dimples of 17.32 mm diameter

flow, commonly known as spent-flow. This crossflow deflects subsequent jets from their intended target position, thus a decline in the overall average heat transfer across the target plate occurs. With the presence of dimples, the spent-flow separates in a higher degree than that caused by post jet-impingement on a flat plate. When the velocities at the jet exits were increased (i.e., higher Re), the velocity of the spent flow consequently increases, this helped to relieve the heat transfer degradation that occurs due to the jet-deflection mentioned earlier.

Effect of Jet-to-Plate Spacing. The jet-to-plate spacing strongly affected the heat transfer results on both flat and dimpled surfaces. At $H/D_j=2$ and $\mathrm{Re}_{D_j}=11500$, the dimpled surface improved the heat transfer by 8%; while a significant improvement was found at the larger spacings as shown in Fig. 5. The distance from the nozzle plate to the bottom of a dimple was 4.5 jet diameters, which might be the end of the potential core according to Cornaro et al. [7] who presented flow visualization of a single jet impinging onto a concave surface. They showed that at the end of the potential core there was a strong radial oscillation of the stagnation point that accelerated the breakdown of the roll-up vortices that struck the surface. This effect ruined the symmetry of the jet making it dissimilar to impingement on a flat plate.

Jet impingement on a dimple plate can be thought as a coupled effect of jet impingement itself and channel-flow caused by the spent-air; the performance depends upon which one dominates. The channel flow enhanced the performance of dimpled surfaces as presented previously by the authors [8]. Three crossflow exit schemes were compared in that work: freely exit (four-way), two-way exit and one-way exit (as used throughout the current study). A significant heat transfer improvement of dimples was shown in the two- and one-way exits, but heat transfer reduction by 10 to 15% was found in the free-exit scheme.

Figure 6 displays the normalized streamwise averaged Nusselt numbers of hemispherical ($D_d=17.32$ mm or $d/D_d=0.25$) dimples at an H/D_j of 4, 8 and 12 for Re=8000 (Phase 1 in Table 1). The results indicated that at $H/D_j=4$ the dimpled surface improved heat transfer less than at $H/D_j=8$ compared to that of the flat plate at the same conditions, and its performance was similar to that at $H/D_j=12$. On average (Fig. 7), at $H/D_j=8$ the dimples raised the heat transfer by 38% compared to the result of the flat plate, 22% at $H/D_j=4$, and 21% at $H/D_j=12$. Notwithstanding, with the presence of dimples of the heat transfer for $H/D_j=2$ slightly decreased at a Re_{D_j} of 5000 and 8000 when compared to that of the flat surface, but 8% improvement was found for $\mathrm{Re}_{D_j}=11500$. At spacings $H/D_j=2$ and 4 with $\mathrm{Re}_{D_j}=11500$, the spacing was narrow enough to form a strong channel flow to hasten the jets after impinging to impact the dimples, and enhance the heat transfer was better than the flat surface at the same condition. But in both these cases one would presume the existence of a recirculation flow inside the dimple itself that would prevent an effective use of the dimple as a heat transfer enhancer; further work including a detailed flow investigation will follow this paper including varying the relative curvature (D_j/D_d) and more results on varying dimple depths. At much larger distances, $H/D_j=12$, the spacing was wider so that the oncoming jets were losing their momentum, even though the jets are likely to impinged below the end of the potential cores. At $H/D_j=8$, the recirculation inside the dimple itself should be less pronounced than at narrower spacings, and had higher momentum than the larger spacing of 12; leading to the best overall performance of all the spacings.

Effect of Impinging Jet Positions. The arrangement of jet holes directly above the dimples exhibited higher heat transfer augmentation than that when impingement occurred on the flat portions, Fig. 8 for $H/D_j=8$. The same was found for the cusped elliptical dimple, Fig. 9. Figure 10 illustrates the normalized overall average Nusselt numbers of both impinging positions for both dimple geometries. The arrangement of the jet holes inline to the dimples produced higher heat transfer than those inline to the flat portions.

From the recorded video for Case 1 (jet holes inline to dimples), the strong crossflow deflected the jets to impinge on the downstream halves of the upstream rows of dimples and for the downstream dimple rows on adjoining flat portions. These deflections caused the dimples to function more properly as turbulence promoter as aforementioned in the effect of the crossflow scheme. However, for Case 2 (jet holes inline to flat portions), the oncoming jets were shifted to impinge onto the upstream rims of

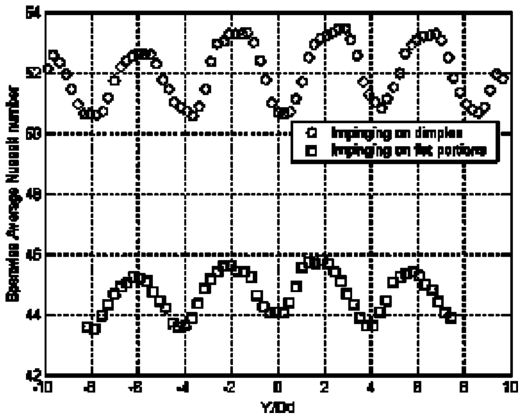

Fig. 8 Spanwise averaged Nusselt numbers of different impinging jet positions on hemispherical dimpled plate $H/D_j=8$ and Re=11500 (Phase 1, Table 1)

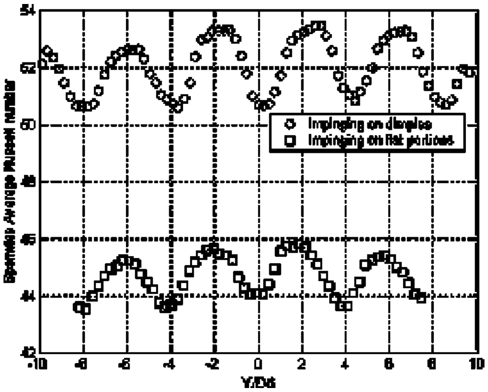

Fig. 9 Spanwisewise averaged Nusselt numbers of different impinging jet positions on a cusped elliptical dimpled plate at $H/D_j=8$ and Re=11500. (Phase 1, Table 1)

dimples, which were located downstream of the corresponding flat portions. The jets then lost momentum once impinged on the upstream rims of dimples, and this led to lower heat transfer improvement compared to Case 1, because the upstream edges could be "sinks" which ejaculated the vortices from the upstream toward the downstream dimples according to Kesarev and Kozlov [1].

Effect of Dimple Geometries. Recalling that both hemispherical and cusped elliptical dimpled shapes having the same wetted cross sectional area or equivalent diameter with the same depth, Fig. 11 shows the comparison of the streamwise average Nusselt numbers at an H/D_j of 4 and 8. For an H/D_j of 4, the hemispherical dimples performed better than the cusped elliptical dimples by 10.78% on average and 6.70% for an H/D_j of 8 (Fig. 12). Considering the degradation caused by the strong crossflow, for an H/D_j of 4, the peaks of heat transfer results of the hemispherical dimples were reduced by 0.68% based on the upstream peak, the cusped elliptical dimples by 1.5% and the flat plate by 6.78%. The cusped elliptical dimple divided the oncoming jet into two parts, and the recirculation occurred inside both dimples that formed a cusped elliptical dimple. This double recirculation was more severe than that inside a single hemispherical dimple. Consequently, the two rolling-up recirculations disturbed the oncoming jet. However, since the three sidewalls constrained the spent air to form a channel flow, this might hasten the recirculation flow to shed along the crossflow. At an H/D_j of 8 both geometries performed better than the other two spacings compared to the flat plate. Further flow visualization is needed to complete this physical explanation. Nevertheless, in terms of economy, manufacturing and performance, the hemispherical shape is more attractive than the cusped elliptical shape.

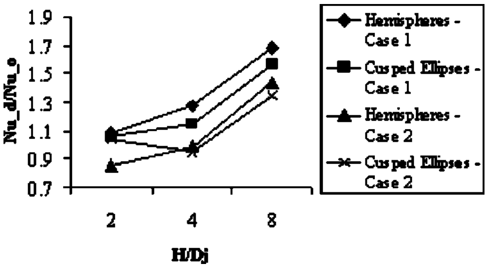

Fig. 10 Comparisons of overall averaged Nusselt numbers of both impinging jet positions to those of the flat surface, maximum crossflow scheme (Figures courtesy of Kanokjaruvijit and Martinez-Botas [9]). Note that Case 1 means jets impinging onto dimples and Case 2 on flat portions

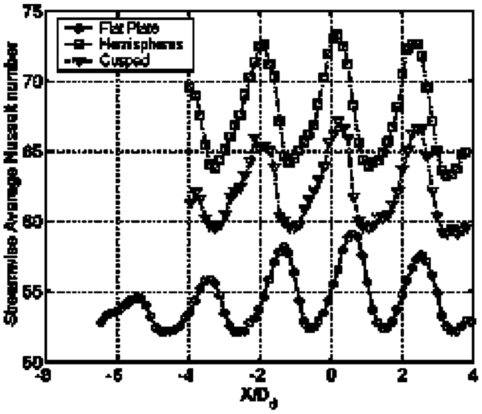

(a) H/Dj = 4

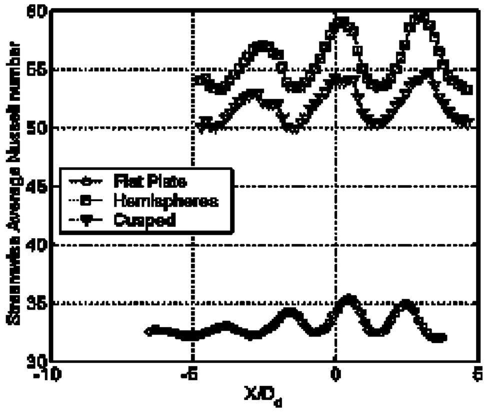

(b) H/Dj = 8

Fig. 11 Plots of streamwise normalized average Nusselt numbers of both dimpled plates compared to those of flat surface (Phase 1, Table 1). (Figures courtesy of Kanokjaruvijit and Martinez-Botas [8])

Effect of Dimple Depth. Different dimple depths resulted in different heat transfer augmentation. They clearly caused the different flow propagation from the dimples themselves. Figure 13 shows the schematic of a dimple plate used to investigate such an effect. Note that the center dimple was staggered and the rest are inline to the jet holes. The plots of local Nusselt numbers for both depths in Figs. 14 and 15 show that the trends in each cross-section for both streamwise and spanwise directions are identical, however, the heat transfer results of $d/D_d=0.15$ are higher than those of $d/D_d=0.25$. The lowest heat transfer was obtained inside the staggered dimple in Fig. 15(*a*).

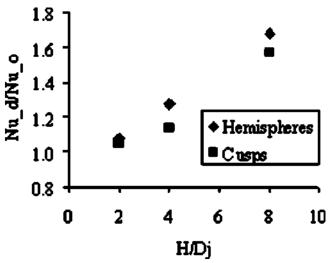

Fig. 12 Comparisons of overall averaged Nusselt numbers of both dimple geometries to those of a flat surface at Re =11500, Phase 1 in Table 1. (Figures courtesy of Kanokjaruvijit and Martinez-Botas [8])

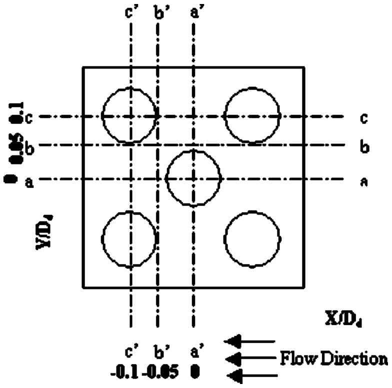

Fig. 13 Schematic of dimpled plate showing local locations with cross-sectional lines: (a–a), (b–b) and (c–c) represent the centerline of the plate (passing the center dimple which is staggered), tangential line and centerline of inline dimples in the streamwise direction, respectively, (a′–a′), (b′–b′), (c′–c′) in the spanwise direction (Phase 2, Table 1). Note that the center dimple is staggered and the rest are inline to the jet holes

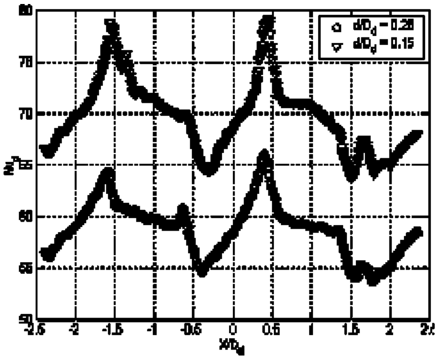

(a) Centerline of the plate (line a-a, Y/D_d = 0)

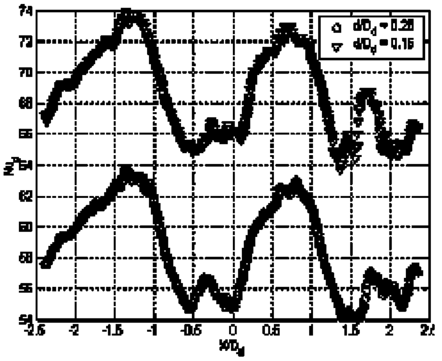

(b) Tangential line (line b-b, Y/D_d = 0.05)

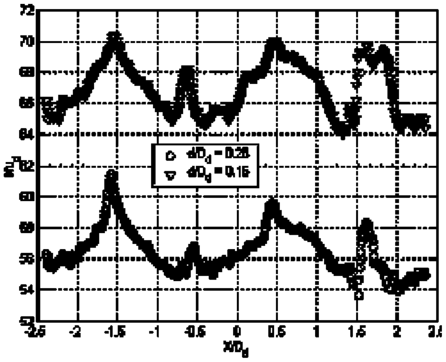

(c) Centerline of inline dimples (line c-c, Y/D_d = 0.1)

Fig. 14 Comparisons of local streamwise Nusselt numbers at different locations from the schematic in Fig. 13

Figure 16(*c*) shows the normalized average Nusselt numbers of d/D_d of 0.15 and 0.25 against Reynolds numbers at $H/D_j=2$ and 4. The results at each H/D_j showed the different trend. At $H/D_j=2$, $\mathrm{Re}_{D_j}=8000$ led to the worst improvement among three Reynolds number, but the opposite result at $H/D_j=4$. At $\mathrm{Re}_{D_j}=8000$ and $H/D_j=2$, $d/D_d=0.15$ resulted in a 23% increase, but $d/D_d=0.25$, a slight reduction. However, the heat transfer was discernibly enhanced at $H/D_j=2$ by $d/D_d=0.15$ around 70% at $\mathrm{Re}_{D_j}=11500$; while $d/D_d=0.25$ augmented 11%. At $\mathrm{Re}_{D_j}=5000$, the deeper dimples caused no difference in the heat transfer from that of the flat surface. Contradictorily, the shallow dimples enhanced 41%. At Re=8000 and $H/D_j=4$, both cases indicated the highest improvement: $d/D_d=0.25$ improved by 39% and $d/D_d=0.15$ by 64%, while at Re=5000 the shallower dimples conducted the highest improvement by 38% compared to the results of the deeper ones.

The deeper dimples caused a higher degree of recirculation than the shallow ones, who entrained the vortices on the wall downstream easier and faster, and this lessened the recirculation penalty. Additionally, when coupled with impingement the shallower dimples obtained the higher momentum from the oncoming jets than the deeper ones. In accordance with Cornaro et al. [7] for an impinging jet on a concave surface, the well-organized vortices were formed at $H/D_j=4$, and the stagnation point oscillated randomly in the radial direction. These happened with a lower Reynolds number such as 6000. When the turbulence intensity was increased, i.e., increasing Reynolds number to some level, the well-formed vortices were broken down as well as the higher degree of the vortex structures dissipating upstream towards the oncoming jet. This might help explain in this study that when increasing the Reynolds number to 11500, the disturbances from the dissipation of the vortices were strong enough to form recirculation, and this caused it to have less heat transfer improvement (compared to the result of the flat surface) than at $\mathrm{Re}_{D_j}=8000$. However, the channel flow-like crossflow moderated the strength of the dissipation.

Nevertheless, at $H/D_j=2$ smaller vortices occurred from the vortex breakdown on the wall with the recirculation, but high momentum. The concavity of the dimples then caused these vortices to roll up, depending on the depths of the dimples. Figure 16(*a*) displays significantly high heat transfer augmentation on $d/D_d=0.15$ at $\mathrm{Re}_{D_j}=11500$. This was possibly due to the higher jet velocity leading to the high velocity of the channel flow formed by the crossflow, which assisted the dimples to function more properly.

Close-up Inside Dimple Cavities. Looking at the detailed heat transfer distribution, the lowest heat transfer occurred inside the dimples. From the video images, for both dimple depths, the maximum heat transfer occurred at the downstream edges of the inline dimples (inline to jet holes), followed by the downstream flat portions, and the rest of the areas inside the dimples (Figs. 18 and 19). However, the lowest heat transfer took place inside the staggered dimples, and some distance further downstream from them. This leads to the idea of heat transfer enhancement happening by three dimples ‘‘teaming up’’: two inline dimples (labeled 1 and 2 in Fig. 17) and 1 staggered dimple (labeled 3) situated downstream between two inline ones. Once the oncoming jets impinged onto the inline dimples, the channel flow formed by the crossflow from upstream propelled the jet to move forward, and the flow inside the dimples acted like a source [2] producing vortices and shedding them in two directions toward the two adjacent

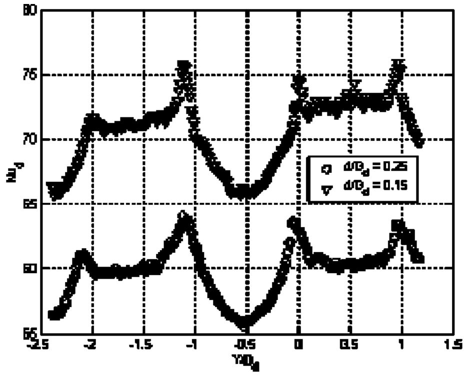

(a) Centerline of the plate (a'-a', $X/D_d = 0$)

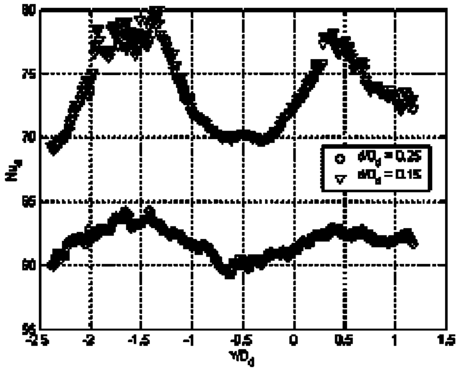

(b) Tangential line (b'-b', $X/D_d = -0.05$)

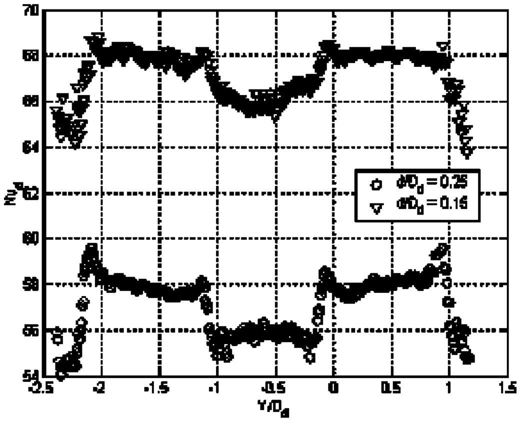

(c) Centerline of inline dimples (c'-c', $X/D_d = -0.1$)

Fig. 15 Comparisons of local spanwise Nusselt numbers at different locations from the schematic in Fig. 14

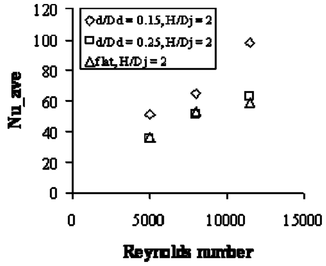

(a) Overall averaged Nusselt numbers of both dimple depths and flat plate at $H/D_j = 2$

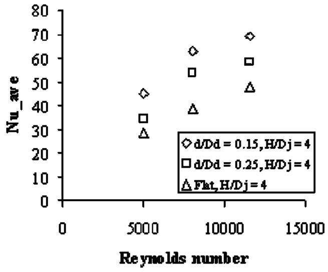

(b) Overall averaged Nusselt numbers of both dimple depths and flat plate at $H/D_j = 4$.

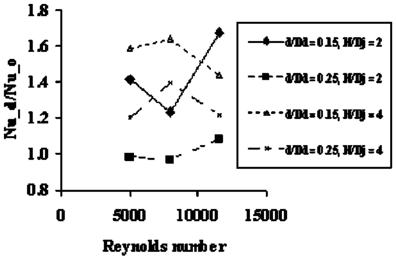

(c) Comparison of normalized average Nusselt numbers of different dimple depths at $H/D_j = 2$ and 4

Fig. 16 Overall heat transfer results of different dimple depths compared with those of the flat plate at $H/D_j = 2$ and 4

staggered dimples. The observation was analogous to the investigation of Terekhov et al. [19] on the parallel flow across a single dimple that the flow propagated, for instance, in 45 degree respect to the direction of the mainstream. Friction factors and detailed pressure distribution across the dimpled plates will be presented in a following paper.

Effect of Taking Into Account Dimple Areas. As foregoing, the experimental data from the hemispherical and cusped elliptical dimples in Phase 1 (Table 1) did not take the dimple areas into account, but the analysis on the dimple imprinted diameter of 40 mm in Phase 2 (Table 1) did. This was because the liquid crystal slurry was accumulated at the bottom of the small dimples when being sprayed. However, the heat conduction at the edges of the dimples was also carefully considered. Figure 19 shows the comparison of Nusselt numbers of dimpled surfaces of the imprinted diameter of 40 mm from three calculation methods for both values of d/D_d: taking the whole area into account, excluding the dimple areas and excluding the dimple edges. Excluding dimple areas led to the reduction of the results by the order of 2 compared to taking the whole area into account. When the edges were taken out of consideration, the results illustrate no significant reduction.

Plenum Total Pressure. Figure 20 exhibits the total pressures measured inside the plenum chamber for both dimple depths at the tested Re_{D_j} and H/D_j; the flat plate is included for a comparison. At the same Re_{D_j}, significant differences of the results of all three plates were not found. At $H/D_j \geqslant 2$, the total pressure was not a function of H/D_j or dimple depth. When the Re_{D_j} was increased from 5000 to 8000, the total pressure was doubled, and likewise from 8000 to 15000. At $H/D_j = 1$, for both $\mathrm{Re}_{D_j} = 8000$ and 11500, the deep dimples ($d/D_d = 0.25$) induced the highest total pressure among the three plates; this could be due to a greater tendency to form rolling-up vortices in the dimples.

Wall Static Pressure. The pressure distribution across a dimpled plate of $d/D_d = 0.25$ at $H/D_j = 4$ $\mathrm{Re}_{D_j} = 11500$ for the maximum crossflow scheme is illustrated in Fig. 21 in both streamwise and spanwise directions. Note that for the streamwise direction (Fig. 21(*a*)), the crossflow direction was from the right leftward. On the locations along the rows of staggered dimples and flat portions, the static pressures display no significant difference across the plate. The interest was drawn to the pressures along the inline dimple row. The highest peaks represent the stagnation points of the impinging jets, which happened inside the

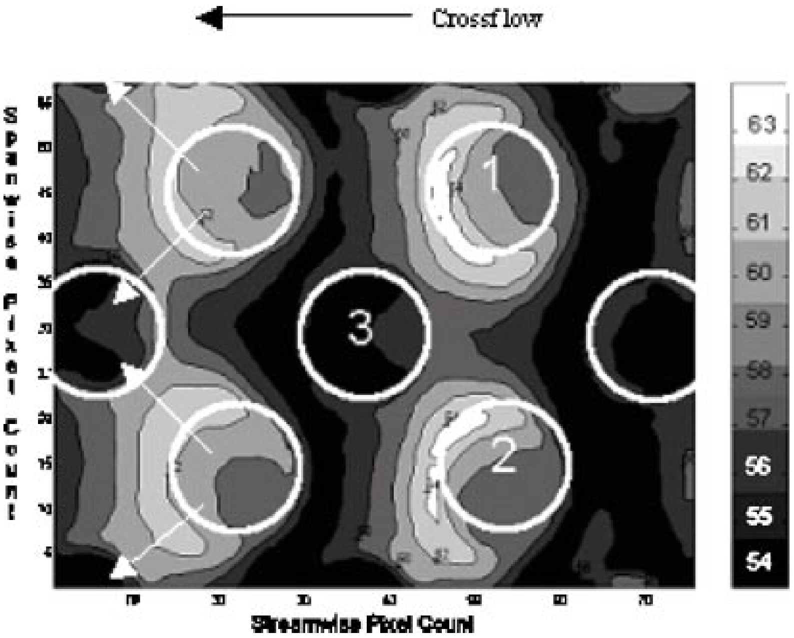

Fig. 17 Contour plot of Nusselt numbers of a dimpled plate of 40 mm diameter and 10 mm depth ($d/D_d=0.25$) at Re=11500 (Phase 2, Table 1). Note that white rings represent dimple positions

inline dimples. They were deflected towards the downstream edges of dimples, and the level of the peaks decreased in the downstream direction where the crossflow became stronger. For the spanwise direction (see Fig. 21(*b*)), the dimples near the sidewalls, where the stronger crossflow was expected, also had the highest pressure, while the values were less near the center of the plate. Therefore, the crossflow formed by the jets after impinging helped to diminish the pressure by reducing the momentum of the oncoming jets.

Conclusions

Experimental results of jet impingement on dimples with the maximum crossflow scheme (one-way spent air exit) showed a large heat transfer enhancement relative to a flat plate for most cases studied.

At a high Reynolds number, the flow contained more energetic eddies. With the presence of dimples, those eddies were broken down into a smaller-scale, and these assisted enhancing the heat

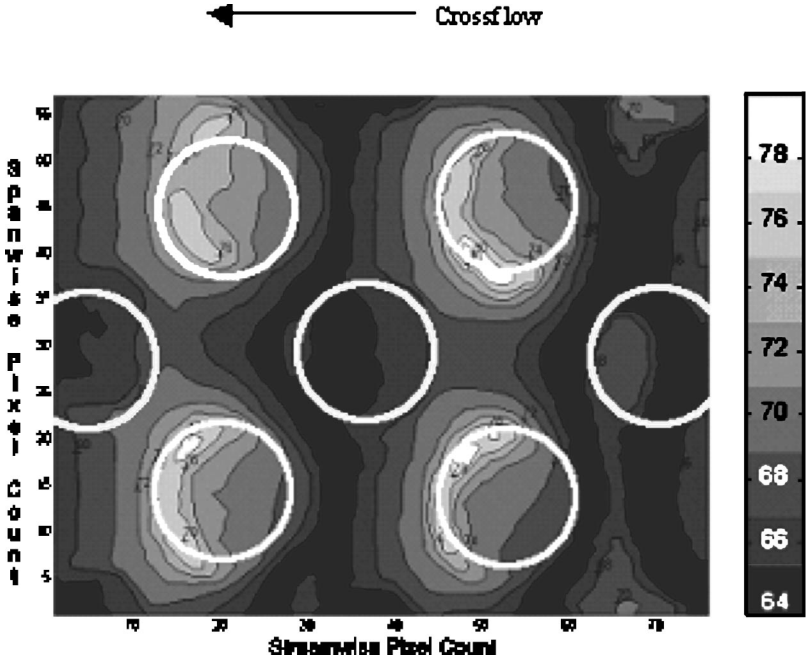

Fig. 18 Contour plot of Nusselt numbers of a dimpled plate of 40 mm diameter and 6 mm depth ($d/D_d=0.15$) at Re=11500 (Phase 2, Table 1)

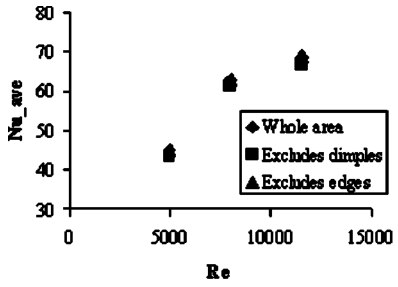

(a). $d/D_d = 0.15$

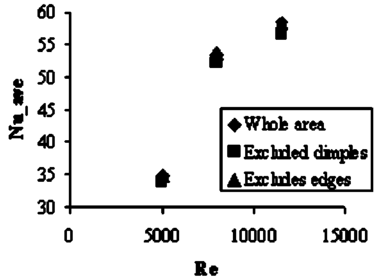

(b). $d/D_d = 0.25$

Fig. 19 Effect of the calculation method of taking into account areas of dimples and dimple edges, $H/D_j=4$

transfer, as illustrated by Re=11500 and $H/D_j=8$ where the heat transfer was improved by 50% on average compared to that of the flat plate.

Jet-to-plate spacing had a significant impact on the heat transfer of the dimple impingement. The narrow spacing could cause the recirculation which diminished the heat transfer. Concurrently, at wide spacings a lesser enhancement was measured. However, the later results on the shallower dimples show significant improvement on heat transfer for the narrow spacing as explained in the following paragraph.

The arrangement of the jet holes inline to the dimples performed better than inline to the flat portions. From the video images, when the jet holes were set inline to the flat portions, the strong crossflow deflected the oncoming jets to impinge on the upstream halves of dimples where a cold region or sink could happen. In addition, the dimples could lessen the momentum of the flow instead of promoting turbulence.

Hemispherical and cusped elliptical dimpled shapes were designed having the same wetted area. Nonetheless, the cusp could divide the oncoming jet into two parts, which formed stronger recirculation than the hemispherical dimple, and this caused the heat transfer reduction.

The depth of the dimples significantly influenced the heat transfer. The shallower dimples ($d/D_d=0.15$) enhances higher heat transfer than the deeper ones ($d/D_d=0.25$) plausibly because the vortices formed inside the dimples could be shed more easily than the deeper dimples. Moreover, the rolling-up of recirculation for the shallow dimples could occur more difficult.

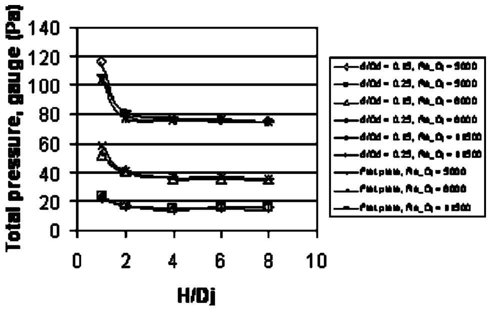

Fig. 20 Plenum pressure measurements compared to those of the flat surface at various H/D_j values (Phase 1, Table 1), $\mathrm{Re}_{D_j}=11500$, Maximum crossflow scheme

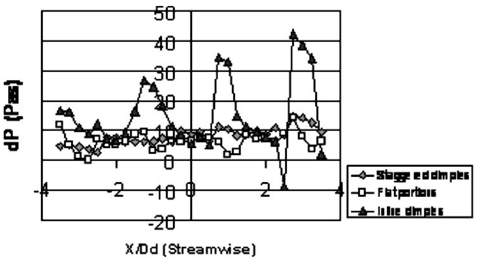

(a) Streamwise surface pressure distribution

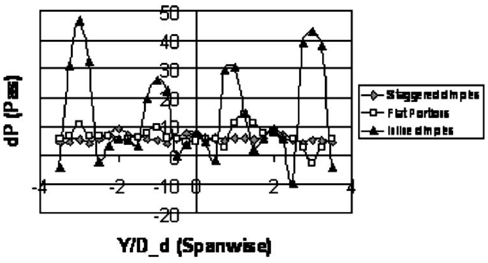

(b) Spanwise surface pressure distribution

Fig. 21 Surface pressure distribution across the dimpled plate, $H/D_j=4$, $\mathrm{Re}_{D_j}=11500$, $d/D_d=0.25$, Maximum crossflow scheme

Observing closely inside the dimples from the films, for both dimple depths the heat transfer augmentation occurred similarly with the highest near the downstream edges of inline dimples. The heat transfer inside a staggered dimple was developed by the two adjacent upstream inline dimples shedding vortices into it.

The plenum total pressure was not affected for jet-to-plate spacings greater than two jet diameters or for the two dimple depth. As expected the main influence on total pressure was due to the Reynolds number. The total pressures of both dimpled plates were not significantly different from those of the flat plate.

The surface static pressure measurements showed that the presence of crossflow assisted lowering the pressure loss on the dimpled plate. This was because the strong crossflow helped reducing the momentum of the oncoming jets toward the dimples. More experiments on static pressure measurements will be carried out in our following paper.

Nomenclature

A_t = total projected area of jet holes
c = thermal capacity of Perspex
d = dimple depth
dP = pressure difference from atmospheric pressure
D_d = dimple diameter
D_j = jet hole diameter
h = heat transfer coefficient
H = distance measured from nozzle plate to target plate
k = thermal conductivity of Perspex
$\dot{m}$ = mass flow rate
Nu_d = Nusselt number of dimpled surface
Nu_0 = Nusselt number of flat surface
Re = Reynolds number based on a single jet, VD_j/ν where $V=\dot{m}/\rho_j A_j$
t = elapsed time
T_i = initial temperature of target plate before impingement began
T_m = bulk fluid temperature

V = jet velocity
X = streamwise distance of target plate
Y = spanwise distance of target plate
z = heat penetration depth in substrate
α = thermal diffusivity of Perspex
ν = dynamic viscosity of air
ρ = density of Perspex
ρ_j = density of air

References

[1] Kesarev, V. S., and Kozlov, A. P., 1993, ''Convection Heat Transfer in Turbulized Flow Past a Hemispherical Cavity,'' Heat Transfer Res., **25**, pp, 156–160.

[2] Afanasyev, V. N., Chudnovsky, Ya. P., Leontiev, A. I., and Roganov, P. S., 1993, ''Turbulent Flow Friction and Heat Transfer Characteristics for Spherical Cavities on a Flat Plate,'' Exp. Therm. Fluid Sci., **7**, pp. 1–8.

[3] Moon, H. K., O'Connell, T., and Glezer, B., 1999, ''Channel Height Effect on Heat Transfer and Friction in a Dimpled Passage,'' ASME Paper No. 99-GT-163.

[4] Mahmood, G. I., Hill, M. L., Nelson, D. L., and Ligrani, P. M., 2000, ''Local Heat Transfer and Flow Structure On and Above a Dimpled Surface in a Channel,'' ASME International Gas Turbine and Aeroengine Congress and Exhibition, Germany, May 8–11, 2000-GT-230.

[5] Kataoka, K., Suguro, M., Degawa, H., Maruo, K., and Mihata, I., 1987, ''The Effect of Surface Renewal Due to Large-Scale Eddies On Jet-Impingement Heat Transfer,'' Int. J. Heat Mass Transfer, **30**, pp. 559–567.

[6] Gau, C., and Chung, C. M., 1991, ''Surface Curvature Effect on Slot-Air-Jet Impingement Cooling Flow and Heat Transfer Process,'' J. Heat Transfer, **113**, pp. 858–864.

[7] Cornaro, C., Fleischer, A. S., and Goldstein, R. J., 1999, ''Flow Visualization of a Round Jet Impinging on Cylindrical Surfaces,'' Exp. Therm. Fluid Sci., **20**, pp. 66–78; Chyu, M. K., Yu, Y., Ding, H., Down, J. P., and Soechting, F. O., 1997, ''Concavity Enhanced Heat Transfer in an Internal Cooling Passage,'' ASME Paper No. 97-GT-437.

[8] Kanokjaruvijit, K., and Martinez-Botas, R. F., 2003(a), ''Jet Impingement Onto a Dimpled Surface with Different Crossflow Schemes,'' Paper No. IGTC2003Tokyo TS-074, 8th International Gas Turbine Congress 2003, Tokyo.

[9] Kanokjaruvijit, K., and Martinez-Botas, R. F., 2003(b), ''Positions of Impinging Jets on Different Geometries of Dimples Considering Effect of Crossflow Scheme,'' 8th UK National Heat Transfer Conference, Oxford, 9–10 September 2003.

[10] Schultz, D. L., and Jones, T. V., 1973, ''Heat-Transfer Measurements in Short-Duration Hypersonic Facilities,'' AGARD-AG-165.

[11] Camci, C., Kim, K., and Hippensteele, S. A., 1992, ''A New Hue Capturing Technique for the Quantitative Interpretation of Liquid Crystal Images Used in Convective Heat Transfer Studies,'' ASME J. Turbomach., **114**, pp. 765–775.

[12] Wang, Z., Ireland, P. T., Jones, T. V., and Davenport, R., 1994, ''A Color Image Processing System for Transient Liquid Crystal Heat Transfer Experiments,'' ASME Paper No. 94-GT-290.

[13] Yuen, C., and Martinez-Botas, R. F., 2003, ''Film Cooling Characteristics of a Single Hole at Various Streamwise Angles: Part 1 Effectiveness,'' Int. J. Heat Mass Transfer, **46**, pp. 221–235.

[14] Yuen, C., and Martinez-Botas, R. F., 2003, ''Film Cooling Characteristics of a Single Hole at Various Streamwise Angles: Part 2 Heat Transfer Coefficient,'' Int. J. Heat Mass Transfer, **46**, pp. 237–249.

[15] Moffat, R., 1990, ''Experimental Heat Transfer,'' 9th International Heat Transfer Conference, Jerusalem, Israel.

[16] Martinez-Botas, R. F., 1993, ''Annular Cascade Aerodynamics and Heat Transfer,'' Doctorate thesis, St. John's College, Oxford University.

[17] Obot, and Trabold, 1987.

[18] Huber, A. M., and Viskata, R., 1994, ''Convective Heat Transfer to a Confined Impinging Array of Air Jets with Spent Air Exits,'' J. Heat Transfer, **116**, pp. 570–576.

[19] Terekhov, V. I., Kalinina, S. V., and Mshvidobadze, Yu. M., 1997, ''Heat Transfer Coefficient and Aerodynamic Resistance on a Surface with a Single Dimple,'' J. Enhanced Heat Transfer **4**, pp. 131–145.

Adiabatic Effectiveness Measurements of Endwall Film-Cooling for a First-Stage Vane

D. G. Knost

K. A. Thole

Mechanical Engineering Department,
Virginia Polytechnic Institute and State University,
Blacksburg, VA 24061

In gas turbine development, the direction has been toward higher turbine inlet temperatures to increase the work output and thermal efficiency. This extreme environment can significantly impact component life. One means of preventing component burnout in the turbine is to effectively use film-cooling whereby coolant is extracted from the compressor and injected through component surfaces. One such surface is the endwall of the first-stage nozzle guide vane. This paper presents measurements of two endwall film-cooling hole patterns combined with cooling from a flush slot that simulates leakage flow between the combustor and turbine sections. Adiabatic effectiveness measurements showed the slot flow adequately cooled portions of the endwall. Measurements also showed two very difficult regions to cool, including the leading edge and pressure side-endwall junction. As the momentum flux ratios were increased for the film-cooling jets in the stagnation region, the coolant was shown to impact the vane and wash down onto the endwall surface. Along the pressure side of the vane in the upstream portion of the passage, the jets were shown to separate from the surface rather than penetrate to the pressure surface. In the downstream portion of the passage, the jets along the pressure side of the vane were shown to impact the vane thereby eliminating any uncooled regions at the junction. The measurements were also combined with computations to show the importance of considering the trajectory of the flow in the near-wall region, which can be highly influenced by slot leakage flows. [DOI: 10.1115/1.1811099]

Introduction

Combustion turbine engines have become an integral part of our daily lives through propelling aircraft, tanks, and large naval ships and providing peaking power on the electrical grid. The technology of the turbine engine needs to continue to grow to provide more power at a higher efficiency in today's more environmentally conscious, yet energy-thirsty, world. The power output and efficiency of a turbine engine depend on the fluid temperature entering the turbine, with engine development moving toward increasing turbine temperatures.

As turbine inlet temperatures continue to rise the metallurgical limits of the machine have been pushed and frequently exceeded. One method of combating the overheating problem is the use of film-cooling holes whereby cooler air is extracted from the compressor, bypasses the combustor, and is injected through discrete holes in the vane and endwall surfaces. Film-cooling hole placement, particularly in the endwall region, has traditionally been based on designer experience. In addition to film cooling, most turbines have a slot at the combustor-turbine interface where cooler gases leak through. If designed properly, this leakage flow could be relied on as a source of coolant. It is also important to recognize the importance of overall aerodynamic penalties for endwall cooling.

The goal of this research was twofold. The first goal was to compare two different film-cooling hole patterns, which were based on different design philosophies. The second goal was to determine how the leakage slot flow at the combustor-turbine interface could be used to cool the turbine platform and also how this slot flow might affect the downstream film cooling. One region in particular that was assessed from a cooling standpoint was the leading-edge region of the vane whereby a range of coolant injection levels were evaluated.

Summary of Past Literature

There have been a number of studies documenting endwall film cooling and a number of studies documenting cooling from the leakage gap at the turbine-combustor junction. As will also be discussed in this summary, there has been only one study presented in the literature that has combined endwall film cooling with coolant leakage from an upstream slot.

Detailed endwall film-cooling results have been conducted by Friedrichs et al. [1–3]. The results of their first study [1], which were all surface measurements or visualization, indicated a strong influence of the secondary flows on the film cooling and an influence of the film cooling on the secondary flows. Their data showed that the angle at which the coolant leaves the hole did not dictate the coolant trajectory, except near the hole exit. Furthermore, the endwall cross flow was altered so that it was turned toward the inviscid streamlines, which was due to the film-cooling injection.

There have been a few studies that have measured endwall heat transfer as a result of injection from a two-dimensional (2D) flush slot just upstream of the vane. Blair [4] measured adiabatic effectiveness levels and heat transfer coefficients for a range of blowing ratios through a flush slot placed just upstream of the leading edges of his single-passage channel. One of the key findings was that the endwall adiabatic effectiveness distributions showed extreme variations across the vane gap with much of the coolant being swept across the endwall toward the suction-side corner. Granser and Schulenberg [5] reported similar adiabatic effectiveness results in that higher values occurred near the suction side of the vane. Based on their measurements, Roy et al. [6], however,

---

Contributed by the International Gas Turbine Institute (IGTI) of THE AMERICAN SOCIETY OF MECHANICAL ENGINEERS for publication in the ASME JOURNAL OF TURBOMACHINERY. Paper presented at the International Gas Turbine and Aeroengine Congress and Exhibition, Vienna, Austria, June 13–17, 2004, Paper No. 2004-GT-53326. Manuscript received by IGTI, October 1, 2003; final revision, March 1, 2004. IGTI Review Chair: A. J. Strazisar.

indicated that the coolant migrated toward the pressure side of the vane. Their measurements indicated reduced values of local heat transfer coefficients at the leading edge when slot cooling was present relative to no slot cooling.

A series of experiments have been reported for various injection schemes upstream of a nozzle guide vane with a contoured endwall by Burd and Simon [7], Burd et al. [8], and Oke et al. [9,10]. In these studies [7–9], coolant was injected from an interrupted flush slot that was inclined at 45 deg just upstream of their vane. Similar to others, they found that most of the slot coolant was directed toward the suction side at low-slot flow conditions. As they increased the percentage of slot flow to 3.2% of the exit flow, their measurements indicated better coverage occurred between the airfoils.

Colban et al. [11,12] reported flow-field and endwall effectiveness contours for a backward-facing slot with several different coolant exit conditions. Their results indicated the presence of a tertiary vortex that developed in the vane passage due to a peaked total pressure profile in the near-wall region. For all of the conditions simulated, the effectiveness contours indicated the coolant from the slot was swept toward the suction surface. While this study was completed for the same vane geometry as that reported in this paper, the slot geometry has been altered to be flush with the endwall surface.

Zhang and Moon [13] tested a two row film-cooling configuration upstream of a contoured endwall. Upstream of these two rows of film-cooling holes was placed either a flush wall or a backward facing step. In making direct comparisons between these two configurations, measured effectiveness levels were reduced considerably in the case of the backward-facing step configuration. They attributed these reduced effectiveness levels to the increased secondary flows that were present.

The only two studies to have combined an upstream slot with film-cooling holes in the passage of the vane were those of Kost and Nicklas [14] and Nicklas [15] and a CFD study previously reported by Knost and Thole [16] as those on this paper. One of the most interesting results from the Kost and Nicklas [14] and Nicklas [15] studies was that they found for the slot flow alone, which was 1.3% of the passage mass flow, the horseshoe vortex became more intense. This increase in intensity resulted in the slot coolant being moved off of the endwall surface and heat transfer coefficients that were over three times that measured for no-slot flow injection. They attributed the strengthening of the horseshoe vortex to the fact that for the no-slot injection, the boundary layer was already separated with fluid being turned away from the endwall at the injection location. Given that the slot had a normal component of velocity, injection at this location promoted the separation and enhanced the vortex. Their adiabatic effectiveness measurements indicated higher values near the suction side of the vane due to the slot-coolant migration.

The CFD study results presented by Knost and Thole [16], for the same geometry and coolant flow conditions as presented in this paper, indicated the presence of a warm ring on the endwall around the vane where no coolant was present despite the combined slot cooling and film cooling. Based on this computational study and lack of experimental data in the literature for a realistic hole pattern combined with an upstream slot representing the combustor-turbine interface, there was a need to verify the cooling problems associated with the endwall of a turbine platform.

Design of Endwall Cooling Schemes

Two realistic cooling hole patterns for the platform of the vane were developed based on industry input, as shown in Fig. 1. Also shown in this figure are iso-velocity contours, hole injection directions, and for pattern 2, the location of a gutter. A gutter, which is the joint between the two mating platforms, has the potential of having coolant leakage, but was not simulated in our studies. The airfoil geometry used in the current study is a commercial first-stage vane previously described by Radomsky and Thole [17]. The vane is two-dimensional with the midspan modeled along the entire span.

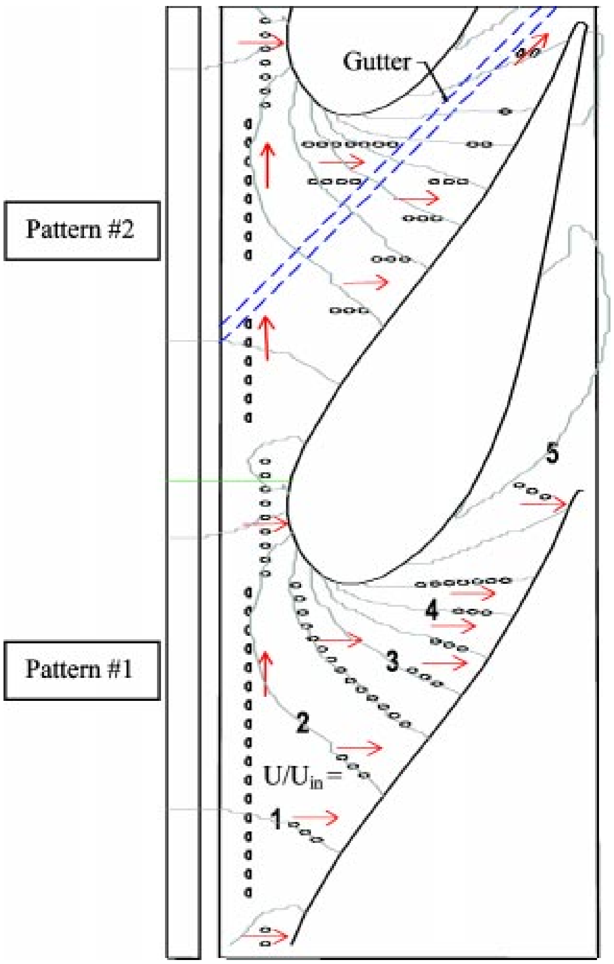

Fig. 1 The two film-cooling patterns that were simulated in this study with iso–velocity contours (U/U_{inlet}) and injection direction for the cooling holes

Table 1 provides a summary of parameters relevant to both cooling-scheme designs. Both cooling hole patterns included a two-dimensional flush slot located $0.31C_a$ upstream of the vane stagnation, representing the combustor-turbine interface. The slot injected at an angle of 45 deg with respect to the endwall and had a slot length (flow-path length) to width (cross-sectional width) of 1.8.

Downstream of the slot, two different endwall cooling hole patterns were placed. All film-cooling holes injected at a 30 deg angle with respect to the endwall surface. The primary difference

Table 1 Summary of Cooling Hole and Slot Geometry

Feature	9× Scale
Re_{in}	2.3×10^5
Cooling hole diameter (cm)	0.46
Cooling Hole L/D	8.3
Hole injection angle	30 deg
P/D for leading edge holes	4/3
P/D for passage holes	3
Slot width (cm)	1.48
Slot length to width	1.8
Upstream slot location of vane	$-0.35C_a$
Slot injection angle	45 deg

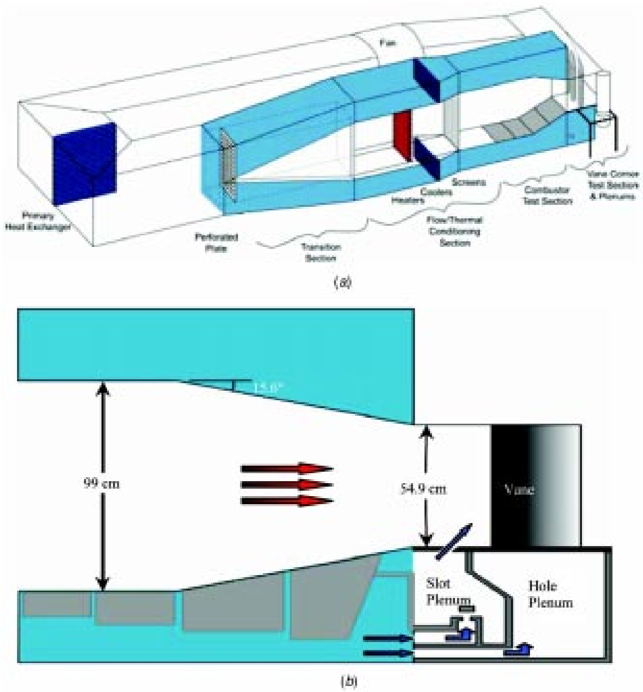

Fig. 2 (***a***) **Illustration of wind tunnel facility,** (***b***) **cooling supply for slot and film cooling holes**

between the two endwall cooling configurations in the leading-edge region was the absence of holes for pattern 2 where there would be a gutter between the two platforms. Inside the passage there are distinct differences between the two cooling hole patterns. Harasgama and Burton [18] suggested that locating film-cooling holes along iso-mach lines would ensure a uniform blowing rate and momentum flux helping to prevent jet liftoff. Hole pattern 1 was designed such that the cooling holes were located along straight lines approximating the iso-velocity contours. Iso-velocity contours were chosen because experiments will be conducted in a low-speed facility with little variation in Mach number. Alternatively, hole pattern 2 was designed such that the holes nearest to the pressure side of the vane lie on the same iso-velocity contours that were used in hole pattern 1, but with the difference being the row of holes was placed along axial lines rather than iso-velocity contours. There was a continuation of the gap left in the rows of holes where the previously mentioned gutterwould reside. While the hole pattern on the iso-velocity lines (pattern 1) provide a uniform blowing ratio given the same supply pressure, the axial hole pattern (pattern 2) is more likely to be cheaper to manufacture.

One of the additional differences between the two cooling hole patterns is that there were 14 more cooling holes for the cooling hole pattern 1 as compared with pattern 2, which was dictated by the designs given by industry (pattern 2 has 78% of the hole area of pattern 1). As a result of this disparity in the number of cooling holes, the coolant flow distribution is different for each of the hole patterns.

Experimental Methodology

Adiabatic endwall temperatures were measured for a range of experimental conditions using a scaled up vane, film-cooling holes, and slot geometries to allow for good measurement resolution. The experiments for this study were performed in a low-speed, closed-loop wind-tunnel facility, shown in Fig. 2(a), that has previously been described by Barringer et al. [19] and Colban et al. [11]. The flow in the wind tunnel is driven by a 50 hp axial vane fan, which is controlled by a variable frequency inverter.

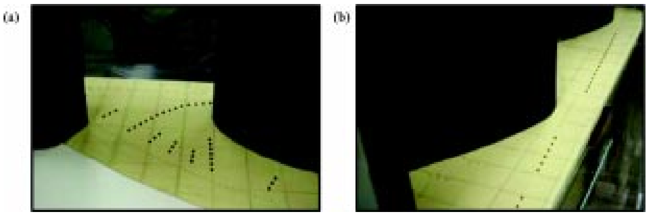

Fig. 3 **Film-cooling holes for** (***a***) **Passage 1 and** (***b***) **the leading edge region**

Downstream of the fan, the flow passes through a primary flow, finned-tube heat exchanger used to cool the bulk flow. After being turned by another 90 deg elbow, the flow encounters a three-way flow split. This flow split is controlled by a perforated plate, which was designed to obtain the proper pressure drop in the main gas path thereby forcing some of the air into the bypass legs. The core flow then passes through a heater bank, a series of screens used for flow straightening, and finally into a two-dimensional converging section. In the vane cascade, two full passages were modeled with three vanes. A bleed is positioned on either side of the two-passage cascade to remove edge effects from the side walls while tailboards ensure periodicity of the flow in the two passages.

As was stated, this facility included three channels: a heated primary channel (representing the main gas path) and two symmetric secondary channels (representing the coolant flow paths). A 35–40° C temperature differential between the coolant and mainstream was achieved by using the heaters in the primary channel and heat exchangers in the secondary channels. While the top secondary flow channel was closed off for these experiments, the bottom secondary flow channel was used for supplying the coolant to the slot and hole plenums, as seen in Fig. 2(b). These two plenums were constructed to provide independent control of the slot and film-cooling flow rates. The front plenum supplied the slot flow while the rear plenum supplied the film-cooling flow. Typical time to achieve steady-state conditions was 3 hr. As these experiments were to be relevant to industrial gas turbines where freestream turbulence levels can be lower than for aeroderivative engines; freestream turbulence effects were not the focus. The inlet turbulence level and length scales were measured, however, to be 1.3% and 4 cm, respectively.

The endwall test plate had a foam thickness of 1.9 cm (0.75 in.), which was chosen because of its low thermal conductivity (0.033 W/mK). To ensure the precision and integrity of the cooling hole pattern, the holes were cut with a five-axis water jet. Portions of the hole patterns are shown in Fig. 3. The endwall surface was painted black to enhance the radiative emissivity of the surface. The slot was constructed from balsa wood, which had the same thermal conductivity as the foam but was stiffer.

Coolant Flow Settings. For every test condition, the dimensionless pressure coefficient distribution was verified to ensure periodic flows were set through the passages (reported previously in [17]). Film-coolant flow rates for each cooling hole could not be controlled because only one plenum provided coolant to the entire endwall cooling hole pattern, and the local static pressure field varied greatly from hole to hole. Friedrichs et al. [1] suggested that a global blowing ratio based on the inlet flow conditions could be characterized by the blowing ratio of a loss-free hole injecting into inlet conditions as calculated from

$$M_{\text{ideal}} = \sqrt{\frac{\rho_c}{\rho_{in}} \cdot \frac{P_{o,c} - p_{s,in}}{P_{o,in} - p_{s,in}}} \tag{1}$$

A modification of this approach was taken for this study in that a global discharge coefficient C_D was derived so that the cumulative flow rate through either cooling pattern could be characterized. The C_D values were obtained from CFD studies and have been previously reported by Knost and Thole [16]. Measurements

Table 2 Discharge Coefficients for Film-Cooling

Slot flow rates $\%m_{\text{exit}}/M_{in}$	Film flow rate $\%m_{\text{exit}}/M_{in}$	Cooling hole patterns	Hole discharge coefficient
—	0.5/1.2	1	1.09
—	0.5/1.5	2	0.81
0.5/0.17	0.5/1.2	1	1.09
0.5/0.18	0.5/1.5	2	0.80
0.5/0.17	0.75/1.8	1	0.84
0.5/0.18	0.75/2.2	2	0.71

of the inlet velocity, average inlet static pressure, and coolant total pressures were obtained, which then allowed the fraction of coolant flow relative to the inlet core flow to be calculated from

$$\frac{\dot{m}_c}{\dot{m}_{\text{core}}}=M_{\text{ideal}}\cdot C_D\cdot\frac{A_{\text{hole}}}{A_{in}}\cdot\#\text{holes} \tag{2}$$

Different global discharge coefficients were used for each of the two cooling patterns, as indicated in Table 2, because the patterns had a number of holes in different locations. Note that these discharge coefficients are greater than one as a result of using a reference pressure as the static pressure at the inlet to the cascade. As the flow accelerates through the cascade the static pressure decreases, causing the discharge coefficient to be greater than one. A discharge coefficient of $C_D=0.6$ was used for the slot flow. Also given in Table 2 is the global mass flux ratio (M_{in}) based on the inlet velocity. Note that for all of the experiments, the density ratio (jet-to-mainstream) was held fixed at 1.12.

Instrumentation and Measurement Uncertainty. An Inframetrics P20 infrared camera acquired the spatially resolved adiabatic temperatures on the endwall. Measurements were taken at 13 different viewing locations to ensure that the entire endwall surface was mapped. From a camera distance of 55 cm, each picture covered an area that was 24 cm by 18 cm with the area being divided into 320 by 240 pixel locations. The spatial integration for the camera was 0.715 mm (0.16 hole dia). The camera images were post calibrated using directly measured temperatures on the endwall by thermocouples that were installed. Thermocouple data was continuously acquired during image collection. The thermocouple measurements had a maximum-to-minimum range of approximately 0.8°C deg with a standard deviation of 0.17°C during the image collection time, which required about 30 min. For the post calibration, the emissivity and background temperature were adjusted until the temperatures from the infrared camera images were within 1°C of the corresponding thermocouple data. Typical emissivity values and typical background temperatures were $\varepsilon=0.89$ and 45°C. Once the images were calibrated, the data was exported to an in-house Matlab® program that was written for image assembly.

Variations in free-stream temperature from passage to passage were less than 1.5°C. Three thermocouples were also located in both the slot and film-cooling plenums with one thermocouple beneath each of the passages and one beneath the center vane. These thermocouples allowed gradients in the coolant supply to be documented. Variation within the plenums was generally less than 0.3°C. Voltage outputs from the thermocouples were acquired by a 32-channel data acquisition module that was used with a 12-bit digitizing card.

An uncertainty analysis was performed on the measurements of adiabatic effectiveness using the partial derivative method described at length by Moffat [20]. The precision uncertainty was determined by taking the standard deviation of six measurement sets of IR camera images with each set consisting of five images. The precision uncertainty of the measurements was ±0.014°C. The bias uncertainty was ±1.0°C based on the calibration of the image. The bias uncertainty of the thermocouples was ±0.5°C. The total uncertainty was then calculated as ±1.0°C for the images and ±0.51°C for the thermocouples. The uncertainty in adiabatic effectiveness η was then found based on the partial derivative of η with respect to each temperature in the definition and the total uncertainty in the measurements. An uncertainty of $\partial\eta=\pm0.082$ at $\eta=0.2$ and $\partial\eta=\pm0.029$ at $\eta=0.9$ were calculated.

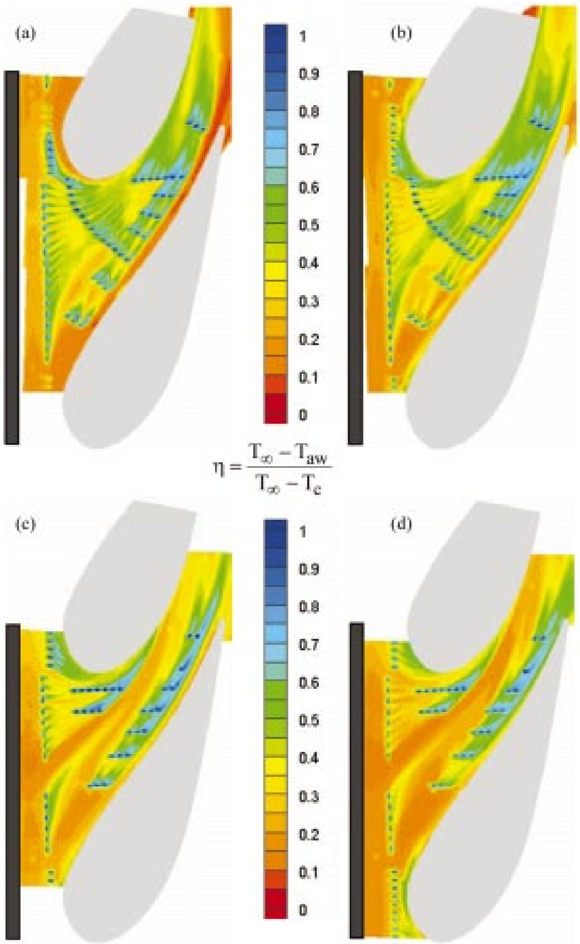

Fig. 4 Contours of adiabatic effectiveness for the baseline film-cooling only cases: (*a*) pattern 1, 0.5% coolant (*b*) pattern #1, 0.75% coolant, (*c*) pattern #2, 0.5% coolant, and (*d*) pattern 2, 0.75% coolant

Discussion of Results

The results from the experiments will be discussed in a logical progression of complexity. First, the cooling provided from the film cooling alone for both endwall patterns will be discussed. Second, the predictions for the combined slot and film-cooling configurations will be compared to the endwall film cooling alone. Finally, there will be a discussion of the leading-edge region and vane pressure-side region as these two regions were found difficult to cool.

Film Cooling Without Slot Injection. The film-cooling cases without slot flow for each of the two patterns are shown in Figs. 4(a)–4(d). The location of the slot, which was not simulated, is shown in black for reference. Each pattern was tested with a low and high film-cooling flow rate of 0.5% and 0.75% of the core flow, respectively. It can be seen in Figs. 4(a)–4(d) that the minimum effectiveness levels are $\eta=0.1$ for all cases The reason for this is that there was a slight cooling effect of the near-wall fluid because of the long 4 m (6.8 C) unheated wall between the heater bank and the test section. The thermal boundary layer at the inlet to the cascade was measured to have a thickness that was 5% of the vane span. As will be shown in later contours, effectiveness levels near zero were measured for some of the cases presented indicating the downturning of hotter fluid onto the endwall.

For pattern 1 at the low film flow rate, shown in Fig. 4(a), a fairly uniform coverage is seen across much of the passage. The leading row of holes near the suction side inject as discrete jets in the direction of the streamlines despite being directed normal to the inlet direction (toward the top of the page). The leading row of holes near the pressure side inject in a more merged pattern toward the injection direction. Just upstream of the stagnation location are quite ineffective at these low-coolant flow conditions, particularly near the pressure side. Those holes near the stagnation location along the suction side are swept around the shoulder leaving an uncooled region at the vane-endwall junction. The jets along the pressure side appear to inject in the streamwise direction following the contour of the vane despite the jet hole being directed axially downstream. Along the pressure side of the vane, however, there is still a warm region with no appearance of coolant.

For the increased film-cooling case of pattern 1, shown in Fig. 4(b), several effects are seen. First the suction-side jets of the leading row still inject as discrete jets, but lower adiabatic effectiveness values present downstream of the holes indicate that the jets are lifting off of the surface. The leading row of holes near the pressure side appear to be slightly more directed with very little coolant present downstream of several of the holes. The leading-edge holes at the stagnation location of pattern 1 for the 0.75% coolant flow rate are far more effective than for the 0.5% coolant flow rate. These higher effectiveness levels at the higher coolant flow are even more apparent along the suction side at cooling the vane-endwall junction. The cooling jets exiting the stagnation holes on the pressure side, however, appear to lift off at the injection location, impact the vane, and convect down the vane onto the endwall. This liftoff is evidenced by the coolant accumulating along the vane-endwall junction near the dynamic stagnation point of the vane. Within the passage, the pressure-side jets penetrate to approximately one cooling-hole diameter closer to the vane as compared with the 0.5% case, thereby reducing, but not eliminating, the warm zone along the pressure side.

For pattern 2 at the low blowing rate, shown in Figure 4(c), the most noticeable feature is the large hot streak through the center of the passage. This hot streak exists in the location where the gutter would be, therefore, including the gutter flow may tend to alleviate the problem. It is also important to remember that pattern 2 has fewer cooling holes, and as such, the coolant distribution is different from pattern 1. Consider the leading-edge row of holes where the holes nearer to the suction side inject with the streamlines for both hole patterns, but the local effectiveness levels are lower for pattern 2 than in the corresponding case for pattern 1. The reason for this difference is that pattern 2 has slightly higher momentum flux ratios for these jets, and as such, there is a tendency for the coolant flow to separate from the wall. These higher momentum flux ratios for pattern 2 has a positive benefit, however, when considering the holes near the stagnation location where the effectiveness levels are much higher for pattern 2 than for pattern 1 at the 0.5% coolant flow. Also, the pressure-side holes in the passage of pattern 2 appear to reduce the uncooled zone along the vane-endwall junction when compared to pattern 1.

The results of increasing the film-cooling flow rate, in pattern 2, to the high-blowing rate are shown in Figure 4(d). The jet detachment of the suction-side leading row of holes appears to be exacerbated, resulting in low effectiveness levels on the endwall. The coolant from the suction-side leading row of holes also appears to be less effective at the high-coolant flow rate and may suffer from blockage by the holes directionally downstream (bottom to top on the image) in the row causing the coolant to lift off. At the stagnation location, there is clearly a separation region of the jets that then impact the vane and wash onto the endwall surface. Within the passage, the pressure-side jets appear well merged and penetrate to the vane-endwall junction, eliminating the hot zone along the second half of the pressure side.

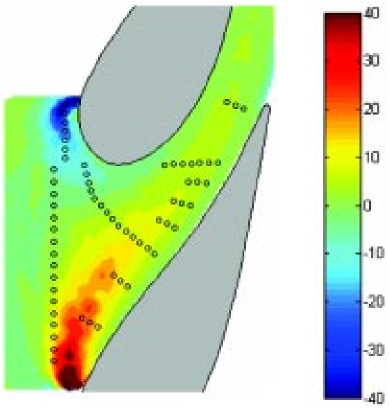

Fig. 5 Contours of the difference between the predicted flow angles at 2% span and midspan are shown for the high 0.75% slot flow case. The hole locations of pattern 1 are shown for reference.

Slot-Flow Combined With Film-Cooling Injection. When placing film-cooling holes, a designer would like to predict the film-coolant trajectory to ensure that the cooling needs of critical areas are met. A first approximation might be made by using a 2D inviscid CFD prediction of the streamlines to predict the path of the coolant. This first approximation was examined by comparing the flow-turning angles at the midspan relative to those near the endwall at the 2% span location. Contour plots of the difference between the flow-turning angles near the wall and those at midspan for a 0.75% slot-flow injection is shown in Fig. 5 (note that there is no film-cooling injection, but the cooling holes for pattern 1 are superimposed for reference). These predictions were computed using FLUENT, whereby the full details are given in a previous publication [16]. These contours indicate the cross flows that are induced in the near wall region for a high slot flow with deviations from the midspan by as much as 40 deg near the stagnation location. As will be discussed when interpreting the film-cooling measurements, it is relatively important to assess these differences when designing an endwall hole pattern.

To compare the influence of the slot flow rate, the 2% span streamlines for both the 0.5% and 1% slot flow cases were superimposed on hole pattern 1 as shown in Fig. 6. It is seen that especially along the upstream portion of the pressure side, and the upstream portion along the suction side to a lesser extent, the near-wall flow trajectory can be dramatically altered depending on the slot flow rate. At a high slot flow rate, the streamlines are drawn toward the suction side of the vane more so than at the lower slot flow rate. The cross flows are also shown to be slightly stronger at the high slot flow rate.

Predicted streamlines in the near-wall region (2% span) for 0.5% slot flow without film cooling are shown superimposed on adiabatic effectiveness measurements of the two patterns with 0.5% slot flow and 0.5% film flow in Figs. 7(a) and 7(b). For both hole patterns, the slot flow is funneled toward the suction side and is not present in the stagnation region. Similar to that of the film-cooling injection without slot flow, the minimum effectiveness level is $\eta = 0.1$, which is due to the unheated entry region to the cascade. It is apparent from these contours that the holes at the stagnation location, similar to those results in Fig. 4(a), are quite ineffective, leaving an uncooled area in the stagnation region. Moreover, it is apparent that the leading row of holes placed in the midpassage is being saturated by coolant and the need for film-cooling holes has been diminished as a result of the coolant from the slot.

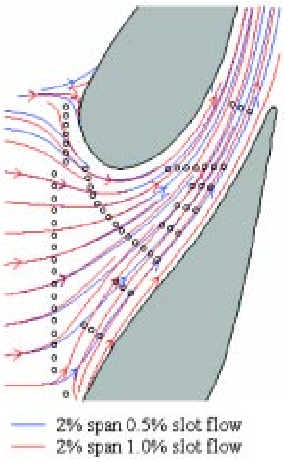

Fig. 6 Predicted streamlines at 2% span for both the 0.5% and 1.0% slot flow rates. The hole locations of pattern 1 are shown for reference.

For both patterns the film-coolant trajectories follow the predicted streamlines quite well in a number of locations. The coolant from the holes in the stagnation region is swept around the suction side and the jets along the pressure side of the vane follow the predictions. The largest difference between the streamlines and the coolant trajectory is for the leading row of holes nearer to the pressure side of the vane outside of the influence of the slot. This location shows that the holes are directed in a cross-pitch direction rather than following the streamlines at this location. It is also seen that the streamlines are more closely followed for pattern 1 relative to pattern 2, which can be explained by the stronger effects that the jets have for pattern 2 (fewer holes with more mass flow per hole).

Predictions of the streamlines at 2% span for the highest 1% slot flow rate are superimposed on measurements of each pattern with 0.75% slot coolant and 0.5% film-cooling in Figs. 8(*a*) and 8(*b*). The case of 0.75% slot coolant without film-cooling was not computed, but the predicted streamlines for the higher slot flow case will still be used to illustrate the effects of the slot flow.

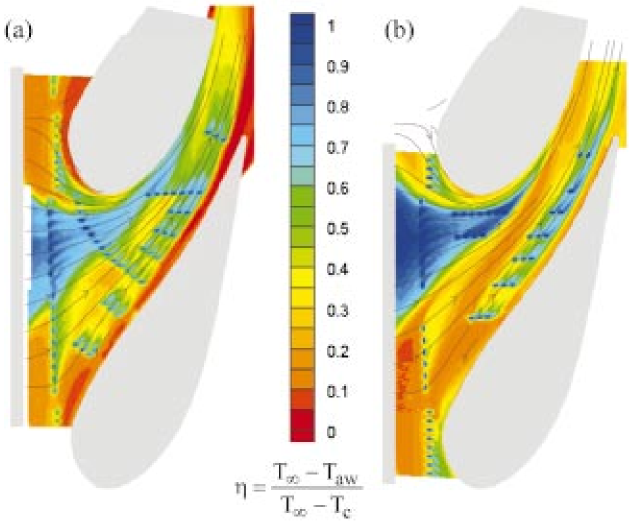

Fig. 7 Predicted streamlines at 2% span for 0.5% slot flow without film cooling are superimposed on measured effectiveness levels for (*a*) pattern 1 with 0.5% slot flow and 0.5% film cooling and (*b*) pattern 2 with 0.5% slot flow and 0.5% film cooling

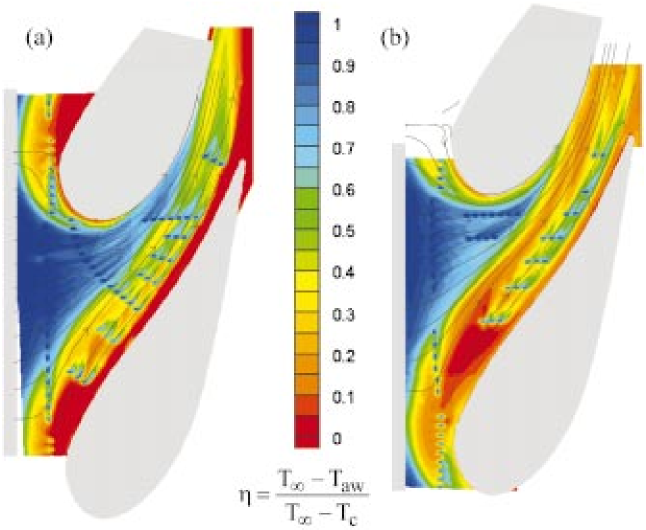

Fig. 8 Predicted streamlines at 2% span for 1% slot without film cooling superimposed for (*a*) pattern 1 with 0.75% slot flow and 0.5% film cooling, and (*b*) pattern 2 with 0.75% slot flow and 0.5% film cooling

When the slot flow is increased to 0.75% of the core flow while the film cooling is maintained at 0.5%, it is seen from Figs. 8(*a*) and 8(*b*) that the slot coolant coverage is dramatically increased. Coolant exits across the entire width of the slot, but is still funneled toward the suction side. Adiabatic effectiveness levels across much of the upstream portion of the endwall are near unity, indicating overcooling by the slot. The leading row of holes over a large portion of the pitch appears to be unnecessary for endwall cooling. Therefore, the coolant emerging from these holes could be redistributed to more advantageous locations. As has consistently been the case, the stagnation holes of pattern 1 at the low film-cooling rate are ineffective leaving an uncooled zone at the leading edge as the coolant is immediately swept around the suction side. Also, the pressure-side jets in the passage inject with the streamlines, once again leaving an uncooled region along the pressure side.

For these high slot flow conditions shown in Figs. 8(*a*) and 8(*b*), it is interesting to note that the minimum effectiveness level is $\eta = 0$ as compared to the previously shown no and low slot flow cases. The reason for these lower effectiveness levels is because of the increased downturning of the fluid above the endwall toward the endwall. These results indicate that for the high slot flow case there is a more pronounced cross-passage flow whereby the slot flow moves endwall fluid toward the suction side of the airfoil. As such, the near-wall upstream boundary layer fluid is replaced with hotter fluid that was entrained toward the endwall from above the 5% vane span location (thickness of the cooled thermal boundary layer).

The near-wall streamlines again predict the coolant trajectories relatively well. The leading row of holes follows the streamlines as do the pressure-side holes both in the up- and downstream regions. Note that there is better agreement with the streamlines for the leading row of holes in the region nearer to the pressure side of the vane for this high-coolant flow condition as compared with lower coolant flow.

When comparing the two hole patterns for combined film-cooling and slot flow cases, there are some noticeable differences. The exit location of the slot flow is seen to have migrated slightly toward the suction side of the vane for pattern 2 relative to pattern 1. This is most likely because of the absence of holes (due to the gutter location) for pattern 2, thus resulting in less flow blockage of the slot flow as compared to pattern 1 with a continual row of holes. Also immediately noticeable is the large hot streak through

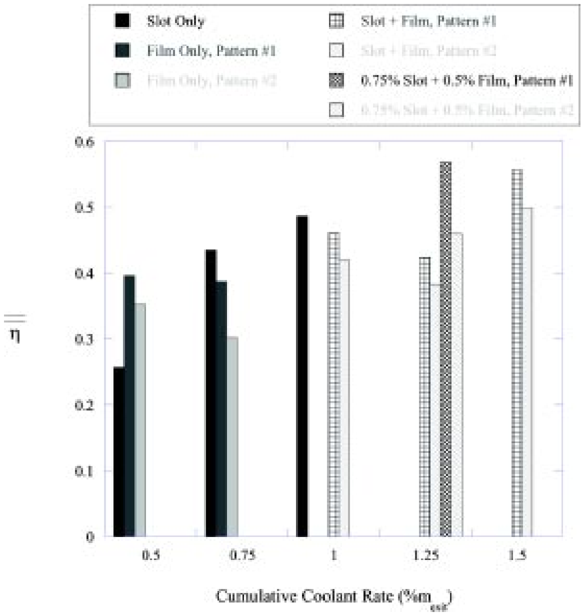

Fig. 9 Area-averaged effectiveness levels for a range of coolant flow rates (percentage is based on total passage flow)

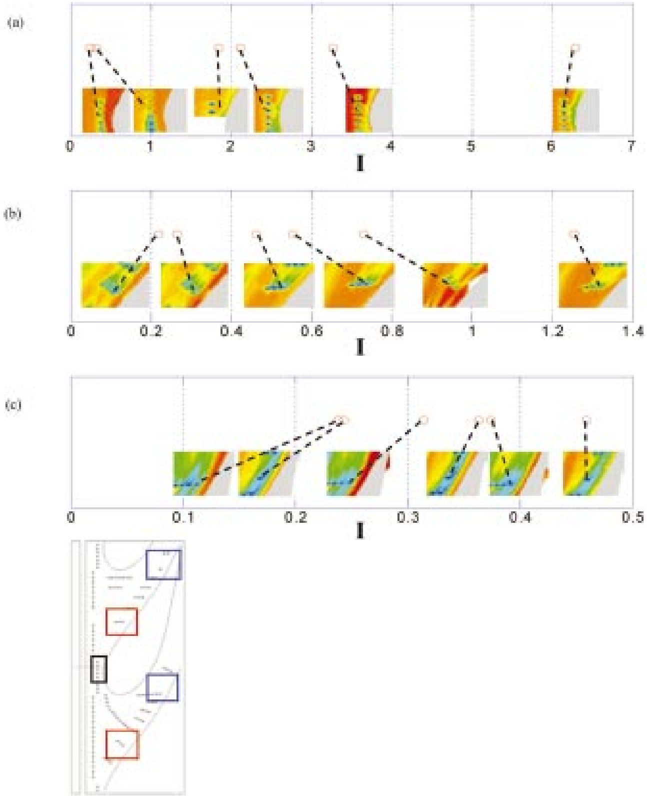

Fig. 10 Momentum flux ratios for holes indicated by the dashed lines are shown in (*a*) leading edge, (*b*) pressure side upstream, and (*c*) pressure side downstream regions. Hole locations are shown to the right

the center of the passage that was present without slot flow for pattern 2. The coolant from the pressure-side leading row of holes, which provided a small measure of relief to the hot streak without the presence of slot flow, appears drawn across the gap and merges with the slot coolant at the upstream rows of passage holes. One more noticeable difference between the two patterns is that the pressure-side jets in the passage of pattern 2 at the low blowing ratio are seen to be more directed than their counterparts in pattern 1 because of the higher momentum due to fewer jets. The coolant, however, still fails to fully penetrate to the vane, leaving a thin uncooled zone along the pressure side for both hole patterns.

Area-averaged adiabatic effectiveness levels, such as those shown in Fig. 9, are one way of deducing an overall comparison of the different cooling methods. This comparison, however, does not allow one to compare hot spots that may arise causing reductions in component life. The averages, shown in Fig. 9, were computed from the axial location $x/C_a = -0.24$, corresponding to the location furthest upstream where the images covered the entire pitch for all cases, to $x/C_a = 0.74$, beyond which there was no optical access. The various cases, of which not all have been shown in this paper, have been grouped by cumulative coolant flow rate to provide a quantification of the effects of distributing coolant between the slot and film-cooling holes.

It is seen that at the lowest coolant flow rate of 0.5%, the film-cooling holes provide a greater average cooling effectiveness than the slot flow alone. When the coolant and slot flow rates are increased to 0.75% of the core flow, however, the slot flow provides the highest average effectiveness level. Note that the slot average effectiveness is only high in the upstream, center portion of the passage, while providing no relief to the vane-endwall junction along both the leading edge and pressure side of the vane. The average effectiveness level of pattern 1 is roughly the same for both coolant flows cases (0.5% and 0.75%), while pattern 2 actually performs worse at the higher coolant flow relative to the lower coolant flow. This worse performance is because of the jet separation and a widening of the hot streak in the center of the passage (these contours are not shown in this paper). At 1% coolant flow, the area averaged effectiveness level is still somewhat higher for the slot flow alone relative to the combined film and slot cases.

The 1.25% grouping consisted of four cases where the coolant was varied between slot and film-cooling holes as shown in Fig. 9. The highest average effectiveness level was measured for pattern 1 at the higher slot flow combined with lower film-cooling flow. Pattern 2 showed the same trend with the high-slot, low-film condition flows outperforming the low-slot, high-film flow case. The higher slot flow rate provided significantly more coolant to the broad uncooled area in the upstream portion of the passage. This, combined with the less directed, streamwise injection of the pressure-side holes, minimized the hot streak for pattern 2.

Finally, the high 0.75% slot flow rate combined with the high film-cooling rate for each pattern is shown for the total 1.5% coolant flow cases in Fig. 9. Pattern 1 showed a slight decrease in average effectiveness levels from the high-slot, low-film case. The reason for these lower average effectiveness levels is because lower local effectiveness levels occurred as the jet liftoff became significant in many regions on the endwall. Pattern 2 exhibited a slightly higher average effectiveness level as the hot ring along the pressure surface was reduced in size.

Leading Edge and Pressure Side Holes. Because these results indicate that the leading-edge and pressure-side regions are so difficult to cool, a further analysis revealed the importance of the local jet momentum flux ratios. The holes within the boxes shown in Fig. 10 were selected as representative holes to analyze. The local momentum flux ratios for each of the holes were calculated from CFD predictions using

$$I = \frac{\rho_j v_j^2}{\rho_\infty v_\infty^2} = \frac{\rho_j (\dot{m}_j / \rho_j A_j)^2}{2(P_{o,c} - p_\infty)} \tag{3}$$

The momentum flux ratios for these holes are also plotted in Figs. 10(*a*)–10(*c*) along with subsets of the effectiveness contours for these representative holes.

Figure 10(a) shows the holes in the stagnation location. The blowing ratios for these holes are seen to be significantly higher than for holes along the pressure side despite the velocity of these jets being lower. This occurs because of the stagnating core flow. At the lowest momentum flux ratios, the coolant from the jets is seen to barely be present. In fact, the contours indicate that there is some coolant present upstream of the injection location and the presence of some coolant being swept around the suction side of the vane. The coolant occurring upstream of the holes is present as a result of the leading-edge horseshoe vortex sweeping the coolant upstream.

As the momentum flux ratio of the jets is increased to slightly above $I \sim 2$ in Fig. 10(a), coolant is swept on the vane endwall. As the momentum flux ratio is increased, the jet impacts the endwall then separates to impact the vane and wash down the vane onto the endwall. These contours for $I \sim 3.2$ show coolant is present on the endwall for this range of momentum flux ratios. At the highest momentum flux ratio case of $I \sim 6$, all holes are fully detached with effectiveness levels along the vane-endwall junction being higher than $I \sim 3.2$. This is because the coolant exits the holes, impacts vane, and is then washed down onto the endwall to provide a cooling benefit.

The momentum flux ratios for the pressure-side holes are important to understand to ensure no uncooled regions near the pressure side of the vane. For the upstream pressure-side holes, presented in Fig. 10(b), the jets appear fully attached up to $I = 0.46$. At $I = 0.55$ the effectiveness levels are not maintained as far downstream of the holes, indicating partial jet liftoff. Also, the upstream-most hole at $I = 0.46$ is drawn away from the vane and toward the center of the passage. At the momentum flux ratio of $I = 0.73$, the jet appears nearly fully detached. This data indicate that as the momentum flux of the jets is increased, the upstream pressure-side jets separate from the wall rather than penetrate to the pressure-side surface of the vane.

The downstream pressure-side jets, shown in Fig. 10(c), appear fully attached in all cases with a maximum momentum flux ratio of only $I = 0.46$, being achieved because of the high mainstream velocities. As the momentum flux ratio was increased, the downstream pressure-side jets penetrated close to the vane finally impacting the vane at the highest momentum flux ratio of $I = 0.46$.

When comparing all holes, separation was induced in the range $0.55 \leqslant I \leqslant 0.73$. The upstream pressure-side holes separated before impacting the vane, while the downstream pressure-side holes were able to penetrate completely to the pressure side of the vane leaving no uncooled regions.

Conclusions

Measurements of endwall adiabatic effectiveness were presented for an extensive test matrix combining both coolant from a flush slot and film cooling from two distinct hole patterns. Film-cooling holes were shown to distribute coolant evenly throughout the passage, with the exception being a large uncooled streak down the center of the passage for the hole pattern that was designed as a provision of a gutter between two vane platforms. With slot and film-cooling flows present, there was a large region in the center of the inlet to the passage that was overcooled. This overcooling was particularly evident for the high (0.75%) slot flow case. For the case with high leakage losses, it seems that is would be beneficial to eliminate those film-cooling holes and use the coolant elsewhere, such as near the leading-edge or vane pressure-side regions. In general, the hole pattern that was derived from constant streamlines was better than the hole pattern that included axially placed holes and a gutter.

Predicted streamlines at 2% span with included slot flow were compared to those at the midspan with the former being superimposed on measurements of film-cooling effectiveness. A considerable deviation between the near-wall and midspan streamlines was observed and shown that the slot flow rate and near-wall effects must be considered when predicting film-coolant trajectory based on streamlines. The film-coolant trajectories as well as the slot-flow trajectory each affected the other. At high slot flows, the near-wall cross flows were increased, which, in turn, swept the jets closer toward the suction surface. At low slot flows, the first row of film-cooling holes provided blockage, allowing more uniform flow to exit the slot.

Film-cooling momentum flux ratios were shown to have a significant impact on cooling performance. The higher momentum flux associated with higher blowing allowed the coolant to penetrate to hard-to-cool areas at the leading edge and along the pressure side in the downstream region. Cooling jets at the leading edge had a tendency to separately impact the vane, and then wash onto the endwall. As the momentum flux ratio was increased for the jets along the pressure side in the upstream portion of the passage, there was a tendency for the jets to separate prior to being able to penetrate closer to the pressure-side surface. This is different from the phenomena for the downstream holes along the pressure-side surface where the jets had less tendency to separate and were able to penetrate to the pressure side of the vane, thereby reducing the warm ring around the vane.

Acknowledgments

This publication was prepared with the support of the US Department of Energy, Office of Fossil Energy, National Energy Technology Laboratory. However, any opinions, findings, conclusions, or recommendations expressed herein are those of the authors and do not necessarily reflect the views of the DOE. The authors thank David Candelori (Pratt & Whitney), Ron Bunker (General Electric), and John Weaver (Rolls-Royce) for their input on the endwall cooling hole patterns.

Nomenclature

C = true chord of stator vane
C_a = axial chord of stator vane
G = gutter in Fig. 1
I = momentum flux ratio
$\dot{m}$ = mass flowrate
M = mass flux ratio
P = vane pitch; hole pitch
P_o, p = total and static pressures
Re_{in} = Reynolds number defined as $\mathrm{Re} = CU_{in}/\nu$
s = distance along vane from flow stagnation
S = span of stator vane
T = temperature
x, y, z = local coordinates
u, v, w = local velocity components
U = velocity magnitude

Greek

η = adiabatic effectiveness, $\eta = (T_\infty - T_{aw})/(T_\infty - T_c)$
ρ = density
ν = kinematic viscosity

Subscripts

ave, - = pitchwise average at a given axial location
ave, = = area average of endwall, slot to trailing edge
aw = adiabatic wall
c = coolant conditions
inlet = inlet conditions
∞ = freestream conditions

References

[1] Friedrichs, S., Hodson, H. P., and Dawes, W. N., 1996, ''Distribution of Film-Cooling Effectiveness on a Turbine Endwall Measured Using the Ammonia and Diazo Technique,'' ASME J. Turbomach., **118**, pp. 613–621.

[2] Friedrichs, S., Hodson, H. P., and Dawes, W. N., 1997, ''Aerodynamic Aspects of Endwall Film-Cooling,'' ASME J. Turbomach., **119**, pp. 786–793.

[3] Friedrichs, S., Hodson, H. P., and Dawes, W. N., 1999, ''The Design of an Improved Endwall Film-Cooling Configuration,'' ASME J. Turbomach., **121**, pp. 772–780.
[4] Blair, M. F., 1974, ''An Experimental Study of Heat Transfer and Film Cooling on Large-Scale Turbine Endwalls,'' ASME J. Heat Transfer, **97**, pp. 524–529.
[5] Granser, D., and Schulenberg, T., 1990, ''Prediction and Measurement of Film Cooling Effectiveness for a First-Stage Turbine Vane Shroud,'' ASME Paper No. 90-GT-95.
[6] Roy, R. P., Squires, K. D., Gerendas, M., Song, S., Howe, W. J., and Ansari, A., ''Flow and Heat Transfer at the Hub Endwall of Inlet Vane Passages-Experiments and Simulations,'' ASME Paper No. 2000-GT-198.
[7] Burd, S. W., and Simon, T. W., 2000, ''Effects of Slot Bleed Injection over a Contoured Endwall on Nozzle Guide Vane Cooling Performance: Part I: Flow Field Measurements,'' ASME Paper No. 2000-GT-199.
[8] Burd, S. W., Satterness, C. J., and Simon, T. W., ''Effects of Slot Bleed Ijection over a Contoured Endwall on Nozzle Guide Vane Cooling Performance: Part II Thermal Measurements,'' ASME Paper No. 2000-GT-200.
[9] Oke, R., Simon, T., Burd, S. W., Vahlberg, R., ''Measurements in a Turbine Cascade Over a Contoured Endwall: Discrete Hole Injection of Bleed Flow,'' ASME Paper No. 2000-GT-214.
[10] Oke, R., Simon, T., Shih, T. Zhu, B., Lin, Y. L., and Chyu, M. ''Measurements Over a Film-Cooled, Contoured Endwall with Various Coolant Injection Rates,'' ASME Paper No. 2001-GT-140.
[11] Colban, W. F., Thole, K. A., and Zess, G., 2002, ''Combustor-Turbine Interface Studies: Part 1: Endwall Measurements,'' ASME J. Turbomach., **125**, pp. 193–202.
[12] Colban, W. F., Lethander, A. T., Thole, K. A., and Zess, G., 2002, ''Combustor-Turbine Interface Studies: Part 2: Flow and Thermal Field Measurements,'' ASME J. Turbomach., **125**, pp. 203–209.
[13] Zhang, L., and Moon, H. K., 2003, ''Turbine Nozzle Endwall Inlet Film Cooling–The Effect of a Back-Facing Step,'' ASME Paper No. GT-2003-38319.
[14] Kost, F., and Nicklas, M., 2001, ''Film-Cooled Turbine Endwall in a Transonic Flow Field: Part I–Aerodynamic Measurements,'' ASME Paper No. 2001-GT-0145.
[15] Nicklas, M., 2001, ''Film-Cooled Turbine Endwall in a Transonic Flow Field: Part II–Heat Transfer and Film-Cooling Effectiveness Measurements,'' ASME Paper No. 2001-GT-0146.
[16] Knost, D. K., and Thole, K. A., 2003, ''Computational Predictions of Endwall Film-Cooling for a First Stage Vane,'' ASME Paper No. GT-2003-38252.
[17] Radomsky, R. W., and Thole, K. A., 2000, ''Flowfield Measurements for a Highly Turbine Flow in a Stator Vane Passage,'' ASME J. Turbomach., **122**, pp. 255–262.
[18] Harasgama, S. P., and Burton, C. D., 1992, ''Film Cooling Research on the Endwall of a Turbine Nozzle Guide Vane in a Short Duration Annular Cascade: Part 1—Experimental Technique and Results,'' ASME J. Turbomach., **114**, pp. 734–540.
[19] Barringer, M. D., Richard, O. T., Walter, J. P., Stitzel, S. M., and Thole, K. A., 2002, ''Flow Field Simulations of a Gas Turbine Combustor,'' ASME J. Turbomach., **124**, pp. 508–516.
[20] Moffat, R. J., 1988, ''Describing the Uncertainties in Experimental Results,'' Exp. Therm. Fluid Sci., **1**, pp. 3–17.

Flow and Heat Transfer in an Internally Ribbed Duct With Rotation: An Assessment of Large Eddy Simulations and Unsteady Reynolds-Averaged Navier-Stokes Simulations

A. K. Saha

Sumanta Acharya

Department of Mechanical Engineering,
Louisiana State University,
Baton Rouge, LA 70803

Large eddy simulations (LES) and unsteady Reynolds averaged Navier-Stokes (URANS) simulations have been performed for flow and heat transfer in a rotating ribbed duct. The ribs are oriented normal to the flow and arranged in a staggered configuration on the leading and trailing surfaces. The LES results are based on a higher-order accurate finite difference scheme with a dynamic Smagorinsky model for the subgrid stresses. The URANS procedure utilizes a two equation k-ε model for the turbulent stresses. Both Coriolis and centrifugal buoyancy effects are included in the simulations. The URANS computations have been carried out for a wide range of Reynolds number ($Re = 12{,}500-100{,}000$), rotation number ($Ro = 0-0.5$) and density ratio ($\Delta\rho/\rho = 0-0.5$), while LES results are reported for a single Reynolds number of 12,500 without and with rotation ($Ro = 0.12, \Delta\rho/\rho = 0.13$). Comparison is made between the LES and URANS results, and the effects of various parameters on the flow field and surface heat transfer are explored. The LES results clearly reflect the importance of coherent structures in the flow, and the unsteady dynamics associated with these structures. The heat transfer results from both LES and URANS are found to be in reasonable agreement with measurements. LES is found to give higher heat transfer predictions (5–10% higher) than URANS. The Nusselt number ratio (Nu/Nu_0) is found to decrease with increasing Reynolds number on all walls, while they increase with the density ratio along the leading and trailing walls. The Nusselt number ratio on the trailing and sidewalls also increases with rotation. However, the leading wall Nusselt number ratio shows an initial decrease with rotation (till $Ro = 0.12$) due to the stabilizing effect of rotation on the leading wall. However, beyond $Ro = 0.12$, the Nusselt number ratio increases with rotation due to the importance of centrifugal-buoyancy at high rotation. [DOI: 10.1115/1.1861917]

Introduction

In internal cooling of turbine blades, coolant air is circulated through serpentine ribbed passages and discharged through bleed holes along the trailing edge of the blade. With rotation, the flow is subjected to Coriolis forces and centrifugal-buoyancy effects. Rotation induces secondary flows that destabilize the flow and enhance heat transfer along one wall while they stabilize the flow and reduce heat transfer along the opposite wall. Centrifugal buoyancy accelerates the flow along the heated walls and, at high rotation numbers, can have a significant effect on the surface heat transfer.

Experimental investigations of flow and heat transfer in smooth and rib-roughened channels have been carried out by a number of different researchers (Han and Park [1]; Han et al. [2]; Han [3]; Wagner et al. [4], and Johnson et al. [5]). More recently, Chen et al. [6] have reported detailed mass transfer (naphthalene sublimation) measurements in a stationary duct having a sharp 180 deg bend. Azad et al. [7] have studied the effect of the channel orientation in a two-pass rectangular duct for both smooth and 45 deg ribbed walls. In a recent study, heat transfer in a rib-roughened rectangular channel with aspect ratio 4:1 has been reported by Griffith et al. [8]. In their study, the trailing surface heat transfer shows strong dependence on the rotation number.

Most of the earlier computational studies on internal cooling passage of the blades have been restricted to three-dimensional steady Reynolds averaged Navier-Stokes (RANS) (SRANS) simulations (Stephens et al. [9]; Rigby et al. [10]; Bo et al. [11], and Iacovides [12]). The flow and heat transfer through a two-pass 45 deg rib-roughened rectangular duct having aspect ratio of 2.0 has been conducted by Al-Qahtani et al. [13] using a Reynolds stress turbulence model. They have found reasonable match with experiments, although in certain regions there are significant discrepancies. In Qahtani et al. [13], it is argued that two equation models are unsatisfactory for rotating ribbed duct flows, and that a second moment closure is needed for accurate predictions.

A key deficiency of SRANS procedures is their inability to properly represent the unsteady dynamics of large scale structures in the turbulence model. Direct numerical simulation (DNS), large eddy simulation (LES), and unsteady RANS (URANS) provide alternative approaches where all or a portion of the unsteady spectrum is resolved. In DNS all scales are resolved, and no modeling is introduced. In LES, all dynamics of turbulent eddies above a cutoff filter (twice the mesh size) are resolved while only the

---

Contributed by the Turbomachinery Division of THE AMERICAN SOCIETY OF MECHANICAL ENGINEERS for publication in the JOURNAL OF TURBOMACHINERY. Manuscript received by the ASME Turbomachinery Division September 19, 2003; final revision received December 7, 2004. Associate Editor: R. S. Bunker.

small scale fluctuations are modeled. In URANS, all turbulent fluctuations are modeled while the large scale rotational motions are resolved as unsteady phenomenon. Thus, URANS aims to capture only the first few fundamental frequencies and models the random motions using a standard turbulence closure.

The turbulent flow in a stationary duct has been investigated using DNS (Huser et al. [14] and Gavrilakis et al. [15]). However, as noted earlier, DNS is computationally expensive. On the other hand, LES gives improved accuracy with reasonable computational resources. Tafti and Vanka [16] have reported LES of flow in a rotating rectangular channel. They have used the Smagorinsky eddy viscosity model for the subgrid scale closure. Piomelli and Liu [17] solved the same problem using a dynamic subgrid scale model. Both the studies could predict all the flow characteristics and show good comparison with experiments. Flow through a rotating square duct has been simulated by Pallares and Davidson [18]. They present turbulent stress budgets in their study. The flow and heat transfer characteristics of the rotating duct with ribbed roughened walls has been investigated numerically using LES by Murata and Mochizuki [19]. The effect of centrifugal buoyancy and the different rib orientations have been considered. Their study reveals that the centrifugal buoyancy in the ribbed duct increases and decreases both the wall shear stress and the heat transfer for the buoyancy-induced aiding and opposing flows respectively. They have also observed that the heat transfer and the friction factor are sensitive to rib orientations.

As discussed earlier, LES is known for its higher temporal and spatial accuracy. However, simulating the flow at a moderate Reynolds number using LES still requires significant computational resources due to the necessary grid resolution. On the other hand, since URANS solves only for the unsteady energetic coherent scales while modeling the rest of the fluctuations, the grid size requirements are considerably more modest. In flows dominated by discrete frequency large scale structures that URANS can resolve, it is conceivable that URANS may provide solutions of reasonable accuracy with moderate computational effort. This is a key goal for the gas turbine industry-improved accuracy with fast turnaround time. Thus, one primary goal for the present study is to explore the accuracy of URANS (using LES and measurements as benchmarks for comparison) for rotating ribbed-duct flows.

The second goal of the present paper is to use URANS to extend the parametric values (Re, Ro, $\Delta\rho/\rho$) to ranges of relevance to gas turbine industry. Results reported in the literature are generally limited to lower parametric ranges since the higher parametric ranges are difficult to achieve experimentally, while computational efforts (primarily SRANS) have been stymied by lack of agreement with rotational data even at moderate parameter values. Since URANS is likely to provide improved accuracy over SRANS, it is justifiable to report computational results over an extended parameter range as done in this paper.

Governing Equations and Boundary Conditions

For LES, the equations solved are the unsteady, homogenously filtered Navier-Stokes equations, along with the incompressibility constraint. For filtering, a top-hat filter has been used. In URANS, the unsteady Reynolds-averaged Navier-Stokes equations are solved where the unsteady term represents temporal variations over time scales larger than the averaging time. The resulting equations for both LES and URANS have the following form where the overbar represents spatially filtered quantities in LES and ensemble-averaged quantities in URANS

$$\frac{\partial \overline{u_i}}{\partial x_i} = 0 \tag{1}$$

$$\frac{\partial \overline{u_i}}{\partial t} + \frac{\partial}{\partial x_j}(\overline{u_j u_i}) = -\frac{\partial \overline{P}}{\partial x_i} + \frac{1}{\mathrm{Re}}\frac{\partial^2 \overline{u_i}}{\partial x_j^2} + \frac{\partial \tau_{ij}}{\partial x_j} - 2\mathrm{Ro}\,\varepsilon_{i2k}u_k - \frac{\mathrm{Bo}}{R_M}(1-\theta)\varepsilon_{i2l}\varepsilon_{l2k}r_k \tag{2}$$

$$\frac{\partial \overline{\theta}}{\partial t} + \overline{\theta}\Lambda + \frac{\partial}{\partial x_j}(\overline{u_j}\overline{\theta}) = \frac{1}{\mathrm{Re\,Pr}}\frac{\partial^2 \overline{\theta}}{\partial x_j^2} + \frac{\partial q_j}{\partial x_j} \tag{3}$$

where $\overline{\theta} = (\overline{T} - \overline{T_w})/(\overline{T_{m1}} - \overline{T_w})$, $\tau_{ij} = -\overline{u_i' u_j'}$, and $q_j = -\overline{u_j' \theta'}$. The terms τ_{ij} and q_j in Eqs. (2) and (3) are the subgrid scale contributions that have to be modeled. Here, T_w is the wall temperature and T_{m1} is the bulk temperature of the fluid evaluated at the inlet section of the computational domain. The unknown function Λ in the energy equation is given by

$$\Lambda = \frac{1}{\overline{T_{m1}} - \overline{T_w}}\frac{\partial}{\partial t}(\overline{T_{m1}} - \overline{T_w})$$

The coupling between $\overline{\theta}$ and Λ can be solved iteratively as described by Wang and Vanka [20].

In the earlier equations the velocities are nondimensionalized with the average velocity u_{av}, all lengths are scaled with the dimensions of the square duct, B (or H), pressure is scaled with ρu_{av}^2 and time is scaled by B/u_{av}. For air ($\mathrm{Pr}=0.7$), the primary parameters that appear in Eqs. (1)–(3) are the Reynolds number Re, the rotation number Ro, and the Buoyancy parameter Bo. These parameters are varied over appropriate ranges in the present study.

The imposition of periodic boundary conditions for the dependent variables needs special attention. The nondimensional pressure P is decomposed into a modified nondimensional pressure, p, and a linear component that varies along the streamwise direction

$$\overline{P}(x,y,z,t) = \overline{p}(x,y,z,t) - \beta(t)x$$

where $\beta(t)$ is the linear component of the nondimensional pressure that has to be adjusted in each time step to get the desired mass flow rate. With the earlier modification, the momentum equations take the following form:

$$\frac{\partial \overline{u_i}}{\partial t} + \frac{\partial}{\partial x_j}(\overline{u_j u_i}) = -\frac{\partial \overline{p}}{\partial x_i} + \delta_{i1}\beta(t) + \frac{1}{\mathrm{Re}}\frac{\partial^2 \overline{u_i}}{\partial x_j^2} + \frac{\partial \tau_{ij}}{\partial x_j} - 2\mathrm{Ro}\,\varepsilon_{i2k}u_k - \frac{\mathrm{Bo}}{R_M}(1-\theta)\varepsilon_{i2l}\varepsilon_{l2k}r_k \tag{4}$$

Subgrid Closure Model. The most commonly used subgrid scale model is based on the gradient transport hypothesis, and correlates τ_{ij} to the mean stain-rate tensor

$$\tau_{ij} = \overline{u_i u_j} - \overline{u_i u_j} = 2\nu_T \overline{S_{ij}} - \frac{\delta_{ij}}{3}\tau_{kk} \tag{5}$$

where δ_{ij} is the Kronecker delta, $\tau_{kk} = -\overline{u_k' u_k'}$, and $\overline{S_{ij}}$ is given by

$$\overline{S_{ij}} = \frac{1}{2}\left(\frac{\partial \overline{u_i}}{\partial x_j} + \frac{\partial \overline{u_j}}{\partial x_i}\right) \tag{6}$$

The eddy viscosity proportional to local large scale deformation is written as

$$\nu_T = C(\overline{\Delta})^2|\overline{S}| \tag{7}$$

Here C is a function of space and time and is to be calculated dynamically at each time step, $\overline{\Delta}$ is the grid filter scale and is given by $\overline{\Delta} = [(\delta x)(\delta y)(\delta z)]^{1/3}$, and $|\overline{S}| = (2\overline{S_{ij}}\,\overline{S_{ij}})^{1/2}$. Lilly [21] and Germano et al. [22] suggested a method to calculate C for each time step and grid point dynamically from the flow field data. In addition to the grid filter, which signifies the resolved and subgrid scales, a test filter is introduced for computation of C. The width

Table 1 Model parameters

C_μ	$C_{\varepsilon 1}$	$C_{\varepsilon 2}$	σ_k	σ_ε
0.09	1.44	1.92	1.0	1.3

of the test filter is larger than the grid filter width. Our computations were carried out using the model suggested by Piomelli and Liu [17]. To avoid ill conditioning of C, a local averaging over adjacent grid cells, following Zang et al. [23], was carried out. Similarly, for energy equation, the subgrid stress is

$$q_j = \overline{u_j}\theta - \overline{u_j\theta} = \frac{\nu_T}{\mathrm{Pr}_t}\frac{\partial\overline{\theta}}{\partial x_j} \tag{8}$$

where Pr_t is subgrid scale or SGS turbulent Prandtl number and is calculated dynamically by the dynamic model described in Moin et al. [24].

Unsteady RANS Turbulence Closure. The URANS simulations in the present study have been carried out using the two equations (k_n and ε_n) model of Kato-Lauder [25]. It has already been pointed out that the URANS solves for the quasi-periodic part of the flow field while modeling the random turbulent fluctuations. The turbulence closure is based on the gradient transport hypothesis, which correlates τ_{ij} to the phase averaged stain-rate tensor

$$\tau_{ij} = 2\nu_T\overline{S}_{ij} - \frac{\delta_{ij}}{3}\tau_{kk} \tag{9}$$

where δ_{ij} is the Kronecker delta, $\tau_{kk} = -\overline{u_k''u_k''}$, and $\overline{S}_{ij}$ is given by

$$\overline{S}_{ij} = \frac{1}{2}\left(\frac{\partial\overline{u_i}}{\partial x_j} + \frac{\partial\overline{u_j}}{\partial x_i}\right) \tag{10}$$

Similarly, q_j is given by

$$q_j = -\overline{u_j''\theta''} = \alpha_T\frac{\partial\overline{\theta}}{\partial x_j} \tag{11}$$

The turbulent eddy viscosity and turbulent thermal diffusivity are given in nondimensional forms as follows:

$$\nu_T = C_\mu \,\mathrm{Re}\, \frac{\overline{k_n^2}}{\overline{\varepsilon_n}} \text{ and } \alpha_T = C_\mu \,\mathrm{Re}\,\mathrm{Pr}\, \frac{\overline{k_n^2}}{\sigma_t\overline{\varepsilon_n}}$$

where $\overline{k_n}$ and $\overline{\varepsilon_n}$ are nondimensional turbulent kinetic energy and dissipation, C_μ is a model constant, and σ_T is the turbulent Prandtl or Schmidt number. For k and ε equations, the Kato Launder [25] is found to be suitable for bluff body flows since it can handle the stagnation zone properly by reducing the turbulent production in this region [25,26]. In this model [25], the production of turbulent kinetic energy is written in terms of rotation and shear of fluid elements instead of only shear. The nondimensional transport equations for k and ε are as follows:

$$\frac{\partial\overline{k}}{\partial t} + \frac{\partial}{\partial x_i}\{\overline{k\overline{u_i}}\} = \frac{1}{\mathrm{Re}}\frac{\partial}{\partial x_i}\left\{\frac{\nu_t}{\sigma_k}\frac{\partial\overline{k}}{\partial x_i}\right\} + P_k - \overline{\varepsilon} \tag{12}$$

$$\frac{\partial\overline{\varepsilon}}{\partial t} + \frac{\partial}{\partial x_i}\{\overline{\varepsilon u_i}\} = \frac{1}{\mathrm{Re}}\frac{\partial}{\partial x_i}\left\{\frac{\nu_t}{\sigma_\varepsilon}\frac{\partial\overline{\varepsilon}}{\partial x_i}\right\} + C_{\varepsilon 1}P_k\frac{\overline{\varepsilon}}{\overline{k}} - C_{\varepsilon 2}\frac{\overline{\varepsilon}^2}{\overline{k}} \tag{13}$$

where, $P_k = C_\mu\overline{\varepsilon\overline{S}}\,\overline{\Omega}$, $\overline{\Omega} = \overline{k}/\overline{\varepsilon}\sqrt{1/2\{(\partial\overline{u_i}/\partial x_j) - (\partial\overline{u_j}/\partial x_i)\}^2}$. The parameters for the earlier equations are given in Table 1.

The periodic boundary conditions for velocities and pressure corresponding to the earlier momentum equations and turbulent kinetic energy and dissipation corresponding to k-ε equations are

$$\overline{\phi}(x + L_x, y, z, t) = \overline{\phi}(x, y, z, t) \tag{14}$$

where $\phi \equiv (u_i, p, k, \varepsilon)$. The corresponding periodic boundary conditions for the energy equations are

$$\frac{\overline{\theta}(x + L_x, y, z, t)}{\overline{\theta}_{m2}} = \frac{\overline{\theta}(x, y, z, t)}{\overline{\theta}_{m1}}$$

where $\overline{\theta}_{m1}$ and $\overline{\theta}_{m2}$ are the nondimensional bulk temperatures at the inlet and outlet of the computational domain.

The channel and obstacle surfaces are treated as no-slip boundaries. Constant wall temperature boundary conditions have been used for the heated walls and rib surfaces. For URANS calculations, normalized kinetic energy is set to zero while zero Neumann boundary conditions are used for the nondimensional dissipation at all walls. Since the near-wall mesh in the LES calculation is sufficiently fine, with the y-plus values of the first set of grid points away from the wall less than 1.0, no wall function or damping is necessary for LES. However, the URANS grid is substantially coarser, and for the near wall modeling in URANS, standard wall functions are used and the grid is generated such that the y-plus values of the first set of points lie between 15 and 40. Earlier studies with URANS have shown that the standard wall function can predict the near-wall flow behavior with reasonable accuracy (Saha et al. [26]).

Numerical Method

The differential equations (Eqs. (1), (3), and (4)) have been solved on a staggered grid by using a modified version of the MAC algorithm of Harlow and Welch [27]. When the flow is incompressible, the pressure and velocity fields have to be solved simultaneously, since the pressure field has to be compatible with the continuity equation. This has been implemented by a two-step procedure: (*a*) a predictor step using current values of pressure that is fully explicit and (*b*) a corrector step in which the correction to velocity and pressure are obtained by ensuring compatibility with the continuity equation. An explicit, second order in time, Adams-Bashforth differencing scheme has been used for the time advancement of the convection and diffusion terms. The complete numerical algorithm is presented in Saha and Acharya [28].

In the present study, diffusion terms have been approximated using second order central differencing. For the advection terms, a third order upwind differencing (Kawamura et al. [29]) has been used. Once the corrected velocities are updated using the continuity equation, the momentum and the energy equations are solved using second order temporal (Adams-Bashforth) differencing scheme. Similarly, the convective and diffusive terms in the energy equations are discretized using the third order upwinding scheme of Kawamura et al. [29] and the second order central differencing scheme respectively.

The present simulations are carried out using a grid size of $114 \times 82 \times 96$ for the LES calculations while a grid size of $62 \times 48 \times 50$ are used for URANS. A nonuniform mesh with cells packed towards all the solid boundaries has been used to resolve the near-wall viscous effects. The URANS code results was tested for grid independence by comparing the results obtained with a $50 \times 32 \times 42$ grid and the $62 \times 48 \times 50$ grid. With the two grids, the surface-averaged Nusselt number along the sidewalls show a difference of 3.6% while the leading and trailing walls reveal a discrepancy of 1.6% and 1.7% respectively. Therefore, all the computations of URANS are carried out using a grid size of $62 \times 48 \times 50$. Typical computational effort required per time step for LES and URANS are 3 min and 30 s, respectively, on a 667 MHz Alpha processor with 1 GB RAM.

The computational domain of interest is shown in Fig. 1, and represents a periodic rib module in the radially outward flowing leg of a coolant passage. The ribs are oriented normal to the flow and placed in a staggered fashion on the leading and trailing surfaces of the duct passage. The pitch-to-rib height ratio is 10 while

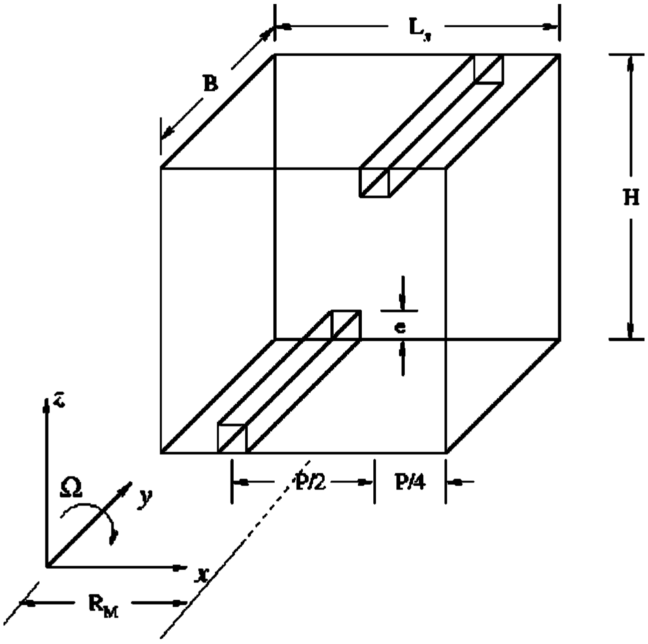

Fig. 1 Geometric model of the problem

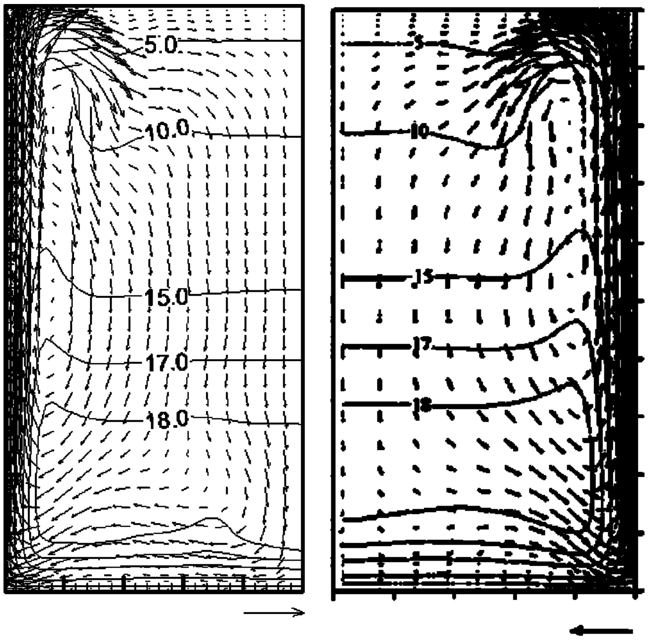

Present   Paralles and Davidson [18]

Fig. 2 Comparison of secondary flow structures and streamwise velocity

the rib height-to-hydraulic diameter ratio is 0.1. The mean radius of rotation, R_M, is 49. These geometrical dimensions correspond to the experimental study of Johnson et al. [5].

As noted earlier, a key objective of the present study is to compare the performance of LES and URANS calculations in a rib-roughened rotating square duct, and their ability in capturing the unsteady dynamics of the flow field. Both the LES and URANS results are compared with experiments. This study differs from the LES study by Murata and Mochizuki [19] in that the present study is carried out at a much higher Reynolds number and for a staggered arrangement of ribs. The present study also uses a considerably finer grid resolution than in Ref. [19], and is based on constant wall temperature boundary conditions that need special treatment.

Validation

The present code has been validated thoroughly for the flow and heat transfer characteristics in a channel flow with periodic array of cylinders (Saha and Acharya [25]). The code has also been validated against published results for the flow past a square cylinder placed in an infinite medium. The computed drag coefficient and the Strouhal number match with the experimental results. The validation of the URANS code is done using the flow past a square cylinder and found good match with experiments (Saha et al. [26]).

The present LES and URANS codes have been validated against published LES results for rotating smooth duct [18], and measurements and computations for rotating ribbed duct [12], respectively. Figure 2 shows LES results of the time-averaged secondary flow velocity vectors and contours of the streamwise velocity, and compares the present predictions with those of Pallares and Davidson [18]. The Reynolds number and the rotation number considered for the comparison are 3900 and 0.12, respectively. The number of grid points in the present study was $82\times82\times82$, while Pallares and Davidson used a grid size of $62\times62\times62$, for a domain size of $6\times1\times1$. The comparison between the two sets of data can be seen to be quite good. The URANS results of the present study have been compared with those of Iacovides [12] for a Reynolds number of 100,000 and rotation number of 0.2. Iacovides [12] solved the steady RANS equations and used a maximum grid size of $74\times62\times30$ for domain dimensions of $1\times1\times1$. In the present study, a grid size of $62\times50\times48$ was used for the unsteady computations. Figure 3 shows the comparison of the streamwise as well as cross-stream velocities at two different locations. The streamwise velocity of the present study matches better with experiments than computations of Iacovides [12] at both locations. On the other hand, the cross-stream velocity underpredicts the experimental value somewhat in the core flow.

Results and Discussions

A single Reynolds number (Re=12,500) has been used for all the LES computations (both the stationary and rotational cases). The rotational case includes the effects of Coriolis forces and centrifugal buoyancy. The rotation number (Ro) and density ratio $(\Delta\rho/\rho)$ considered in the present study for LES are 0.12 and 0.13, respectively. The URANS simulations are carried out for a Reynolds range of 12,500–100,000, a rotational number range of 0–0.5 and a density ratio range of 0–0.5.

Instantaneous LES Flow Field. Figure 4 shows the velocity vector superimposed on the temperature contours at the mid transverse plane $(y=0)$ for both the stationary and rotating cases. Both the cases show clear evidence of separating shear layers shed from the ribs. For both the cases, the flow reattaches downstream of the ribs on both ribbed walls. The strength of vortices near the leading and trailing walls are comparable for the stationary case while, for the rotating case, the vortical structures are stronger near the trailing (or unstable) side compared to the leading (or stable) side. The recirculation region behind the rib on the leading surface is larger (relative to the trailing surface of the rotating case) with rotation. This behavior is linked to the fact that the Coriolis-induced secondary flows move the bulk flow away from the leading surface towards the trailing wall resulting in an increase in magnitude of the velocity near the trailing surface and a reduction in the magnitude of velocity near the leading wall. Further, the peak-to-peak fluctuations in the velocity signals (not shown here) near the two walls (outside the viscous sublayer) reveals that turbulence levels are suppressed along the leading surface, which lowers the eddy viscosity and therefore decreases the spreading rate of the shear layer and delays reattachment. Another difference between the

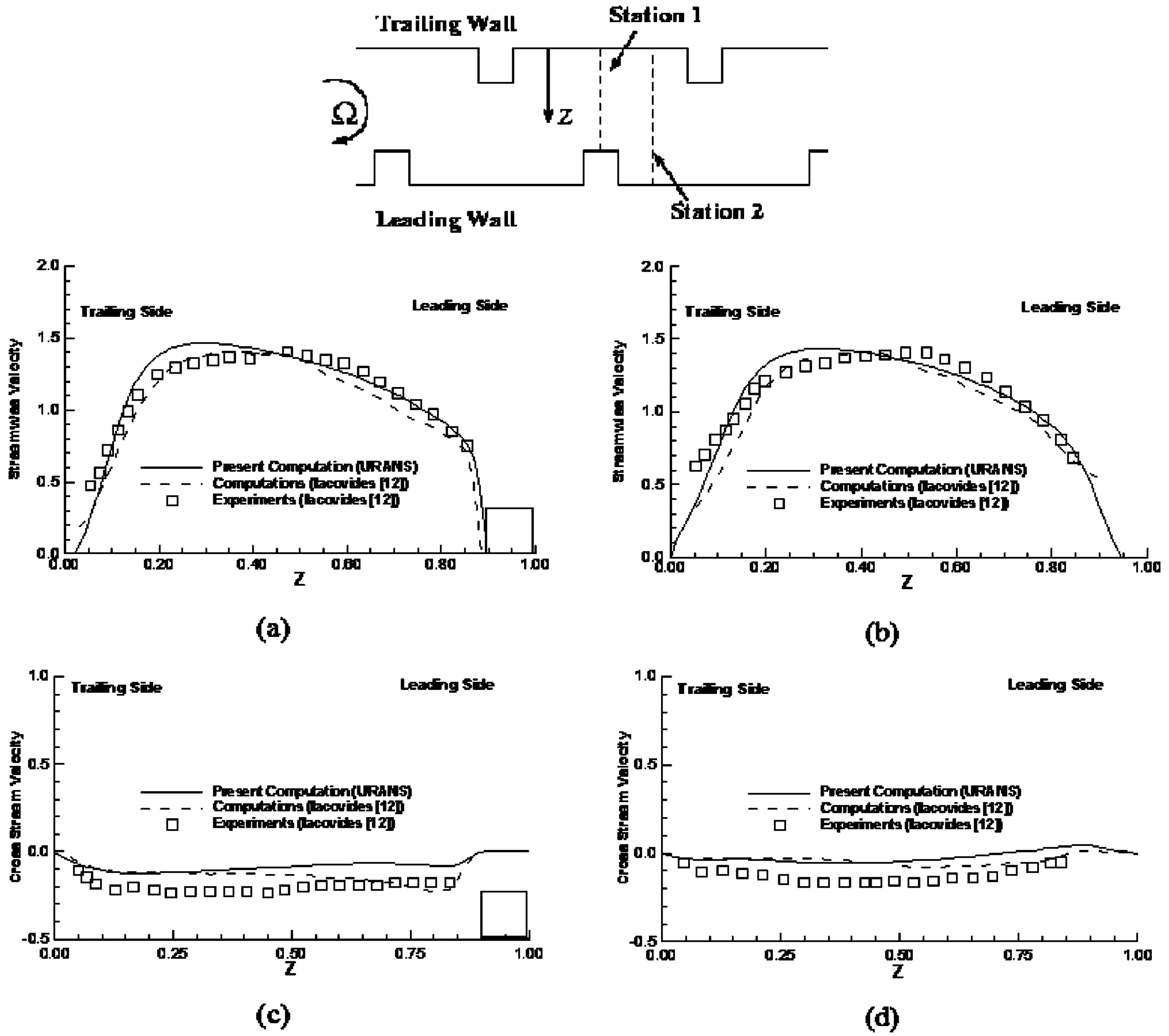

Fig. 3 Comparison of streamwise velocity at (*a*) station 1 and (*b*) station 2 and cross-stream velocity at (*c*) station 1 and (*d*) station 2

two cases is that the bulk flow for the rotational case has greater vorticity than the stationary case. Rotation produces a velocity gradient in the bulk mean flow that leads to additional vorticity across the entire width of the channel. The temperature distributions between the two cases reveal significant differences. For the stationary case, the incoming coolant fluid (nondimensional temperature of 1) is distributed almost symmetrically between the two walls (nondimensional temperature of 0). For the rotational case, the temperature of the bulk fluid becomes asymmetric because high momentum cold fluid is pushed towards the trailing side by the Coriolis-induced secondary flows. Thus, for the stationary case, both walls and the rib experience fluid of comparable temperature, while for the rotational case, the ribs as well as the wall on the trailing side are exposed to colder fluid compared to the leading side. Thus the heat transfer on the trailing surface is expected to be higher. Further, due to the higher velocity of the trailing edge separated shear layer, the shedding of the vortices from the trailing edge ribs is stronger, and due to its consequent interaction with the boundary layer, mixing is enhanced leading to higher heat transfer rates from the trailing side.

The secondary velocity vectors superimposed on the temperature contours at $x=0.5$ are presented in Fig. 5 for the stationary and rotating cases, and show that the secondary flow is stronger with rotation. The flow near the ribbed walls shows more vortical structures than along the two smooth sidewalls (Fig. 5(*a*)). At this x location, the flow near both the leading and trailing walls for the stationary case exhibits similar structures. For the rotating case (Fig. 5(*b*)), stronger vortical structures are observed along the unstable/trailing wall compared to the stable/leading wall. The unstable side is dominated by higher momentum fluid, and therefore the secondary vortices formed are stronger. The stationary case shows low temperature fluid located centrally in the core region since there are no rotational effects (Fig. 5(*a*)). On the other hand, the rotating case depicts the shift of the cold bulk flow towards the unstable side creating a larger zone of recirculation in the stable side. The effect of this larger recirculation results in higher temperature of the fluid near the stable region.

The variation of Nusselt number on the two walls (leading and trailing) is presented in Fig. 6 for the stationary case. The Nusselt number variations on the two ribbed walls are of comparable magnitude. There is clear evidence of patches or streaks of low temperature (high Nusselt number) fluid near the walls. These patches are a consequence of the colder core fluid being entrained into the near wall flow structures. The low Nusselt number region in the

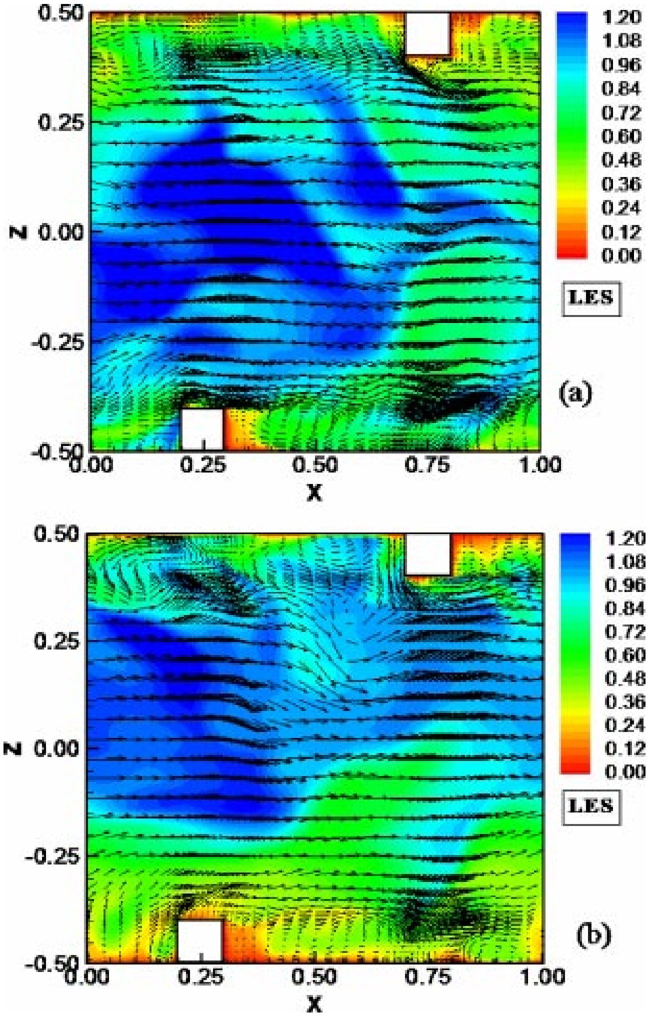

Fig. 4 Instantaneous velocity vectors and temperature contours at $y=0.0$ for (*a*) Ro=0.0 and (*b*) Ro=0.12 and $\Delta\rho/\rho=0.13$, Re=12,500 (top: trailing wall; bottom: leading wall)

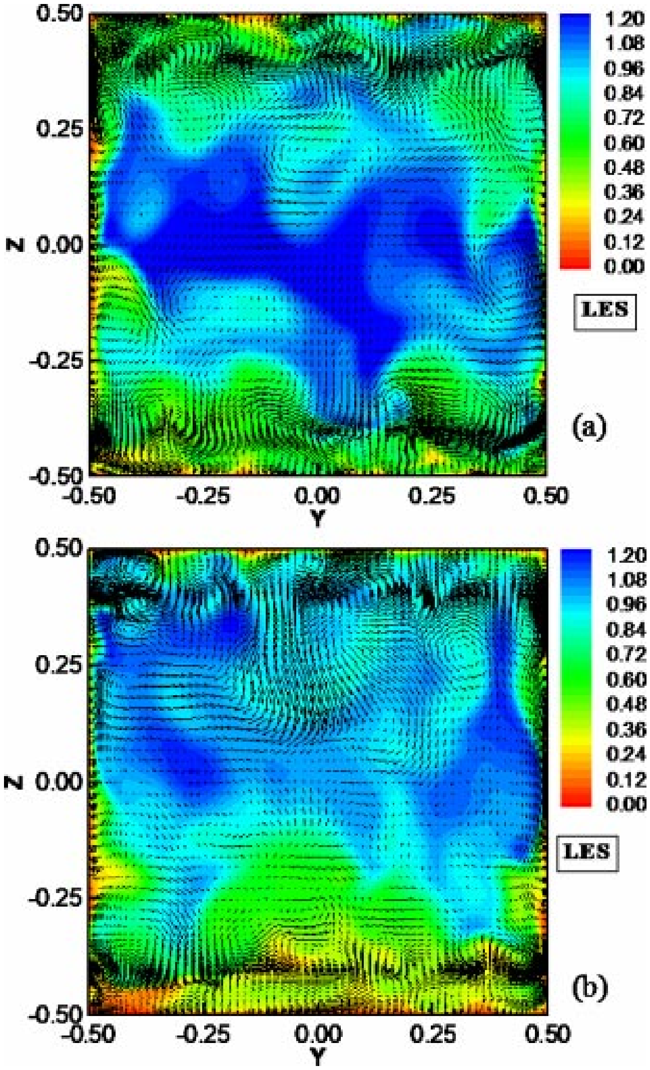

Fig. 5 Instantaneous secondary flow structures superimposed on temperature contours at $x=0.5$ for (*a*) Ro=0.0 and (*b*) Ro=0.12 and $\Delta\rho/\rho=0.13$, Re=12,500 (top: trailing wall; bottom: leading wall)

recirculation region behind the ribs extends roughly 1.5 rib heights downstream and is nearly two dimensional. On the other hand, the separation zone upstream of the ribs appears to be more three dimensional with low temperature streaks (high Nusselt number) that are stretched in the spanwise direction.

The Nusselt number distributions for the rotational case (Figs. 7(*a*) and 7(*b*)) shows very different behavior near the leading and trailing wall regions. There are larger zones of high Nusselt number along the unstable side of the wall produced by the Coriolis forces that drive the coolant fluid from the core regions toward the trailing or unstable side. The low temperature streaks (high Nusselt number) are generally oriented in the streamwise direction except upstream of the rib where the thermal streaks are oriented in the spanwise direction.

Figure 8 depicts the isosurfaces of spanwise vorticity ($\omega_y = \pm 20$). Two different types of spanwise vortices are seen in the vicinity of the ribs. One is a wall generated vorticity (dark grey color near the leading wall and light grey color near the trailing wall) and the other is shear layer vorticity (generated due to the separation at the corners of the ribs). For the stationary case, the magnitudes associated with both vortical structures are almost same on either of the walls. The separating shear layer shows clear evidence of reattachment and is seen to be discontinuous or shredded along the span of the ribs. In contrast, the separating shear layer in the flow past a cylinder placed in infinite medium shows continuity along its span upto a certain streamwise distance (at least 1–2 diameters downstream) while being shed downstream. The tearing of shear layer in the present case may be attributed to the interaction between the wall vortices and the shear layer vortices, which are of opposite sign. The rotational case reveals that the shear layer on the stable side is seen to be moving parallel to the wall and there is no reattachment of the shear layer in the vicinity of the rib. On the other hand, the reattachment of the shear layers near the top unstable wall is quite evident, and the structures are more prominent and stronger because of the higher momentum fluid present near the unstable side.

An isosurface of temperature for both the cases (Fig. 9) can provide information on the mixing of the core fluid with the near-wall regions. The thermal structures themselves appear to be comparable in size to the flow structures. Upstream of the rib, the structures appear to be stretched in the transverse direction, but reorient themselves to be in the streamwise direction downstream of the ribs. The stationary case (Fig. 9(*a*)) reveals somewhat finer structures compared to the rotational case. The rotational case (Fig. 9(*b*)) clearly shows that the isocontours are lifted off the stable surface to a greater degree compared to the unstable surface and also relative to the stationary case; this shows less entrain-

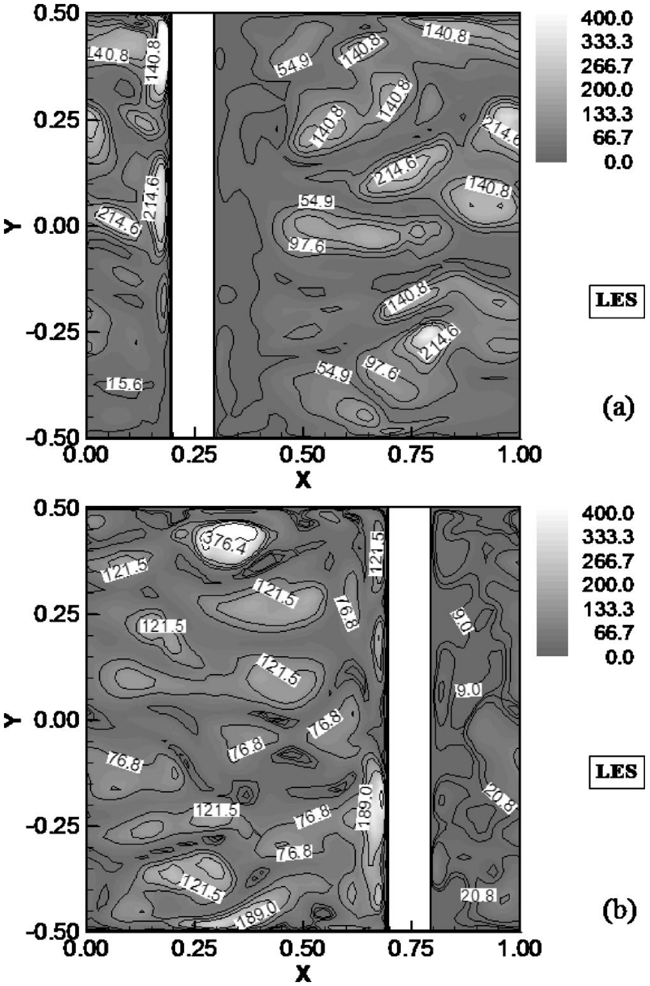

Fig. 6 Instantaneous Nusselt number contours of the stationary case for $\Delta\rho/\rho=0.13$, Re=12,500 (*a*) leading wall and (*b*) trailing wall

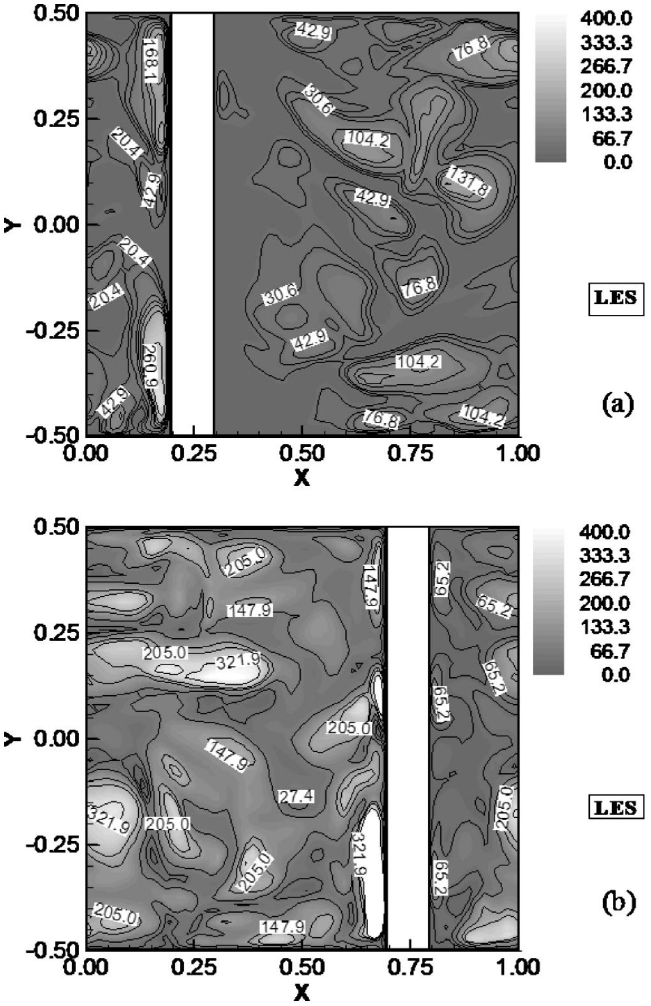

Fig. 7 Instantaneous Nusselt number contours of the rotating case for $\Delta\rho/\rho=0.13$, Re=12,500 (*a*) leading wall and (*b*) trailing wall

ment and mixing of the core fluid near the stable surface relative to the entrainment along the unstable surface, and relative to the stationary case.

Comparison of LES and URANS. Most of the URANS cases do not show strong unsteadiness at low rotation numbers. Only mild unsteadiness is observed in the pressure as well as k and ε fields. However, at high rotation numbers ($\text{Ro}\geqslant 0.25$), strong unsteadiness in the velocity field is observed, and will be discussed later. Since LES is carried out at low Reynolds number (Re =12,500), rotation number (Ro=0 or 0.12) and density ratio ($\Delta\rho/\rho=0.13$), comparison of LES with URANS is done with respect to the mean flow and temperature fields because for these parameter ranges the URANS computations are only mildly unsteady, while LES results expectedly show greater unsteadiness.

Figure 10 delineates the time-averaged velocity vector fields superimposed on the temperature contours at the midtransverse plane. The zoomed-in views near the ribs are also shown for both the cases. Though both LES and URANS represent similar overall mean flow structures, the flow near the ribs in LES is quite different from the URANS. In URANS, only one vortex (separating shear layer) is seen in the downstream of both the ribs while LES shows additional small corner vortices along with the separating shear layer vortices. Because of these additional vortices, the heat transfer along the downstream rib surface is stronger for LES than URANS. This fact is clear from the smaller high temperature region near the ribs in LES. The strength of the separating shear layers formed downstream of the ribs is greater in LES than URANS. The single corner vortex formed in front of the ribs is found to be bigger in LES than those in URANS. Therefore, the overall heat transfer from the ribs in LES is stronger than URANS. The relative contribution of heat transfer from the ribs to the overall heat transfer on the leading wall is about 34% and 24% for LES and URANS, respectively. The corresponding values on trailing wall are 37% and 25%, respectively.

The time-averaged temperature distribution for URANS and LES are presented in Fig. 11 at the midstreamwise plane. There is a distinct difference in the temperature contours for the two cases. The effect of rotation on the temperature field is clearly discerned through the two lobes in the temperature field. The temperature contours in the LES results show the formation of two small counter-rotating lobes along the midportion of the trailing surface, and correspondingly there is little dip in the temperature contours in this region (not seen in the URANS). It is quite clear that the zone near the leading surface show higher temperatures in URANS compared to LES. The stronger unsteady flow in LES helps in the near-wall mixing, and in bringing the temperature down, leading to higher heat transfer rates (see Table 2). The time-averaged Nusselt number distribution near the trailing wall is plotted in Fig. 12. In the LES results, both the temperature contours in Fig. 11 and the Nusselt number contours in Fig. 12 show asymmetry about the axial mid plane ($y=0$). The averaging is done for over 15 flow-through time periods, and this is generally

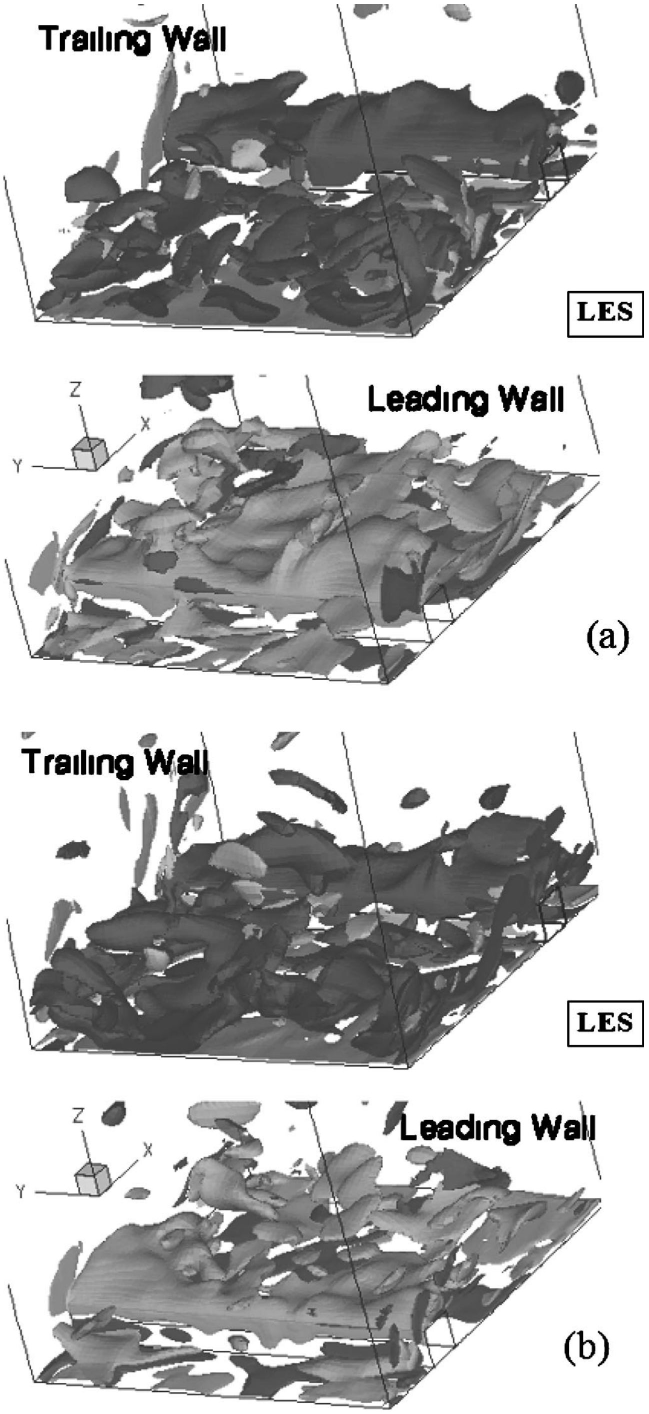

Fig. 8 **Isosurface of spanwise vorticity ($\omega_y = \pm 20.0$) for (*a*) Ro $= 0.0$ and (*b*) R $= 0.12$ and $\Delta\rho/\rho = 0.13$**

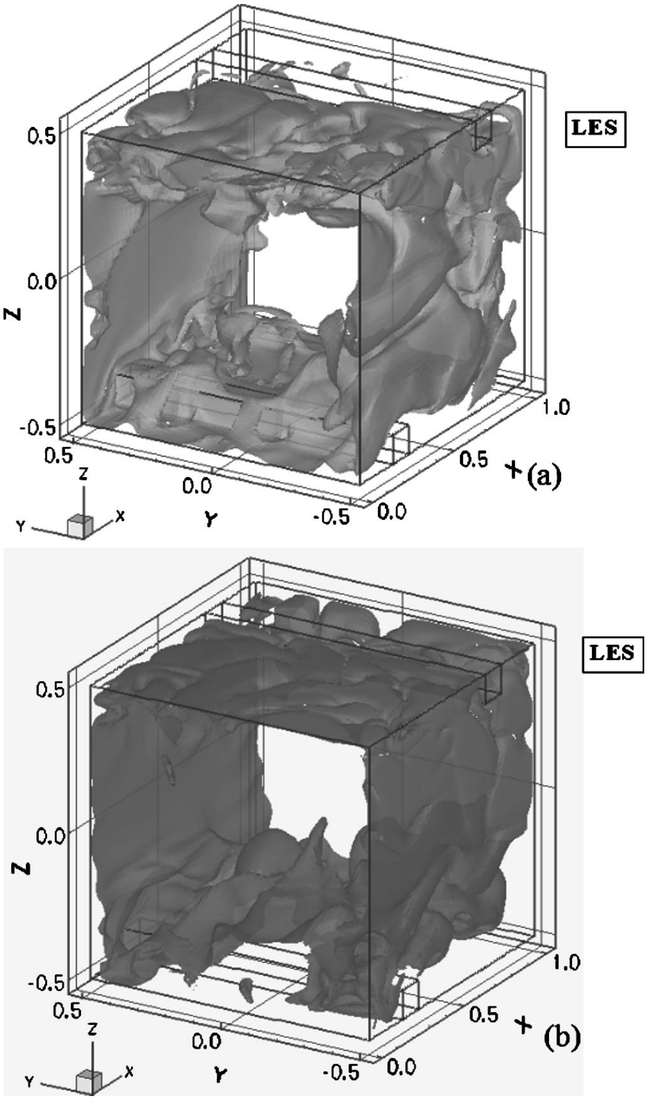

Fig. 9 **Isosurface of temperature ($\theta = 0.6$) for (*a*) Ro $= 0.0$ and (*b*) R $= 0.12$ and $\Delta\rho/\rho = 0.13$ for LES (top: trailing wall; bottom: leading wall)**

long enough to statistically resolve turbulent fluctuations. Increasing the averaging time to 20 flow-through time periods did not improve the asymmetry. Therefore, this means the presence of a low-frequency unsteadiness in the flow system. URANS is unable to capture this because of its diffusive nature.

Comparison of Nusselt number contours from URANS and LES reveals that URANS gives higher Nusselt number over most of the regions on the wall. However, the heat transfer on the wall just before the ribs and from the ribs surfaces is significantly higher with LES, and leads to a higher overall heat transfer rate. The three dimensionality of temperature field near the trailing wall is seen in both LES and URANS simulations. The deviation from the two dimensionality in temperature distribution downstream of the rib in URANS shows that the reattachment is affected by the presence of side walls. However, these variations are reduced in LES due to the additional mixing and transport predicted by LES.

Table 2 presents the comparison of time-averaged Nusselt number for URANS, LES, and experiments. The experiment corresponds to a four pass ribbed duct [5]. The reported experimental data in the present study are taken from the downstream regions in the first pass that show near periodic behavior in heat transfer. It should, however, be noted that the ribs used in the experiments do not have sharp corners, and the measured Nusselt numbers in the experiments does not show perfectly periodic behavior. All the Nusselt number reported in the present study have been normalized with respect to smooth channel Nusselt number ($\mathrm{Nu}_0 = 0.0176\mathrm{Re}^{0.8}$). The heat transfer on the ribbed walls are nearly 2.5–3 times higher, while that along the smooth side walls are nearly 1.5 times higher compared to the smooth channel case. For the rotational case, the trailing/unstable surface reveals the highest heat transfer (nearly 1.5 times greater than stationary values) and, as already discussed, this is because of the secondary flows generated by the Coriolis forces, and the associated high velocity bulk

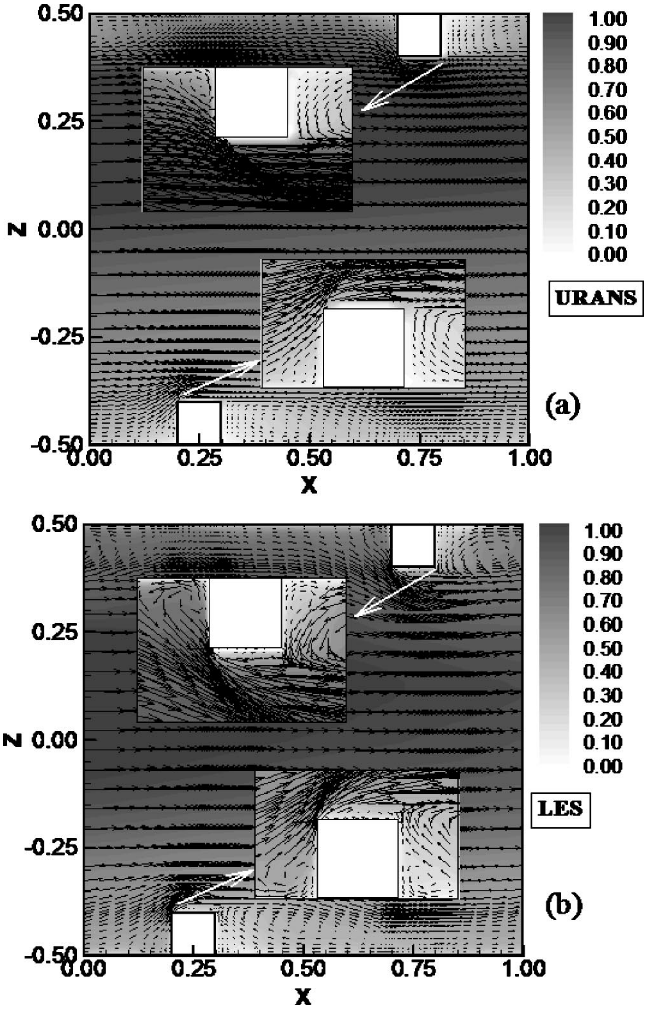

Fig. 10 Time-averaged velocity vectors and temperature contours at $y=0.0$ for Ro=0.12 and $\Delta\rho/\rho=0.13$, Re=12,500 (*a*) URANS and (*b*) LES (top: trailing wall; bottom: leading wall)

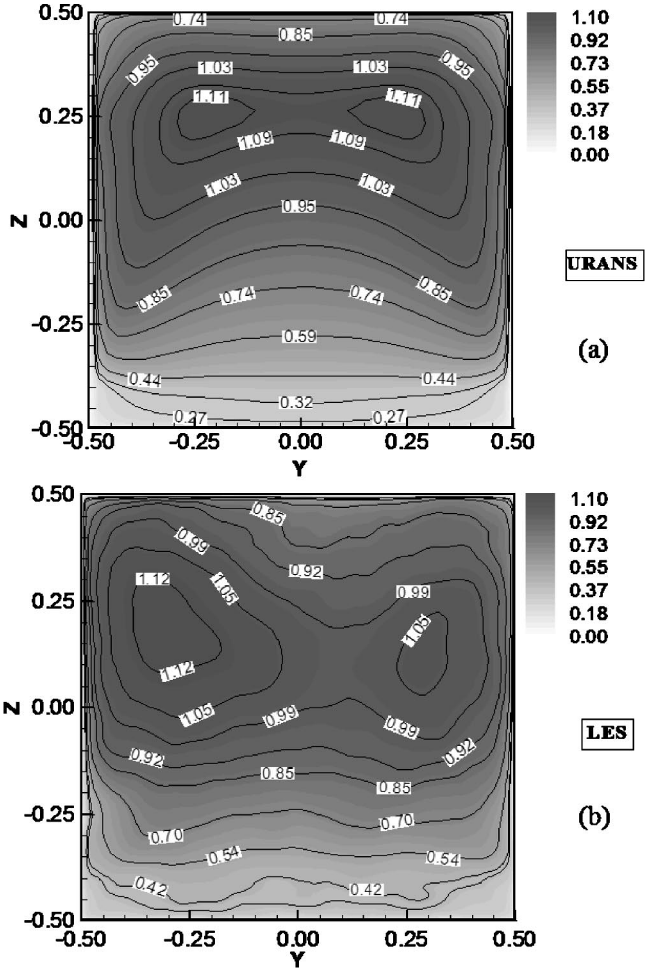

Fig. 11 Time-averaged temperature contours at $x=0.5$ for Ro $=0.12$ and $\Delta\rho/\rho=0.13$, Re=12,500 (*a*) URANS and (*b*) LES (top: trailing wall; bottom: leading wall)

fluid and higher fluctuations near the trailing surface. Correspondingly, the heat transfer along the leading wall is less (factor of about 0.7 relative to the stationary values) because of the lower bulk flow velocity and decreased velocity and temperature fluctuations. The sidewalls show enhanced heat transfer (factor of about 1.4) compared to the stationary case since rotation results in additional secondary flow.

Comparisons among URANS, LES, and experiments show that the Nusselt number ratios for both stationary as well as rotating cases reveal similar levels of agreement with data, with the predictions agreeing to within 20–25% on the leading and trailing walls and to less than 15% on the sidewalls. The heat transfer surface area with square ribs (computations) is nearly 10% larger than the rounded ribs in the measurements (all Nusselt numbers are based on projected areas), and therefore slightly higher predicted values should be expected. In view of this, one can conclude that the present predictions with both URANS and LES appear to be quite reasonable. The LES results show higher heat transfer on all walls for both the stationary and the rotating cases compared to the corresponding URANS cases. The URANS model is dissipative in nature and thus damps the flow structures. Consequently, the heat transfer is less in URANS since the fluctuations of energetic structures that are responsible for high heat transfer is reduced.

Since LES computations are expensive, and both URANS and LES appear to give reasonable agreement with measurements, the parametric effects of the Reynolds number, rotation number and density ratio are simulated using only URANS. These results are described next.

Effect of Re. The effect of Reynolds number is carried out using a rotation number of 0.12 and density ratio of 0.13. Figure 13 represents the velocity vector plots superimposed on temperature contours for two Reynolds numbers namely, 25,000 and 100,000 at a midstreamwise plane ($x=0.5$). At both Reynolds

Table 2 Comparison of Nusselt number (normalized with $\mathrm{Nu}_0=0.0176\mathrm{Re}^{0.8}$ for simulations and experiments

Re=12,500, $(\Delta\rho/\rho)=0.13$	Sidewall	Leading wall	Trailing wall
URANS (no rotation), square ribs (Std k-ε)	1.51	2.82	2.82
LES (no rotation), square ribs (dynamic model)	1.65	3.10	3.14
Johnson et al. [5], rounded ribs (no rotation)		2.47	2.50
URANS, square ribs (Std k-ε) (Ro=0.12)	2.11	1.83	4.20
LES, square ribs, (dynamic model) (Ro=0.12)	1.99	2.08	4.45
Johnson et al. [5], rounded ribs (Ro=0.12)	1.86	1.75	3.72

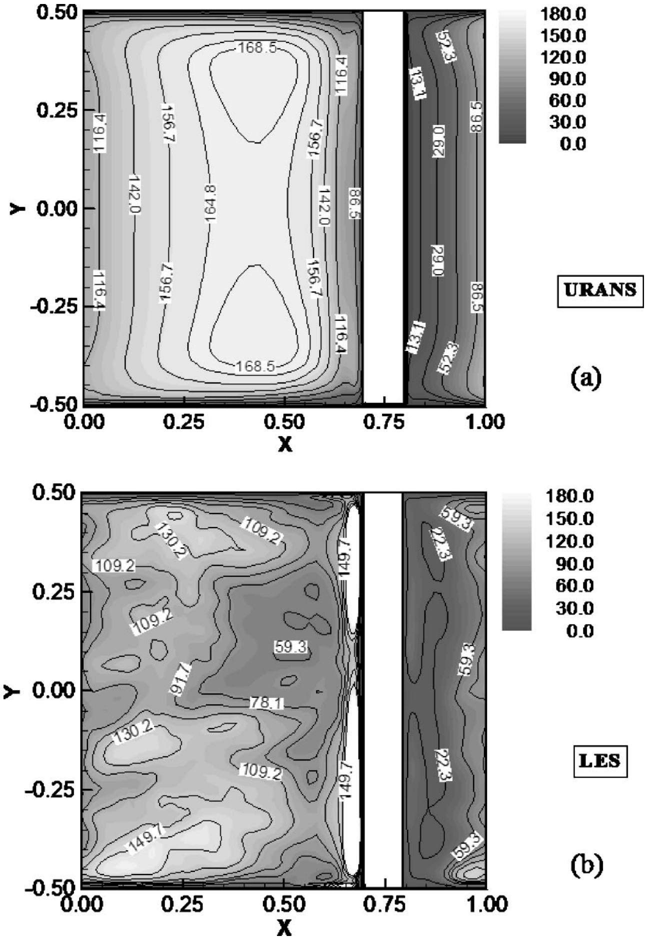

Fig. 12 Time-averaged Nusselt number contours on the trailing wall for Ro=0.12 and $\Delta\rho/\rho$=0.13, Re=12,500 (*a*) URANS and (*b*) LES

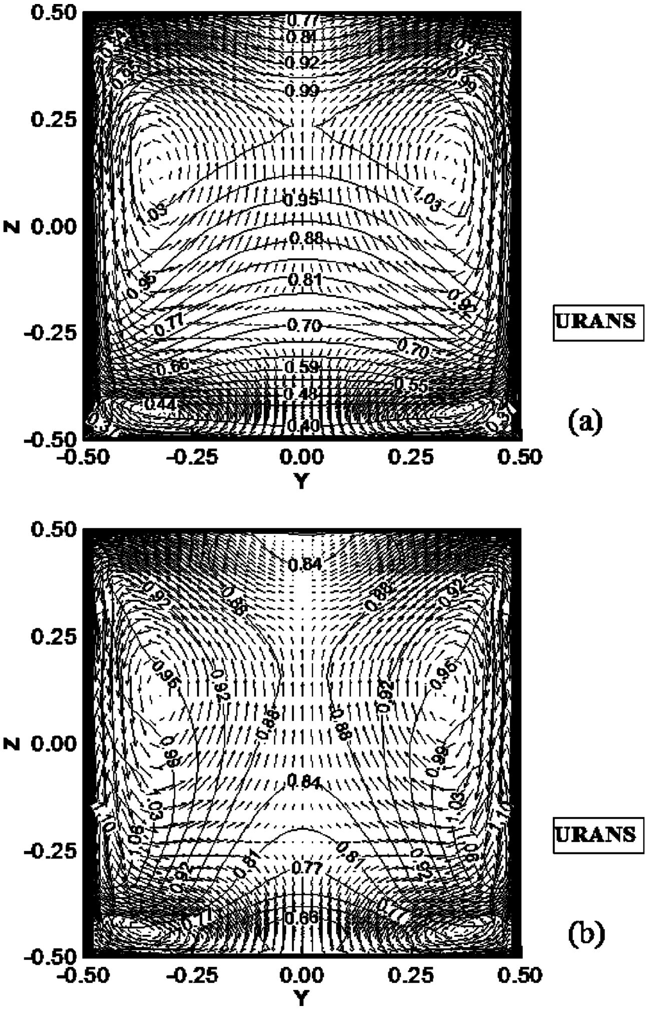

Fig. 13 Secondary flow structures superimposed on temperature contours at x=0.5 for (*a*) Re=25,000 and (*b*) Re=100,000, Ro=0.12 and $\Delta\rho/\rho$=0.13 (top: trailing wall; bottom: leading wall)

numbers, there is clear evidence of strong secondary flow in the form of two counter rotating vortices induced by the Coriolis forces. The presence of the ribs distorts the secondary flow structures, and this is reflected in the pair of secondary vortices observed near the leading surface (Fig. 13(*a*)). The flow structures at the two Reynolds numbers do not reveal significant differences. However, differences are observed between the temperature distributions of the two cases, with the core fluid at Re=100,000 at a higher temperature than at Re=25,000. The higher temperature of the core fluid at the higher Reynolds number decreases the relative heat transfer ratio (with respect to the smooth wall heat transfer) from the leading and trailing walls. The Nusselt number distributions on the trailing wall at Re=25,000 and 100,000 are shown in Figs. 14(*a*) and 14(*b*), respectively. The effect of the two counter rotating secondary vortices is clearly seen in the two high Nusselt number patches near the trailing wall (Fig. 14(*a*)). The symmetric pair of high Nusselt number zones moves towards the sidewalls and become elongated in the streamwise direction at higher Reynolds number. At the same time, the low heat transfer zone just downstream of the rib shrinks down with the increase in Reynolds number. While the general distributions at the two Reynolds numbers are similar, lower surface temperatures (higher Nusselt numbers) are noted at the higher Re.

Figure 15 shows the effect of the Reynolds number on the Nusselt number ratio for all three walls namely, the trailing, leading, and sidewalls. For comparisons, the data of Johnson et al. [5] are also plotted in the same graph. The present results show good match with that of Johnson et al. [5] for the leading and side walls. The present simulation overpredicts (by about 10–15%) the trailing wall Nusselt number ratio for Re=12,500 while it underpredicts (by less than 10%) at Re=25,000. However, in general, the agreement with the data in the Re range of 12,000–25,000 is excellent. While the Nusselt number itself increases with Re, the Nusselt number ratio decreases with increasing Re values indicating that for ribbed ducts with or without rotation, $\mathrm{Re}^{0.8}$ is not the appropriate scaling. The trailing wall shows a greater dependence on the Reynolds number; this Re dependence appears to be greater at the lower Re values ($\mathrm{Re} < 50{,}000$), and decreases somewhat for $\mathrm{Re} > 50{,}000$. For smooth ducts, the increase in Reynolds number results in the decrease in viscous sublayer. However, for ribbed duct, the separation of the shear layer from the front edge of the rib causes disturbance to the viscous sublayer and as a result the sublayer becomes less sensitive to the Reynolds number. One potential reason for the observed Re dependence in both smooth and ribbed ducts is that the hydrodynamic and thermal boundary layers decrease with an increase in Reynolds number, and therefore, the spatial interaction and momentum transport between the separated shear layer and the boundary layer reduces. This decrease in momentum exchange causes a reduction in the heat transfer with increasing Reynolds number.

Effect of Density Ratio. To investigate the effect of density ratio, the Reynolds number and rotation number are fixed at 25,000 and 0.12, respectively, while the density ratio is varied

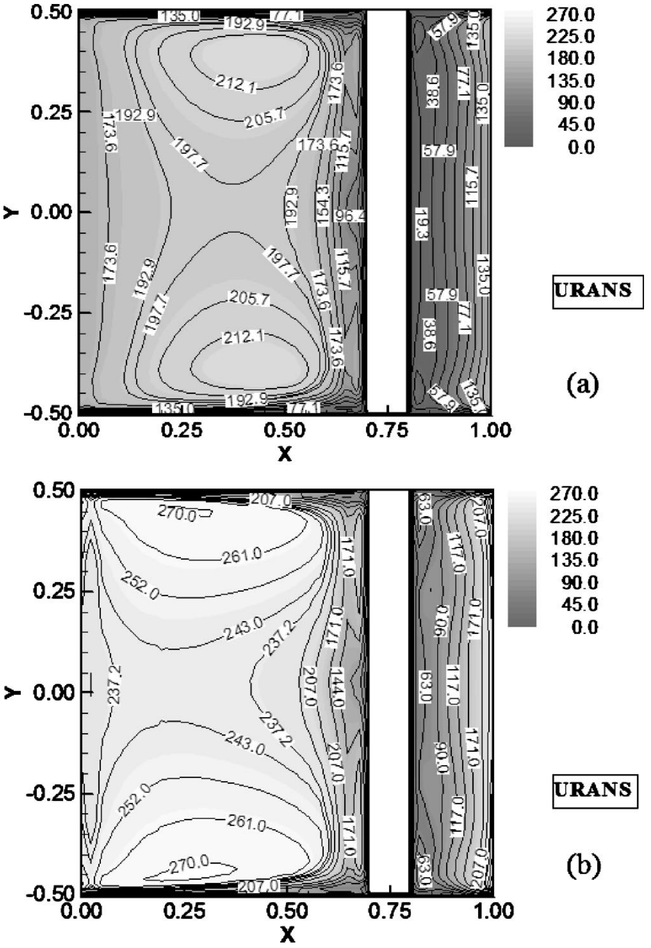

Fig. 14 Nusselt number contours on the trailing wall at (*a*) Re=25,000 and (*b*) Re=100,000 for Ro=0.12 and $\Delta\rho/\rho=0.13$

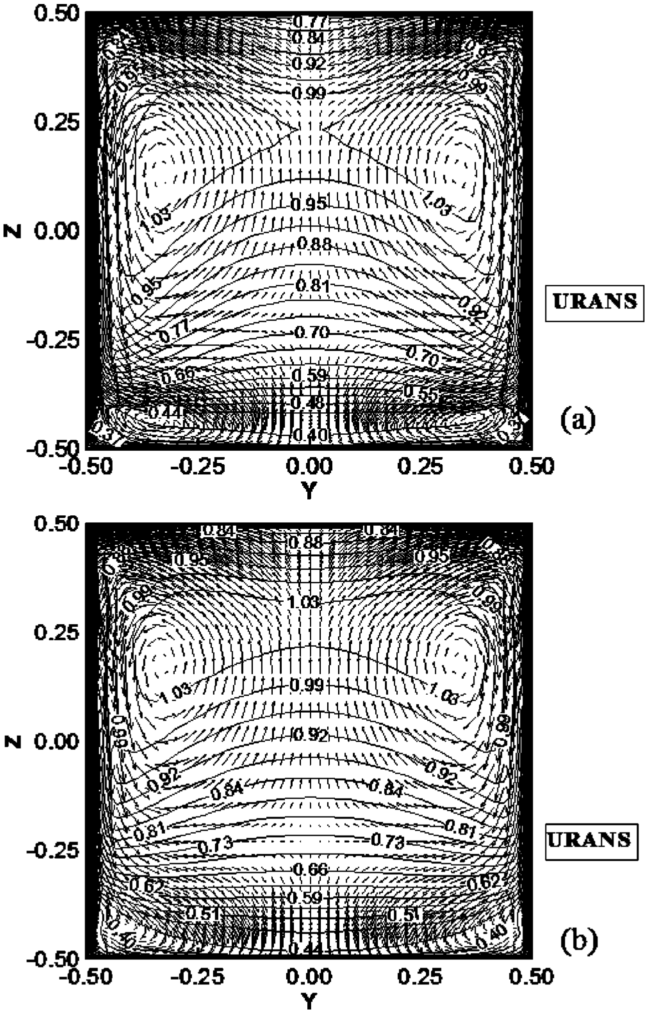

Fig. 16 Secondary flow structures superimposed on temperature contours (*x*=0.5) at (*a*) $(\Delta\rho/\rho)=0.13$ and (*b*) $(\Delta\rho/\rho)=0.5$ for Ro=0.12 and Re=25,000 (top: trailing wall; bottom: leading wall)

between 0 and 0.5. In the present paper, the variation in the buoyancy parameter is achieved by varying the density ratio while keeping the rotation constant. The buoyancy force is governed by both the centrifugal forces acting on the fluid and the density gradient in the fluid. With the wall temperatures higher than the core temperature, as in the present case, the direction of buoyancy is radially inward and opposite to the main flow direction. The opposing direction of buoyancy can produce complex effects including increased turbulence production and thickening of the boundary layer. In Johnson et al. [5], it has been shown that centrifugal buoyancy leads to an increase in heat transfer along both leading and trailing walls.

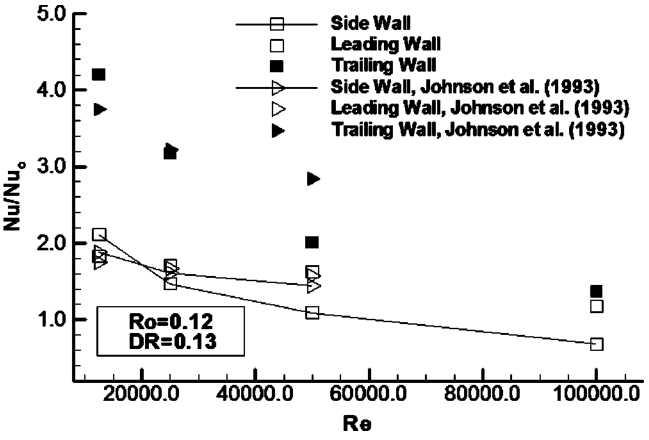

Fig. 15 Effect of Reynolds number on Nusselt number ratio for Ro=0.12 and $(\Delta\rho/\rho)=0.13$

Figures 16(*a*) and 16(*b*) show the velocity vectors at the mid streamwise plane ($x=0.5$) for $(\Delta\rho/\rho)=0.13$ and 0.5, respectively. No significant differences are observed in the flow pattern between the two vector plots with the primary differences being in the relative magnitudes of the velocity and temperature. One distinct difference is that the rib generated secondary flow structure near the bottom is smaller at $(\Delta\rho/\rho)=0.5$. The corresponding thermal field looks almost similar except that the low temperature region is shifted closer to the trailing side with increasing density ratio, and therefore the near-wall temperature at $(\Delta\rho/\rho)=0.5$ is lower than that at $(\Delta\rho/\rho)=0.13$.

To further explore the behavior near the leading surface, the Nusselt number distributions on the leading walls for $(\Delta\rho/\rho)=0.13$ and 0.5 are presented in Figs. 17(*a*) and 17(*b*) respectively. With increasing density ratio, higher Nusselt number in the attached flow regions is observed, and at the same time the higher temperature zones (low heat transfer) before and after the ribs are smaller in size. However, these differences are relatively small, and in general, the leading surface heat transfer appears to be relatively insensitive to density ratio. These observations are con-

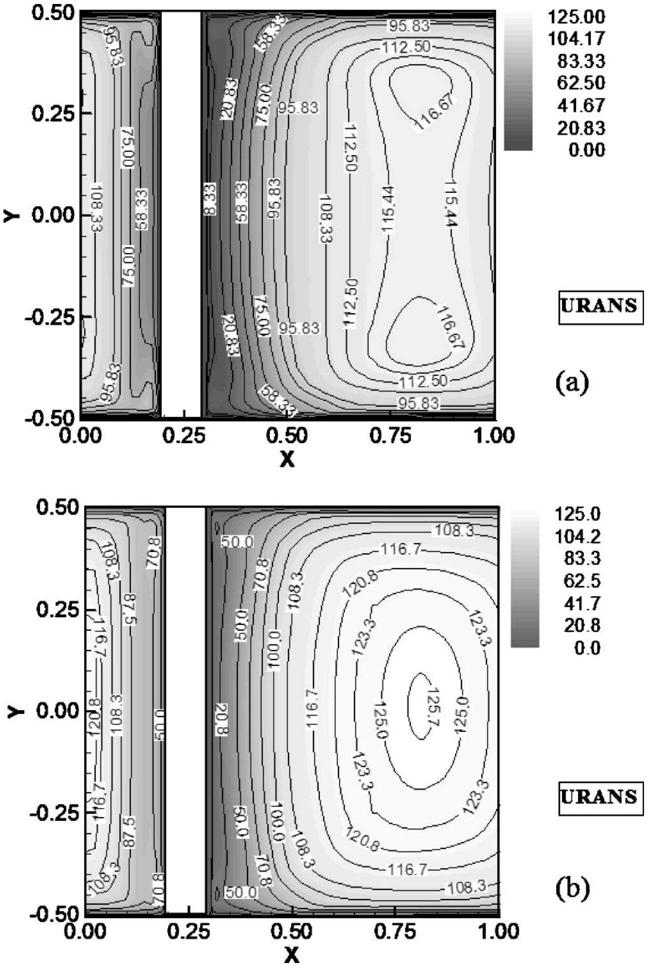

Fig. 17 Nusselt number contours on the leading wall at (*a*) $(\Delta\rho/\rho)=0.13$ and (*b*) $(\Delta\rho/\rho)=0.5$ for Ro=0.12 and Re=25,000

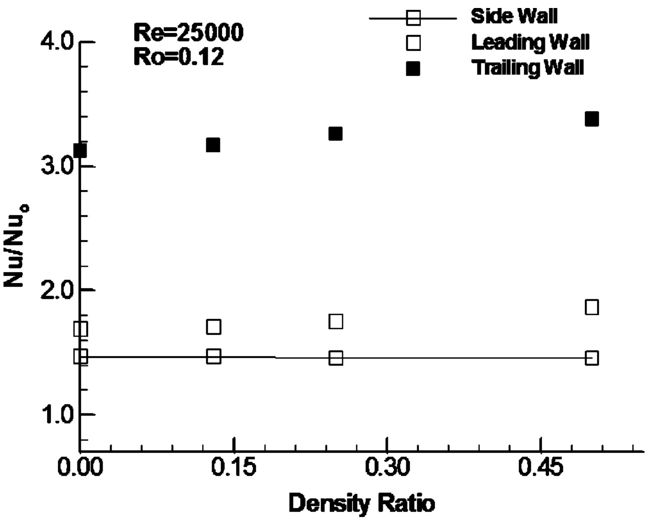

Fig. 18 Effect of density ratio $(\Delta\rho/\rho)$ on Nusselt number ratio for Ro=0.12 and Re=25,000

sistent with the measurements of Johnson et al. [5] who reported that for a Ro=0.12, rather small enhancements of leading wall heat transfer with the density ratio are obtained for a ribbed duct.

Figure 18 depicts the variation of Nusselt number with density ratio along the trailing, leading and sidewalls at Ro=0.12 and Re=25,000. Both the leading and trailing surfaces show a monotonic increase in Nusselt number ratio with the density ratio. The increase is rather modest and is about 10% as the density ratio is increased from 0 to 0.5. The sidewall Nusselt number ratio is relatively insensitive to the density ratio.

Effect of Rotation Number. Rotational effects are studied by varying the rotation number between 0 and 0.5 while keeping the Reynolds number and the density ratio fixed at 25,000 and 0.13, respectively. As discussed earlier, the centrifugal buoyancy parameter represents the combined effect of rotation and density ratio. Therefore, it is important to note that the variation of rotation gives the combined effect of rotation and buoyancy.

For Ro=0.12 and below, the flow field predicted by URANS is essentially steady. However, at a rotation number of 0.25 and more, the flow field reveals strong unsteadiness and is discussed here. A sequence of time dependent flow structures at three different times for Ro=0.5 is presented in Fig. 19. The temporal variation of vertical velocity as a function of time at the center of the domain is shown in Fig. 19(*a*). It is clear that the flow field at Ro=0.5 shows quasi-periodic behavior. Clear evidence of multiple frequencies is observed from the signal trace. The snapshots of velocity vectors with superimposed temperature field at $x=0.5$ are presented in Figs. 19(*b*)–19(*d*) at three different times. It is interesting to note that the double rolls seen in other cases at low rotation number bifurcates and two pairs of counter rotating rolls are observed. The middle two rolls show larger oscillations compared to the two side rolls. The continuous growth and shrinkage of the rolls can be seen in the sequence of figures. The corresponding temperature variations also show clear unsteady behaviour.

The time-averaged secondary flow field and Nusselt number variation on trailing wall corresponding to Ro=0.5 are plotted in Fig. 20. At $x=0.5$, two symmetric pairs of rolls can be clearly seen in the secondary flow pattern in Fig. 20(*a*). Due to the higher rotation, the bulk fluid is pushed towards the trailing wall and the zone near the trailing wall is dominated by cold fluid and higher vorticity secondary flow. The maximum vorticity in the core of the secondary flow is 6.0 while the corresponding value at low rotation (Ro=0.12) is about 1.3. As a result of the stronger secondary flow, the heat transfer increases with rotation along the trailing and sidewalls. The secondary flow pattern at Ro=0.5 appears to be intrinsically different than at a lower rotation number (Ro =0.12 in Fig. 16) with four eddies at Ro=0.5, and secondary flow directed away from the midregions of the trailing surface instead of being directed towards the trailing surface. The Nusselt number distribution along the trailing wall is shown in Fig. 20(*b*), and clearly shows two separate zones of low temperatures. At higher rotation numbers, the Nusselt numbers show a little asymmetry. This behavior is caused by very low frequency present in the flow. Averaging of this low frequency demand very long averaging time. The percentage change in the values of Nusselt number on the confining walls are checked by increasing the total time of averaging by 1.5 times, and no noticeable difference is observed. The minimum period for which averaging is done is more than 15 flow through times. The high temperature (low heat transfer) region in the middle is a consequence of the central downwash away from the trailing surface.

Figure 21 shows the mean velocity vectors along with the temperature contours at the midtransverse plane ($y=0$). At this high rotation number, the velocity distribution looks different from the other cases discussed so far. The fluid is pushed strongly towards the trailing surface to the extent that there is no formation of corner vortices in front of the rib. The separating shear layer at the trailing edge is so strong that it penetrates nearly to the center of the domain. On the other hand, the velocity near the leading edge reduces to the extent that the flow structures near the leading surface are significantly altered. Two large vortices, one before

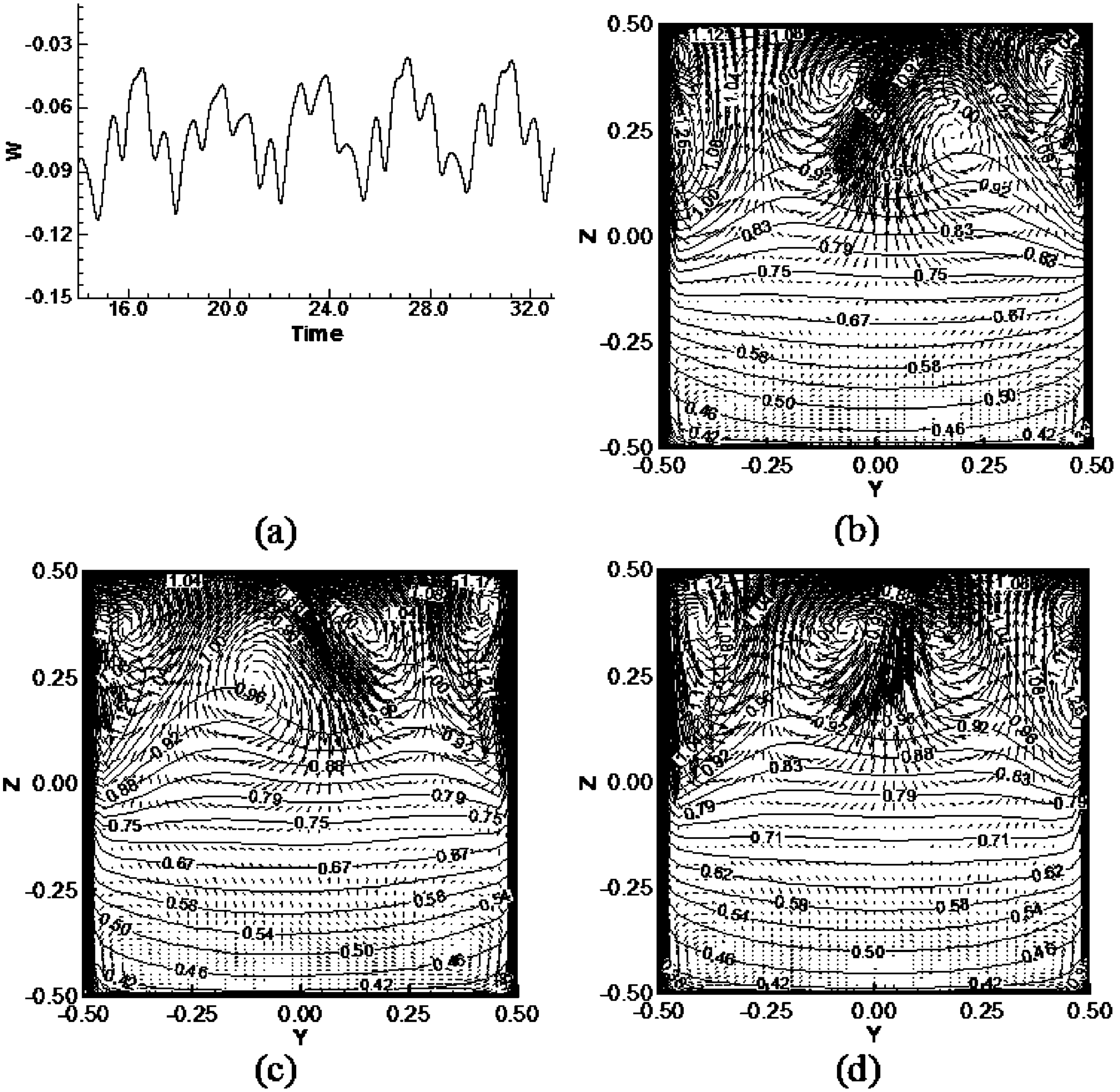

Fig. 19 (*a*) Signal traces of the vertical velocity at $x=0.5$, $y=0$, $z=0$, (*b*)–(*d*) secondary flow structures superimposed on temperature contours ($x=0.5$) at (*b*) time=14.53, (*c*) 25.88, and (*d*) 32.90 for Re=25,000, $(\Delta\rho/\rho)=0.13$ and Ro=0.5 (URANS) (top: trailing wall; bottom: leading wall)

and one after the rib, are formed without any evidence of a separating shear layer at the rib edge. Due to high rotation the vorticity of the bulk flow also increases.

Figure 22 presents the line plot showing the variation of Nusselt number ratio for various rotation numbers. The trailing surface shows a continuous increase in Nusselt number ratio as the rotation number is increased. This is expected since the rotation-induced secondary flows push the cold core fluid towards the trailing wall and increase the velocities and turbulent fluctuations near the trailing wall. The leading wall shows an initial drop in the Nusselt number ratio until a Ro=0.12. Beyond Ro=0.12, the Nusselt number ratio increases with a further increase in rotation, but does not exceed the stationary case value. It has already been discussed that the increase in rotation number causes an increase in the buoyancy forces and it is this effect that is partly responsible for increasing the heat transfer at the leading wall. To investigate this further, simulation is performed at Ro=0.25 without any buoyancy. The Nusselt number ratios along the side, leading, and trailing walls for no buoyancy case are found to be 1.51, 1.69, and 3.30, respectively, and are less than the corresponding values of 1.53, 1.84, and 3.47 with a density ratio of 0.13. The other factors that may play a role in the leading wall heat transfer at high Ro are the large vortices generated upstream and downstream of the rib. Johnson et al. [5] also observed similar behavior. They found that in the lower rotation number range (0–0.23), there is a decrease in the Nusselt number ratio on the leading wall and the ratio increases with further increase in rotation. The same behavior is seen here except the minimum point is located at Ro=0.12. The lower Ro number at which the transition in the trend occurs

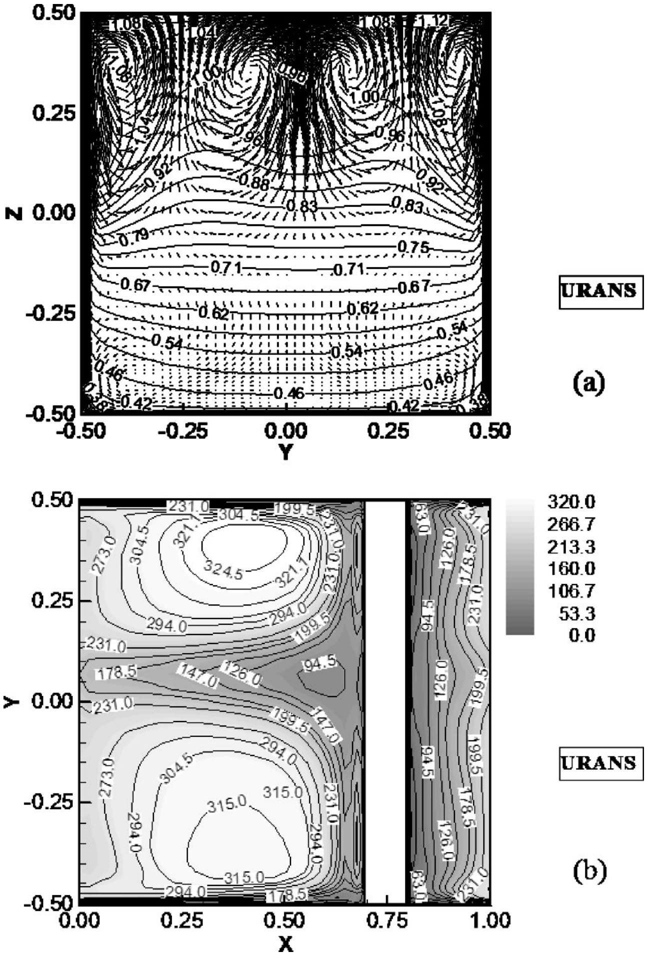

Fig. 20 Time averaged (*a*) secondary flow and temperature contours at $x=0.5$, (top: trailing wall); bottom: leading wall. (*b*) Trailing wall Nusselt number distribution for Re=25,000, $(\Delta\rho/\rho)=0.13$ and Ro=0.5

may be related to the square rib profile used in the present study, while in Ref. [5] a rounded rib profile was used. The sidewalls reveal increasing heat transfer with rotation since higher rotation causes stronger secondary flow.

Concluding Remarks

Results from LES and URANS of flow and heat transfer in a rotating ribbed duct with isothermal walls and staggered ribs are presented. The effect of Coriolis forces and centrifugal buoyancy are included in the simulations. The following conclusions emerge from the present study.

- Heat transfer predictions with LES and URANS agree well (within 20%) with experimental data in rotating smooth and rotating ribbed ducts over a wide range of Reynolds number and Rotation numbers.
- The LES results reveal that the flowfield is characterized by unsteady coherent structures, and that these structures play an important role in the mixing and heat transfer. The thermal structures downstream of the rib have streamwise orientations similar to the flow structures. The URANS results show only mild unsteadiness at Ro less than 0.25, but exhibit significant flow unsteadiness and dynamics of the secondary flow structures at a rotation number of 0.5. The secondary flow exhibits four eddies at Ro=0.5 compared to two eddies at a lower Ro. The different secondary flow patterns substantially influence the heat transfer distributions on the trailing wall.

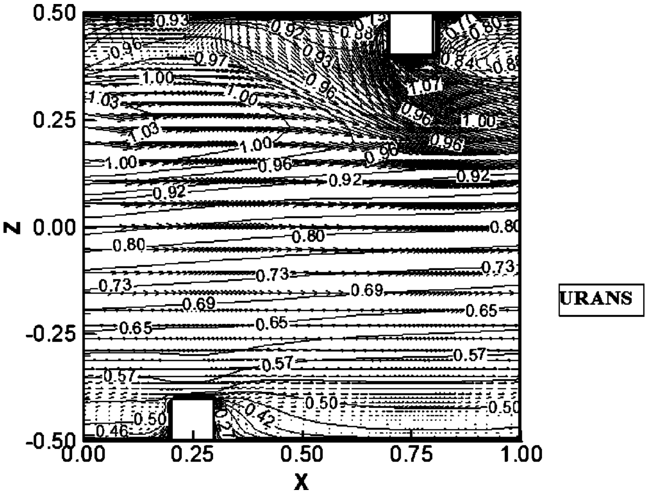

Fig. 21 Time averaged vectors on temperature contours at $y=0.0$ for Re=25,000, $(\Delta\rho\rho)=0.13$ and Ro=0.5. (top: trailing wall; bottom: leading wall)

- With increasing Re, the heat transfer ratio decreases monotonically with the trailing wall exhibiting the greatest dependence. The $\mathrm{Re}^{0.8}$ scaling is clearly inadequate for ribbed duct flows.
- Rotation causes heat transfer on the trailing and sidewalls to increase monotonically. However, the leading wall shows an initial decrease in heat transfer until Ro=0.12. The leading wall heat transfer increases beyond Ro=0.12 because of the increased effect of centrifugal buoyancy at high rotation. However, it does not exceed the stationary duct value. The Nusselt numbers on both leading and trailing surfaces are higher with centrifugal-buoyancy effects included.
- With increasing density ratio, the leading and trailing walls show an increase in the Nusselt number ratio. However, along the sidewalls the Nusselt number ratio is relatively insensitive to the density ratio.

Acknowledgments

This work was supported by a grant from the South Carolina Institute for Energy Studies under the auspices of the DOE-ATS program. Their support is gratefully acknowledged. The authors would also like to thank Mayank Tyagi for his valuable discussions.

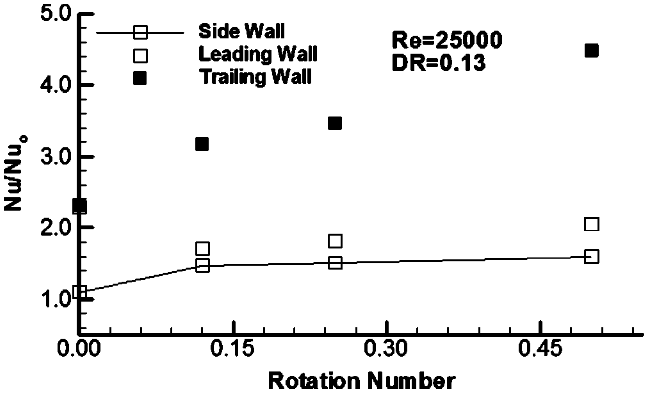

Fig. 22 Effect of rotation number on Nusselt number ratio for Re=25,000, $(\Delta\rho/\rho)=0.13$

Nomenclature

B = width of the duct
Bo = buoyancy parameter, $(\Delta\rho/\rho)\mathrm{Ro}^2 R_M$
e = height of the ribs
H = hydraulic diameter (height) of the duct
K = thermal conductivity of fluid/solid
L_x = streamwise extent of the periodic domain
Nu = $-[(\partial\theta/\partial n)|_{n=0}]/(\theta_w-\theta_b)$
P = total pressure, pitch of the array of ribs
p = periodic component of pressure
Pr = Prandtl number, ν/α
q_j = turbulent thermal subgrid stress
Re = Reynolds number, $u_{\mathrm{av}}B/\nu$
r_j = radius of rotation
R_M = mean radius of rotation
Ro = rotation number, $\Omega B/u_{\mathrm{av}}$
t = time
T = temperature
$\overline{u},\overline{v},\overline{w}$ = nondimensional filtered velocity in x, y, and z directions
u',v',w' = nondimensional unfilterd velocities in x, y, and z directions (LES)
u'',v'',w'' = nondimensional incoherent or random components velocities in x, y, and z directions (URANS)
u_z = friction velocity
y-plus = y expressed in wall coordinates $(=yu_{\tau/\nu})$

Greek Symbols

β = mean pressure gradient
ε_{ijk} = alternating tensor
δ_{ij} = Kronecker delta
θ = nondimensional periodic component of temperature, $(T-T_w)/(T_{m1}-T_w)$
$\Delta\rho/\rho$ = coolant-to-density ratio, $(T_w-T_b)/T_w$
ω_i = instantaneous vorticity, $\varepsilon_{ijk}\partial u_k/\partial x_j$
τ_{ij} = subgrid stress
$\delta x,\delta y,\delta z$ = mesh spacing in x, y, z directions

Subscripts

b = bulk
w = wall
$m1,m2$ = periodic planes

References

[1] Han, J. C., and Park, J. S., 1988, "Developing Heat Transfer in Rectangular Channel With Rib Turbulators," Int. J. Heat Mass Transfer, **31**(1), pp. 183–195.

[2] Han, J. C., Ou, S., Park, J. S., and Lei, C. K., 1989, "Augmented Heat Transfer in Rectangular Channels of Narrow Aspect Ratios with Rib Turbulators," Int. J. Heat Mass Transfer, **32**(9) pp. 1619–1630.

[3] Han, J. C., 1988, "Heat Transfer and Friction Characteristics in Rectangular Channels With Rib Turbulators," ASME J. Heat Transfer, **110**, pp. 321–328.

[4] Wagner, J. H., Johnson, B. V., Graziani, R. A., and Yeh, F. C., 1992, "Heat Transfer in Rotating Serpentine Passages With Trips Normal to the Flow," ASME J. Turbomach., **114**, pp. 847–857.

[5] Johnson, B. V., Wagner, J. H., and Steuber, G. D., 1993, "Effect of Rotation on Coolant Passage Heat Transfer," NASA Contractor Report-4396, Vol. II.

[6] Chen, Y., Nikitopoulos, D. E., Hibbs, R., Acharya, S., and Myrum, T. A., 2000, "Detailed Mass Transfer Distribution in a Ribbed Coolant Passage with a 180°," Int. J. Heat Mass Transfer, **43**, pp. 1479–1492.

[7] Azad, G. S., Uddin, M. J., Han, J.-C., Moon, H.-K., and Glezer, B., 2002, "Heat Transfer in a Two-Pass Rectangular Rotating Channel with 45° angled rib turbulators," ASME J. Turbomach., **124**, pp. 251–259.

[8] Griffith, T. S., Al-Hadhrami, L., and Han, J. C., 2002, "Heat Transfer in Rotating Rectangular Cooling Channels $(\mathrm{AR}=4)$ with Angled Ribs," ASME J. Heat Transfer, **124**, pp. 617–625.

[9] Stephens, M. A., Shih, T. I.-P., and Civinskas, K. C., 1995, "Computation of Flow and Heat Transfer in a Rectangular Channel with Ribs," AIPP paper no. 95-0180.

[10] Rigby, D. L., Steinthorsson, E., and Ameri, A. A., 1997, "Numerical Prediction of Heat Transfer in a Channel with Ribs and Bleed," ASME paper no. 97-GT-431.

[11] Bo, T., Iacovides, H., and Launder, B. E., 1995, "Developing Buoyancy-Modified Turbulent Flow in Ducts Rotating in Orthogonal Mode," ASME J. Turbomach., **117**, pp. 474–484.

[12] Iacovides, H., 1998, "Computation of Flow and Heat Transfer Through Rotating Ribbed Passage," Int. J. Heat Fluid Flow, **19**, pp. 393–400.

[13] Al-Qahtani, M., Jang, Y.-J., Chen, H.-C., and Han, J. C., 2002, "Prediction of Flow and Heat Transfer in Rotating Two-Pass Rectangular Channels with 45° Rib Turbulators," ASME J. Turbomach., **124**(2), pp. 242–250.

[14] Huser, A., Biringen, S., and Hatay, F. F., 1994, "Direct Simulation of Turbulent Flow in a Square Duct: Reynolds-Stress Budgets," Phys. Fluids, **6**(9), pp. 3144–3152.

[15] Gavrilakis, S., 1992, "Numerical Simulation of Low Reynolds Number Turbulent Flow Through a Straight Square Duct," J. Fluid Mech., **244**, pp. 101–129.

[16] Tafti, D. K., and Vanka, S. P., 1991, "A Numerical Study of the Effects of Spanwise Rotation on Turbulent Channel Flow," Phys. Fluids A, **3**(4), pp. 642–656.

[17] Piomelli, U., and Liu, J., 1995, "Large-Eddy Simulation of Rotating Channel Flows Using a Localised Dynamic Model," Phys. Fluids, **7**, pp. 839–848.

[18] Pallares, J., and Davidson, L., 2000, "Large Eddy Simulations of Turbulent Flow in a Rotating Square Duct," Phys. Fluids, **12**(11), pp. 2878–2894.

[19] Murata, A., and Mochizuki, S., 2001, "Effect of Centrifugal Buoyancy on Turbulent Heat Transfer in an Orthogonally Rotating Square Duct with Transverse or Angled Rib Turbulators," Int. J. Heat Mass Transfer, **44**, pp. 2739–2750.

[20] Wang, G., and Vanka, S. P., 1995, "Convective Heat Transfer in Periodic Wavy Passages," Int. J. Heat Mass Transfer, **38**(17), pp. 3219–3230.

[21] Lilly, D. K., 1992, "A Proposed Modification of the Germano Subgrid-Scale Closure Method," Phys. Fluids A, **4**, pp. 633–635.

[22] Germano, M., Piomelli, U., Moin, P., and Cabot, W. H., 1991, "A Dynamic Subgrid-Scale eddy Viscosity Model," Phys. Fluids A, **3**, pp. 1760–1765.

[23] Zang, Y., Street, R. L., and Koseff, J. R., 1993, "A Dynamic Subgrid-Scale Model and Its Application to Turbulent Recirculating Flows," Phys. Fluids A, **5**, pp. 3186–3196.

[24] Moin, P., Squires, K., Cabot, W., and Lee, S., 1991 "A Dynamic Subgrid-Scale Model for Compressible Turbulence and Scalar Transport," Phys. Fluids A, **3**, pp. 2746–2757.

[25] Kato, M., and Launder, B. E., 1993, "The Modelling of Turbulent Flow around Stationery and Vibrating Square Cylinders," *Proc. 9th Symposium on Turbulent Shear Flows*, Kyoto, Japan, Vol. 10-4.

[26] Saha, A. K., Biswas, G., and Muralidhar, K., 2001, "Two-Dimensional Study of the Turbulent Wake Behind a Square Cylinder Subject to Uniform Shear," ASME J. Fluids Eng., **123**, pp. 595–603.

[27] Harlow, F. H., and Welch, J. E., 1965, "Numerical Calculation of Time-Dependent Viscous Incompressible Flow of Fluid with Free Surfaces," Phys. Fluids, **8**, pp. 2182–2188.

[28] Saha, A. K., and Acharya, S., 2001, "Three-Dimensional Flow and Heat Transfer Calculations in Micro-Channel Heat Exchangers," HTD-366-3, Proceeding of the ASME Heat Transfer Division, IMECE 2001, New York, NY, 11–16 November, Vol. 3.

[29] Kawamura, T., Takami, H., and Kuwahara, K., 1986, "Computation of High Reynolds Number Flow around a Circular Cylinder with Surface Roughness," Fluid Dyn. Res., **1**, pp. 145–162.

Nusselt Numbers and Flow Structure on and Above a Shallow Dimpled Surface Within a Channel Including Effects of Inlet Turbulence Intensity Level

P. M. Ligrani
Professor,
Fellow ASME

N. K. Burgess
Graduate Student

S. Y. Won
Graduate Student

Convective Heat Transfer Laboratory,
Department of Mechanical Engineering,
University of Utah,
Salt Lake City, UT 84112-9208

Experimental results from a channel with shallow dimples placed on one wall are given for Reynolds numbers based on channel height from 3,700 to 20,000, levels of longitudinal turbulence intensity from 3% to 11% (at the entrance of the channel test section), and a ratio of air inlet stagnation temperature to surface temperature of approximately 0.94. The ratio of dimple depth to dimple print diameter δ/D *is 0.1, and the ratio of channel height to dimple print diameter* H/D *is 1.00. The data presented include friction factors, local Nusselt numbers, spatially averaged Nusselt numbers, a number of time-averaged flow structural characteristics, flow visualization results, and spectra of longitudinal velocity fluctuations which, at a Reynolds number of 20,000, show a primary vortex shedding frequency of 8.0 Hz and a dimple edge vortex pair oscillation frequency of approximately 6.5 Hz. The local flow structure shows some qualitative similarity to characteristics measured with deeper dimples (*δ/D *of 0.2 and 0.3), with smaller quantitative changes from the dimples as* δ/D *decreases. A similar conclusion is reached regarding qualitative and quantitative variations of local Nusselt number ratio data, which show that the highest local values are present within the downstream portions of dimples, as well as near dimple spanwise and downstream edges. Local and spatially averaged Nusselt number ratios sometimes change by small amounts as the channel inlet turbulence intensity level is altered, whereas friction factor ratios increase somewhat at the channel inlet turbulence intensity level increases. These changes to local Nusselt number data (with changing turbulence intensity level) are present at the same locations where the vortex pairs appear to originate, where they have the greatest influences on local flow and heat transfer behavior.* [DOI: 10.1115/1.1861913]

Introduction

Dimples are used on the surfaces of internal flow passages because they produce substantial heat transfer augmentations, with pressure drop penalties which are smaller than many other types of heat augmentation devices, such as pin fins and rib turbulators. Arrays of dimples accomplish this: (i) by ejecting multiple pairs of vortices, which increase secondary advection, and local, three-dimensional turbulence transport, as they advect downstream, and (ii) by not protruding into the flow, and therefore, by not increasing losses due to form drag [1–3]. Also important are the unsteadiness associated with vortex pair shedding, and the reattachment of the shear layer which forms across the top of each dimple. Dimples are also attractive heat transfer augmentation devices because they generally require uncomplicated manufacturing procedures, particularly if the dimple shape is a spherical indentation. Because of this characteristic, dimples do not add extra weight onto a component, especially if surface material is removed to form the dimples. On thinner materials, an indentation producing device can be used to form the dimples, which then gives protrusions on the opposite side. This then leads to another advantage because substantial heat transfer augmentations are also provided by the array of protrusions [4,5].

A number of heat transfer studies from Russia utilize dimples. These studies employ flows over flat walls with regular arrays of spherical pits [6], flows in annular passages with a staggered array of concave dimples on the interior cylindrical surface [7], flows in single hemispherical cavities [8,9], flows in diffuser and convergent channels each with a single hemispherical cavity [10], and flows in a narrow channel with spherically shaped dimples placed in relative positions on two opposite surfaces [11]. Heat transfer augmentations as high as 150%, compared to smooth surfaces, are reported, sometimes with appreciable pressure losses [7]. Other recent data shows that the enhancement of the overall heat transfer rate is about 2.5 times smooth surface values over a range of Reynolds numbers, and pressure losses are about half the values produced by conventional rib turbulators [12]. A computational simulation of flows over dimpled surfaces in a channel gives flow structures, flow streamlines, temperature distributions, and resulting surface heat transfer distributions for similar geometries and flow conditions [13]. Moon et al. [14] give data that show that improvements in heat transfer intensification and pressure losses remain at approximately constant levels for different Reynolds numbers and channel heights. Mahmood et al. [1] describe the mechanisms responsible for local and spatially averaged heat transfer augmentations on flat channel surfaces with an array of dimples on one wall for one channel height, equal to 50% of the dimple print diameter. Other recent investigations consider flow

---

Contributed by the International Gas Turbine Institute (IGTI) of THE AMERICAN SOCIETY OF MECHANICAL ENGINEERS for publication in the ASME JOURNAL OF TURBOMACHINERY. Paper presented at the International Gas Turbine and Aeroengine Congress and Exhibition, Vienna, Austria, June 13–17, 2004, Paper No. 2004-GT-54231. Manuscript received by IGTI, October 1, 2003; final revision, March 1, 2004. IGTI Review Chair: A. J. Strazisar.

and heat transfer in single spherical cavities [15], the effects of dimple depth on vortex structure and surface heat transfer [16], the effects of deep dimples on local surface Nusselt number distributions [2], the combined influences of aspect ratio, temperature ratio, Reynolds number, and flow structure [3], and the flow structure due to dimple depressions on a channel surface [17].

The present study is unique and different from existing studies because the effects of shallow dimples, with a ratio of dimple depth to dimple print diameter δ/D of 0.1, are investigated. Of particular interest are the effects of different inlet turbulence intensity levels on local Nusselt numbers, spatially averaged Nusselt numbers, and friction factors. The experimental results, measured on a test surface with shallow dimples, placed on one wall of a channel, are given for Reynolds numbers based on channel height from 3,700 to 20,000, levels of longitudinal turbulence intensity from 3% to 11% (at the entrance of the channel test section), and a ratio of air inlet stagnation temperature to surface temperature of approximately 0.94. The ratio of channel height to dimple print diameter H/D is 1.00. As such, the present experiment is designed to model internal cooling passages of the airfoils employed in gas turbines used for utility power generation. However, the improvements in surface heat transfer augmentation produced by arrays of dimples are also useful in a variety of other practical applications, including electronics cooling, heat exchangers, micro-scale passages, bio-medical devices, and combustion chamber liners.

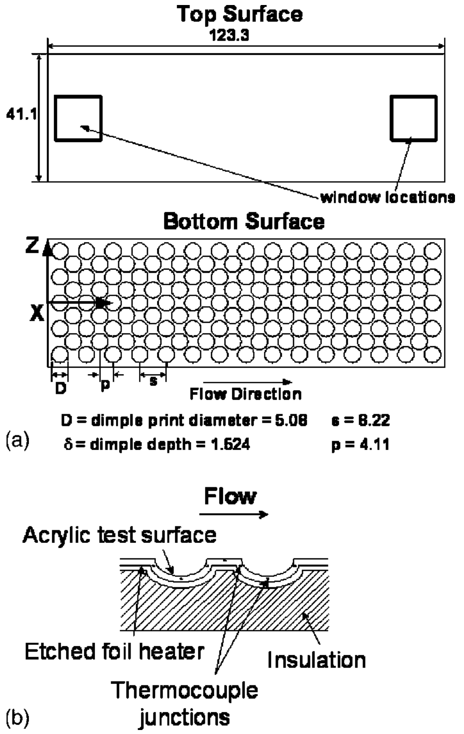

Fig. 1 Schematic diagrams of: (a) The top and bottom dimpled test surfaces, and (b) cross-sectional view of the heated test surface. All dimensions are given in cm.

Experimental Apparatus and Procedures

Channel and Test Surface for Heat Transfer Measurements. A schematic of the facility used for heat transfer measurements is given by Burgess et al. [2] and by Mahmood and Ligrani [3]. The air used within the facility is circulated in a closed-loop. One of three circuits is employed, depending upon the Reynolds number requirements in the test section. For Reynolds numbers Re_H less than 10,000, a 102 mm inner diameter pipe is used, which is connected to the intake of an ILG Industries 10P type centrifugal blower. For Reynolds numbers between 10,000 and 25,000, the 102 mm pipe is connected to the intake of a Dayton 7C554 radial drive blower. For higher Reynolds numbers, a 203 mm inner diameter pipe is employed with a New York Blower Co. 7.5 HP, size 1808 pressure blower. In each case, the air mass flow rate from the test section is measured (upstream of whichever blower is employed) using an ASME standard orifice plate and Validyne M10 digital pressure manometer. The blower then exits into a series of two plenums (0.9 m square and 0.75 m square). A Bonneville cross-flow heat exchanger is located between two of these plenums. As the air exits the heat exchanger, it enters the second plenum, from which the air passes into a rectangular bell mouth inlet, followed by a honeycomb, two screens, and a two-dimensional nozzle with a contraction ratio of 10. This nozzles leads to a rectangular cross-section, 411 mm by 50.8 mm inlet duct which is 1219 mm in length. This is equivalent to 13.5 hydraulic diameters (where hydraulic diameter is 90.4 mm). Boundary layer trips are employed on the top and bottom surfaces of the inlet duct, just upstream of the test section, which follows with the same cross-section dimensions. It exits to a 0.60 m square plenum, which is followed by two pipes, each containing an orifice plate, mentioned earlier.

Figure 1(*a*) presents geometric details of the test section, including the bottom dimpled test surface, and the top smooth surface. Dimple geometry details are then given in Fig. 2. In the present study, a total of 29 rows of dimples are employed in the streamwise direction, with 4 or 5 dimples in each row. The dimples are positioned on the surface in a staggered array. Note that the amount of rounding around the perimeter of each dimple (where the dimple joins the flat part of the test surface) has an important influence on heat transfer and skin friction augmentations. Also identified in Fig. 1(*a*) is the test section coordinate system employed for the study. Note that the *Y* coordinate is normal from the test surface.

Local Nusselt Number Measurement. All exterior surfaces of the facility (between the heat exchanger and test section) are insulated with Styrofoam (k=0.024 W/mK), or 2 to 3 layers of 2.54 cm thick, Elastomer Products black neoprene foam insulation (k=0.038 W/mK) to minimize heat losses. Calibrated copper-constantan thermocouples are located between the three layers of insulation located around the entire test section to determine conduction losses. Between the first layer and the 3.2 mm thick acrylic, dimpled test surface is a custom-made Electrofilm etched-foil heater (encapsulated between two thin layers of Kapton) to provide a constant heat flux boundary condition on the bottom dimpled test surface. This custom-made heater is designed so that it follows the convex contour of the test surface behind each dimple (Fig. 1(*b*)).

The bottom dimpled acrylic surface contains 24 copper-constantan thermocouples. Each of these thermocouples is located 0.05 cm just below this surface to provide measurements of local

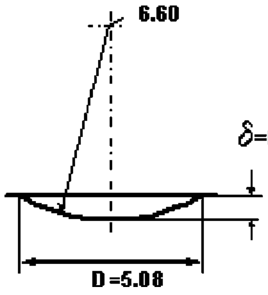

Fig. 2 Schematic diagram of individual dimple geometry details for the present study. All dimensions are given in cm.

surface temperatures, after correction for thermal contact resistance and temperature drop through the 0.05 cm thickness of acrylic. Acrylic is chosen because of its low thermal conductivity ($k=0.16$ W/mK at 20°C) to minimize streamwise and spanwise conduction along the test surface, and thus minimize "smearing" of spatially varying temperature gradients along the test surface. The surface of the acrylic is painted flat black to improve its surface emissivity for the infrared imaging. The power to the foil heater is controlled and regulated using a variac power supply. Energy balances, performed on the heated test surface, then allow determination of local magnitudes of the convective heat flux.

The mixed-mean stagnation temperature of the air entering the test section is measured using five calibrated copper-constantan thermocouples spread across the inlet cross section. To determine this temperature, measured temperatures are corrected for thermocouple wire conduction losses, channel velocity variations, as well as for the differences between stagnation and recovery temperature. Magnitudes of the local mixed mean temperatures at different locations though the test section, T_{mx}, are then determined using energy balances, and the mixed mean temperature at the inlet of the test section. Because of the way in which it is measured, this inlet temperature is also a stagnation value. The thermal conductivity k used to determine local Nusselt numbers is based on this inlet stagnation temperature. Because mixed mean temperature variations through the test section are always less than 3.0°C, thermal conductivity magnitudes based on inlet stagnation temperature are only slightly different from values based on local mixed mean temperature.

Five calibrated copper-constantan thermocouples are also spread over the exit of the test section duct. Mixed-mean temperatures, estimated from temperatures measured with these five thermocouples (and accounting for velocity variations across the channel cross-section), match values determined from energy balances within a few percent for all experimental conditions investigated. All measurements are obtained when the test facility is at steady-state, achieved when each of the temperatures from the 24 thermocouples (on the bottom dimpled test surface) vary by less than 0.1°C over a 10 min period.

To determine the surface heat flux (used to calculate heat transfer coefficients and local Nusselt numbers), the total convective power level, provided by the etched foil heater, is divided by the flat, projected test surface area corresponding to that foil heater. Spatially resolved temperature distributions along the bottom test surface are also determined using infrared imaging in conjunction with thermocouples, energy balances, digital image processing, and *in situ* calibration procedures. To accomplish this, the infrared radiation emitted by the heated interior surface of the channel is captured using a VideoTherm 340 Infrared Imaging Camera, which operates at infrared wavelengths from 8 to 14 μM. Temperatures, measured using the calibrated, copper-constantan thermocouples distributed along the test surface adjacent to the flow, are used to perform the *in situ* calibrations simultaneously as the radiation contours from surface temperature variations are recorded.

This is accomplished as the camera views the test surface through a custom-made, zinc-selenide window (which transmits infrared wave lengths between 6 and 17 μm) located on the top wall of the test section. Reflection and radiation from surrounding laboratory sources are minimized using an opaque shield which covers the camera lens and the zinc-selenide window. As shown in Fig. 1, this window can be positioned either at an upstream location or a downstream location. Note that the downstream location is located just above the 26th to 29th rows of dimples downstream from the leading edge of the test surface. Twelve thermocouple junction locations are present in the infrared field viewed by the camera. The exact spatial locations and pixel locations of these thermocouple junctions and the coordinates of a 12.7 by 12.7 cm field of view are known from calibration maps obtained prior to measurements. During this procedure, the camera is focused, and rigidly mounted and oriented relative to the test surface in the same way as when radiation contours are recorded. Voltages from the thermocouples are acquired using a Hewlett-Packard 44422T data acquisition card installed in a Hewlett-Packard 3497A data acquisition control unit, which is controlled by a Hewlett-Packard A4190A Series computer.

With these data, gray scale values at pixel locations within video taped images from the infrared imaging camera are readily converted to local Nusselt number values. Because such calibration data depend strongly on camera adjustment, the same brightness, contrast, and aperture camera settings are used to obtain the experimental data. The *in situ* calibration approach rigorously and accurately accounts for these variations.

The images from the infrared camera are recorded as 8-bit gray scale directly into the memory of a Dell Dimension XPS T800r PC computer using a Scion Image Corporation Frame grabber video card, and SCION IMAGE V.1.9.2 software. Three sets of 60 frames are recorded at a rate of one frame per second. All of 180 resulting images are then ensemble averaged to obtain the final gray scale data image. This final data set is then imported into MATLAB version 6.0.0.88 (Release 12) software to convert each of 256 possible gray scale values to local Nusselt number at each pixel location using calibration data. Each individual image covers a 300 pixel by 300 pixel area.

Friction Factors. The wall static pressures are measured along the test section simultaneously as the heat transfer measurements are conducted, using 12 static pressure taps, located 25.4–80 mm apart along one of the test section side walls. These measurements are made in the test section with the dimples, as well as in a baseline test section with smooth surfaces on all four walls. The friction factors are then determined from streamwise pressure gradient magnitudes. The pressures from the wall pressure taps are measured using Celesco LCVR pressure transducers. The signals from these transducers are processed using Celesco CD10D Carrier-Demodulators. Voltages from the Carrier-Demodulators are acquired using a Hewlett-Packard 44422A data acquisition card installed in a Hewlett-Packard 3497A data acquisition control unit, which is controlled by a Hewlett-Packard A4190A Series computer. With this apparatus, 100 sequential measurements are acquired and measured from each pressure transducer, over a time period of about 20 s.

Time-Averaged Flow Velocity Components and Pressure. A second experimental facility, with the same interior dimensions and also described by Burgess et al. [2] and Mahmood and Ligrani [3], is used for flow visualizations and measurements of flow structural characteristics. Within this apparatus, a 1.27 mm diameter miniature five-hole pressure probe, manufactured at the University of Utah especially for such measurements, is used to obtain time-averaged surveys of total pressure, static pressure, and the three mean velocity components [18,19]. These data are then used to deduce distributions of streamwise vorticity. To obtain the surveys, the probe employed is mounted on an automated two-dimensional traverse, and inserted into the test section through a slot lined with foam to prevent air leakage. The centerline of this probe is traversed as close as about 5 mm from the test section top wall, and as close as approximately 5 mm from the test section bottom wall. The output ports of the probe are connected either to Validyne DP103-06 pressure transducers (to measure differential pressures up to 2.5 mm of water), or Celesco LCVR pressure transducers (to measure differential pressures up to 20.0 mm of water). Signals from the transducers are then processed using Celesco CD10D Carrier-Demodulators. Voltages from the Carrier-Demodulators are acquired using a Hewlett-Packard 44422A data acquisition card installed in a Hewlett-Packard 3497A data acquisition control unit. This control unit, two Superior Electric type M092-FD310 Mitas stepping motors on the two-dimensional traverse, a Superior Electric Modulynx Mitas type PMS085-C2AR controller, and a Superior Electric Modulynx Mitas type

PMS085-D050 motor drive are controlled by a Hewlett-Packard A4190A Series computer. Contour plots of measured quantities are generated using a polynomial interpolating technique (with DELTAGRAPH software) between data points. In each survey plane, 1560 data points are spaced 2.54 mm apart. Data obtained at each one of these locations is time-averaged over a period of about 30 s. Additional details of the five-hole probe measurement procedures, including calibration details and procedures to account for velocity gradients and finite spatial resolution, are given by Ligrani et al. [18,19].

Flow Visualization of Instantaneous Flow Structure. Flow visualization using smoke is used to identify vortex structures and other secondary flow features. Smoke from three horizontally oriented smoke wires is employed for this purpose. These are located 6.0, 12.0, and 18.0 mm from the bottom test surface at $X=205.5$ mm, which is above the center of the fifth dimple row along the shallow dimple test surface. To produce sheets of smoke, each wire is first coated with Barts Pneumatics Corp. super smoke fluid and then powered using a Hewlett-Packard 6433B DC power supply. With this arrangement, the smoke forms into single thin planes parallel to the test surface. As the smoke is advected downstream, the secondary flows which accompany vortex and secondary flow development cause the smoke to be rearranged in patterns which show the locations and distributions of these flow phenomena. Smoke patterns are illuminated in spanwise-normal light planes located at $X=616.5$ mm (above the center of the fifteenth dimple row) using a thin sheet of light provided by a Colotran ellipsoidal No. 550, 1000 Watt spot light, and a slits machined in two parallel metal plates. Images are recorded using a Panasonic WV-BP330 CCTV video camera. The analog images from this camera are acquired and then digitized using a Scion Image Corporation Frame grabber video card, and SCION IMAGE V.1.9.2 software. The resulting images are then further processed using a Dell P4 Precision 330 PC computer. An additional discussion of many of the procedures used for flow visualization is provided by Ligrani [20].

Longitudinal Turbulence Intensity Measurements and Spectra of Longitudinal Velocity Fluctuations. A single, horizontal-type platinum-plated tungsten hot-wire sensor, with a diameter of 5.0 μm and a length of 2.54 mm, is employed to measure the time varying longitudinal component of velocity at the inlet of the test section, and within the test section. The time-averaged longitudinal velocity, longitudinal turbulence intensity, and turbulence length scale are then determined from these measurements. When the probe is traversed over a measurement plane, it is positioned and controlled using the same two-dimensional traverse, controller, and drive as are employed with the five-hole pressure probe. When the hot-wire sensor is used to measure the inlet turbulence intensity level, the sensor is located in the center of the channel cross-section ($Z=0$ cm, $Y=2.54$ cm), at $X=2.0$ cm, which is just above parts of dimples in the first streamwise row.

The hot-wire probe is driven by a Disa 55M10 constant-temperature hot-wire anemometer bridge with an overheat ratio of 1.6. The analog signal from this bridge is then processed using a Dantec 56N20 signal conditioner with a low-pass, anti-aliasing filter set to 1.0 kHz. The time-varying output voltage signal is then sampled at a 2.0 kHz rate using a DATEL PCI441D I/O board installed in the Dell Precision 530 PC workstation. During each measurement, 60,000 voltage values are sampled over a 30 s period. Data are acquired using LABVIEW 6.1 software and then processed further using MATLAB 6.1 software, including determination of the turbulence length scale. This is accomplished by integrating the autocorrelation functions which are deduced from the time-varying longitudinal velocity signals. The entire measurement system, including the hot-wire sensor, is calibrated along the centerline of the channel. A Kiel type pressure probe, wall static taps, and a copper-constantan thermocouple are used to measure and determine the total pressure, static pressure, static temperature, and streamwise velocity at the test section location where the calibration is conducted.

Power spectra density profiles of streamwise velocity fluctuations (u') are obtained using 4096 (2^{12}) point of Fast-Fourier-Transforms (FFT). Each power spectra density profile is determined from an ensemble average of 100 individual profiles obtained over overlapping time intervals which are spread over a total time period of 30 s.

Uncertainty Estimates. Uncertainty estimates are based on 95% confidence levels and are determined using methods described by Kline and McClintock [21] and Moffat [22]. The uncertainty of temperatures measured with thermocouples is $\pm 0.15°$C. The spatial and temperature resolutions achieved with the infrared imaging are about 0.5 mm and 0.8°C, respectively. This magnitude of temperature resolution is due to uncertainty in determining the exact locations of thermocouples with respect to pixel values used for the *in situ* calibrations. The local Nusselt number uncertainty is then about ±6.8%. Corresponding Nusselt number ratio uncertainty is about ±0.14 (for a ratio of 1.50), or ±9.4%. Note that all uncertainties of local Nusselt numbers consider variations of surface heat flux which may be present due to small changes of the thickness of the acrylic which comprises the dimpled test surface. The friction factor ratio uncertainty is approximately ±5.0% for f/f_o equal to 1.40. Reynolds number uncertainty is about ±2.0% for Re_H of 17,800. The experimental uncertainties of time-averaged magnitudes of local total pressure (relative to atmospheric pressure), local static pressure (relative to atmospheric pressure), local streamwise velocity, and local streamwise vorticity are ±4.0%, ±4.0%, ±2.5%, and ±8.0%, respectively. The estimated uncertainties of the time-averaged magnitudes of the spanwise and normal velocity components are about ±8.0%, and ±10.0%, respectively. The estimated uncertainty of the time-averaged magnitude of the longitudinal Reynolds normal stress (or the mean-square of the fluctuating velocity component) is about ±5.0%.

Experimental Results and Discussion

Baseline Nusselt Numbers. Two different sets of baseline Nusselt numbers are measured for two different purposes. In both cases, constant-property baseline Nusselt numbers are measured in a smooth rectangular test section with smooth walls on all surfaces and no dimples, for a ratio of inlet stagnation temperature to a surface temperature of 0.93–0.94 and an inlet turbulence intensity level of 3.3%. The baseline measurements are also time-averaged, and made in the downstream portion of the test section, where the channel flow is hydraulically and thermally fully developed. The *first set* is measured in a channel with an aspect ratio of 4 with heating on all four channel surfaces (with constant heat flux boundary condition around the entire test section) to verify the experimental apparatus and procedures employed. The *second set* is measured in a channel with an aspect ratio of 8 (which is the same aspect ratio employed for the present dimple surface measurements) to provide baseline Nusselt numbers Nu_o to normalize values measured on the dimpled surface. In this case, only the bottom channel surface is heated to provide the same type of thermal boundary condition as when the dimples are installed. Except for the absence of the dimples, all geometric characteristics of the channel are then the same as when the dimpled test surface is installed.

Baseline Nusselt numbers for both sets of conditions are shown in Fig. 3. Also included in this figure is the Dittus–Boelter smooth circular tube correlation [23], which is given by

$$\mathrm{Nu}_o = 0.023\mathrm{Re}_{Dh}^{0.8}\mathrm{Pr}^{0.4} \tag{1}$$

The agreement between Eq. (1) and the first set of baseline data (obtained with all four walls heated), shown in Fig. 3 for the entire range of Reynolds numbers Re_{Dh} examined, provides a check on the experimental apparatus and procedures. This first set of

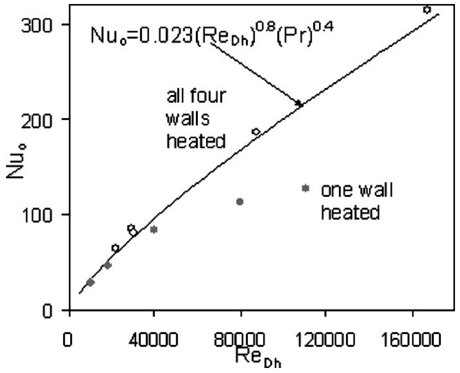

Fig. 3 Baseline, constant property Nusselt numbers, measured with smooth channel surfaces and constant heat flux boundary condition, for a ratio of inlet stagnation temperature to surface temperature of 0.93–0.94, as dependent upon Reynolds number based on hydraulic diameter. Data are given for all four walls heated, and for one wall heated.

spatially-averaged Nusselt numbers are determined from measurements made on the top and bottom walls.

Because of the different thermal boundary conditions employed, Fig. 3 shows that baseline Nusselt numbers with heating only on one wall are generally lower than the values given by Eq. (1), when compared at the same Reynolds number based on hydraulic diameter. The lower values are due to larger differences between local wall temperature and local mixed mean temperature for the same magnitudes of surface heat flux. As mentioned, the baseline values are employed to normalize dimpled surface Nusselt numbers. In some cases, this is accomplished by interpolating between the darkened data points in Fig. 3 using a polynomial equation.

Augmentation of the Longitudinal Turbulence Intensity. The device used to augment turbulence intensity levels at the inlet of the test section is shown in Fig. 4. It consists of two plenums, each of which supplies a row of injection holes located on each side of the channel. A splitter plate is then also located along the mid-plane of the channel. The plenum supply pressure level can be varied to alter the magnitude of the longitudinal turbulence intensity. The value with no jets is 3.3%. Values as high as about 11%, are possible with a plenum supply pressure of about 38 psia. For this range of supply pressures, magnitudes of the turbulence length scale range from about 10.7 mm to about 16.8 mm.

To determine the longitudinal turbulence intensity, the instantaneous velocity signal u is expressed as the sum of a time-averaged component $\overline{u}$ and a fluctuating component u', such that

$$u_i=\overline{u}+u_i',$$

where the subscript i denotes one instantaneous result. The turbulence intensity is then the root-mean-square of the fluctuating component divided by the magnitude of the mean component. An autocorrelation function (ACF) for one location in the flow is used to calculate the integral length scale (or the turbulence length scale), by integrating the autocorrelation function with respect to the time lag. The result is subsequently multiplied by the mean velocity to get the integral length scale, which is representative of the sizes of the largest eddies in the turbulent flow field.

Effects of Inlet Turbulence Intensity Level on Local Nusselt Number Tatios. The local Nusselt number ratios are given in Fig. 5, which are measured with shallow dimples on one channel surface and heating on one channel surface, for $\delta/D=0.1$, $H/D=1$, $Re_H=17{,}800$, $Tu=0.033$, and no augmentation of turbulence intensity levels. Note that the baseline Nusselt numbers, used for normalization of the values presented, are obtained using the same thermal boundary conditions and heating arrangement as when dimples are used on the measurement surface. In addition, heat transfer coefficients and heat flux values (used to determine Nusselt numbers) are based on flat projected areas in both cases. Here, the Nu_o values used for normalization are measured at $Tu=0.33$ and the same Reynolds numbers as the Nusselt numbers measured on the dimpled surface.

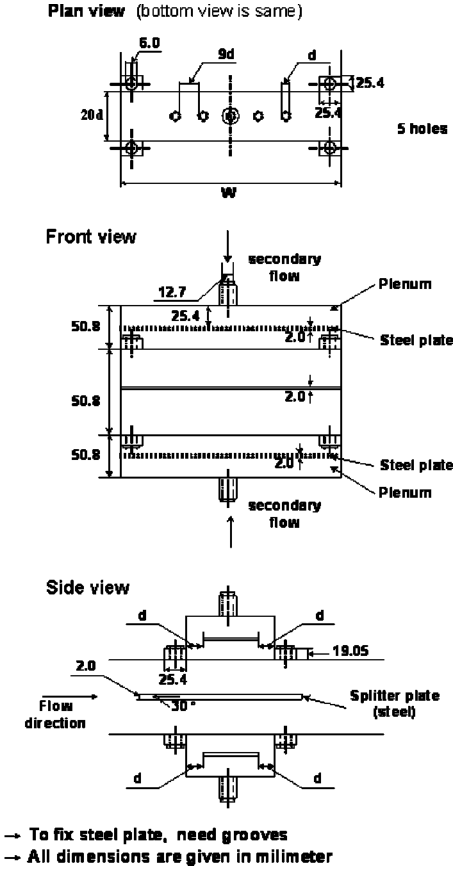

Fig. 4 Apparatus employed to increase the magnitude of the longitudinal turbulence intensity in the channel

The bulk flow direction in Fig. 5 is from left to right in the direction of increasing X/D. Each $\delta/D=0.1$ dimple is located in the vicinity of each circular Nusselt number distribution. Note that the position of each dimple is indicated using a dashed circular line. Also notice that local Nu/Nu_o values are lowest in the upstream halves of the dimples. Each of these is positioned beneath

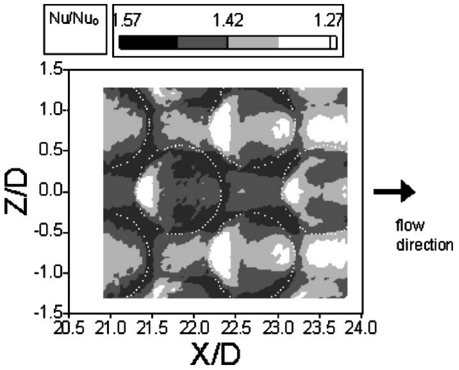

Fig. 5 Local Nusselt number ratio data from a channel with shallow dimples on one channel surface, and heating on one channel surface, for $\delta/D=0.1$, $H/D=1$, $Tu=0.033$, and $Re_H=17{,}800$

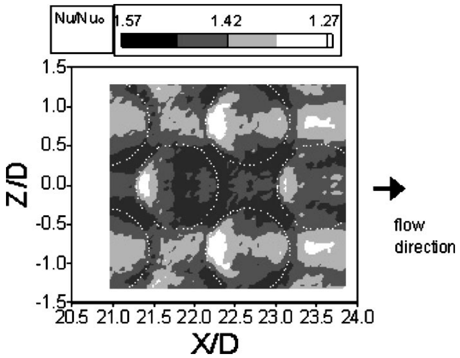

Fig. 6 Local Nusselt number ratio data from a channel with shallow dimples on one channel surface, and heating on one channel surface, for $\delta/D=0.1$, $H/D=1$, $Tu=0.069$, and $\mathrm{Re}_H=18{,}100$

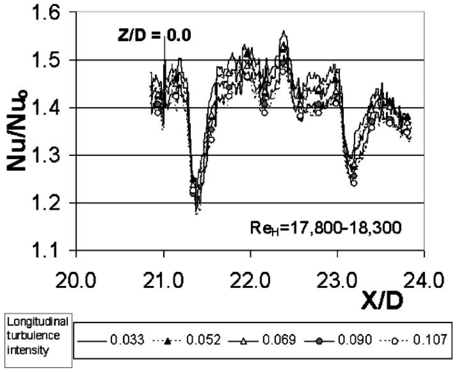

Fig. 7 Local Nusselt number ratios along the test surface spanwise centerline, $Z/D=0.0$, for different levels of channel inlet longitudinal turbulence intensity Tu from a channel with shallow dimples on one channel surface, and heating on one channel surface, for $\delta/D=0.1$, $H/D=1$, and $\mathrm{Re}_H=17{,}800-18{,}300$

a region of re-circulating flow, where advection velocities in the flow located adjacent to the surface are very low. Nusselt number ratios then increase progressively with X/D along the dimpled surface. The values then become highest near the diagonal and downstream edges of the dimples, and on the flat surfaces just downstream of these locations. Here, local Nu/Nu_o augmentations are as high as 1.6 because of reattachment of the shear layer which forms across the top of each dimple, and because of the multiple vortex pairs which are periodically shed from each dimple. For $\delta/D=0.1$, $H/D=1.0$, and $\mathrm{Re}_H=17{,}800$, one relatively large vortex pair is shed from the central part of each dimple, and two smaller vortex pairs are shed from the spanwise edges of each dimple. These edge formed vortex pairs then strengthen as they advect downstream next to the edges of other dimples. This is discussed in more detail later in the paper, and occurs because of the staggered arrangement of the dimples on the test surface, which causes each "edge" vortex pair to be located first on the right edge of a dimple, then on the left edge of another dimple, and so on. The result is interconnected regions of high local Nusselt number ratios, located diagonally between adjacent dimples, as shown in Fig. 5. Similar qualitative Nu/Nu_o variations are present on dimpled surfaces with $\delta/D=0.2$ [1] and $\delta/D=0.3$ [2], even though local quantitative Nu/Nu_o ranges and magnitudes generally increase as δ/D increases.

Figure 6 shows local Nusselt number ratio data from a channel with shallow dimples on one channel surface, and heating on one channel surface, for $\delta/D=0.1$, $H/D=1$, $\mathrm{Re}_H=18{,}100$, and $Tu=0.069$. These data are thus obtained with an augmented turbulence intensity level at the channel entrance, and are presented to show the effects of turbulence distribution, with only small quantitative variations as the turbulence intensity level is altered. Such small quantitative differences are most apparent near dimple spanwise edges, within the downstream portions of dimples, and on the flat surfaces just downstream of dimple rims, where local $\mathrm{Nu}/\mathrm{Nu}_o$ values decrease somewhat as Tu increases. This is partly because of changes to the vortices shed by the dimples, which occur as the level of inlet turbulence intensity changes.

Additional information on local Nu/Nu_o variations with are presented in Figs. 7 and 8. Figure 7 presents local Nusselt number ratios along the test surface spanwise centerline, $Z/D=0.0$, and Fig. 8 presents local Nusselt number ratios along a line of constant $X/D=23.18$. In each of these figures, data are given for different levels of inlet longitudinal turbulence intensity Tu for the channel with shallow dimples on one channel surface, and heating on one channel surface, for $\delta/D=0.1$, $H/D=1$, and $\mathrm{Re}_H=17{,}800-18{,}300$. Both of these figures show that Nusselt number ratios, measured at different levels of channel inlet longitudinal turbulence intensity Tu, are similar within the upstream parts of the dimples, where local values are also lowest. Local ratios then generally show slight decreases as Tu increases within the downstream portions of the dimples, and on the flat surfaces just downstream of the dimples, but in most cases, variations with increasing Tu are relatively small. In each case, local and spatially averaged Nusselt number ratios (like the ones shown in Fig. 9) are thus either approximately constant as Tu increases from 0.033 to 0.107, or decrease slightly at a particular location as Tu increases from 0.033 to 0.107. The decreases, when present, are due to slightly diminished transport capabilities of the vortices and sec-

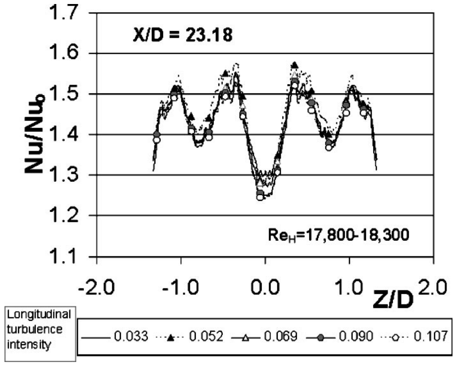

Fig. 8 Local Nusselt number ratios along a line of constant $X/D=23.18$, for different levels of channel inlet longitudinal turbulence intensity Tu from a channel with shallow dimples on one channel surface, and heating on one channel surface, for $\delta/D=0.1$, $H/D=1$, and $\mathrm{Re}_H=17{,}800-18{,}300$.

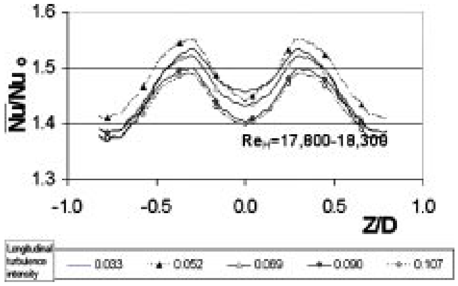

Fig. 9 Nusselt number ratios streamwise-averaged over one period of dimple surface geometry, for different levels of channel inlet longitudinal turbulence intensity Tu from a channel with shallow dimples on one channel surface, and heating on one channel surface, for $\delta/D=0.1$, $H/D=0$, and $\mathrm{Re}_H=17{,}800-18{,}300$.

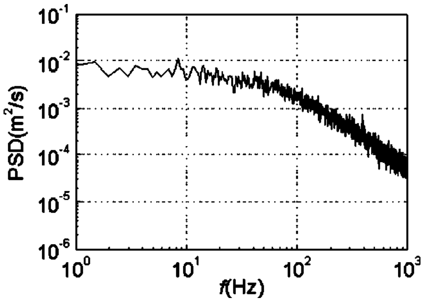

Fig. 10 Ensemble-averaged spectrum of longitudinal velocity fluctuations measured at $X/D=6.27$, $Z/D=0$, and $Y/D=0.05$, just downstream of the downstream edge of dimples in the seventh row, for $Re_H=20{,}000$, $\delta/D=0.1$, $H/D=1$, and $Tu=0.033$.

ondary flows shed by the dimples. This is partially a result of increased turbulent diffusion of vorticity, and diminished magnitudes of vortex secondary flows.

Instantaneous and Time-Averaged Flow Structure Characteristics. Additional information on the unsteadiness associated with the vortices shed from the dimples is provided by ensemble-averaged spectra of longitudinal velocity fluctuations, which are presented in Figs. 10 and 11 for $Re_H=20{,}000$ and $Tu=0.033$. The data in the first of these figures are given for $Z/D=0$, $Y/D=0.05$, and $X/D=6.27$, which is a location just downstream of the centerline of the central dimple in the seventh row. This is a location which is affected by the large, primary vortex pair which is shed from the central portion of each individual dimple. The spectrum in Fig. 10 provides evidence that the shedding frequency of the primary vortex pair is about 8.0 Hz, which is consistent with flow visualization results like the ones shown in Fig. 12 (accounting for the different Reynolds numbers for the two data sets). Here, a time sequence of visualized flow structures is presented for an illuminated spanwise-normal plane at $X/D=12.14$ (which is just above the central part of the central dimple in the 15th row) for $Re_H=3{,}700$ and $Tu=0.033$. As time proceeds, the intermittent appearance, emergence, ejection, and disappearance of the primary vortex pair, and the smaller edge vortex pairs (on either side) are apparent. The primary pair unsteadiness is a result of periodic shedding, and thus, is associated with relatively large-scale unsteady, secondary-flow events near the dimpled surface. Figure 10 also shows smaller-amplitude peaks at multiples of 8 Hz, which are due to harmonic oscillations associated with primary vortex pair shedding. Local spectra maxima at frequencies less than 8 Hz are associated with other large-scale unsteady secondary flow events near the dimpled surface.

The power spectral density distribution in Fig. 11 is given for $Z/D=0.5$, $Y/D=0.05$, and $X/D=6.27$, which is also positioned in a measurement plane just downstream of the seventh row of dimples, but at a spanwise location which is mostly affected by the vortex pairs which form and develop along dimple spanwise edges. A number of local maxima are evident in the plot. The one positioned at a frequency of 6.5 Hz is believed to be a result of the oscillations associated with the edge vortex pairs. Harmonic peaks are also evident, along with another separate primary spectral peak at a frequency of about 14.0 Hz.

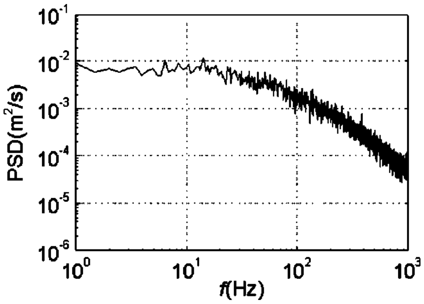

Fig. 11 Ensemble-averaged spectrum of longitudinal velocity fluctuations measured at $X/D=6.27$, $Z/D=0.5$, and $Y/D=0.05$, just downstream of the downstream edge of dimples in the seventh row, for $Re_H=20{,}000$, $\delta/D=0.1$, $H/D=1$, and $Tu=0.033$

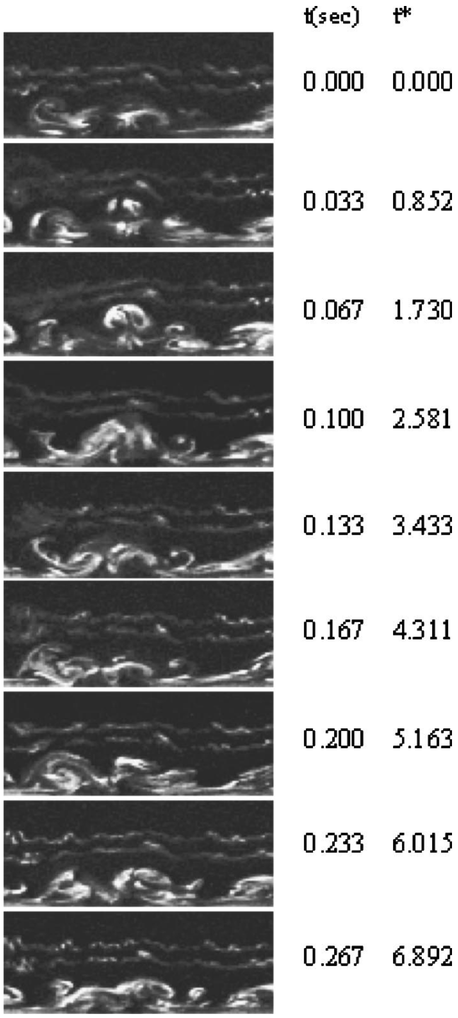

Fig. 12 Time sequence of flow images visualized in a spanwise-normal plane located at $X/D=12.14$, which is just above the central part of the central dimple in the fifteenth row, for $Re_H=3{,}700$, $\delta/D=0.1$, $H/D=1$, and $Tu=0.033$

Figures 13(*a*)–13(*g*) present surveys of time averaged quantities, which are measured over a spanwise-normal plane located at $X/D=6.27$, which is also positioned in a measurement plane just downstream of the seventh row of dimples. These data are also given for $Re_H=20{,}000$ and $Tu=0.033$. These data are presented for a higher Reynolds number than those used to obtain the flow visualization data because overall experimental uncertainties are lower as Reynolds number increases. Note that the bulk flow direction is into the plane of the paper of each contour plot, that the dimples are located at the bottom of each plot, and that all data are normalized. For the normalizations employed, P_a is ambient pressure, ρ_a is fluid density, and $\overline{V}$ is the streamwise flow velocity averaged over the channel cross section.

The surveys of streamwise velocity u_x (Fig. 13(*a*)), total pressure P_o (Fig. 13(*b*)), and static pressure P (Fig. 13(*c*)) all show relatively small deficits near the dimpled surface at locations

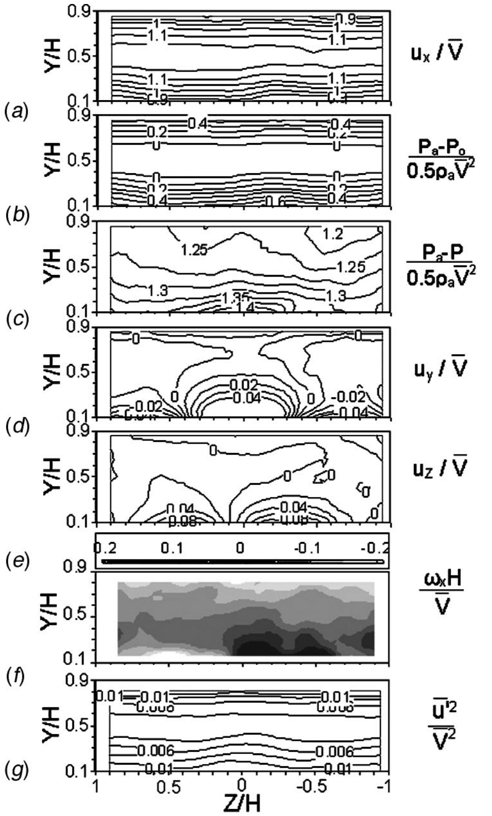

Fig. 13 Surveys of different time-averaged quantities measured in a spanwise-normal plane at $X/D=6.27$, just downstream of the downstream edge of dimples in the seventh row, for $\delta/D=0.1$, $H/D=1$, $Tu=0.033$, and $Re_H=20{,}000$. (a) Normalized streamwise velocity. (b) Normalized total pressure. (c) Normalized static pressure. (d) Normalized normal velocity. (e) Normalized spanwise velocity. (f) Normalized streamwise vorticity. (g) Normalized Reynolds normal stress.

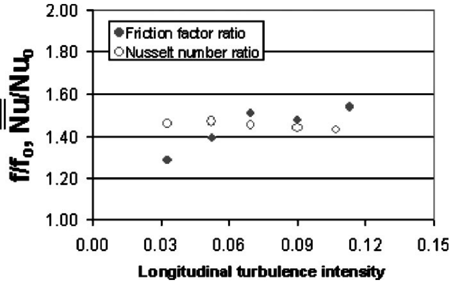

Fig. 14 Dimpled channel friction factor ratios and globally averaged dimpled channel Nusselt number ratios, for different levels of channel inlet longitudinal turbulence intensity Tu from a channel with shallow dimples on one channel surface, and heating on one channel surface, for $\delta/D=0.1$, $H/D=1$, and $Re_H=17{,}800-18{,}300$

where an upwash region is present (in the vicinity of $Z/H=0$) above the central part of the central dimple in the seventh row. The spanwise and normal velocity component data (u_y and u_z in Figs. 13(*d*) and 13(*e*), respectively) are used to determine the distribution of local streamwise vorticity ω_x, shown in Fig. 13(*f*). Variations of normal and spanwise velocity components in Figs. 13(*d*) and 13(*e*) are mostly due to secondary flow motions from the different vortex pairs which develop in the channel. Notice the large positive magnitudes of normal velocity u_y located near $Z/H=0$, which indicate secondary flow motion away from the surface in the upwash region. These are positioned just above the central part of the dimpled surface at Y/H from 0 to 0.4 and at Z/H from −0.3 to +0.3. Spanwise velocity magnitudes u_z are then in the positive and negative directions on either side of this extended upwash region, depending mostly upon location within and relative to the upwash region and the primary vortex pair.

Positive and negative regions of vorticity, associated with the primary vortex pair, like the ones seen earlier in flow visualization results, are apparent in Fig. 13(*f*). In the time-averaged flow field, the two vortices in this pair are located on either side of the upwash region located near $Z/H=0$. Other less-important regions of positive and negative vorticity are also apparent in Fig. 13(*f*) nearby the regions containing the primary vorticity. Separate signatures of time-averaged vorticity from the edge-vortex pairs are not readily apparent in this figure. The only vortex signatures which are evident in Fig. 13(*f*) are from the nearest row of dimples located just upstream of the measurement plane. No variations appear to be produced by dimples located in the sixth streamwise row (or the next to last upstream row), which is different from the variations present for dimples with $\delta/D=0.2$ [17].

Another interesting feature of the data in Fig. 13 are the connections between streamwise vorticity, deficits of total pressure, deficits of streamwise velocity, variations of normal velocity, and variations normalized Reynolds normal stress (Fig. 13(*g*)). Figure 13(*g*) shows one region of high normal stress located very near the dimpled surface at Z/H from −0.5 to +0.5, which is at the same locations as the primary vortex pair, the large extended upwash region evident in the $u_y/\overline{V}$ distribution, and the deficits of streamwise velocity and total pressure. The augmented normal stress levels are thus due to increased production of turbulence kinetic energy, at locations where local shear magnitudes and strain rates are increased. From the results presented in Figs. 12 and 13, it is evident that such shear magnitudes, strain rates, local vorticity magnitudes, and normalized normal stresses all increase significantly within the extended upwash region as Y/H decreases and the dimpled surface is approached.

Effects of Inlet Turbulence Intensity Level on Globally Averaged Nusselt Number Ratios and Friction Factor Ratios. Globally averaged Nusselt numbers are determined by averaging local data over one complete period of dimple geometry. These averages are thus conducted in both the spanwise and streamwise directions over a rectangular area from the center to center of adjacent dimples in the 27th and 29th rows. The baseline Nusselt numbers Nu_o (used for normalization) are obtained at $Tu=0.033$, and the same Reynolds numbers as the Nusselt numbers measured on the dimpled surface.

Figure 14 presents dimpled channel friction factor ratios and globally averaged dimpled channel Nusselt number ratios, for different levels of channel inlet longitudinal turbulence intensity Tu from a channel with shallow dimples on one channel surface, and heating on one channel surface, for $\delta/D=0.1$, $H/D=1$, and $Re_H=17{,}800-18{,}300$. The friction factor magnitudes a range from 1.28 to 1.57, and thus, the present dimpled surface friction factor ratios are less than magnitudes measured in several types of turbulated passages, where f/f_o range from 2.5 to 75 [24]. Figures 15(*a*) and 15(*b*) give globally averaged thermal performance parameters for the same channel configuration and experimental conditions. In all cases, heat transfer coefficients and heat flux magnitudes are based on flat projected areas. In Fig. 14, the Nusselt number ratios decrease very slightly as Tu increases, whereas friction factor ratios increase significantly as Tu increases. As a result, both thermal performance parameters decrease as Tu increases in Figs. 15(*a*) and 15(*b*). The highest values of the two performance parameters are thus produced at the lowest magnitudes of channel inlet longitudinal turbulence intensity Tu. This is partially a result of slightly diminished transport capabilities of

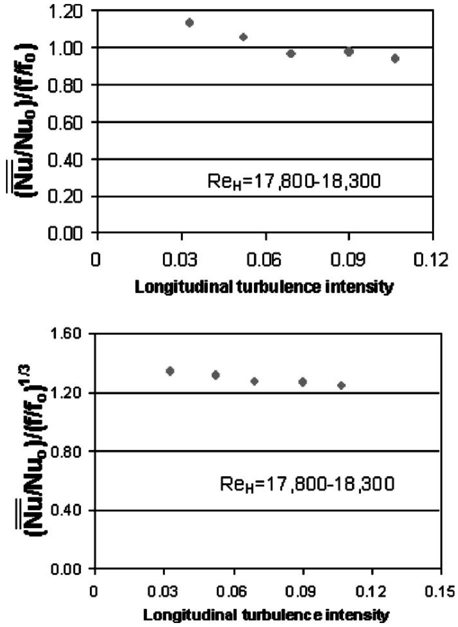

Fig. 15 Globally averaged dimpled channel thermal performance parameters, for different levels of channel inlet longitudinal turbulence intensity *Tu* from a channel with shallow dimples on one channel surface, and heating on one channel surface, for $\delta/D=0.1$, $H/D=1$, and Re_H=17,800–18,300

the vortices and secondary flows shed by the dimples (because of increased turbulent diffusion of vorticity), and the increases of local flow shear stress values which are tied to increased flow mixing.

Summary and Conclusions

Experimental results from a channel with shallow dimples placed on one wall are given for Reynolds numbers based on channel height from 3,700 to 20,000, levels of longitudinal turbulence intensity from 3%–11% (at the entrance of the channel test section), and a ratio of air inlet stagnation temperature to surface temperature of approximately 0.94. The ratio of dimple depth to dimple print diameter δ/D is 0.1, and the ratio of channel height to dimple print diameter H/D is 1.

Spectra of longitudinal velocity fluctuations, measured at a Reynolds number of 20,000, show a primary vortex shedding frequency of 8.0 Hz and a dimple edge vortex pair oscillation frequency of approximately 6.5 Hz. These frequencies are consistent with variations observed in time-sequences of instantaneous flow visualization images. Other time-averaged, local flow structural characteristics show some qualitative similarity to characteristics measured with deeper dimples (δ/D of 0.2 and 0.3), with smaller quantitative changes from the dimples as δ/D decreases. For all three δ/D values, one relatively large vortex pair is periodically shed from the central part of each dimple, and two smaller vortex pairs oscillate periodically near the two spanwise edges of each dimple. Local Nusselt number ratio data for $\delta/D=0.1$ also show qualitative similarity to characteristics measured with deeper dimples (but with smaller quantitative variations). This is because the highest local values are present within the downstream portions of dimples, as well as near dimple spanwise and downstream edges for both situations.

Local Nusselt number ratios generally show slight decreases as *Tu* increases within the downstream portions of the dimples, and on the flat surfaces just downstream of the dimples, but in most cases, variations with increasing *Tu* are relatively small. In each case, local and spatially averaged Nusselt number ratios are thus either approximately constant as *Tu* increases from 0.033 to 0.107, or decrease slightly at a particular location as *Tu* increases from 0.033 to 0.107. The decreases (when present) due to slightly diminished transport capabilities of the vortices and secondary flows shed by the dimples. This is believed to be partially due to increased turbulent diffusion of vorticity, and diminished magnitudes of vortex secondary flows.

Acknowledgments

The work presented in this paper was conducted under the sponsorship of Pratt & Whitney-Canada Corp., Agreement 013800, PO 4500314218. Mr. Tim Blaskovich, and Dr. Toufik Djeridane were project monitors. Mr. Qiang Zhang is acknowledged for his efforts in measuring inlet turbulence intensity levels.

Nomenclature

D = dimple print diameter
Dh = channel hydraulic diameter
f = frequency
f = channel friction factor
f_o = baseline friction factor measured in a channel with smooth surfaces and no dimples
H = channel height
h = heat transfer coefficient based on flat projected surface area, $\dot{q}o''/(T_w-T_{mx})$
k = thermal conductivity
Nu = local Nusselt number, hD_h/k
Nu_o = baseline Nusselt number in a channel with smooth surfaces and no dimples
p = streamwise spacing of adjacent dimple rows
P = local static pressure
P_o = local total pressure
P_a = ambient atmospheric pressure at test section inlet
Pr = molecular Prandtl number
PSD = power spectra distribution
$\dot{q}o''$ = surface heat flux based on flat projected surface area
Re_H = Reynolds number based on channel height, $H\overline{V}/\nu$
Re_{Dh} = Reynolds number based on channel hydraulic diameter, $Dh\overline{V}/\nu$
s = streamwise spacing of every other dimple row
t = time
t^* = non-dimensional time, $t\overline{V}/H$
T = temperature
Tu = longitudinal turbulence intensity at inlet of channel test section, $(\overline{u'^2})^{1/2}/\overline{V}$
u = local streamwise instantaneous velocity
u_x = local time-averaged streamwise component of velocity
u_y = local time-averaged normal component of velocity
u_z = local time-averaged spanwise component of velocity
$\overline{V}$ = streamwise bulk velocity averaged over the channel cross-section
X = streamwise coordinate measured from test section inlet
Y = normal coordinate measured from test surface dimple horizon
Z = spanwise coordinate measured from test section center-line

Greek Symbols

ν = kinematic viscosity
δ = dimple depth

ρ_a = static density
ω_x = local time-averaged streamwise vorticity

Subscripts

mx = time-averaged, local mixed-mean value
w = local wall value

Superscripts

‘ = fluctuating component
– = spatially averaged value or time-averaged value
= = globally averaged value.

References

[1] Mahmood, G. I., Hill, M. L., Nelson, D. L., Ligrani, P. M., Moon, H.-K., and Glezer B., 2001, “Local Heat Transfer and Flow Structure On and Above a Dimpled Surface in a Channel,” ASME J. Turbomach., **123**, No. 1, pp. 115–123.

[2] Burgess, N. K., Oliveira, M. M., and Ligrani, P. M., 2003, “Nusselt Number Behavior on Deep Dimpled Surfaces Within a Channel,” ASME J. Heat Transfer, **125**, No. 1, pp. 11–18.

[3] Mahmood, G. I., and Ligrani, P. M., 2002, “Heat Transfer in a Dimpled Channel: Combined Influences of Aspect Ratio, Temperature Ratio, Reynolds Number, and Flow Structure,” Int. J. Heat Mass Transfer, **45**, No. 10, pp. 2011–2020.

[4] Mahmood, G. I., Sabbagh, M. Z., and Ligrani, P. M., 2001, “Heat Transfer in a Channel With Dimples and Protrusions on Opposite Walls,” AIAA J. Thermophys. Heat Transfer, **15**, No. 3, pp. 275–283.

[5] Ligrani, P. M., Mahmood, G. I., Harrison, J. L., Clayton, C. M., and Nelson, D. L., 2001, “Flow Structure and Local Nusselt Number Variations in a Channel With Dimples and Protrusions on Opposite Walls,” Int. J. Heat Mass Transfer, **44**, No. 23, pp. 4413–4425.

[6] Afanasyev, V. N., Chudnovsky, Y. P., Leontiev, A. I., and Roganov, P. S., 1993, “Turbulent Flow Friction and Heat Transfer Characteristics for Spherical Cavities on a Flat Plate,” Exp. Therm. Fluid Sci., **7**, pp. 1–8.

[7] Belen’kiy, M. Y., Gotovskiy, M. A., Lekakh, B. M., Fokin, B. S., and Dolgushin, K. S., 1994, “Heat Transfer Augmentation Using Surfaces Formed by a System of Spherical Cavities,” Heat Transfer Res., **25**, No. 2, pp. 196–203.

[8] Kesarev, V. S., and Kozlov, A. P., 1994, “Convective Heat Transfer in Turbulized Flow Past a Hemispherical Cavity,” Heat Transfer Res., **25**, No. 2, pp. 156–160.

[9] Terekhov, V. I., Kalinina, S. V., and Mshvidobadze, Y. M., 1995, “Flow Structure and Heat Transfer on a Surface With a Unit Hole Depression,” Russ. J. Eng. Thermophys., **5**, pp. 11–33.

[10] Schukin, A. V., Koslov, A. P., and Agachev, R. S., 1995, ‘study and Application of Hemispherical Cavities For Surface Heat Transfer Augmentation,” ASME Paper No. 95-GT-59, ASME 40th International Gas Turbine and Aeroengine Congress and Exposition, Houston, Texas.

[11] Gortyshov, Y. F., Popov, I. A., Amirkhanov, R. D., and Gulitsky, K. E., 1998, “studies of Hydrodynamics and Heat Exchange in Channels With Various Types of Intensifiers,” Proceedings of 11th International Heat Transfer Congress, 6, pp. 83–88.

[12] Chyu, M. K., Yu, Y., Ding H., Downs, J. P., and Soechting, F. O., 1997, “Concavity Enhanced Heat Transfer in an Internal Cooling Passage,” ASME Paper No. 97-GT-437, ASME 42nd International Gas Turbine and Aeroengine Congress and Exposition, Orlando, Florida.

[13] Lin, Y.-L., Shih, T. I.-P., and Chyu, M. K., 1999, “Computations of Flow and Heat Transfer in a Channel With Rows of Hemispherical Cavities,” ASME Paper No. 99-GT-263, ASME 44th International Gas Turbine and Aeroengine Congress and Exposition, Indianapolis, Indiana.

[14] Moon, H.-K., O’Connell, T., and Glezer, B., 1999, “Channel Height Effect on Heat Transfer and Friction in a Dimpled Passage,” ASME Paper No. 99-GT-163, ASME 44th International Gas Turbine and Aeroengine Congress and Exposition, Indianapolis, Indiana.

[15] Terekhov, V. I., and Kalinina, S. V., 2002, “Flow and Heat Transfer in a Single Spherical Cavity: State of the Problem and Unanswered Questions (Review),” Thermophysics and Aeromechanics, **9**, No. 4, pp. 475–496.

[16] Isaev, S. A., Leontiev, A. I., Kudryavtsev, N. A., and Pushnyi, I. A., 2003, “The Effect of Rearrangement of the Vortex Structure on Heat Transfer Under Conditions of Increasing Depth of a Spherical Dimple in the Wall of a Narrow Channel,” Teplofiz. Vys. Temp., **41**, No. 2, pp. 268–272.

[17] Ligrani, P. M., Harrison, J. L., Mahmood, G. I., and Hill, M. L., 2001, “Flow Structure Due to Dimple Depressions on a Channel Surface,” Phys. Fluids, **13**, No. 11, pp. 3442–3451.

[18] Ligrani, P. M., Singer, B. A., and Baun, L. R., 1989, “Miniature Five-Hole Pressure Probe for Measurement of Three Mean Velocity Components in Low Speed Flow,” J. Phys. E, **22**, No. 10, pp. 868–876.

[19] Ligrani, P. M., Singer, B. A., and Baun, L. R., 1989, “Spatial Resolution and Downwash Velocity Corrections for Multiple-Hole Pressure Probes in Complex Flows,” Exp. Fluids, **7**, No. 6, pp. 424–426.

[20] Ligrani, P. M., 2000, “Flow Visualization and Flow Tracking as Applied to Turbine Components in Gas Turbine Engines,” Meas. Sci. Technol., **11**, No. 7, pp. 992–1006.

[21] Kline, S. J. and McClintock, F. A., 1953, “Describing Uncertainties in Single Sample Experiments,” Mech. Eng. (Am. Soc. Mech. Eng.), **75**, pp. 3–8.

[22] Moffat, R. J., 1988, “Describing the Uncertainties in Experimental Results,” Exp. Therm. Fluid Sci., **1**, No. 1, pp. 3–17.

[23] Lienhard, J. H., 1987, *A Heat Transfer Textbook*, 2nd ed., Prentice-Hall Inc., Englewood Cliffs, New Jersey, pp. 338–343.

[24] Ligrani, P. M., Oliveira, M. M., and Blaskovich, T., 2003, “Comparison of Heat Transfer Augmentation Techniques,” AIAA J., **41**, No. 3, pp. 337–362.

Semiu A. Gbadebo
Whittle Laboratory,
University of Cambridge,
Madingley Road,
Cambridge CB3 0DY, UK

Nicholas A. Cumpsty
Rolls-Royce Plc,
Derby, UK

Tom P. Hynes
Whittle Laboratory,
University of Cambridge,
Madingley Road,
Cambridge CB3 0DY, UK

Three-Dimensional Separations in Axial Compressors

Flow separations in the corner regions of blade passages are common. The separations are three dimensional and have quite different properties from the two-dimensional separations that are considered in elementary courses of fluid mechanics. In particular, the consequences for the flow may be less severe than the two-dimensional separation. This paper describes the nature of three-dimensional (3D) separation and addresses the way in which topological rules, based on a linear treatment of the Navier-Stokes equations, can predict properties of the limiting streamlines, including the singularities which form. The paper shows measurements of the flow field in a linear cascade of compressor blades and compares these to the results of 3D computational fluid dynamics (CFD). For corners without tip clearance, the presence of three-dimensional separation appears to be universal, and the challenge for the designer is to limit the loss and blockage produced. The CFD appears capable of predicting this.
[DOI: 10.1115/1.1811093]

Introduction

Regions of three-dimensional (3D) separations have been identified as an inherent flow feature of the corner formed by the suction surface and endwall of axial compressors. Also referred to as corner separations, these separations contribute greatly to passage blockage, which effectively places a limit on the loading and static pressure rise achievable by the compressor. In addition, the subsequent mixing of the flow in the separated region with the main passage flow may lead to a considerable total pressure loss and a consequent reduction in compressor efficiency. A number of studies have discussed the importance of three-dimensional flows in axial compressors and pumps where 3D separations were clearly evident on the suction surface and/or endwall corner of both stator as well as rotor blades. Among these are Dring et al. [1], Joslyn and Dring [2], Dong et al. [3], McDougall [4], Schultz et al. [5], Zierke and Straka [6], Place [7], Bolger [8] and Friedrichs et al. [9].

Although the deleterious consequences of 3D separations have been identified by these and other authors, effective management and control of these effects has been very difficult to achieve. This is perhaps primarily because the nature and characteristics of 3D separations in turbomachines are not clearly understood, nor are the mechanisms and factors that influence their growth and ultimate size.

Part of the difficulty in coming to grips with the flow in 3D separated regions concerns the apparent complexity of the flow, as demonstrated by surface flow visualization techniques. Because of the relative ease with which these surface flow patterns are attained, they remain, by far, the most comprehensive body of available data and a tempting tool of choice for exploring this problem. Figure 1 shows experimental and computed surface streamlines in the separated region of the hub/endwall region for a cascade of modern prescribed velocity distribution (PVD) stators near its design incidence. As we shall show later in this paper, this is a relatively simple case—as incidence is increased for this cascade and the separation grows in size, the complexity of these patterns will increase considerably. One of the aims of this paper is to discuss how these patterns are constrained by various general theorems of topology.

Description of 3D Separations

There is clear evidence that separations in three-dimensional flows do not behave in the simple way that is associated with those in two-dimensional (2D) or axisymmetric cases, where separation from the surface is identified at the point where the shear stress vanishes and by the inception of reversed flow. Three-dimensional separation can occur with no reverse flow and nonzero friction [10]. As also pointed out by Délery [11], there are a wide variety of flows where the phenomenon of 3D separation appears nearly independent of Reynolds number (Re), which is in stark contrast to two-dimensional separations. Three-dimensional separated flows observed over delta wings, downstream of the base of a missile, in front of blunt obstacles, and over bodies of revolution are virtually identical to those observed over the same objects in small water tunnels of relatively low velocity. Typical examples are the water tunnel visualizations by Werle [12–15].

While the velocity is zero at the surface itself, it is not so at points only a small height h above the surface. ‘‘Surface streamlines’’ are the streamlines or direction of fluid particles infinitesimally close to the surface (i.e., as h tends to zero). These also lie very closely along the surface shear stress or skin-friction lines and can be expressed [10] as

$$\frac{dy}{dx} = \lim_{h\to 0}\frac{v}{u} = \left(\frac{\partial v/\partial z}{\partial u/\partial z}\right)_{h=0} = \left(\frac{\tau_y}{\tau_x}\right)_{h=0} \tag{1}$$

where z is normal to the surface, and u and v are the components of the velocity along the tangential (x and y) directions, respectively.

The behavior of flow over a surface associated with separation usually results in a pattern of lines emanating from critical points where the shear stress vectors (τ_x and τ_y) are identically zero. Various authors (notably Legendre [16–18], Lighthill [19], Perry and Fairlie [20], Tobak and Peake [21], Perry and Chong [22] and Dallmann [23], have built on and applied the ideas of Poincaré [24] on singular points of differential equations to the Navier-Stokes and continuity equations in the vicinity of critical points. Because of the close proximity to the surface, velocity vectors can be approximated as a linear function of space coordinates with constant coefficients (which are function of time in case of unsteady flows). In a plane that corresponds to the surface, the coefficients usually form a 2×2 Jacobian matrix. Critical points can be classified by the pattern of surface streamlines observed in their vicinity, which are determined by the trace (p) and determinant (q) of the matrix. These can be written as

---

Contributed by the International Gas Turbine Institute (IGTI) of THE AMERICAN SOCIETY OF MECHANICAL ENGINEERS for publication in the ASME JOURNAL OF TURBOMACHINERY. Paper presented at the International Gas Turbine and Aeroengine Congress and Exhibition, Vienna, Austria, June 13–17, 2004, Paper No. 2004-GT-53617. Manuscript received by IGTI, October 1, 2003; final revision, March 1, 2004. IGTI Review Chair: A. J. Strazisar.

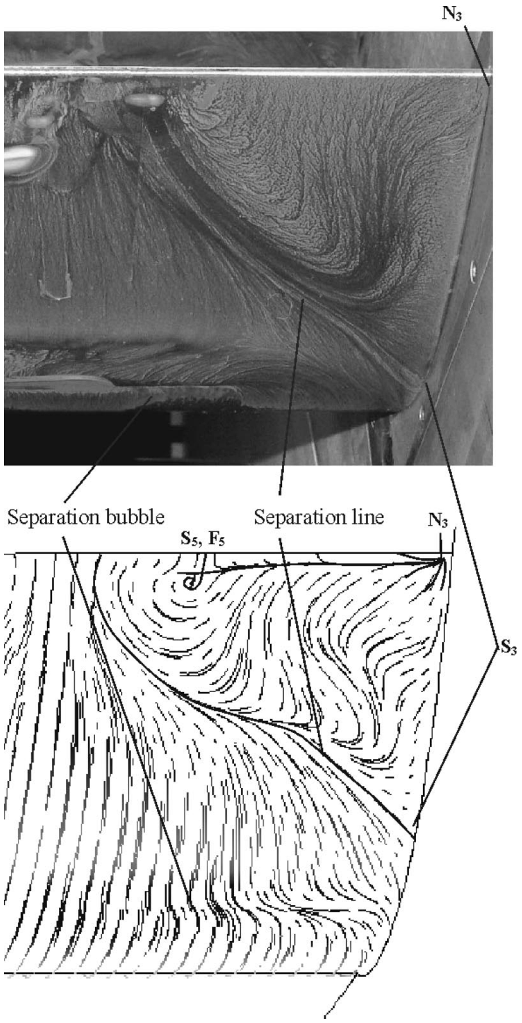

Fig. 1 Suction surface flow pattern and the numerical limiting streamlines for cascade 2, $i=0.0$ deg (S=Saddle; N=Node; F=Focus)

$$p=\frac{\partial u}{\partial x}+\frac{\partial v}{\partial y} \tag{2}$$

$$q=\frac{\partial u}{\partial x}\frac{\partial v}{\partial y}-\frac{\partial u}{\partial y}\frac{\partial v}{\partial x} \tag{3}$$

The complete range of critical points that can, in theory, occur, as described by Dallmann [23], are shown, in Fig 2.

Tobak and Peake [21] and Perry and Chong [22] have shown that all critical points that occur on the axes of Fig. 2 (which includes 2D separations) or on the parabola shown, are *topologically unstable*. They argue that slight changes to conditions or geometry will result in their disappearance or evolution into one of the remaining stable types. The stable critical points are:

- Saddle point: a point through which two particular (critical) lines pass, each acting as barriers in the field of limiting streamlines or skin-friction lines, making one set of streamlines inaccessible to the adjacent set
- Regular node: a point common to an infinite number of limiting streamlines
- Spiral node or focus: a point around which an infinite number of limiting streamlines spiral, which, for example, can denote a vortex lifting off the surface.

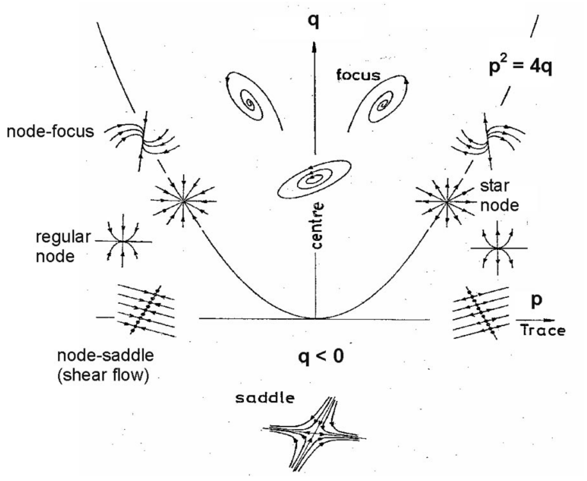

Fig. 2 Classification of critical points (from [23])

They further show that a pattern having streamlines that join two saddle points is topologically unstable, as are coincident critical points unless they occur at sharp corners between surfaces.

Following Hunt et al. [25] the above definitions can be interpreted in terms of separations and attachments. The two critical lines of a saddle point act as separation and attachment lines, respectively; the adjacent limiting streamlines converging along the former and diverging away from the latter. A nodal point is a separation point where all the limiting streamlines converge to it, and it is a point of attachment where the limiting streamlines issue from it. A focus of separation is observed where the adjacent streamlines spiral into it, while it is a focus of attachment, where the limiting streamlines around it spiral outward.

Critical points obey certain rules that are directly related to the topological class of object on which they exist. The most important of these, Flegg [26], also known as the *index rule*, places a condition on the number of each type of critical point that can occur on surfaces of a given type. If all regular nodes, foci, and degenerate critical points, such as centers and star nodes (see Fig. 2), are counted as nodes and each is assigned an index of 1, while a saddle point is assigned an index of -1, then

$$\sum \text{indices} = \sum N - \sum S \tag{4}$$

where N and S are the number of nodes and saddles, respectively. Then it follows that

$$\sum \text{indices} = 2-2g \tag{5}$$

where the genus g is a property of the topological class of the surface. It can be shown [27] that a single blade passage with no tip gaps has $g=1$, while a passage involving a tip gap has $g=0$ such that the index rule gives

$$\sum N - \sum S = 0 \quad (\text{no tip gap}) \tag{6}$$

$$\sum N - \sum S = 2 \quad (\text{with tip gap}) \tag{7}$$

There have been a number of postulates about which arrangements and appearance of critical points will be associated with separation lines. Eichelbrenner and Oudart [28] suggest that a separation line be considered as an "envelope" of the limiting streamlines on the surface. Maskell [29] also hypothesized that it is possible to have a vortex layer or "vortex sheet" separation, which involves ordinary nonsingular points. In the study of 3D separations described here for blade passages with no tip gap, the separation lines encountered have been largely those of the type described by Lighthill [19]. The separation line is itself a surface streamline to which other surface streamlines are asymptotes rather than being an envelope to which they join tangentially. Lighthill was also of the opinion that a separation line must originate and terminate at critical points and that it will trace a smooth curve on the wall, which forms the base of a stream surface whose streamlines have all entered the fluid through a saddle point. The term ''streamline'' is used here to refer to the computed patterns and the oil traces. ''Streakline'' is more generally accurate, but for steady flow, these are equivalent and the more familiar term is used.

Sizing of 3D Separations in Axial Turbomachines

The region of 3D separation is usually bounded on the suction surface and the endwalls by their respective separation lines. Hence, the spread of the region on the suction surface can be quantified in terms of the spanwise extent of the separation line from the endwall (expressed nondimensionally as a fraction of chord) and the origin of the separation lines near the suction surface endwall corner (also expressed as a fraction of chord from the leading edge). These are relatively easy to assess from the pattern of surface streamlines from either experimental or numerical flow visualization. More problematical is to quantify how thick the separated layer is, as measured from the suction surface, at the trailing edge. As suggested by Gbadebo [27], the thickness of the 3D separated layer can simply be denoted using the concept of *relative* displacement thickness. At any radial location, the relative displacement thickness is defined as the displacement thickness minus the midspan displacement thickness. Since flow usually does not separate at the midspan, except during complete blade stall, the net or relative displacement thickness at those radial locations away from midspan toward the endwall will be equivalent to the contribution from the separated boundary layer. Thus the average thickness of the separated layer between, say the hub and midspan, normalized by the blade chord, can be given as

$$\delta^*_{\mathrm{eff}}=\frac{\dfrac{2}{R}\displaystyle\int_{r_{\mathrm{hub}}}^{r_{\mathrm{mid}}}[\delta^*(r)-\delta^*_{\mathrm{midspan}}]dr}{c} \tag{8}$$

where displacement thickness is given as

$$\delta^*(r)=\int_0^{\delta}\left[1-\frac{\rho v(r,s)}{\rho_{fs}V_{fs}}\right]ds \tag{9}$$

There is usually no defined edge of the suction surface boundary layer until about 5% span from the endwall because of the coupling between the suction surface and endwall boundary layer at the corner. Where the free stream velocity V_{fs} is not well defined, it can be approximated by the local midpitch velocity.

For the compressor cascades used in this study, the nominal flow direction at the trailing edge is axial. It is, therefore, convenient to use the axial velocity for the above expressions. This will also give a realistic estimate of the layer's thickness because reverse flow (negative axial velocities), which is always a characteristic feature of the separated region, will be accounted for.

Cascade Facilites and Experimental Procedure

An experimental investigation was carried out on two sets of low-speed compressor cascades. The first, referred to as cascade 1, consists of five blades with a standard NACA65 thickness distribution on a circular arc camber line. The second cascade, referred to as cascade 2, consists of five modern prescribed velocity distribution (PVD) blades. On this was more detailed measurement, and analysis was performed. The geometric, flow, and inlet boundary layer integral parameters for both cascades are summarized in Table 1. Cascade 1 was operated only at zero incidence. Although cascade 2 was operated at −7.0 deg and 0.0 deg incidence, experimental results for only zero incidence are presented. The inlet flow Reynolds number based on chord for cascade 1 is about twice that for cascade 2. The inlet Mach number for both cascades was approximately 0.07, and their inlet free stream turbulence intensity measured with a single hotwire probe was found to be about 1.5% rms. Surface mounted tufts were used for flow visualization on cascade 1, while oil and dye flow visualization was utilized for cascade 2.

Table 1 Cascades geometry and inlet boundary layer parameters

Geometric parameters		
	Cascade1	Cascade2
Profile	NACA-65	PVD
Chord (m)	0.3	0.1515
s/c	0.6	0.926
h/c	1.45	1.32
t/c	0.05	0.1
α_1	45.0 deg	41.0 deg
Camber angle	45.5 deg	42.0 deg
Stagger angle	22.25 deg	15.0 deg
Aerodynamic parameters		
Incidence	0.0 deg	0.0 deg
Re (inlet)	4.8×10^5	2.3×10^5
2D DF	0.47	0.49
de Haller No.	0.75	0.8
Inlet boundary layer parameters		
δ (mm)	11.5	5.23
δ^* (mm)	1.497	0.507
θ (mm)	1.21	0.29
H	1.24	1.75

Downstream area traverses for both cascades were carried out at about 50% axial chord from the trailing edge. A Kiel probe, positioned in the nominal flow direction (axial), was used for cascade 1 so that only total pressure loss was measured. The area traverse for cascade 2 was performed using a three-hole probe; the uncertainty in the yaw angle measurement was estimated to be ±0.6 deg, uncertainty of total pressure was ±1.0% of dynamic head, and the uncertainty in the measurement of the dynamic head was calculated to be ±2.5%. A hot-wire area traverse was used to measure the radial variation of the relative displacement thickness at the trailing edge for cascade 2 and used for comparison with CFD predictions. The comparison is qualitative in the sense that, even though the hot-wire was positioned normal to the nominal (axial) direction, it is unable to distinguish reverse flow in the separated region. Nevertheless, the profile is believed to be adequate for comparison purposes.

Computational Procedure

The code employed is MULTIP, a fully three-dimensional Reynolds-Averaged Navier-Stokes solver of Denton [30]. The code uses a scheme that is second-order accurate in space and solutions can be obtained for flows from very low Mach number of about 0.1 to supersonic flows. The calculations were carried out using a control volume formulation on an ''H''-type mesh. Shear stress is modeled using a thin-shear approximation to the Navier-Stokes equation, and an eddy viscosity mixing length is used for turbulence modeling. The experimentally measured inlet profiles of stagnation pressure and absolute flow angles were used to define the inlet conditions, while the measured inlet and exit static pressures were used as a guide for fixing the pressure ratio.

Initial grid sensitivity tests showed that the grid size in the spanwise direction has the most influence on the solution, particularly the separated pattern of the limiting streamlines. Since separated flows are usually characterized by free shear layers as well as strong viscous effects, a highly refined mesh right from the

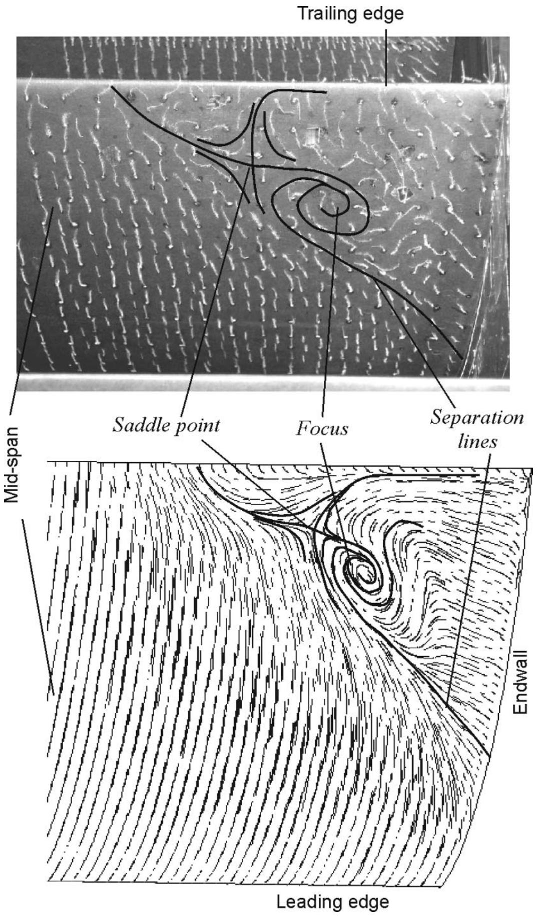

Fig. 3 Suction surface flow pattern and the numerical limiting streamlines for cascade 1, $i=0.0$ deg

adjoining surfaces of the suction surface and/or endwall corner toward the free stream was found necessary to achieve a realistic prediction of the size of the separated region. About 11 grid points were used to resolve the boundary layer on the blade surfaces while 17 grid points were used for the boundary layer on the Endwall. Together these were found adequate to resolve the three-dimensional boundary layer along the corner. This level of grid refinement ensures the adequacy of the thin shear layer approximation for viscosity in the code, which assumes the first grid point from the surface to be at a y^+ of 11.0. The grid points in the pitchwise, streamwise and spanwise directions were $49\times159\times99$. The solutions converged smoothly to an average residual error in the midspan meridional velocity of between 0.02 to 0.08%, depending on the magnitude of separations, at an average of about 14,000 time steps.

Results and Discussion

Suction Surface Limiting Streamline Pattern. Tuft visualization on the suction surface and the computed streamlines for cascade 1 are shown in Fig. 3. The agreement can be seen to be good. A separation line (marked by convergence of neighboring streamlines) can be seen originating at about 35% chord from the leading edge at the endwall. It stretches diagonally and winds into a focus (vortex). The same line passes through a saddle point adjacent to the focus and extends to a distance along the span equal to about 60% of chord length from the endwall at the trailing edge.

For cascade 2, the oil-streak pattern of the separated region on the suction surface and the corresponding numerical limiting streamlines are presented in Fig. 1. Once again these figures show excellent agreement between experiment and computation. The suction surface separation line originates at about 37% chord from the leading edge at the suction surface/endwall corner and terminates at the trailing edge at a distance also equivalent to about 60% of chord length from the endwall. On the suction surface of the airfoil, at about 20% chord from the leading edge, the formation of a separation bubble, as a result of laminar-turbulent boundary layer transition, is clearly visible. This is captured numerically, following the specification in the calculation of the transition location where it is indicated by the measured suction-surface static pressure.

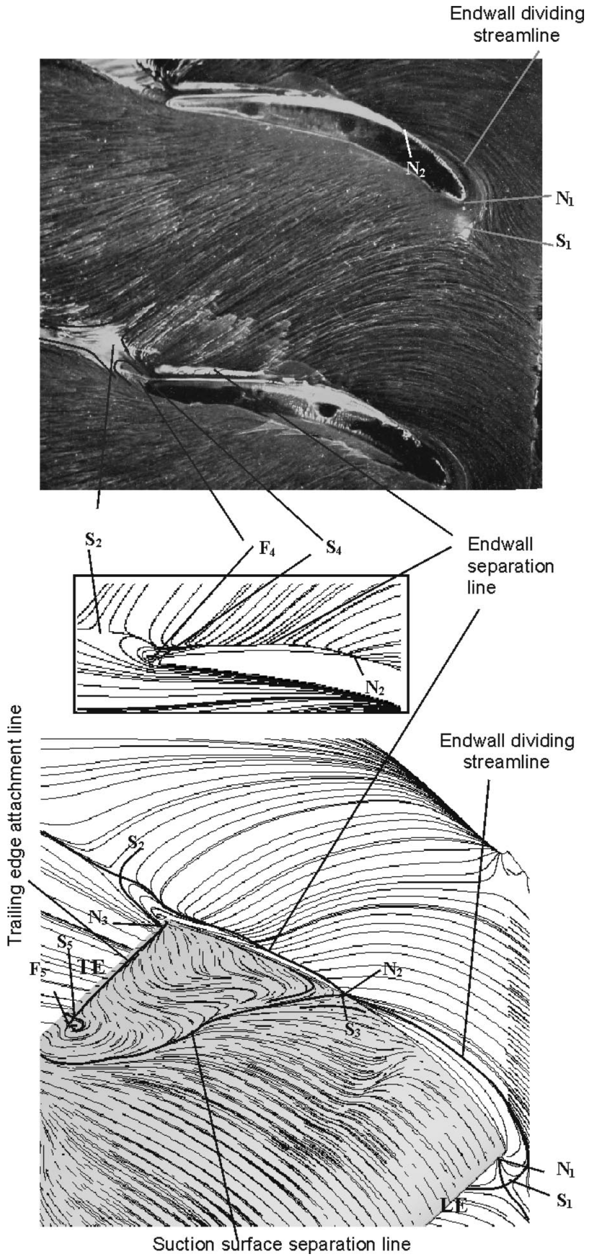

Fig. 4 Endwall oil-streak pattern and the numerical limiting streamlines for cascade 2, $i=0.0$ deg (S=Saddle; N=Node; F=Focus)

Critical Points in the Surface Flow Pattern and Application of the Index Rule. Using cascade 2 as an example, the endwall oil streak lines and the numerical streamlines shown in Fig. 4 can be seen to reveal the leading-edge saddle point of separation and the corresponding nodal point of attachment labeled (N_1, S_1).

Also observable on the endwall corner is the point at which the suction side leg of the dividing streamline (which forms the base of the horse-shoe vortex) interacts with the suction surface. This can be seen to be the common point from which the suction surface and the endwall separation lines originate. Close inspection of the endwall/suction surface corner of Fig. 4 suggests that this point takes the form of a multiple (node-saddle) critical point [a node (N_2) on the endwall and a saddle point (S_3) on the suction surface]. As mentioned earlier, a multiple node-saddle critical point like this is topologically unstable unless it remains in the corner between surfaces. On the endwall, the nodal point arm of the critical point links up with the trailing-edge saddle point to form a pair (N_2,S_2). On the suction surface, the saddle point arm pairs up with the nodal point of attachment at the trailing edge corner, i.e., (S_3,N_3). On the endwall, at the trailing-edge corner, is a less obvious pair of saddle and focal points of attachment (S_4,F_4). Lastly, a saddle-focus pair (S_5,F_5) can be seen on the suction surface at a distance of about 55% chord from the endwall at the trailing edge. The nodal point of attachment N_3 is the origin of the attachment line, which acts as one of the critical lines of saddle point S_5.

By applying the topological rule (recall that foci count as nodes), it can be seen that an equal number of nodes and saddles exist within the blade passage. In other words,

$$\sum N - \sum S = 5 - 5 = 0 \tag{10}$$

This conforms with the finding of Gbadebo [27] (Eq. (6)) that the flow in the single-blade passage is topologically equivalent to that on the surface of a single torus.

Formation of 3D Separations. Following the observation of the formation of critical points in Fig. 4, it is clear that the leading-edge horseshoe vortex and its associated dividing streamlines that emanate from the leading-edge stagnation (saddle) point, and which form the base of the vortex system, play a major role in the mechanism of 3D separation. The suction-side leg of the horseshoe vortex experiences the combined effect of the streamwise and circumferential pressure gradients. Since it originates from a zero wall-shear-stress point, its shear-stress relative to those of the other skin-friction lines presumably will be at a minimum level. The influence of the adverse streamwise pressure gradient on this dividing streamline makes its shear stress again drop to zero on a critical point that forms when it reaches the suction surface and/or endwall corner. The node-saddle critical point (N_2 and S_3), which occurs as a node on the endwall and as a saddle point on the suction surface, marks the origin of 3D separation and is characterized by the emergence of separation lines on both the suction surface and the endwall.

Just downstream of the nodal point arm (N_2) on the endwall, the limiting streamlines along the corner can, with close inspection, be seen reversing direction as they approach the suction surface, presumably because of high static pressure that is building up along the corner. The limiting streamlines then converge along the separation line, which appears as an envelope of the limiting streamlines. This can also be observed in the endwall oil-streak pattern in Fig. 4. Because this node-saddle critical point occurs as a saddle point on the suction-surface part of the corner, the suction-surface separation line appears to form an asymptote of the neighboring streamlines, limiting streamlines near the saddle point. This can be seen in the oil-flow pattern and numerical streamlines of Fig. 1, as well as Fig. 4. The trailing-edge saddle point S_2, on the endwall, acts as a divide between the limiting streamlines undergoing flow reversal (under greater influence of the adverse pressure gradient) on the suction-surface corner and those proceeding normally downstream.

The above observation appears to agree with Lighthill's [19] criterion for the occurrence of 3D separation, which implies that a separation line should originate and terminate at critical points. From Fig. 4, the separation line on the endwall originates from the nodal point N_2 and terminates downstream via saddle point S_2. The suction-surface separation line also originates at the corner saddle point S_3 and extends to the trailing edge, near the midspan, where it terminates, but without encountering any critical point. However, the separation line on the suction surface of cascade 1 also emanates from a critical point, as shown in Gbadebo [27], but as Fig. 3 shows, it embraces the focal point of separation (i.e., a spiral node) and then continues its journey to the trailing edge via the saddle point.

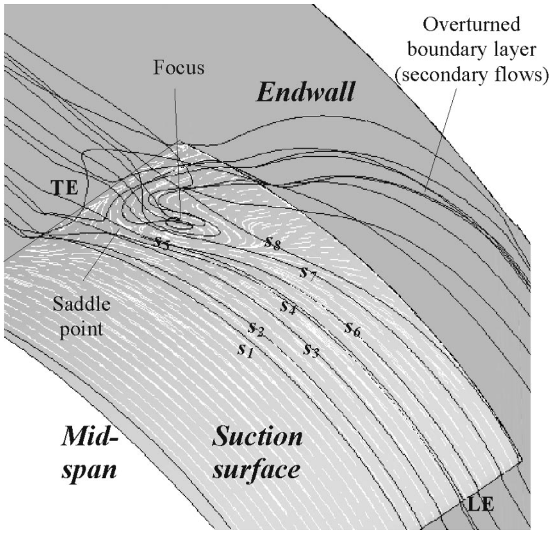

Fig. 5 Streamlines in the outer separated region of cascade 1, $i=0.0$ deg (here $s=$streamline number)

Flow Structure in the Outer Separated Region. The limiting streamlines described above are more or less the footprint of a complex fluid motion in the outer field within the 3D separated region. The strong agreement between the experimentally observed surface flow patterns and calculated streamlines, therefore, promotes confidence for further numerical visualization to be carried out in order to understand the flow structure in the separated region away from the surfaces.

Some streamlines in the outer separated region are plotted for cascade 1 in Fig. 5. This shows the endwall boundary layer, which turns more sharply toward the suction surface and interacts with the suction surface boundary layer in the separated region. The figure also illustrates how the flow lifts off via the focus on the suction surface, which forms the base of a 3D focus of separation. Downstream running streamlines from within the suction surface boundary layer, such as streamlines s_5 and s_7, as labeled in the figure, can also be seen to lift off into the main flow after encountering the saddle point on the surface.

It should be pointed out that the calculations are steady, so any unsteady effect on the flow field is suppressed. In this respect, there is no guarantee that the flow pattern calculated represents either the time-mean or the instantaneous flow actually occurring.

As shown in Fig. 6, it is evident that the 3D separated region in cascade 2 is also filled with fluid from both the separated suction surface boundary layer and the endwall boundary layer. Separation from the suction surface occurs when the endwall boundary layer streamlines, which are driven toward the suction surface by the circumferential pressure gradient, reverse direction because of the adverse streamwise pressure gradient and then encounter the streamlines on the suction-surface boundary layer coming from upstream. This process can be seen to cause the interaction and convergence of streamlines, such as s_8 and s_9, which then lift off the surface along the separation line. As shown in the figure, some of the overturned endwall boundary layer streamlines impinge on the suction surface along the trailing-edge attachment line, and the

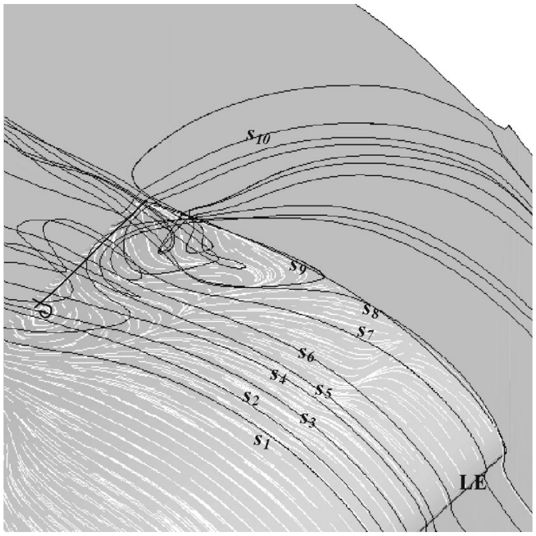

Fig. 6 Streamlines in the outer separated region of cascade 2, $i=0.0$ deg (here s = streamline number)

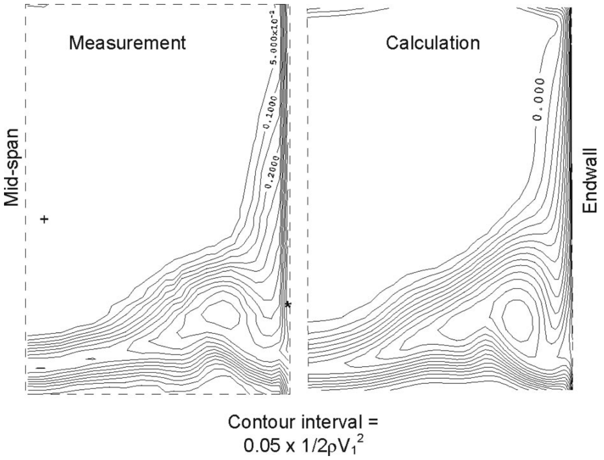

Fig. 8 Comparison of measured and calculated contours of exit total pressure loss for cascade 2, $i=0.0$ deg

weaker ones can even be seen meeting the surface and reversing direction well before the trailing edge because of the combined effects of the streamwise and circumferential pressure gradients. Particularly noticeable are the streamlines, which roll into a vortex after interacting with the suction surface.

Thickness of the 3D Separated Layer. The hot-wire measurement and the numerical computation of the spanwise variation of relative displacement thickness (i.e., the extra thickness of the separated layer over the midspan value) at the trailing edge of cascade 2 are compared in Fig. 7. The average thickness of the separated layer (δ^*_{eff}) from the measurement is about 4% chord while the CFD predicts it to be about 6% chord. As remarked before, this difference is thought to be because the hot wire is unable to detect the reverse flow associated with the separated region, hence, under estimating the thickness. However, both curves show similar trends and reasonably good qualitative agreement.

Cascade Performance. The surprisingly good agreement between the measured and predicted surface flow patterns for both cascades is matched by the measured and calculated total pressure loss contours. As shown in Fig. 8 for cascade 2, the measured and predicted maximum loss at the core are respectively 60% and 65% of inlet dynamic head and the loss core for both is centered around 15% chord from the endwall and about 17% chord from the suction surface. Figure 9 shows, for example, measured and predicted surface static pressure distribution at 10% span from the endwall, while the measured spanwise profiles of pitchwise averaged exit flow angles are compared with the CFD in Fig. 10. Both figures can be seen to show good agreement, which is attributable to the realistically predicted size of 3D separated region in the blade passage.

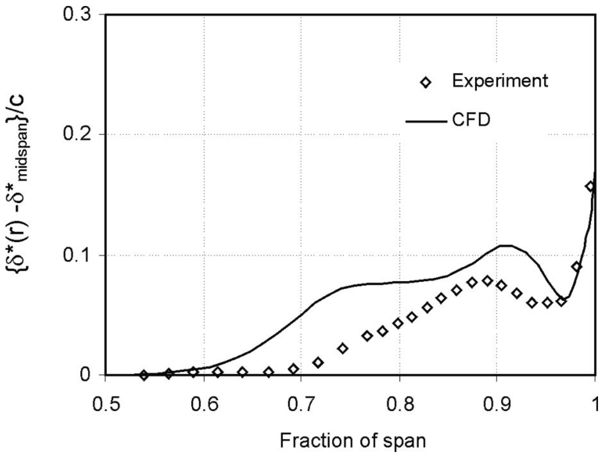

Fig. 7 Comparison of measured and calculated relative displacement thickness at the trailing edge of cascade 2, $i=0.0$ deg

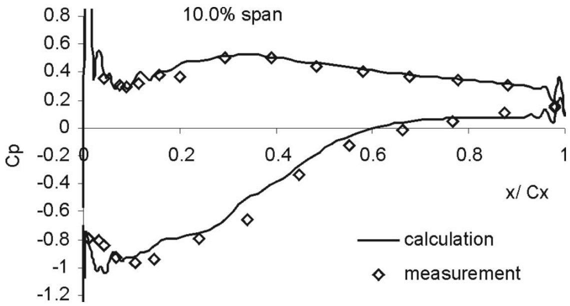

Fig. 9 Comparison of measured and calculated surface static pressure distribution for cascade 2, $i=0.0$ deg

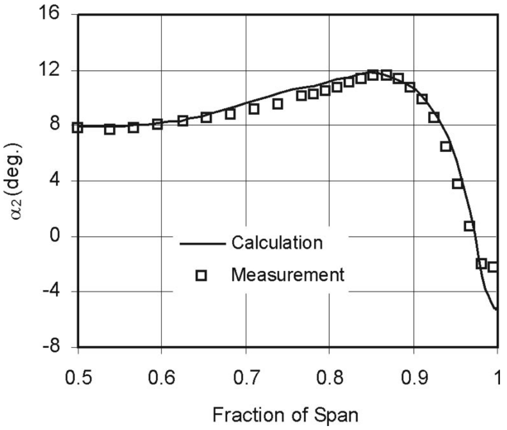

Fig. 10 Spanwise profile of pitchwise averaged exit flow angles for cascade 2, $i=0.0$ deg

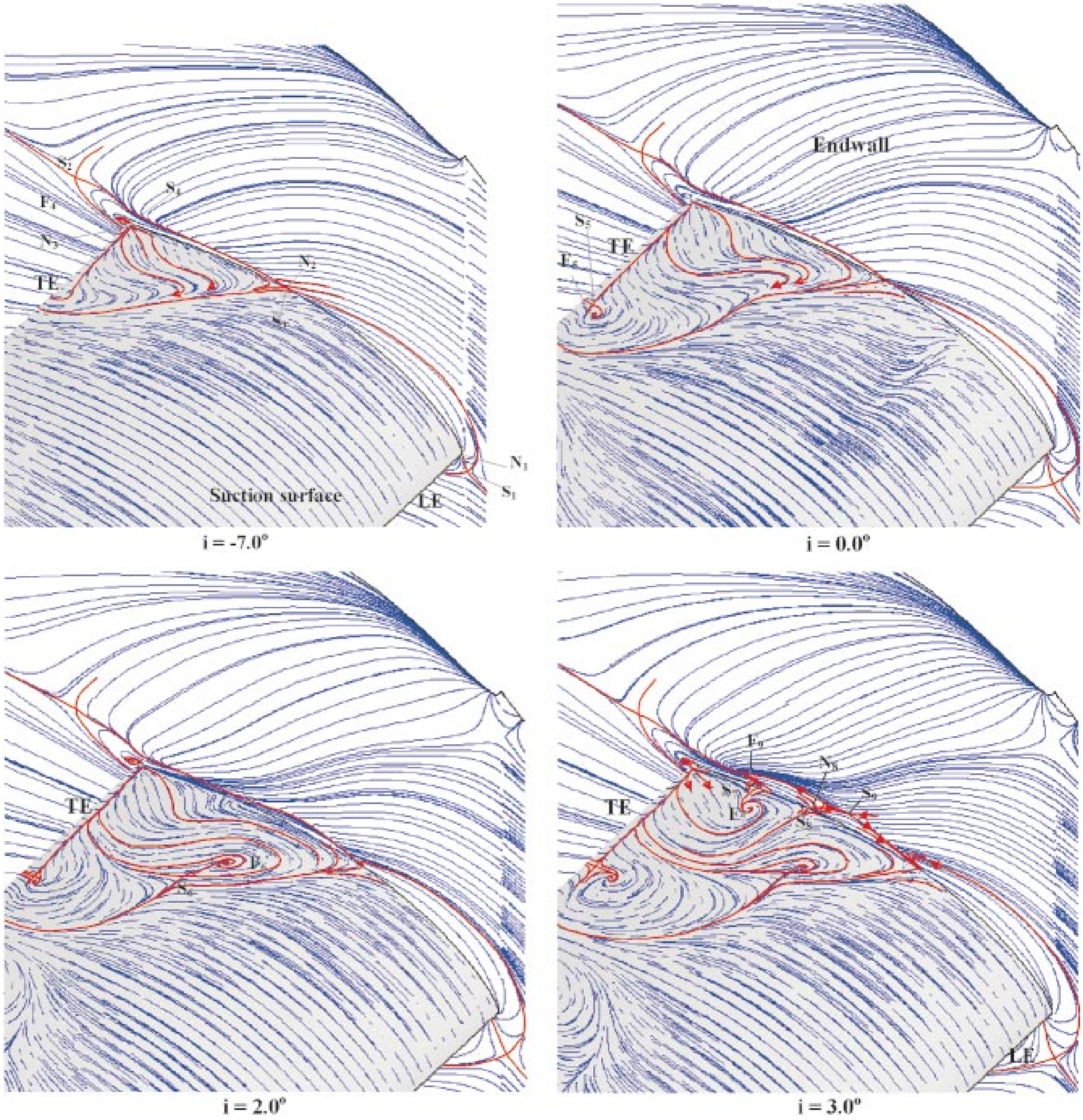

i = -7.0°

i = 0.0°

i = 2.0°

i = 3.0°

Fig. 11 Influence of incidence on the topology of separated surface flow pattern on cascade 2 (*S*=Saddle; *N*=Node; *F*=Focus)

Influence of Incidence on the Topological Structure and Size of 3D Separation. Figure 11 compares the suction surface and endwall limiting streamline patterns computed for incidence of −7.0, 0.0, +2.0, and +3.0 deg. As might be expected, an increase in the chordwise extent of the separated region from the leading-edge and the spanwise extent from the endwall is evident with increased incidence. Close inspection of the predicted surface singularities shows that apart from the four critical point pairs, similar to pairs (S_1, N_1) to (S_4, F_4) enumerated in Fig. 4, no apparent critical point occurs on the suction surface within the blade passage at −7.0 deg incidence. Although the flow patterns at other negative incidences are not shown, the pair (S_5, F_5) at the trailing edge does not appear until zero incidence. The increase in incidence to +2.0 deg leads to the emergence of the saddle-focus pair (S_6, F_6) on the suction surface, which lies at a distance of about 27% chord from the endwall and 70% chord from the leading edge. By just increasing the incidence to +3.0 deg, the 3D separated region grows very rapidly such that three additional pairs of critical points emerge as shown in the figure. The topological rule (of equal number of nodes and saddles) is again confirmed. At this +3.0 deg incidence, the endwall separation line can be seen to wrap into focus F_9, via saddle point S_9. Close inspection of saddle-node (S_8, N_8) shows that the two critical points occur at the same point on the endwall corner—a saddle point on the suction surface arm of the corner (S_8) and node (N_8) on the endwall. This, similar to multiple node-saddle point (N_2, S_3), from where the separation lines originate, is topologically unstable unless it remains on the corner. It may, for example,

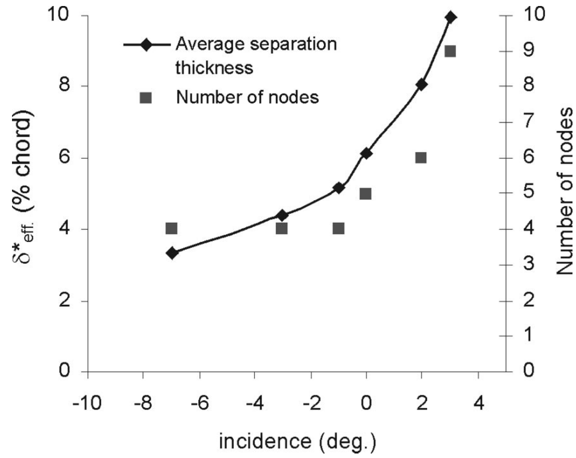

Fig. 12 Influence of incidence on the predicted number of nodes within half of the blade passage and average thickness of 3D separated layer at the trailing edge of cascade 2

bifurcate into a full saddle and a node on the endwall with further increase in incidence. The presence of the node (N_8) causes the endwall separation line to be pushed away from the suction surface, indicating more thickening of the separated layer close to the endwall. Taking a closer look at the suction surface, the main separation line can be seen to have advanced to midspan at the trailing edge, where it merges with the separation line growing from the other endwall. This marks the limit of the spanwise spread of 3D separation from the endwall at the trailing edge and any increase in incidence beyond $+3.0$ deg, for this cascade can only increase its perpendicular thickness from the suction surface.

The influence of incidence on the predicted average thickness of 3D separation from the suction surface at the trailing edge is shown in Fig. 12. Also plotted in the figure is the total number of nodes that formed within the half passage at each incidence tested. In the range of incidence between -7.0 deg and zero, the increase in the thickness is fairly modest. There is also no increase in the number of critical points until around zero incidence. From zero to positive incidence, the rapid increase in the spread of separation is accompanied by the emergence of more critical points on the suction surface and the endwall, as shown in Fig. 11, and is reflected in the rapid rise in the average separation thickness.

As a conjecture, which it was not possible to confirm, the increase in blockage is not smooth and continuous with increase in incidence (as implied by the line through the points), but possibly a series of steps that correspond to an increase in the number of nodes.

Conclusions

The following conclusions can be drawn from this study:

- For a blade joining an endwall with no clearance, the presence of corner separations appears to be universal. The assessment of a design as aerodynamically good or bad hinges on the thickness of the separated region measured normal to the solid surfaces; in other words, on the blockage of the flow area.
- The corner separations are three-dimensional, and the conditions for their formation are quite different from the more familiar separations in two dimensions. Whereas the formation of separation in two dimensions is easily explained and understood (though it may be difficult to predict accurately for turbulent boundary layers), the formation of three-dimensional separation is not easily explained or described. The rules associated with the size and growth of 3D separations are not those applicable to 2D boundary layers and 2D separation.
- Although 3D separations are formed by complicated processes, they may be predicted with current 3D Reynolds-Averaged Navier-Stokes codes fairly easily and with surprising accuracy. In particular the complex patterns of the limiting surface streamlines are well predicted because, in the limit as a wall is approached, the shape of these streamlines is the result of equilibrium between pressure stresses and laminar viscous stresses at the wall.
- The pattern of surface streamlines is constrained by topological rules governing the singular points, both for the type of singularity and the number. The experimental surface streamlines, as well as the computed surface streamlines, are compatible with these rules.
- It was found that as the incidence onto the blade was increased, the number of singular points increased and there was a good correlation for the cascade examined between the number of singularities and the thickness of the separated region. It is reasonable to assume that changing the blade design to give more turning and larger pressure rise, but keeping zero incidence, will also increase the number of critical points as well as blockage. For well-designed blade rows, the 3D separation may sometimes be small enough to ignore or overlook.
- The engineering requirement for corner separation analysis is primarily to predict the blockage, which requires the size or thickness of the separated flow to be found. With a realistic prediction of the size of 3D separation, the influence of any design change on the size of the separation and resulting blockage can be assessed with increased confidence.
- The size of the separated region normal to the surface is believed to be sensitive to the turbulent entrainment processes at the outer edge of the layer. Because of the limitations in turbulence modeling in turbomachinery, it must be recognized that Reynolds-Averaged Navier-Stokes methods will be found to be subject to error in determining the effective thickness and blockage of the 3D separation, even though the surface patterns are well predicted.
- The conclusions here are drawn from experiments and computations for compressor blades. Surface flow visualization on turbine blade rows shows complex three-dimensional patterns with evidence of similar singularities and separations. Because of the larger turning in turbine blades, the streamline patterns on the blade surfaces show even greater divergence from the normally assumed 2D flow pattern. Most emphatically, this paper does not purport to be the last word on the topic of three-dimensional flow features in compressor blade passages, but rather an early step in trying to understand more completely the processes that are taking place.

Acknowledgments

This work was supported by Rolls-Royce Plc, the Applied Research Program of the Ministry of Defense, the Department of Trade and Industry Aeronautic Research Program, and QinetiQ Ltd. The authors are very grateful for this and for their permission to publish. The authors would also like to thank Prof. J. D. Denton for the use of his CFD code. The opinions expressed here are those of the authors and not necessarily those of Rolls-Royce plc or any other organization.

Nomenclature

A = area
c = chord
C_p = pressure coefficient
F = focus
g = genus (see Eq. (5))
h = blade height (span), height from surface
H = shape factor$=\delta^*/\theta$
i = incidence
LE = leading edge
N = node
P = pressure
PS = pressure surface/side

r = radius, radial distance
Re = Reynolds number
rms = root mean square
s = pitchwise distance
S = saddle point
SS = suction surface/side
t = blade thickness
TE = trailing edge
u = velocity in x-direction
u^* = friction velocity $\sqrt{\tau_w/\rho}$
v = velocity in y-direction
x = axial distance
y = distance perpendicular to x in the same plane
y^+ = wall function (zu^*/ν)
Y_p = total pressure loss coefficient
z = distance perpendicular to the surface

Greek Symbols

α = absolute flow angle
β = blade (metal) angle
δ = boundary layer thickness
δ^* = displacement thickness
θ = momentum thickness
ρ = density
ν = kinematic viscosity
τ_w = wall shear stress
$\sum$ = summation

Subscripts

mid = midheight
e, eff = effective
fs = free stream
h = hub
s = static
1 = inlet
2 = exit

References

[1] Dring, R. P., Joslyn, H. D., and Hardin, L. W., 1982, ''An Investigation of Compressor Rotor Aerodynamics,'' ASME J. Turbomach., **104**(1), pp. 84–96.

[2] Joslyn, D. H., and Dring, R. P., 1985, ''Axial Compressor Stator Aerodynamics,'' ASME J. Heat Transfer, **107**, pp. 485–493.

[3] Dong, Y., Gallimore, S. J., and Hodson, H. P., 1987, ''Three-Dimensional Flows and Loss Reduction in Axial Compressors,'' ASME J. Turbomach., **109**(3), pp. 354–361.

[4] McDougall, N. M., 1988, ''Stall Inception in Axial Compressors,'' Ph.D. thesis, University of Cambridge, UK.

[5] Schultz, H. D., Gallus, H. E., and Lakshminarayana, B., 1990, ''Three-Dimensional Separated Flow Field in the Endwall Region of an Annular Compressor Cascade in the Presence of Rotor-Stator Interaction: Part 1-Quasi-Steady Flow Field and Comparison with Steady State Data,'' ASME J. Turbomach., **112**(4), pp. 669–678.

[6] Zierke, W. C., and Straka, W. A., 1996, ''Flow Visualization and the Three-Dimensional Flow in an Axial Flow Pump,'' J. Propulsion Power, **12**(2), pp. 250–259.

[7] Place, J. M. M., 1997, ''Three-Dimensional Flow in Axial Compressors,'' PhD thesis, University of Cambridge, UK.

[8] Bolger, J. J. 1999, ''Three-Dimensional Design of Compressor Blading,'' PhD thesis, University of Cambridge, UK.

[9] Friedrichs, J., Baumgarten, S., Kosyna, G., and Stark, U., 2000, ''Effect of Stator Design on Stato Boundary Layer Flow in a Highly Loaded Single-Stage Axial Flow Low-Speed Compressor,'' ASME Paper 2000-GT-616.

[10] Chang, P. K., 1970, *Separation of Flow*, Pergamon Press, New York, Interdisciplinary and Advanced Topics in Science and Engineering, Vol. 3.

[11] Délery, J. M., 2001, ''Robert Legendre and Henry Werle: Toward the Elucidation of Three-Dimensional Separation,'' Annu. Rev. Fluid Mech., **33**, pp. 129–154.

[12] Werlé H., 1974, *Le Tunnel Hydrodynamique au Service de la Recherche Aérospatiale*. ONERA Publ. **156**, p. 23.

[13] Werlé H., 1982, ''Flow Visualization Techniques for the Study of High Incidence Aerodynamics,'' AGARD-VKI Lect. Ser., pp. 121–124.

[14] Werlé H., 1983, ''Visualisation des Écoulements Tourbillonnaires Tridimensionnels,'' AGARD-FDP Conf. Aerodynamics of Vortical Type Flows in Three-Dimensions, Rotterdam, April 25–27, p. 25.

[15] Werlé H., 1986, ''Possibilités D'essai Offertes par les Tunnels Hydrodynamiques à Visualisation de l'Onera Dans les Domaines Aéronautiques et Navals,'' AGARD-CP 413, p. 26.

[16] Legendre, R., 1956, ''Separation de l'Ecoulement Laminaire Tridimensionnel,'' Recherche Aeronautique **54**, pp. 3–9.

[17] Legendre, R., 1965, ''Lignes de Courant d'un Écoulement Continu,'' La Rech. Aerosp., **105**, pp. 3–9.

[18] Legendre, R., 1966, ''Vortex Sheet Rolling up Along Leading Edges of Delta Wings,'' Prog. Aerosp. Sci., **7**, pp. 7–33.

[19] Lighthill, M. J., 1963, ''Attachment and Separation in Three-Dimensional Flows,'' *Laminar Boundary Layers*, L. Rosenhead, ed., Oxford Univ. Press, Oxford, UK, pp. 72–82.

[20] Perry, A. E., and Fairlie, B. D., 1974, ''Critical Points in Flow Patterns,'' Adv. Geophys., **18B**, pp. 299–315.

[21] Tobak, M., and Peake, D. J., 1982, ''Topology of Three-Dimensional Separated Flows,'' Annu. Rev. Fluid Mech., **14**, pp. 61–85.

[22] Perry, A. E., and Chong, M. S., 1987, ''A Description of Eddying Motions and Flow Patterns Using Critical Point Concepts,'' Annu. Rev. Fluid Mech., **19**, pp. 125–155.

[23] Dallmann, U., 1983, ''Topological Structures of Three-Dimensional Flow Separation,'' DFVLR, IB 221-82-A07, Gottingen, Germany.

[24] Poincaré, H., 1928, *Oeuvres de Henri Poincaré, Tome I*, Gauthier-Villars, Paris.

[25] Hunt, J. C. R., Abell, C. J., Peterka, J. A., and Woo, H., 1978, ''Kinematical Studies of Flow Around Free or Surface-Mounted Obstacles; Applying Topology to Flow Visualization,'' J. Fluid Mech., **86**, Part 1, pp. 179–200.

[26] Flegg, G. C., 1974, *From Geometry to Topology*, English Universities Press, London.

[27] Gbadebo, S. A., 2003, ''Three-Dimensional Separations in Compressors,'' Ph.D. thesis, University of Cambridge, UK.

[28] Eichelbrenner, E. A., and Oudart, A., 1955, ''Method de Calcul de la Couche Limite Tridimensionelle, Application a un Corps Fusele Incline sur le Vent,'' ONERA Publication 76, Chatillon.

[29] Maskell, E. C., 1955, ''Flow Separation in Three Dimensions,'' RAE Farnborough Report No. Aero. 2565, Nov.

[30] Denton, J. D., 1999, ''Multistage Turbomachinery Flow Calculation Program-MULTIP,'' Whittle Laboratory, University of Cambridge, UK.

Experimental Investigation of a Transonic Aspirated Compressor

Brian J. Schuler

Jack L. Kerrebrock

Ali Merchant

Gas Turbine Laboratory,
Department of Aeronautics and Astronautics,
Massachusetts Institute of Technology,
Cambridge, MA 02139

The experimental investigation of a transonic aspirated stage demonstrating the application of boundary layer aspiration to increase stage work is presented. The stage was designed to produce a pressure ratio of 1.6 at a tip speed of 750 ft/s resulting in a stage work coefficient of 0.88. The primary aspiration requirement for the stage is a bleed fraction 0.5% of the inlet mass flow on the rotor and stator suction surfaces. Additional aspiration totaling 2.8% was also used at shock impingement locations and other locations on the hub and casing walls. Detailed rotor and stator flow field measurements, which include time-accurate and ensemble-averaged data, are presented and compared to three-dimensional viscous computational analyses of the stage. The stage achieved a peak pressure ratio of 1.58 and through-flow efficiency of 90% at the design point. In addition, the stage demonstrated good performance with an aspiration lower than the design requirement, and a significant off-design flow range below that predicted by the computational analysis. [DOI: 10.1115/1.1860575]

1 Introduction

Compressor performance measured in terms of pressure ratio, efficiency, and operability are limited by the boundary layer behavior within the compressor stage. Blade surface and end-wall boundary layer growth limits the achievable stage pressure ratio at a given rotational speed. The thickness of the blade boundary layer also contributes significantly to the stage losses, stage work, and mass flow. Therefore, judicious removal of the boundary layer fluid within the compressor stage can result in well-attached boundary layers, which can yield both higher pressure ratio and higher efficiencies than those achieved by conventional stages. The distinguishing factors in applying suction on a compressor are the thermodynamic impact of removing the high entropy flow on subsequent blade rows [1], and the reduction in blockage development achieved by controlling the boundary layer growth on the blades and end walls. Both of these can have a beneficial impact on the efficiency.

Although a direct consequence of using aspiration is a higher pressure ratio due to the capability of increasing the blade loading, the higher loading can also be exploited to lower the blade speed while maintaining the same total pressure ratio. This alternative has several attractive advantages: (i) reduction or elimination of shock losses and corresponding shock-boundary layer interaction losses, (ii) large noise reduction, (iii) lighter components due to lower structural stresses, and (iv) increased flow range, because the blades have better off-design performance at subsonic conditions, as shown in the controlled diffusion cascade study of Hobbs and Weingold [2].

The experiment by Reijnan [3] on a transonic rotor showed an improvement in turning and pressure rise of the five blades that were modified to aspirate the flow. The experimental data also showed that the boundary layer control modified the stall behavior of the rotor. This paper presents experimental results on the first fully aspirated transonic compressor stage. The objective of this study is to demonstrate the aerodynamic performance, particularly, the blade performance and loading capability at design and off-design conditions, achieved with aspiration at low tip speeds.

The aspirated stage was designed using the quasi-3D MISES integral boundary layer solver [4] coupled with an axisymmetric solver described by Merchant [5]. The stage was designed to achieve a pressure ratio of 1.6 at tip speed of 750 ft/s. The low blade speed design resulted in a stage work coefficient of 0.88, a meanline flow coefficient of 1.13, and a peak diffusion factor of 0.57. The rotor has a free vortex design resulting in constant work over the span. A tip shroud was included in the design to eliminate tip clearance flows. The primary aspiration requirement on the rotor and stator blade surfaces is 0.5% of the inlet mass flow. Although additional aspiration of 2.8% is used at various locations on the hub and shroud, no attempt was made to optimize their location and quantity. Therefore, the total aspiration is not indicative of the optimal aspiration requirement for such a design.

The efficiencies presented in this paper are calculated from an appropriately averaged pressure ratio and temperature ratio of the through flow. Studies on the potential impact of aspirated flow on the system-level efficiency have been presented by Kerrebrock et al. [1], Kerrebrock [6], and McCabe [7].

The paper first discusses the design point CFD analyses performed using APNASA. This is followed by a description of the stage mechanical design and experimental facility. The experimental data is discussed in detail and compared to the CFD analysis, and the important results and implications of the work are enumerated. Aspiration and suction are used interchangeably in this paper.

2 3D Viscous CFD Analysis

The three-dimensional (3D) viscous analysis presented in this section was calculated using the APNASA code developed by Adamczyk [8,9]. The code solves the 3D Reynolds-averaged Navier-Stokes equations using a finite volume cell-centered scheme discretized on a structured hexahedral H-type mesh. The code uses a two-equation standard k-ε turbulence model of Launder and Spalding to estimate the eddy viscosity. A multistage model developed by Adamczyk [8,9] referred to as the average passage flow model is used to interact the blade rows at various stages in the flow path. The code was modified with a simple transpiration boundary condition on the blade and flow path surfaces to model suction. The suction mass flow is specified as a fraction of the stage inlet mass flow uniformly distributed over the suction slot. The model also incorporates a test for mass flow choking based on the slot area and flow conditions at the slot inlet.

The grid used for the present calculation has 255 axial, 51 circumferential, and 51 spanwise points. The design suction slot location was not matched exactly in the viscous calculation be-

---

Contributed by the International Gas Turbine Institute (IGTI) of THE AMERICAN SOCIETY OF MECHANICAL ENGINEERS for publication in the ASME JOURNAL OF TURBOMACHINERY. Paper presented at the International Gas Turbine and Aeroengine Congress and Exhibition, Amsterdam, The Netherlands, June 3–6, 2002; Paper No. 2002-GT-30370. Manuscript received by IGTI, December 1, 2001, final revision, March 1, 2003. Associate Editor: E. Benvenuti.

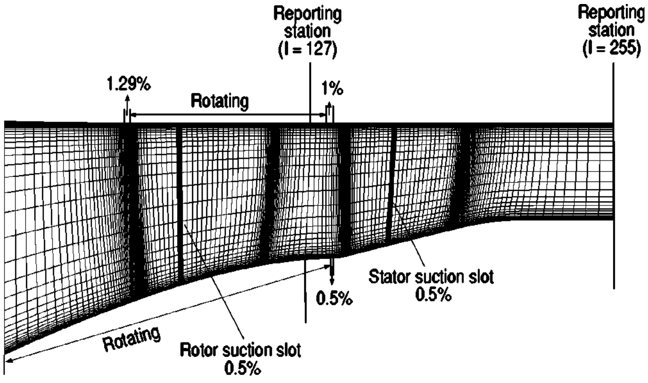

Fig. 1 3D viscous APNASA calculation grid suction configuration

cause the code requires the slot to be specified along a constant spanwise grid line. The slot axial location was matched in an average sense by selecting a grid line that resulted in the least deviation from the prescribed slot location. The blade geometry derived from the quasi-3D MISES design was altered by fitting leading-edge and trailing circles to meet grid-generation constraints. The diverging trailing-edge geometry of the blades was not completely resolved because the grid required pairs of suction and pressure side points with the same axial location.

The case presented below was calculated at an inlet mass flow of 63.9 lbs/s. This solution was found to have the best overall performance and was designated as the design point. The stage pressure ratio is 1.59 with an isentropic efficiency of 89.3%. A total suction of 3.79% was prescribed in the calculation. The distribution at various locations is shown in Fig. 1. The shock impingement suction on the hub and shroud were not included in the calculation.

Figure 2 shows contours of a Mach number in the rotor at 95% span. The contours show a peak Mach number of 1.22 followed by a weak shock. Aspiration is applied just downstream of the shock, and a thinning of the boundary layer is visible in the flow field contours. The flow remains well attached downstream of the slot and diffuses uniformly in the core flow to an exit Mach number of 0.66. The impact of the diverging trailing edge is seen in the Mach number decrease on the pressure side just upstream of the trailing edge.

Figure 3 shows contours of Mach number in the stator flow field at 10% span. The inlet Mach number is 1.09 with a peak Mach number of 1.27 just upstream of the passage shock. Aspiration is applied just downstream of the shock. The flow remains well attached through the subsonic diffusion part of the flow and diffuses to an average exit Mach number of 0.6. The impact of the diverging trailing edge is seen in the flow field contours near the trailing edge similar to the rotor. The flow is turned approximately 53 deg at this section.

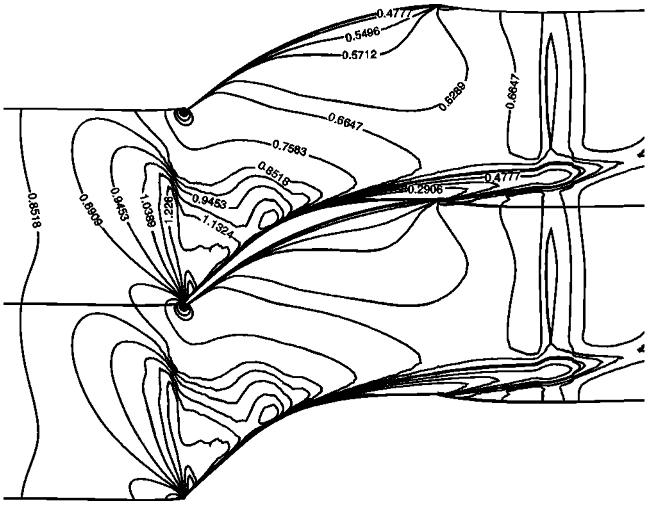

Fig. 2 Rotor 95% span Mach number contours

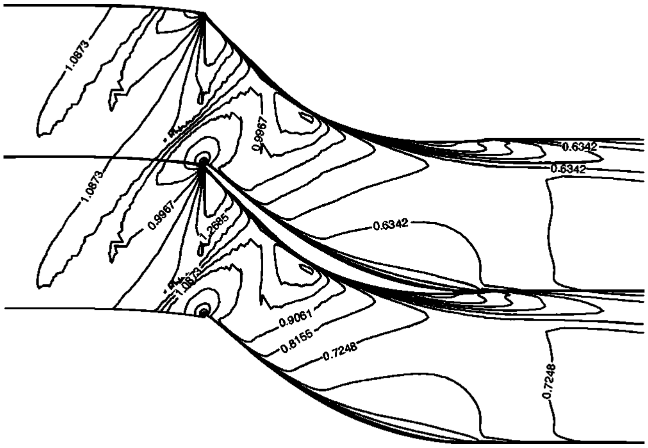

Fig. 3 Stator 10% span Mach number contours

3 Mechanical Design

The mechanical design of the stage and overall experiment are described in detail by Schuler [10]. The rotor and stator were machined as integral blisks. The rotor disk has a tip shroud, which provides a convenient path for transporting the bleed flows outside the flow path. Figure 4 shows a cross section of the stage with suction removal paths. Orifices on the rotor and stator casing are designed to choke at the design bleed flows, and the bleed flows are transported through channels to the main dump tank of the test facility. The bleed passages are machined into the suction side of the rotor and stator blades. Cover plates with 0.015 in. bleed slots were used to cover the suction surface of the blades. The cover plates were preshaped to match the curvature of the blade surfaces. The geometry parameters of the stage are given in Table 1.

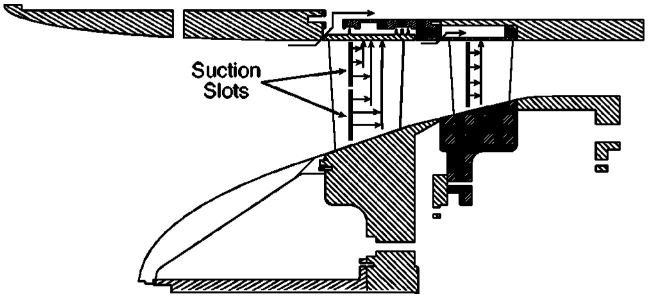

Fig. 4 Assembly cross section and suction scheme

Table 1 Stage geometry parameters

Stage tip diameter (in.)	20.7
Rotor inlet $R_{\mathrm{hub}}/R_{\mathrm{tip}}$	0.62
Rotor tip solidity	1.4
Stator hub solidity	2.1
Rotor mean chord (in.)	1.0
Stator mean chord (in.)	1.0
Rotor aspect ratio	1.2
Stator aspect ratio	1.1

4 Experimental Facility

The fan stage was tested in the MIT blow down compressor facility. The design, construction, and primary testing procedures of the facility are described by Kerrebrock [11]. Since the inception of the blow down compressor, several validations of the test procedure have been performed. The facility is equipped with a fast-acting valve [12] that allows rapid testing. The facility is instrumented with several high-frequency response pressure transducers to capture the flow field within the test section and the necessary pressures within the supply and dump tanks. An important part of the data collection system is the four-way probe, which measures total pressure, static pressure, total Mach number, tangential angle, and radial angle. The calibration and data reduction procedure, which is critical for obtaining accurate data, is described by Reijnen [3].

High-frequency pressure transducers are also placed within the casing of the stage to measure the casing static pressures upstream and downstream of the stage as well as between the rotor and stator. The downstream casing pressure, along with the exit Mach number set by the choke plate area ratio, gives an estimate of the stage total pressure ratio and can be used to rapidly predict the overall stage performance. An optical encoder with 400 lines per revolution is used to measure the speed of the rotor. The encoder also has the option of producing a once per revolution pulse so that the test is always triggered with the rotor in the same position.

5 Experiment Results

The design point data for the rotor and stator exits are presented in this section. The rotor total pressure and flow angle measurements are presented as time-accurate data and as an ensemble average of 7 rotor revolutions or 175 blade passes. The data at 28%, 65%, and 92% span locations is presented. The rotor data is measured at an axial distance of 1.1 in. downstream of the rotor tip trailing edge, and the stator data is measured 1 in. downstream of the stator trailing edge. The data collected at this location is compared to the APNASA solution corresponding to the same axial location. For all these plots, the pressure side is the left side of the wake, and the suction side is the right side of the wake. The complete data set can be found in Schuler [13]. The APNASA solution was used to fill in the gaps below 28% span and above 92% span to calculate the averaged performance downstream of the rotor and stator. The APNASA solution was scaled to match the experimental data at 28% and 92% span locations. The rotor efficiency was calculated from the mass-averaged total temperature and total pressure downstream of the rotor, the stage efficiency was calculated from the mass-averaged total pressure downstream of the stator.

5.1 Rotor Design Point Performance. Figure 5 presents a comparison between the pitch-averaged radial variation of total pressure from the experiment and the APNASA analysis. The experimental data shows excellent agreement with the CFD analysis at 28%, 47%, and 65% span. The two measurements closest to the tip, at 84% and 92% span, show a lower total pressure than the values predicted by APNASA. The flow region below 28% span could not be surveyed because the probe could not safely traverse so close to the hub. It is interesting to note the uniformity of the total pressure profile predicted by the CFD calculation, indicating that near-design intent performance was obtained in the CFD calculation. The reduction in total pressure near the hub is caused by the strong secondary flow, which can be attributed to the incoming hub boundary layer. The tip region also shows the presence of secondary flows. In contrast to compressors with tip clearance, the rotating tip shroud on this rotor results in nearly uniform total pressure up to the tip.

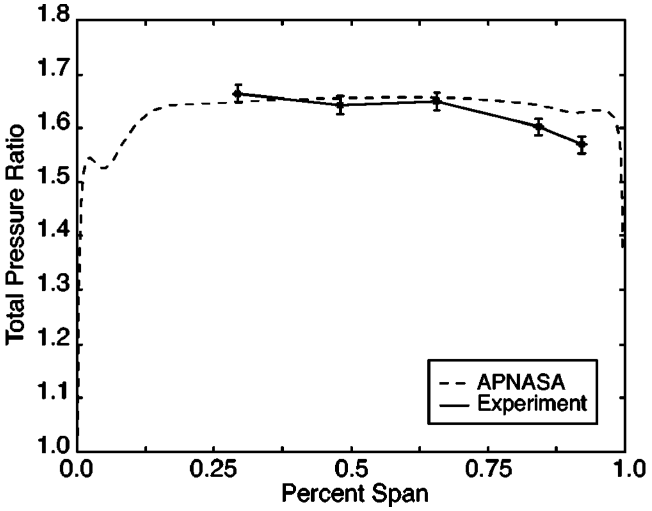

Fig. 5 Comparison of experimental spanwise total pressure distribution to APNASA analysis

Figure 6 presents a comparison between the spanwise pitch-averaged radial variation of total temperature from the experiment and the APNASA analysis. The total temperature is calculated from the Euler turbine equation using flow angle measurements made with the four-way probe. The experimental data shows that the rotor produces a lower total temperature rise than APNASA predicts in the lower half of the span, whereas better agreement is seen between the experiment and APNASA in the upper half of the span. Lower span locations could not be surveyed, as explained above. The uniform total temperature profile shows that the design intent was well captured. The presence of secondary flow discussed above can be clearly identified in the total temperature profile at the hub. At the tip, the work added to the flow by the rotating shroud is clearly seen. The difference between the measured and computed radial variations is discussed further in Sec. 9.

Table 2 presents a comparison between the stage performance at the design point calculated from the experimental data and the APNASA solution. The rotor and overall stage experimental performance are in good agreement with the APNASA prediction. The stator total pressure loss predicted by APNASA is 3%, whereas the experimental data indicate approximately 3.7%. The rotor and stage efficiencies are also in good agreement. In particular, it is interesting to note the high rotor efficiency predicted by APNASA and confirmed by the experimental data.

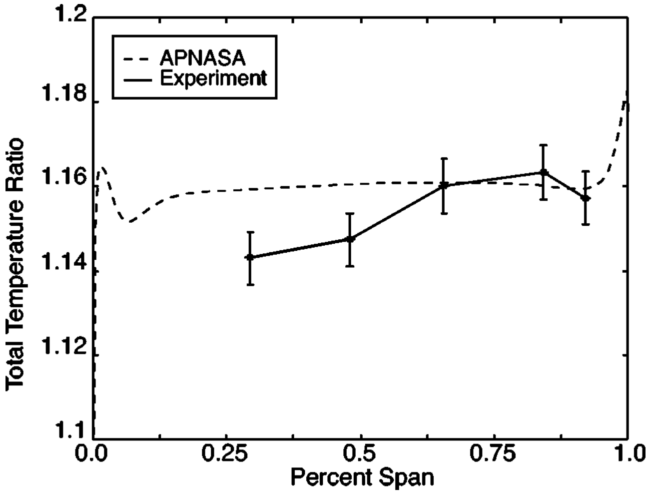

Fig. 6 Comparison of experimental spanwise total temperatire distribution to APNASA

Table 2 Experimental and computational stage design point performance

	APNASA	Experiment
Rotor pressure ratio	1.64	1.62
Stage pressure ratio	1.59	1.57
Corrected mass flow (lbm/s)	63.9	64.2
Rotor isentropic efficiency	0.96	0.97
Stage isentropic efficiency	0.89	0.90

5.2 Pitchwise Variation, 28% Span. Figures 7 and 8 show the ensemble-averaged total pressure and tangential flow angle data of 175 blade passes, or 7 rotor revolutions, at the 28% span location. The ensemble-averaged data is compared to APNASA analysis prediction at the same axial and spanwise position. The experimental data and CFD data are aligned such that the center of each wake is at the same pitchwise position. The predicted total pressure profile is in good agreement with the experimental data in the core flow. The APNASA analysis predicts the wake width to be 20% of the pitch, and the experimental data shows a slightly narrower wake of 15% of the blade pitch. Although the wake width is in good agreement, APNASA significantly over predicts the wake depth. The analysis predicts a minimum total pressure ratio of 1.50, whereas the data show the minimum total pressure ratio to be 1.57. Overall, the APNASA analysis underpredicts the total pressure ratio at this streamline than indicated by the experimental data.

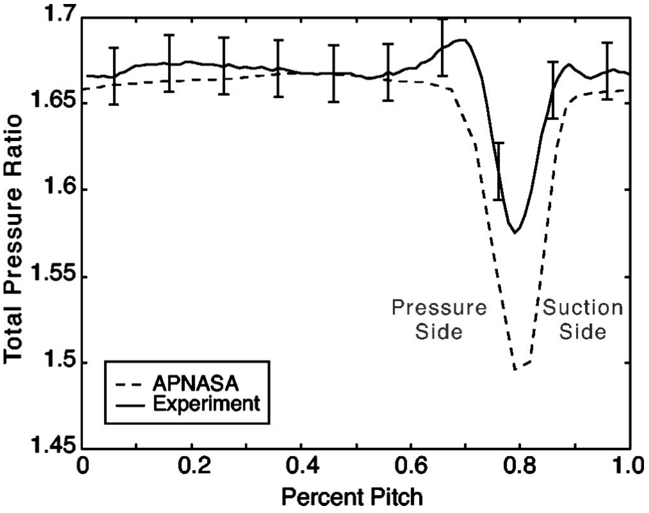

Fig. 7 Pitchwise total pressure profile at 28% rotor span

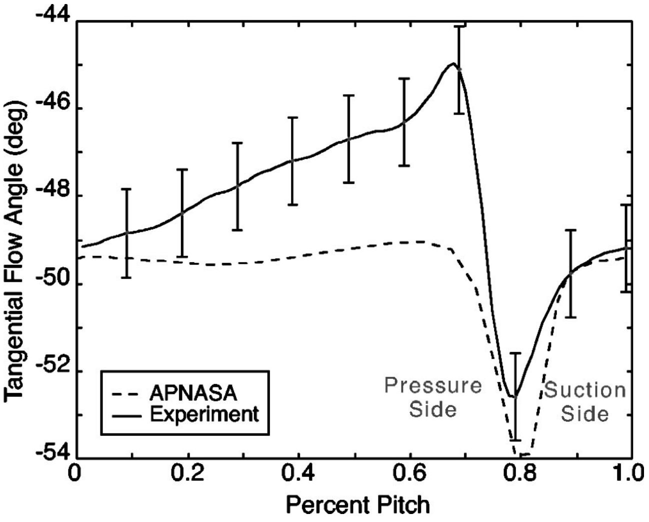

Fig. 8 Pitchwise tangential angle profile at 28% rotor span

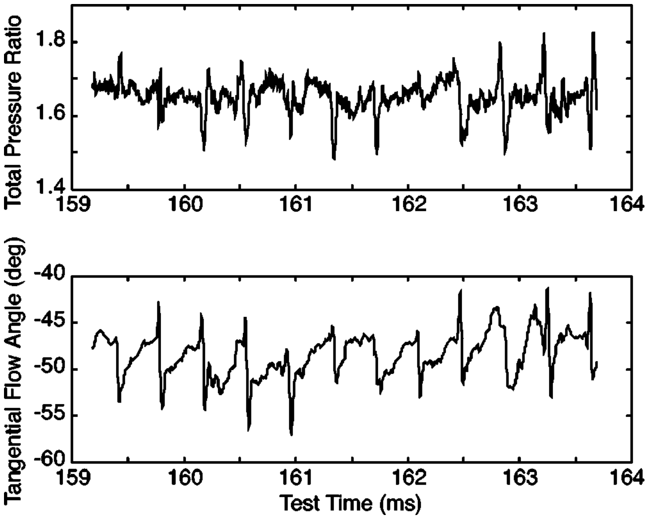

Fig. 9 Time-accurate total pressure and tangential angle at 28% rotor span

The pitchwise tangential flow angle profile shown in Fig. 8 indicates that the APNASA analysis overpredicts the turning in the core flow. The analysis predicts a nearly constant tangential flow angle of −49.5 deg in the core flow, whereas the experimental data shows a roughly linear decrease in turning from −49.5 deg to a minimum turning of −45 deg on the pressure side of the wake. The APNASA analysis predicts an overturning of −54 deg in the wake, while the experimental data only shows an overturning of −52.5 deg.

Figure 9 shows the time-accurate data traces of total pressure and tangential flow angle at the 28% span location that were used to calculate the ensemble-averaged plots.

5.3 Pitchwise Variation, 65% Span. Figure 10 shows the ensemble-averaged total pressure data taken at the 65% span location compared to the APNASA analysis prediction for the same axial and radial location. Excellent agreement is seen between the experimental data and the APNASA analysis. The experimental data show a total pressure ratio range of 1.66–1.68 in the core

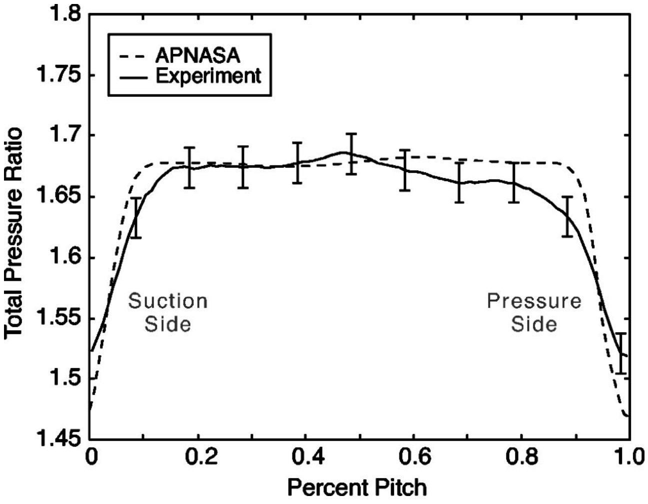

Fig. 10 Pitchwise total pressure profile for 65% rotor span

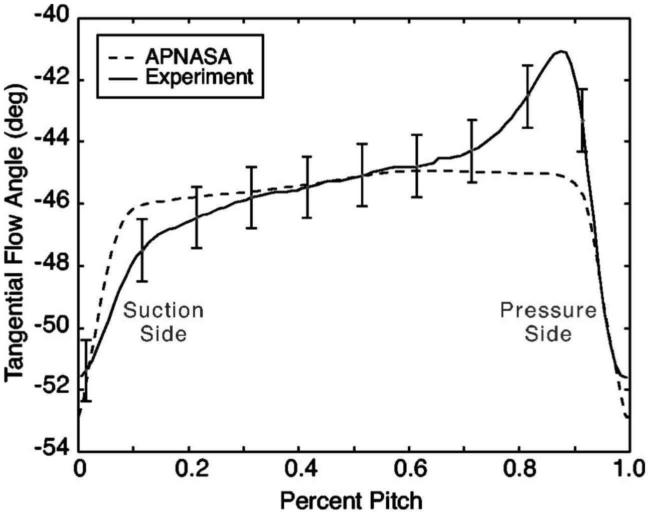

Fig. 11 Pitchwise tangential angle profile for 65% rotor span

flow, whereas APNASA predicts a total pressure ratio range of 1.67–1.68. Good agreement is also seen in the wake flow between the experimental data and APNASA. Both the experiment and APNASA show a wake width of approximately 20% of the blade pitch. The wake depth, however, is overpredicted by APNASA to be 1.47, while the experimental data show a minimum total pressure ratio of 1.52.

Figure 11 shows the ensemble-averaged tangential angle data taken at the 65% span location compared to the APNASA prediction. The APNASA analysis and the experimental data differ by ∼2 deg in the core flow. The experimental data range from approximately −46 deg on the suction side of the wake to approximately −44 deg of turning near the pressure side of the wake. The APNASA prediction shows a range from −42 deg to −44 deg of turning over the same pitch. Once again the experimental data show an underturning of the flow to a peak of −41 deg on the pressure side of the wake. In the wake flow, the APNASA analysis predicts a maximum overturning of −53 deg compared to the experimental data, which show a peak overturning of −51 deg.

Figure 12 shows the time-accurate total pressure and tangential flow angle data from the four-way probe at the 65% span location that were used to calculate the ensemble-averaged plots.

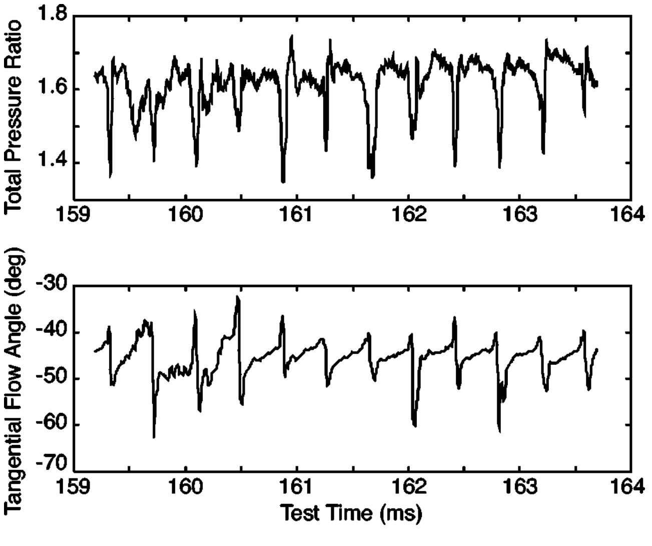

Fig. 12 Time-accurate total pressure and tangential angle for 65% rotor span

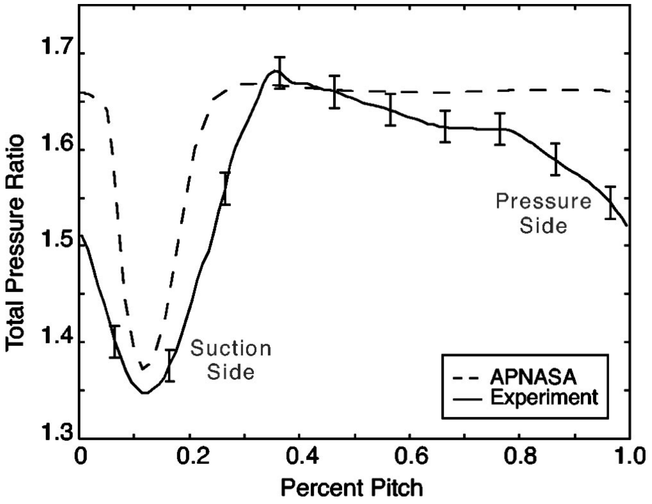

Fig. 13 Pitchwise total pressure profile at 92% rotor span

5.4 Pitchwise Variation, 92% Span. Figure 13 shows the ensemble-averaged total pressure ratio data at the 92% span compared to the APNASA solution at the same spanwise and axial locations. Although the overall pressure ratio and wake depth are in good agreement, a decrease in the experiment total pressure ratio is seen near the pressure side. The experimental total pressure ratio varies from 1.67 to 1.62, whereas APNASA predicts a nearly constant total pressure ratio of 1.66 in the core. The APNASA analysis predicts a wake width of 20% pitch, whereas the experimental data show a wake width of approximately 40% of the blade pitch. The wider wake on the pressure side may be indicative of a pressure-side separation. This may be attributed to the following factors: (i) negative incidence cause by the length of the rotating shroud upstream of the rotor, or the amount of endwall suction upstream of the rotor, and (ii) flow recirculation in the shock bleed holes on the tip shroud. The wake depth in the analysis and the experimental data are in good agreement. The APNASA analysis predicts a minimum total pressure ratio of 1.37, and the experimental data show a minimum total pressure ratio of 1.35.

Figure 14 shows a comparison between the ensemble-averaged tangential angle data at 92% span and the APNASA analysis. The experimental data show a tangential flow angle variation from −44 to −40 deg in the core flow compared to the APNASA analysis

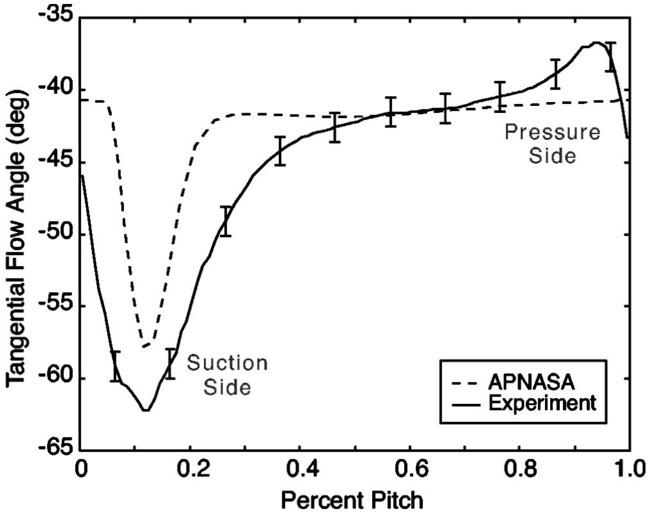

Fig. 14 Pitchwise tangential angle profile at 92% rotor span

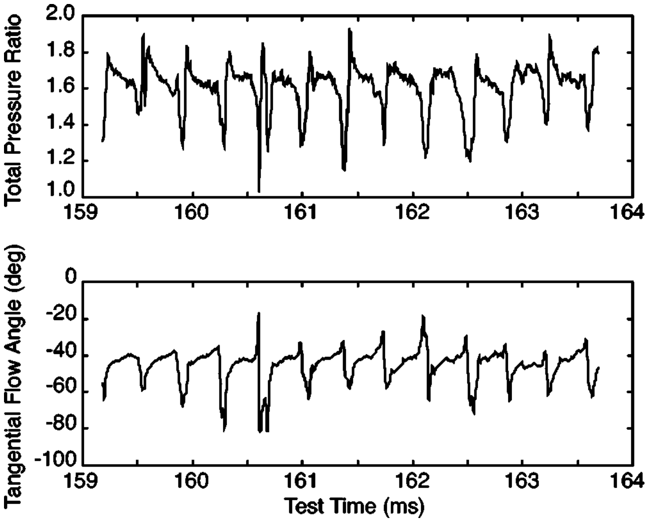

Fig. 15 Time-accurate total pressure and tangential flow angle at 92% rotor span

prediction, which ranges from −41 to −42 deg. The experimental data show a mild underturning of the flow to −37 deg near the pressure side of the wake. This is lower than the 28% and 65% span locations and may be linked to the pressure-side separation discussed above. The APNASA analysis predicts a maximum overturning of the flow of −57 deg in the wake, whereas the experimental data show a maximum overturning of −62 deg.

Figure 15 shows the instantaneous total pressure and tangential angle measurements from the four-way probe at the 92% span location.

5.5 Blade to Blade Variation. The time-accurate data traces in the previous section highlight the significant unsteadiness in the rotor exit flow from one blade passing to the next. Figure 16 shows the blade-to-blade variation in total pressure for the 65% span location. In the core flow, the total pressure variation is about 4% of the mean value, whereas in the wake flow there is a significant increase up to 15% of the value in the core flow. The source of this unsteadiness and its impact on the rotor performance are discussed in Sec. 9.

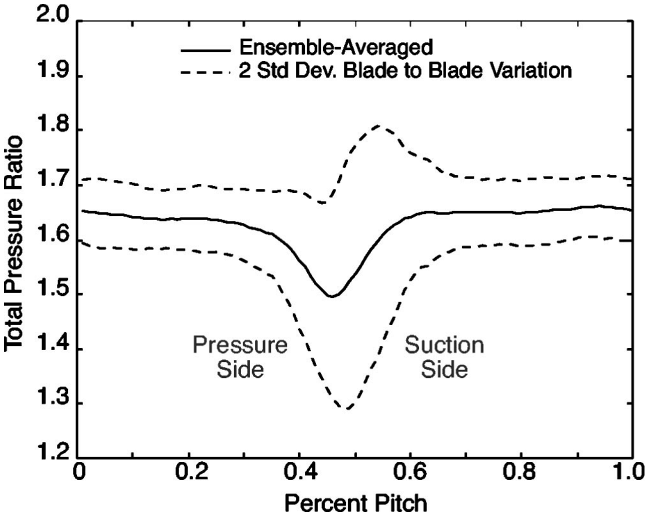

Fig. 16 Blade to blade variation in the total pressure at 65% rotor span

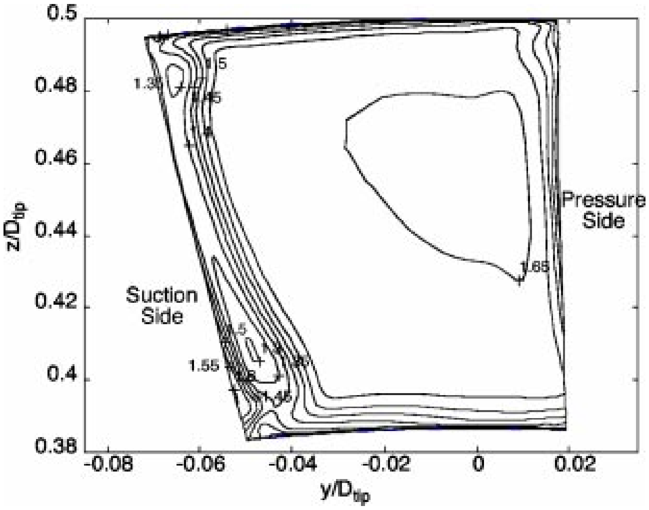

Fig. 17 Stator exit total pressure contour predicted by APNASA

6 Stator Design Point Performance

The stator performance can be effectively characterized by the total pressure at the exit plane. Experimental data was collected in a grid of four spanwise points by six pitchwise points located approximately 1 in. downstream of the stator trailing edge. The four spanwise points are located at 20%, 40%, 60%, and 80% span, where 0% span is the hub and 100% span is the casing. The six pitchwise points are clustered around the wake with two points in the main flow. The points are located at 0%, 5%, 30%, 80%, 90%, and 95% pitch.

Figure 17 shows the total pressure contour from the APNASA analysis at the same axial location as the four-way probe location. Figure 18 shows the time-averaged values of total pressure measured with the four-way probe at each location with an interpolated contour plot superimposed over the measured values. The features observed in the APNASA solution are also clearly visible in the experimental data, in particular, the thicker wake on the suction side and low total pressure regions near the hub and tip on the suction indicating strong secondary flows. The extent and position of the high loss regions are also reasonably close to the APNASA prediction. The experiment predicts a higher peak total pressure value of 1.7 on the pressure side of the blade compared to 1.66 predicted by APNASA.

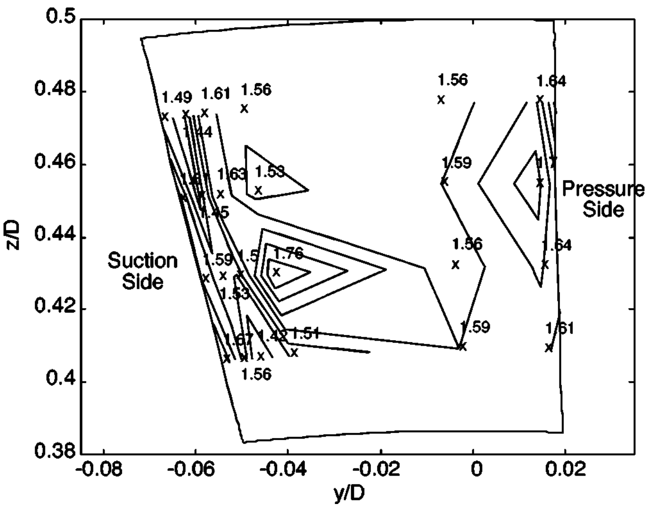

Fig. 18 Time-averaged total pressure data from stator exit

Table 3 Comparison of Design and Measured Suction Values

Suction location	Design	Measured
Rotor casing	1.3%	0.72%
Rotor blade and shroud	0.95%	0.84%
Stator casing and vane	1.95%	0.85%

7 Measured Stage Aspiration

The layout of the stage aspiration channels is shown in Fig. 4. Three suction channels in the casing insert carry the suction flows from the rotor and stator to the dump tank. The total and static pressure measured in the channels, combined with the cross-sectional area of the channels and the number of channels, are used to calculate the total mass flow through the channels. The geometry of the suction channels was not changed during any of the experimental runs.

Three main channels remove the bleed flow, and only the mass flow in these channels, not the individual suction locations, is measured. The first channel carries the rotor casing suction, the second channel carries the rotor blade surface and shroud suction, and the third channel carries the stator casing, shroud, and blade surface suction. The stator hub (inner diameter) suction is not measured. Table 3 shows the comparison of measured and design suction values in the channels. The measured total rotor blade and shroud suction closely matches the design value, whereas the measured upstream rotor casing suction and total stator suction are approximately 45% below the design value.

8 Off-Design Performance

Tests at off-design throttle points on the design speedline showed that the stage did not exhibit rotating stall as low as 79% of the design mass flow. The design speedline is shown in Fig. 19. The speedline is almost linear down to 83% of the design mass flow and shows a somewhat rapid decrease at the last data point at 79% of the design mass flow. The stage produced a lower pressure ratio compared to the CFD analysis performed using APNASA and one by Pratt & Whitney [14], but the choking mass flow is higher than that predicted by the CFD analyses.

It is interesting to note the positive slopes and nearly linear behavior of the speedline at lower mass flows. The CFD analysis was unable to predict solutions below 96% of the design mass flow. This may be due to the exit pressure numerical boundary condition used in the codes. Fig. 19 also shows the theoretical speedline calculated using Euler's turbine equation

$$\tau = 1 + M_0^2(\gamma - 1) r_{ex}[1 - \phi \mathrm{AVR}\tan(\beta_{ex})]$$

$$\pi = [1 + \eta(\tau - 1)]^{\gamma/(\gamma-1)} \qquad (1)$$

Here, M_0 is the blade rotational Mach number, r_{ex} is the radius of the exiting streamline, *AVR* is the axial velocity ratio, ϕ is the flow coefficient, β_{ex} is the rotor exit relative flow angle, and η is the stage core flow efficiency. The values chosen for calculating the speedline were taken at the stage meanline and held constant, leaving the stage pressure ratio as a function of ϕ. The stage efficiency was assumed to be 90%.

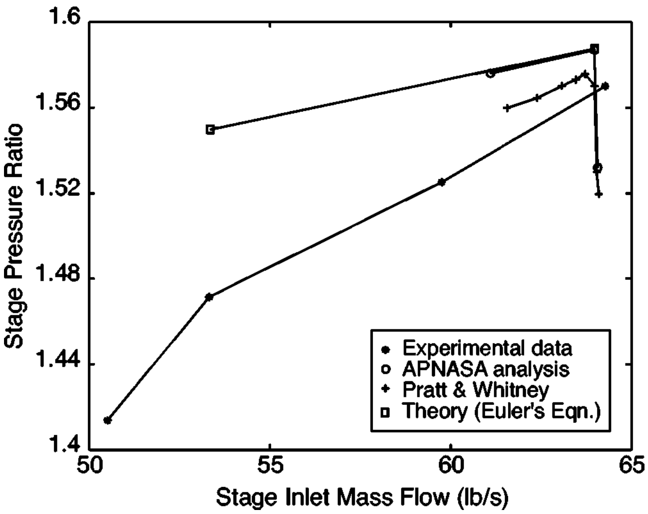

Fig. 19 Off-design performance of aspirated fan stage

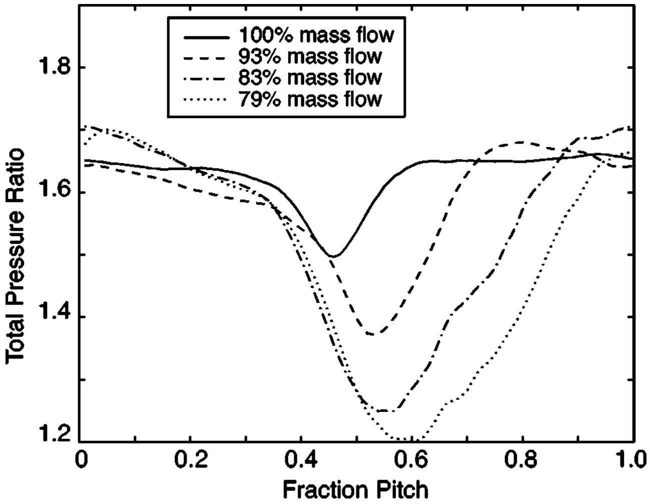

Fig. 20 Pitchwise total pressure at rotor exit for 65% span at different mass flows

The negative exit angle at the meanline results in a positive slope of the total pressure characteristic. The stability of the stage, however, is determined by the slope of the exit static pressure characteristic, which must have a negative slope up to the stall point, as shown by Merchant [5]. The slope of the theoretical speedline is in good agreement with the CFD analyses and also shows very little deviation from the experimental one. This indicates that there is little change in the stage efficiency and deviation of rotor flow angles over a significantly larger flow range than a conventional nonaspirated stage. Schuler [13] has examined the loading characteristic of the blades at off-design condition in order to explain the large flow range achieved by the stage.

Figure 20 shows the ensemble-averaged total pressure variation across the pitch at the 64% spanwise location downstream of the rotor. The total pressure wakes of the rotor get wider and deeper as the mass flow decreases. At the design mass flow, the rotor wake covers approximately 15% of the blade pitch, whereas the 79% mass flow test shows the wake covering approximately 50% of the blade pitch.

Figure 21 shows the time-accurate total pressure data taken at 40% span and 5% pitch downstream of the stator for design mass flow and 79% design mass flow runs. The lower mass flow run shows a larger variation in total pressure than the design mass flow run, and in addition, the wakes are not as sharp and distinct as the wakes at the design flow condition. However, both sets of data clearly show no evidence of rotating stall cells.

9 Spanwise Loss Redistribution in the Rotor Wakes

A comparison of the ensemble-averaged data with the APNASA calculations at different radial locations showed differences in the spanwise distributions of total pressure and total temperature. In addition, the blade-to-blade variation of total pressure in the experimental data indicated a large amount of unsteadiness in the flow field. This suggests that the unsteadiness in the flow

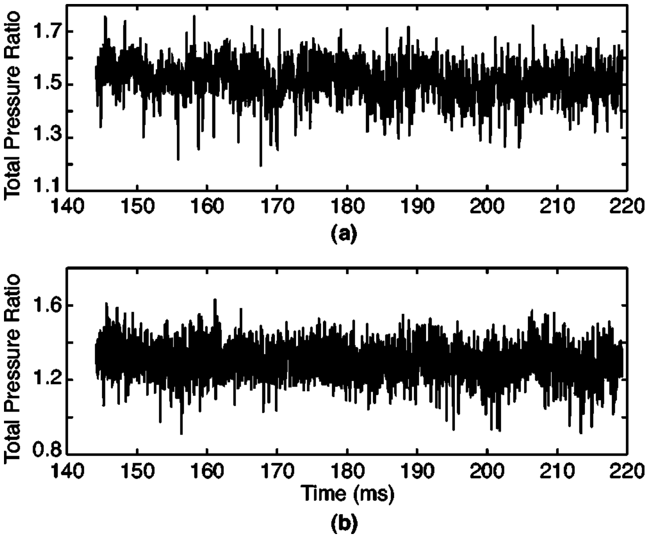

Fig. 21 Time-accurate total pressure data at (*a*) 100% and (*b*) 79% mass flow

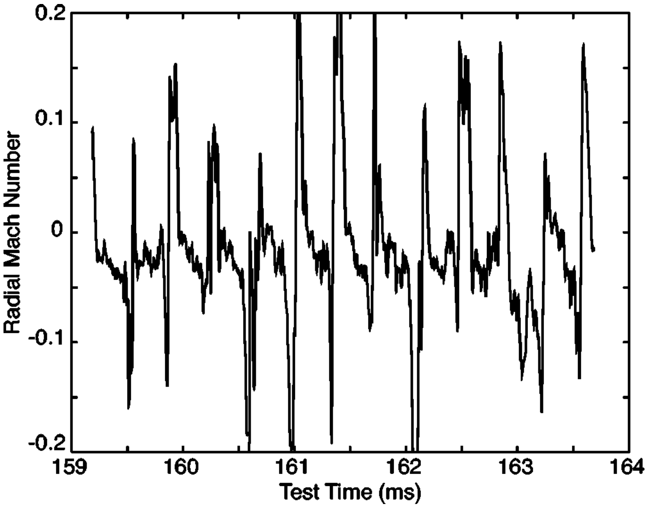

Fig. 22 Time-accurate radial Mach number distribution at 92% span

field and the discrepancy in the measured and calculated spanwise profiles may be attributed to radial transport of fluid in the wakes due unsteady vortex shedding.

Gertz [15] has shown the existence of regular arrays of vortex streets in the wakes of a transonic rotor in data gathered in the MIT blow down compressor facility. These were also identified on the same compressor stage in an experiment by Strazisar and Powell [16] through the bimodal character of the velocity probability density distribution (PDD). Following the two-dimensional (2D) vortex fitting model of Gertz [15], and subsequent extension to spanwise flows by Kotidis [17], a vortex shedding model was developed for the aspirated fan stage. The present model improves on Kotidis' approach, which only considered flows within the vortex core, by including the spanwise flows throughout the wake. The flow outside the vortex cores has a significant effect on the amount of mass that can be exchanged between stream tubes.

The result of these calculations is that the radial velocities within the wake are roughly constant from the 28% span location to the 84% span location with the spanwise flow directed toward the tip region. The 92% span location shows both positive and negative velocities, indicating that there is flow both into and out of the region. These radial velocities in the wake are supported by the experiment. Time-accurate measurements of radial velocity at the 92% span location are shown in Fig. 22. APNASA predicts radial Mach numbers at the same radial location of less than 0.02. The measurements at other radial locations also show large variation in radial Mach number in the wake compared to the APNASA solutions. The difference can be attributed to the absence of the unsteady vortex shedding in the APNASA calculation.

The spanwise mass redistribution calculated from the vortex-shedding model can be used to estimate its impact on the measured values of total pressure and total temperature. The results of adjusting the flow properties downstream of the rotor to remove the effects of transport are shown in Fig. 23. The measured experimental efficiency with the experimental error bars is shown along with the predicted efficiency distribution from the APNASA calculation. The two adjusted efficiency distributions are also shown: one that includes mixing losses and one that only redistributes the flow properties. The "no mixing" distribution shows very little change from the measured values, whereas the "mixed" efficiency distribution shows a more uniform profile and approaches the efficiency profile predicted by the APNASA solution. Given that the distance from the rotor trailing edge to the probe location is small, it is possible that the wake flows are not completely mixed out. Therefore, the true solution lies between the efficiency profile corrected without mixing and the profile corrected with mixing.

Figure 23 shows that the stage has an efficiency higher than the design efficiency in the hub region of the rotor. The tip region shows an efficiency lower than the design efficiency. It is interesting to note that the measured average efficiency of the rotor agrees with the APNASA prediction. The vortex model indicates that one of the reasons for the discrepancy between the measured efficiency distribution and the APNASA distribution is spanwise transport within the blade wake due to unsteady vortex shedding. This radial tranport causes the spanwise redistribution of flow properties, which accounts partially for the difference between the measured and predicted efficiency distributions. Therefore, in order to more accurately predict the rotor performance, a vortex model similar to the one used here should be incorporated into existing 3D viscous computational tools.

10 Conclusions

The analysis and testing of a transonic aspirated compressor stage have been presented in this paper. The experimental stage performance and detailed flow field data clearly validate the utility

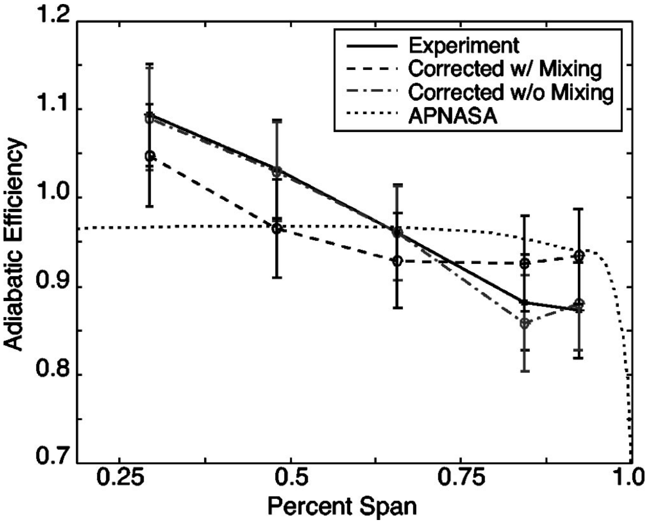

Fig. 23 Effect of spanwise transport on efficiency distribution

of aspiration for increasing stage work. More detailed observations and conclusions about this research are enumerated below:

1. The stage achieved near-design performance in terms of pressure ratio and efficiency. Detailed design-point data are in good agreement with the CFD analysis, particularly when the unsteady effects observed in the experiment are included in the data reduction. The rotor outflow measurements of total pressure ratio and rotor exit flow angle show good agreement with the APNASA analysis. The stator total pressure contours are in good agreement in terms of the magnitude and flow features predicted by the CFD analysis.
2. Although the overall stage efficiency was close to 90%, the rotor showed an extremely high efficiency of 97% for a transonic rotor. This can be attributed to: (i) elimination of the tip clearance flow due to the tip shroud, (ii) well-attached thin boundary layers on the blade surfaces due to aspiration, and (iii) advanced blade design features. The high loss in the stator can be primarily attributed to a mismatch in the rotor-stator design [13].
3. The off-design performance of the stage on the 100% design speedline is also a significant result. The experimental data show unstalled stage performance at least down to 53 lbs/s, which is 83% of the design-point mass flow. The stage also did not exhibit rotating stall at any of the data points. This was inferred from the time-accurate data downstream of the rotor. The stage performance follows the trend predicted by theory and 3D viscous CFD analyses. An important implication of these observations is that aspiration is effective in maintaining stage performance at off-design conditions.
4. Although no explicit aspiration sensitivity study was performed, the lower aspiration fractions measured in the experiment indicate the low sensitivity of the stage performance to the required aspiration fraction. The stage demonstrated adequate performance at 35% lower aspiration than the design value. In particular, the measured rotor and stator aspiration were 70% and 45% of the design requirement.
5. The use of an unsteady vortex-shedding model has provided useful insight into the phenomenon of loss redistribution in the rotor wakes induced by the vortex shedding. In addition, it also explains the high efficiency (above 1) measured at the hub. The CFD predictions can be corrected with the model resulting in a better data match with the measured distribution.
6. Finally, the experimental results validate the design and analysis system. This includes the through-flow quasi-3D design system, predicting the aspiration requirement and the subsequent 3D CFD analysis of the final design.

Acknowledgments

We would like to thank Mark Drela and Alan Epstein for their guidance and contribution to this research, and John Adamczyk and his team at NASA for many contributions to this research and for carrying out the many APNASA calculations. Research presented in this paper was supported by AFOSR and funded by DARPA under the MAFC program.

References

[1] Kerrebrock, J. L., Reijnen, D. P., Ziminsky, W. S., and Smilg, L. M., 1997, “Aspirated Compressors,” *ASME IGTI Conference*, ASME, New York, Paper No. 97-GT-525.
[2] Hobbs, D. E., and Weingold, H. D., 1984, “Development of Controlled Diffusion Aerofoils for Multistage Compressor Applications,” ASME J. Eng. Gas Turbines Power **106**(1), pp. 271–278.
[3] Reijnen, D. P., 1997, “Experimental Study of Boundary Layer Suction in a Transonic Compressor,” Ph.D. thesis, MIT, Cambridge, MA.
[4] Drela, M., and Giles, M. B., 1987, “Viscous-Inviscid Analysis of Transonic and Low Reynolds Number Airfoils,” AIAA J. **25**(10), pp. 1347–1355.
[5] Merchant, A. A., 1999, “Design and Analysis of Axial Aspirated Compressor Stages,” Ph.D. thesis, MIT, Cambridge, MA.
[6] Kerrebrock, J. L., 2000, “The Prospects for Aspirated Compressors,” *AIAA Conference*, AIAA, Washington, DC, AIAA Paper No. 2000-2472.
[7] McCabe, N., 2001, “A System Study on the Use of Aspirated Technology in Gas Turbine Engines,” M.S. thesis, MIT, Cambridge, MA.
[8] Adamczyk, J. J., 1985, “Model Equation for Simulating Flows in Multistage Turbomachines,” ASME J. Turbomach. **103**(2), pp. 430–437.
[9] Adamczyk, J. J., Celestina, M. L., and Mulac, R. A., 1986, “A Model for Closing the Inviscid Form of the Average-Passage Equation System,” ASME J. Turbomach. **108**, pp. 180–186.
[10] Schuler, B. J., 1998, “Mechanical Design of an Experimental Aspirated Compressor,” M.S. thesis, MIT, Cambridge, MA.
[11] Kerrebrock, J. L., 1975, “The MIT Blowdown Compressor Facility,” Gas Turbine Laboratory Report No. 108, MIT, Cambridge, MA.
[12] Ziminsky, W. S., 1996, “Design of a High Pressure Ratio Transonic Compressor Stage With Active Boundary Layer Control,” M.S. thesis, MIT, Cambridge, MA.
[13] Schuler, B. J., 2001, “Experimental Investigation of an Aspirated Fan Stage,” Ph.D. thesis, MIT, Cambridge, MA.
[14] Saxena, V., and Lord, W., 1999 (personal communication).
[15] Gertz, J. B., 1986, “Unsteady Design-point Flow Phenomena in Transonic Compressors,” Gas Turbine Laboratory Report No. 188, MIT, Cambridge, MA.
[16] Strazisar, A. J., and Powell, J. A., 1981, “Laser Anemometer Measurements in a Transonic Axial Flow Compressor Rotor,” ASME J. Eng. Power **103**(2), pp. 430–437.
[17] Kotidis, P. A., 1989, “Unsteady Radial Transport in a Transonic Compressor Stage,” Gas Turbine Laboratory Report No. 199, MIT, Cambridge, MA.

M. Vahdati

A. I. Sayma

Mechanical Engineering Department,
Imperial College,
Exhibition Road,
London SW7 2BX, UK

C. Freeman
Rolls-Royce plc,
PO Box 31, Moor Lane,
Derby DE24 8BJ, UK

M. Imregun
Mechanical Engineering Department,
Imperial College,
Exhibition Road,
London SW7 2BX, UK

On the Use of Atmospheric Boundary Conditions for Axial-Flow Compressor Stall Simulations

This paper describes a novel way of prescribing computational fluid dynamics (CFD) boundary conditions for axial-flow compressors. The approach is based on extending the standard single passage computational domain by adding an intake upstream and a variable nozzle downstream. Such a route allows us to consider any point on a given speed characteristic by simply modifying the nozzle area, the actual boundary conditions being set to atmospheric ones in all cases. Using a fan blade, it is shown that the method not only allows going past the stall point but also captures the typical hysteresis loop behavior of compressors. [DOI: 10.1115/1.1861912]

1 Introduction

The performance of an axial flow compressor, either a fan assembly or a core compressor, is often summarised in the form of a pressure-rise versus mass flow characteristic curve, representing nominally steady and axisymmetric flow operation. At a given shaft speed, the operating zone is bounded by the blades choking at high mass flow–low pressure, or the blades stalling at low mass flow–high pressure. Both boundaries are associated with severe instabilities, though here we will be focussing on stall-related events. Stall margin can be degraded substantially during the engine operation due to various factors such as inlet distortions resulting from nonaxisymmetric intakes or wakes shed from fuselage or wings or cross wind [1,2]. Sudden flow variations during rapid maneuvres can also be detrimental.

Since the avoidance of stall is a major design consideration, a considerable amount of research effort has been devoted to understanding the physical mechanisms that give rise to stall. After the initial inception stage, it is not clear which conditions will cause surge or rotating stall. If the latter occurs, there are no rules to determine its speed, its circumferential and radial extent as well as the number of rotating cells. So far, due to modeling difficulties, much of the stall research has been experimental [3,4] or based on simplified models [5] though realistic numerical simulations are becoming possible with dramatic increases in hardware and software. In any case, it is very difficult to capture the required local detail using an experimental approach and hence a numerical modeling route is very attractive. However, in spite of dramatic advances in hardware and software, the simulation of turbomachinery flows near stall is fraught with difficulties. First, because of inherent unsteadiness, the flow representation must be time-accurate, nonlinear, and viscous. Second, the turbulence model must be able to cope with flow separation and re-attachment. Third, appropriate inlet and outlet boundary conditions must be imposed. However, when the flow conditions are uniform at the boundaries, the flow is stable at lower working lines but numerical difficulties occur at higher working lines. It is well-known that rigid boundary conditions, based on imposing given exit pressure distributions, are not suitable for stall studies. For instance, in the case of rotating stall, the downstream exit pressure profiles are neither known nor constant in time. Similarly, at high working lines, the flow becomes genuinely unsteady near the stall boundary, and the imposition of a radially constant exit static pressure is likely to result in numerical instabilities, the so-called “numerical stall.” The situation can be remedied by introducing a downstream variable nozzle, thus allowing the pressure behind the fan to adjust automatically while the pressure behind the nozzle is fixed. Such an approach makes the computational domain “less stiff” and provides a powerful natural boundary condition for stall studies. Moreover, since the aim is to simulate, as much as possible, engine and rig tests, nozzle area changes can be used to move to any point on the compressor characteristic. The application of such a methodology for computing a part-speed characteristic of a fan blade will be presented in the next section. Not only a more accurate characteristic is obtained, but also the stall boundary is reached without any numerical problems, an outcome which is not possible by using fixed-valued radial static pressure profiles.

2 Case Study

2.1 Computational Tool. The flow code used is an edge-based upwind solver that uses unstructured meshes [6]. The time stepping is done in an implicit fashion and hence very large CFL numbers can be used without creating numerical instabilities in the solution algorithm. Time accuracy is ensured by using a dual time stepping technique with inner Jacobi and outer Newton iterations. The code can be run in viscous mode via Reynolds-averaged Navier–Stokes equations with Baldwin–Barth, Spalart–Allmaras and q-zeta turbulence models. The flow geometry is described using general grids of three-dimensional (3D) elements such as tetrahedra, hexahedra and wedges, a feature that offers great flexibility for modeling complex shapes, such as casing treatment geometries.

2.2 Study of Stall. Two sets of calculations, with two different boundary condition strategies, were performed along the 70%

Contributed by the Turbomachinery Division of THE AMERICAN SOCIETY OF MECHANICAL ENGINEERS for publication in the ASME JOURNAL OF TURBOMACHINERY. Manuscript received March 1, 2004; final revision, August 27, 2004. Editor: D. Wisler.

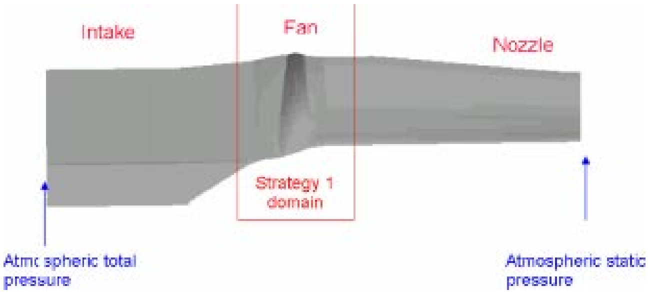

Fig. 1 Computational domains for Strategies 1 and 2

speed characteristic of a large aero-engine fan. The domain for Strategy 1 excludes the intake and the variable nozzle of Fig. 1 and may be viewed as a standard 3D single-passage calculation for this type of blade. The computational domain for Strategy 2 includes the upstream and downstream extensions, namely a symmetric intake with a spinner and a variable nozzle.

As listed in Table 1 different boundary conditions are used for the two modeling strategies. For Strategy 1, corrected atmospheric pressure and temperature are imposed at the inlet to compensate for the intake losses. More significantly, a radially constant static pressure, whose values determine the actual point on the characteristic, is used at the exit. On the other hand, for Strategy 2, atmospheric total pressure and temperature are imposed at the intake inlet, while atmospheric static pressure is imposed at the nozzle exit. A critical difference between the two strategies is that both the inlet and outlet boundary conditions remain the same for all the points on the characteristic for the latter. Different points on the characteristic are obtained by changing the area of the exit nozzle, the path from choke to stall requiring an area decrease and vice versa. The annulus geometry downstream of the fan was modified to change the nozzle area. However, the nozzle area was kept fixed for a given computation at a given operating point.

The characteristics obtained from the two modeling strategies are compared to measured data in Fig. 2. Up to the working line, which corresponds to a normalized flow rate of about 1.0, both strategies yield very similar steady-state flow results, which in turn are in very good agreement with the measured data. However, Strategy 1, that employs constant-value radial static pressure profiles, is unable to provide a solution beyond a mass flow of 0.98. On the other hand, with Strategy 2, it was not only possible to go past the stall point but also to obtain a hysteresis loop, characteristic of compressor behavior at surge (Fig. 2). Once the compressor is operating near the stall boundary, the flow is no longer steady since both the mass flow and the pressure ratio begin to vary with time and Strategy 1 computations can no longer yield a flow solution. However, in Strategy 2 calculations, the pressure rise across the fan adjusts itself automatically, though the computations at stall need to be conducted in a time-accurate fashion. The nozzle boundary condition mechanism is based on a delicate balance which requires that a static pressure rise across the fan must be offset by a static pressure drop in the downstream nozzle. If the inlet total pressure is the same as the exit static pressure, the boundary conditions are consistent with the zero flow case. If the exit static to inlet total pressure ratio is set as high as the minimum fan pressure ratio during the stall loop, the boundary conditions remain consistent with the overall minimum flow rate. If the ratio is set higher than the minimum fan pressure ratio during the stall loop, the fan flow (static pressure rise) becomes inconsistent with the nozzle flow (static pressure drop) and the flow rate changes in an attempt to reach equilibrium. Starting from a drop in the mass flow, the hysteresis loop, can be described as follows. As the mass flow decreases, the pressure rise also decreases and the system moves to a lower pressure ratio along a constant throttle-area line. In this new operating condition at a reduced pressure ratio, the mass flow increases and the fan tries to move to its original working line. This causes an increase in the pressure ratio and the mass flow drops.

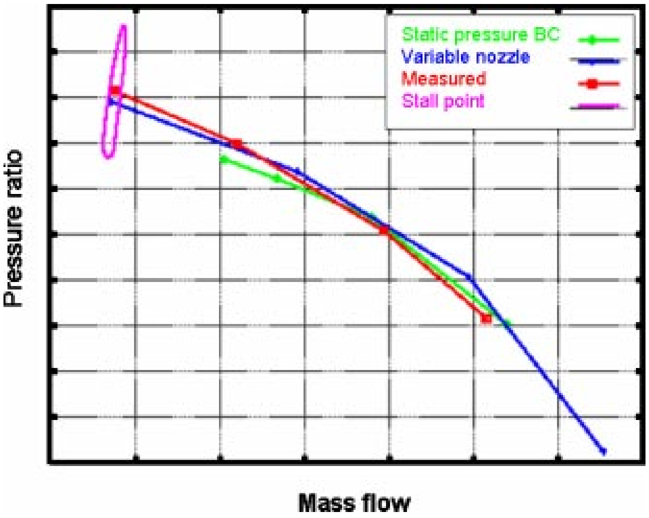

Fig. 2 Compressor characteristic at 70%. Strategy 1 predictions, Strategy 2 predictions and measured data

The hysteresis characteristic in Fig. 2 was determined from the pressure and mass flow time histories of the time-accurate calculations at stall. The corresponding mean value, part of the predicted data curve in Fig. 2, compares very well to the corresponding measured characteristic point. A further set of calculations was made for the design speed and the stall boundary was determined from the hysteresis loop. The predicted and measured results for both speeds are plotted in Fig. 3. Using this technique, the stall line can be determined accurately, though a straight line is used in Fig. 3 for illustration purposes. Finally, as can be seen from Fig. 4, the stall loop is repeated in time, here shown as engine revolution.

Table 1 Comparison of Strategies 1 and 2

	Strategy 1 Without nozzle or intake	Strategy 2 With nozzle and intake
Inlet boundary condition	Corrected atmospheric total pressure 2 flow angles Total temperature	Atmospheric total pressure Atmospheric total temperature Axial flow
Outlet boundary condition	Radially-constant static pressure	Atmospheric static pressure
Point control	Change back pressure	Change nozzle area
Calculation type	Steady-state	Steady-state Time-accurate at stall

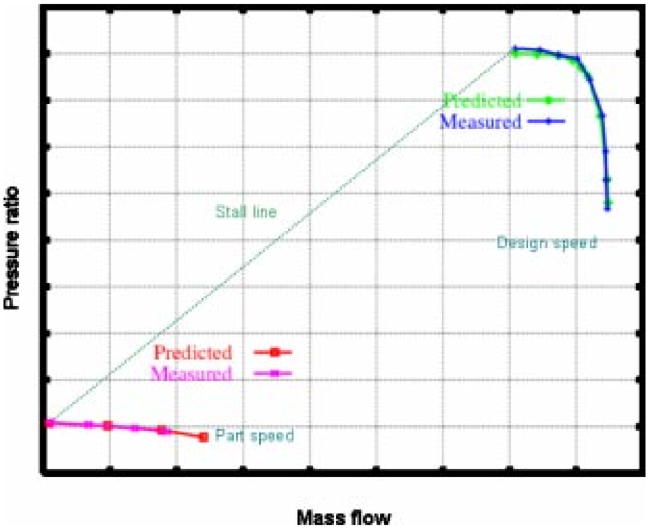

Fig. 3 Computed vs measured at design speed and 70% part-speed

2.3 Further Considerations[1].

- During the Strategy 2 computations, which include an extended domain and variable-area downstream nozzle, constant atmospheric static pressure is used as the exit boundary condition and the area of the nozzle is decreased to approach the stall boundary. The purpose of the extended domain is to provide solution stability by allowing the flow to develop more naturally downstream of the fan. The nozzle has two purposes. First it provides a means of controlling the actual operating point on a given speed characteristic by area change. Second, as will be discussed later, it goes some way towards making the varying flow inside the domain and the radially constant exit static pressure compatible by providing a stabilizing mechanism since the fan pressure rise is balanced by the nozzle static pressure drop. (At the limit, if the nozzle is choked at stall, the flow inside the domain will become totally independent of the exit static pressure, though this was not the case during the computations since there is less flow near stall.) In any case, the steady-state Strategy 1 computations were repeated with an extended domain but without a nozzle and it was not possible to reach the stall boundary. However, the new computations converged quicker near stall, or at a high working line, and managed to get closer to the stall boundary than the standard-domain computations.

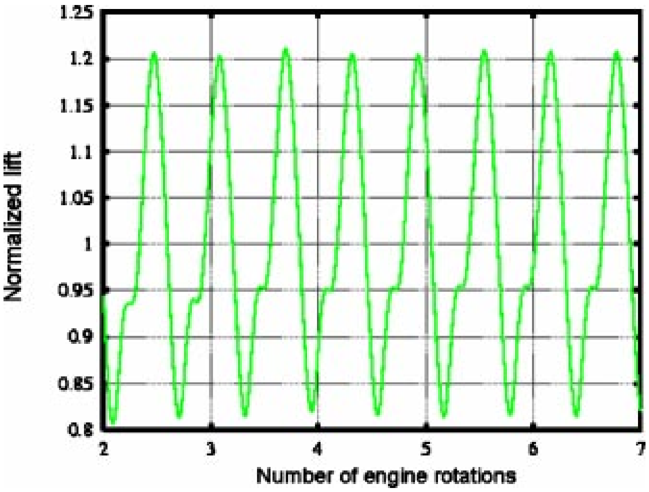

Fig. 4 Time history for blade lift

- Intuitively, it may be speculated that the main effect of the extended domain is to make the flow more uniform towards the exit boundary, thus making it more compatible with the imposed exit static pressure. It can, therefore, be argued that if extended-domain Strategy 1 computations are conducted in a time-accurate fashion, the stall boundary may be reached without a nozzle. However, no convergence was obtained in spite of several attempts.
- Away from stall, changing the value of the exit pressure is equivalent to changing the nozzle area and this can be observed from Fig. 2 by noticing the similarity of the speed characteristic predicted by the two strategies until the stall boundary is reached. However, as discussed above, the nozzle is needed to provide stability once the stall boundary is reached.
- Since the fan introduces swirl to the flow and there are no flow straightening devices, such as outflow guide vanes (OGVs), in the model, a certain amount of swirl may well reach the outflow boundary, thus creating an incompatibility with the imposed radial-equilibrium boundary condition. However, because of the additional length provided by the extended domain and the presence of the nozzle, it is unlikely that the flow behind the fan will have been affected by the imposed boundary conditions.

3 Concluding Remarks

(i) The variable-nozzle method not only provides a means of obtaining the compressor characteristic past stall but is also explains why standard single passage steady-state computations are ill-conditioned near the stall boundary;
(ii) the proposed variable-nozzle method can easily be extended to detailed surge modeling. The inclusion of two large plenum volumes, one upstream of the intake and the other downstream of the nozzle, will allow the direct use of atmospheric conditions at both ends, as in the current stall study. This issue will be addressed in a forthcoming paper.

Acknowledgment

The authors thank Rolls-Royce plc for sponsoring the work and allowing its publication.

References

[1] Freeman, C., 1992, "The Effect of Aircraft Inlets on the Behavior of Aero Engine Axial Flow Compressors," VKI Lecture Series, Axial Flow Compressors, 1992–02
[2] Day, I. J., 1992, "Stall and Surge in Axial Flow Compressors," VKI Lecture Series, Axial Flow Compressors, 1992–02.
[3] Longley, J. P., and Hynes, T. P., 1990, "Stability of Flow Through Multi-stage Axial Compressors," ASME J. Turbomach., **112**(1), pp. 126–132.
[4] Weigl, H. J., Paduano, J. D., Fréchette, L. G., Epstein, A. H., Greitzer, E. M., Bright, M. M., and Strazisar, A. J., 1998, "Active Stabilization of Rotating Stall and Surge in a Transonic Single-Stage Compressor," ASME J. Turbomach., **120**(4), pp. 625–636.
[5] Moore, F., and Greitzer, E. M., 1986, "A Theory of Post-Stall Transients in Axial Compressors—Part I: Development of the Equations," ASME J. Eng. Gas Turbines Power, **108**(1), pp. 371–379.
[6] Sayma, A. I., Vahdati, M., Sbardella, L., and Imregun, M., 2000, "Modeling of 3D Viscous Compressible Turbomachinery Flows using Unstructured Hybrid Grids," AIAA J., **38**(6), pp. 945–954.

---

[1] The contribution of the Reviewers is gratefully acknowledged.

Active Control of Tip Clearance Flow in Axial Compressors

Jin Woo Bae[1]
Gas Turbine Laboratory,
Massachusetts Institute of Technology,
Cambridge, MA

Kenneth S. Breuer
Division of Engineering,
Brown University,
Providence, RI

Choon S. Tan
Gas Turbine Laboratory,
Massachusetts Institute of Technology,
Cambridge, MA

Control of compressor tip clearance flows is explored in a linear cascade using three types of fluidic actuators; normal synthetic jet (NSJ; unsteady jet normal to the mean flow with zero net mass flux), directed synthetic jet (DSJ; injection roughly aligned with the mean flow), and steady directed jet (SDJ), mounted on the casing wall. The effectiveness of each active control technique is determined in terms of its ability to achieve: (1) reduction of tip leakage flow rate, (2) mixing enhancement between tip leakage and core flow, and (3) increase in streamwise momentum of the flow in the endwall region. The measurements show that the NSJ provides mixing enhancement only, or both mixing enhancement and leakage flow reduction, depending on its pitchwise location. The DSJ and SDJ actuators provide streamwise momentum enhancement with a consequent reduction of clearance-related blockage. The blockage reduction associated with the use of NSJ is sensitive to actuator frequency, whereas that with the use of DSJ is not. For a given actuation amplitude, DSJ and SDJ are about twice as effective as NSJ in reducing clearance-related blockage. Further the DSJ and SDJ can eliminate clearance-related blockage with a time-averaged momentum flux roughly 16% of the momentum flux of the leakage flow. However, achieving an overall gain in efficiency appears to be hard; the decrease in loss is only about 30% of the expended flow power from the present SDJ actuator. Guidelines for improving the efficiency of the directed jet actuation are presented. [DOI: 10.1115/1.1776584]

Introduction

Background and Technical Goal. The relative motion between rotor tips and stationary casing wall in axial compressors requires finite spacing between the two. The most common way to achieve this is to have a finite clearance (~0.01 of blade span) at the rotor tip. The pressure difference across the blade causes a leakage flow through the tip clearance from the pressure surface to the suction surface of the blade. This tip leakage flow dominates the aero-thermodynamic behavior of the flow in the tip region and has a strong impact on pressure rise capability, compressor efficiency, and stability. The influence of tip leakage flow manifests itself in two manners: a blockage that effectively reduces the pressure rise capability and a loss that affects the efficiency of the compressor.

Even though the detrimental effects of an increase in tip clearance are well known (Wisler [1], Smith [2], and Cumpsty [3]), compressors often operate with tip clearances that are larger than aerodynamically desirable due to changes in tip clearance during operations and limitations in manufacturing tolerances. Consequently, there is strong motivation to look for means to relieve the stringent requirement on tight tip clearance and manage the compressor tip clearance flow to minimize its impact on performance. A potential technique for accomplishing this is active flow control and this constitutes the overall technical goal of the work described in this paper on the use of fluidic actuators to beneficially affect the behavior of compressor tip clearance flow.

This paper is organized as follows. First we introduce the control schemes explored in this paper. Then the experimental setup is described. Experimental results and their analyses are discussed subsequently. Finally we present a summary and conclusions.

Approach. Tip clearance flow control using the following three types of fluidic actuators mounted on the casing wall is examined: normal synthetic jet (NSJ; unsteady jet with zero net mass flux normal to the mean flow), directed synthetic jet (DSJ; injection roughly aligned with the mean flow), and steady directed jet (SDJ). Three metrics are used to measure the effectiveness of tip clearance flow control: (i) reduction of the tip leakage flow rate, (ii) mixing enhancement between the defect region of the tip clearance vortex and the primary stream flow, and (iii) streamwise momentum enhancement.

The first scheme is to address the problem at the source by reducing the rate of the leakage flow using NSJ, as illustrated in **Fig. 1**. The momentum flux of NSJ modifies the streamline next to the casing wall so to effectively reduce the tip clearance. Because the leakage jet is driven by the pressure difference across the blade, which is largely set by the midspan loading (Storer [4]), reduced clearance size will result in a reduced leakage flow rate.

The second scheme, namely mixing enhancement, is to make the wake-like velocity defect region more uniform as illustrated in **Fig. 2**, thus reducing the growth of the defect region, which determines the flow blockage in the blade passage. The idea is to exploit a fluid dynamic mechanism/process that may exist to efficiently promote momentum transfer/transport from the high momentum main flow to the low momentum flow in the endwall region.

The third one (momentum injection) is to energize the retarded flow in the endwall region using momentum flux of the DSJ or SDJ as shown in **Fig. 3**.

Experimental Setup

Introduction. A linear cascade has been designed and fabricated to be tested in a low-speed wind tunnel. Because of the cost-effectiveness and experimental simplicity versus rotating rigs, cascade tunnels have been used to study tip clearance flows (Storer and Cumpsty [5], Heyes et al. [6], Bindon [7], and Saathoff and Stark [8]). Moreover Khalid [9] pointed out the dominant role of the tip clearance on endwall flow structure by using a computational method eliminating different physical effects one at a time, which showed that for this configuration the relative motion of the casing wall or the endwall boundary layer skew results in minor changes in the endwall flow field.

---

[1] Presently at Display Division, ILJIN Diamond, Korea.

Contributed by the International Gas Turbine Institute and presented at the International Gas Turbine and Aeroengine Congress and Exhibition, Atlanta, GA, June 16–19, 2003. Manuscript received by the IGTI December 2002; final revision March 2003. Paper No. 2003-GT-38661. Review Chair: H. R. Simmons.

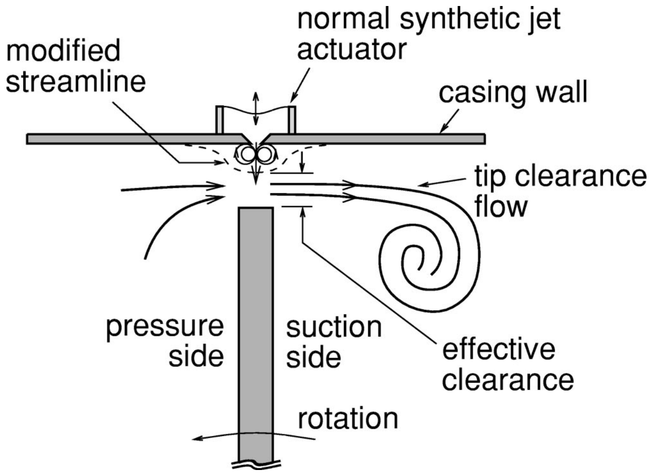

Fig. 1 Illustration of tip leakage flow rate reduction scheme

Table 1 Summary of cascade design parameters

Airfoil	G.E. E^3 rotor B tip section
Chord, C	0.190 m
Pitch, s	0.177 m
Span, h	0.305 m
Camber	30.7°
Stagger	56.9°
Reynolds number	$\geqslant 1.0\times 10^5$
Inlet flow angle, β_{in}	62.7°
Exit flow angle, β_{ex}	51.8°
Diffusion factor	0.40

Linear Cascade Wind Tunnel. **Table 1** summarizes the design parameters of the cascade test section, intended to be geometrically representative of a rotor tip section in a modern aero-engine compressor. The schematic of the cascade test section is shown in **Fig. 4**. The inlet of the test section is attached to the 0.30 m×0.30 m contraction exit of a wooden wind tunnel settling chamber. There are five blade contour slots on the bottom wall with the blades inserted into the test section from the bottom and held by brackets underneath the bottom wall.

Two blades are instrumented with static pressure taps to check the midspan loading distribution. All the blades are interchangeable and three central blades in the test section are cantilevered at the roots to allow variable tip clearances. A 7 mm wide transition strip made out of 50-grit sandpaper is glued on the suction surface of each blade at 42%C from the leading edge to allow operation at low Reynolds number without laminar separation. The outlet screen pressurizes the test section so that wall boundary layers can be removed by bleeding to atmospheric pressure through slots. There are endwall bleed slots on the top and bottom walls near the inlet of the test section as shown in the schematic. Periodicity is achieved by adjusting the bleed ports on the sidewalls.

The jet actuator is attached to the endwall as shown in **Fig. 4** and sits in a slot machined through the casing wall. The angle of the two exit sidewalls downstream of the blades is set by the midspan exit flow angle as obtained from the MISES code, [10].

To assess the effects of actuation on the time-averaged performance of the compressor cascade, total pressure is surveyed using a Kiel probe in the survey plane, 5%C downstream of the trailing edge plane as shown in **Fig. 4**. The Kiel probe with 3.2 mm outer diameter head manufactured by United Sensor is attached to a three-axis TSI® traverse table model 9400, which has 0.01 mm position resolution with built-in backlash compensation loop. The traversing is programmed and performed automatically over the survey area (1 pitch×0.5 span) with a mesh size of 19 (pitchwise) ×13 (spanwise).

Uncertainties in each measurement are estimated by small-sample method (Kline and McClintock [11]) with odds 20:1 and are presented as error bars in each data plot throughout the paper.

Flow Blockage. The effect of tip clearance size on pressure rise is quantified by measuring the endwall blockage as a function of tip clearance size. The flow blockage is defined as

$$A_b=\int\left(1-\frac{U_x}{U_{x,\mathrm{edge}}}\right)dA.$$

In computing the blockage from the total pressure loss coefficient survey data, it is assumed that the survey plane static pressure is uniform and equal to the exit static pressure measured with the taps on the casing wall and the flow is unidirectional in the direc-

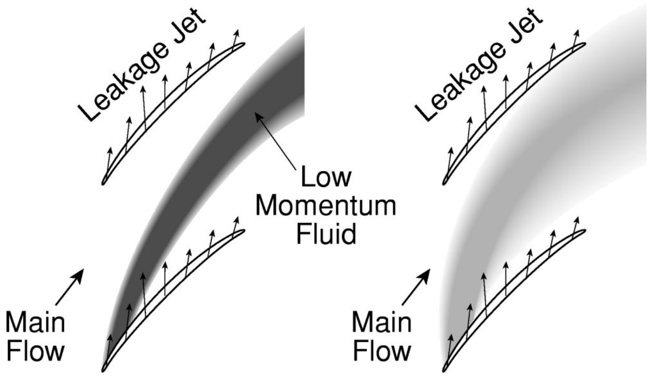

Baseline Case **Forced-Mixing Case**

Fig. 2 Illustration of mixing enhancement scheme

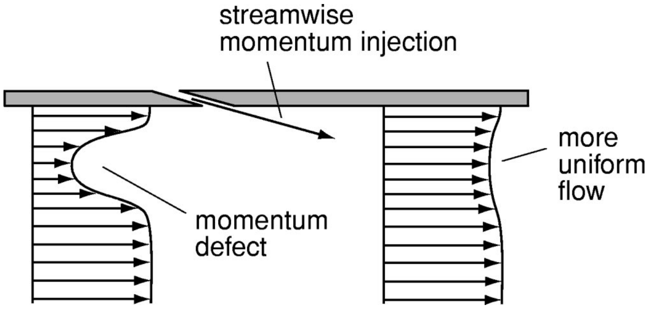

Fig. 3 Illustration of streamwise momentum injection scheme

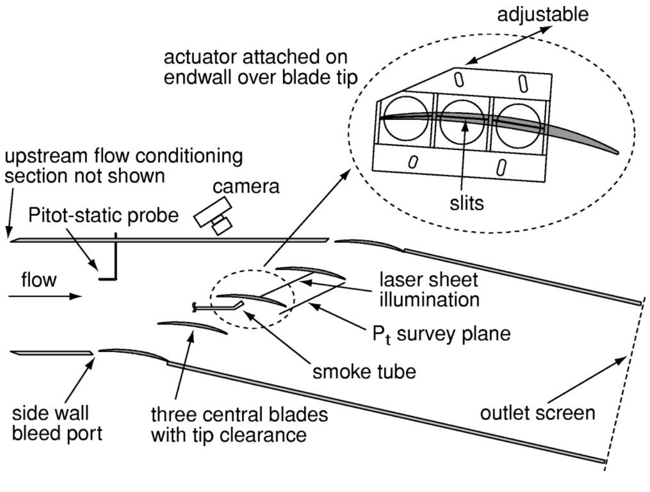

Fig. 4 Schematic of cascade wind tunnel test section

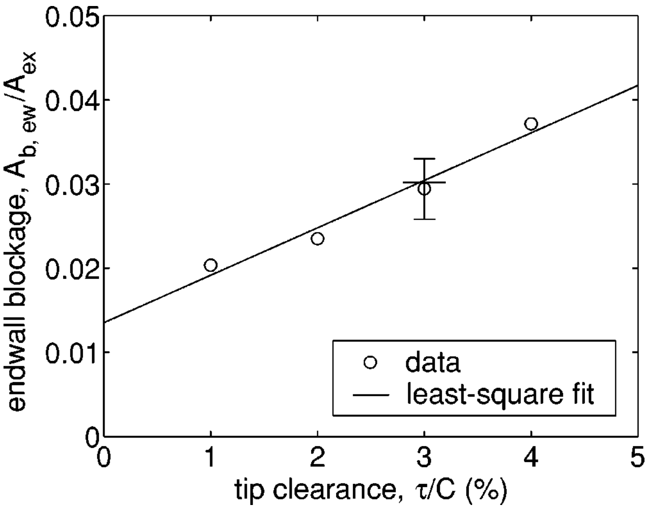

Fig. 5 Endwall blockage measured 5%*C* downstream of trailing edge plane versus tip clearance size. No actuation is applied.

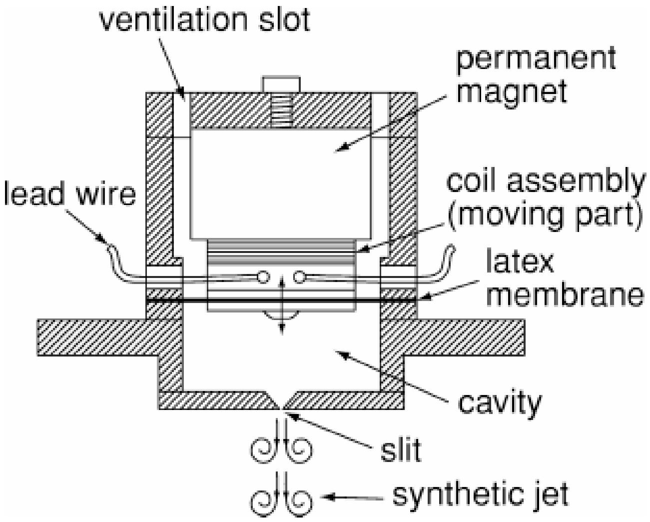

Fig. 6 Schematic of the synthetic jet actuator used in the cascade rig. Configuration of the normal synthetic jet (NSJ) actuator with slit

tion of the mass-averaged exit flow angle near midspan predicted by MISES. The axial velocity in the plane is then

$$U_x = U_\infty \sqrt{(1-\omega - C_{P,ex})}\cos\beta_{ex}\,.$$

The endwall blockage is computed by subtracting the blockage associated with the blade surface boundary layers from the total blockage:

$$A_{b,ew} = A_b - \left(\delta^* \times \frac{h}{2}\right)$$

where δ^* is the displacement thickness of the blade wake near midspan and h is the length of the blade span. The endwall blockage versus tip clearance size is shown in **Fig. 5** where the endwall blockage is normalized by the exit area, $A_{ex} = s \times h$. The uncertainty introduced by the assumption and the measurement error is estimated for 3%C clearance and the uncertainty bound with 95% confidence level is shown in **Fig. 5**. The solid line is the least-square fit of the data points. The endwall blockage increases approximately linearly with tip clearance.

The tip clearance-related blocked area, $A_{b,\mathrm{tip}}$ is obtained by subtracting the endwall blockage at 0%C clearance, i.e., the y-intercept of the least-square fit line multiplied by the exit area, from the endwall blockage, $A_{b,ew}$. Changes in endwall blockage can be directly related to changes in tip clearance-related blockage and hence it can be used to measure the effectiveness of the fluidic actuation on the reduction of the tip clearance-related blockage.

Actuator. The schematic of the actuator used is shown in **Fig. 6**. This actuator is widely known as synthetic jet actuator (Amitay et al. [12], Smith et al. [13]) and it consists of a vibrating membrane, a cavity, and a slit (for NSJ) or holes (for DSJ). There are three isolated synthetic jet actuators inline in the direction normal to **Fig. 6**.

The normal synthetic jet (NSJ) actuator has three straight slits that are shaped to approximately follow the camberline of the blade (**Fig. 4**) while the directed synthetic jet (DSJ) actuator has four tilted holes per actuator (12 holes total) that are directed approximately to the chordwise direction and tilted by 25 deg from the casing wall (**Fig. 7 and Fig. 8**). The actuator covers the first 70%C from the leading edge because most of the benefit associated with actuation is expected to be attained near the leading edge (Khalid et al. [14]). To study the dependence on pitchwise location of the actuator, the casing wall with the actuator has been made adjustable in the pitchwise direction as indicated in **Fig. 4** and **Fig. 8**. The dimensions of the actuator are summarized in **Table 2**.

For SDJ actuation, the housing of the voice coil actuator and membrane is replaced with a plenum that supplies regulated shop air to the 12 holes on the plates. The flow rate into the plenum is regulated using a pressure regulator and a needle valve and is measured using a flow meter.

Normal Synthetic Jet Actuation

The effects of actuation on the time-averaged change in tip clearance-related blockage and loss were determined and are outlined in the following paragraphs. Specifically, we examine the

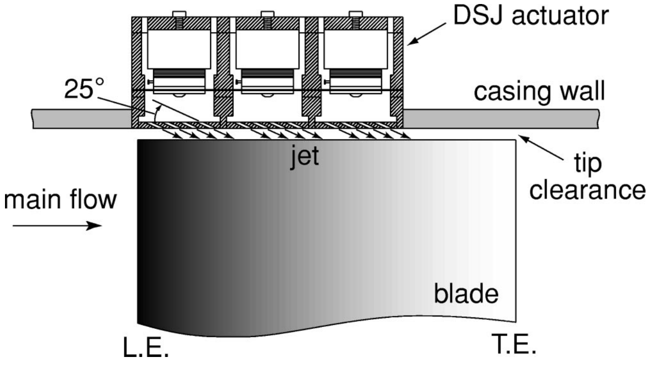

Fig. 7 Schematic of the DSJ actuator mounted on the casing wall

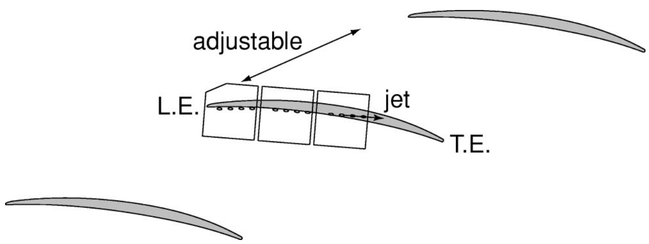

Fig. 8 Schematic of the directed synthetic jet (DSJ) actuator mounted on the casing wall showing the direction of the jet

Table 2 Dimensions of synthetic jet actuator

External length	136.5 mm
External width	47.6 mm/85.7 mm (including mounting flanges)
External height	56.1 mm
Cavity volume per actuator	1.52×10^4 mm^3
Slit/hole plate thickness	3.18 mm
Slit width (NSJ)	0.254 mm
Slit area per actuator (NSJ)	10.5 mm^2
Hole diameter (DSJ)	1.59 mm
Hole length (DSJ)	7.51 mm
Hole area per actuator (DSJ)	7.92 mm^2

influence of four parameters: actuator type (NSJ, DSJ, or SDJ), pitchwise location of the actuator on the casing relative to blade tip location, amplitude of actuation, and frequency at which the actuation is applied. The parametric dependence of the tip clearance-related blockage and loss on the actuation amplitude and frequency is assessed. The flow processes responsible for the observed change in the blockage and loss are also identified.

Effect of NSJ on Total Pressure Contours. **Figure 9(*b*)** and **(*c*)** show the contour plots of ω taken with two pitchwise locations of the NSJ actuator: **(*b*)** directly over the blade tip and **(*c*)** approximately over the vortex core[2] as indicated by the arrows. There is noticeable change in the contours for both locations compared to the baseline in **(*a*)**. Quantitative measurements are discussed below.

Scaling of NSJ Actuator Amplitude. The momentum coefficient of the actuator (momentum of the actuator jet normalized by the momentum of the leakage flow) is used as a measure of the actuation amplitude. The leakage flow momentum is approximated based on the far upstream flow velocity. Although the magnitude of the leakage jet velocity varies over the blade chord, it scales with U_∞ and is well approximated by U_∞ for different tip clearance sizes (Bae [15]). The momentum coefficient is thus defined as

$$C_{\mu,\tau}=\frac{\rho U_{J,\mathrm{peak}}^2 A_J}{\rho U_\infty^2 \tau C}.$$

Figure 10 shows the tip clearance-related blockage versus amplitude of actuation for two tip clearances. The NSJ actuator is placed at a pitchwise location 0.25*s* (25% pitch) from the camberline of the center blade so that it is approximately over the vortex core. The blockage (mostly dominated by that associated with tip leakage flow) has been normalized by the baseline blockage of each clearance. The data set collapses onto a single curve with the implication that the actuator momentum scales with the leakage flow momentum. Most of the tip clearance-related blockage can be eliminated using the NSJ actuator at $C_{\mu,\tau}$ of approximately 1.5.

The endwall blockages taken with two upstream velocities are plotted against the actuator amplitude in **Fig. 11**. The horizontal lines are the baseline blockages without actuation at each clearance (**Fig. 5**). The two data sets form a single trend when plotted nondimensionally against $C_{\mu,\tau}$ showing that the definition of $C_{\mu,\tau}$ appropriately reflects the dependence of the blockage reduction on the far upstream velocity.

Dependence on Forcing Frequency of NSJ. The blockage reduction achieved with the use of NSJ exhibits considerable sen-

---

[2] The actuator covers 70%C from L.E. Therefore, the NSJ slits upstream of the survey plane are approximately over the vortex core, although the arrow projected onto the survey plane appears to be closer to SS than the core.

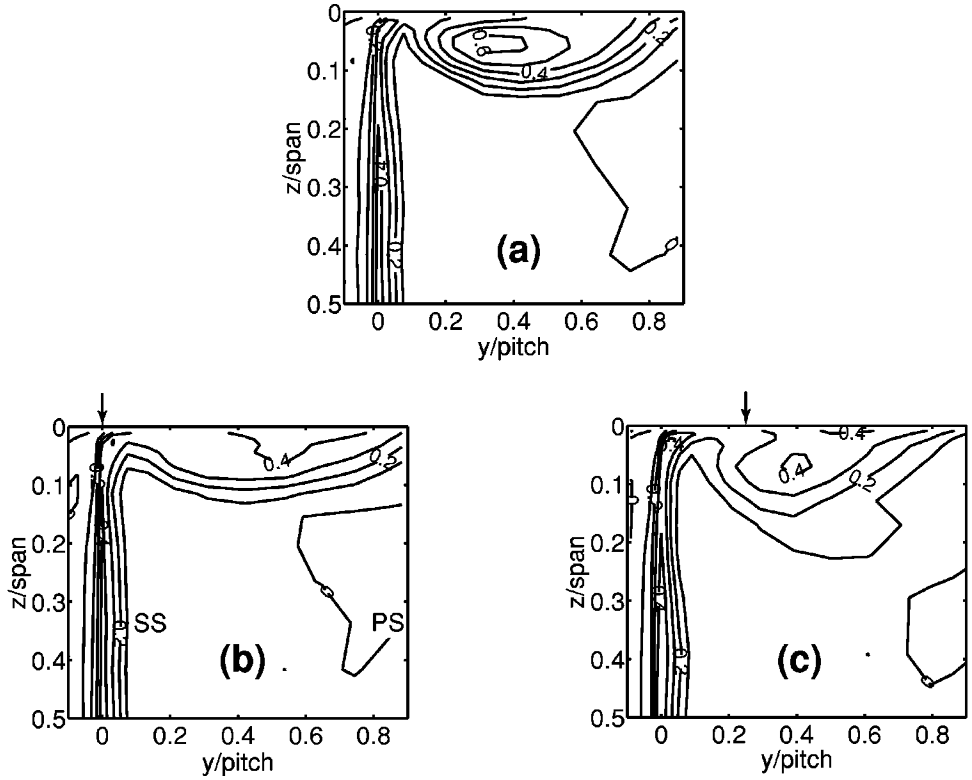

Fig. 9 Contours of ω measured 5%C downstream of trailing edge plane: (*a*) baseline without actuation, $\tau=3\%C$; (*b*) NSJ directly over blade tip (at 0% pitch), $C_{\mu,\tau}=0.88$, $F_C^+=1.0$; (*c*) NSJ over vortex core (at 25% pitch), $C_{\mu,\tau}=0.88$, $F_C^+=1.0$. Arrows indicate pitchwise locations of NSJ slits.

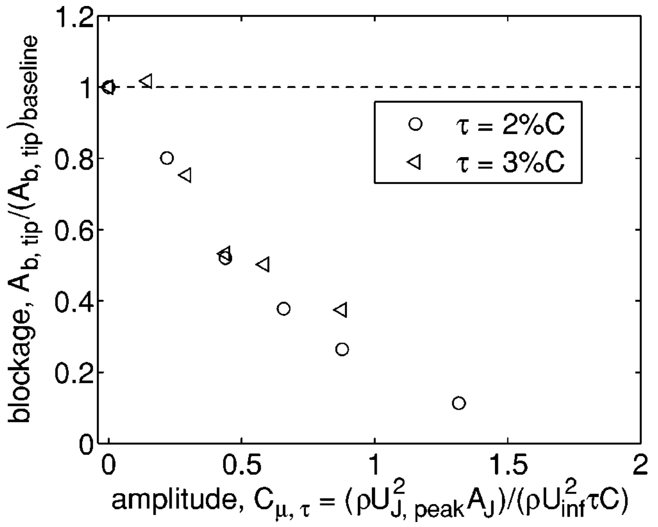

Fig. 10 Tip clearance-related blockage versus NSJ actuator amplitude. Actuator near the vortex core. $F_C^+=1.0$.

sitivity to the forcing frequency. Thus we need to first identify/define a reduced frequency parameter, which scales this sensitivity. It was suggested that the observed reduction in blockage is associated with the instability of the shear layer developed at the blade tip as in the mixing enhancement of two-dimensional wall-bounded jets (Katz et al. [16] and Tsuji et al. [17]). If that is the case, the frequency should scale with the height of the wall jet or the tip clearance size τ. **Figure 12** shows the frequency response of the endwall blockage taken with NSJ actuator placed at 25% pitch. There are two data sets with two tip clearance sizes. In **Fig. 12(*a*)**, the tip clearance size τ is used to non-dimensionalize the forcing frequency as follows:

$$\beta_\tau = \frac{2\pi f \tau}{U_\infty}.$$

The blockage is the most responsive when forced at $\beta_\tau = 0.05 \sim 0.25$. However, the troughs of the endwall blockage for the two data sets do not line up vertically as indicated with the dashed line, implying that the flow mechanism is not related to the shear layer instability.

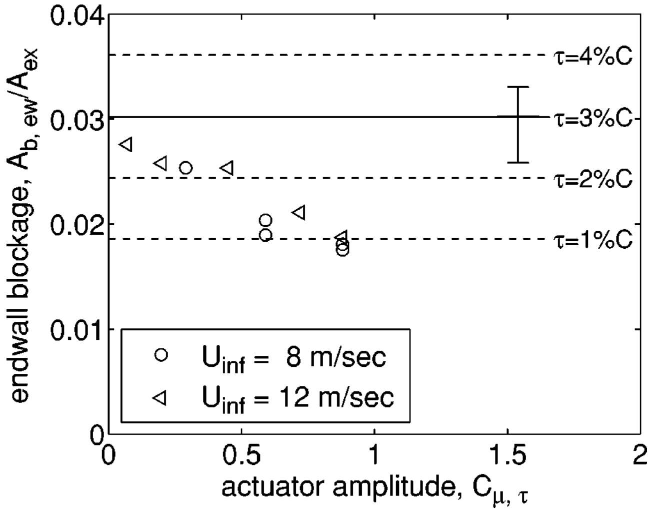

Fig. 11 Endwall blockage versus $C_{\mu,\tau}$ with NSJ directly over blade tip. Data sets taken for two upstream velocities. $\tau=3\%C$, $F_C^+=1.0$.

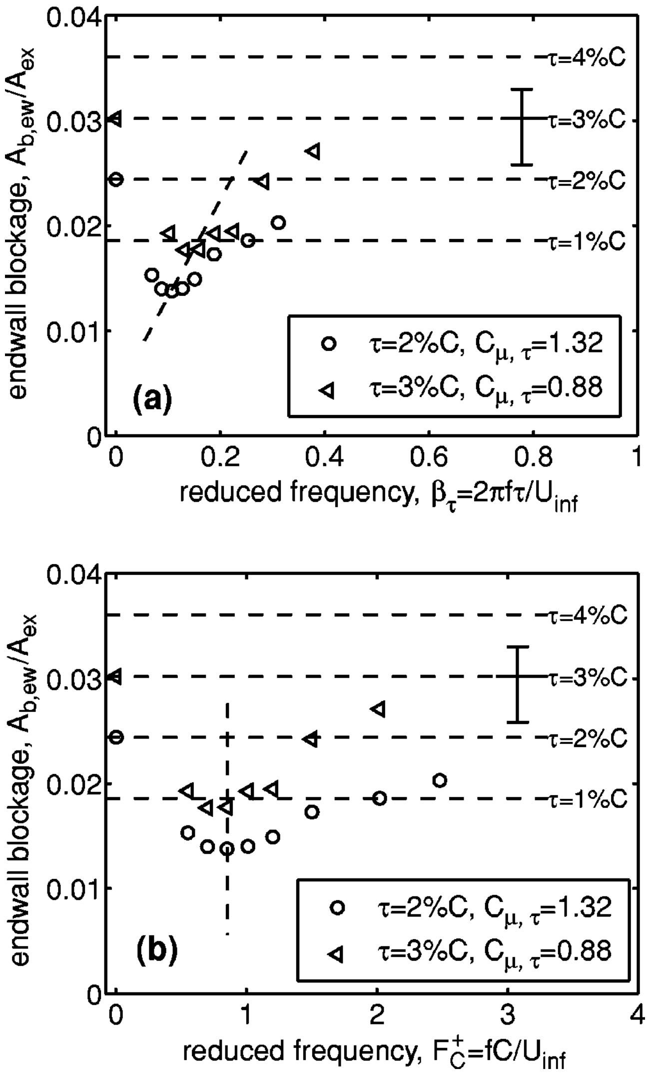

Fig. 12 Frequency dependence of blockage reduction with NSJ actuator over the vortex core: (*a*) using clearance size τ; (*b*) using blade chord *C* as length scale

In **Fig. 12(*b*)**, the blade chord length C is used instead of τ to non-dimensionalize the forcing frequency as follows[3]:

$$F_C^+ = \frac{fC}{U_\infty}.$$

The blockage is the most responsive when forced at a reduced frequency F_C^+ of about 0.75 and the troughs of the endwall blockage for the two data sets both nearly line up vertically.

A similar trend is obtained for data taken with the NSJ actuator acting directly over the blade tip, for three tip clearances. Again, the blockage troughs line up vertically at a reduced frequency F_C^+ of about 1.0 when the blade chord length is used to nondimensionalize the forcing frequency, [15].

It is deduced that the most effective frequency for blockage reduction using the NSJ corresponds to the periodic unsteadiness of the tip clearance vortex. Bae [15] put forward a hypothesis that the mechanistic origin of this tip vortex unsteadiness is analogous to the Crow instability associated with trailing vortices downstream of wing, [18].

---

[3] The factor of 2π only appears in the definition of β_τ. The above definition of β_τ is typically used in the wall jet stability community, while that of F_C^+ is in the flow separation control community.

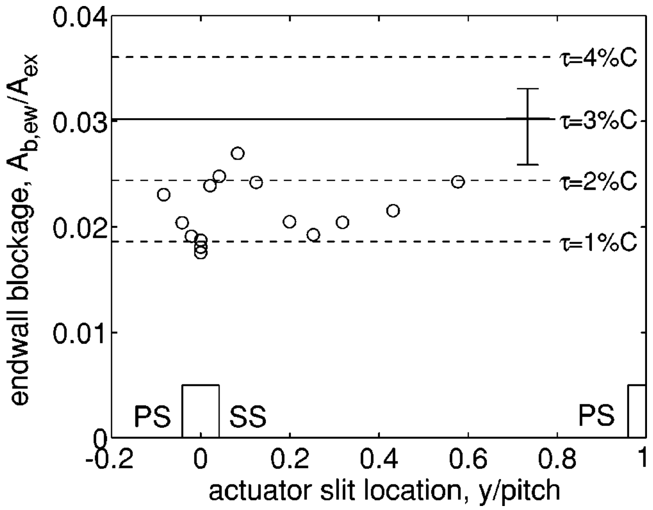

Fig. 13 Endwall blockage versus pitchwise location of the NSJ actuator. $\tau/C=3\%$, $C_{\mu,\tau}=0.88$, and $F_C^+=1.0$.

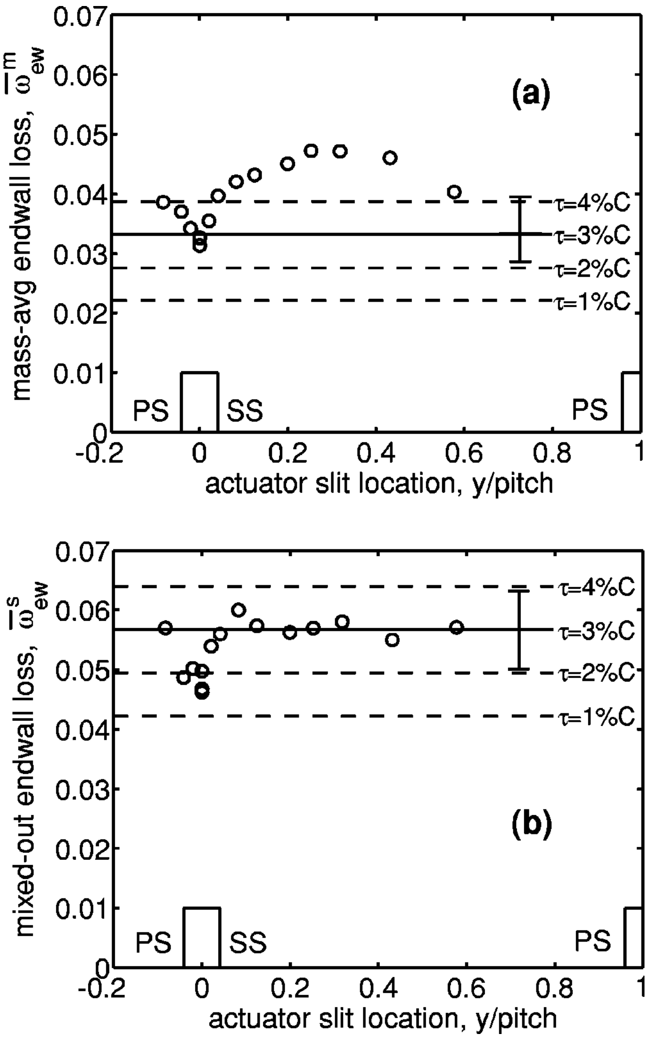

Fig. 14 Endwall total pressure loss coefficient versus pitchwise location of NSJ actuator. $\tau/C=3\%$, $C_{\mu,\tau}=0.88$ and $F_C^+=1.0$: (*a*) mass-averaged ω; (*b*) stream thrust-averaged (or fully mixed-out) ω.

Dependence on Pitchwise Location of NSJ. The casing wall with the actuator is adjustable in the pitchwise direction and the survey of total pressure loss coefficient was carried out with various pitchwise NSJ slit locations. **Figure 13** shows the dependence of the blockage reduction on the pitchwise location of the NSJ actuator with $3\%C$ clearance. The baseline blockage without actuation is indicated with a solid horizontal line. The locations of the blades are indicated in the bottom of the figure. There are two local optimum pitchwise locations for blockage reduction: one right over the blade tip and the other over the vortex core. At these optimum pitchwise locations, the tip clearance-related blockage is reduced by about 66%, which is equivalent to the baseline case with $1\%C$ clearance. The actuator amplitude and frequency were fixed at $C_{\mu,\tau}=0.88$ and $F_C^+=1.0$. The bulk flow process responsible for the blockage reduction will be discussed later.

Total pressure loss coefficient variation with pitchwise location of the NSJ is shown in **Fig. 14**. **Figure 14**(***a***) shows that the mass-averaged loss increases with actuation compared to the baseline (the solid horizontal line) except for the data with the actuator over the blade tip where it remains more or less the same. The mass-averaged loss is largest at around 0.25 *pitch* where the blockage reduction is locally largest as shown in **Fig. 13**. Tip clearance-related loss at 0.25 *pitch* is increased by roughly 83% to the same level as the extrapolated baseline case with $5.5\%C$ clearance. **Figure 14**(***b***) shows the stream thrust-averaged (i.e. mixed-out) loss vs. the pitchwise location of the NSJ actuator. The stream thrust-averaged loss remains more or less the same as the baseline when the actuator is away from the blade tip. However, when the actuator is right over the blade, the tip clearance-related stream thrust-averaged loss is reduced by about 33% so that it is the same as the baseline case with $2\%C$ clearance.

Bulk Flow Process Associated With NSJ Actuation. The dependence of the blockage reduction on the forcing frequency excludes momentum injection as a source because the same time-averaged momentum results in almost no change in blockage at frequencies far away from the optimum, as shown in **Fig. 12**. Two possible bulk flow processes associated with the NSJ actuation can be suggested as responsible for the reduction in tip clearance-related blockage: leakage flow reduction and mixing enhancement. Kang et al. [19] showed that the NSJ actuation does not change the leakage flow rate when placed away from the blade tip. Blockage reduction with the actuator over the vortex core is thus attributed to the mixing enhancement. Mixing enhancement shortens the distance for mixing and consequently increases the mass-averaged loss, although the stream thrust-averaged loss is not changed (See **Fig. 14** at $y=0.25$ pitch).

The blockage reduction with the NSJ actuator over the blade tip is a combination of the two flow processes. As observed by Kang et al. [19] the NSJ actuator can reduce the amount of the leakage flow for a given pressure difference across the blade when it is placed over the blade tip. One can indirectly quantify the reduction in the leakage flow rate in the cascade experiment from the stream thrust-averaged loss measurements shown in **Fig. 14**(***b***). The reduction in the stream thrust-averaged loss with the NSJ actuator over the blade tip is attributed to a reduction in the leakage flow rate. The model of Storer and Cumpsty [20] suggests that for fixed midspan loading tip clearance-related loss increases linearly with the leakage flow rate. The 33% reduction in the tip clearance-related stream thrust-averaged loss shown in **Fig. 14**(***b***) leads one to conclude that the leakage flow rate is reduced by about 33% due to the NSJ actuation over the blade tip. The 33% reduction in the leakage flow rate results in a 33% reduction of tip clearance-related blockage and loss, which are proportional to the leakage flow rate, as summarized in the second row of **Table 3**. About half of the blockage reduction is thus viewed as due to the leakage flow reduction.

As described in Bae et al. [21], the NSJ actuator over the blade

Table 3 Effects of each flow process and their combined effects on tip clearance-related blockage and loss explaining observations with the NSJ actuator over the blade tip

	Blockage	Mass-Averaged Loss	Fully Mixed-Out Loss
Leakage flow reduction	↓ Decrease by 33%	↓ Decrease by 33%	↓ Decrease by 33%
Mixing enhancement	↓ Decrease by 33%	↑ Increase by 33%	- Same
Net effect	↓↓ Decrease by 66%	- Same	↓ Decrease by 33%

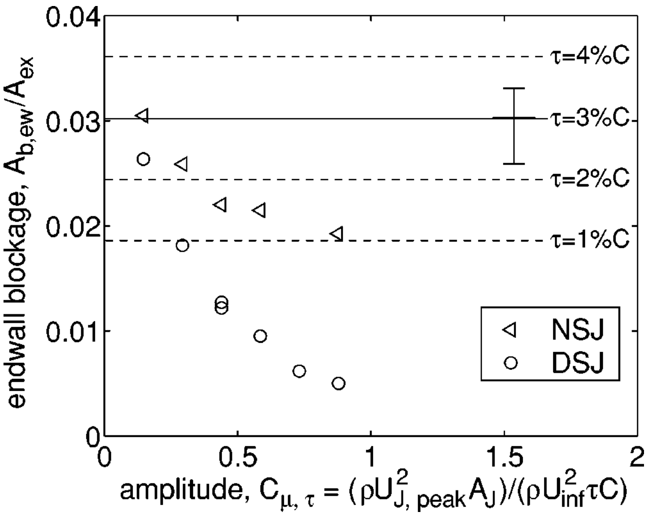

Fig. 16 Comparison between DSJ (placed near the pressure surface of the blade) and NSJ (placed near the vortex core). $\tau = 3\% C$. Both actuators at $F_C^+ = 1.0$.

tip also brings about mixing enhancement with the other half of the blockage reduction attributed to this effect. The net effects of the two flow processes on the tip clearance-related blockage, mass-averaged, and stream thrust-averaged losses are listed in **Table 3**. The net effect on the mass-averaged loss remains the same as a result of the compensating effect of the tip leakage flow reduction and the mixing enhancement. In summary, both leakage flow reduction and mixing enhancement are responsible for the reduction in blockage with the NSJ actuator over the blade tip and their contributions are roughly the same.

Directed Jet Actuation

Effect of DSJ on Total Pressure Contours. **Figure 15** shows a representative result of the DSJ actuation compared with the baseline. There are substantial changes in the endwall flow.

As with the experiments on the NSJ, the dependence on the amplitude, frequency, and pitchwise location of the DSJ actuator were determined. We also compare the use of a SDJ (steady directed jet) against a DSJ to determine if steady injection of momentum with the same time-averaged value as that from the DSJ yields similar benefit.

Dependence on Amplitude of DSJ. The response of the endwall blockage with the use of DSJ actuation is compared with that with the use of NSJ actuation in **Fig. 16**. The endwall blockage is plotted against the actuator amplitude with each actuator placed at one of its most effective pitchwise locations for blockage reduction, i.e., for the case where the DSJ actuator is placed near the pressure side of the blade ($y = -0.04$ pitch) and for the situation where the NSJ actuator is placed near the vortex core. The forcing frequency is $F_C^+ = 1.0$ for both. The DSJ actuator is about twice as effective as the NSJ actuator in reducing the endwall blockage for a given amplitude $C_{\mu,\tau}$. In addition, at a $C_{\mu,\tau}$ of about 1.0, it eliminates most of the endwall blockage, not only that associated with the tip clearance flow but also that associated with the endwall boundary layer.

Dependence on Forcing Frequency of the DSJ. The blockage reduction with the DSJ is less sensitive to frequency than the NSJ. The variations in the data taken at two Reynolds numbers are less than the measurement uncertainty and no significant trend in the frequency response is observed. This suggests that the change in the flow process due to the DSJ is different from that of the NSJ. In particular it appears that the time-averaged momentum is more important than the unsteadiness in reducing the blockage with the use of the DSJ. Specific details on the flow process will be discussed later.

Dependence on Pitchwise Location of the DSJ. **Figure 17** shows endwall blockage versus pitchwise location of the DSJ actuator. The actuator frequency and the amplitude are fixed at $F_C^+ = 1.0$ and $C_{\mu,\tau} = 0.88$. A substantial reduction in the endwall

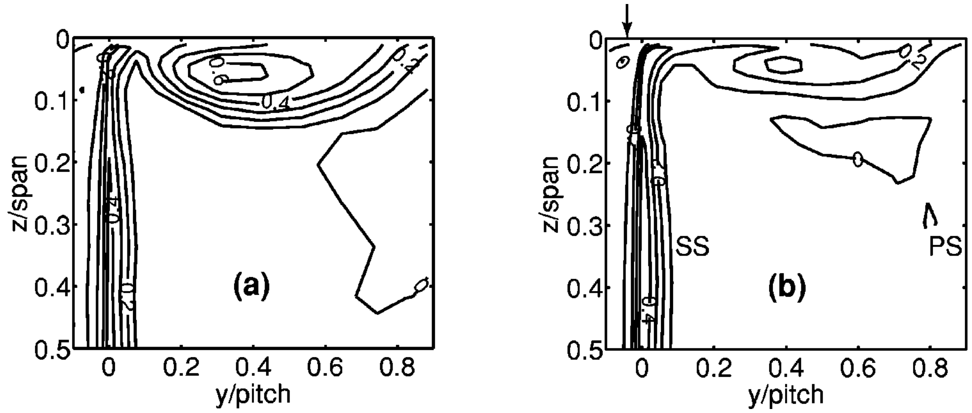

Fig. 15 Contours of ω measured 5%C downstream of trailing edge plane: (*a*) baseline without actuation, $\tau = 3\% C$; (*b*) DSJ directly over blade PS ($y = -0.04$ pitch), $C_{\mu,\tau} = 0.88$, $F_C^+ = 1.0$. Arrows indicate locations of DSJ holes.

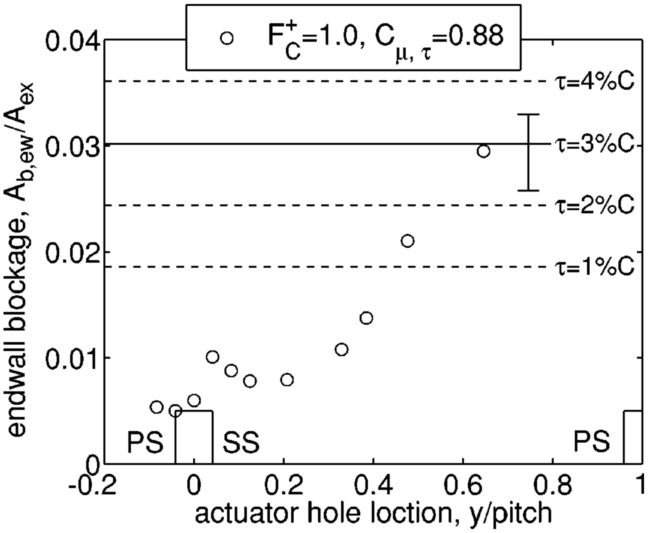

Fig. 17 Endwall blockage versus pitchwise location of DSJ actuator. $\tau=3\%C$.

blockage is achieved when the DSJ is located near the pressure side of the blade ($y=-0.04$ pitch) or the tip clearance vortex core.

Figure 18 shows mass-averaged and stream thrust-averaged total pressure loss coefficients. Unlike NSJ, the DSJ reduces both of them significantly from the baseline when the DSJ is located within -0.08 pitch and 0.6 pitch.

Comparison Between DSJ and SDJ. The measurements with the DSJ actuation presented above have elucidated two aspects to support the hypothesis that momentum injection is mainly responsible for the observed blockage reduction with the use of DSJ. The first is that the reduction is not sensitive to the actuation frequency. The second is that the DSJ reduces both blockage and loss in the endwall region. SDJ (steady directed jet) experiments have been carried out to examine the hypothesis by establishing the bulk behavior, time-averaged momentum of the directed jet and blockage reduction. **Figure 19** shows the comparison between the DSJ and the SDJ. Note that $C_{\mu,\tau}$ of the DSJ has been time-averaged (Bae [15]). The data essentially collapse to a single curve verifying that the time-averaged $C_{\mu,\tau}$ is the important parameter in reducing the blockage with the use of directed jets.

Figure 19 shows that the tip clearance-related endwall blockage can be completely eliminated using directed jets with a time-averaged momentum flux that is about 13 to 19% of the momentum flux of the leakage flow. In other words, endwall blockage can be reduced to the level of the extrapolated baseline with zero clearance when directed jets are applied at a time-averaged momentum coefficient of roughly 0.16.

Effect on Overall Efficiency. As presented above, all three actuators (NSJ, DSJ, and SDJ) are capable of mitigating the endwall blockage associated with tip leakage flow. We now examine the loss associated with the tip leakage. To determine whether the reduction in endwall loss with the use of directed jets results in an improvement in the overall efficiency, the reduction in the endwall flow power deficit must be compared with the flow power expended by the actuator. The endwall flow mechanical power deficit is

$$\Pi_{\text{deficit}}=\frac{\dot{m}_{in}}{\rho}(P_{t,\infty}-\overline{P}_t^m)=\frac{\dot{m}_{in}q_\infty\overline{\omega}_{ew}^m}{\rho}=Q_{in}q_\infty\overline{\omega}_{ew}^m$$

$$=U_\infty\cos\beta_{in}\frac{hs}{2}q_\infty\overline{\omega}_{ew}^m.$$

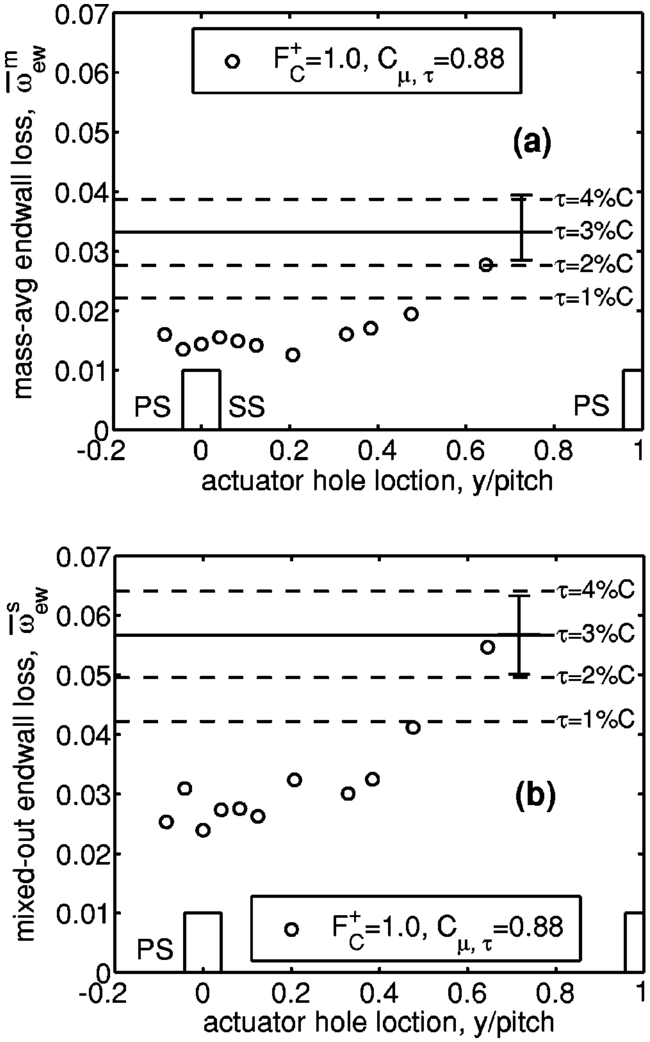

Fig. 18 Endwall total pressure loss coefficient versus pitchwise location of the DSJ actuator ($\tau=3\%C$): (*a*) mass-averaged ω; (*b*) stream thrust-averaged (or fully mixed-out) ω.

The time-averaged flow power expended by the directed jets is

$$\Pi_J=\overline{(Q_Jq_J)}=\frac{1}{2}\rho A_J\overline{U_J^3}=\frac{1}{2}\rho A_J(0.26\times U_{J,\text{peak}}^3).$$

The factor of 0.26 in the above equation is from time-averaging the DSJ injection cycle (Bae [15]). The ratio of endwall loss reduction to expended flow power, η_J is thus

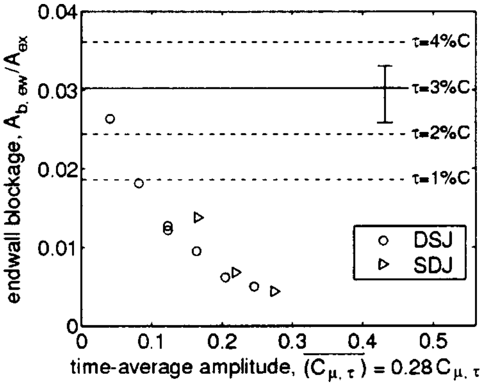

Fig. 19 Comparison between the DSJ and the SDJ (steady directed jet). Holes of both actuators are placed over the pressure surface of the blade. $\tau=3\%C$. DSJ at $F_C^+=1.0$.

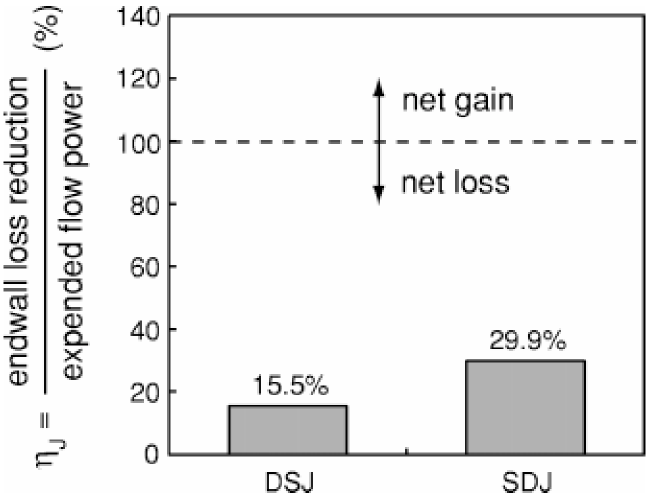

Fig. 20 Ratio of endwall loss reduction to expended flow power of directed jet actuation at $\overline{C}_{\mu,\tau}=0.25$.

$$\eta_J=\frac{\Delta\Pi_{\text{deficit}}}{\Pi_J}\times 100=\frac{(\Pi_{\text{deficit}})_{\text{baseline}}-(\Pi_{\text{deficit}})_{\text{control}}}{\Pi_J}\times 100(\%).$$

Figure 20 shows the values of η_J for the DSJ and the SDJ at $\overline{C}_{\mu,\tau}=0.25$. Only about 16% of the flow power expended by the DSJ and about 30% of the flow power expended by the SDJ are regained in increasing the flow power measured 5%C downstream of the trailing edge plane (or in reducing the mass-averaged total pressure loss) and the remainder is lost. Consequently, there is a net loss in the flow power with the use of directed jet actuation.

The difference in the η_J of the DSJ and the SDJ is because the flow power scales with the cube of the jet velocity. The cyclic DSJ has a peak jet velocity about twice the SDJ velocity for the same time-averaged momentum coefficient. The amount of the reduction in Π_{deficit} is the same for both the DSJ and the SDJ for a given time-averaged momentum coefficient. Therefore, a higher Π_J of the DSJ for the same $\Delta\Pi_{\text{deficit}}$ results in a lower η_J compared to the SDJ.

Even for the SDJ, η_J is very low, when compared to boundary layer separation control wherein active control benefits from great leverage achieving about 1600% return on the input electrical power to the actuator (McCormick [22]). The ratio η_J that is well below 100% in the current tip leakage flow control suggests that there is no leverage for loss reduction, which one can take advantage of, at least with the schemes considered in this study.

The two reasons for η_J being less than 100% are: (i) the relative angle between the directed jet and the main flow, and (ii) the mixing process of the high velocity jet with the passage flow. We can examine how much loss is attributed to each. To examine the effect of the relative flow angle, it is assumed that only the jet flow power associated with the velocity component parallel to the main flow is regained in increasing blade passage flow power. Recovered flow power of the jet decreases with relative angle as shown in **Fig. 21**(***a***). The relative angle in spanwise direction is 25 deg as illustrated in **Fig. 7** and the corresponding recovery rate is 74% of the expended flow power. In other words, 26% of the jet flow power is lost due to the relative angle between the jet and the main flow.

Mixing between the actuator jet and the blade passage flow also incurs loss. $U_{J,\text{peak}}$ of the DSJ is about $6.3U_\infty$, and U_J of the SDJ is about $3.4U_\infty$ at $\overline{C}_{\mu,\tau}=0.25$. Loss due to mixing between two streams with different magnitude of velocities can be estimated using a control volume analysis with the result shown in **Fig. 21**(***b***) where estimated recovery rate of the expended flow power is plotted against the velocity ratio between the jet and the blade passage flow. The recovery rate of the expended flow power decreases quickly from 100% as the velocity ratio increases and is 46% with a velocity ratio of 3.4 (for the SDJ). The remaining 54% of the flow power is lost in the mixing process.

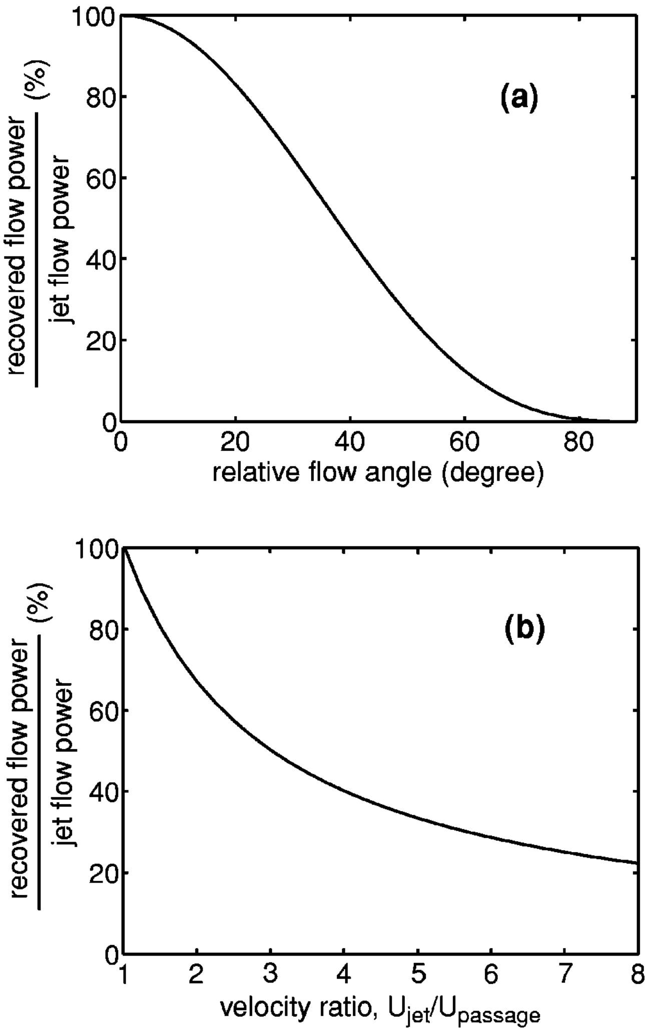

Fig. 21 Estimated recovery rate of expended flow power: (*a*) as function of relative angle between the jet and main flow; (*b*) as function of the velocity ratio for a fixed momentum injection

Thus, the estimated overall recovery rate of the flow power η_J considering losses due to relative angle and high jet velocity is 34% ($=0.74\times 0.46$) for the SDJ; this accounts for the observed η_J of 30% shown in **Fig. 20**. The mixing loss associated with a high jet velocity is the dominant loss mechanism of the present directed jet actuators. To increase the efficiency of the actuation while reducing the blockage, the jet must be aligned with the main flow direction and the velocity ratio must be reduced close to unity. In particular, the η_J of the present DSJ and SDJ can be improved by reducing the jet velocity while keeping the momentum coefficient the same.

Summary and Conclusions

Control of compressor tip clearance flows has been explored in a linear cascade using three types of fluidic actuators: a normal synthetic jet, a directed synthetic jet, and a steady directed jet, all mounted on the casing. The results are summarized as follows:

1. The NSJ provides mixing enhancement only, or both mixing enhancement and leakage flow reduction, depending on its pitchwise location. The DSJ and SDJ actuators provide streamwise momentum enhancement. Consequently, all three actuators result in a reduction of clearance-related blockage.
2. For a given actuation amplitude, the DSJ and SDJ are about twice as effective as the NSJ in reducing clearance-related blockage. Further the DSJ and SDJ can eliminate clearance-related blockage with a time-averaged momentum flux roughly 16% of the momentum flux of the leakage flow.
3. Effective pitchwise locations of actuator jets for blockage reduction are near the blade tip or the clearance vortex core.
4. The decrease in loss is only about 30% of the expended flow power from the present SDJ actuator, which is the best among the actuators considered. To improve the efficiency of the directed jet actuation, both the direction and the magnitude of the jet velocity must be made close to the main flow velocity.
5. The period of the optimum unsteady forcing for the blockage reduction with the use of NSJ is of the order of the convective time through the blade passage.

The present work has the following implications on tip clearance flow control in axial compressors:

- Actuations based on mixing enhancement and/or leakage flow reduction are not as effective as those based on streamwise momentum injection.
- Steady directed jet (SDJ) is effective in reducing tip clearance-related blockage at design and should be further explored for its potential benefit relative to compressor stability.

Acknowledgment

This work was funded by DARPA/AFOSR under Grant F49620-97-1-0526 with Dr. W. Tang of DARPA and Dr. T. J. Beutner of AFOSR as technical monitors and program managers. In addition, the first author was supported on the Jonathan Whitney Central Fellowship grant for the last semester and would like to thank M.I.T. Dean B. E. Staton for providing the support. We would like to thank Dr. Beutner of AFOSR for taking a personal interest in the work and providing many useful suggestions and comments, Dr. Greitzer of MIT, Dr. Marble of Caltech, and Dr. N. A. Cumpsty of Rolls-Royce for useful technical comments and discussions. Finally, the help and the suggestions given by Dr. Mark Jones and the reviewers toward improving the technical clarity of the paper are gratefully acknowledged.

Nomenclature

Symbols

A_b = blocked area due to blockage
$A_{b,ew}$ = endwall blocked area
$A_{b,\mathrm{tip}}$ = tip clearance-related blocked area
A_{ex} = blade passage exit area $= h \times s$
A_J = jet area
C = blade chord
$C_{\mu,\tau}$ = momentum coefficient $= (\rho U_{J,\mathrm{peak}}^2 \delta)/(\rho U_L^2 \tau)$ or $(\rho U_{J,\mathrm{peak}}^2 A_J)/(\rho U_\infty^2 \tau C)$ (in cascade)
$\overline{C}_{\mu,\tau}$ = time-averaged momentum coefficient $= \overline{(\rho U_J^2 A_J)}/(\rho U_\infty^2 \tau C)$ (in cascade)
f = frequency (Hz)
F_C^+ = reduced frequency $= fC/U_\infty$ (in cascade)
h = span (blade height)
P_t = total pressure
$P_{t,\infty}$ = far upstream reference total pressure
Q = flow rate $= AU$
q_∞ = far upstream reference dynamic head $= 0.5\rho U_\infty^2$
Re_C = Reynolds number $= U_\infty C/\nu$
s = pitch (spacing between blades)
U = flow velocity
U_x = axial flow velocity
$U_{x,\mathrm{edge}}$ = edge axial flow velocity
$U_{J,\mathrm{peak}}$ = peak center velocity of synthetic jet leaving actuator slit (or hole)
U_∞ = reference flow velocity far upstream
y = pitchwise location
β_{in} = cascade inlet flow angle
β_{ex} = cascade exit flow angle
β_τ = reduced frequency $= 2\pi f \tau/U_L$ or $2\pi f\tau/U_\infty$ (in cascade)
δ^* = displacement thickness
η_J = ratio of endwall loss reduction to expended flow power
Π = flow power
τ = tip clearance size
ω = total pressure loss coefficient $= (P_{t,\infty} - P_t)/q_\infty$
$\overline{\omega}_{ew}^m$ = mass-averaged endwall total pressure loss coefficient
$\overline{\omega}_{ew}^s$ = stream thrust-averaged endwall total pressure loss coefficient

Acronyms

NSJ = normal synthetic jet
DSJ = directed synthetic jet
SDJ = steady directed jet
L.E. = leading edge of blade
T.E. = trailing edge of blade
PS = pressure surface (or side)
SS = suction surface (or side)

References

[1] Wisler, D. C., 1985, ‘‘Loss Reduction in Axial-Flow Compressors Through Low-Speed Model Testing,’’ ASME J. Turbomach., **107**, pp. 354–363.
[2] Smith, L. H., Jr., 1958, ‘‘The Effect of Tip Clearance on the Peak Pressure Rise of Axial-flow Fans and Compressors,’’ *ASME Symposium on Stall*, ASME, New York, pp. 149–152.
[3] Cumpsty, N. A., 1989, *Compressor Aerodynamics*, Longman Group, London, 345.
[4] Storer, J. A., 1991, ‘‘Tip Clearance Flow in Axial Compressors,’’ Ph.D. dissertation, Department of Engineering, University of Cambridge, Jan.
[5] Storer, J. A., and Cumpsty, N. A., 1990, ‘‘Tip Leakage Flow in Axial Compressors,’’ ASME Paper No. 90-GT-127.
[6] Heyes, F. J. G., Hodson, H. P., and Dailey, G. M., 1992, ‘‘The Effect of Blade Tip Geometry on the Tip Leakage Flow in Axial Turbine Cascades,’’ ASME J. Turbomach., **114**, pp. 643–651.
[7] Bindon, J. P., 1989, ‘‘The Measurement and Formation of Tip Clearance Loss,’’ ASME J. Turbomach., **111**, pp. 257–263.
[8] Saathoff, H., and Stark, U., 2000, ‘‘Endwall Boundary Layer Separation in a High-Stagger Compressor Cascade and a Single-Stage Axial-Flow Low-Speed Compressor,’’ Forschung im Ingenieurwesen, **65**(8), pp. 217–216.
[9] Khalid, S. A., 1995, ‘‘The Effect of Tip Clearance on Axial Compressor Pressure Rise,’’ Ph.D. thesis, Gas Turbine Laboratory, Massachusetts Institute of Technology, Cambridge, MA, Feb.
[10] Drela, M., and Youngren, H., 1995, *A User's Guide to MISES 2.1*, MIT Computational Aerospace Science Laboratory, MIT, Cambridge, MA.
[11] Kline, S. J., and McClintock, F. A., 1953, ‘‘Describing Uncertainties in Single-Sample Experiments,’’ CME, Chart. Mech. Eng., **Jan.**, pp. 3–8.
[12] Amitay, M., Honohan, A., Trautmann, M., and Glezer, A., 1997, ‘‘Modification of the Aerodynamic Characteristics of Bluff Bodies Using Fluidic Actuators,’’ Paper No. AIAA 97-2004.
[13] Smith, D. R., Amitay, M., Kibens, V., Parekh, D., and Glezer, A., 1998, ‘‘Modification of Lifting Body Aerodynamics Using Synthetic Jet Actuators,’’ Paper No. AIAA 98-0209.

[14] Khalid, S. A., Khalsa, A. S., Waitz, I. A., Tan, C. S., Greitzer, E. M., Cumpsty, N. A., Adamczyk, J. J., and Marble, F. E., 1998, ''Endwall Blockage in Axial Compressors,'' ASME Paper No. 98-GT-188.

[15] Bae, J., 2001, ''Active Control of Tip Clearance Flow in Axial Compressors,'' Ph.D. thesis, MIT, Cambridge, MA, June.

[16] Katz, Y., Horev, E., and Wygnanski, I., 1992, ''The Forced Turbulent Wall Jet,'' J. Fluid Mech., **242**, pp. 577–609.

[17] Tsuji, Y., Morikawa, Y., Nagatani, T., and Sakou, M., 1977, ''The Stability of a Two-Dimensional Wall Jet,'' Aeronaut. Q., **XXVIII** (Nov.), pp. 235–246.

[18] Crow, S. C., 1970, ''Stability Theory for a Pair of Trailing Vortices,'' AIAA Paper No. 70-53.

[19] Kang, E., Breuer, K. S., and Tan, C. S., 2000, ''Control of Leakage Flows Using Periodic Excitations,'' Paper No. AIAA 2000-2232.

[20] Storer, J. A., and Cumpsty, N. A., 1993, ''An Approximate Analysis and Prediction Method for Tip Clearance Loss in Axial Compressors,'' ASME Paper No. 93-GT-140.

[21] Bae, J., Breuer, K. S., and Tan, C. S., 2000, ''Control of Tip Clearance Flows in Axial Compressors,'' AIAA Paper No. 2000-2233.

[22] McCormick, D. C., 2000, ''Boundary Layer Separation Control With Directed Synthetic Jets,'' Paper No. AIAA 2000-0519.

Numerical Study of Unsteady Flow in a Centrifugal Pump

Kitano Majidi
Technische Universitaet Berlin,
Carnotstr. 1A,
D-10587, Germany
e-mail: kitano.majidi@tu-berlin.de

Computational fluid dynamics (CFD) analysis has been used to solve the unsteady three-dimensional viscous flow in the entire impeller and volute casing of a centrifugal pump. The results of the calculations are used to predict the impeller/volute interaction and to obtain the unsteady pressure distribution in the impeller and volute casing. The calculated unsteady pressure distribution is used to determine the unsteady blade loading. The calculations at the design point and at two off-design points are carried out with a multiple frame of reference and a sliding mesh technique is applied to consider the impeller/volute interaction. The results obtained show that the flow in the impeller and volute casing is periodically unsteady and confirm the circumferential distortion of the pressure distribution at the impeller outlet and in the volute casing. Due to the interaction between impeller blades and the tongue of the volute casing the flow is characterized by pressure fluctuations, which are strong at the impeller outlet and in the vicinity of the tongue. These pressure fluctuations are died away in the casing as the advancement angle increases. These reduced pressure fluctuations are spread to the discharge nozzle; the pressure fluctuations are also reflected to the impeller inlet and they affect the mass flow rate through the blade passages. [DOI: 10.1115/1.1776587]

Introduction

Single-stage centrifugal turbo-machines are mostly designed with a spiral volute casing. The asymmetric shape of the spiral volute and tongue results in a circumferential distortion of the flow conditions at the outlet of the impeller. This distortion is especially pronounced at off-design points. The circumferential non-uniformity of the pressure field causes unbalanced radial forces that must be considered by designing rotor-bearing systems.

Due to the relative movement between impeller and volute casing the flow at the outlet of the impeller is strongly interacting with the volute flow. The unsteady interaction between these components generates pressure fluctuations, which are responsible for unsteady dynamic forces. These unsteady dynamic forces give rise to vibration of the pump components and generate hydraulic noises. The physics of the hydrodynamic forces and the reasons of the vibration and noise generation are extensively reported in [1].

Considerable attention has already been focused to study the unsteady interaction in centrifugal turbomachines. Both experimental and numerical approaches have contributed to the understanding of the complex flow fluctuations due to the unsteady interaction. There are numerous examples of the experimental investigations of which Arndt et al. [2], Kaupert and Staubli [3], and Hagelstein et al. [4] are a representative sample. In addition, some numerical studies have been undertaken to capture the unsteady interaction and to predict the pressure fluctuations. Some of the studies, e.g., Hillewaert and Van den Braembussche [5], consider the flow as inviscid and some authors, e.g., Longatte and Kueny [6], use a two-dimensional model. In recent years, improved computational algorithms as well as hardware development have contributed to enhance CFD capability. It is now feasible to use CFD codes for a realistic prediction of the complex three-dimensional turbulent flow in the entire pump and perform unsteady calculations see, for example, Zhang et al. [7] and González et al. [8,9]. However, the knowledge about the unsteady pressure fluctuations and the unsteady blade loading is still not satisfying. Furthermore, the design of the centrifugal pumps has already reached a level that only through a detailed understanding of the internal flow an increase of the overall performance can be achieved. Due to the curved passages inside the impeller and the volute the flow is to be considered as three-dimensional. Additionally, since the flow following blade passages as well as the volute casing interacts with viscous boundary layers, secondary flows are generated. Therefore, a correct simulation of the impeller/volute interaction requires the simultaneous solution of the three-dimensional unsteady Navier-Stokes equations in both the impeller and volute.

Centrifugal Pump and Test Conditions

The impeller considered in this study is a commercial one. It is shrouded and has five backswept blades. The blade profile varies between the hub and the shroud. The blade angle at the inlet varies from 18.5 deg (from tangential) at the shroud to 30.0 deg at the hub. The blade angle at the outlet is 23.5 deg. The single volute casing is unvaned. The shape of the single volute casing is designed according to the theory of a constant average velocity for all sections of the volute (Stepanoff, [10]). The main dimensions and characteristic of the investigated pump and the test conditions for this study are presented in **Table 1.**

Numerical Model and Computational Methods

The numerical simulations have been carried out using the commercial code CFX-TASCflow. The flow solver of the code employs for incompressible turbulent flow the continuity equation and the three-dimensional time-averaged Navier-Stokes equations. In this study, the eddy-viscosity assumption is used to model the Reynolds stresses. The eddy viscosity is determined by means of the Standard k-ε turbulence model. The walls are modeled using a log-law wall function. The transport equations are discretized using an element based conservative finite volume method.

The numerical calculations are carried out with a multiple frame of reference approach, whereby the impeller flow field is solved in a rotating frame and the casing in a fixed one. The grid for these two frames of reference should be generated separately. The employed code requires provision of structured or block-structured grids. **Figure 1** shows the computational grids used to model the impeller and the volute. Both of the grids are block structured. The grid of the impeller models all impeller blades and passages. In order to enhance a fully developed flow before enter-

---

Contributed by the International Gas Turbine Institute (IGTI) of THE AMERICAN SOCIETY OF MECHANICAL ENGINEERS for publication in the ASME JOURNAL OF TURBOMACHINERY. Paper presented at the International Gas Turbine and Aeroengine Congress and Exhibition, Vienna, Austria, June 13–17, 2004, Paper No. 2004-GT-54099. Manuscript received by IGTI, October 1, 2003; final revision, March 1, 2004. IGTI Review Chair: A. J. Strazisar.

Table 1 Main characteristics of the investigated pump

Impeller:	
$d_2 = 508$ mm	Impeller outlet diameter
$b_2 = 72.5$ mm	Impeller outlet passage width
Volute Casing:	
$d_3 = 523$ mm	Base circle diameter
$b_3 = 94.3$ mm	Volute width at the base circle
Design Point:	
$\dot{m}_{\text{opt}} = 730.0$ kg/s	Mass flow rate
$H = 46.68$ m	Total head
$n = 1482$ rpm	Rotational speed
$N_s = 68$ min^{-1}	Specific speed
Test Conditions:	
(1) Mass flow rate = 730.0 kg/s	$(\dot{m}/\dot{m}_{\text{opt}} = 1)$
(2) Mass flow rate = 541.04 kg/s	$(\dot{m}/\dot{m}_{\text{opt}} = 0.74)$
(3) Mass flow rate = 978.2 kg/s	$(\dot{m}/\dot{m}_{\text{opt}} = 1.34)$

ing the impeller, some part of the suction nozzle is also modeled. Therefore, the inlet surface of the impeller was extended upstream of the physical inlet region of the blades. The grid of the impeller is generated in 16 blocks, i.e., one block for the suction nozzle, five blocks for the inlet region, one block for each of the five impeller passages and each of the regions connecting blade passages with the inlet surface of the volute. All of these sub grids are pinched H-grids. The grid for the impeller has 476,568 nodes. The blades are defined as solid bodies, therefore only 76% of the nodes are active nodes. The grid of the casing is generated in two blocks, one for the volute casing and one for the discharge nozzle, and has 356,664 nodes.

As already mentioned the numerical calculations are carried out with a multiple frame of reference. The two frames of reference are connected in such a way that for steady state calculations the relative position of the impeller and casing does not change through the calculations, i.e., that the grids of the impeller and the casing are connected by means of a frozen-rotor interface. For unsteady calculations the grids are connected by means of a rotor/stator interface, i.e., that they change their relative position through the calculation according to the angular velocity of the impeller. The reference change occurs as the flow crosses the interfaces; the appropriate transformation occurs across the interface without any interface averaging. The rotor/stator approach accounts for the interaction between two frames.

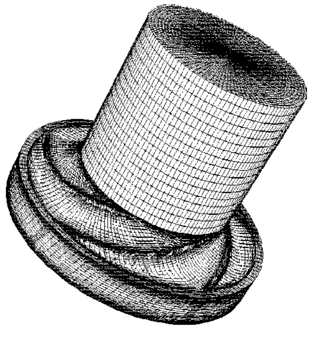

Impeller

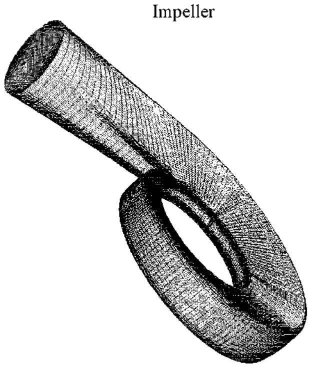

Volute casing

Fig. 1 Grids of the computational domain

For the steady-state calculations the following boundary conditions are assumed: At the inlet of the computational domain the mass flow rate, the turbulence intensity, the eddy length scale and a reference pressure at one grid point are specified. It is assumed, that the absolute velocity vectors at the inlet are perpendicular to the inlet grid surface and point into axial direction. The turbulent intensity was assumed to be 5%. Furthermore, the eddy length scale was assumed to be 10% of the diameter at the inlet plane. At the outlet for all variables (with exception of pressure) a zero-gradient condition was assumed. Both in the fixed frame and in the rotating frame the solid walls, i.e., the impeller blades, hub and shroud, the casing walls and the walls of the suction nozzles, are modeled using a no-slip boundary condition.

For unsteady calculations in a previous study, the same boundary conditions as for the steady state calculations were assumed. The results are published in [11]. Some authors, e.g., Gonzalez et al. [9] and Longatte and Kueny [6], suggested that the assumption of a fixed mass flow rate at the inlet of the computational domain is physically unsuitable for unsteady calculations and in particular for considering the rotor/stator interaction. Therefore, in the present study for unsteady calculations the following boundary conditions are used: instead of a fixed mass flow rate at the inlet the total absolute pressure, and at the outlet the static pressure in a single grid face are specified.

The time step of the unsteady calculations has been set to $2.0243 {*} 10^{-4}$ seconds. This time step is related to the rotational speed of the impeller and is chosen in such a way that one complete impeller revolution is performed after each 200 time steps. The chosen time step is small enough to get the necessary time resolution. The number of iterations in each time step has been set to 4. This number of iterations is in most cases sufficient to reduce the maximum residuals by three orders of magnitude. The average values of residuals (rms values) reduce by four orders of magnitude. All parameter settings, for example the time step and the number of iterations in each time step, have been retained unchanged for all test conditions. The calculations are carried out for four and half impeller revolutions, i.e., for 900 time steps, at the design point—test condition 1—as well as for five impeller revolutions, i.e., for 1000 time steps, at both off-design points—test conditions 2 and 3. At each test condition at first a steady-state calculation is carried out and the result is used to initialize the unsteady calculation at this test point.

Results and Discussions

The results of the unsteady calculations are discussed for different nodal points which are shown in **Fig. 2** (the nodal points are shown exaggeratedly big in order to distinguish them). The nodal points are selected in one blade passage (passage 3) and in the volute casing and in the discharge nozzle of the casing. In the blade passage the points 1PM, 2PM, 1SM, and 2SM are located at midspan of the passage, whereby the points 1PM and 2PM are located at the blade pressure side at the inlet and outlet of the blade passage respectively. The points 1SM and 2SM are located at the suction side (P stands for pressure side, S for suction side, and M for midspan). The nodal points 1VM and 2VM are located in volute midspan at different angular advancements φ, measured from the volute tongue. The nodal points 1TM and 2TM are located directly at the tongue at midspan of the volute casing, whereby the point 1TM is located at the impeller side of the tongue (at $\varphi = 0$) and the point 2TM is located at the discharge nozzle side of the tongue. The points 1DM and 2DM are located respectively at begin and end of the discharge nozzle at midspan

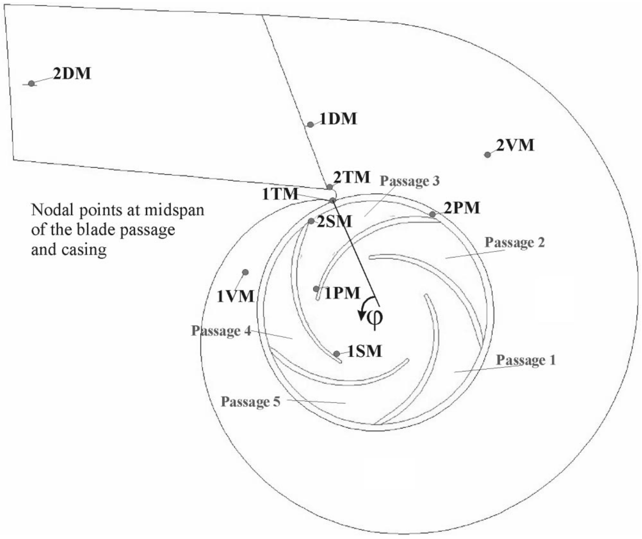

Fig. 2 Location of the investigated nodal points, as well as the relative position of the impeller and volute casing at time=0 (starting the unsteady calculations, initiated from steady-state solutions)

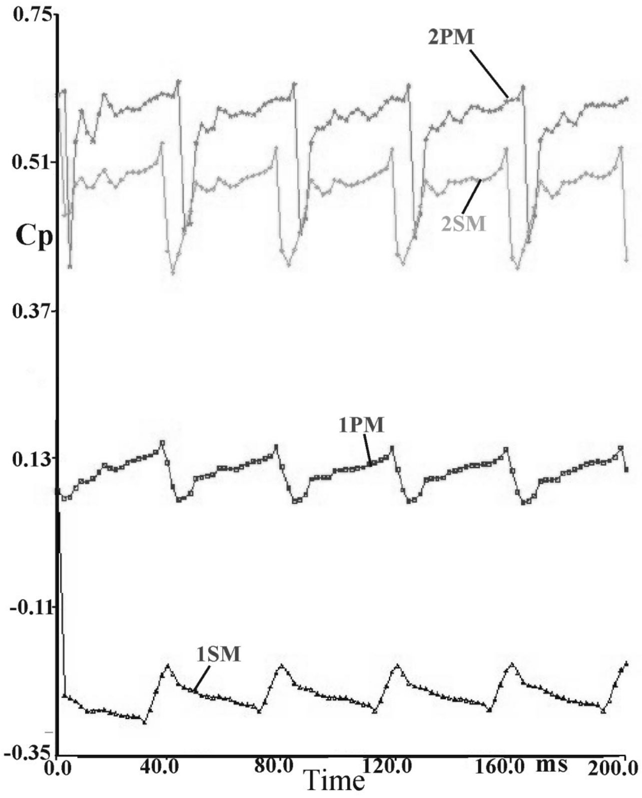

Fig. 4 Unsteady pressure distribution at midspan of the blade passage at $\dot{m}/\dot{m}_{\mathrm{opt}}\approx 0.74$

of the casing. Furthermore, **Fig. 2** shows the relative position of the impeller and casing for steady state calculations as well as at time$=0$ of unsteady calculations.

Unsteadiness Inside the Impeller. In **Fig. 3**, the time histories of the pressure coefficient Cp at the investigated nodal points inside the blade passage are shown, where the time-average of the computed mass flow rate closely captures the design mass flow rate. By the set of boundary conditions used in the present approach, i.e., total pressure at the inlet of the computational domain and the static pressure at a single grid face at the outlet, the design mass flow rate can only roughly be adjusted. For the results presented here, a time-average value of 734.1 kg/s ($\dot{m}/\dot{m}_{\mathrm{opt}}=1.005$) has been computed. The static pressure is normalized using a dynamic pressure based on the impeller outlet tip velocity:

$$Cp=\frac{p-p_{\mathrm{ref}}}{0.5\rho u_2^2}. \tag{1}$$

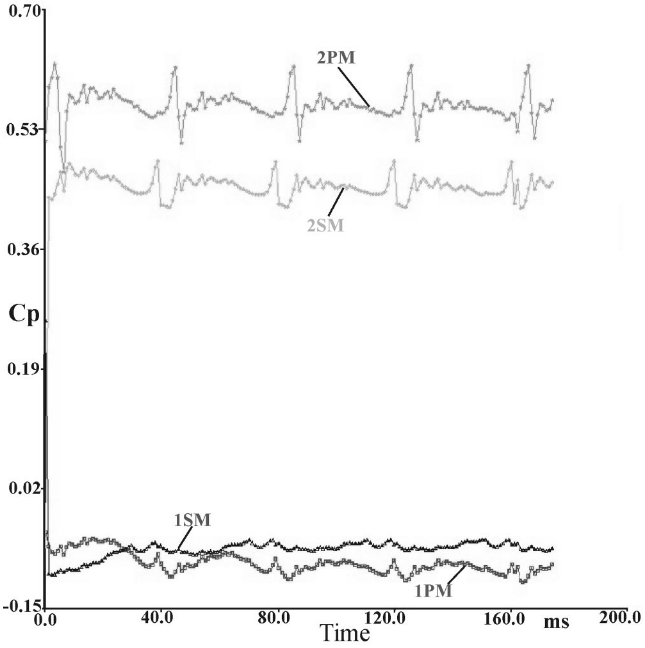

Fig. 3 Unsteady pressure distribution at midspan of the blade passage at $\dot{m}/\dot{m}_{\mathrm{opt}}\approx 1.0$

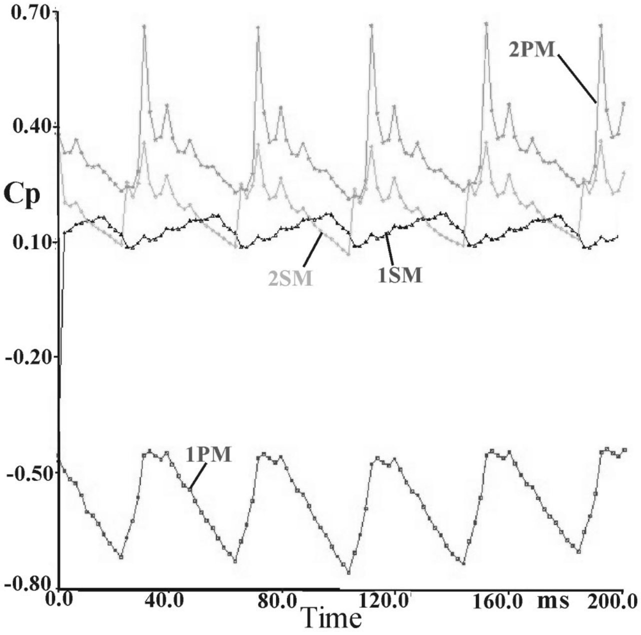

Fig. 5 Unsteady pressure distribution at midspan of the blade passage at $\dot{m}/\dot{m}_{\mathrm{opt}}\approx 1.34$

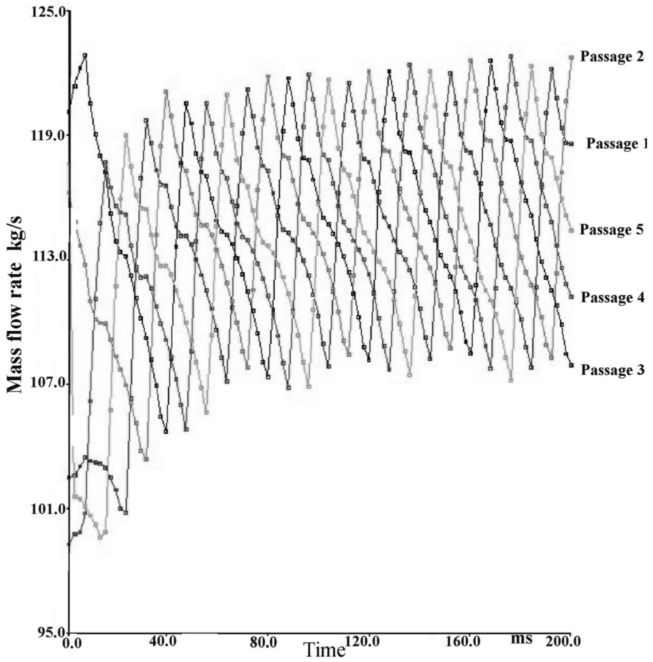

Fig. 6 Unsteady mass flow rate through each blade passage at $\dot{m}/\dot{m}_{opt}\approx 0.74$

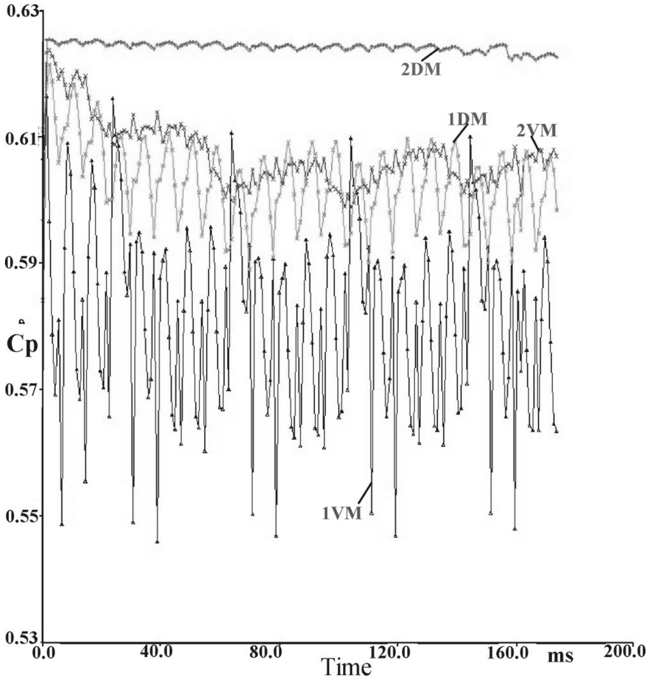

Fig. 8 Unsteady pressure distribution in the volute casing at $\dot{m}/\dot{m}_{opt}\approx 1.0$

As it can be seen in **Fig. 3**, the final periodic unsteady solution is achieved after one impeller revolution, whereby each impeller revolution needs 200 time steps (40,486 ms). At the design point (**Fig. 3**) the calculations are carried out for four and half impeller revolutions, i.e., for 900 time steps. And at both off-design points, **Figs. 4 and 5**, for five impeller revolutions, i.e., for 1000 time steps.

According to **Fig. 3** negative Cp values at the inlet of the blade passage can be observed. A negative Cp refers to a pressure that is lower than the pressure at the reference point, which is selected at the impeller eye. Furthermore, at the inlet of the blade passage in the immediate vicinity of the leading edge, a pressure surplus on the suction side (nodal point 1SM) compared to the corresponding values on pressure side (nodal point 1PM) can be observed. This result indicates a negative blade incidence, which is actually typical for mass flow rates in excess of the design mass flow rate. Indeed, as already mentioned, the mass flow rate exceeds marginally the design mass flow rate.

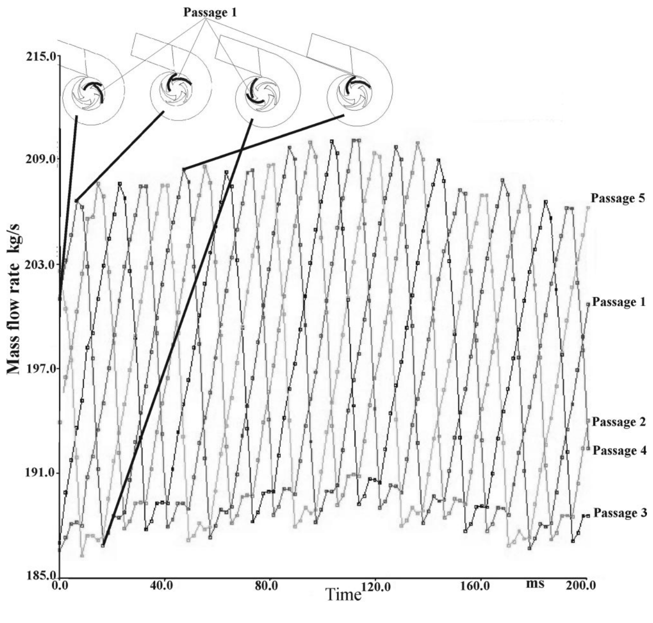

Fig. 7 Unsteady mass flow rate through each blade passage at $\dot{m}/\dot{m}_{opt}\approx 1.3$

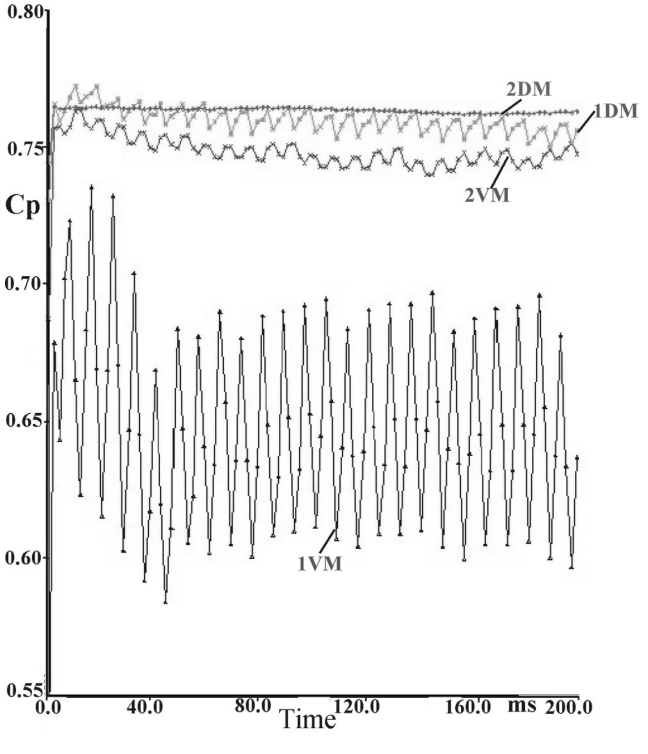

Fig. 9 Unsteady pressure distribution in the volute casing at $\dot{m}/\dot{m}_{opt}\approx 0.74$

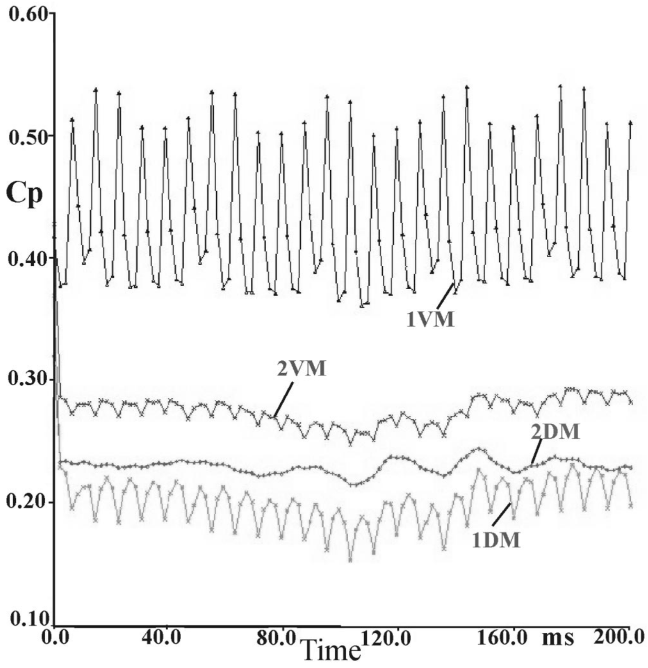

Fig. 10 Unsteady pressure distribution in the volute casing at $\dot{m}/\dot{m}_{\mathrm{opt}}\approx 1.34$

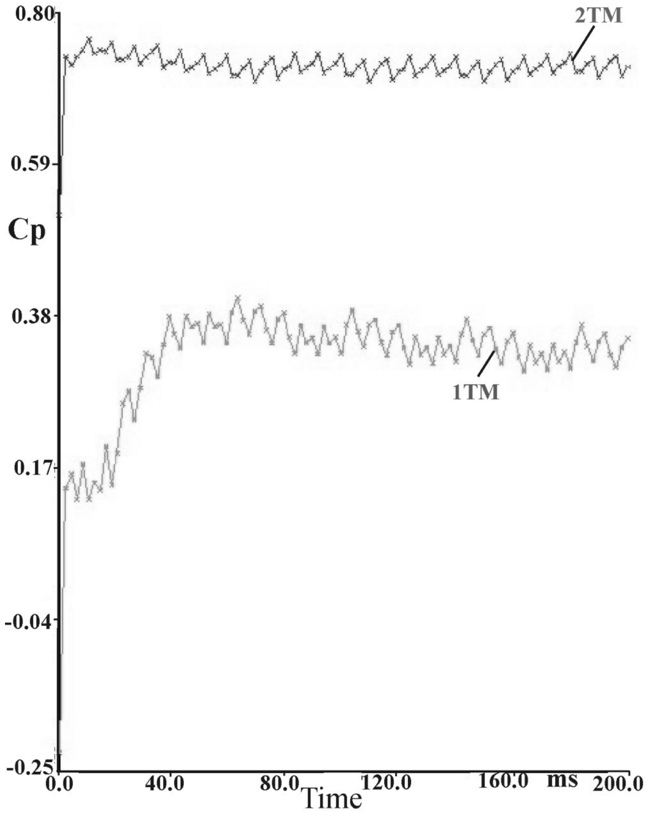

Fig. 12 Unsteady pressure distribution at the tongue of the casing at $\dot{m}/\dot{m}_{\mathrm{opt}}\approx 0.74$

Figures 4 and 5 show the time histories of the pressure coefficients in the blade passage at off-design points $\dot{m}/\dot{m}_{\mathrm{opt}}\approx 0.74$ and $\dot{m}/\dot{m}_{\mathrm{opt}}\approx 1.34$, respectively. The phenomenon in **Fig. 3**—a negative blade incidence—can also be observed in **Fig. 5**, but much more intensely. According to **Fig. 4**, representing a part load operation point, at the inlet of the blade passage the pressure at the nodal point 1PM is higher than at the suction side nodal point 1SM.

Considering **Figs. 3–5**, it can be seen that the amplitude of the pressure fluctuations within the impeller passage grows in magnitude as the trailing edge of the blade is approached. The Comparison of **Fig. 3** with **Figs. 4 and 5**, shows that the amplitudes of the pressure fluctuations at off-design points are considerably larger than the amplitudes at the design point. However, the amplitude of the pressure fluctuations at a mass flow rate higher than the design

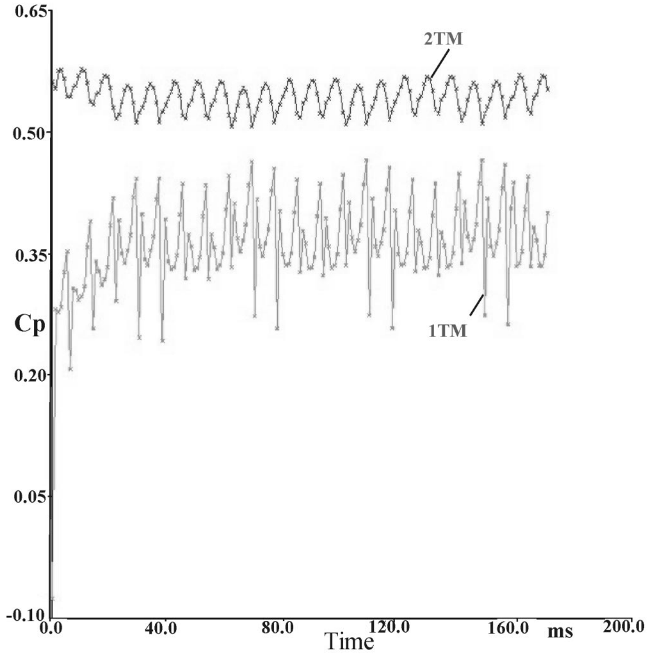

Fig. 11 Unsteady pressure distribution at the tongue of the casing at $\dot{m}/\dot{m}_{\mathrm{opt}}\approx 1.0$

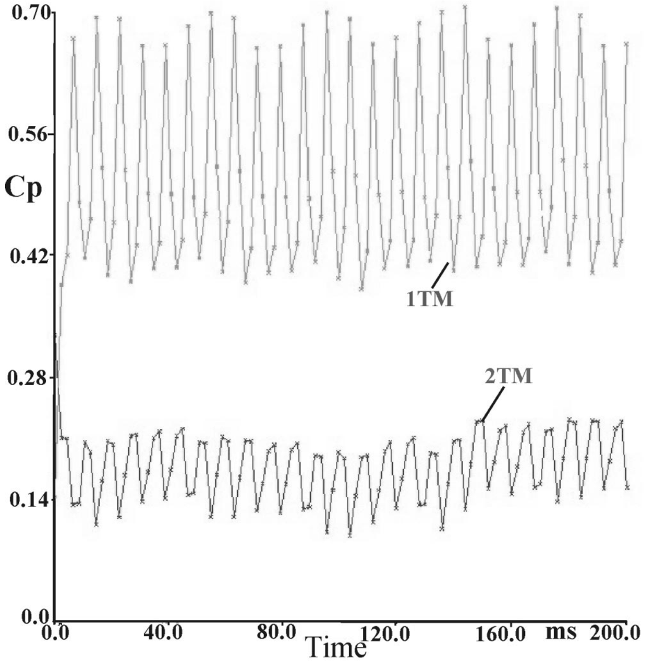

Fig. 13 Unsteady pressure distribution at the tongue of the casing at $\dot{m}/\dot{m}_{\mathrm{opt}}\approx 1.34$

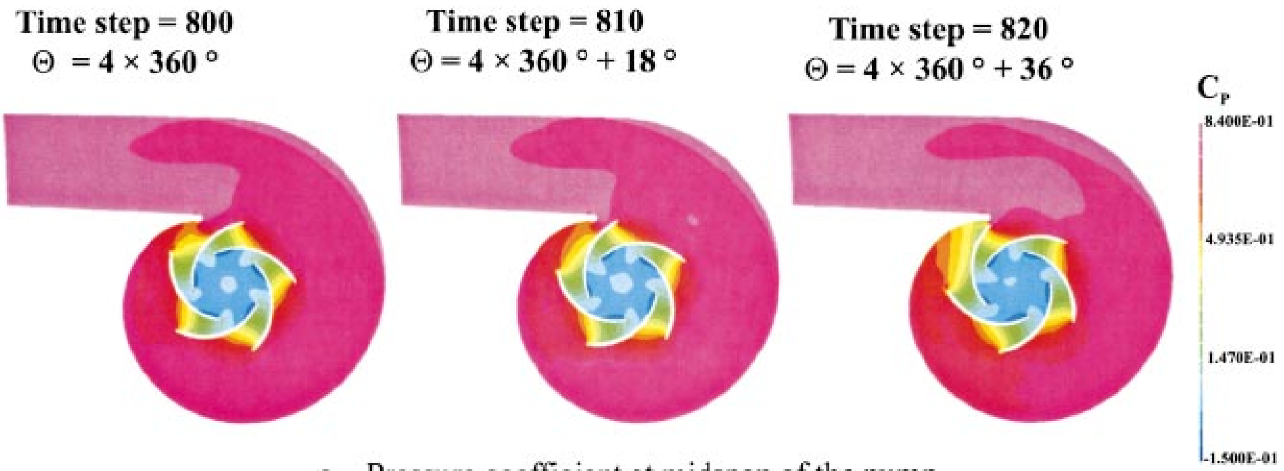

a Pressure coefficient at midspan of the pump

b Pressure coefficient in the cross-sectional plane of the volute casing

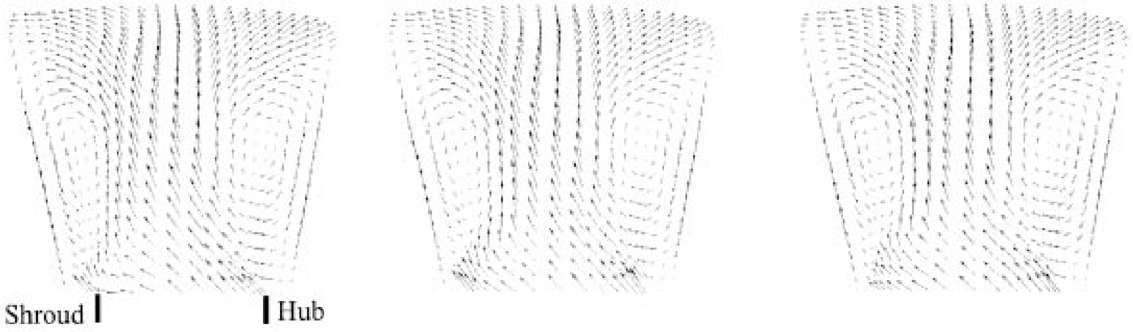

c Secondary flow in the cross-sectional plane of the volute casing

Fig. 14 Pressure distribution at midspan of the pump (*a*), pressure distribution (*b*), and secondary flow (*c*) in the cross-sectional plane of the volute casing at angular advancement $\varphi=60$ deg at three different time steps at off-design point ($\dot{m}/\dot{m}_{opt}\approx 0.74$), [13]

point is obviously more critical. Comparing the pressure fluctuations at the pressure side (nodal points 1PM and 2PM) to suction side (nodal points 1SMand 2SM) reveals that in all operating points the amplitude of the pressure fluctuations on the pressure side of the blade passage is larger than on the suction side.

Since the flow is incompressible, strong pressure fluctuations at the impeller outlet caused by the interaction between the blades and tongue of the volute casing, are reflected upstream to the impeller inlet (see the pressure distribution for nodal points 1PM, 1SM). Thus, pressure fluctuations at the impeller inlet influence the mass flow rate through the blade passages, as it can be seen from **Figs. 6 and 7**. According to these Figs. the mass flow rate through each blade passage varies with time according to the relative position of the blade passage to the tongue of the volute casing. The periodic pressure distribution at the impeller-inlet and outlet leads to a periodic flow, which results in a cyclic acceleration and deceleration of the fluid flow inside each blade passage. At the upper part of **Fig. 7**, the relative position of the passage 1 to the tongue of the volute casing at time step zero as well as exemplary at the begin and at the end of one deceleration and one acceleration-phase are shown; they are linked to the corresponding points of the graph for passage 1. Deviations of the exact repeatability in **Figs. 6 and 7** are partly numerical. However, also in a real pump an exact repeatability of mass flow rates through

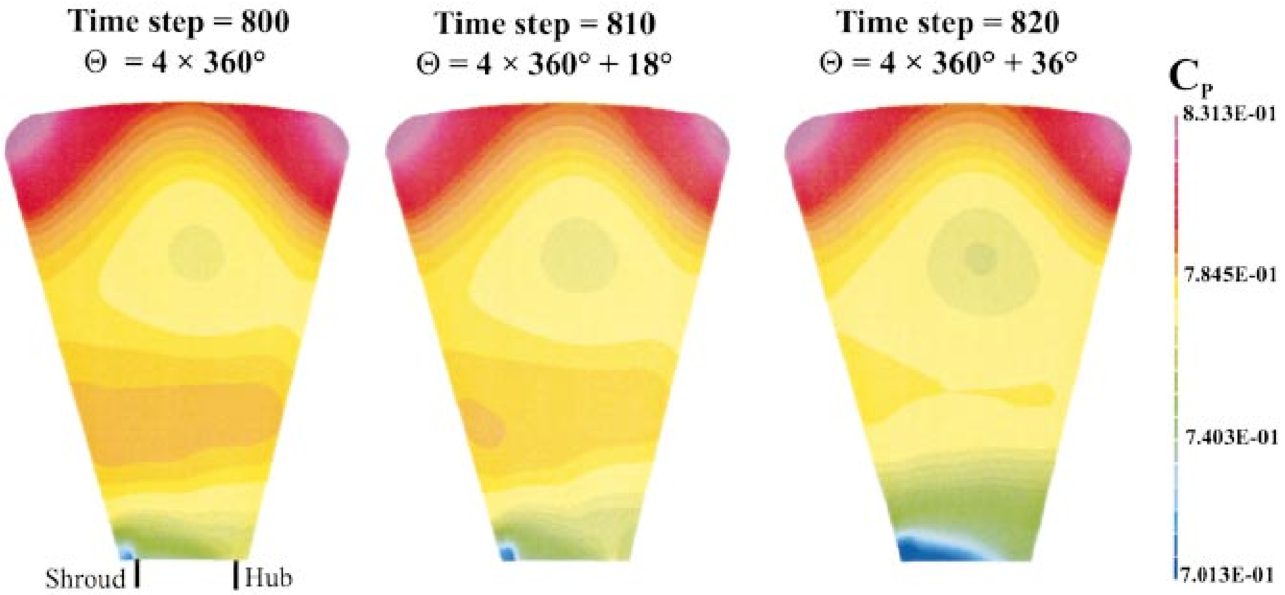

a Pressure coefficient in the cross-sectional plane of the volute casing

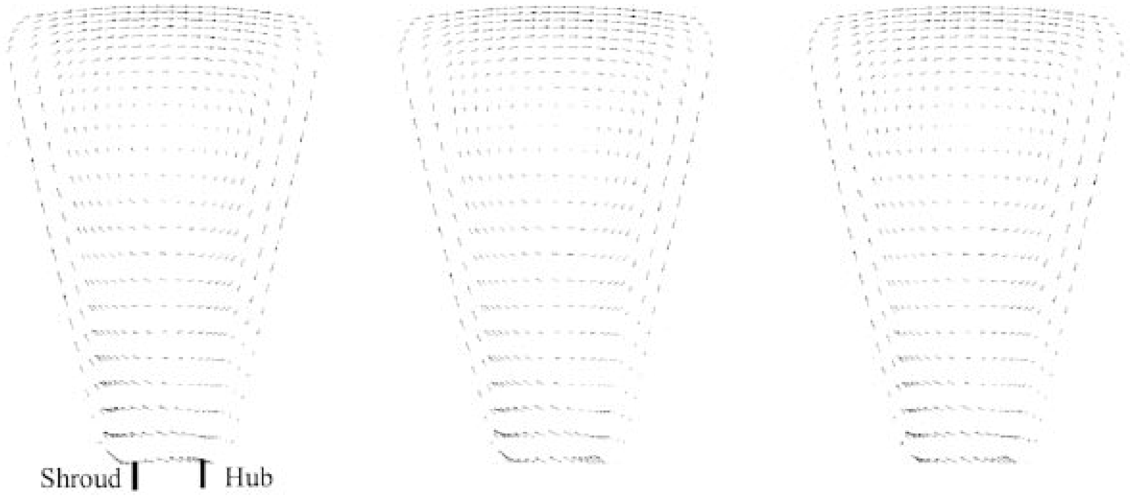

b Secondary flow in the cross-sectional plane of the volute casing

Fig. 15 Pressure distribution (*a*) and secondary flow (*b*) in the cross-sectional plane of the volute casing at angular advancement $\varphi = 260$ deg at three different time steps at off-design point $(\dot{m}/\dot{m}_{opt} \approx 0.74)$

each blade passage at every impeller revolution can not be achieved, since the initial values at each impeller revolution vary slightly.

Unsteadiness Inside the Volute-Casing. The time histories of the pressure coefficient Cp at the investigated nodal points in the volute casing and at the tongue of the casing are shown in **Figs. 8–13**, where both design and off-design points are taken into account. By Considering **Figs. 8–10** it is evident, that pressure fluctuations assume most pronounced intensities in points located closest to the tongue, e.g., points 1VM, 1 TM. The amplitude of these pressure fluctuations die away with advancement of φ (2VM), but is still significant at the discharge nozzle (1DM). At the outlet of the discharge nozzle (2DM) the pressure fluctuations have almost vanished.

According to **Figs. 11–13**, the pressure fluctuations at the impeller side of the tongue, nodal point 1TM, are strong and have large amplitudes. At the discharge side of the tongue at nodal point 2TM these pressure fluctuations have died away and thus, the amplitudes of the fluctuations are considerably smaller.

Contour Plots at Various Instances. The unsteady calculations capture the interaction between the tongue and the blades. **Figure 14**(***a***) shows the contour plots of the pressure coefficient at the midspan of the impeller at three different time steps. According to this figure the tongue and the blades are interacting strongly. As each blade approaches the tongue, very strong pressure fluctuations in the vicinity of the tongue can be observed. These pressure fluctuations are propagated in the volute and are spread to the discharge nozzle. The fluctuations are also reflected

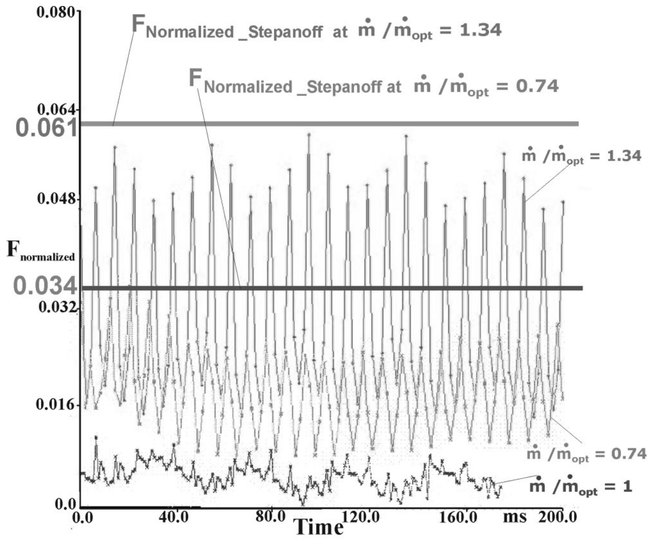

Fig. 16 Unsteady blade loading at different test conditions

in the impeller and are spread to the inlet region. Part (b) of this figure shows the distribution of the pressure coefficient at the cross-sectional plane of the volute casing at the advancement angle $\varphi=60$ deg at the same time steps as in part (a). In order to distinguish the pressure fluctuations, the minimum and maximum values of the color scale of contours remain in all the time steps the same. It means contour level scales are consistent between all time steps. It is to distinguish that at different time steps the pressure fluctuates strongly (colors vary strongly), but the pressure gradients in the cross-sectional plane remain in all time steps almost the same, at all the time steps there are two pronounced minimum value regions in the pressure distribution of the cross-sectional plane. These pressure gradients are arising from the passage curvature (centrifugal forces) and they are in combination with boundary layers responsible for the secondary flows in the volute casing. Since these pressure gradients do not vary with time, the secondary flow, shown in part (c) of **Fig. 14**, does not vary too. The secondary vectors are the projections of the calculated velocity vectors onto the investigated cross-sectional plane. The centers of the vortices of the secondary flow in part (c) correspond to the two pronounced minimum value regions in part (b) of the figure. The high velocity core in the cross section is driven by the impeller.

In **Fig. 15**, the pressure coefficient as well as secondary flow velocity vectors are depicted in a cross-sectional plane of the casing at an angular advancement of $\varphi=260$ deg. By considering **Fig. 15**, it is obvious that pressure fluctuations die away with increasing angular advancement φ (the colors remain in all time steps almost unchanged). In this cross-sectional plane only one deficit region can be observed and correspondingly the secondary flow has only one vortex. As already mentioned, the secondary flows are caused by pressure gradients perpendicular to the flow direction, whereby the pressure gradients depend on the passage curvature; they vary according to the shape of the cross-sectional plane and according to the local radius of the spiral volute (see, for example [12]).

Blade Loading Results. Using the calculated pressure distribution in the impeller, the magnitude of blade loading can be estimated. To calculate the blade loading the static pressure was integrated over the entire surface of the blades. The unsteady pressure distribution results in an unsteady blade loading, which is shown in **Fig. 16**. The blade loading is normalized using the following equation:

$$F_{\text{normalized}}=\frac{F_{\text{radial}}}{0.5\rho u_2^2 \pi d_2 b_2}, \tag{2}$$

where ρ means the density of the fluid, d_2 is the impeller diameter, and b_2 is the width of the impeller at the outlet. Applying Eq. (2) to different test conditions, blade loading appears to assume—as expected—much larger values at off-design conditions (1.3 and 0.74 mass flow ratios). According to **Fig. 16**, at off design points—specially at 1.3 mass flow ratio—the amplitudes of the fluctuations due to flow unsteadiness are equal to the average net blade loading values. This unsteady blade loading gives rise to dynamic effects, which are one of the most important reasons of vibration and hydraulic noises. In order to appraise the virtue of the present unsteady computational approach with semi-empirical correlation given by Stepanoff [10] may be used. Stepanoff has suggested that the radial thrust due to due to the nonuniformity of the circumferential pressure distribution is a function of total head, H, impeller diameter, d_2, impeller width, b_2, and an experimental coefficient K_r

$$F_{\text{radial\_Stepanoff}}=K_r \rho g H d_2 b_2. \tag{3}$$

The coefficient K_r depends on the operating point and reaches its maximum at shutoff:

$$K_r=(0.36\cdots\cdots 0.6)\left[1-\left(\frac{\dot{m}}{\dot{m}_{\text{opt}}}\right)^2\right]. \tag{4}$$

Comparing normalized time-averaged loading values (**Fig. 16**), numerical calculations appear to be less responsive to off-design conditions. On the other hand, the coefficient in Eq. (4) is more or less uncertain in the setup considered here.

Conclusion

The results obtained show that the flow field in the impeller and volute casing of centrifugal pumps is periodically unsteady. It was confirmed that due to the interaction between impeller and volute casing the flow is characterized with pressure fluctuations, which are strong at impeller outlet and at the vicinity of the tongue. The large amplitudes of the pressure fluctuations at impeller outlet and in tongue region die away in the casing as the advancement angle increases. These reduced pressure fluctuations are spread to the discharge nozzle and are reflected to the impeller inlet. Using the unsteady pressure distribution inside the impeller, unsteady blade loading, which is one of the most important reasons of vibration, was calculated. The comparison of the numerical results obtained in this study with the published experimental results show a qualitative good agreement of the results considering the behavior of the unsteady pressure fluctuations.

Nomenclature

b_2 = outlet passage width of the impeller
Cp = pressure coefficient
d_2 = outlet diameter of the impeller
F_{radial} = radial force (blade loading)
p = pressure
u_2 = impeller outlet tip velocity
ρ = density

References

[1] Gülich, J. F., 1999, *Kreiselpumpen, Ein Handbuch für Entwicklung, Anlagenplanung und Betrieb*, Springer, Berlin.
[2] Arndt, N., Acosta, A. J., Brennen, C. E., and Caghey, T. K., 1990, "Experimental Investigation of Rotor-Stator Interaction in a Centrifugal Pump With Several Vaned Diffusers," ASME J. Turbomach., **112**, pp. 98–107.
[3] Kaupert, K. A., and Staubli, T., 1999, "The Unsteady Pressure Field in a High

Specific Speed Centrifugal Pump Impeller—Part I: Influence of the Volute,'' ASME J. Fluids Eng., **121**, pp. 621–629.
[4] Hagelstein, D., Hillewaert, K., Van den Braembussche, R. A., Engeda, A., Keiper, R., and Rautenberg, M., 2000, ''Experimental and Numerical Investigation of the Flow in a Centrifugal Compressor Volute,'' ASME J. Turbomach., **122**, pp. 22–31.
[5] Hillewaert, K., and Van den Braembussche, R. A., 1999, ''Numerical Simulation of Impeller-Volute Interaction in Centrifugal Compressors,'' ASME J. Turbomach., **121**, pp. 603–608.
[6] Longatte, F., and Kueny, J. L., 1999, ''Analysis of Rotor-Stator-Circuit Interactions in a Centrifugal Pump,'' ASME Paper FEDSM99-6866.
[7] Zhang, M., Wang, H., and Tsukamoto, H., 2002, ''Numerical Analysis of Unsteady Hydrodynamic forces on a Diffuser Pump Impeller due to Rotor-Stator Interaction,'' ASME Paper FEDSM2002-31181.
[8] González, J., Fernández, J., Blanco, E., and Santolaria, C., 2002, ''Numerical Simulation of the Dynamic Effects Due to Impeller-Volute Interaction in a Centrifugal Pump,'' ASME J. Fluids Eng., **124**, pp. 348–355.
[9] González, J., Santolaria, C., Blanco, E., and Fernández, J., 2002, ''Unsteady Flow Structure on a Centrifugal Pump: Experimental and Numerical Approaches,'' ASME Paper FEDSM2002-31182.
[10] Stepanoff, A. J., 1957, *Centrifugal and Axial Flow Pumps*, Krieger Publishing Company, Malabar, FL.
[11] Majidi, K., 2003, ''Numerical Calculation of Impeller/Volute Interaction in a Centrifugal Pump,'' *Proceedings of the 5th European Conference on Turbomachinery Fluid Dynamics and Thermodynamics*, pp. 597–606.
[12] Majidi, K., and Siekmann, H. E., 2000, ''Numerical Calculation of Secondary Flow in Pump Volute and Circular Casing Using 3D Viscous Flow Techniques,'' Int. J. Rotating Machinery, **6**(4), pp. 245–252.
[13] Majidi, K., 2004, ''Unsteady Radial Thrust of a Centrifugal Pump due to the Impeller/Volute Interaction,'' *Proceedings of the 10th International Symposium on Transport Phenomena and Dynamics of Rotating Machinery*, Pacific Center of Thermal-Fluids Engineering, Paper ISROMAC10-2004-032.

Thermoacoustic Modeling of a Gas Turbine Combustor Equipped With Acoustic Dampers

Valter Bellucci

Bruno Schuermans

Dariusz Nowak

Peter Flohr

ALSTOM (Switzerland) Ltd,
CH-5405 Baden-Dättwil, Switzerland

Christian Oliver Paschereit
Technical University of Berlin,
D-10623 Berlin, Germany

In this work, the TA3 thermoacoustic network is presented and used to simulate acoustic pulsations occurring in a heavy-duty ALSTOM gas turbine. In our approach, the combustion system is represented as a network of acoustic elements corresponding to hood, burners, flames and combustor. The multi-burner arrangement is modeled by describing the hood and combustor as Multiple Input Multiple Output (MIMO) acoustic elements. The MIMO transfer function (linking acoustic pressures and acoustic velocities at burner locations) is obtained by a three-dimensional modal analysis performed with a Finite Element Method. Burner and flame analytical models are fitted to transfer function measurements. In particular, the flame transfer function model is based on the time-lag concept, where the phase shift between heat release and acoustic pressure depends on the time necessary for the mixture fraction (formed at the injector location) to be convected to the flame. By using a state-space approach, the time domain solution of the acoustic field is obtained. The nonlinearity limiting the pulsation amplitude growth is provided by a fuel saturation term. Furthermore, Helmholtz dampers applied to the gas turbine combustor are acoustically modeled and included in the TA3 model. Finally, the predicted noise reduction is compared to that achieved in the engine. [DOI: 10.1115/1.1791284]

1 Introduction

In gas turbines operating with lean premix flames, the suppression of acoustic pulsations is an important task related to the quality of the combustion process and to the structural integrity of engines. Pressure pulsations may occur when acoustic resonance frequencies are excited by heat release fluctuations independent on the acoustic field (“loudspeaker” behavior of the flame). Heat release fluctuations can also be generated by acoustic fluctuations in the premixed stream. The feedback mechanism inherent in such a process may lead to combustion instabilities, the amplitude of pulsations being limited only by nonlinear effects (“amplifier” behavior of the flame).

To predict the acoustic field generated in gas turbine combustors, the combustion system may be lumped into several elements (e.g., hood, burners, flames, combustor, cooling channels, etc.) that are combined in a *thermoacoustic network* [1–6]. This approach has the advantage that different network elements are modeled using different acoustic models. In particular, annular hoods and annular combustors may be represented by means of approximate analytical solutions of the wave equation. Multi-burner arrangements are simulated by modeling the hood and combustor as Multiple Input Multiple Output (MIMO) elements, described by a transfer function linking acoustic pressures and acoustic velocities at burner locations [2–4]. A more accurate prediction of the hood and combustor is obtained by using Finite Element Methods (FEM) [5,6]. When the geometrical extent of burners and flames is small compared to acoustic wavelengths, only plane wave propagation may be considered. This “compactness” assumption restricts the application of the network approach to the low-frequency regime. Compact burners and compact flames are treated as two-port elements, where acoustic pressure and acoustic velocity upstream and downstream of the element are coupled linearly via a four-element transfer matrix. An $L-\zeta$ model is usually employed to describe the burner transfer function by means of burner “end-correction” (measuring hood and combustor air mass oscillations induced by burner air fluctuations) and “loss coefficient” (measuring the acoustic dissipation in the burner) [7]. The flame transfer matrix describes the interaction process between periodic heat release and an acoustic field. For lean premix flames, the sensitivity of heat release fluctuations to equivalence ratio oscillations may represent a strong feedback mechanism. In the *time-lag* approach, equivalence ratio oscillations are generated at the fuel injector location and then convected to the flame, this time-delay depending on the fluid dynamic field between the injector and the flame [1–5]. The combustion system stability is analyzed by determining the network eigenfrequencies. In linear and stable networks, pressure pulsation is also predicted in the frequency domain. In general, pulsation spectra may be obtained in the time domain by introducing nonlinearities to limit the growth of pressure amplitude [4,5].

In this work we present the *TA3* thermoacoustic network used for simulating the thermoacoustic response of a GT11N2 ALSTOM heavy-duty gas turbine. In *TA3*, the hood and the combustor are represented by means of three-dimensional FEM modal expansion. For the $L-\zeta$ representation of burners, the end-correction is obtained by FEM applied to a combustor/burners/hood model and the loss coefficient from impedance tube acoustic measurements. The flame is modeled as a gas dynamic discontinuity whose transfer function is measured in an atmospheric combustion test rig. A time-lag model of the flame transfer function is fitted to the experimental data. All the network element models are formulated in the time domain using a state-space representation and interconnected to obtain the model of the entire network system [8]. The stability analysis is then performed by computing the system eigenfrequencies. The time domain solution is obtained by including nonlinear saturation of the heat release term.

In addition to the above features, *TA3* can also simulate the effect of Helmholtz dampers applied to the combustion system for suppressing acoustic pulsations. A Helmholtz damper consists of a volume with a neck through which the fluid inside the resonator communicates with an external medium [9]. In combustion applications, a cooling flow must be maintained through the resonator in order to prevent overheating. When applying a resonator to an

---

Contributed by the International Gas Turbine Institute (IGTI) of THE AMERICAN SOCIETY OF MECHANICAL ENGINEERS for publications in the ASME JOURNAL OF TURBOMACHINERY. Paper presented at the International Gas Turbine and Aeroengine Congress and Exhibition, Vienna, Austria, June 13–17, 2004, Paper No. 2004-GT-53977. Manuscript received by IGTI, October 1, 2003; final revision, March 1, 2004. IGTI Review Chair: A. J. Strazisar.

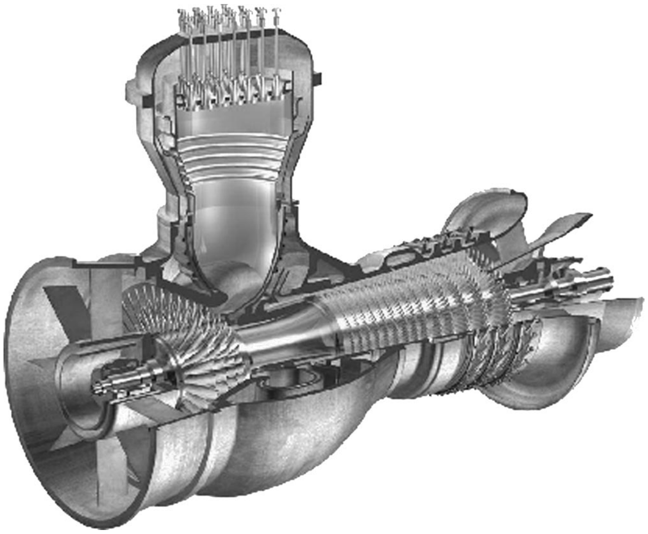

Fig. 1 GT11N2 ALSTOM gas turbine

enclosure, the resonator resonance frequency is tuned to the frequency of the eigenfrequency to be damped in the enclosure. The effect of the damper is then to replace the original eigenfrequency with two new acoustic modes, whose pressure amplitude may be made very small by appropriately tuning the resonator damping [10,11]. Therefore, for a specific eigenfrequency the use of Helmholtz dampers enhances the stability of the system by increasing the modal damping. In the present work, Helmholtz dampers applied to the GT11N2 combustor are acoustically modeled and included in the *TA3* network. Finally, the predicted noise reduction is compared to that achieved in the engine.

2 Thermoacoustic Modeling of Engine

The GT11N2 ALSTOM gas turbine is shown in Fig. 1. On the top of the silo combustors, both EV17i premix burners [12] and Helmholtz resonators are mounted. The thermoacoustic response of the engine is simulated by means of a *TA3* network including a hood, burners, flames, a combustor and resonators.

2.1 Hood and Combustor. Hood and combustor are modeled by means of FEM modal analysis applied to the real geometries. However, the only openings modeled on the boundary surface are those corresponding to burners and resonators. Therefore, both hood air supply channels and combustor exit are assumed acoustic closed boundaries. This assumption is motivated by the large area jump between air supply channels and hood and by the large flow Mach number at the combustor exit. By assuming acoustic wavelengths much larger than burner and resonator dimensions, the acoustic pressure $\hat{p}_j$ and normal acoustic velocity $\hat{u}_j$ are assumed uniform on the opening area A_j centered on the boundary at $\vec{x}_j$ (see Fig. 2). The acoustic unknowns $\hat{p}_j$ and $\hat{u}_j$ are expressed by making use of Green's functions and modal expansion [9]. It reads as

$$\hat{p}_j = i\omega\rho c^2 G(\vec{x}_j,\vec{x}_k) A_k \hat{u}_k, \tag{1}$$

where the Green's function $G(\vec{x}_j,\vec{x}_k)$ is defined as

$$G(\vec{x}_j,\vec{x}_k) = \sum_{n=0}^{N} \frac{\psi_n(\vec{x}_j)\psi_n(\vec{x}_k)}{V\Lambda_n(\omega^2 - 2i\omega\alpha - \omega_n^2)}, \tag{2}$$

with $\Lambda_n = \int_V \psi_n^2 dV$. In our notation, the acoustic velocity is defined as positive when its direction points outside the volume. Equation (1) describes the MIMO system relating the K velocities to the K pressures at volume openings. The eigenfunctions ψ_n and eigenfrequencies ω_n are the solutions of the problem

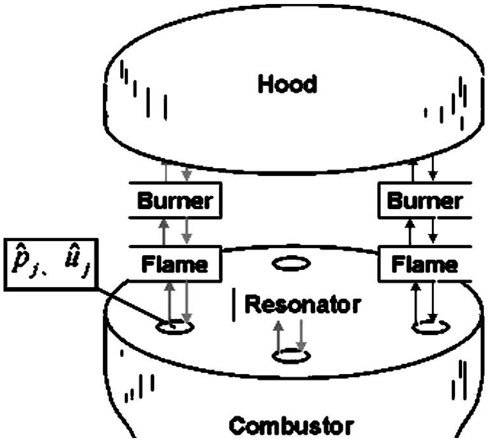

Fig. 2 Thermoacoustic network elements

$$c^2\nabla^2\psi + \omega^2\psi = 0, \tag{3}$$

$$\nabla\psi\cdot\vec{n} = 0 \quad \text{on} V \text{ boundary}. \tag{4}$$

The acoustic damping is directly introduced in Eq. (2) by means of the modal damping coefficient α. Therefore, as a solution of the real problem (3)–(4) both eigenfunctions and eigenfrequencies are real functions. The modal expansion approach does not include mean flow effects, such effects are considered negligible because of the small flow Mach number. ψ_n and ω_n are obtained numerically by applying FEM [13]. A hood and a combustor mode are shown in Fig. 3. Equation (1) yields the exact solution for $N = \infty$. However, a limited number of modes (depending on the frequency range of interest) is generally sufficient to represent the network element.

2.2 Burners. Acoustically compact burners are described by the 2×2 transfer matrix $\mathbf{T}$ defined by the expression

$$\begin{bmatrix} \hat{p}_2/(\rho_2 c_2) \\ \hat{u}_2 \end{bmatrix} = \begin{bmatrix} T_{11} & T_{12} \\ T_{21} & T_{22} \end{bmatrix} \begin{bmatrix} \hat{p}_1/(\rho_1 c_1) \\ \hat{u}_1 \end{bmatrix}. \tag{5}$$

The transfer function $\mathbf{T}(\omega)$ linearly relates acoustic pressure and acoustic velocity on both the sides of the one-dimensional acoustic element. The burner transfer function has been measured in the atmospheric impedance tube shown in Fig. 4. The test rig consists

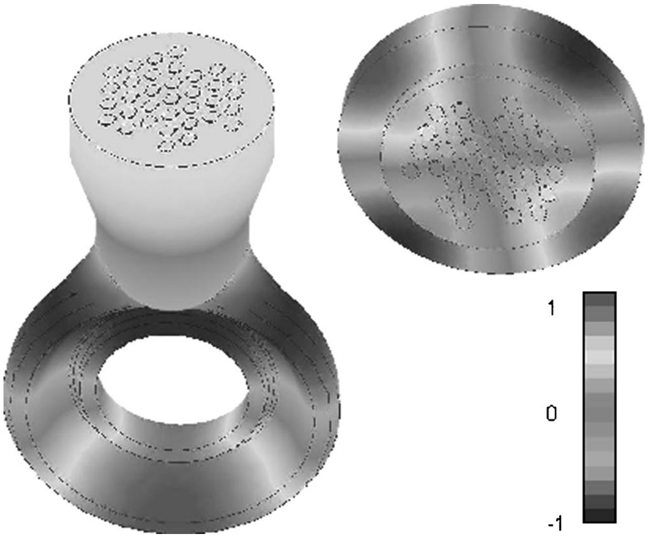

Fig. 3 Example of combustor mode (left) and hood mode (right)

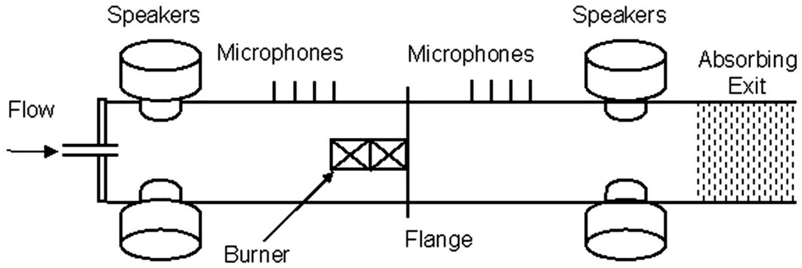

Fig. 4 Impedance tube test rig

of a hollow steel tube with a circular cross section. The tube diameter ensures that plane wave propagation occurs inside the tube for frequencies below the maximum of interest (cut-off frequency). The burner is mounted on the impedance tube flange and an air flow may also be introduced to simulate the engine burner speed. Several loudspeakers emitting pure toned frequency signals at various frequency intervals are used for the acoustic forcing. The response to this excitation is then measured using arrays of microphones mounted along the top side of the tube. Acoustic pressure and acoustic velocity upstream and downstream of the burner can be calculated from the microphone data using the Multi-Microphone Method [7]. Therefore, the burner transfer function relating the cross sections 1 and 2 (upstream and downstream of the burner, respectively) is obtained from Eq. (5). In our approach we locate both sections 1 and 2 at the burner exit, i.e., the burner is modeled as an acoustic discontinuity. An example of measured magnitudes of burner transfer function elements is reported in Fig. 5. Magnitude and phase measurements show that the burner transfer function may be expressed by means of the $L-\zeta$ model [7]

$$\mathbf{T}=\begin{bmatrix} 1 & i\rho\omega L+\rho\zeta u \\ 0 & 1 \end{bmatrix}. \tag{6}$$

Note that contrary to the hood and combustor, mean flow effects are taken into account in the burner model. The pressure loss term ζ obtained from impedance tube measurements is also employed in engine simulations. In the range of variation of the burner velocity, no significant ζ variations were observed. The measured end-correction L reported in Fig. 5 is a function of the test rig area changes upstream and downstream of the burner [14]. To obtain the end-correction for the engine geometry, FEM and *TA3* simulations of the combustion system model including the hood, burners and the combustor are performed. Then, the burner end-correction of the *TA3* model is tuned to obtain the same eigenfrequencies of the FEM model. The FEM combustion system model is shown in Fig. 6 together with the acoustic mode corresponding to the engine pulsation peak (determinated later in this work). Note that in spite of the complicated geometry, the accuracy of the FEM burner modeling is proved by the FEM transfer function also reported in Fig. 5. The result of this end-correction calibration is illustrated in Fig. 7. The end-correction calibration does not account for flow effects, in agreement with the small sensitivity shown by impedance tube measurements with respect to the burner speed.

2.3 Flames. The thermoacoustic dynamics of the EV17i burner flame depends on the several physical mechanisms affecting the heat release process (fuel injection, mixing, convective and diffusive transport, flame stabilization, chemical kinetics). The flame transfer function is the crucial element to perform accurate thermoacoustic simulations. In our approach, we measure flame transfer functions using the atmospheric combustion facility shown in Fig. 8 [1]. The test rig consists of a plenum chamber and a combustion chamber, respectively, upstream and downstream of

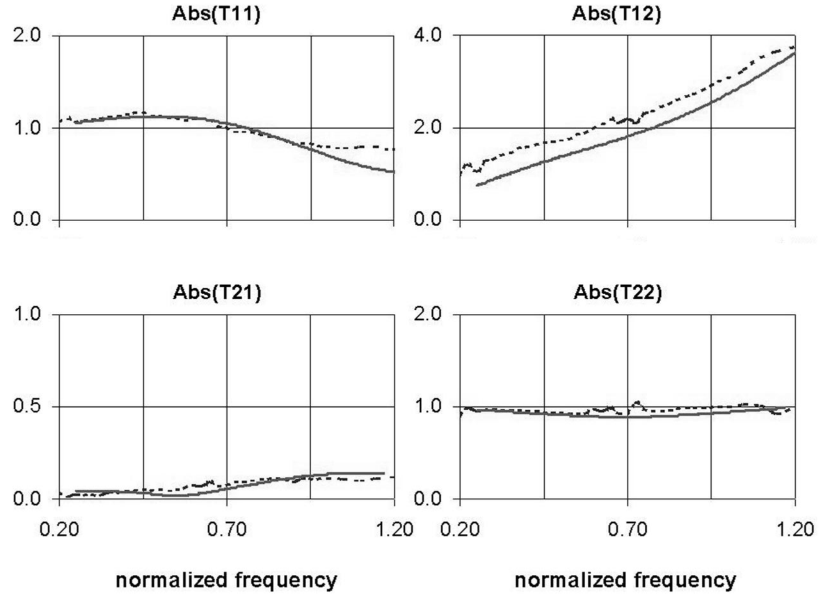

Fig. 5 Magnitude of burner transfer function terms. Dashed line: impedance tube measurements; solid line: FEM simulation

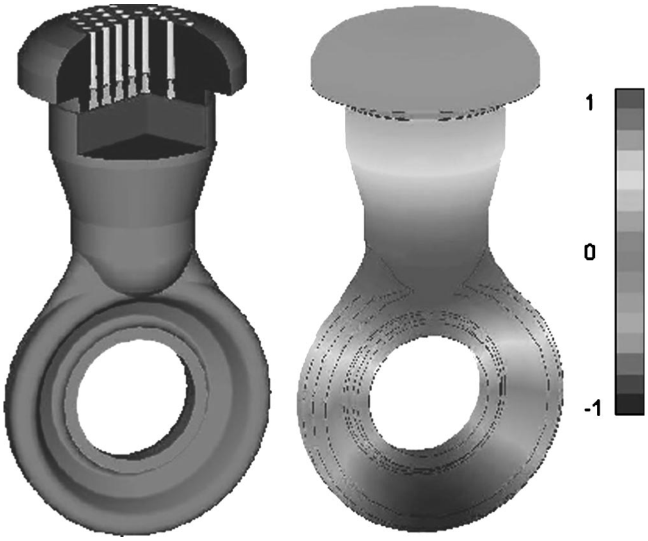

Fig. 6 FEM model (left) and example of the acoustic mode (right) of the combustion system

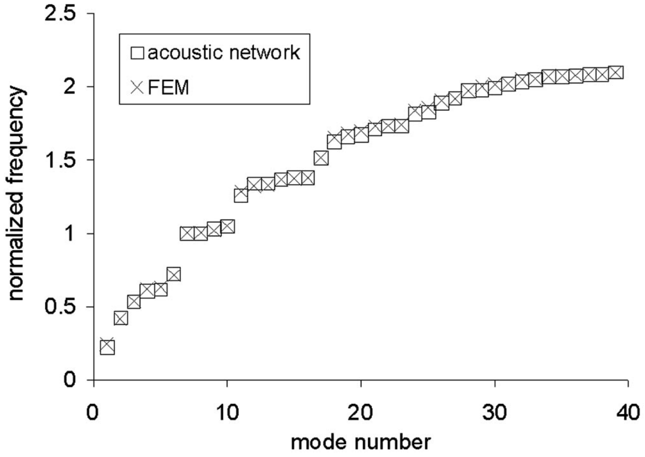

Fig. 7 A comparison of combustion system eigenfrequencies: FEM vs network results

the burner. The acoustic boundary condition of the exhaust system can be adjusted from almost anechoic (reflection coefficient <0.15) to open end reflection. Controlled excitation of the burner flow is accomplished by a circumferential array of loudspeakers. Pressure fluctuations are measured using water-cooled microphones. Like for the burner, the Multi-Microphone Method is used to obtain the transfer function of a zero-thickness flame (acoustic discontinuity) located at the burner exit. However, the flame acts also as a sound source independent of the acoustic field. To model the acoustic source behavior of the flame, a frequency dependent source term $\mathbf{S}=[S_p, S_u]^T$ is added to the right-hand side of Eq. (5). The term $\mathbf{S}=[S_p, S_u]^T$ is modeled by measuring in the combustion test rig the frequency spectra of the combustion noise term. Then, a transfer function $\mathbf{S}_H$ is fitted to the magnitude of the combustion noise frequency spectra. Finally, the source term is obtained by filtering a randomly generated time signal with the transfer function $\mathbf{S}_H$. Both the flame transfer function and the source term measurements are performed under atmospheric conditions in a broad range of variation of the burner speed and the flame temperature. An example of the flame transfer function measurement is reported in Figs. 9–10.

The measured flame transfer functions also give more physical insight into the interactions occurring in the flame. A theoretical expression for flame transfer functions is obtained starting from the acoustic jump relations written for planar flames in low-Mach number flows. They read [15] as

$$\hat{p}_2 = \hat{p}_1 \tag{7}$$

$$\hat{u}_2 = \hat{u}_1 + u_1\left(\frac{T_2}{T_1} - 1\right)\left(\frac{\hat{Q}}{Q} - \frac{\hat{p}_1}{p_1}\right). \tag{8}$$

In Eq. (7), the coefficient T_{12} defined in Eq. (5) is zero. On the contrary, Fig. 9 shows that $|T_{12}|$ is different from zero in the low frequency region. However, in this frequency region the accuracy of measurements is lower and frequencies are lower than the lowest frequency of interest for engine spectrum predictions. By neglecting flame speed fluctuations, heat release fluctuations are expressed as [16]

$$\frac{\hat{Q}}{Q} = \frac{\hat{\rho}_1}{\rho_1} + \frac{\hat{Y}_{f,1}}{Y_{f,1}}. \tag{9}$$

By assuming isentropic flow upstream of the flame, density fluctuations are given by

$$\frac{\hat{\rho}_1}{\rho_1} = \frac{\hat{p}_1}{\gamma_1 p_1}. \tag{10}$$

Fuel mass fraction fluctuations at the injector location are given by

$$\frac{\hat{Y}_{f,i}}{Y_{f,i}} = -\frac{\hat{u}_i}{\overline{u}_i} - \frac{\hat{p}_i}{\gamma_i \overline{p}_i}, \tag{11}$$

where we have assumed that the fuel mass flow rate is much smaller than the air mass flow rate. Furthermore, fuel mass flow rate fluctuations have been neglected in Eq. (11) because of the large injector pressure drop. Following the time-lag approach, $\hat{Y}_{f,i}$ is convected by the mean flow to the flame during the time delay τ necessary to fluid elements to travel from the injector to the flame. Therefore, one has

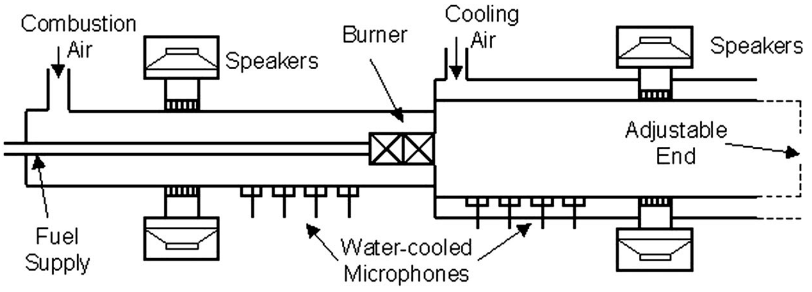

Fig. 8 Combustion test facility for flame transfer function measurements

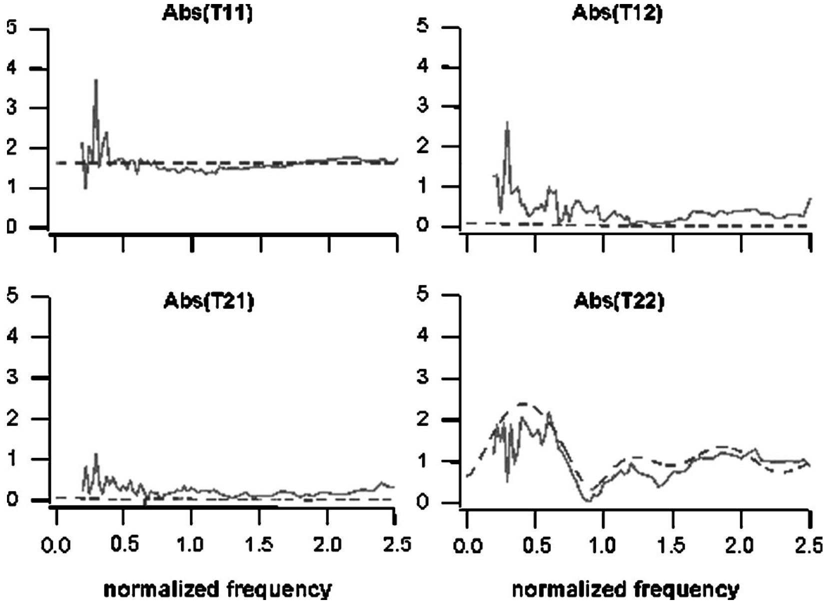

Fig. 9 Flame transfer function magnitude. Solid line: measurements; dashed line: analytical model.

$$\frac{\hat{Y}_{f,1}}{Y_{f,1}} = \frac{\hat{Y}_{f,i}}{Y_{f,i}} e^{-i\omega\tau} e^{-(1/2)\,\omega^2\sigma^2}, \tag{12}$$

where σ is the standard deviation of the Gaussian distribution of time delays [16]. The time delay distribution accounts for effects due to distributed fuel injection, non planar flame shape and time delay diffusion. The values of τ and σ are generated from fits to experimental transfer functions. By employing values of τ and σ dependent on the burner speed and flame temperature, a good agreement between an analytical model and measurements is obtained for all the EV17i operating conditions. Figures 9–10 show the comparison for one of the burner operating points.

2.4 Helmholtz Dampers. A schematic of a cooled GT11N2 Helmholtz resonator is shown in Fig. 11. The cooling air is supplied by the hood and enters the resonator through an opening located on the resonator volume. The neck mouth communicates directly with the combustion chamber. Both the resonator neck and volume are modeled as ducts where plane acoustic wave propagation occurs. The relation between acoustic impedances at duct extremities 1 and 2 in Fig. 11 is given by [17]

$$Z_1 = \frac{\dfrac{i}{\Gamma}(e^{k\ell\Gamma} - e^{-k\ell\Gamma}) + Z_2(e^{k\ell\Gamma} + e^{-k\ell\Gamma})}{(e^{k\ell\Gamma} + e^{-k\ell\Gamma}) + Z_2(e^{k\ell\Gamma} - e^{-k\ell\Gamma})}, \tag{13}$$

where the Γ factor is given by the Kirchhoff solution

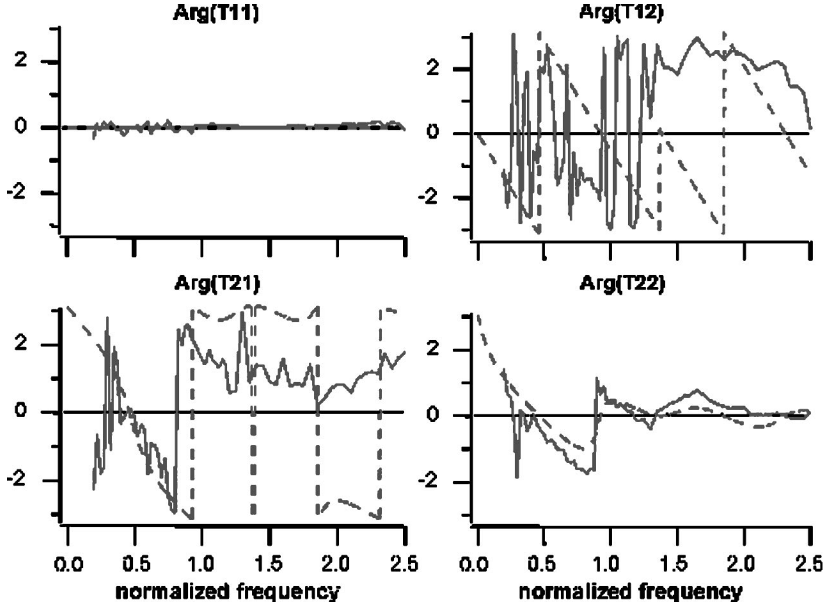

Fig. 10 Flame transfer function phase. Solid line: measurements; dashed line: analytical model.

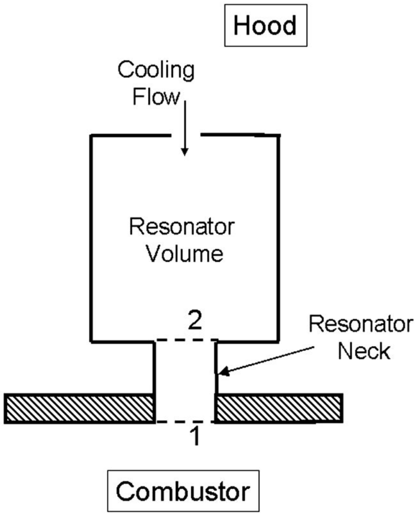

Fig. 11 GT11N2 cooled Helmholtz damper

$$\Gamma = i + \frac{i+1}{\sqrt{2}\mathrm{Sh}}\left(1+\frac{\gamma-1}{\sqrt{\mathrm{Pr}}}\right). \tag{14}$$

The area jump between the neck and the resonator volume is modeled by forcing the continuity of $\hat{p}$ and $\hat{u}A$. Furthermore, at neck ends an additional transfer function must be considered to account for end-resistance and end-reactance. The end-resistance is due to the area change pressure drop. The end-reactance accounts for the fluid mass inside the combustor that is involved in fluctuations by the air fluctuating inside the neck. The correspondent transfer function is expressed by Eq. (6), where the end-correction and pressure loss coefficient are functions of cooling flow velocity, area expansion and frequency [14]. The Helmholtz dampers were also tested in the impedance lab under atmospheric conditions. Figure 12 reports the comparison between measured and computed reflection coefficients for a GT11N2 resonator with cooling flow throughout.

3 Thermoacoustic Network

The combustion system elements are assembled together in the Thermo-Acoustic 3-dimensional (*TA3*) network written in the MATLAB environment [18]. Using the frequency domain formulation employed in the previous section, the stability analysis of the combustion system is performed by computing the eigenvalues of the resulting linear system. The real part of eigenvalues gives the frequency of pulsation peaks. The growth rate (i.e., the eigenvalue imaginary part) determines the stability of the system. Using *TA3*, pulsation spectra are also computed by post-processing the time domain solution. The time domain representation of Eq. (1) corresponds to K second order differential equations relating $2K$ unknowns. Noting that a differential equation of any order can be represented as a system of first order differential equations and that all the terms of the Green's function (2) have the same poles ω_n, Eq. (1) can be expressed in the time domain by a *state-space* formulation consisting of $2N+K$ first order differential equations in $2N+2K$ unknowns. It reads [8] as

$$\frac{\partial \mathbf{y}}{\partial t} = \mathbf{A}\mathbf{y} + \mathbf{B}\mathbf{u}', \tag{15}$$

$$\mathbf{p}' = \mathbf{C}\mathbf{y} + \mathbf{D}\mathbf{u}', \tag{16}$$

where

$$\mathbf{y} = [y_1, \ldots, y_{2N}]^T,$$

$$\mathbf{p}' = [p_1, \ldots, p_K]^T, \quad \mathbf{u}' = [u_1, \ldots, u_K]^T,$$

$$\mathbf{A} = \begin{bmatrix} 0 & -\omega_n & & & \\ \omega_n & -2\alpha & & & \\ & & \ddots & & \\ & & & 0 & -\omega_n \\ & & & \omega_n & -2\alpha \end{bmatrix},$$

$$\mathbf{B} = \begin{bmatrix} 0 & \ldots & 0 \\ -\psi_1(\vec{x}_1)A_1 & \ldots & -\psi_1(\vec{x}_K)A_K \\ & \vdots & \\ 0 & \ldots & 0 \\ -\psi_N(\vec{x}_1)A_1 & \ldots & -\psi_N(\vec{x}_K)A_K \end{bmatrix},$$

$$\mathbf{C} = \frac{\rho c^2}{V}\begin{bmatrix} 0 & \dfrac{\psi_1(\vec{x}_1)}{\Lambda_1} & & 0 & \dfrac{\psi_N(\vec{x}_1)}{\Lambda_N} \\ \vdots & \vdots & \cdots & \vdots & \vdots \\ 0 & \dfrac{\psi_1(\vec{x}_K)}{\Lambda_1} & & 0 & \dfrac{\psi_N(\vec{x}_K)}{\Lambda_N} \end{bmatrix},$$

$$\mathbf{D} = 0.$$

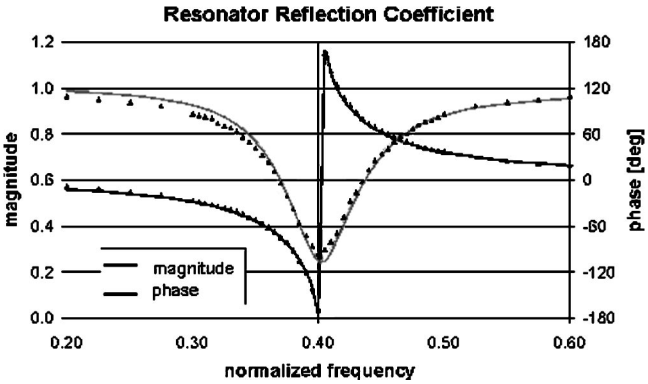

Fig. 12 Reflection coefficient of GT11N2 cooled resonator. Solid line: analytical model; triangles: impedance lab measurements.

The state-space representation is also used to model burners, flames and resonators. In particular, the flame model contains a time delay term and is of infinite order in time domain. In order to avoid systems of infinite order, the time delay is approximated by a *Padé approximation*. The entire system can now be modeled by interconnecting all the outputs of the subsystems to the inputs of their "neighbors" (see Fig. 2). Special care is taken to ensure that the system is causal and stable. The source terms in the flame module provides the external excitation. Unbounded amplitude growth in time is avoided by non-linear fuel saturation, that is introduced by applying the function H to fuel mass fraction fluctuations of Eq. (9). It reads [5] as

$$H\{Y'_{f,1}(t)\} = \begin{cases} Y'_{f,1}(t) & \text{if } |Y'_{f,1}(t)| < Y_{f,\lim} \\ \operatorname{sign}[Y'_{f,1}(t)]Y_{f,\lim} & \text{if } |Y'_{f,1}(t)| > Y_{f,\lim} \end{cases}$$

The computational time for a single spectrum simulation is in MATLAB of the order of 0.5 min.

4 Results

The *TA3* GT11N2 model has been used to simulate baseload conditions. Both engine and *TA3* spectra reported in Fig. 13 were obtained without employing any resonator tuned at the pulsation peak frequency. The atmospheric flame transfer function was employed without any pressure scaling, assuming the natural gas

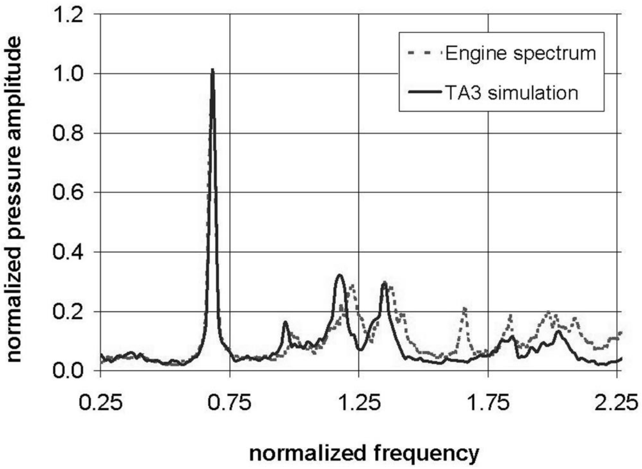

Fig. 13 GT11N2 spectrum without resonators at peak frequency: engine vs TA3 network.

chemical kinetics independent of pressure. The fuel saturation parameter $Y_{f,\lim}$ of Eq. (17) was fitted to the engine spectrum, leading to an accurate pulsation amplitude prediction over the frequency range of interest. After having calibrated the model, different engine operating conditions could be successfully simulated without any variation of the calibration parameters. In particular, Fig. 14 shows *TA3* and engine spectra for an engine configuration with resonators tuned at the pulsation peak frequency. Also in this case, a good agreement between simulations and measured spectrum was achieved. The pulsation amplitude reduction with resonators is about 50%, showing the effectiveness of using Helmholtz resonators for gas turbine acoustic damping.

5 Conclusions

The *TA3* thermoacoustic network has been presented and applied to the prediction of pulsation spectra in a heavy-duty ALSTOM gas turbine combustor. The use of the thermoacoustic network approach has the advantage that the different network elements may be described by different acoustic models singularly validated. Therefore, a Finite Element Method description of the hood and the combustor accounted for the geometrical complexity of the two elements, the physics being described by the wave equation without mean flow effects. In the low-frequency range, burners, flames and resonators have been treated as compact elements (one-dimensional from the point of view of the internal acoustic field). The burner transfer function has been measured and fitted to an $L-\zeta$ model. To obtain the burner end-correction for the engine geometry, a method based on the Finite Element Method analysis of the "cold" (i.e., without flame) combustion system has been proposed. Flame transfer function measurements have permitted us to identify equivalence ratio fluctuations as the main mechanism responsible for acoustic-flame feedback. The acoustic elements have been assembled in the *TA3* network and the time solution has been obtained. The experimental–numerical combined process behind the *TA3* network leads to very fast and accurate engine spectrum computation. In particular, the correct prediction of the effects of acoustic dampers applied to gas turbine combustors have been demonstrated.

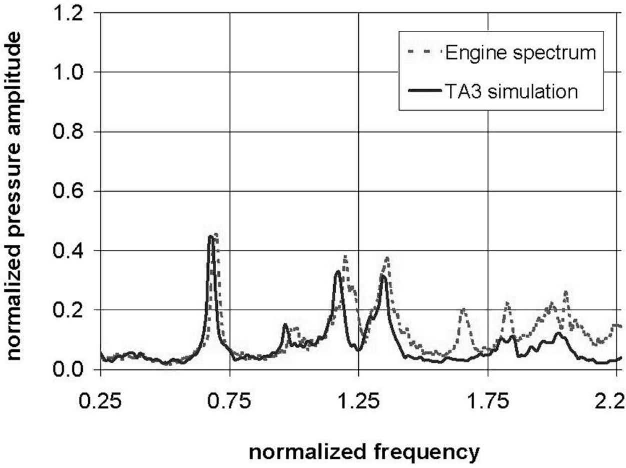

Fig. 14 GT11N2 spectrum with resonators at peak frequency: engine vs TA3 network.

Nomenclature

$(\cdot)$ = mean flow quantities
$(\cdot)'$ = acoustic perturbations
$\widehat{(\cdot)}$ = Laplace transform of acoustic perturbations
A = cross sectional area of burners or resonators
c = speed of sound
G = Green's function
H = fuel saturation function
k = wave number $=\omega/c$
K = number of openings on hood or combustor
ℓ = length of resonator ducts
L = end-correction
$\vec{n}$ = outward normal vector
N = number of acoustic modes
p = pressure
Pr = Prandtl number
Q = heat release per unit area and time
Sh = shear number $=\sqrt{\omega A/(\pi\nu)}$
T = temperature.
$\mathbf{T}$ = transfer matrix
u = normal flow velocity
V = volume of the hood or combustor
$\vec{x}$ = coordinate of burner exit or resonator neck mouth
$\mathbf{y}$ = state variables
Y_f = fuel mass fraction
Z = acoustic impedance normalized by ρc
α = acoustic damping coefficient
γ = specific heat ratio
Γ = plane wave attenuation factor
ζ = pressure loss coefficient
λ_n = mode normalization factor
ν = kinematic viscosity
ρ = density
σ = standard deviation of τ distribution
τ = time delay
ψ_n = acoustic mode
ω = circular frequency$=2\pi\cdot$frequency
ω_n = acoustic eigenfrequency

Subscripts

1 = acoustic element upstream section
2 = acoustic element downstream section
i = injector location

References

[1] Paschereit, C. O., Flohr, P., and Schuermans, B., 2001, "Prediction of Combustion Oscillations in Gas Turbine Combustors," AIAA Paper 2001-0484, Reno, NV, January 8–11.
[2] Akamatsu, S., and Dowling, A., 2001, "Three-Dimensional Thermoacoustic Oscillations in a Premix Combustor," ASME Paper 2001-GT-0034, New Orleans, LA, June 8–11.
[3] Dowling, A. P., and Stow, S. R., 2003, "Modal Analysis of Gas Turbine Combustor Acoustics," J. Propul. Power, **19**, pp. 751–764.
[4] Schuermans, B., Bellucci, V., and Paschereit, C. O., 2003, "Thermoacoustic

Modeling and Control of Multi Burner Combustion Systems,'' ASME Paper GT-2003-38688, Atlanta, GE, June 16–19.

[5] Pankiewitz, C., and Sattelmayer, T., 2002, ''Time Domain Simulation of Combustion Instabilities in Annular Combustors,'' ASME Paper GT-2002-30063, Amsterdam, The Netherlands, June 3–6.

[6] Evesque, S., and Polifke, W., 2002, ''Low-Order Acoustic Modelling for Annular Combustors: Validation and Inclusion of Modal Coupling,'' ASME Paper GT-2002-30064, Amsterdam, The Netherlands, June 3–6.

[7] Schuermans, B., Polifke, W., and Paschereit, C. O., 1999, ''Modeling Transfer Matrices of Premixed Flames and Comparison with Experimental Results,'' ASME Paper 1999-GT-0132, Indianapolis, IN, June 7–10.

[8] Schuermans, B., Bellucci, V., Nowak, D., and Paschereit, C. O., 2002, ''Modelling of Complex Thermoacoustic Systems: A State-Space Approach,'' *9th International Congress on Sound and Vibration*, Orlando, FL, July 8–11.

[9] Morse, P. M., and Ingard, K., 1968, *Theoretical Acoustics*, McGraw-Hill, New York.

[10] Fahy, F. J., and Schofield, C., 1980, ''A Note on the Interaction Between a Helmholtz Resonator and an Acoustic Mode of an Enclosure,'' J. Sound Vib., **72**, pp. 365–378.

[11] Bellucci, V., Paschereit, C. O., Flohr, P., and Magni, F., 2001, ''Acoustic Pulsations in Industrial Gas Turbines,'' ASME Paper 2001-GT-0039, New Orleans, LA, June 8–11.

[12] Paschereit, C. O. et al., 2002, ''Combustion Control by Extended EV Burner Fuel Lance,'' ASME Paper GT-2002-30462, Amsterdam, The Netherlands, June 3–6.

[13] *SYSNOISE 5.4 Documentation*, 1999, LMS International, Brussels, Belgium.

[14] Bellucci, V., Paschereit, C. O., and Flohr, P., 2002, ''Impedance of Perforated Screens with Bias Flow,'' AIAA Paper 2002–2437, Breckenridge, CO, June 17–19.

[15] Chu, B. T., 1953, ''On the Generation of Pressure Waves at a Plane Flame Front,'' *Fourth Symposium (International) on Combustion*, Massachusetts Institute of Technology, pp. 603–612.

[16] Bellucci, V., Schuermans, B., Paschereit, C. O., and Flohr, P., 2001, ''Thermoacoustic Simulation of Lean Premixed Flames Using an Enhanced Time-Lag Model,'' AIAA Paper 2001-2794, Anaheim, CA, June 11–14.

[17] Tijdeman, H., 1975, ''On the Propagation of Sound Waves in Cylindrical Tubes,'' J. Sound Vib., **39**, pp. 1–33.

[18] Using MATLAB *Version 6*, 1999, MathWorks, Natick, MA.

Experimentally Verified Numerical Optimization of a Three-Dimensional Parametrized Turbine Vane With Nonaxisymmetric End Walls

Marc G. Nagel

Ralf-D. Baier

MTU Aero Engines
Aerodynamics Turbine/Compressor (TEAD),
Dachauer Str. 665,
80995 München, Germany

A three-dimensional optimization procedure on the basis of a transitional Navier-Stokes code has been developed and tested. It allows complete three-dimensional parameterization of the flow channel for improved engine component design. Both the aerofoils and the end walls are three-dimensionally parameterized to permit full design control over the wetted surface. The end wall curvature is in fact controlled by the superposition of an axisymmetric and a nonaxisymmetric parameterization. The target comprises profile and secondary losses. The optimization procedure was applied to a low-loss turbine vane and resulted in an aerodynamic design with considerably reduced losses. Vanes and end walls were then manufactured according to this optimization. The high-speed cascade wind tunnel measurements performed on these parts confirm the computational results.

[DOI: 10.1115/1.1773848]

Introduction

Improving aircraft engine component efficiencies beyond the high level already achieved by aerodynamic means is an ambitious task, which requires innovative ideas and methodological approaches.

A promising suggestion is to make full use of the geometrical degrees-of-freedom available in aerodynamic design. In the 1970s first studies were conducted to investigate e.g. traditionally neglected annulus design options for the improvement of aerofoil performance. Twenty years ago even nonaxisymmetric annulus contouring has already been proposed. In many of these investigations attempts were made at designing aerofoils and end walls independently of each other. In some papers, annulus contouring was assessed positively, whereas others claimed it to be disadvantageous. An explanation for the contradictory opinions is that in some investigations initially a front loaded aerofoil was transformed by end wall contouring to an aft loaded aerofoil which resulted in a subsequent positive rating. In others the rating was negative as an aft loaded aerofoil was found to be simply overloaded.

The appropriate methodological approach is an integrated design of both aerofoil and annulus shape. With the resulting enlarged design space, however, the calculation effort increases considerably for two reasons: first because of the higher-dimensional search regions and, secondly, because the quasi-three-dimensional methods can no longer be used. Instead, time-consuming three-dimensional methods are required. This new task with search operations in a high-dimensional design space is not particularly suitable for engineer-in-the-loop type approaches. Numerical optimization is therefore needed, which has already found widespread application in aerodynamic design. This paper presents the systematic mastering of the complexity of a fully three-dimensional parameterization by computational means, which is the result of a five-year project.

Three-Dimensional Design Space. The three-dimensional design space for the flow channel of a blade row of a turbomachine is on principle established by the parameterized wetted surface. It comprises both the blade surface and the surface of the annulus.

The blade surface can be described by two-dimensional aerofoil shapes, parameterizable by various methods, in combination with a radial stacking function for these two-dimensional sections. **Fig. 1** shows the parameterization of an aerofoil section split up by four spline functions.

Figure 2 gives an overview of the most important three-dimensional blade shaping possibilities. Various combinations of these stacking laws are common practice.

Figure 3 summarizes the possibilities of flow channel design. It distinguishes between axisymmetric and nonaxisymmetric annulus profiling. Nonaxisymmetric end-wall contouring within the row offers the freedom—as the sketch shows—to choose noncontinuous circumferential functions, whereas platform contouring just in front of the row has to satisfy certain continuity conditions.

Scope. The scope of the project described in this paper covers the computational generation of innovative shapes. This concept bases on in the first impressive steps in the optimization of technical systems. In the late 1960s, some innovative fluid mechanical devices, like a nozzle for two-phase flow, have been designed by means of optimization algorithms, [1]. The designs obtained were genuinely new and absolutely unexpected from the human designer's point of view. Decisive for the results was the combination of an explorative search based on the principles of biological evolution and the use of experiments with adaptive walls within the optimization loop. An even more elegant approach would be to choose a flow configuration, which inherently fulfils a minimisation functional as the ice formation method does, [2].

The authors of this paper followed a similar approach: First they wanted to create new advantageous blade row geometries (in this case algorithmically) and secondly, analyze and understand the innovative configuration. In the absence of obviously experimentally modifiable aerofoil and end-wall contours, the flow had to be simulated. This required an additional validation step for the simulation process. Another particular difficulty was that, due to

---

Contributed by the International Gas Turbine Institute and presented at the International Gas Turbine and Aeroengine Congress and Exhibition, Atlanta, GA, June 16–19, 2003. Manuscript received by the IGTI December 2002; final revision March 2003. Paper No. 2003-GT-38624. Review Chair: H. R. Simmons.

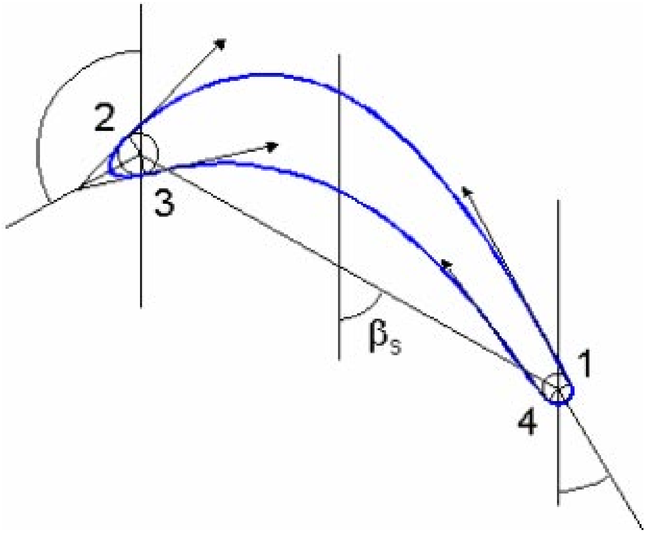

Fig. 1 Parameterization of aerofoil section

limited computing resources only NLP (nonlinear programming) was employed, instead of explorative search strategies like GA (genetic algorithm), ES (evolutionary strategy), or SA (simulated annealing).

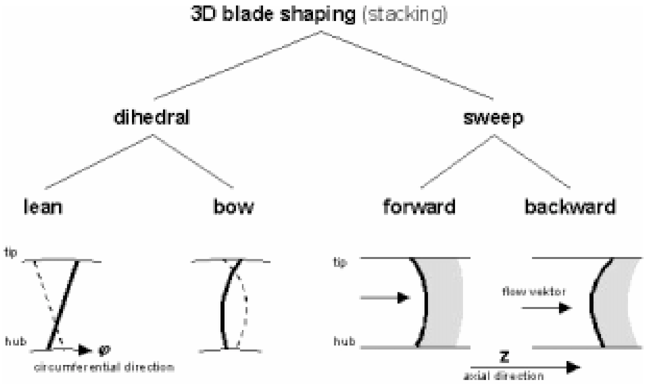

Fig. 2 Some principal radial stacking procedures

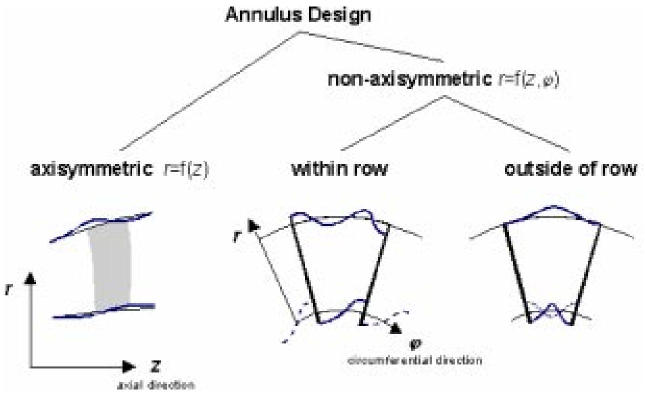

Fig. 3 Basic flow channel design options

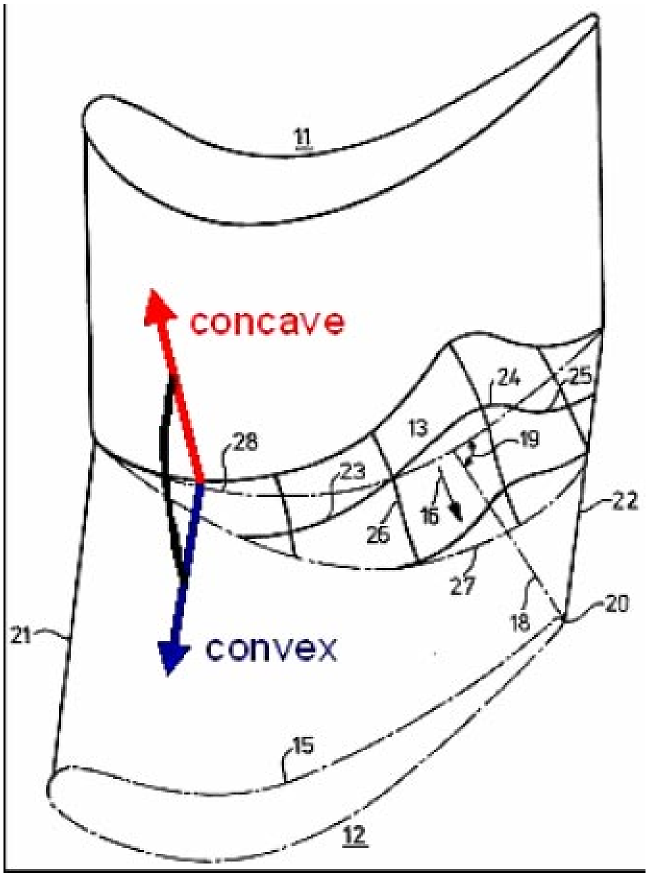

Fig. 4 Curvature design by Bischoff [3]

End-Wall Profiling. One of the first proposals to reduce secondary flow losses by using non-axisymmetric end walls is presented in [3]. The basic idea is to reduce the pressure gradient between suction and pressure sides at the wall by compensating the convex curvature of the blade's suction side by a concave curvature on the wall (**Fig. 4**).

Since then a couple of papers dealing with nonaxisymmetric end walls has been published, with the topics ranging from HP NGV via LP cascade and rig investigations, [4–7]. The latter claims stage efficiency improvements by at least 0.5%. The basic idea of Bischoff, i.e., to influence the transverse pressure gradient by shaping the end-wall curvature, was taken up successfully by [8].

Optimization Process

The backbone of the optimization process is an unconditionally stable evaluation chain (**Fig. 5**). The most important elements are described below.

The complete optimization system was built up with tools and processes appropriate for three-dimensional engine component design.

Search Algorithm. The numerical optimization algorithm is a single element in the process chain. A well-established gradient method, i.e., the SQP-method DONLP2 in ANSI-C implementation has been used, [9]. The gradient computations are performed in parallel on different processors.

Flow Solver and Meshing. The simulation code used is the extensively validated RANS 3D compressible transitional Navier-Stokes solver TRACE-S, which is the result of a joint development of the Institute of Propulsion Technology of the DLR Cologne and MTU Aero Engines in Munich. It should suffice to describe the features of TRACE-S in short, since more detailed descriptions of its performance are available for example by [10]. TRACE-S is a block-structured, finite volume code with implicit

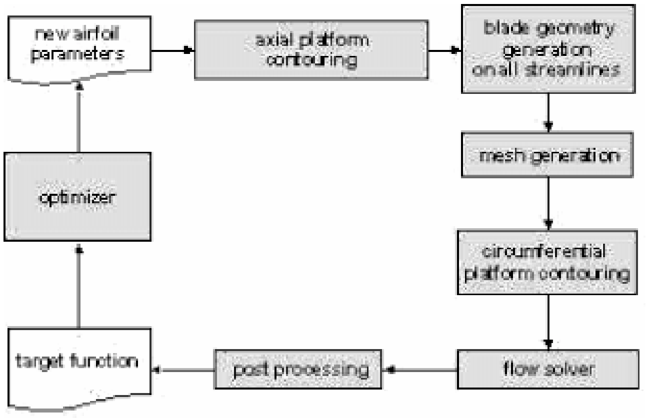

Fig. 5 Optimization process

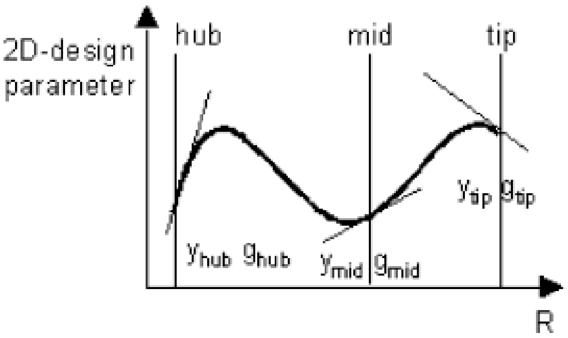

Fig. 6 Radial parameterization of two-dimensional aerofoil sections

time integration in combination with a Roe-upwind scheme. The code is vectorized and able to use shared as well as distributed memory parallelization.

From the available turbulence models the k-ε model was selected for optimization and the Wilcox k-ω two-equation model in low-Reynolds version with compressibility extension for fine mesh recalculations. The equations are time-discretized by 2×2 block-implicit time stepping. The transition model employed is based on the modified correlations of Abu-Ghannam and Shaw [11]. For information about the implementation see [12].

The computational mesh consists of two blocks. The vane under investigation is discretised with one O-type grid around the aerofoil and an H-type grid for covering the major part of the channel. To resolve the boundary layer the dimensionless wall distance y^+ on the aerofoil of 1, was selected.

Geometry Generator. The geometry consists of three parts: the blade generator, the axial platform, and the circumferential platform contouring parts, existing as different modules for the time being.

The blade geometry is defined on two-dimensional blade sections along streamlines. On the individual streamlines each blade section consists of a base frame of a quasi-blade chord with a length and a stagger angle and two short segments at the ends. Symmetrical circuit sections are placed over both ends. The angle of the short segments corresponds to the angle of the leading edge and the trailing edge, respectively. The segment lengths correspond to the leading edge and trailing edge thicknesses. Between the compound points 1 and 2, a spline describes the suction-side shape (**Fig. 1**). Between the compound points 3 and 4, a spline specifies the pressure-side shape. At each compound point the slope, the curvature and the aspect ratio parameters of slope and curvature can be influenced. The symmetrical slopes of the curves at points 2/3 and 1/4 represent the wedge angles at the leading and trailing edge, respectively. Thus a targeted possibility to influence the shape of the pressure and suction-side geometry is available to the user. All influencing parameters are nondimensionalized values, which give the designer a feeling of proportions irrespective of the actual size of the blade.

The parameters controlling the shape of an aerofoil section like in **Fig. 1** are radially linked by an additional radial parameterization to ensure a radially smooth three-dimensional blade (**Fig. 6**). In this case the decision was made in favor of fifth-order polynoms (six variables). The polynoms for the blade section parameters were modified by the value and the slope at hub, tip, and a selectable point in between. The three-dimensional blade shape is controlled by these geometry variables.

The axial end-wall profiling is shown in **Fig. 7**. On the basis of the quasi-three-dimensional annulus contour the shape and curvature of the end wall can be controlled locally as can be seen from the upper curves in **Fig. 7**, which consist of two spline segments each. The arrows again symbolize the stretching factors for surface control. A change of the axial end wall contour leads also to a change of the blade shape, due to the blade definition on streamlines.

Circumferential end wall contouring is achieved by multiplicatively composing two univariate functions to obtain a bivariate contour modulation $\Delta r(\varphi,z)$, which is dependent on the circumferential and axial coordinate within the row, [13,14]. A shape function f_S, which is prescribed between suction and pressure sides, controls the curvature in circumferential direction, whereas a so-called decay function f_D prescribed on both suction and pressure sides on hub and/or casing leads to a modulation Δr equal to zero at the inlet and outlet of the row (**Fig. 8**). This approach has the advantage that it limits the additional design variables to a few essential ones. $\Delta r(\varphi,z)$ is transformed from a rectangular computational domain $\Delta r(y,x)=f_S(y)\cdot f_D(x)$. **Figure 9** gives an example of this composition in the computational domain where the decay function itself is composed of two functional parts.

Postprocessing and Target Function. The target function is composed of a weighted addition of various absolute postprocessor results, where the integral flux averaged loss, calculated by the flow solver, accounted for the major part. The difference

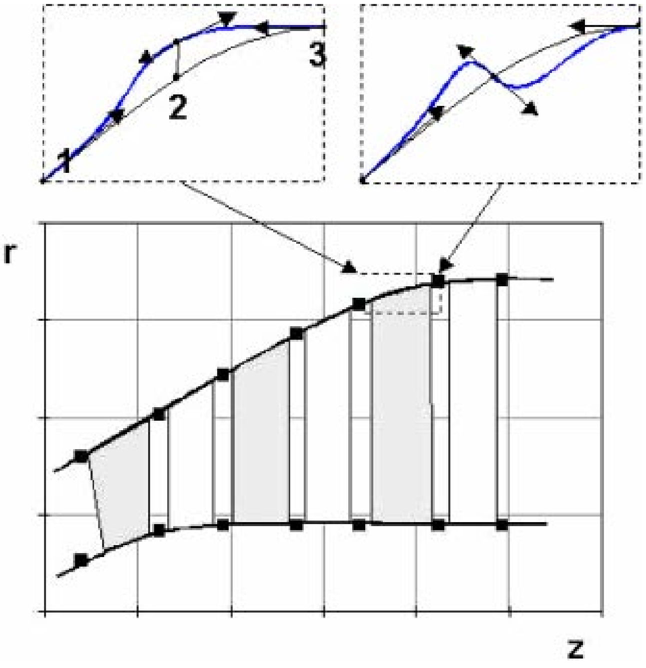

Fig. 7 Axisymmetric end-wall profiling

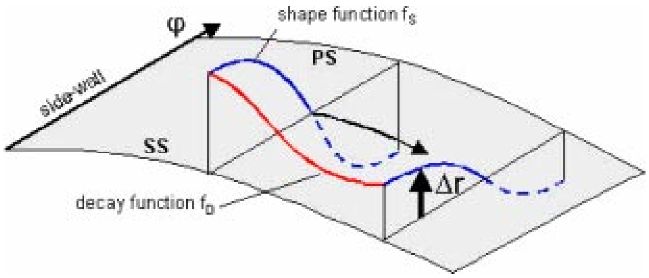

Fig. 8 End-wall profiling between suction and pressure sides

between calculated outflow angle distribution and secondary flow free S2 outflow angle distribution is useful for estimation of the secondary flows. The maximum derivation and the integrated area between the two curves to cover oscillations as well as the secondary kinetic energy (SKE) are considered to a small extent. To maintain the same blade loading during the optimization cycle boundary conditions are defined. The most important is compliance with the integral flux averaged outflow angle in circumferential direction. With a S1 postprocessor evaluation criteria for the blade pressure distributions on the streamlines are calculated. Their application is useful as wide open boundary conditions to restrict the search area inside the area of validity of the employed numerical models, for example. The analysis of these values on all streamlines soon result in numerous aerodynamic boundary conditions. Thus, the optimization of the new technology is not adversely affected.

Optimization Test Case

The numerical optimization system for engine component improvements could best demonstrate its performance by an experimental validation allowing precise and highly significant measurements. Therefore a large-scale linear cascade for a high-speed wind tunnel has been chosen as test case. It is noted that the design coordinate system and the experimental one differ, since the experimental results are given in Cartesian coordinates. For comparisons both systems are brought into accordance. Using a cascade as test case has some further implications. There was no need to include structural constraints offering the chance to generate a pure aerodynamic optimum. Subsequently the geometrical changes could be big, which was desirable from a testing perspective, since this truly challenged the design system. Though the results would not be directly transferable to a multistage component it was expected to computationally generate new ideas for secondary flow reduction.

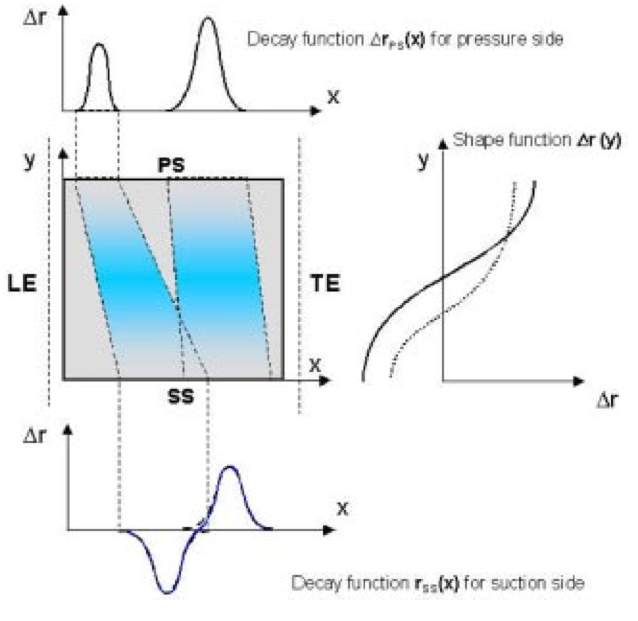

Fig. 9 End-wall contour modulation in a rectangular domain

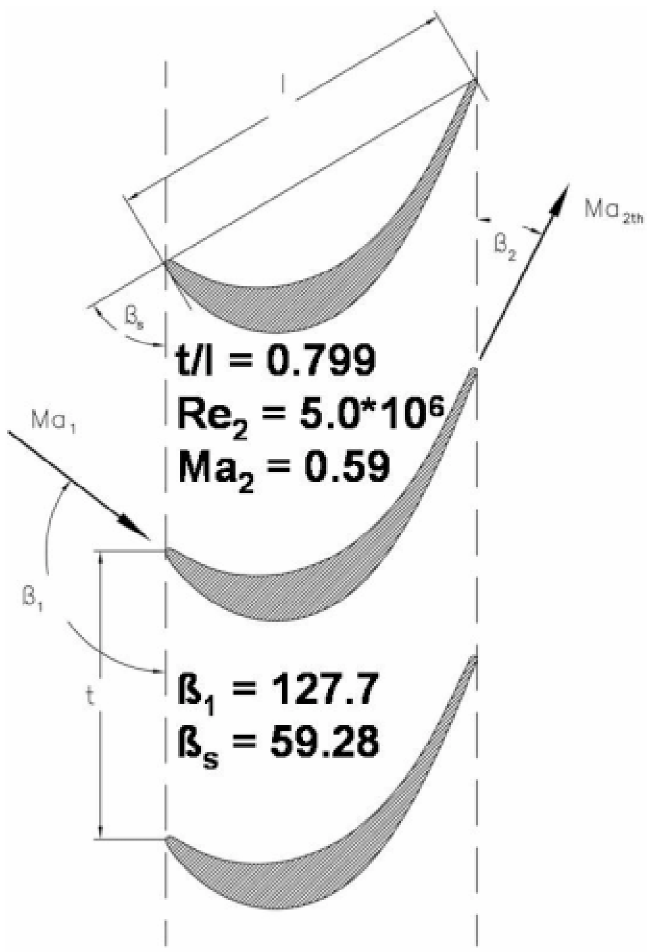

Fig. 10 Reference Cascade T106

The aft loaded aerofoil (T106) derived from a low-pressure turbine has been selected since it is considered as a good reference and starting point and moreover allows comparison with the earlier work of [15]. Exhaustive investigations on the base line cascade are reported in [16].

Figure 10 shows the original prismatic aerofoil. In order to obtain a realistic acceleration ratio both end walls, in contrast to the original design, are divergent by an angle of $\lambda = 15$ deg. See **Fig. 11** for the installation in the large-scale cascade High-Speed Cascade Wind Tunnel of the Universität der Bundeswehr München.

Numerical Optimization

The flow solver TRACE-S accepts only boundary conditions in cylinder co-ordinates. For this reason, the midspan of the wind tunnel cascade was modeled quasi linear on a radius of 10 meters. The symmetry of the cascade permitted the performance of numerical calculations for half-span only. The flow channel was discretized by an OH-topology calculating mesh with 160,000 nodes (half-span). The integral flow evaluation was performed numerically (last grid plane) and experimental at $x/l_{ax} = 1.5$. To provide a basis for the optimization the cascade had been parameterized by pre-processors. To achieve an axial contouring of the casing wall between blade, inlet plane and outlet plane, the radius and the

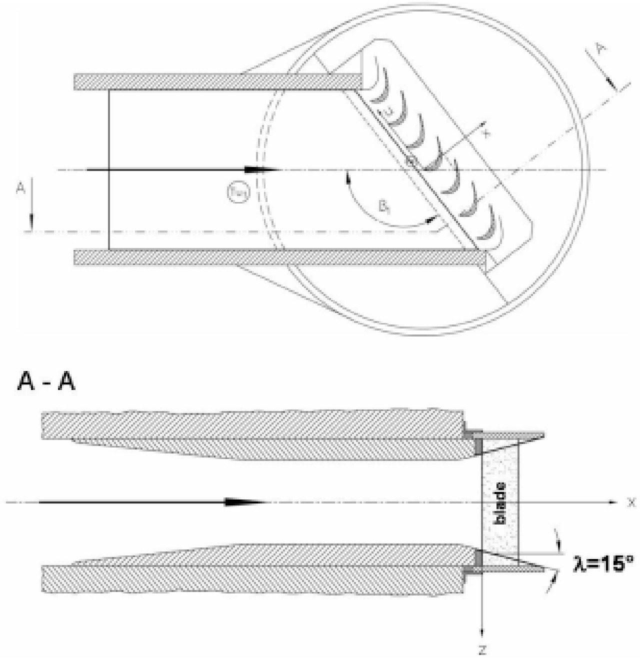

Fig. 11 Cascade T106 in HGK wind tunnel

slope of the interference point of the parameterization were enabled. With an S2 calculation 21 streamlines were defined through the blade passage. The streamlines were concentrated towards the casing sidewall. The blade shape is defined on these streamlines with the outlined parameterization above.

The blade sections were stacked over the trailing edge. In order to modify the blade shape at the leading edge, the parameter wedge angle, the leading edge angle, and the thickness were enabled. The parameters enabled for the trailing edge were wedge angle and trailing edge angle. The spline on the suction side was controlled by the aspect ratios and the curvature of the slope at point 1 and 2. The pressure side was controlled only by the aspect ratio of the slope at point 3. The stagger angle was enabled to control the flow angles in circumferential direction at the outlet plane. All these variables of one blade section normally generate six variables via the radial parametrization for a full blade. Here, only the values at midspan, at the tip and the slope at tip were essential as independent variables, because of the symmetrical wind tunnel application. A possible modification of the radial shape of the stacking curve in circumferential or axial direction was not enabled to allow the design effects to be examined without lean or bow. Additionally, at the tip wall, one bump was parameterized for nonaxisymmetric platform contouring.

As variables of the bump the start and end positions on the suction and pressure side were enabled. Also, the flatness at the middle interface points and the amplitudes of the interface points in radial direction on the suction and the pressure side were released. The shape function was fixed as a half cosine. In total, 43 geometry variables were enabled at reasonable intervals between fixed upper and lower limits. These variables constitute the degree-of-freedom of the optimization task.

About 70 boundary conditions for the optimization were defined in total. The flow solver calculations during the main function calls were parallelized on two processors, all other calculations ran as single processor jobs. The optimization of this cascade comprised 82 main function steps, including the starting point. Overall 542 target function evaluations were executed with k-ε turbulence model and transition criteria on the suction side.

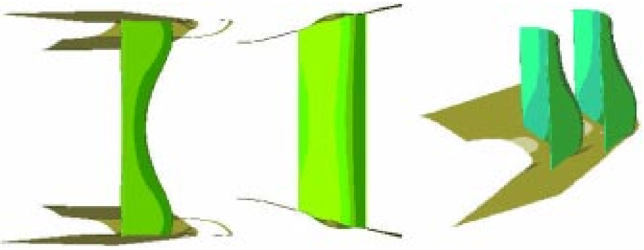

Fig. 12 Loss minimized flow channel (Airfoil: T106Dopt)

Results

Loss-Minimized Flow Channel. The automatically generated, optimized geometry T106opt is shown in **Fig. 12** and **Fig. 13**. This geometry was calculated with a fine mesh (875 k grid nodes) for half-span, before the cascade was manufactured. All numerical results shown in the following are the outcome of this calculation. The shape is strongly three-dimensional to counteract the three-dimensional flow effects. As the focus was on an integral improvement, the geometry does not show the stacking of optimal two-dimensional blade sections, but an ideal three-dimensional solution. Near the end wall the suction side is bulged outwards. The suction side is longer than the pressure side, due to the nonaxisymmetrical end-wall contouring. This must be considered when looking at the profile pressure distributions. The integral flux averaged outflow angle in circumferential direction remained within the limited interval. The mass flow is almost identical to the mass flow of the original starting cascade geometry.

Comparison With the Measurements. For the experimental analysis the optimized blade was instrumented on four sections. The position and the shape of the sections can be seen in **Fig. 14**. Together with the end wall instrumentation, 137 static pressure tappings were incorporated. In the wind tunnel, static pressure

Fig. 13 Aerofoil T106Dopt

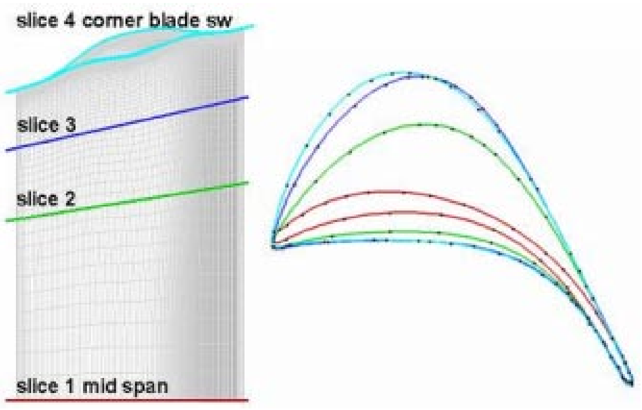

Fig. 14 Instrumentation planes, pressure taps

measurements using these pressure tappings were performed. The outflow of the cascade was measured by a five-hole probe.

In **Fig. 15** shows the numerical (lines) and the experimental (symbols) cp-distributions of the four sections, where the midspan shows increased loading. The transverse pressure gradient at the end wall (section 4) is markedly reduced. The same applies to the secondary. Despite the somewhat exceptional static pressure distributions, the agreement between numerical and experimental results is rather good.

The radial distribution of the outflow angle in circumferential direction is shown in **Fig. 16**. The achieved improvement is reflected by the fact, that overturning could be almost eliminated. The interval between over and underturning is clearly smaller. The peaks have moved towards the end wall. In the radial loss distribution this behavior is reproduced. The starting geometry shows a distribution of a highly loaded turbine cascade. This is amplified by the divergent end walls.

The optimized cascade (**Fig. 17**) exhibits a shifting of the loss region towards the end wall and a lower loss peak. The decrease in secondary flows leads to a homogenized outflow (see also [13]).

The comparison of experimental and numerical results for the outflow at $x/l_{ax}=1.5$ is shown in **Fig. 18**. The position of the loss centres and even their values are well represented by the calculation. The integral losses in total pressure of the optimized geometry were reduced by 22% relative to the starting cascade. The secondary kinetic energy SKE was reduced by 60%.

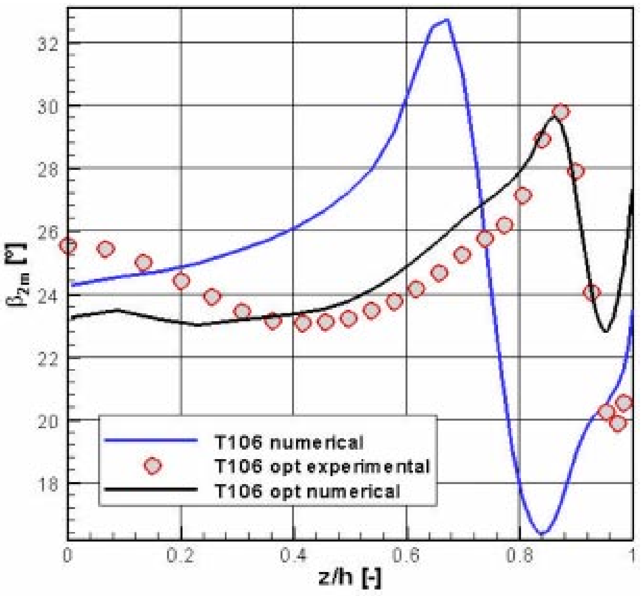

Fig. 16 Radial distribution of the outflow angle in circumferential direction (106D: initial; 106Dopt: optimized)

In **Fig. 19** shows the oil-paint pictures of the suction side of one blade (front, rear) and the end wall at the design point. Examination of the end wall picture must consider the non-axisymmetric end wall contouring which is hardly visible. Due to the longer suction side, the end wall area near the suction side shows a strong depression.

In the end-wall picture, a half-circle shaped flow separation far upstream of the leading edge is visible. This separation develops due to the strong divergence of the end wall, which is similar to an overcritical diffusor. Another reason is the potential effect of the blade leading edge active upstream. The separated material flows in a wide arc on both leading edge sides into the end-wall depres-

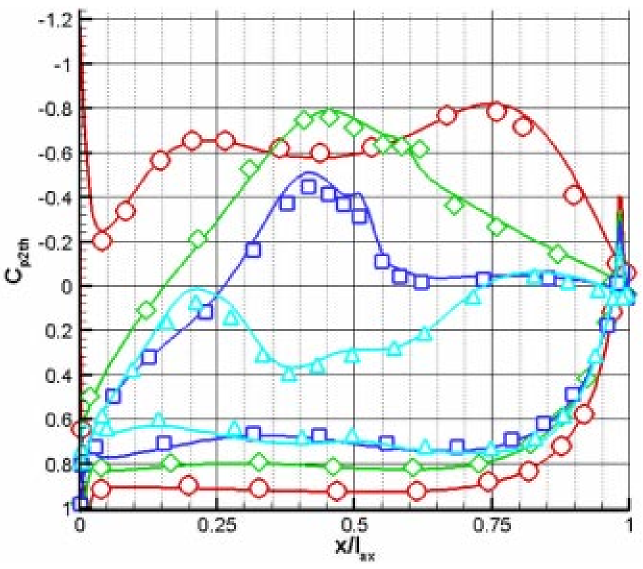

Fig. 15 Comparison of profile pressure distributions numerical/experimental in four measurement planes

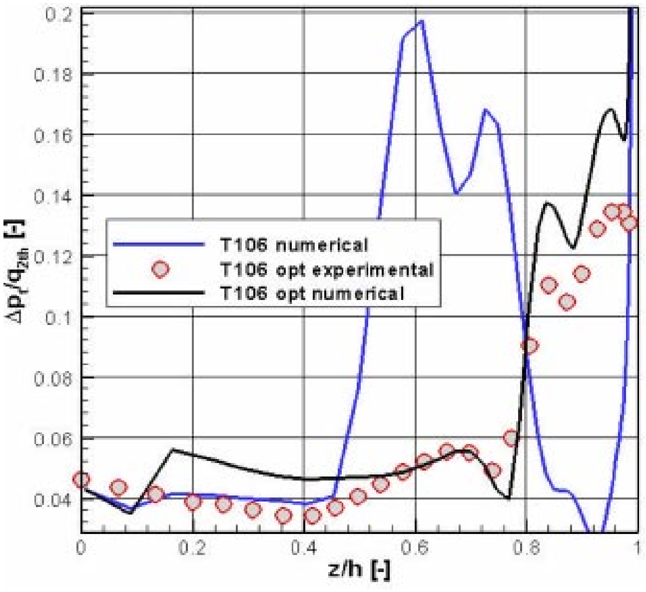

Fig. 17 Radial loss distribution (106D: initial; 106Dopt: optimized)

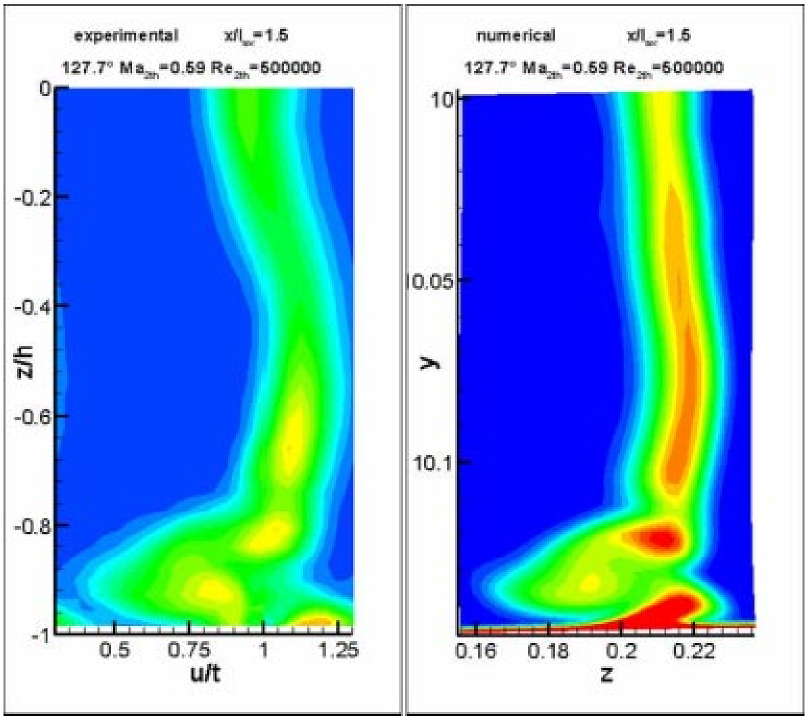

Fig. 18 Comparison of experimental and numerical distribution of total pressure loss at $x/l_{ax}=1.5$

sion at the ridge of the section thickness. In the separated flow (shear layer) no rotation is observable. Behind the separation a new small boundary layer is built up. This boundary layer creates a small horseshoe vortex at the leading edge. The suction side leg runs directly into the corner profile end wall. More downstream the boundary layer fluid, normally creating the channel vortex, is transported to the end-wall depression as well. On the suction side of the blade at midsection a wide zone of two-dimensional flow is visible. Despite the high loading, in accordance with the pressure distribution, no separation occurs. Near the end wall a separation is apparent at a short distance behind the point of maximum section thickness. This separation moves downstream towards midblade. Outside the two-dimensional midsection flow sector the separation is washed backward. The separation bubble obviously is filled with the low-energetic boundary layer material coming out of the end-wall depression. Thereby, the boundary layer material is re-energized. It feeds the main flow almost without building up dissipating vorticity. The remaining fluid out of the end-wall depression is accelerated in downstream direction. It leads to a roll up and a late generation of a small channel vortex.

A comparable computation at a lower Reynolds number of 200,000 still shows an improvement of the losses. In experimental tests even at a Reynolds number of 80,000, no laminar separation at midspan could be observed. Other numerical optimizations using the original cascade but different target functions all show the tendency towards a bulged suction side near the end wall. The application of the nonaxisymmetric end wall contouring always resulted in a suction side longer than the pressure side. The transport mechanisms of the secondary flows could obviously be eliminated effectively that way. For each individual blade shape a particular position of the bump was found. Thus, the position of the bump varied within a wide range. The best target function was found with a longer suction side while the pressure side remained roughly the same shape. The nonaxisymmetric end-wall contouring widens the blade passage narrowed by the suction side.

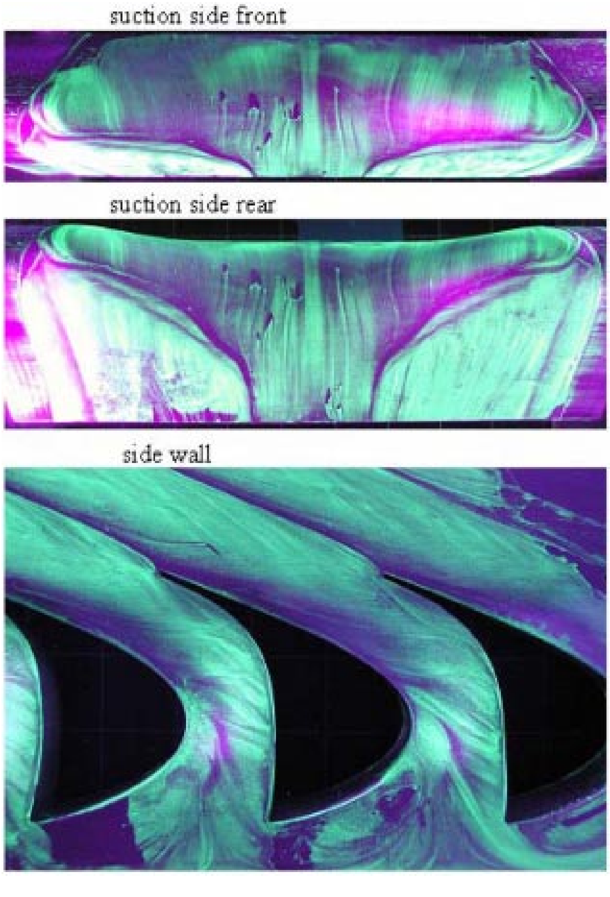

Fig. 19 Flow visualization

Conclusions

Two objectives were pursued under this project. The first was to generate an innovative turbine cascade design with the help of numerical optimization and the second to verify the results experimentally. Both targets have been achieved. The optimized blade channel design turned out to be genuinely novel in the sense that aerodynamicists in a limited number of manual design loops neither would have achieved such loss reduction, nor would they have tried to use such extreme geometrical means. It has to be pointed out that, due to time restrictions, no explorative optimization strategies like evolutionary strategies, genetic algorithms, or simulated annealing could be used. These strategies will be included in further investigations. The optimization result has been achieved using merely the SQP method, which is known for high local search performance, only.

A major risk in optimisations using simulation codes is that interesting results may be produced, which would, however, not withstand thorough physical analysis. Such results would turn out to be artefacts resulting from the combination of sophisticated mathematical search algorithms and false or incomplete physical modelling in the simulation code. Therefore, it is of utmost importance that the optimization results be carefully verified, especially if they are beyond the traditional design space. This task has been also accomplished. For both the pressure distribution and the secondary loss development the experiment fully confirms the simulation of the geometry proposed by the optimizer.

Acknowledgments

The authors acknowledge gratefully the inspiring support of Prof. Leonhard Fottner, who, until his sudden death in the summer of 2002, headed of the Institute of Jet Propulsion at the University of the Armed Forces Munich.

Nomenclature

$C_{p,x}$ = $[p_x - p_2]/[p_{t1} - p_2]$
h = blade height (m)
l = chord length (m)
g = slope
Ma = Mach number
p = pressure (hPa)
q = dynamic pressure (hPa)
Re = Reynolds number
r = radius (m)
t = pitch (m)
Tu = turbulence intensity
u = coord. in circumferential direction (wind tunnel) (m)
x = blade surface position (design system) axial coord. (wind tunnel) (m)
z = axial coordinate (design system) radial coordinate (wind tunnel) (m)
β = flow angle in circumferential direction (deg)
β_s = stagger angle (deg)
φ = circumferential coordinate (deg)

Abbreviations

HGK = high-speed cascade wind tunnel
LE = leading edge
PS = pressure side
RANS = Reynolds-averaged Navier-Stokes
SQP = sequential quadratic programming
SS = suction side
TE = trailing edge

Subscripts

1 = cascade inlet plane
2 = cascade exit plane
$2th$ = downstream conditions for isentropic flow
ax = axial
m = mass averaged
t = total
x = local

References

[1] Rechenberg, 1973.
[2] LaFleur, R. S., and Langston, L. S., 1993, ‘‘Drag Reduction of a Cylinder/Endwall Junction Using the Ice Formation Method,’’ ASME J. Fluids Eng., **115**.
[3] Bischoff, H., 1983, Patentschrift DE 3202855 C1, MTU Motoren- und Turbinen Union, Munich.
[4] Rose, M. G., 1994, ‘‘Non-Axisymmetric Endwall Profiling in the HP NGV's of an Axial Flow Gas Turbine,’’ ASME Paper 94-GT-249.
[5] Hartland, J. C., Gregory-Smith, D. G., Harvey, N. W., and Rose, M. G., 1999, ‘‘Non-Axisymmetric Turbine End Wall Design: Part II Experimental Validation,’’ ASME Paper 99-GT338.
[6] Rose, M. G., Harvey, N. W., Seaman P., Newman D. A., and McManus D., 2001, ‘‘Improving the Efficiency of the TRENT 500 HP Turbine Using Non-Axisymmetric End Walls: Part 2, Experimental Validation,’’ ASME Paper 2001-GT-0505.
[7] Harvey, N. W., Brennan G., Newman, D. A., and Rose, M. G., 2002, ‘‘Improving Turbine Efficiency Using Non-Axisymmetric End Walls: Validation in the Multi-Row Environment and With Low Aspect Ratio Blading,’’ ASME Paper GT-2002-30337.
[8] Hartland, J. C., and Gregory-Smith, D. G., 2002, ‘‘A Design Method for the Profiling of End Walls in Turbines,’’ ASME Paper GT-2002-30433.
[9] Spellucci P.: *DONLP2, User's Guide*, Technical University Darmstadt, FB4, AG8.
[10] Gier, J., Ardey, S., Eymann, S., Reinmöller, U., and Niehuis, R., 2002, ‘‘Improving 3D Flow Characteristics in a Multistage LP Turbine by Means of Endwall Contouring and Airfoil Design Modification. Part 2: Numerical Simulation and Analysis,’’ ASME Paper 2002-GT-30353.
[11] Abu-Ghannam, B. J., and Shaw, R., 1980, ‘‘Natural Transition of Boundary Layers—The Effects of Turbulence, Pressure Gradient, and Flow History,’’ J. Mech. Eng. Sci., **22**(5).
[12] Gier, J., Ardey, S., and Heisler, A., 2000, ‘‘Analysis of Complex Three-Dimensional Flow in a Three-Stage LP Turbine By Means of Transitional Navier-Stokes Simulation,’’ ASME 2000-GT-0645.
[13] Nagel, M., Fottner, L., and Baier, R.-D., 2001, *Optimization of Three Dimensionally Designed Turbine Blades and Side Walls*, Bangalore ISABE-2001-1058.
[14] Baier, R.-D., 2001, ‘‘Dreidimensionale Schaufelkanalgestaltung: Umfangskonturierung der Seitenwand von Turbinenbeschaufelungen,’’ MTUM-N01TPA-0007, MTU Aero Engines, Munich.
[15] Duden, A., Raab, I., and Fottner, L., 1998, Controlling the Secondary Flows in a Turbine Cascade by 3D Airfoil Design and Endwall Contouring. ASME Paper 98-GT-72.
[16] Duden, A., 1999, ‘‘Strömungsbeeinflussung zur Reduzierung der Sekundärströmungen in Turbinengittern,’’ dissertation, Universität der Bundeswehr München.

The Unsteady Development of a Turbulent Wake Through a Downstream Low-Pressure Turbine Blade Passage

R. D. Stieger[1]

H. P. Hodson

Engineering Department,
Whittle Laboratory,
Cambridge University,
Madingley Road,
Cambridge, UK

This paper presents two-dimensional LDA measurements of the convection of a wake through a low-pressure turbine cascade. Previous studies have shown the wake convection to be kinematic, but have not provided details of the turbulent field. The spatial resolution of these measurements has facilitated the calculation of the production of turbulent kinetic energy, and this has revealed a mechanism for turbulence production as the wake convects through the blade row. The measured ensemble-averaged velocity field confirmed the previously reported kinematics of wake convection while the measurements of the turbulence quantities showed the wake fluid to be characterized by elevated levels of turbulent kinetic energy (TKE) and to have an anisotropic structure. Based on the measured mean and turbulence quantities, the production of turbulent kinetic energy was calculated. This highlighted a TKE production mechanism that resulted in increased levels of turbulence over the rear suction surface where boundary-layer transition occurs. The turbulence production mechanism within the blade row was also observed to produce more anisotropic turbulence. Production occurs when the principal stresses within the wake are aligned with the mean strains. This coincides with the maximum distortion of the wake within the blade passage and provides a mechanism for the production of turbulence outside of the boundary layer. [DOI: 10.1115/1.1811094]

Introduction

The unsteady flow field in low-pressure (LP) turbines is governed by a combination of potential and convective interactions [1]. Of these, the convected wakes from upstream blade rows play the most significant role due to their effect on the blade-surface boundary layers. Indeed, unsteady wake-induced transition phenomena have been exploited in the design of high-lift LP turbines, which have up to 30% fewer blades than traditional LP turbines [2,3].

A number of researchers have described the kinematics governing the convection of a wake through a cascade. Early work by Meyer [4] used potential flow solutions to model wake convection as the convection of a perturbation jet through the blade row. Numerous numerical studies have further shown that the wake convection is primarily a kinematic phenomenon (e.g., [5,6]).

However, the kinematics of the wake convection is only partly responsible for the effects of the wake on the blade-surface boundary layer. The primary effect of the wake convection is to dictate boundary-layer transition, and, therefore, the turbulence of the wake and the convection of turbulence quantities through the blade row are also of importance. Indeed, the transition models of Addison and Hodson [7], Doorly and Oldfield [8], and La Graff et al. [9] all neglect the negative jet effect and use the wake convection simply to transport wake turbulence, which acts to initiate transition. However, the work of Stieger and Hodson [10] and Stieger et al. [11] has shown that transition phenomena on LP turbine blades with high levels of diffusion may be initiated by instability mechanisms and are thus dependant on the kinematics of the wake convection as well as the wake turbulence.

To date, few measurements exist of the unsteady wake convection through a turbine blade row. The measurements of Schulte [12] provide a guide to the mean flow through a LP turbine passage, however, these measurements lack resolution and details of the turbulence quantities. Halstead [13] reports data from the inlet and exit of individual blade rows in a two-stage machine.

This paper presents two-dimensional (2D) LDA measurements of the wake convection through the T106 LP turbine cascade. These measurements are of high spatial resolution and provide information of the mean flow and full 2D turbulence quantities through the direct measurements of Reynolds stresses. As such, the data provides a database for validation of numerical predictions.

Experimental Details

The measurements reported in this paper were performed on a bar-passing cascade facility at the Whittle Laboratory of Cambridge University. The bar-passing cascade, shown in Fig. 1, simulates the unsteady wake-passing environment of a turbomachine by traversing bars across the inlet flow. No attempt is made to simulate the unsteady potential field of adjacent blade rows.

The unsteady wake-passing flow conditions were chosen to match those of a repeating stage of the T106 profile. The Reynolds number based on chord and time mean isentropic exit velocity of 12.6 m/s was $\mathrm{Re}=1.6\times10^5$. The flow coefficient was $\phi=0.83$. The bar pitch matched the cascade pitch so that $s_b/s_c=1$ $(f_r=0.68)$. The bar diameter of 2.05 mm was chosen to match the loss of a representative turbine blade, and the axial gap is representative of that found in LP turbines. The inlet flow angle was set to the design value of 37.7 deg. Flow turning due to the moving bars was not taken into consideration.

The unsteady flow field was measured using a commercial 2D LDA system. Light was supplied by a 5 W Argon-Ion laser. A 2D probe was used with a 1.95 beam expander and a lens of 500 mm

---

[1] Currently at Rolls-Royce plc, SinA-76, Rolls-Royce, Derby DE24 8EJ, UK. e-mail: rory.stieger@rolls-royce.com

Contributed by the International Gas Turbine Institute (IGTI) of THE AMERICAN SOCIETY OF MECHANICAL ENGINEERS for publication in the ASME JOURNAL OF TURBOMACHINERY. Paper presented at the International Gas Turbine and Aeroengine Congress and Exhibition, Vienna, Austria, June 13–17, 2004, Paper No. 2004-GT-53061. Manuscript received by IGTI, October 1, 2003; final revision, March 1, 2004. IGTI Review Chair: A. J. Strazisar.

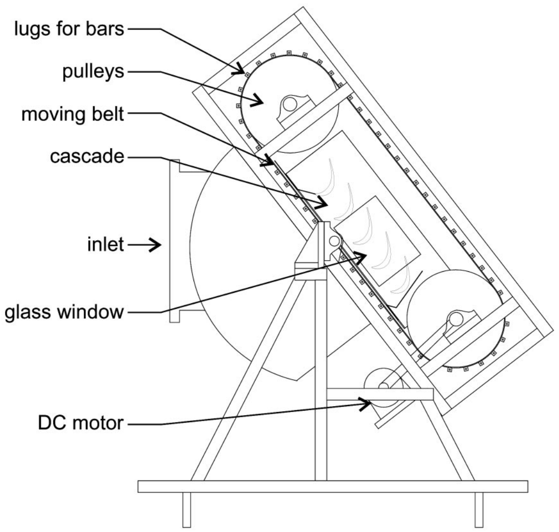

Fig. 1 Bar passing cascade with T106 profile.

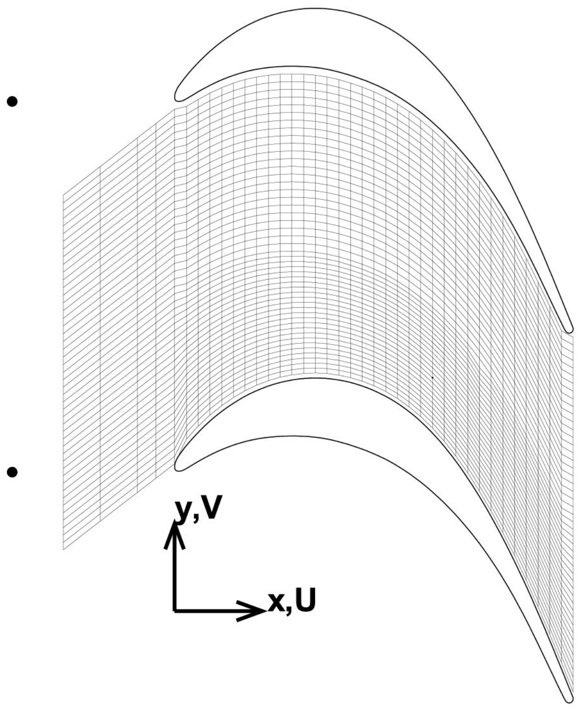

Fig. 2 Grid for 2D LDA measurements of the convection of a bar wake through the T106 LP turbine cascade

focal length. The optical configuration resulted in a measuring volume of $0.077\times 0.076\times 1.0116$ mm for the 514.5 nm beam and $0.073\times 0.072\times 0.963$ mm for the 488 nm beam. A backward scatter configuration was used, and the receiving optics included a Dantec 55X35 color separator and two Dantec 9057X0081 photomultiplier tubes. Dantec BSA signal processors were used to process the photomultiplier outputs.

Seeding of the flow was by means of smoke generated by a Dantec SPT smoke generator using Shell Ondina oil. The smoke was injected into the constant area section of the wind tunnel through the trailing edge of a streamlined injector tube. The point of injection was approximately 3 m upstream of the test section and upstream of the honeycomb, contraction, and final screens of the wind tunnel. The effect of the injector on the flow was thus immaterial. Phase Doppler anemometry measurements showed the characteristic size of the smoke particles used to be 1.5 μm. At each traverse point a maximum of 1×10^5 samples were collected in up to 60 s. This corresponded to a maximum of approximately 2500 wake-passing cycles. Validated data rates typically varied from 1.5 to 5 kHz. The coincidence filtering was performed by software to reject any samples not detected by both photomultipliers within a 5 μs window corresponding to twice the sample record length.

Ensemble averaging of the LDA data was performed relative to a once per bar trigger. The wake-passing period was divided into 128 time bins. Each coincident measurement was then assigned to a time bin according to its time relative to the trigger signal. The statistics of each time bin were then calculated with a residence time weighting to remove velocity bias, as suggested by George [14].

All data presented in this paper are nondimensional. All velocities are nondimensionalised by the measured isentropic exit velocity (V_{2is}), and all spatial coordinates are nondimensionalized by blade chord C.

The measurement grid consisted of 35 tangential traverses evenly spaced in the axial direction within the blade row. A further four traverses were performed upstream of the leading edge of the cascade. Each tangential traverse consisted of 48 points. The beam pairs of the LDA intersect at a half angle of 4.3 deg, therefore, in order to make measurements close to the blade surfaces, it was necessary to incline the probe so that neither of the beams was obstructed by the blade. The traverses in the blade-to-blade plane were thus performed in two stages, with 24 points equally spaced from the suction surface and then, after altering the probe inclination, 24 equally spaced from the pressure surface. The suction-side traverses were performed at a marginally smaller spacing than those from the pressure side. The velocity measured with the inclined LDA probe is insignificantly different from that measured with a normal probe (less than 0.5%), and for this reason, it was considered unnecessary to apply a correction to the measurements.

The blade surface was painted matt black to minimize flare from the intersecting beams. However, a narrow strip at midspan was left unpainted to avoid contaminating the midspan static-pressure tappings. Therefore, all measurements were performed at 45% span. The measurement grid with the blades and bars superimposed together with the definitions of the coordinate directions and velocity components are shown in Fig. 2.

Kinematics of Wake Convection Through a Turbine Cascade

The unsteady flow can most easily be visualized by the perturbation velocity, which is defined as the difference between the ensemble average and the time-averaged velocities according to

$$\langle U_p^*\rangle = \langle U^*\rangle - \overline{U^*}$$

$$\langle V_p^*\rangle = \langle V^*\rangle - \overline{V^*}$$

The perturbation velocity vectors are shown at six equally spaced time instants through the wake-passing cycle in Fig. 3. The location and shape of the wake is easily identified.

The velocity perturbation vectors of Fig. 3 provide a clear picture of the negative jet effect described by Meyer [4]. The wake segment within the blade row is clearly identified as a perturbation jet pointing toward the source of the wake. It should be noted that Meyer considered the negative jet to be a perturbation to the freestream, whereas the negative jet presented here is the perturbation to the time mean flow. This negative jet has a component of velocity across the blade passage that causes the wake fluid to convect toward, and impinge upon, the suction surface. This is apparent in Figs. 3(d)–3(f) where the wake fluid impinging on the surface splits into two perturbation streams, one pointed down-

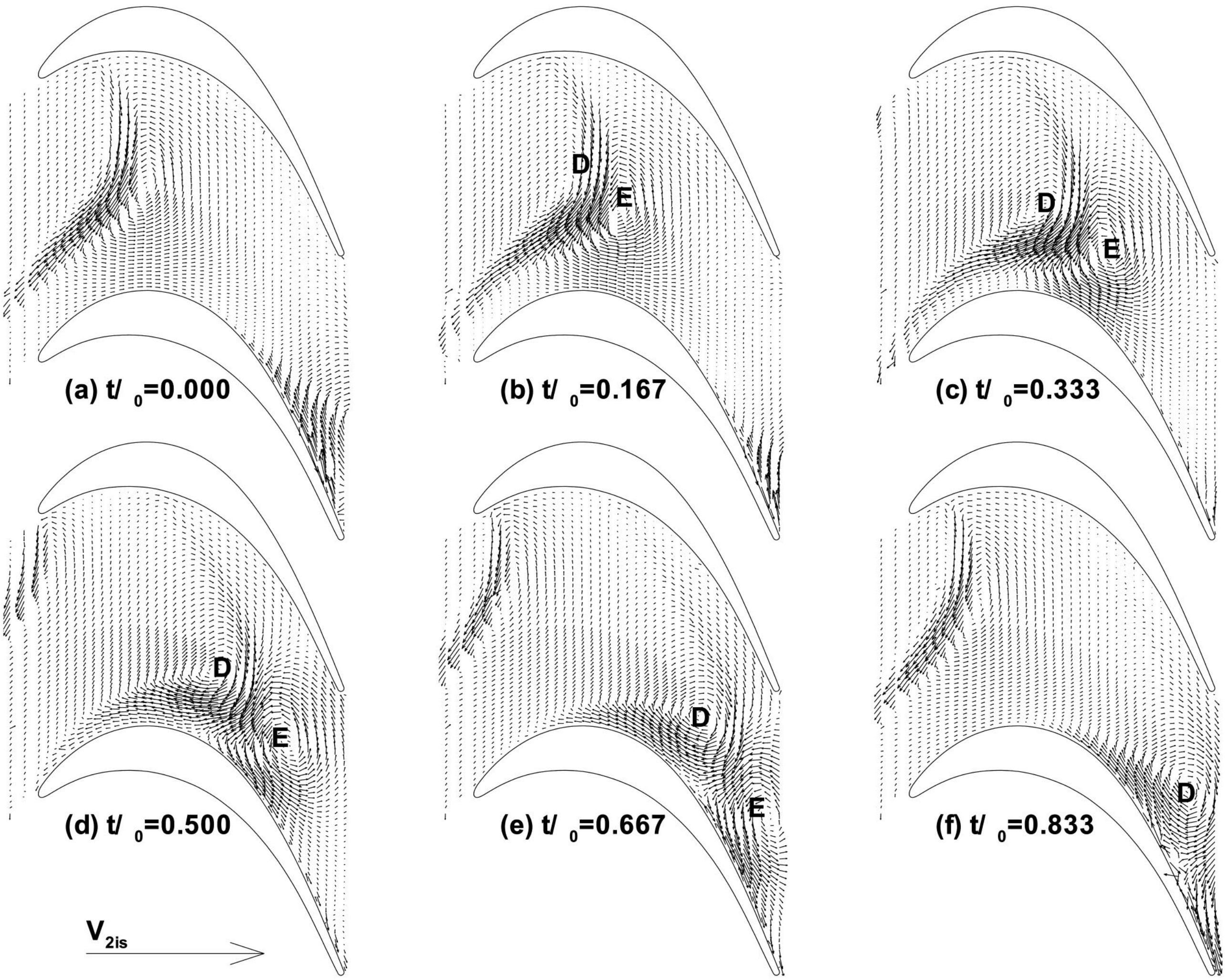

Fig. 3 Perturbation velocity vectors from 2D LDA measurements at six equispaced time instants through the wake-passing cycle. T106, Re=1.6×10^5, $s_b/s_c=1$, $\phi=0.83$, $f_r=0.68$

stream along the blade and the other upstream along the blade. Thus, downstream of the wake center the perturbation from the negative jet accelerates the flow, while upstream of the wake center the perturbation decelerates the flow and enhances any adverse pressure gradients, while making boundary layer profiles more inflectional.

The convection of the wake segment within the blade row is characterized by bowing, reorientation, elongation, and stretching (see [1]). All these processes are visible in Fig. 3. Bowing of the wake fluid is most evident in Figs. 3(*a*) and 3(*b*) and originates near the leading-edge plane where the midpassage velocities are higher than the velocities near the blade surfaces. The wake fluid convects with the local velocity and distorts into the bowed shape. The reorientation of the wake segment occurs due to the circulation of the blade. The velocities near the suction surface are higher than near the pressure surface, and therefore, fluid near the suction surface convects through the passage more rapidly, resulting in a reorientation of the wake segment. This is most clearly seen by comparing the angles of the two wake segments toward the pressure side of the passage in Fig. 3(*e*). The difference in convection velocities also causes the wake segment to elongate, and this, in turn, decreases the wake width to conserve the vorticity of the wake fluid. Comparing the wake width in Figs. 3(*a*) and 3(*e*), the decrease in wake width is only apparent on the pressure side of the passage. Near the suction side of the passage, the width of the wake increases. As the first part of the wake reaches the leading edge, it is accelerated over the suction surface of the blade and moves away from the upstream edge of the wake thus increasing the wake width on the suction side of the passage. This stretching process is visible along the suction surface in Figs. 3(*c*) and 3(*d*).

The velocity gradients along the leading half of the pressure surface are not as strong as on the suction surface; therefore, this stretching effect is less pronounced on the pressure surface. The combined effect of all the above results in the wake fluid building up on the suction surface with a tail pointing upstream and toward the pressure side, as seen most clearly in Fig. 3(*e*).

The wake fluid entering the blade row consists of two concentrated strips of vorticity of equal magnitude and opposite sign. These strips of vorticity are distorted during the convection of the wake through the blade row and create two swirling flows at labels *D* and *E* in Fig. 3. Although these structures appear to be a pair of counterrotating vortices, it should be noted that the vorticity is confined to the wake fluid and the vortical structures apparent in the perturbation velocity vectors result from the definition of the perturbation velocity vectors relative to the time-averaged flow.

Convection of Wake Turbulence Through a Turbine Cascade

The use of 2D LDA allows the simultaneous measurement of both components of the velocity vector in the measurement plane.

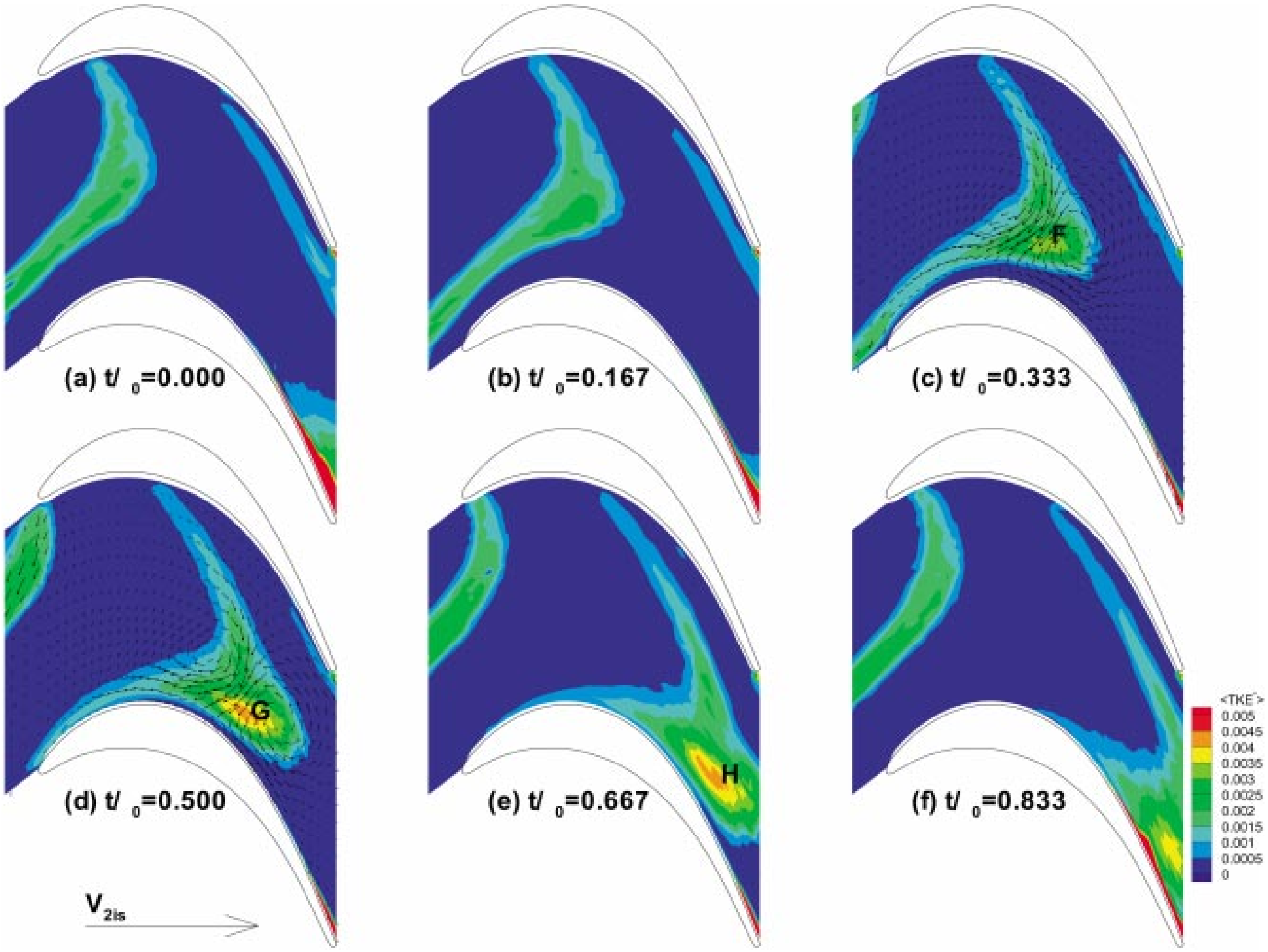

Fig. 4 Nondimensional turbulent kinetic energy (TKE) from 2D LDA measurements at six equispaced time instants through the wake-passing cycle. Perturbation velocity vector superimposed (*c*) and (*d*). T106, Re$=1.6\times10^5$, $s_b/s_c=1$, $\phi=0.83$, $f_r=0.68$

From these measurements it is possible to calculate the ensemble-averaged flow velocity and the 2D Reynolds stresses.

Turbulent Kinetic Energy. The ensemble-average nondimensional turbulent kinetic energy (TKE) for the 2D flow was calculated from the 2D LDA measurements according to

$$\langle \mathrm{TKE}^* \rangle = \tfrac{1}{2}(\langle u'^{2*} \rangle + \langle v'^{2} \rangle^*)$$

and is presented in Fig. 4 at a series of six equally spaced time instants through the wake-passing cycle. The kinematic wake convection described above is apparent from the elevated regions of TKE.

Along the pressure side of the channel, the TKE of the wake fluid is observed to drop as it convects through the blade row. A combination of elongation of the wake center line and the convective transport away from the pressure surface is responsible for this reduction in TKE. Similarly, the stretching that results as the blade chops the wake causes the TKE to reduce over the forward part of the suction surface. This is evident in Figs. 4(*c*) and 4(*d*).

The highest levels of TKE outside of the boundary layer occur in Figs. 4(*d*) and 4(*e*). These high regions of TKE, labeled *G* and *H*, occur where the wake fluid accumulates near the suction surface. The perturbation velocity vectors, a few of which are superimposed in Figs. 4(*c*) and 4(*d*), indicate that the peak TKE occurs slightly below the centers of the counter rotating "vortex" pair. The elevated TKE does not penetrate to the boundary layer. In this region the turbulence intensity based on isentropic exit velocity is $Tu=7\%$ whereas the wake centerline turbulence intensity at the leading edge plane is $Tu=5\%$. The increase in the level of TKE is seen to begin in Fig. 4(*c*) at label F and continue through Figs. 4(*d*)–4(*f*), although it is the extent and not the level that increases between G and H.

The response of the boundary layer to the wake passing can be seen in Fig. 4(*f*), where very high levels of turbulent kinetic energy are observed near the rear of the suction surface. The boundary-layer response to wake passing is described in Stieger and Hodson [10] and Stieger et al. [11].

The measured ensemble averaged Reynolds stresses were used together with the ensemble average velocity derivatives calculated from Green's theorem to evaluate the ensemble averaged nondimensional production of TKE in the blade-to-blade plane according to

$$\langle P^*_{\mathrm{TKE}} \rangle = -\langle u'^{2*} \rangle \frac{\partial \langle U^* \rangle}{\partial x^*} - \langle v'^{2*} \rangle \frac{\partial \langle V^* \rangle}{\partial y^*} - \langle u'v'^* \rangle \left(\frac{\partial \langle U^* \rangle}{\partial y^*} + \frac{\partial \langle V^* \rangle}{\partial x^*} \right)$$

The results are presented in Fig. 5 with the labels copied from Fig. 4. It is apparent that the increased levels of TKE are a direct result of TKE production. The highest production levels occur at labels *F* and *G* in Figs. 5(*c*,*d*) and it is these regions of high production that subsequently lead to regions of high TKE at *G* and *H* in Fig. 4.

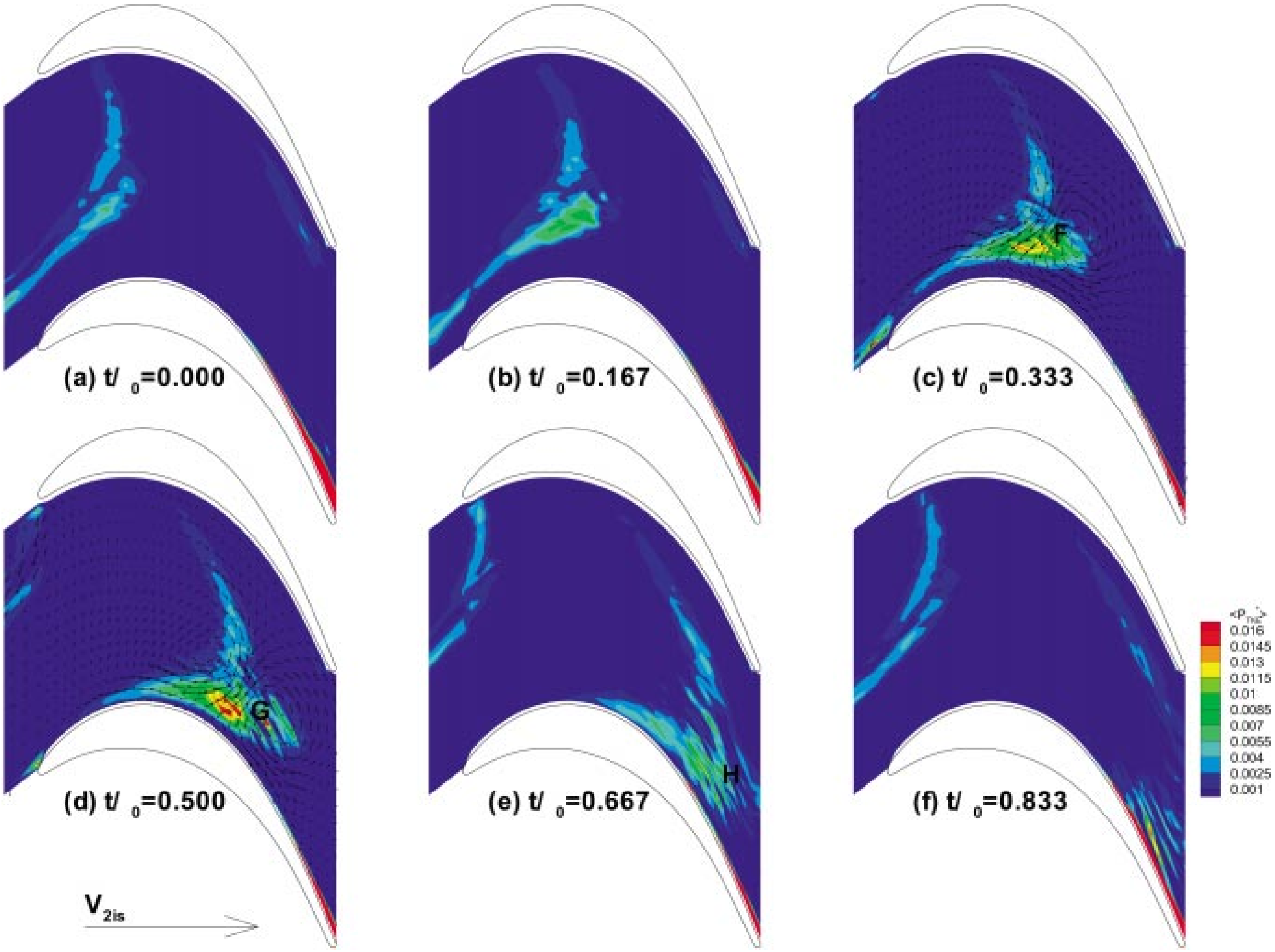

Fig. 5 Nondimensional production of TKE (P^{*}_{TKE}) from 2D LDA measurements at six equispaced time instants through the wake-passing cycle. Perturbation velocity vector superimposed (*c*) and (*d*). T106, $Re=1.6\times10^5$, $s_b/s_c=1$, $\phi=0.83$, $f_r=0.68$

The production of TKE occurs when the turbulence extracts work from the mean flow. This occurs in regions having high turbulent stresses and high spatial velocity gradients. The turbulent stresses are confined to the wake fluid and so production occurs when the wake fluid enters regions of high spatial velocity gradients. Indeed, Stieger and Hodson [10] measured very high levels of TKE production in the boundary layer on the rear part of the suction surface. The high levels of TKE production measured in Fig. 4(*a*) are confined to the edge regions of the wake fluid where the high levels of turbulent stresses in the wake fluid coincide with the shear layers of the edge of the wake. However, it is not only the magnitudes, but also the relative directions of the turbulent stresses and the strain rate of the mean flow that are important for the production of TKE. If the turbulent stresses and velocity gradients are aligned, the turbulent production is enhanced. This is the case at label F in Fig. 4 where the peak levels of TKE production are measured.

Anisotropy. An isotropic turbulent flow is one having the same characteristics of turbulence in all directions. For any turbulent flow, it is possible to define the principal stress direction ψ as that orientation having zero shear stress according to

$$\langle\psi\rangle=\frac{1}{2}\tan^{-1}\left(\frac{2\langle u'v'^{*}\rangle}{\langle u'^{2}*\rangle-\langle v'^{2}*\rangle}\right)$$

The principal normal stresses may then be found by a coordinate transformation to align the measured turbulence quantities to the calculated principal directions

$$\langle u_{\psi}'^{2}*\rangle=\langle u'^{2}*\rangle\cos^{2}\langle\psi\rangle+\langle v'^{2}*\rangle\sin^{2}\langle\psi\rangle$$
$$+2\langle u'v'^{*}\rangle\sin\langle\psi\rangle\cos\langle\psi\rangle$$
$$\langle v_{\psi}'^{2}*\rangle=\langle u'^{2}*\rangle\sin^{2}\langle\psi\rangle+\langle v'^{2}*\rangle\cos^{2}\langle\psi\rangle$$
$$-2\langle u'v'^{*}\rangle\sin\langle\psi\rangle\cos\langle\psi\rangle$$

A measure of the anisotropy may then be inferred by taking the modulus of the ratio of these principal turbulent stresses. The resulting parameter,

$$\langle\alpha\rangle=\left|\frac{\langle u_{\psi}'^{2}*\rangle}{\langle v_{\psi}'^{2}*\rangle}\right|\quad\cdots\quad\text{if }\langle u_{\psi}'^{2}*\rangle>\langle v_{\psi}'^{2}*\rangle$$

$$\langle\alpha\rangle=\left|\frac{\langle v_{\psi}'^{2}*\rangle}{\langle u_{\psi}'^{2}*\rangle}\right|\quad\cdots\quad\text{if }\langle v_{\psi}'^{2}*\rangle>\langle u_{\psi}'^{2}*\rangle$$

is chosen to be greater than unity with a value of unity indicating isotropy.

Figure 6 shows contours of α, and it is apparent that the wake fluid is anisotropic while the undisturbed fluid is essentially isotropic. High levels of anisotropy in the wake fluid are seen to

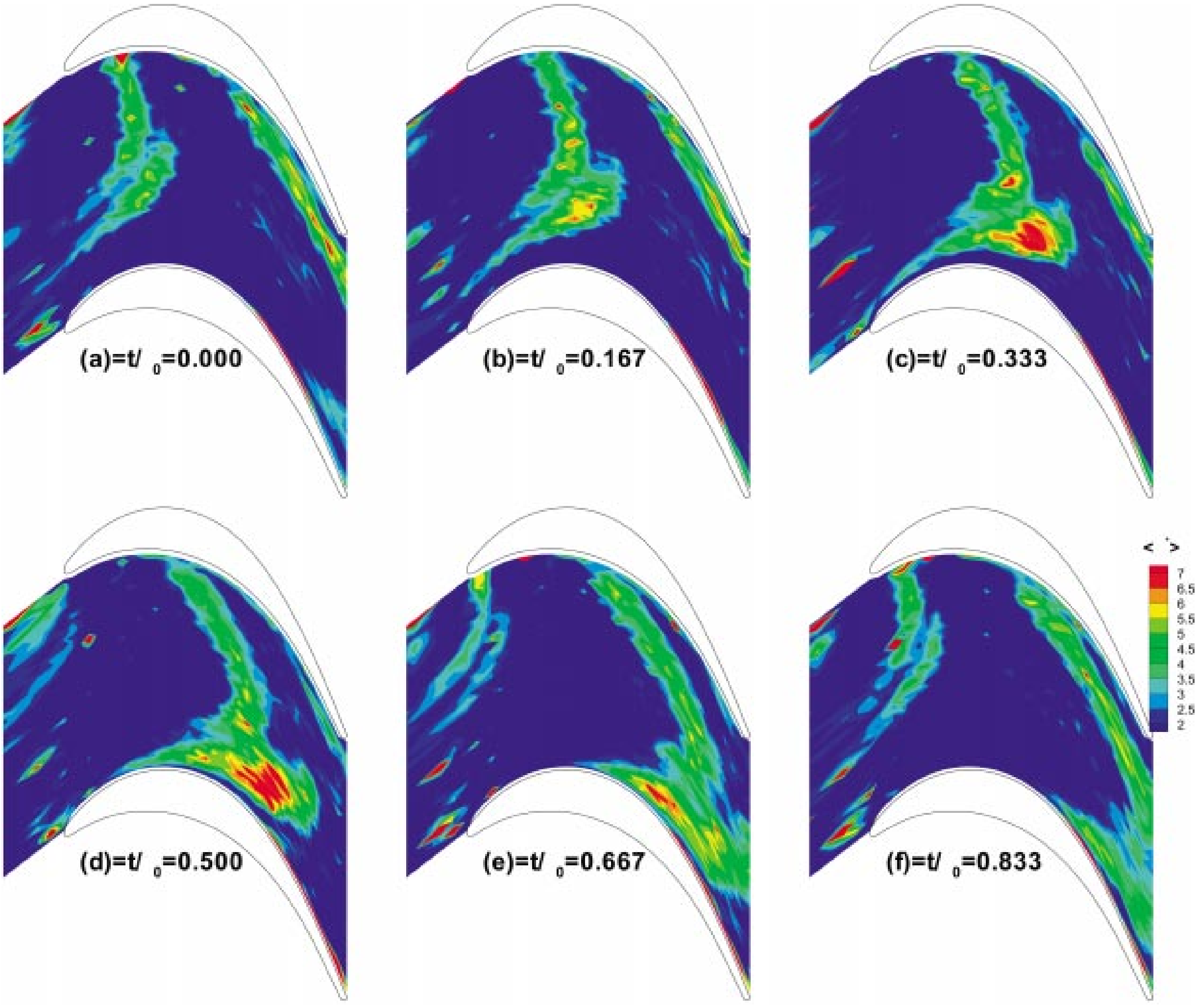

Fig. 6 Anisotropy (α) from 2D LDA measurements at six equispaced time instants through the wake-passing cycle. T106, Re$=1.6\times10^5$, $s_b/s_c=1$, $\phi=0.83$, $f_r=0.68$.

coincide with the regions of high TKE production. The very high levels of anisotropy in Figs. 6(*c*), 6(*d*) do not persist to the trailing edge plane and are already reduced in Fig. 6(*e*).

The wake fluid near the pressure surface can also be seen to become isotropic as it convects through the bladerow. This is the same region identified as having low TKE due to stretching of the wake center line in Fig. 4.

The components $\langle u'^2_\psi \rangle$ and $\langle v'^2_\psi \rangle$ of the principal stress vectors are plotted in Fig. 7. Figure 7(*a*) corresponds to the same time as the plot of the production of TKE in Fig. 5(*a*). At this time the TKE production is limited to the edges of the wake where the wake shear layer and turbulent stresses coexist. A comparison of Figs. 7(*a*) and 7(*c*) shows that the orientation of the principal stresses relative to the wake center line are essentially unchanged. Thus, as the wake is reorientated by the kinematics of wake convection, the orientation of the principal stresses changes relative to the mean flow field. Indeed, the principal stress vectors of Fig. 7(*c*) are aligned with the principal strain rate vectors in the region of peak TKE production. This is shown in the exploded box of Fig. 7(*c*) where the principal stress-vector components and principal strain-rate vectors are superimposed.

A comparison of the region of high TKE production, labeled F in Fig. 5(*c*), and the corresponding region in Fig. 7(*a*) shows that the high TKE production results from the alignment of the principal turbulent stress components and the spatial velocity gradients (strain rate). This alignment of turbulent stresses and mean velocity strain is the mechanism whereby TKE is produced within the blade passage. Note that the principal stress-component vectors and principal strain-rate vectors point in opposite directions in accordance with the equation for TKE production.

Conclusions

Measurements of the wake convected through a turbine blade row were made using 2D LDA. The resolution of the measurement grid and the availability of the Reynolds stress components of the 2D flow provide a detailed description of the ensemble-averaged mean and turbulent flow fields.

The measurements confirm that the wake convection may be described by simple kinematics with the wake fluid being bowed, reorientated, elongated, and stretched as it passes through the blade passage.

Measurements of the convected wake turbulence showed increased levels of TKE due to the production of TKE. The wake fluid was shown to be anisotropic, and the turbulence production within the blade row was observed to yield anisotropic turbulence.

The production of TKE outside of the boundary layers was shown to be strongest in regions where the Reynolds stresses and the strain rate field of the flow were aligned. This mechanism for TKE production occurs outside of the boundary-layer flow and provides a means by which the convection of a turbulent wake through a blade row may increase the levels of turbulence.

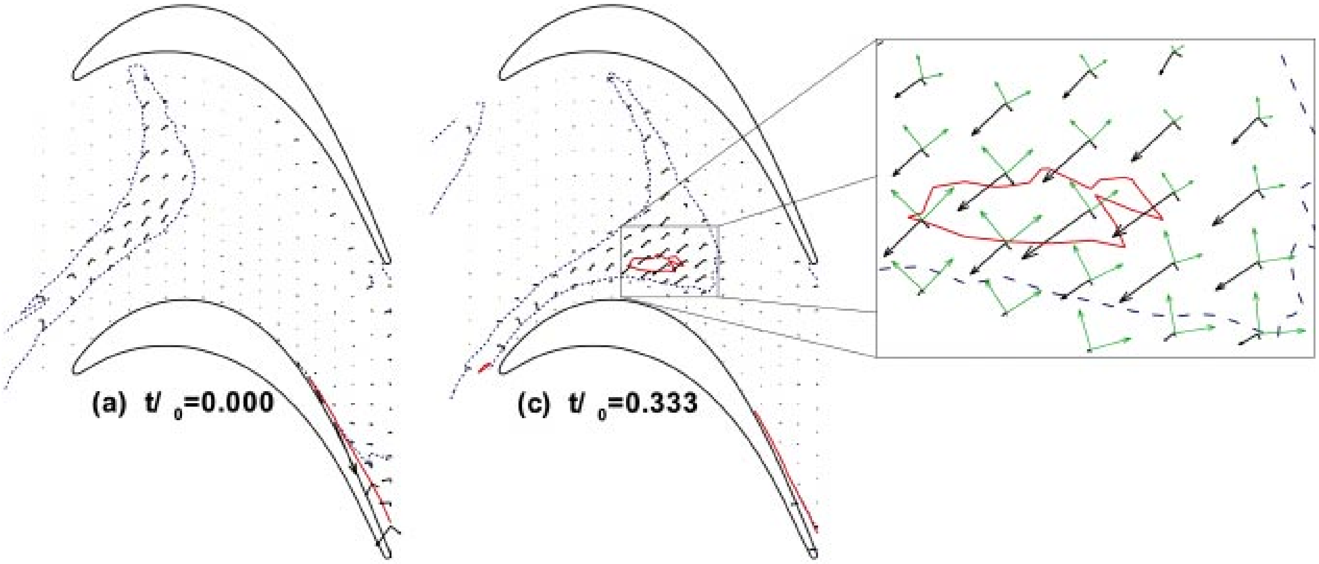

Fig. 7 Vectors of principal stress components $\langle u'^2_\psi \rangle$ and $\langle v'^2_\psi \rangle$ at (*a*) $t/\tau_0 = 0.00$ and (*c*) $t/\tau_0 = 0.333$. Contour of $\langle P^*_{\mathrm{TKE}} \rangle = 0.01$ and $\langle \mathrm{TKE}^* \rangle = 0.001$ (dotted line) highlight the position of the wake and TKE production. The exploded box shows principal stress components and principal strain vectors in region of peak TKE production.

Acknowledgments

The first author would like to acknowledge the financial support of the ORS and a Peterhouse Research Studentship. The funding of EPSRC Grant No. GR/L96660/01 is also gratefully acknowledged.

Nomenclature

C = chord
f_r = reduced frequency $f_r = fC/U_{bar}$
P_{TKE} = production of TKE
Re = Reynolds number
s_b/s_c = ratio of bar pitch to cascade pitch
TKE = turbulent kinetic energy
Tu = turbulence intensity
U, V = velocity components
U_p, V_p = perturbation velocity components
$u'^2, v'^2, u'v'$ = turbulent stress components
u'_ψ, v'_ψ = principle turbulent stresses
V_{2is} = isentropic exit flow velocity
x, y = linear co-ordinates
α = anisotropy measure
ϕ = flow coefficient $\phi = V_{axial}/U_{bar}$
ψ = principal stress direction
$\langle \rangle$ = ensemble average quantity
$*$ = nondimensional quantity
$\overline{x}$ = time average of x

References

[1] Hodson, HP, 1998, "Bladerow Interactions In Low Pressure Turbines," *Blade Row Interference Effects Axial Turbomachinery Stages*, Von Karman Institute, Brussels, Belgium, in VKI Lecture Series No. 1998-02, Feb 9.
[2] Howell, R. J., Hodson, H. P., Schulte, V., Schiffer, H-P., Haselbach, F., and Harvey, N. W., 2001, "Boundary Layer Development on the BR710 and BR715 LP Turbines-The Implementation of High Lift and Ultra High Lift Concepts," ASME Paper No. 2001-GT-0441.
[3] Cobley, K., Coleman, N., Siden, G., and Arndt, N., 1997, "Design of New Three Stage Low Pressure Turbine for BMW Rolls-Royce BR715 Engine," ASME Paper No. 97-GT-419.
[4] Meyer, R. X., 1958, "The Effects of Wakes on the Transient Pressure and Velocity Distributions in Turbomachines," ASME J. Basic Eng., **80**, pp. 1544–1552.
[5] Hodson, H. P., 1985, "A Blade-to-Blade Prediction of Wake-Generated Unsteady Flow," ASME J. Eng. Gas Turbines Power, **107**.
[6] Giles, M. B., 1987, "Calculation of Unsteady Wake/Rotor Interactions," *AIAA 25th Aerospace Sciences Meeting*, Reno, AIAA Paper 87-0006.
[7] Addison, J. S., and Hodson, H. P., 1992, "Modelling of Unsteady Transitional Boundary Layers," ASME J. Turbomach., **114**(3), pp. 580–589.
[8] Doorly, D. L., and Oldfield, 1985, "Simulation of the Effects of Shock Wave Passing on a Turbine Rotor Blade," ASME Paper No. 85-GT-112.
[9] La Graff, J. E., Ashworth, D. A., and Schultz, D. L., 1989, "Measurements and Modelling of the Gas Turbine Blade Transition Process as Disturbed by Wakes," ASME J. Turbomach., **111**, pp. 315–322.
[10] Stieger, R. D., and Hodson, H. P., 2003, "The Transition Mechanism of Highly Loaded LP Turbine Blades," ASME Paper No. GT2003-38304.
[11] Stieger, R. D., Hollis, D., and Hodson, H. P., 2003, "Unsteady Surface Pressures Due to Wake Induced Transition in a Laminar Separation Bubble on a LP Turbine Cascade," ASME Paper No. GT2003-38303.
[12] Schulte, V., 1995, "Unsteady Separated Boundary Layers in Axial-flow Turbomachinery," Ph.D. dissertation, Cambridge Univ., Cambridge, England.
[13] Halstead, D. E., 1997, "Flowfield unsteadiness and turbulence in multistage low pressure turbines," *Conf. Boundary layer transition in turbomachines*, Syracuse Univ., Minnowbrook, Sep 7–10.
[14] George, W. K., 1975, "Limitations to Measuring Accuracy Inherent in the Laser-Doppler Signal," *Proc. LDA Symp.*, Copenhagen.

A. Bonfiglioli
DIFA Università della Basilicata,
Contrada Macchia Romana,
85100 Potenza, Italy
email: bonfiglioli@unibas.it

P. De Palma
e-mail: depalma@poliba.it

G. Pascazio
e-mail: pascazio@poliba.it

M. Napolitano
e-mail: napolita@poliba.it

DIMeG and CEMeC,
Politecnico di Bari,
via Re David, 200,
70125 Bari, Italy

An Implicit Fluctuation Splitting Scheme for Turbomachinery Flows

This paper describes an accurate, robust and efficient methodology for solving two-dimensional steady transonic turbomachinery flows. The Euler fluxes are discretized in space using a hybrid multidimensional upwind method, which, according to the local flow conditions, uses the most suitable fluctuation splitting (FS) scheme at each cell of the computational domain. The viscous terms are discretized using a standard Galerkin finite element scheme. The eddy viscosity is evaluated by means of the Spalart-Allmaras turbulence transport equation, which is discretized in space by means of a mixed FS-Galerkin approach. The equations are discretized in time using an implicit Euler scheme, the Jacobian being evaluated by two-point backward differences. The resulting large sparse linear systems are solved sequentially using a preconditioned GMRES strategy. The proposed methodology is employed to compute subsonic and transonic turbulent flows inside a high-turning turbine-rotor cascade. [DOI: 10.1115/1.1777576]

1 Introduction

In the last decades, computer performance has improved dramatically with respect to both speed and memory size, such that the relative cost of a given computation has been reduced by approximately a factor of ten every ten years, [1]. At the same time, the use of computational fluid dynamics (CFD) has experienced an exponential growth, and this has greatly influenced the design and development of modern airplanes, advanced turbomachinery, and internal combustion engines. In fact, it is now possible to compute very complex flows (flows about an entire airplane or inside one or more blade passages of a turbomachinery rotor and/or stator), with computational meshes using millions of cells, within only order of hours computational (CPU) time. Therefore, the still necessary, but often very costly, real world experimental analyses are fortunately then limited to the final design choices, since preliminary designs can be analyzed by very fast and inexpensive computer runs.

Nowadays, most CFD codes for turbomachinery applications are often based on numerical methods originally developed for external flow applications. These flow codes solve the steady-state Reynolds-averaged compressible Navier-Stokes equations by means of time-marching explicit or implicit schemes, and their convergence rate is accelerated by various techniques such as local time stepping, implicit residual smoothing (for the case of explicit schemes), multigrid, etc. As far as the spatial discretization is concerned, conservative finite volume (or element) discretizations are typically applied to the conservation-law form of the governing equations, so as to correctly capture flow discontinuities such as shocks and contact surfaces. The dissipation required to avoid spurious oscillations is either added artificially to the scheme, in case the advection terms in the equations are discretized using centered differences, [2], or it is ‘‘naturally’’ contained in the scheme itself, if an ‘‘upwind’’ discretization is used for such terms, [3]. Finally, in order to solve flows of engineering interest, the aforementioned methods employ turbulence models of increasing complexity, namely, algebraic models, differential models, and large eddy simulation techniques. To date, it is still unfeasible for realistic problems to resolve all time and length scales of the unsteady Navier-Stokes equations, namely, to perform a direct numerical simulation. Therefore, CFD is still far from becoming the perfect design tool for both aerospace and turbomachinery applications, mainly due to serious limitations in the modeling of turbulence and laminar/turbulent flow transition, but also because most numerical methods do not properly account for the multidimensional nature of compressible flows.

This last difficulty has been recently alleviated by the last three authors of this paper, who have developed and optimized a nonlinear hybrid fluctuation splitting (FS) scheme which, according to the local flow conditions, uses the most suitable FS spacial discretization among the matrix LDA and PSI schemes, [4,5], which are optimal for subsonic and supersonic flow conditions respectively, and the monotone matrix N scheme, [4,5], which can capture shocks monotonically. A Runge-Kutta explicit integration procedure with multigrid was used to time-march the solution to its steady state. The hybrid scheme has proven extremely accurate for both inviscid and viscous transonic flows, the first-order-accurate monotone N scheme being used only at shock cells, [6]. On the other hand, for turbulent flow calculations, due to the very high aspect-ratio of the near-wall computational cells, the explicit integration procedure lacks both robustness and efficiency, [7]. Therefore, the first author of this paper has concentrated his efforts towards optimizing the efficiency of the solution procedure, [8]. The resulting new method uses an implicit Euler time discretization which requires the evaluation of the Jacobian of the discrete residual with respect to the dependent variable. This Jacobian is evaluated using a first-order-accurate finite difference. The resulting large sparse linear system is solved using a preconditioned GMRES strategy.

It is now possible to provide an accurate, robust and efficient numerical scheme, by combining the hybrid FS spacial discretization presented in Ref. [6] with the implicit time integration procedure described in Ref. [8]. In this paper, such a scheme is provided and applied successfully to compute subsonic and transonic flows through a high-turning turbine-rotor cascade.

2 Governing Equations and Numerical Method

2.1 Navier-Stokes Equations. The compressible Navier-Stokes equations are written in vector form as

$$\frac{\partial U}{\partial t} = -\nabla \cdot (\mathcal{F}^{i} - \mathcal{F}^{v}) = \mathrm{Res}^{i}(U) + \mathrm{Res}^{v}(U), \qquad (1)$$

Contributed by the Turbomachinery Division of THE AMERICAN SOCIETY OF MECHANICAL ENGINEERS for publication in the JOURNAL OF TURBOMACHINERY. Manuscript received by the ASME Turbomachinery Division, April 15, 2004; final revision, April 17, 2004. Associate Editor: D. C. Wisler.

where U is the vector of the conservative variables and $\mathcal{F}^i$ and $\mathcal{F}^v$ are the inviscid and viscous flux tensors, respectively. The fluid is assumed to be a perfect gas with constant specific heats, and the laminar viscosity is modeled according to Sutherland's law. For turbulent flows of interest here, the eddy viscosity is added to the laminar molecular viscosity and is computed according to the Spalart-Allmaras [9] one-equation turbulence model:

$$\frac{\partial\tilde{\nu}}{\partial t}=-\mathbf{u}\cdot\nabla\tilde{\nu}+c_{b1}\tilde{S}\tilde{\nu}+\frac{1}{\sigma\,\mathrm{Re}}[\nabla\cdot((\nu+\tilde{\nu})\nabla\tilde{\nu})+c_{b2}(\nabla\tilde{\nu})^2]-\frac{1}{\mathrm{Re}}\left[c_{w1}f_w-\frac{c_{b1}}{k^2}f_{t2}\right]\left[\frac{\tilde{\nu}}{d}\right]^2. \tag{2}$$

In Eq. (2), $\tilde{\nu}$ is proportional to the kinematic eddy viscosity, and the right-hand side terms represent convection, production, diffusion, and destruction of the turbulent viscosity, respectively. See Ref. [9] for details. The transition triggering terms have been omitted in Eq. (2), since only fully turbulent flows are considered. Finally, the turbulent Prandtl number is set equal to 0.9 to evaluate the turbulent heat fluxes.

2.2 Numerical Method for Scalar Equation. In this section, a multidimensional discretization method, which is second-order accurate in space, is presented for the two-dimensional scalar advection equation. Such a new *truly multidimensional* methodology allows for a more realistic model of compressible flow propagation when compared to classical methods such as flux difference or flux vector splitting, which are based on one-dimensional flux splitting along directions aligned with the grid.

Consider the linear advection equation for the scalar variable u with velocity $\boldsymbol{\lambda}=a\mathbf{i}+b\mathbf{j}$:

$$\frac{\partial u}{\partial t}=-\left(a\frac{\partial u}{\partial x}+b\frac{\partial u}{\partial y}\right). \tag{3}$$

The computational domain is assumed to be discretized by triangular elements. If the variable u is also assumed to vary linearly over each triangle, the discrete fluctuation, namely the flux balance over the cell, can be evaluated exactly as

$$\phi_T=-\sum_{j=1}^{3}k_ju_j,\quad k_j=\frac{1}{2}\boldsymbol{\lambda}\cdot\mathbf{n}_jl_j, \tag{4}$$

$\mathbf{n}_j$ being the inward unit normal to the edge opposing node j, and l_j its length.

Fluctuation splitting schemes are obtained by two main steps: (i) the fluctuation is distributed among the nodes of each triangle; (ii) the solution at each node i of the computational domain is obtained by summing up all nodal contributions (arising from the set of triangles Δ_i sharing node i) as

$$u_i^{n+1}=u_i^n+\frac{\Delta t}{S_i}\sum_{T\in\cup\Delta_i}\phi_{T,i}. \tag{5}$$

Several FS schemes have been proposed in the literature, the final goal being a monotone and second-order-accurate scheme, an impossible task for any linear scheme, [10]. The majority of such schemes are of the (multidimensional) upwind type: with reference to **Fig. 1**, linearly interpolated values of u at the inflow and outflow points of the cell can be evaluated as

$$u_{\mathrm{in}}=\frac{\sum_{j=1}^{3}k_j^-u_j}{\sum_{j=1}^{3}k_j^-},\quad u_{\mathrm{out}}=\frac{\sum_{j=1}^{3}k_j^+u_j}{\sum_{j=1}^{3}k_j^+}, \tag{6}$$

where $k_j^+=\max(0,k_j)$, $k_j^-=\min(0,k_j)$. Then, the fluctuation, ϕ_T, can be written in compact form as [11]:

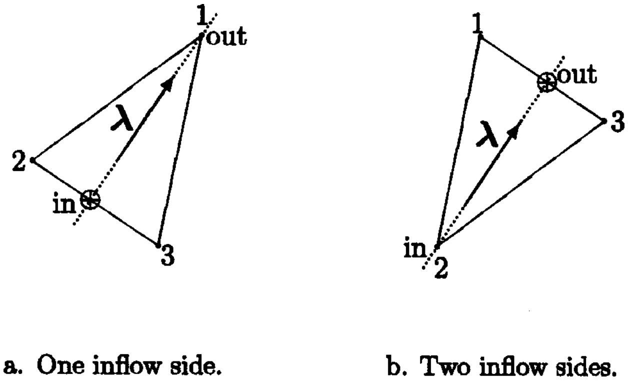

a. One inflow side.   b. Two inflow sides.

Fig. 1 Defninition of inflow and outflow points

$$\phi_T=-\sum_{j=1}^{3}k_ju_j=-\sum_{j=1}^{3}k_j^+(u_{\mathrm{out}}-u_{\mathrm{in}}). \tag{7}$$

Equation (7) shows that the fluctuation is zero when u takes the same values at both the inflow and outflow points, namely, when it is constant along streamlines. Upwind schemes are obtained by assigning to each downstream node j, $k_j\geqslant 0$, a fraction of the cell fluctuation. For the trivial configuration shown in **Fig. 1(*a*)**, the entire fluctuation is assigned to the only downstream node, and the resulting FS scheme is both positive and second-order accurate. For the nontrivial configuration shown in **Fig. 1(*b*)**, different choices of the splitting criterion characterize the different schemes such as the N, LDA, and PSI scheme, [10], which are here briefly recalled:

(i) The N scheme, which is the optimal first-order accurate upwind scheme, is obtained as

$$\phi_j^N=-k_j^+(u_j-u_{\mathrm{in}}). \tag{8}$$

(ii) The LDA scheme, which is a linear second-order-accurate upwind scheme, is obtained as

$$\phi_j^{LDA}=-k_j^+(u_{\mathrm{out}}-u_{\mathrm{in}}). \tag{9}$$

(iii) In order to design a scheme satisfying both properties P (positivity, namely capability of providing monotone solutions) and LP (linearity preserving, namely capability of preserving exact initial linear solution which is equivalent to second-order accuracy, [11]), it is necessary to make the distribution nonlinear. As proposed in Refs. [12] and [13], a nonlinear advection velocity can be used in Eq. (3) without changing the steady-state residual:

$$\boldsymbol{\lambda}^{\omega}=\boldsymbol{\lambda}+\omega\mathbf{s},\quad \mathbf{s}=\frac{-u_y\mathbf{i}+u_x\mathbf{j}}{|\nabla u|}. \tag{10}$$

In such a way, a degree-of-freedom, namely, the auxiliary speed ω, is introduced to determine the appropriate advection velocity for the sought upwind scheme. The strategy used to evaluate ω makes use of the *level line*, namely, the line of constant u. Such a strategy is briefly recalled here for completeness. In the two-target configuration (with respect to $\boldsymbol{\lambda}$), see **Fig. 1(*b*)**, two situations may occur: (i) the level line passing through the upwind node 2 cuts the outflow edge, i.e., $(u_3-u_2)(u_1-u_2)<0$ (**Fig. 2(*a*)**); (ii) the level line passing through the upwind node 2 does not cut the outflow edge, i.e., $(u_3-u_2)(u_1-u_2)>0$ (**Fig. 2(*b*)**). In both cases one looks for two values of $\boldsymbol{\lambda}^{\omega}$ being aligned with the two sides 2-1 and 2-3, respectively, $\boldsymbol{\lambda}_1^{\omega}$ and $\boldsymbol{\lambda}_3^{\omega}$. In the first case only one of such $\boldsymbol{\lambda}^{\omega}$ is downwind so that the scheme is one target. In particular, if $(u_1-u_3)\phi_T<0$, see **Fig. 2(*a*)**, the entire fluctuation is sent to node 1 and ω is computed by requiring that $k_3^{\omega}=0$, namely

$$\omega=-\frac{\boldsymbol{\lambda}\cdot\mathbf{n}_3}{\mathbf{s}\cdot\mathbf{n}_3}; \tag{11}$$

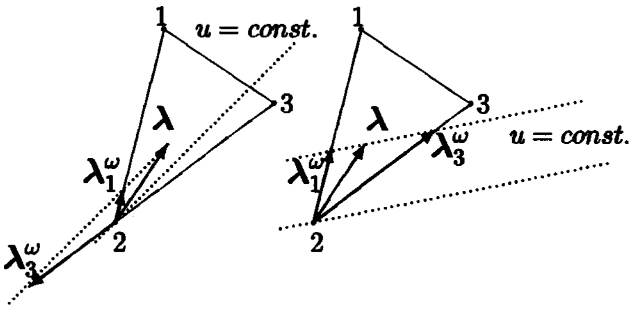

a. One target. **b. Two targets.**

Fig. 2 Nonlinear scheme configurations

for $(u_1-u_3)\ \phi_T>0$, the entire fluctuation is sent to node 3 and ω is computed by requiring that $k_1^\omega=0$, namely

$$\omega=-\frac{\boldsymbol{\lambda}\cdot\mathbf{n}_1}{\mathbf{s}\cdot\mathbf{n}_1}. \tag{12}$$

In the second situation, see **Fig. 2(*b*)**, both $\boldsymbol{\lambda}^\omega$ are downwind so that the scheme must be two-target and the distribution is performed according to the *N* scheme.

2.3 Numerical Method for the Navier-Stokes Equations. The fluctuation splitting methodology is extended to the solution of the Euler and Navier-Stokes equations by the following procedure. The Euler equations

$$\frac{\partial U}{\partial t}=-\boldsymbol{\nabla}\cdot\boldsymbol{\mathcal{F}}^i=\mathrm{Res}^i(U), \tag{13}$$

are discretized on a computational domain composed of linear finite elements. The discrete conservative flux balance over each cell T, namely, the fluctuation $\Phi_{U,T}$, can be written in terms of appropriate fluxes through the sides of the cell (see, e.g., [4,5]) as

$$\Phi_{U,T}=\bar{R}\Phi_T,\quad \Phi_T=-\sum_{j=1}^{d+1}\frac{l_j}{d}\bar{\mathbf{A}}\cdot\mathbf{n}_jQ_j=-\sum_{j=1}^{d+1}K_jQ_j. \tag{14}$$

In Eq. (14), $\bar{R}$ is the cell-averaged projection matrix from the characteristic variables, Q, to the conservative ones, U; Φ_T is the fluctuation in the variables Q; d is the number of space dimensions; $\bar{\mathbf{A}}$ is the Jacobian tensor with respect to the characteristic variables Q; and

$$K_j=\frac{l_j}{d}\bar{\mathbf{A}}\cdot\mathbf{n}_j. \tag{15}$$

Due to the hyperbolic nature of the system, K_j can be written as

$$K_j=(\bar{R}_K\bar{\Lambda}_K\bar{L}_K)_j=(\bar{R}_K\bar{\Lambda}_K^+\bar{L}_K)_j+(\bar{R}_K\bar{\Lambda}_K^-\bar{L}_K)_j=K_j^++K_j^-. \tag{16}$$

In Eq. (16), $\bar{R}_{K,j}$ and $\bar{L}_{K,j}$ are the right and left eigenvector matrices of K_j, whereas $\bar{\Lambda}_{K,j}^+$ and $\bar{\Lambda}_{K,j}^-$ are the corresponding positive and negative eigenvalue matrices. Generalizing the results obtained for the scalar equations, and introducing the following vectors,

$$Q_{\mathrm{in}}=\left(\sum_{j=1}^{d+1}K_j^-\right)^{-1}\left(\sum_{j=1}^{d+1}K_j^-Q_j\right),$$

$$Q_{\mathrm{out}}=\left(\sum_{j=1}^{d+1}K_j^+\right)^{-1}\left(\sum_{j=1}^{d+1}K_j^+Q_j\right), \tag{17}$$

the linear matrix LDA scheme, which is linearity preserving, [10], is obtained as

$$\Phi_j=-K_j^+[Q_{\mathrm{out}}-Q_{\mathrm{in}}]. \tag{18}$$

Such a scheme is very accurate for subsonic smooth flows and can be considered the optimal compact FS scheme for such conditions. For supersonic flows, different characteristic variables, W, are employed, which, for two-dimensional flows, allow one to recast the Euler system into an equivalent set of four scalar advection equations, [14]. These are then discretized by the nonlinear (scalar) PSI scheme, [10], which can be written as

$$\hat{\Phi}_j=-K_j^{nl+}(W_j-W_{\mathrm{in}}^{nl}), \tag{19}$$

where K_j^{nl+} is computed by generalizing the procedure described in the scalar section using the nonlinear Jacobian $\hat{\bar{\mathbf{A}}}^{nl}$, as defined in [15]. Finally, in order to compute transonic flows with strong shocks, it is necessary to use locally a monotone scheme, namely, the matrix N scheme of Ref. [5], given as

$$\hat{\Phi}_j=-K_j^{l+}(W_j-W_{\mathrm{in}}^{l}), \tag{20}$$

where K_j^l and W_{in}^l are computed using the Jacobian $\bar{\mathbf{A}}_W$ (Ref. [15]). In order to pinpoint the "shock cells" where such a lower-order scheme needs to be employed, and disregarding those cells where the transition from supersonic flow conditions to subsonic ones is smooth enough to be properly handled by the LDA scheme, it is necessary to characterize computational cells uniquely. By a careful analysis of the flow properties across a normal shock, it is concluded that "shock cells" are characterized by (i) average cell Mach number $M<1$; (ii) at least one supersonic node; and (iii) at least one subsonic node with its local Mach number lower than 0.9. The choice of such a value is arbitrary indeed. The proposed one is such that the lower order scheme is used for normal shocks and makes the overall approach very robust while still limiting the use of the lower-order scheme to a very small number of cells, [16]. In conclusion, at every step of the computational process, the present hybrid approach flags all elements of the computational domain and distributes the residuals for each of them using Eq. (18) at subsonic cells, Eq. (19) at supersonic ones, and Eq. (20) at "shock cells."

The viscous terms are discretized using a standard Galerkin finite element scheme. Consider the generic node i of the computational domain and the area/volume S_i composed by all elements sharing node i. The standard procedure used in finite element analysis is applied to the divergence of the viscous fluxes, to provide

$$\int_{S_i}\psi_i\boldsymbol{\nabla}\cdot\boldsymbol{\mathcal{F}}^v\mathrm{d}S=-\int_{S_i}\boldsymbol{\nabla}\psi_i\cdot\boldsymbol{\mathcal{F}}^v\mathrm{d}S-\oint_{\partial S_i}\psi_i\boldsymbol{\mathcal{F}}^v\cdot\mathbf{n}\,\mathrm{d}s, \tag{21}$$

where ψ_i is the linear tent function and $\mathbf{n}$ is the inward unit vector normal to the boundary ∂S_i. The second term in the right-hand side of Eq. (21) is zero since $\psi_i=0$ on ∂S_i, so that

$$\int_{S_i}\psi_i\boldsymbol{\nabla}\cdot\boldsymbol{\mathcal{F}}^v\mathrm{d}S=-\sum_T\left[\frac{l_{iT}\mathbf{n}_{iT}}{2S_T}\cdot\int_{S_T}\boldsymbol{\mathcal{F}}^v\,\mathrm{d}S\right]. \tag{22}$$

In Eq. (22), the sum is extended over all elements meeting at node i, and the subscript iT refers to the face of the element T opposite to the vertex i.

The convective and source terms in the turbulence transport Eq. (2) are discretized in space by means of the PSI scheme and the centered scheme, respectively, whereas the diffusive terms are discretized by the standard Galerkin scheme.

The residuals of the Reynolds-averaged Navier-Stokes equations at each node i are finally computed by collecting all terms, to give

$$\left(\frac{\partial U}{\partial t}\right)_i=\frac{1}{S_i}\sum_T(\Phi_{U,T})_i-\sum_T\left[\frac{l_{iT}\mathbf{n}_{iT}}{2S_T}\cdot\int_{S_T}\boldsymbol{\mathcal{F}}^v\,\mathrm{d}S\right]=R(U)_i. \tag{23}$$

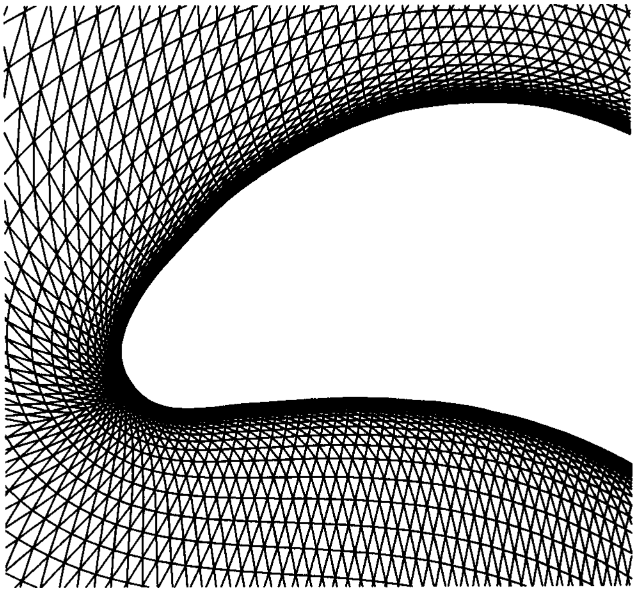

Fig. 3 Local view of the coarse grid at the leading edge

The time derivative in Eq. (23) is approximated using a two-point backward finite difference, and the residual is evaluated implicitly. Linearizing $R(U)$ about time level n, the following scheme is obtained:

$$\left(\frac{S}{\Delta t}I-\left(\frac{\partial R}{\partial U}\right)\right)_i (U^{n+1}-U^n)_i=R(U)_i^n. \tag{24}$$

Equation (24) represents a large nonsymmetric sparse linear system to be solved at each time step. In the present computations the Jacobian, $\partial R/\partial U$, is evaluated numerically using first-order-accurate differences. The sparse matrix technology required to solve Eq. (24) is provided by the PETSc library, [17]. The linear solver is based on an ILU(0) preconditioned GMRES algorithm, restarted every 30 linear iterations. The time step, Δt, is varied, after each nonlinear iteration, so as to equal the ratio between the initial and the current nonlinear residual, thus rapidly reaching very large values.

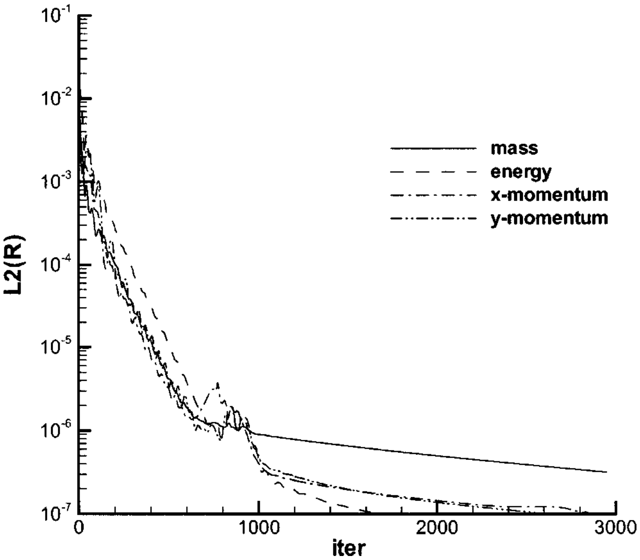

Fig. 4 Convergence histories for the $M_{2,is}=0.81$ case

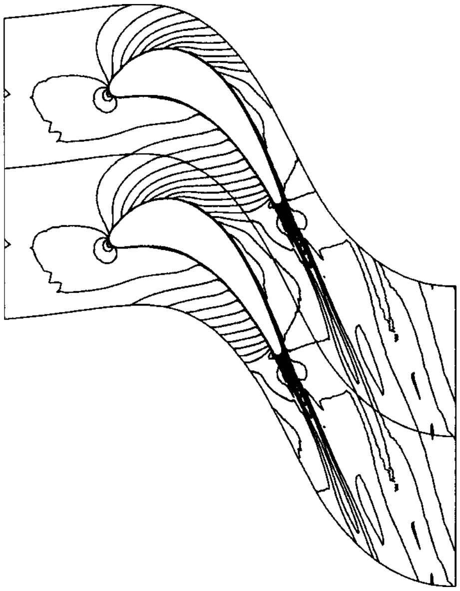

Fig. 5 Coarse grid: Mach number contours for $M_{2,is}=0.81$ ($\Delta M=0.05$)

The turbulence transport Eq. (2) is discretized in time and is solved by the same implicit method, one nonlinear iteration being performed at the end of each nonlinear iteration of the flow equations.

Standard characteristic boundary conditions are imposed at inflow and outflow points. Both velocity components at the wall nodes are set to zero, whereas the zero heat-flux condition is naturally enforced by omitting the boundary heat-flux contributions at the wall cell sides. Concerning the turbulence equation, the values of $\tilde{\nu}$ are prescribed at inlet points ($\tilde{\nu}=0.01$) and at wall points ($\tilde{\nu}=0$), and are linearly extrapolated at outlet points.

3 Results

The proposed numerical method has been employed to compute subsonic and transonic flows through the high-turning VKI LS59

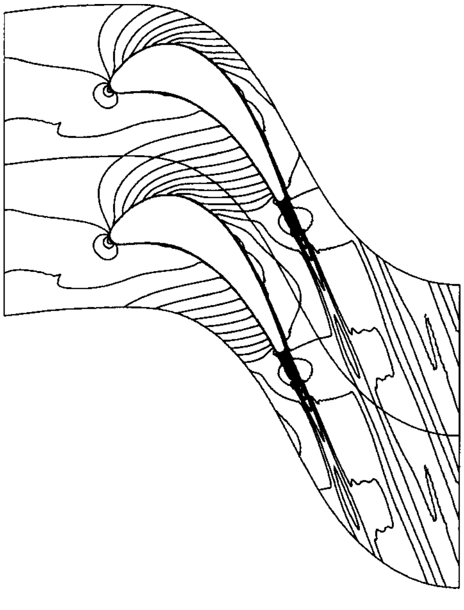

Fig. 6 Fine grid: Mach number contours for $M_{2,is}=0.81$ ($\Delta M=0.05$)

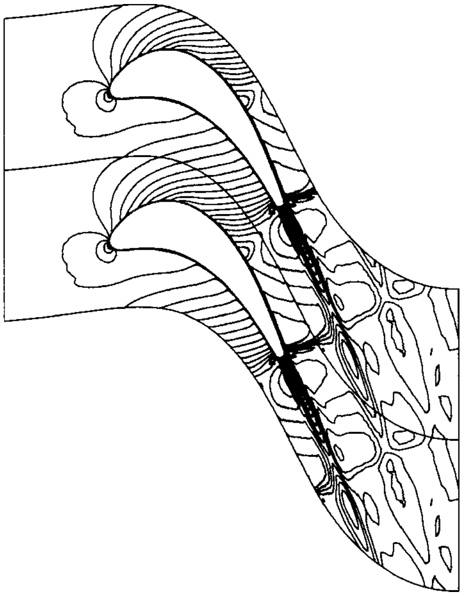

Fig. 7 Coarse grid: Mach number contours for $M_{2,is}=1$ ($\Delta M=0.05$)

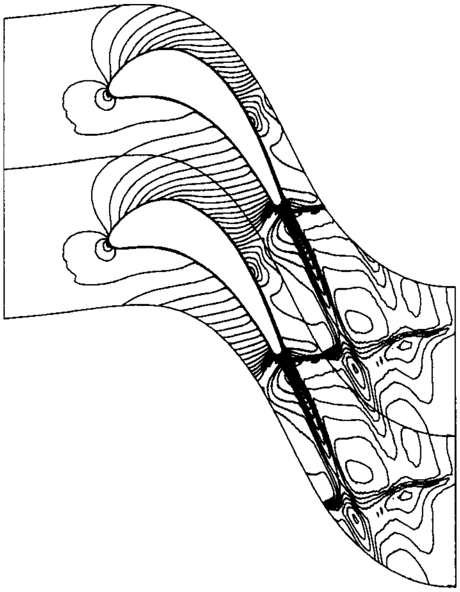

Fig. 9 Coarse grid: Mach number contours for $M_{2,is}=1.11$ ($\Delta M=0.05$)

turbine-rotor cascade. Experimental data are available in the literature, [18,19], indicating that the flow is nearly two-dimensional. End-wall effects and aspect-ratio influence are practically negligible, so that a two-dimensional flow computation is adequate.

Four flow conditions have been considered, with isentropic exit Mach number, $M_{2,is}$, equal to 0.81, 1, 1.11, and 1.2, respectively; the corresponding Reynolds numbers, based on the blade chord, c, and exit conditions, are 8.22×10^5, 7.44×10^5, 7×10^5, 6.63×10^5, whereas the inlet flow angle with respect to the axial direction is always 30 deg. Two grids have been employed, containing 24576 and 98304 triangular elements and 257 and 513 points on the blade, respectively. The maximum corresponding distances between the profile and the first grid point are $10^{-4}\,c$ ($y^+\approx4$) and $0.5\times10^{-4}\,c$ ($y^+\approx2$). The unstructured grids have been obtained by structured ones by dividing each quadrilateral cell into two triangles. **Figure 3** provides a local view of the coarse grid around the leading edge of the blade. For all computations, starting from rest, a residual drop of three orders of magnitude is obtained in about 40 and 160 minutes, which corresponds to about 200 iterations, on a single-processor (EV5.6-500 MHz) DIGITAL computer, for the coarse and fine grids, respectively. Such CPU times are two orders of magnitude lower than the ones corresponding to the explicit procedure employed in [7]. **Figure 4** provides the convergence histories of the L_2 norm of the residual for each conservation equation corresponding to the $M_{2,is}=0.81$ case. **Figures 5–12** show the Mach number contours for the four exit Mach number flow cases and for the two grid resolutions. In all cases, the complex structure of the flow is well predicted, and the shocks are captured sharply and monotonically even on the coarse grid. This demonstrates the remarkable accuracy of the hybrid FS

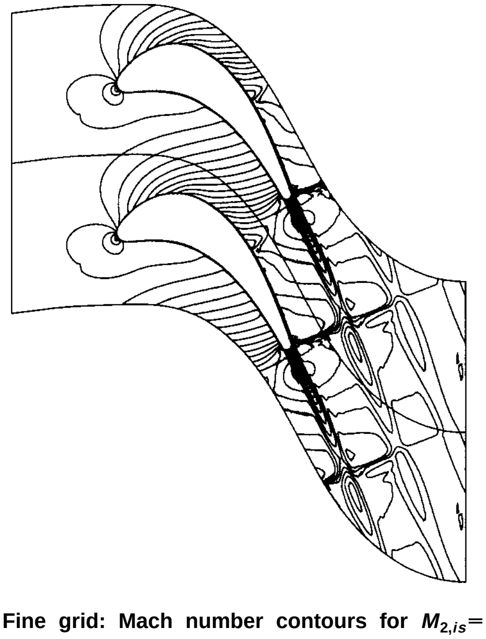

Fig. 8 Fine grid: Mach number contours for $M_{2,is}=1$ ($\Delta M=0.05$)

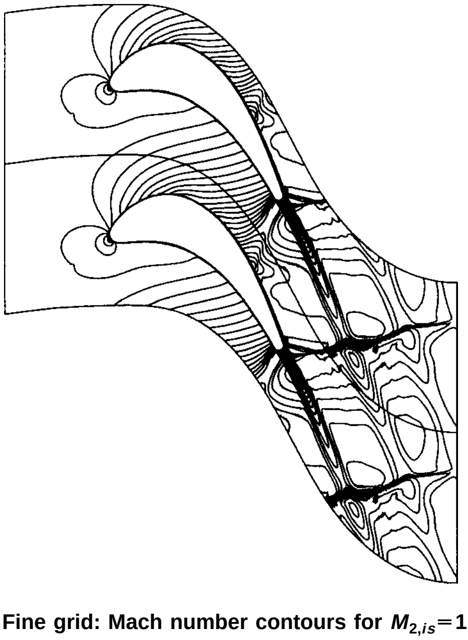

Fig. 10 Fine grid: Mach number contours for $M_{2,is}=1.11$ ($\Delta M=0.05$)

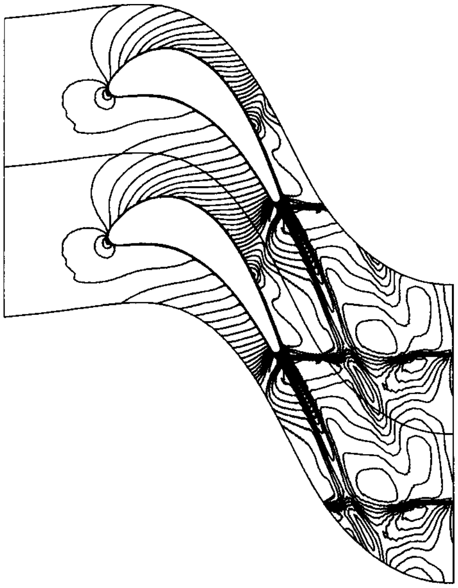

Fig. 11 Coarse grid: Mach number contours for $M_{2,is}=1.2$ ($\Delta M=0.05$)

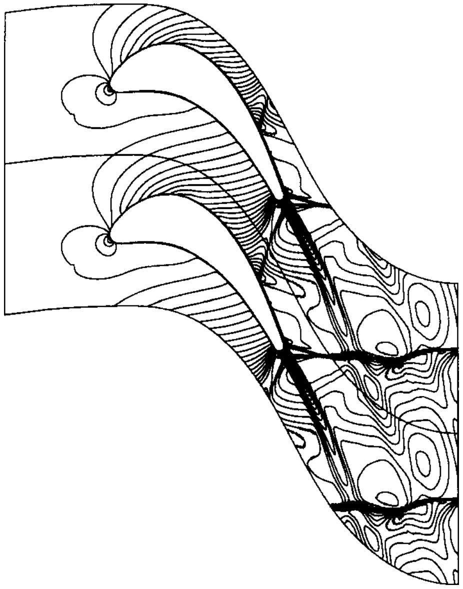

Fig. 12 Fine grid: Mach number contours for $M_{2,is}=1.2$ ($\Delta M=0.05$)

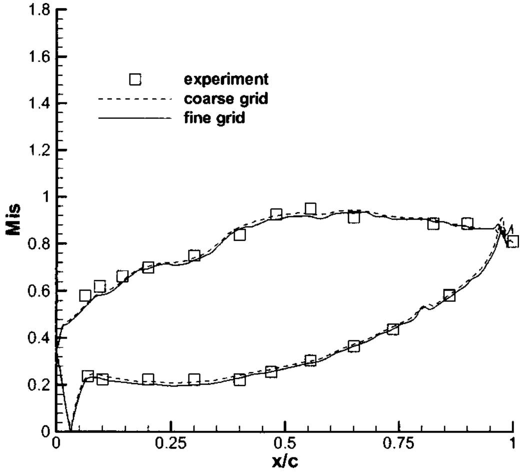

Fig. 13 Isentropic Mach number distributions along the blade for $M_{2,is}=0.81$

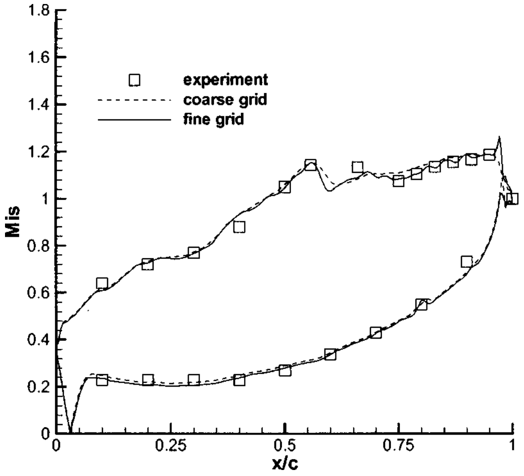

Fig. 14 Isentropic Mach number distributions along the blade for $M_{2,is}=1$

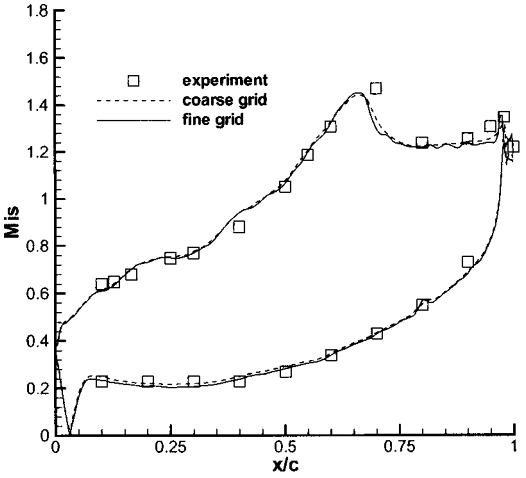

Fig. 15 Isentropic Mach number distributions along the blade for $M_{2,is}=1.11$

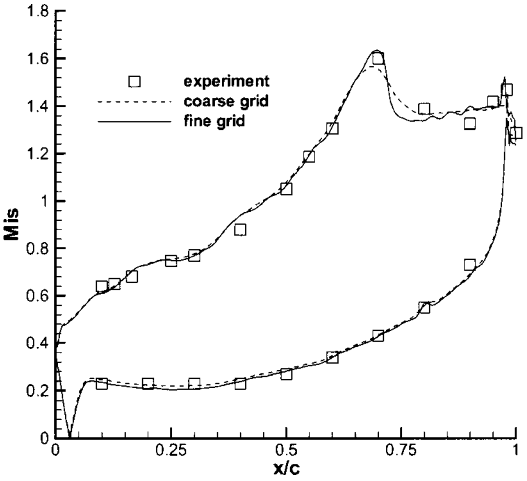

Fig. 16 Isentropic Mach number distributions along the blade for $M_{2,is}=1.2$

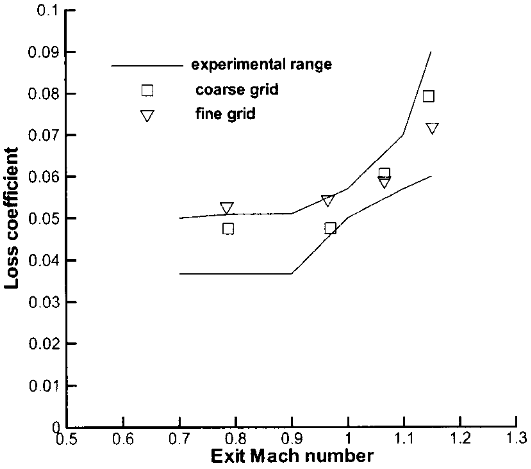

Fig. 17 Loss coefficient

formulation. The saw-tooth patterns barely visible near the shock for some flow cases, see, e.g., **Fig. 8**, is probably due to the local distortion of the grid with respect to the flow. In particular, for the $M_{2,is}=1.2$ flow case, the λ shock at the trailing edge of the suction side of the blade is already captured on the coarse grid and clearly evident on the fine one. Comparing such a solution with the corresponding one provided in [20], it can be seen that such a flow feature is missed by classical numerical schemes such as Jameson's scheme even on grids comparable with the present fine one. The computed isentropic Mach number distributions along the blade are shown in **Figs. 13–16** along with the experimental results obtained by Sieverding [18,19]. The coarse-grid solutions are practically grid-converged, except at the suction surface shock location for the $M_{2,is}=1.2$ flow case. All the fine grid solutions can be seen to agree well with the experimental data. The computed values of the pitchwise-mass-averaged loss coefficient $(1-w^2/w_{is}^2$, w being the velocity) 0.6 chords downstream of the cascade are given in **Fig. 17**, together with the experimental results obtained on four European wind tunnels, [19]. It appears that the fine grid is required to evaluate such a very sensitive property, accurately. Nonetheless, the errors of the coarse-grid predictions are lower than the range of the experimental data. Finally, the pitchwise-mass-averaged exit flow angles are given in **Fig. 18**. For such an integrated quantity, the coarse and fine grid results practically coincide and are in the middle of the experimental range.

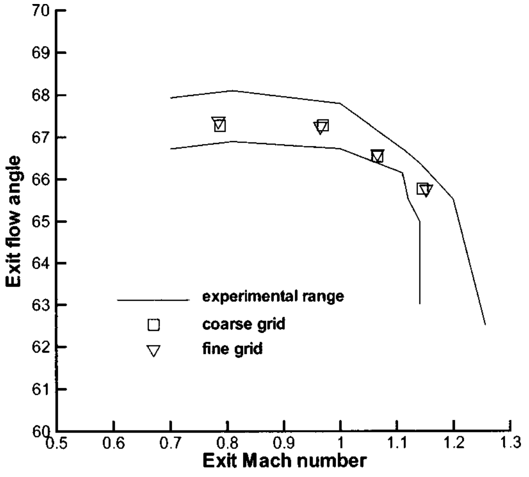

Fig. 18 Exit flow angle

4 Conclusions

An implicit hybrid fluctuation splitting scheme has been developed for solving steady compressible flows in two dimensions. Results are presented for subsonic and transonic turbulent flows through a high-turning turbine-rotor cascade, which demonstrate the accuracy of the spacial discretization and the robustness and efficiency of the implicit Newton-GMRES integration procedure. The proposed methodology is currently being extended to three-dimensional steady flows as well as to time-dependent flows, via a dual-time-stepping approach.

Acknowledgments

This research is supported by MIUR/COFIN2001 and MIUR/COFIN2003.

References

[1] Tannehill, J. C., Anderson, D. A., and Pletcher, R. H., 1997, *Computational Fluid Mechanics and Heat Transfer*, Second Ed., Taylor and Francis, London.
[2] Jameson, A., Schmidt, W., and Turkel, E., 1981, "Numerical Simulation of the Euler Equations by Finite Volume Methods Using Runge-Kutta Time Stepping Schemes," AIAA Paper 81-1259.
[3] Roe, P. L., 1981, "Approximate Riemann Solvers, Parameter Vectors and Difference Schemes," J. Comput. Phys., **43**(2), pp. 357–372.
[4] van der Weide, E., and Deconinck, H., 1996, "Positive Matrix Distribution Schemes for Hyperbolic Systems, With Applications to the Euler Equations," 3rd ECCOMAS CFD Conference, Paris.
[5] Catalano, L. A., De Palma, P., Pascazio, G., and Napolitano, M., 1997, "Matrix Fluctuation Splitting Schemes for Accurate Solutions to Transonic Flows," *Lecture Notes in Physics*, 490, Springer-Verlag, Berlin, pp. 328–333.
[6] De Palma, P., Pascazio, G., and Napolitano, M., 1999, "A Hybrid Multidimensional Upwind Scheme for Compressible Steady Flows," AIAA Paper 99-3513.
[7] De Palma, P., Pascazio, G., and Napolitano, M., 2001, "A Multidimensional Upwind Solver for Steady Compressible Turbulent Flows," CFD Journal, Special No., pp. 287–295.
[8] Bonfiglioli, A., 1998, "Multidimensional Residual Distribution Schemes for the Pseudo-Compressible Euler and Navier-Stokes Equations on Unstructured Meshes," *Lecture Notes in Physics*, **515**, Springer-Verlag, Berlin, pp. 254–259.
[9] Spalart, P. R., and Allmaras, S. R., 1994, "A One-Equation Turbulence Model for Aerodynamical Flows," Rech. Aerosp., **1**, pp. 5–21.
[10] Struijs, R., Deconinck, H., and Roe, P. L., 1991, "Fluctuation Splitting Schemes for the 2D Euler Equations," VKI LS 1991-01, Computational Fluid Dynamics, von Karman Institute, Belgium.
[11] Paillère, H., 1995, "Multidimensional Upwind Residual Distribution Schemes for the Euler and Navier-Stokes Equations on Unstructured Grids," Ph.D. thesis, Université Libre de Bruxelles, Belgium, June.
[12] Mizukami, A., and Hughes, T. J. R., 1985, "A Petrov-Galerkin Finite Element Method for Convection-Dominated Flows: An Accurate Upwinding Technique for Satisfying the Maximum Principle," Comput. Methods Appl. Mech. Eng., **50**, pp. 181–193.
[13] Roe, P. L., 1990, "Optimum Upwind Advection on a Triangular Mesh," ICASE Report No. 90-75.
[14] van Leer, B., Lee, W. T., and Roe, P. L., 1991, "Characteristic Time-Stepping or Local Preconditioning of the Euler Equations," AIAA Paper 91-1552.
[15] De Palma, P., Pascazio, G., and Napolitano, M., 1998, "A Hybrid Fluctuation Splitting Scheme for Transonic Inviscid Flows," 4th ECCOMAS CFD Conference, Athens.
[16] De Palma, P., Pascazio, G., and Napolitano, M., 2002, "A Hybrid Fluctuation Splitting Scheme for Two-Dimensional Compressible Steady Flows," *Innovative Methods for Numerical Solution of Partial Differential Equations*, M. M. Hafez and J. J. Chattot, eds., World Scientific Publishing, Singapore, pp. 303–333.
[17] Balay, S., Gropp, W. D., Curfman McInnes, L., and Smith, B. F., 1998, PETSc home page http://www.mcs.anl.gov/petsc.
[18] Sieverding, C. H., 1973, "Experimental Data on Two Transonic Turbine Blade Sections and Comparisons With Various Theoretical Methods," VKI Report No. LS59, von Karman Institute, Belgium.
[19] Kiock, R., Lethaus, F., Baines, N. C., and Sieverding, C. H., 1986, "The Transonic Flow Through a Plane Turbine Cascade as Measured in Four European Wind Tunnels," ASME J. Eng. Gas Turbines Power, **108**, pp. 277–285.
[20] Arnone, A., and Swanson, R. C., 1993, "Navier-Stokes Solver for Turbomachinery Applications," ASME J. Turbomach., **115**, pp. 305–313.

Stephen K. Roberts
e-mail: skrobert@connect.carleton.ca

Metin I. Yaras
e-mail: metin_yaras@carleton.ca

Department of Mechanical and Aerospace Engineering,
Carleton University,
3135 Mackenzie Building,
1125 Colonel By Drive,
Ottawa, ON K1S 5B6, Canada

Modeling Transition in Separated and Attached Boundary Layers

This paper presents a mathematical model for predicting the rate of turbulent spot production. In this model, attached- and separated-flow transition are treated in a unified manner, and the boundary layer shape factor is identified as the parameter with which the spot production rate correlates. The model is supplemented by several correlations to allow for its practical use in the prediction of the length of the transition zone. Second, the paper presents a model for the prediction of the location of transition inception in separation bubbles. The model improves on the accuracy of existing alternatives, and is the first to account for the effects of surface roughness. [DOI: 10.1115/1.1860570]

Keywords: Boundary Layer Transition, Transition Modeling

Introduction

Since the concept of the turbulent spot was initially proposed by Emmons [1], extensive experimental research efforts have been dedicated to uncovering the mechanisms leading to transition inception (e.g., [2–6]) and the process of growth and merging of turbulent spots into a fully turbulent boundary layer (e.g., [7–9]). Studies such as these have increased our understanding of the transition process and have identified the flow parameters that significantly affect this process, namely, freestream turbulence intensity [10,11], turbulence length scale [12,13], streamwise pressure gradients [14–16], streamline curvature [17,18], periodic impingement of wakes [19–21], and surface roughness [22,23].

The ultimate mathematical model for the transition process already exists in the form of the unsteady Navier-Stokes equations. Until relatively recently, however, lack of computing power has prevented the numerical solution of these equations with sufficient resolution to predict the details of turbulence production, convection, diffusion and dissipation in transitioning or turbulent flows. Such direct numerical simulations (DNS) are now being used as numerical wind tunnels to shed light onto fundamental features of transition and turbulence [24–27], which are extremely difficult to observe through physical experiments. However, the available computing power has imposed limits on the range of flow Reynolds numbers that can be considered in such simulations [27,28], which will remain so for the foreseeable future.

There has been considerable research focusing on predicting transition through the use of low-Reynolds-number turbulence models (e.g., [29–31]). In the authors' opinion, however, there are no fundamental grounds for these turbulence models to capture the proper physics of the transition process, for they have been tailored to predict the near-wall region of fully turbulent boundary layers. Flow phenomena key to the transition process, such as amplification of instabilities leading to the inception of turbulent spots and the distinct spreading patterns of these spots, are concealed by the Reynolds-averaging process. Nonetheless, there have been numerous attempts to make these models mimic transition phenomena by drawing analogies between the cross-stream variation of turbulence near a solid surface and the streamwise variation of turbulence during transition. Such methods employ a subgroup of models based on the turbulence Reynolds number rather than on wall proximity. Proper execution of this approach requires the presence of freestream disturbances, which limits the transition process to that of the bypass type, triggered by diffusion of freestream turbulence into the shear layer. Savill [32] showed that low-Re turbulence models fail to predict both the transition onset location and the length of the transition zone accurately. The latter trend was noted by Schmidt and Patankar [31] as well, who also showed that these models are sensitive to the streamwise start location of calculations and to the initial profiles of turbulence quantities. The poor performance of low-Reynolds-number turbulence models in attached flow is likely to prevail in separated-flow transition as well.

There have been attempts to improve the transition prediction performance of low-Reynolds-number turbulence models through the use of intermittency functions (e.g., [33]). Such methods are more general than the basic low-Reynolds-number turbulence modeling approach, in the sense that they explicitly account for spot formation and growth rates. However, the underlying assumption of similarity between the turbulence structure in the turbulent spots and in the fully turbulent boundary layer remains, and the location of transition inception needs to be estimated through other means, typically empirical correlations. Hobson and Weber [34] attempted to use the turbulence model of Spalart and Allmaras [35] together with the intermittency function of Solomon et al. [36] for separation-bubble transition and found that the internal structure of the bubble was not predicted well. More recently, transport equations have been developed for predicting the streamwise variation of intermittency rather than relying on empirical relations (e.g., [37,38]). The model of Suzen and Huang [38] also accounts for the cross-stream variation of flow intermittency. The authors reported reasonable accuracy for the prediction of the transition length, with the transition inception location determined through an empirical correlation. However, in the context of the previous discussion on the use of low-Re turbulence models to predict the turbulence generation within turbulent spots, the present authors remain doubtful of the feasibility of achieving consistent prediction accuracy with such models.

Large eddy simulation (LES) has relatively recently emerged as a compromise between the excessive computing requirements of DNS and the lack of general applicability of Reynolds-average Navier-Stokes (RANS) formulations to turbulent and transitional flows. In this method, the larger turbulent structures are computed explicitly, while the smaller scale turbulence is modeled, which is commonly referred to as sub-grid-scale modeling [39]. This approach has been shown to have the potential to provide substantially more consistent prediction of turbulent flows than has been accomplished by modeling the complete range of turbulence scales [40]. Because a large range of turbulence scales naturally develop during such simulations, prediction of transition inception

---

Contributed by the International Gas Turbine Institute (IGTI) of THE AMERICAN SOCIETY OF MECHANICAL ENGINEERS for publication in the ASME JOURNAL OF TURBOMACHINERY. Paper presented at the International Gas Turbine and Aeroengine Congress and Exhibition, Vienna, Austria, June 13–17, 2004, Paper No. 2004-GT-53664. Manuscript received by IGTI, October 1, 2003; final revision, March 1, 2004. IGTI Review Chair: A. J. Strazisar.

and turbulent spot propagation is theoretically within the capability of this method. This has been confirmed through case studies in the published literature (e.g., [40,41]). However, the LES computing requirements for high-Re flows are within the range that still makes LES unattractive for regular use in industry. Additionally, the feasibility of sub-grid-scale turbulence models that are equally effective away as well as in close proximity of solid boundaries remains the focus of extensive research. Hence, it will be some time before this technique matches the reliability and efficiency of the well proven semi-empirical modeling approach for the prediction of the transition process.

Based on these observations, for the foreseeable future, semi-empirical mathematical tools appear to be the most accurate and time efficient means for modeling turbulent spot inception and propagation. The present study begins with a review of existing models for predicting transition inception and transition length, and proposes models that account for the effects of a broader range of flow and geometric parameters, calibrated against an extensive set of experimental data.

Review of Semi-Empirical Transition Models

Transition from laminar to turbulent flow in boundary layers is known to take place through the inception and spreading of turbulent spots, which in planform view resemble an arrowhead, with the tip pointing in the downstream direction (e.g., [1,42]). Once formed, these spots are convected downstream while they spread in the streamwise, spanwise, and cross-stream directions, until merging with each other to form a fully turbulent boundary layer. The length of the transition zone is therefore dictated by the inception, convection, and spreading rates of the turbulent spots. For modeling purposes, the state of the boundary layer in the transition zone is conventionally described by the intermittency, γ, which is the fraction of time that a given location in the boundary layer resides within turbulent spots. Emmons [1] showed this to be a continuous Poisson process. Ignoring variations in the intermittency in the cross-stream and spanwise directions, this may be mathematically expressed as

$$\gamma(x) = 1 - e^{-\int n(x)dx \int g_x(x)dx \int g_z(x)dx} \tag{1}$$

where n represents the inception rate of turbulent spots at a given location, and g_x and g_z respectively represent the streamwise and spanwise spreading rates of these spots.

Inception of Turbulent Spots. The uniformly distributed spot production assumed in Emmons' [1] theory is not supported by the concentrated inception of spots observed in the experiments of Schubauer and Klebanoff [43]. Recently, Johnson and Fashifar [8] observed the presence of a finite streamwise band within which spot inception takes place. Nonetheless, this band is sufficiently narrow to justify Narasimha's [9] hypothesis of concentrated breakdown, whereby spot inception occurs at random times and spanwise locations at one streamwise location. Another underlying assumption in Emmons' theory is that the inception of a turbulent spot is not affected by the proximity of other spots. However, it has been demonstrated experimentally [8] that turbulent spots are less likely to be produced in close proximity of each other. This may be, in part, due to the existence of a calmed region following the passage of a turbulent spot [8,42]. Despite evidence of deviations from the assumptions of concentrated breakdown and spot formation that is uninfluenced by other spots, the level of success with transition models based on Narasimha's hypothesis [9,36] suggests these deviations to be small.

The inception of turbulent spots in an attached boundary layer is typically preceded by the growth of instability (Tollmien-Schlichting) waves, which is for the most part a linear process, becoming nonlinear shortly before breakdown into turbulent spots (e.g., [5,24]). This transition mode, known as natural transition, is encountered in relatively low disturbance environments and has recently been observed to potentially be the dominant mechanism of transition also in instances where the boundary layer separates prior to transition onset [24]. In cases of separated flow, the highly inflectional mean velocity profile downstream of the point of separation tends to substantially reduce the streamwise length of instability growth leading to transition inception (e.g., [44–46]). In an environment with large disturbances, such as elevated freestream turbulence and substantial surface roughness, the relatively long process of linear growth of instability waves is bypassed, leading to the formation of turbulent spots shortly after exposure of the laminar boundary layer to such disturbances (e.g., [10,47]).

Regardless of whether transition is of the natural or bypass mode, experimental studies have shown that the rate of turbulent spot inception is affected by the local freestream turbulence and streamwise pressure gradient [14,48], and surface roughness, as indicated indirectly by the measurements of Pinson and Wang [23]. The random occurrence of turbulent spots prevents direct measurement of their inception rates. Thus, conclusions regarding the trends in spot inception rates have been deduced from the transition length and spot propagation characteristics in the transition zone. The level of success in experimentally quantifying the inception rate of turbulent spots is therefore closely coupled to the extent of our understanding of their convection and spreading characteristics.

Convection and Spreading of Turbulent Spots. Since the work of Emmons [1], numerous studies have documented the development of turbulent spots as they are convected downstream. These studies measured the structure and spreading of spots in the horizontal plane (e.g., [7,49]) or in the vertical plane of symmetry [7]. More recently, measurements have been undertaken to fully document the three-dimensional spot structure (e.g., [42]). Such three-dimensional measurements have identified distinct regions of turbulence generation at the leading edge and along the lateral extremes of the spots. Through these studies, the local pressure gradient has been confirmed as the parameter dominating the spreading rate of turbulent spots.

Transition Models.

Location of Transition Inception. In attached boundary layers, the widely accepted parameter for correlating the location of transition inception is the Reynolds number based on momentum thickness, Re_θ. Among the numerous transition inception formulations, those of Mayle [50] (Eq. (2)) and Abu-Ghannam and Shaw [3] (Eqs. (3)) are the ones cited most frequently in turbomachinery blade studies.

$$\mathrm{Re}_{\theta ts} = 400\, Tu^{-0.625} \tag{2}$$

$$\mathrm{Re}_{\theta ts} = 163 + \exp\left(F(\lambda_\theta) - \frac{F(\lambda_\theta)}{6.91}\overline{Tu}\right) \tag{3a}$$

where $\mathrm{Re}_{\theta ts}$ is the Reynolds number based on momentum thickness at the transition inception location, $\overline{Tu}$ is the average freestream turbulence level between the leading edge and transition inception location, and $F(\lambda_\theta)$ in Eq. (3*a*) is a function of Thwaites' pressure gradient parameter $(\lambda_\theta = (\theta^2/\nu)dU_e/dx)$, defined as

$$F(\lambda_\theta) = 6.91 + 12.75\lambda_\theta + 63.64\lambda_\theta^2 \quad \{\lambda_\theta \leqslant 0\} \tag{3b}$$

$$F(\lambda_\theta) = 6.91 + 2.48\lambda_\theta - 12.27\lambda_\theta^2 \quad \{\lambda_\theta \geqslant 0\} \tag{3c}$$

Although the model of Abu-Ghannam and Shaw [3] has the advantage of accounting for the effects of both freestream turbulence and streamwise pressure distribution, for flows with high turbulence intensity it has been artificially forced to correspond to the stability limit for natural transition of $\mathrm{Re}_{\theta ts}=163$. Mayle's [50] correlation is not constrained by this stability limit, but it does not account for the effects of pressure gradient. For freestream turbulence intensities typical of turbomachinery blade rows, it is known that transition inception in an attached boundary layer is not strongly affected by the streamwise pressure distribution [13,50]. Thus, Eq. (2) is suitable for such applications. The experimental results from an earlier phase of the present research [13], covering a range of pressure gradients and freestream turbulence levels, were predicted reasonably well by both of these models.

For transition in short separation bubbles, the location of transition inception has been found to correlate well with the state of the boundary layer at the point of separation.

Mayle [50]

$$\mathrm{Re}_{ts} - \mathrm{Re}_{s} = 300\,\mathrm{Re}_{\theta s}^{0.7} \tag{4}$$

where Re_s and Re_{ts} are the Reynolds numbers based on the streamwise locations of separation (x_s) and transition inception (x_{ts}), respectively.

Roberts [51]

$$\mathrm{Re}_{s-ts} = 2.5 \times 10^4 \log_{10}\{\coth[TF(\%)/10]\} \tag{5}$$

In this equation, TF is Taylor's [52] turbulence factor [$TF = Tu_{\mathrm{ref}}(L/\lambda_s)^{0.2}$], where λ_s is the integral length scale of freestream turbulence, and L is the length of the surface along which the boundary layer develops.

Hatman and Wang [44]

$$\mathrm{Re}_{ts} = 1.0816\,\mathrm{Re}_s + 26{,}805 \tag{6}$$

Yaras [53]

$$\mathrm{Re}_{ts} = 1.04\,\mathrm{Re}_s + 6.3 \times 10^4\{1 - \tanh^3[TF'(\%)]\} \tag{7}$$

where $TF' = \max[TF, (\%)1\%]$.

Among these models, the latter two have been found to be more accurate when compared to the experimental transition data that have been measured at Carleton University over the past several years [45,53,54]. While the models of Hatman and Wang [44] and Yaras [53] agree well with each other at low freestream turbulence levels, only the latter model is applicable to elevated free-stream turbulence conditions.

Length of Transition. Early efforts to model the transition region for attached boundary layers (e.g., [1,9]), did so without the benefit of more refined measurements of streamwise propagation rates and spreading angles that have become available more recently [7,42,49]. Nonetheless, the concentrated breakdown hypothesis described earlier, along with the further assumption of constant spreading rates in the streamwise and lateral directions, led to the well-known intermittency model of Narasimha [9]:

$$\gamma(x) = 1 - e^{-(n\sigma/U_e)(x - x_{ts})^2} \quad \{x \geqslant x_{ts}\} \tag{8}$$

where n is the spot inception rate and σ is a spot propagation parameter given by

$$\sigma = U_e(U_{TE}^{-1} - U_{LE}^{-1})\tan(\alpha) \tag{9}$$

In Eq. (9), α is the lateral spot spreading half-angle, and U_{LE} and U_{TE} are the spot leading- and trailing-edge convection velocities, respectively.

*Spot Inception Rate***.** Narasimha [9] proposed a nondimensional inception rate parameter formulated as

$$N = \frac{n\sigma\theta_{ts}^3}{\nu} \tag{10}$$

Based on experimental data primarily for low values of λ_θ [2,3,43,55], Narasimha proposed a value of $N = 0.7 \times 10^{-3}$, for freestream turbulence levels above 0.1%.

More recently, Fraser et al. [14] established a dependence of N on both streamwise pressure gradient and turbulence level through experimental data compiled from various sources and proposed the following model:

$$N = \frac{47.23 \times 10^{-3}}{(10 - e^{1.7-\mathrm{Tu}/2})^2} \times e^F \tag{11a}$$

$$F = -10\sqrt{\lambda_{\theta ts}} + 300\lambda_{\theta ts}{}^4 \quad \{\lambda_{\theta ts} \geqslant 0\} \tag{11b}$$

$$F = \lambda_{\theta ts}(1 - 55\lambda_{\theta ts}{}^2) \times (2.6\mathrm{Tu} + 3.6\sqrt{\mathrm{Tu}} - 86) \quad \{\lambda_{\theta ts} \leqslant 0\} \tag{11c}$$

Based on additional experimental data, Gostelow et al. [48] suggested the following alternative expressions for N:

$$N = 8.6 \times 10^{-4} e^{2.134\lambda_{\theta ts}\ln \mathrm{Tu}_{ts} - 59.23\lambda_{\theta ts} - 0.564 \ln \mathrm{Tu}_{ts}} \; \{\lambda_{\theta ts} \leqslant 0\} \tag{12a}$$

$$N = 8.6 \times 10^{-4} e^{-0.564 \ln \mathrm{Tu}_{ts} - 10\sqrt{\lambda_{\theta ts}}} \quad \{\lambda_{\theta ts} \geqslant 0\} \tag{12b}$$

In experiments by the present authors [13], Eq. (12*b*) was found to provide accurate predictions of the spot production rates, while Eq. (12*a*) was found to overestimate these measurements. Replacement of the factor 8.6 in Eq. (12*a*) with 3.0 provided a better agreement between measurements and predictions [13], although this created a slight discontinuity at $\lambda_{\theta ts} = 0$.

*Spot Propagation Rate***.** The intermittency model of Narasimha (Eq. (8)) has been found to agree well with measurements in flows with both favorable and mild adverse pressure gradients (e.g., [9,48,56]), provided that the pressure gradient does not vary significantly within the transition region. If the pressure gradient varies significantly within the transition region, which is often the case with turbomachinery blades, then the intermittency distribution may deviate from the distribution given by Eq. (8). Chen and Thyson [57] postulated that this discrepancy is due to changes in the convection velocity of the turbulent spots, caused by the streamwise pressure gradient, and suggested that their rate of convection should scale on the local freestream velocity. However, Walker et al. [58] noted that this adjustment is insufficient to establish good agreement with experimental results.

The failure of the model of Chen and Thyson [57] is attributed to the fact that the streamwise and spanwise spreading rates of turbulent spots vary significantly with λ_θ, as was documented by Gostelow et al. [7]. Based on these findings, Solomon et al. [36] proposed the following expression:

$$\gamma = 1 - e^{-n\int_{x_{ts}}^{x}[\sigma/\tan(\alpha)U]dx\int_{x_{ts}}^{x}\tan(\alpha)dx} \tag{13}$$

In this equation, $\sigma/[\tan(\alpha)U]$ and $\tan(\alpha)$ represent the streamwise and spanwise spreading of turbulent spots, respectively. Based on the experimental data compiled by Gostelow et al. [7] for λ_θ values between −0.06 and 0.06, the following expressions for the spot-spreading characteristics were proposed:

$$a = 4 + 22.14/(0.79 + 2.72e^{47.63\lambda_\theta}) \tag{14}$$

$$\sigma = 0.03 + 0.37/(0.48 + 3.0e^{52.9\lambda_\theta}) \tag{15}$$

More recently, Eq. (15) was updated by D'Ovidio et al. [59] to extend the range of λ_θ to −0.12:

$$\sigma = 0.024 + 0.604/(1 + 5e^{66\lambda_\theta}) \tag{16}$$

Experiments by the present authors [13], conducted over a range of pressure distributions, freestream turbulence, and flow Reynolds numbers, provided indirect evidence that these spot propagation parameters are adequately described by the pressure gradient parameter, without any need for further adjustment due to freestream turbulence and Reynolds number.

Johnson and Ercan [12] proposed an alternative approach for modeling the intermittency distribution in the transition zone, with a focus on conditions with elevated levels of freestream turbulence ($Tu > 2\%$). The model relaxes the assumption of concentrated spot production, and bases the spot production rate on the near-wall and freestream turbulence length scales in addition to

Table 1 Summary of experimental configurations

Study	Test-section config.	$\mathrm{Re}_L(\times 10^5)$	$\mathrm{Tu}_{\mathrm{ref}}(\%)$	Smooth surface	Rough surface	C_p dist.	Hotwire type
RY	Flat plate	3.5–9.3	0.5–9.0	×	×	Adv., blade	Single
VSP	Flat plate	3.5	8.7	×		Fav.	X-wire
V	Cascade	1.0–3.0	8.7	×		Blade	X-wire
VH	Flat plate	0.5–3.0	7.0	×		Fav.	Single
DV	Flat plate	13.9–18.3	1.4–3.9*	×		Fav., adv.	Single

*Estimated from turbulence grid and test section geometry

the local freestream turbulence intensity and pressure gradient. The model also includes new expressions for the spot propagation parameter σ and spreading angle α, although these differ from the predictions based on Eqs. (14) and (16) mostly for high adverse pressure gradients ($\lambda_\theta < -0.10$). The model was validated through comparisons with experimental data published by Gostelow and his co-workers. Compared to the model of Solomon et al. [36] (Eq. (13)), prediction of the intermittency distribution was improved in the early and late stages of transition.

Finally, there appears to be a substantial lack of effort on modeling the transition length in separation bubbles. As the location of reattachment is generally well correlated with the completion of transition, and the reattachment location is the more relevant information for the prediction of the downstream boundary layer development, the tendency has been to develop correlations for the reattachment location instead. Two recently proposed models are as follows:

Hatman and Wang [44]

$$\mathrm{Re}_r = 1.0608\ \mathrm{Re}_s + 34{,}890 \tag{17}$$

Yaras [53]

$$\mathrm{Re}_r = 1.04\ \mathrm{Re}_s + 8.05 \times 10^4[1 - \tanh^3(TF'(\%))] - 2.0 \times 10^4 \tag{18}$$

where $TF' = \max[TF(\%), 1\%]$.

The uncertainty of the experimental data on which these correlations are based is expected to be somewhat higher than for the locations of separation and transition inception. This is because of the unsteady nature of the reattachment location and the greater subjectivity involved in interpreting the location of reattachment through the shape of the time-averaged velocity profile, a peak in the turbulence intensity, or a combination of the two. It would therefore be useful to establish correlations for the intermittency distributions in the separated shear layer from which the end of the transition process can be deduced with higher precision. In recent studies by the current authors [54], Volino [60], and Gostelow and Thomas [61], intermittency distributions in separation bubbles have been measured with sufficient streamwise resolution to provide the experimental basis for the development of such mathematical models.

Description of Experiments

The experimental data compiled herein have been extracted mostly from the authors' own studies [13,54] (identified by RY, as in Table 1). In order to confirm the absence of any trends in these results that may be unique to the wind tunnel and instrumentation used by the authors, results from several other research facilities have been included in the data set. The additional data are those published by Volino and co-workers (VH, VSP) [11,62], Volino (V) [60], and Devasia (DV) [56]. The data set encompasses a range of flow Reynolds numbers, streamwise pressure gradients, freestream turbulence levels, and surface roughness conditions that are typical of gas turbine applications, and includes cases with attached flow [11,13,56,62] and separation-bubble transition [54,60].

With the exception of the most recent experiments of Volino (V) [60], the noted wind-tunnel transition studies were performed using a flat test surface, with a well-defined location for the beginning of the boundary layer development. In each case, streamwise pressure distributions were imposed the test surface through the use of a contoured test-section ceiling. The ceiling was configured to yield streamwise pressure gradients that are favorable [11,56,62], adverse [13,56], or resemble those typically encountered on the suction surface of turbine blades [13,54,60]. The test surfaces were wide enough to ensure two-dimensional flow development at the spanwise locations of the boundary layer measurements. Variations in freestream turbulence were realized by the use of turbulence-generating grids, placed sufficiently upstream of the test surface to yield isotropic and homogeneous turbulence. Surface roughness variations, which were limited to the studies of the present authors, were achieved through the use of commercially available materials that provided random roughness patterns.

The experiments of Volino (V) [60] were performed in a single-passage rectilinear cascade test section. The blade geometry was chosen such that the Pak-B pressure distribution was reproduced in an incompressible flow. Through comparison of the transition trends prevailing on this blade to those observed on flat surfaces in the remainder of the studies considered here, the effects of convex surface curvature on boundary layer transition may be inferred. Only three of the ten test cases published by Volino [60] are included in the current study, namely those with high freestream turbulence and Reynolds numbers based on the suction surface length of 100,000–300,000. In the remaining seven test cases, the transition process occurred too rapidly to yield intermittency distributions with sufficient streamwise resolution for the purposes of the present study.

The noted experimental data sets are summarized in Table 1. The relevant flow parameters from the authors' previous studies [13,54,63,64] are presented in Tables 2 and 3. Three different pressure distributions were investigated in these studies; the pressure distributions identified as C_{p1} and C_{p2} are similar to those prevailing on the suction side of low-pressure turbine blades. The initial acceleration for these two pressure distributions is approximately the same, but the subsequent adverse pressure gradient is stronger in the case of the C_{p1} distribution. The designation C_{p3} corresponds to a nearly constant adverse pressure gradient that begins at the leading edge of the test surface and is milder than that encountered in the downstream portions of the C_{p1} and C_{p2} pressure distributions. Streamwise distributions of the acceleration parameter $(\eta = (\nu/U_e^2)dU_e/dx)$ corresponding to these pressure distributions are given in Fig. 1.

Proposed Transition Model

Location of Transition Inception. As shown in Fig. 2, the experimental results from earlier phases of the present research [13], covering a range of favorable and adverse pressure gradients, and freestream turbulence levels between 1.7% and 3.3% are predicted reasonably well by the model of Abu-Ghannam and Shaw [3], given by Eq. (3) in the previous section and shown by

Table 2 Flow parameters at transition inception: Attached-flow test cases [13,54,63,64]

C_p Dist.	$\mathrm{Re}_L(\times 10^3)$	Re_{kts}	$k_{\mathrm{rms}}/\theta_{ts}(\times 10^{-3})$	$\mathrm{Tu}_{\mathrm{ref}}$ (%)	TF (%)	$\eta_{ts}(\times 10^{-7})$	$\lambda_{\theta ts}(\times 10^{-2})$	$\mathrm{Re}_{\theta ts}$	H_{ts}	$\log_{10}(N)$
1	350	0.3	2.0	6.4	14.0	33.2	9.5	167	1.7	−4.1
1	350	109	347	4.5	11.2	−12.5	−12.2	312	2.2	−0.1
1	470	0.4	2.3	4.4	11.2	31.2	11.4	191	1.8	−3.6
1	470	0.3	1.6	6.8	15.7	33.2	12.8	199	1.7	−3.8
1	470	37	131	2.4	5.3	6.6	5.2	278	1.9	−3.5
1	470	22	89	4.1	10.3	−5.2	−3.1	245	2.0	−2.4
1	470	40	141	4.1	10.2	−2.1	−1.7	286	2.0	−2.4
1	470	145	411	2.5	5.8	−16.3	−20.5	354	2.5	−0.2
1	470	151	568	4.5	11.2	−11.3	−8.1	266	2.1	−1.2
2	350	0.3	1.9	8.9	20.8	32.3	10.1	177	1.7	−3.8
2	470	0.4	2.2	6.8	15.1	37.7	11.1	171	1.8	−3.9
2	470	0.3	1.8	9.0	21.0	39.6	13.7	185	1.6	−3.8
3	350	0.2	0.9	2.3	6.7	−6.5	−3.4	227	2.6	−2.4
3	350	0.2	0.9	3.7	8.0	−8.4	−4.6	226	2.6	−2.7
3	350	0.2	1.1	4.3	11.3	−10.9	−3.4	176	2.3	−3.0
3	350	0.2	1.8	6.2	13.2	−9.4	−1.4	122	2.2	−3.8
3	470	0.2	1.2	2.2	6.0	−7.5	−4.3	239	2.6	−2.8
3	470	0.6	2.9	3.9	9.4	−8.5	−5.6	258	2.4	−3.0
3	470	0.3	1.9	4.4	11.4	−6.1	−1.3	141	2.2	−3.6
3	470	0.3	2.6	6.1	13.1	−7.7	−0.8	98	2.1	−3.8
3	650	0.3	0.9	0.7	0.9	−5.0	−6.6	364	2.9	−1.7
3	650	0.4	1.7	2.5	6.3	−7.0	−3.3	216	2.4	−2.9
3	650	0.4	2.0	3.8	9.0	−6.2	−3.2	226	2.2	−2.8
3	650	0.4	2.7	4.6	11.9	−3.4	−0.7	139	2.1	−3.6
3	930	0.5	1.5	0.5	0.6	−4.2	−5.1	351	2.8	−1.5
3	930	0.3	1.6	3.8	9.6	−1.9	−0.6	175	2.1	−3.4
3	930	0.5	3.2	6.5	14.0	−4.3	−1.3	168	1.9	−3.7

the solid lines in Fig. 2. This agreement is achieved without having to adjust the value of $\mathrm{Re}_{\theta ts}$ predicted by the model to account for a bias created by the measurement technique of Abu-Ghannam and Shaw [3], as suggested by Fraser et al. [14] and Dey and Narasimha [65]. It must be recognized, however, that the scatter in the data observed in Fig. 2, which is comparable to the scatter of the original data set of Abu-Ghannam and Shaw [3], translates into an uncertainty in the predicted Re_θ at transition onset of 15–20%. This level of precision may be inadequate in certain instances. For example, for the separation-bubble transition measurements of the present authors [54], where the streamwise pressure distribution is typical of the suction side of a turbine blade, the model of Abu-Ghannam and Shaw [3] predicts attached flow transition instead. Such a difference could be critical in the estimation of profile losses and heat transfer patterns on a turbine blade. The transition process in separation bubbles was shown by Yaras [45] to be sensitive to the pressure gradient history of the boundary layer prior to separation. Since this is most probably the result of the effect of such history on the streamwise development of instabilities in the boundary layer, similar effects are just as likely in instances of attached-flow transition. Such effects cannot be accounted for with the parameters currently appearing in the model of Abu-Ghannam and Shaw [3]. Thus, although this model is in fair agreement with the data of the present authors, and is

Table 3 Flow parameters at separation and transition inception: Separation-bubble test cases [13,54,63,64]

$\mathrm{Re}_L(\times 10^3)$	$k_{\mathrm{rms}}/\theta_s(\times 10^{-3})$	Re_{ks}	$\mathrm{Tu}_{\mathrm{ref}}$ (%)	TF (%)	$\eta_s(\times 10^{-7})$	$\lambda_{\theta s}(\times 10^{-2})$	$\mathrm{Re}_{\theta s}$	$\mathrm{Re}_s(\times 10^3)$	$\mathrm{Re}_{ts}(\times 10^3)$	$\mathrm{Re}_{s-ts}(\times 10^3)$	$\mathrm{Re}_r(\times 10^3)$	H_s	H_{ts}	$\log_{10}(N)$
350	1.3	0.3	0.6	1.7	−4.7	−3.3	263	244	285	34	271	3.1	8.1	0.5
350	1.4	0.4	0.6	1.2	−9.6	−6.4	258	261	302	36	293	3.2	8.7	0.3
350	1.3	0.3	2.2	5.9	−15.8	−10.1	252	242	271	32	280	3.0	6.4	0.6
350	1.3	0.4	4.2	8.9	−10.3	−8.4	285	270	280	23	274	3.0	4.3	0.1
350	62	16	0.7	1.4	−22.5	−13.8	257	255	289	30	295	3.0	4.2	0.9
350	66	17	2.2	5.6	−3.8	−3.0	258	273	286	31	302	3.0	5.7	0.3
350	56	16	4.4	10.8	−8.1	−6.5	288	268	273	7	274	3.0	3.3	−0.6
350	110	28	0.7	1.3	−15.4	−10.2	257	264	287	35	284	3.1	5.6	0.5
350	97	28	2.2	5.4	−16.8	−13.9	287	266	278	19	280	3.0	4.5	−0.2
350	94	29	4.2	10.3	−13.5	−13.4	314	286	287	4	294	2.9	3.2	−0.4
350	347	99	0.7	1.7	−16.7	−13.8	286	271	280	17	278	3.5	4.7	0.2
350	340	109	2.4	6.2	−24.4	−24.9	321	309	312	4	309	3.7	3.6	−0.2
470	1.6	0.5	0.4	0.7	−6.2	−5.8	306	339	390	45	357	3.1	6.8	0.8
470	1.6	0.5	0.4	0.6	−8.2	−7.7	305	349	392	47	390	3.0	7.3	0.7
470	1.5	0.5	2.3	5.9	−11.5	−11.1	309	339	362	38	359	3.0	5.2	0.6
470	1.5	0.5	3.4	8.4	−9.1	−9.0	312	336	356	31	342	2.9	4.4	0.3
470	78	25	0.6	0.8	−13.5	−13.4	316	410	448	38	438	3.1	5.7	0.9
470	49	22	2.3	5.4	−16.6	−32.7	444	362	372	17	367	2.8	3.2	0.3
470	98	37	0.5	0.7	−11.3	−16.2	376	352	380	35	378	3.0	5.3	0.3
470	405	137	0.6	0.9	−13.7	−15.8	338	378	381	8	383	3.5	4.2	−0.1

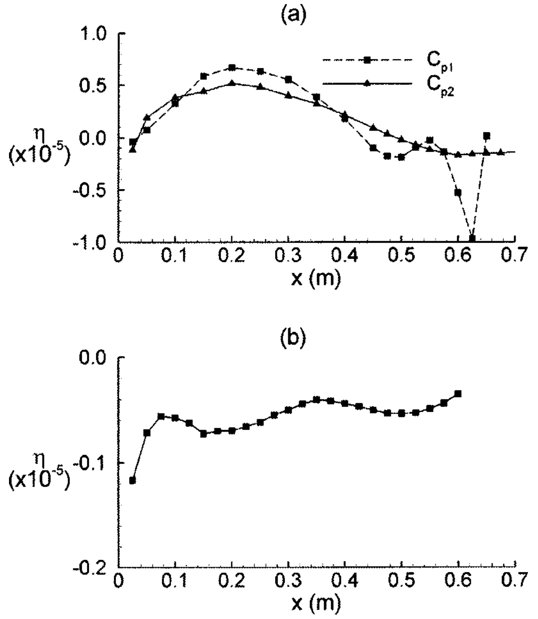

Fig. 1 Representative distributions of the acceleration parameter η for the test cases of Roberts and Yaras [13,54,63,64]: (*a*) C_{p1} and C_{p2} pressure distributions, (*b*) C_{p3} pressure distribution

herein put forward as the one favored over alternative models available in the published literature, the potential for further improvements remains.

The data points identified by the grey symbols in Fig. 2 correspond to surfaces with a range of distributed roughness with heights of approximately $0.1 < k_{\text{rms}}/\theta_{ts} < 0.6$. The physics of the observed effect of surface roughness on the location of transition inception is discussed elsewhere [63,64]. Although a significant effect of roughness on $\text{Re}_{\theta ts}$ is evident, the relative sparseness of the data set prevents reliable enhancement of Abu-Ghannam and Shaw's [3] model. Further measurements are needed before attempting such improvements that would make the model more relevant for the performance prediction of in-service gas turbine blades.

In instances of transition in separation bubbles, the correlation of Yaras [53] (Eq. (7)) provides reliable estimates of the location of transition inception, including cases with elevated levels of freestream turbulence. The model mimics the empirical trend of reduced sensitivity of Re_{ts} to freestream turbulence as *Tu* increases. Re_x typically does not vary significantly between the separation and transition inception locations. This is due to the decreasing freestream velocity partially offsetting the increase in the streamwise coordinate *x*. As a result, it is more difficult to capture the slight upstream movement of the transition inception point with increasing freestream turbulence at elevated levels of turbulence through a correlation based on Re_{ts}. This can be better accomplished if the dependent parameter Re_{ts} is replaced with the Reynolds number based on the streamwise distance between the separation and transition inception locations Re_{s-ts}. Re_{s-ts} correlates closely with the Reynolds number at the separation point $\text{Re}_{\theta s}$ and decreases with increasing freestream turbulence as shown in Fig. 3. The proposed correlation is

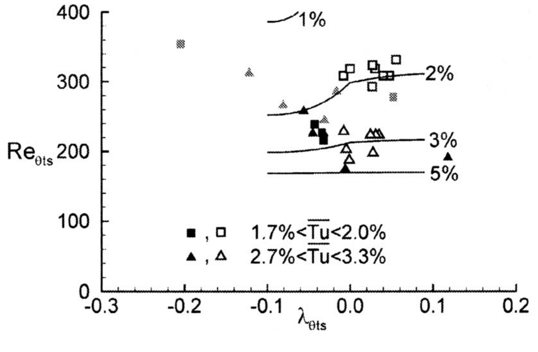

Fig. 2 Comparison of present experimental results (filled symbols) to the experimental data (hollow symbols) and correlation (lines) of Abu-Ghannam and Shaw [3]. (The present rough-surface test cases are shown in grey.)

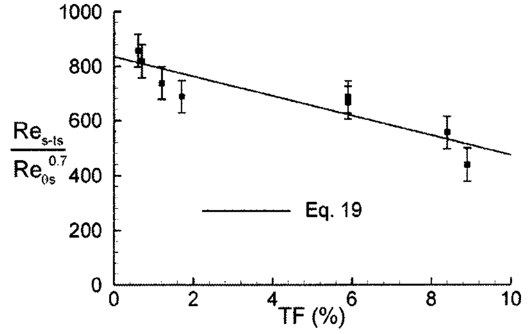

Fig. 3 Sensitivity of the transition inception location in the separation bubble to freestream turbulence (smooth surfaces)

$$\text{Re}_{s-ts} = [835 - 36TF(\%)]\text{Re}_{\theta s}^{0.7} \tag{19}$$

Recent experiments by the authors identified the effects of distributed surface roughness on the location of transition inception in separation bubbles [63,64]. This effect is demonstrated in terms of the parameters of the proposed model in Fig. 4. The upstream movement of the transition point with increased surface roughness height is clearly evident, and the rate of this movement appears to increase somewhat with freestream turbulence. The proposed transition-inception model (Eq. (19)) can be made to account for surface roughness effects through the following modification:

$$\text{Re}_{s-ts} = \left\{ 835 - 36TF(\%) - [1{,}400 + 25e^{0.45TF(\%)}]\frac{k_{\text{rms}}}{\theta_s} \right\}\text{Re}_{\theta s}^{0.7} \tag{20}$$

Length of Transition. The proposed transition length model is based on the following expression for the streamwise intermittency distribution [36]:

$$\gamma = 1 - e^{-n\int_{x_{ts}}^{x}[\sigma/\tan(\alpha)U]dx\int_{x_{ts}}^{x}\tan(\alpha)dx} \tag{21}$$

As was noted earlier, this expression has its roots in the work of Emmons [1] and has been brought to the present level of formulation through the studies of Narasimha [9] and Solomon et al.

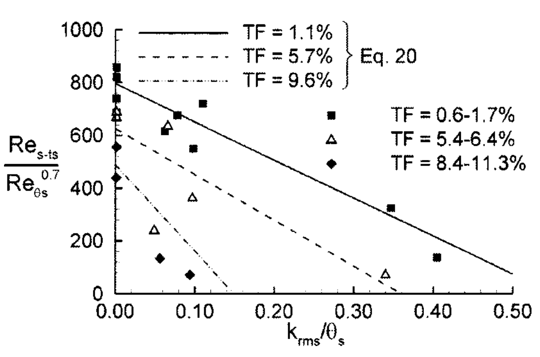

Fig. 4 Sensitivity of the transition inception location to surface roughness and freestream turbulence

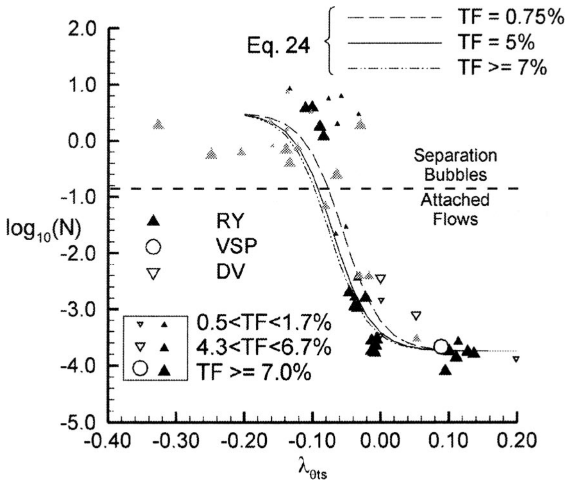

Fig. 5 Variation of the spot inception parameter with $\lambda_{\theta ts}$ and Taylor's turbulence factor. (Rough surface measurements [63,64] are shown in grey.)

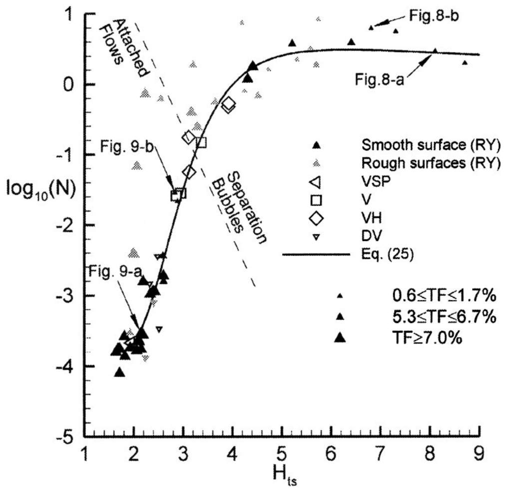

Fig. 6 Variation of the spot production parameter with the shape factor at transition inception. (Symbols filled in grey indicate measurements over a rough surface.)

[36]. Since this formulation for intermittency has been demonstrated to be consistent with the physics of the transition process based on numerous experimental studies, it has been adopted in the present modeling effort. The length of the transition zone is quantified through the streamwise distance over which Eq. (21) yields intermittency values greater than 0 and less than 1. The location of transition inception x_{ts} appearing in this expression is obtained from the models proposed in the previous section. The parameters σ and α representing the spot spreading rate are obtained from the following expressions, as proposed by Solomon et al. [36] and D'Ovidio et al. [59]:

$$a = 4 + 22.14/(0.79 + 2.72e^{47.63\lambda_\theta}) \quad (22)$$

$$\sigma = 0.024 + 0.604/(1 + 5e^{66\lambda_\theta}) \quad (23)$$

The intermittency distributions based on the experimental results of the present authors for a range of streamwise pressure gradients, freestream turbulence levels, and surface roughness conditions [13,54,63,64] have been found to be consistent with the dependence of α and σ on only λ_θ. This has been observed to be true in both attached-flow [13,63] and separated-flow [54,63,64] transition. The remaining parameter required for estimating the intermittency distribution through Eq. (21) is the spot inception rate n. As was discussed previously, starting with the work of Narasimha [9], this parameter has traditionally been extracted from the nondimensional inception rate parameter, $N = n\sigma\theta_{ts}^3/\nu$, and the most recent model, as given by Eq. (12) (with Eq. (12*a*) scaled as per the authors' recent experimental results) correlate this parameter to λ_θ and freestream turbulence at the transition inception location. Figure 5 presents measured results for the variation of N with λ_θ and freestream turbulence level. The majority of the data points, as identified with filled symbols, were measured by the present authors [13,54,63,64] and are observed to be consistent with the results of others. In the figure, the size of the symbols increases with increasing freestream turbulence level. Unlike the earlier data sets used for correlating N to λ_θ and freestream turbulence, Fig. 5 includes results from transition in separation bubbles. In the figure, the attached-flow and separated-flow transition regimes are separated approximately by a straight dashed line. Despite somewhat larger scatter, the rate of spot production is observed to remain fairly constant in separation-bubble transition for the displayed ranges of magnitudes of λ_θ and freestream turbulence. Equation (12), on the other hand, would predict a linear increase in $\log_{10}(N)$ with increasing adverse pressure gradient, rather than leveling off as suggested by the data. As a result, the following correlation is proposed, which is consistent with the experimental results throughout the $\lambda_{\theta ts}$ range of Fig. 5,

$$\log_{10}(N) = -3.75 + \frac{8.5}{2 + 35e^{35[\lambda_\theta - f(TF)]}} \quad (24a)$$

$$f(TF) = \frac{2.9 - 0.25TF(\%)}{100 + 1.4TF(\%)[1 + TF(\%)]} \quad (24b)$$

This correlation is formulated such that it provides similar results to Eq. (12) in the −0.1 to 0.08 $\lambda_{\theta ts}$ range, for turbulence intensities varying from 0.5% to 6.5%, since this earlier correlation was calibrated against an extensive data set in this range. The turbulence intensity Tu, appearing in the earlier expressions for N, is now replaced by TF. This was done in recognition of the fact that the effect of turbulence intensity on the transition process ought to be influenced by the length scale of the freestream turbulence eddies. In the absence of length-scale information for freestream turbulence, Eq. (24) may still be used to obtain estimates of N by using Tu in place of TF. The data points shown with grey symbols in Fig. 5 correspond to a range of rough-surface conditions and will be discussed shortly.

A more effective approach to estimating the spot production rate parameter N is evident from the results shown in Fig. 6. Excluding the rough-surface conditions identified by grey symbols, a strong dependence of N on the boundary-layer shape factor at the point of transition inception is observed. This is consistent with the established dependence of N on the freestream turbulence level and streamwise pressure gradient, for both factors are known to affect the shape factor. However, the notably lower scatter in Fig. 6 than that observed in Fig. 5 may suggest the boundary layer shape factor to be more directly relevant to the rate of turbulent spot production. The trends in Fig. 6 suggest the following correlation between N and H_{ts}:

$$\log_{10}(N) = \frac{0.55H_{ts} - 2.2}{1 - 0.63H_{ts} + 0.14H_{ts}^2} \quad \{1.6 \leqslant H_{ts} \leqslant 8.5\} \quad (25)$$

The use of this correlation to estimate N requires that H_{ts} be known. In instances of attached-flow transition, this information can be obtained most efficiently by the use of an integral method, such as the method of Thwaites [66], for the streamwise development of the laminar boundary layer up to the point of transition inception. Based on the data published by White [67], H can be correlated to λ_θ through

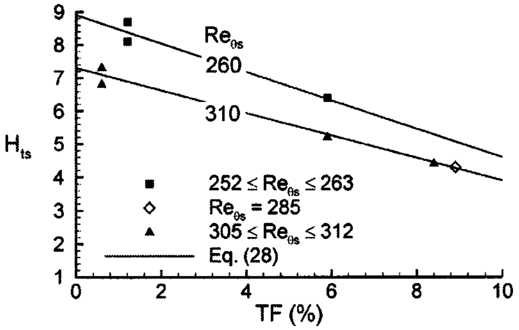

Fig. 7 Variation of H_{ts} with turbulence level and $Re_{\theta s}$ for separation-bubble transition (smooth surfaces)

$$H = \frac{2.61 + 20.3\lambda_\theta}{1 + 9.43\lambda_\theta + 8.35\lambda_\theta^2} \quad \{-0.09 \leq \lambda_\theta \leq 0.25\} \qquad (26)$$

The effect of freestream turbulence on H is not accounted for in this empirical correlation and can be estimated from the following expression, which is based on the experimental results of the present authors:

$$\frac{H}{H_T} = 1 - 0.03TF(\%) \quad \{TF(\%) \leq 11\} \qquad (27)$$

where H_T is the shape factor estimated from Eq. (26).

For estimating the shape factor at the point of transition inception in separation bubbles, the following correlation is proposed for smooth surfaces, over the ranges of $250 \leq Re_{\theta s} \leq 310$ and $TF \leq 10\%$, based on the experimental data shown in Fig. 7.

$$H_{ts} = (17.2 - 0.032\,Re_{\theta s}) - (0.9 - 0.0018\,Re_{\theta s})TF(\%) \qquad (28)$$

In summary, the proposed model for predicting the length of the transition zone, unified for attached- and separated-flow transition, consists of Eqs. (21)–(23) and (25). These are supplemented by Eqs. (3) or (20) to predict the streamwise location of transition inception, by Eq. (10) to relate n to N, and by Eqs. (26)–(28) to predict the shape factor at this point, if necessary.

For two of the separated-flow transition cases labeled in Fig. 6, the predicted intermittency distribution, hence, transition length, is compared to the measured values in Fig. 8 The spot production parameter N of the test case corresponding to Fig. 8(*b*) is off of the trend line (Eq. (25)) in Fig. 6 by about one standard deviation. Thus, the difference in the extent of agreement of the predicted and experimental intermittency distributions in Fig. 8 provides an indication of the effect of the scatter in the measured values of N on the prediction accuracy of the transition length. This effect is noted to be relatively small.

Similarly, the measured and predicted intermittency distributions for two attached-flow transition cases (labeled in Fig. 6) are compared in Fig. 9. Again, Fig. 9(*b*) corresponds to a test case that represents the extent of scatter in the measured values of N. The effect of the uncertainty in the N values on the prediction accuracy of the transition length is observed to be small. For reference, the predictions based on N values estimated through Eq. (12), with Eq. (12*a*) modified as per the authors' recent observations [13], are also included in these figures. Since both Eqs. (12) and (25) are calibrated against the same attached-flow transition data set, the accuracy of the prediction is similar with the two models.

Effect of Surface Roughness on Transition Length. For attached-flow transition, presence of roughness is noted to increase N for a given $\lambda_{\theta ts}$ (Fig. 5) or H_{ts} (Fig. 6). This trend is particularly evident in Fig. 6, where H_{ts} assumes a nearly constant value of 2 for the attached-flow transition cases over rough surfaces. The rough-surface data points shown in the figure for attached-flow transition correspond to a range of roughness heights of about $0.1 < k_{\mathrm{rms}}/\theta_{ts} < 0.6$, with a trend toward increasing spot production rate with increasing height of roughness elements. It therefore appears that although freestream turbulence affects the spot production rate primarily through its influence on

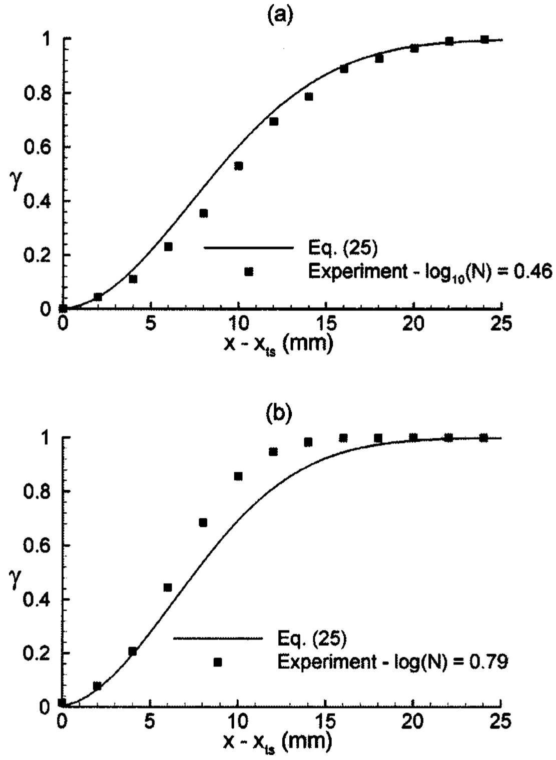

Fig. 8 Intermittency distributions for two separated-flow transition cases (as labeled in Fig. 6)

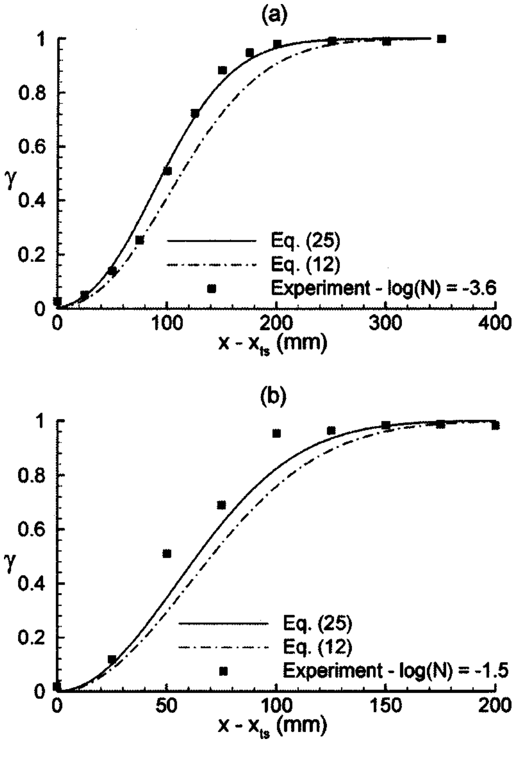

Fig. 9 Intermittency distributions for two attached-flow transition cases (as labeled in Fig. 6)

the cross-stream distribution of velocity as described by the shape factor, surface roughness has a more direct effect. This is an intuitive result, for the sweep and ejection processes leading to generation of turbulent spots take place deep within the boundary layer where they can be readily affected by the local flow perturbations created by the roughness elements. A fairly consistent trend of increasing N with increasing rms roughness height was observed by the authors for the data points displayed in Fig. 6. However, further experiments are desirable before an extension of the proposed correlation for N may be attempted to include rough surface conditions in the attached-flow transition regime.

Finally, as shown in Fig. 6, the spot production rate in instances of separation-bubble transition does not appear to be sensitive to surface roughness, with the exception of two data points. In the majority of the separated-flow transition cases shown in this figure, the separated shear layer was determined to be well above the crests of the roughness elements in the vicinity of the streamwise location of transition inception. Thus, the process leading to the generation of turbulent spots is not expected to be affected by the flow perturbations of the roughness elements to the same extent as in instances of attached-flow transition. This may be the explanation for the lack of sensitivity of the spot production rate to surface roughness in these cases. Consequently, for surface roughness conditions typical of in-service gas turbine blades, the proposed model for predicting the length of the transition zone remains applicable for the separated-flow regime.

Conclusions

Through analysis of an extensive experimental data set, a strong correlation of the turbulent spot production rate with the boundary layer shape factor is identified. Based on this observation, a unified model is proposed for predicting the spot production rate in separated- and attached-flow regimes, for both favorable and adverse streamwise pressure gradients and a range of freestream turbulance levels. The model is shown to maintain the prediction accuracy of an existing model for the attached-flow regime and is the first to allow prediction of the spot production rate in the separated regime. Additionally, in the separated-flow transition regime, the model is shown to remain applicable for rough surface conditions typical of turbomachinery blades.

The model proposed for predicting the length of the transition zone is complemented by a model for locating the streamwise position of transition inception in separation bubbles. The proposed model provides improvements over existing alternatives both in terms of the precision of the predictions, and in its ability of accounting for the effects of freestream turbulence and surface roughness.

Acknowledgments

The authors wish to acknowledge the financial support of Pratt & Whitney Canada in this project. The cooperation of Professor R. J. Volino (U.S. Naval Academy) and Professor J. Dey (Indian Institute of Science) in providing the experimental data for the present comparisons is also greatly appreciated.

Nomenclature

C_p = surface static pressure coefficient
g_x, g_z = functions describing the streamwise and spanwise growth of turbulent spots
H = boundary layer shape factor
H_T = predicted boundary layer shape factor based on the experimental data of Thwaites (Eq. (26))
k_{rms} = rms surface roughness height
L = length of test surface $(L=1.22\text{ m})$
N = spot production parameter (Eq. (10))
n = spot production rate, $(\text{ms})^{-1}$
Re_k = Reynolds number based on rms roughness height
Re_s = Reynolds number based on streamwise distance between the leading edge and the separation location (x_s), and the freestream velocity atx_s (U_{es})
Re_x = Reynolds number based on streamwise distance from the leading edge
Re_L = reference Reynolds number $\text{Re}_L = U_{\text{ref}}L/\nu$
Re_θ = Reynolds number based on momentum thickness
TF = Taylor's turbulence factor $TF = Tu_{\text{ref}}(L/\lambda_s)^{0.2}$
Tu = local freestream turbulence intensity (%)
Tu_{ref} = reference turbulence intensity (%) measured 10 mm upstream of the test-surface leading edge
Tu = average Tu (%) from the leading edge to x_{ts}
U_e = local freestream velocity, m/s
U_{LE} = turbulent spot leading-edge convection velocity, m/s
U_{ref} = reference velocity, measured 10 mm upstream of the leading edge of the test surface
U_{TE} = turbulent spot trailing-edge convection velocity, m/s
x, y, z = streamwise, wall-normal, and spanwise coordinates
α = turbulent spot spreading half-angle
γ = intermittency of the boundary layer
θ = momentum thickness
η = acceleration parameter $\eta = (\nu/U_e^2)dU_e/dx$
λ_s = integral length scale of turbulence, measured 10 mm upstream of the test-surface leading edge
λ_θ = Thwaites' pressure gradient parameter $\lambda_\theta = (\theta^2/\nu)dU_e/dx$
ν = kinematic viscosity, m^2/s
σ = spot propagation parameter (Eq. (9))

Subscripts

r = reattachment
s = separation
$s-ts$ = denotes the streamwise distance between the separation and transition inception locations
te = transition completion
ts = transition inception

References

[1] Emmons, H. W., 1951, "The Laminar-Turbulent Transition in a Boundary Layer—Part I," J. Aeronaut. Sci. **18**(7), pp. 490–498.
[2] Schubauer, G. B., and Skramstad, H. K., 1948, "Laminar Boundary-Layer Oscillations and Transition on a Flat Plate," NACA TN 909.
[3] Abu-Ghannam, B. J., and Shaw, R., 1980, "Natural Transition of Boundary Layers: The Effects of Turbulence, Pressure Gradient and Flow History," J. Mech. Eng. Sci. **22**(5), pp. 213–228.
[4] Johnson, M. W., and Dris, A., 2000, "The Origin of Turbulent Spots," ASME J. Turbomach., **122**(1), pp. 88–92.
[5] Kachanov, Y. S., 2000, "Three-dimensional Receptivity of Boundary Layers," Eur. J. Mech. B/Fluids **19**, pp. 723–744.
[6] Klebanoff, P. S., Tidstrom, K. D., and Sargent, L. M., 1961, "The Three-dimensional Nature of Boundary-layer Transition," J. Fluid Mech. **12**, pp. 1–42.
[7] Gostelow, J. P., Melwani, N., and Walker, G. J., 1996, "Effects of Streamwise Pressure Gradient on Turbulent Spot Development," ASME J. Turbomach. **118**, pp. 737–743.
[8] Johnson, M. W., and Fashifar, A., 1994, "Statistical Properties of Turbulent Bursts in Transitional Boundary Layers," Int. J. Heat Fluid Flow **15**(4), pp. 283–290.
[9] Narasimha, R., 1985, "The Laminar-Turbulent Transition Zone in the Boundary Layer," Prog. Aerosp. Sci. **22**, pp. 29–80.
[10] Blair, M. F., 1982, "Influence of Free-Stream Turbulence on Boundary Layer Transition in Favorable Pressure Gradients," ASME J. Eng. Power **104**, pp. 743–750.
[11] Volino, R. J., and Hultgren, L. S., 2000, "Measurements in Separated and Transitional Boundary Layers Under Low-Pressure Turbine Airfoil Conditions," ASME Paper No. 2000-GT-0260.
[12] Johnson, M. W., and Ercan, A. H., 1997, "Predicting Bypass Transition: A Physical Model Versus Empirical Correlations," ASME Paper No. 97-GT-475.
[13] Roberts, S. K., and Yaras, M. I., 2003, "Measurements and Prediction of Free-Stream Turbulence and Pressure-Gradient Effects on Attached-Flow Boundary-Layer Transition," ASME Paper No. GT-2003-38261.
[14] Fraser, C. J., Higazy, M. G., and Milne, J. S., 1994, "End-Stage Boundary Layer Transition Models for Engineering Calculations," Proc. Inst. Mech. Eng., Part C: J. Mech. Eng. Sci. **208**, pp. 47–58
[15] Gostelow, J. P., and Blunden, A. R., 1989, "Investigations of Boundary Layer

Transition in an Adverse Pressure Gradient," ASME J. Turbomach. **111**, pp. 366–375.

[16] Sharma, O. P., and Wells, R. A., Schlinker, R. H., and Bailey, D. A., 1982, "Boundary Layer Development on Turbine Airfoil Suction Surfaces," ASME J. Eng. Power **104**, pp. 698–706.

[17] Kim, J., Simon, T. W., and Russ, S. G., 1992, "Free-Stream Turbulence and Concave Curvature Effects on Heated, Transitional Boundary Layers," ASME J. Heat Transfer **114**, pp. 338–347.

[18] Schultz, M. P., Volino, R. J., 2001, "Effects of Concave Curvature on Boundary Layer Transition Under High Free-Stream Turbulence Conditions," ASME Paper No. 2001-GT-0191.

[19] Stieger, R. D., and Hodson, H. P., 2003, "The Transition Mechanism of Highly-Loaded LP Turbine Blades," ASME Paper No. GT2003-38304.

[20] Dong. Y., and Cumpsty, N. A., 1990, "Compressor Blade Boundary Layers: Part 2—Measurements With Incident Wakes," ASME J. Turbomach. **112**, pp. 231–240.

[21] Schobeiri, M. T., and Rakde, R. E., 1994, "Effects of Periodic Unsteady Wake Flow and Pressure Gradient on Boundary Layer Transition Along the Concave Surface of a Curved Plate," ASME Paper No. 94-GT-327.

[22] Cummings, M. J., and Bragg, M. B., 1996, "Boundary-Layer Transition Due to Isolated Three-Dimensional Roughness on an Airfoil Leading Edge," AIAA J. **34**(9), pp. 1949–1952.

[23] Pinson, M. W., and Wang, T., 1997, "Effects of Leading-edge Roughness on Fluid Flow and Heat Transfer in the Transitional Boundary Layer Over a Flat Plate," Int. J. Heat Mass Transfer **40**(12), pp. 2813–2823.

[24] Lang, M., Rist, U., and Wagner, S., 2004, "Investigations on Controlled Transition Development in a Laminar Separation Bubble by Means of LDA and PIV," Exp. Fluids, **36**, pp. 43-52.

[25] Alam, M., and Sandham, N. D., 2000, "Direct Numerical Simulation of Short Laminar Separation Bubbles With Turbulent Reattachment," J. Fluid Mech. **410**, pp. 1–28.

[26] Rai, M. M., and Moin, P., 1993, "Direct Numerical Simulation of Transition and Turbulence in a Spatially Evolving Boundary Layer," J. Comput. Phys. **109**, pp. 169–192.

[27] Maucher, U., Rist, U., Kloker, M., and Wagner, S., 1999, "DNS of Laminar-Turbulent Transition in Separation bubbles," *High Performance Computing in Science and Engineering '99*, E. Krause, and W. Jäger, eds., Springer-Verlag, New York, pp. 279–294.

[28] Ducros, F., Comte, P., and Lesieur, M., 1996, "Large-Eddy Simulation of Transition to Turbulence in a Boundary Layer Developing Spatially Over a Flat Plate," J. Fluid Mech. **326**, pp. 1–36.

[29] Wilcox, D. C. (1977), "A Model for Transitional Flows," AIAA 77-126.

[30] Rodi, W., and Sheuerer, G., 1985, "Calculation of Laminar-Turbulent Boundary Layer Transition on Turbine Blades," *AGARD Conference Proceedings No.* 390, pp. 18.1–18.13.

[31] Schmidt, R. C., Patankar, S. V., 1991, "Simulating Boundary Layer Transition With Low-Reynolds-Number $k-\varepsilon$ Turbulence Models: Part 1—An Evaluation of Prediction Characteristics," ASME J. Turbomach. **113**, pp. 10–17.

[32] Savill, A. M., 1992, "Evaluating Turbulence Model Predictions of Transition—An ERCOFTAC SIG Project," Appl. Sci. Res. **51**, p. 555.

[33] Savill, A. M., 1993, "Some Recent Progress in the Turbulence Modeling of By-pass Transition" *Near-Wall Turbulent Flows*, R. M. C., So, B. E. Speziale and B. E. Launder (eds.), Elsevier Science, New York, pp. 829–848.

[34] Hobson, G. V., and Weber, S., 2000, "Prediction of a Laminar Separation Bubble Over a Controlled-Diffusion Compressor Blade," ASME Paper No. 2000-GT-277.

[35] Spalart, P. R, and Allmaras, S. R., 1992, "A One-Equation Turbulence Model for Aerodynamic Flows," AIAA 92-0439.

[36] Solomon, W. J., Walker, G. J., and Gostelow, J. P., 1996, "Transition Length Prediction for Flows With Rapidly Changing Pressure Gradients," ASME J. Turbomach. **118**, pp. 744–751.

[37] Steelant, J., and Dick, E., 1996, "Modeling of Bypass Transition With Conditioned Navier-Stokes Equations Coupled to an Intermittency Transport Equation," Int. J. Numer. Methods Eng. **23**, pp. 193–220.

[38] Suzen, Y. B., and Huang, P. G., 2000, "An Intermittency Transport Equation for Modeling Flow Transition," AIAA 2000-0287.

[39] Lesieur, M., and Métais, O., 1996, "New Trends in Large-Eddy Simulations of Turbulence," Annu. Rev. Fluid Mech., pp. 45–82.

[40] Rodi, W., Gerziger, J. H., Breuer, M., and Pourquié, M., 1997, "Status of Large Eddy Simulation: Results of a Workshop," ASME J. Fluids Eng. **119**, pp. 248–262.

[41] Huai, X, Joslin, R. D., and Piomelli, U., 1997, "Large-Eddy Simulation of Transition to Turbulence in Boundary Layers," Theor. Comput. Fluid Dyn. **9**, pp. 149–163.

[42] Chong, T. P., and Zhong, S., 2003, "On the Three-Dimensional Structure of Turbulent Spots," ASME Paper No. GT-2003-38435.

[43] Schubauer, G. B., and Klebanoff, P. S., 1955, "Contributions on the Mechanics of Boundary-Layer Transition," NACA TN 3489.

[44] Hatman, A., and Wang, T., 1999, "A Prediction Model for Separated Flow Transition," ASME J. Turbomach. **121**, pp. 594–602.

[45] Yaras, M. I., 2001, "Measurements of the Effects of Pressure-Gradient History on Separation-Bubble Transition," ASME Paper No. 2001-GT-0192.

[46] Lou, W., and Hourmouziadis, J., 2000, "Separation Bubbles Under Steady and Periodic-Unsteady Main Flow Conditions," ASME Paper No. 2000-GT-0270.

[47] Volino, R. J., and Simon, T. W., 1995, "Bypass Transition in Boundary Layers Including Curvature and Favorable Pressure Gradient Effects," ASME J. Turbomach. **117**, pp. 166–174.

[48] Gostelow, J. P., Blunden, A. R., and Walker, G. J., 1994, "Effects of Free-Stream Turbulence and Adverse Pressure Gradients on Boundary Layer Transition," ASME J. Turbomach. **116**, pp. 392–404.

[49] Zhong, S., Chong, T. P., and Hodson, H. P., 2002, "On the Spreading Angle of Turbulent Spots in Non-Isothermal Boundary Layers With Favourable Pressure Gradients," ASME Paper No. GT-2002-30222.

[50] Mayle, R. E., 1991, "The Role of Laminar-Turbulent Transition in Gas Turbine Engines," ASME J. Turbomach. **113**, p. 509–537.

[51] Roberts, W. B., 1975, "The Effect of Reynolds Number and Laminar Separation on Axial Cascade Performance," ASME J. Eng. Power **97**, pp. 261–274.

[52] Taylor, G. I., 1939, "Some Recent Developments in the Study of Turbulence," *Proc. of 5th Int. Congress Appl. Mech.*, J. P. Den Hartog and H. Peters, eds., Wiley, New York, pp. 294–310.

[53] Yaras, M. I., 2002, "Measurements of the Effects of Freestream Turbulence on Separation-Bubble Transition," ASME GT-2002-30232.

[54] Roberts, S. K., and Yaras, M. I., 2003, "Effects of Periodic-Unsteadiness, Free-Stream Turbulence and Flow Reynolds Number on Separation-Bubble Transition," ASME Paper No. GT-2003-38262.

[55] Gostelow, J. P., and Ramachandran, R. M., 1983, "Some Effects of Free Stream Turbulence on Boundary Layer Transition," *Proc. of 8th Australasian Fluid Mech. Conf.*, Newcastle University, Newcastle, NSW, Australia, pp. 12C.1–12C.4

[56] Devasia, K. J., 1974, "A Study of the Effect of Pressure Gradients on Transition in the Boundary Layer on a Flat Plate," M. Eng. Thesis, Dept. of Aeronautical Eng., Ind. Inst. of Sci., Bangalore, India.

[57] Chen, K. K., and Thyson, N. A., 1971, "Extension of Emmons' Spot Theory to Flows on Blunt Bodies," AIAA J. **5**, pp. 821–825.

[58] Walker, G. J., Subroto, P. H., and Platzer, M. F., 1988, "Inviscid Interaction Analysis of Low Reynolds Number Airfoil Flows Involving Laminar Separation Bubbles," ASME Paper No. 88-GT-32.

[59] D'Ovidio, A., Harkins, J. A., and Gostelow, J. P., 2001, "Turbulent Spots in Strong Adverse Pressure Gradients Part 2—Spot Propagation and Spreading Rates," ASME Paper No. 2001-GT-0406.

[60] Volino, R. J., 2002, "Separated Flow Transition under Simulated Low-Pressure Turbine Airfoil Conditions—Part 1: Mean Flow and Turbulence Statistics," ASME J. Turbomach. **124**, pp. 645–655.

[61] Gostelow, J. P., and Thomas, R. L., 2005, "Response of a Laminar Separation Bubble to an Impinging Wake." ASME J. Turbomach., **127**, pp. 35–42.

[62] Volino, R. J., Shultz, M. P., and Pratt, C. M., 2001, "Conditional Sampling in a Transitional Boundary Layer Under High Free-Stream Turbulence Conditions," ASME Paper No. 2001-GT-0192.

[63] Roberts, S. K., and Yaras, M. I, 2004, "Boundary-Layer Transition Over Rough Surfaces With Elevated Free-Stream Turbulence," ASME Paper No. GT2004-53668.

[64] Roberts, S. K., and Yaras, M. I., 2004, "Effects of Surface Roughness on Boundary-Layer Transition in Separation-Bubbles," ASME Paper No. GT2004-53667.

[65] Dey, J., and Narasimha, R., 1988, "An Integral Method for the Calculation of 2-D Transitional Boundary Layers," Report 88 FM 7, Indian Inst. of Sci., Bangalore, India.

[66] Thwaites, B., 1949, "Approximate Calculation of the Laminar Boundary Layer," Aeronaut. Q. **7**(1), pp. 245–280.

[67] White, F. M., 1991, *Viscous Fluid Flow*, 2nd Ed., McGraw-Hill, New York, p. 614.

Nonsynchronous Vibration (NSV) due to a Flow-Induced Aerodynamic Instability in a Composite Fan Stator

A. J. Sanders
Honeywell Engines,
Systems and Services,
Phoenix, AZ 85034
e-mail:al.sanders@honeywell.com

This paper describes the identification and prediction of a new class of nonsynchronous vibration (NSV) problem encountered during the development of an advanced design composite fan stator for an aircraft engine application. Variable exhaust nozzle testing on an instrumented engine is used to map out the NSV boundary, with both choke- and stall-side instability zones present that converge toward the nominal fan operating line and place a limit on the high-speed operating range. Time-accurate three-dimensional viscous CFD analyses are used to demonstrate that the NSV instability is being driven by dynamic stalling of the fan stator due to unsteady shock-boundary layer interaction. The effects of downstream struts in the front frame of the engine are found to exasperate the problem, with the two fat service struts in the bypass duct generating significant spatial variations in the stator flow field. Strain gage measurements indicate that the stator vanes experiencing the highest vibratory strains correspond to the low static pressure regions of the fan stator assembly located approximately 90 degrees away from the two fat struts. The CFD analyses confirm the low static pressure sectors of the stator assembly are the passages in which the flow-induced NSV instability is initiated due to localized choking phenomena. The CFD predictions of the instability frequency are in reasonable agreement with the strain gage data, with the strain gage data indicating that the NSV response occurs at a frequency approximately 25% below the frequency of the fundamental bending mode. The flow patterns predicted by the CFD analyses are also correlated with the results of an engine flow visualization test to demonstrate the complex nature of the flow field. [DOI: 10.1115/1.1811091]

Introduction

High cycle fatigue (HCF) of turbomachinery components is an important area of concern in the design and development of aircraft engines. The fundamental excitation sources for many HCF problems are the unsteady aerodynamic forces that act on the rotating and stationary airfoil rows. Historically, the unsteady aerodynamic drivers have been classified as either flutter or forced response. Flutter problems arise when the vibratory response is self-excited, i.e., the motion-induced unsteady aerodynamics are the source of the excitation. Forced response problems arise when a periodic forcing function coincides with one of the natural modes of vibration of a given blade or vane row. In general, the primary forcing functions considered are wakes, shocks, and potential flow fields generated by both the upstream and downstream airfoil rows.

However, there is no reason to believe that the forcing function to a given blade or vane row has to be externally generated, i.e., the excitation could be generated within the airfoil passage itself. In fact there have been many observations of flow-induced aerodynamic instabilities in a variety of other disciplines. A prime example is the phenomena of vortex shedding behind bluff bodies, such as circular cylinders. This vortex shedding occurs at a frequency proportional the flow velocity, with alternate vortices shed from the cylinder in a very regular fashion. For high Reynolds number flows, the shedding phenomena have been observed to occur at a nearly constant Strouhal number ($\mathrm{St}=0.20$), defined as the ratio of the product of the shedding frequency times the cylinder diameter divided by the freestream velocity [1]. For elastic bodies this shedding can lead to very high levels of vibration if the shedding frequency coincides with one of the natural modes of vibration [2,3].

These vortex shedding phenomena hve also been observed for deeply stalled airfoils, with large-scale vortices shed from the upper surface at a Strouhal number of approximately 0.20 when the projected chord length normal to the flow was used as the characteristic dimension [4]. However, in this same work a low frequency periodic oscillation was also observed for lower angles of attack near the onset of static stall in which the Strouhal number was an order of magnitude lower ($\mathrm{St}=0.02$). These low frequency fluctuations imparted much larger unsteady forces to the airfoil than those observed at the higher angles of attack, with a separation zone originating in the leading edge region causing the airfoil to periodically switch between stalled and unstalled states. Numerical simulations were carried out using a two-dimensional Navier-Stokes analysis [5,6] with the Baldwin-Lomax algebraic turbulence model in which transition was assumed to occur at the leading edge. Nonreflecting boundary conditions were used at the inlet and exit of the computation domain, with the low frequency oscillation predicted to occur at Strouhal number of 0.03, which compared reasonably well with the measured Strouhal number of 0.02.

Camp [7] has postulated that these vortex shedding phenomena can be amplified by resonant duct or cavity modes in the turbomachine annulus. Recall that the frequency of the vortex shedding is proportional to the flow velocity because it occurs at a constant Strouhal number. When the vortex shedding frequency is nearly coincident with a duct resonance, the vortex shedding will lock-on to the acoustic frequency and large amplitude unsteadiness can be

---

Contributed by the International Gas Turbine Institute (IGTI) of THE AMERICAN SOCIETY OF MECHANICAL ENGINEERS for publication in the ASME JOURNAL OF TURBOMACHINERY. Paper presented at the International Gas Turbine and Aeroengine Congress and Exhibition, Vienna, Austria, June 13–17, 2004, Paper No. 2004-GT-53492. Manuscript received by IGTI, October 1, 2003; final revision, March 1, 2004. IGTI Review Chair: A. J. Strazisar.

generated. The coincidence of these two frequencies is not as rare as one would expect because there are numerous duct acoustic resonant frequencies corresponding to different circumferential and radial mode orders. Camp presented data from a low-speed compressor that revealed the characteristics of these lock-on phenomena, with step changes in the frequency content of the acoustic signal occurring as the flow rate was varied to excite acoustic modes of different circumferential orders.

There have also been studies that show the tip clearance flow field can exhibit periodic oscillations. Mailach et al. [8] performed experiments in a low-speed research compressor and observed that strong periodic interactions of the tip clearance flow occurred for large clearances near the stall boundary. The rotating tip flow instability exhibited a cell wavelength spanning approximately two rotor blade pitches and propagated around the annulus at 50–60% of the rotational speed, i.e., a strong periodic interaction occurred between every other blade. The tip instability was found to exhibit a broadband hump in the frequency spectrum, with the center frequency correlated to a Strouhal number using the radial extent of the clearance vortex as the characteristic length scale.

Lenglin and Tan [9] utilized a three-dimensional viscous CFD analysis to demonstrate the inherently unsteady character of the tip clearance flow in the rotor relative frame. They found that the predicted Strouhal number of the unsteadiness based on the rotor chord was 0.7. The fluctuating clearance flow was found to generate unsteady loading fluctuations in the tip region as large as 30% of the local value of the static pressure coefficient. Kielb et al. [10] performed multipassage three-dimensional viscous simulations and found that an NSV problem observed in a compressor was driven by coupled suction-side vortex unsteadiness and a tip flow instability. The simulation predicted an aerodynamic excitation frequency in the rotor relative frame that was in reasonable agreement with the strain gage test data. However, the comparison of the CFD predictions with casing Kulite data were poor, indicating either the circumferential wave speed and/or the nodal diameter of the unsteadiness predicted by the CFD analysis was incorrect.

This paper describes a new class of NSV problem encountered during the development of an advanced design composite fan stator that exhibits characteristics similar to dynamic stall. A combination of factors lead to the onset of the NSV instability, including the close aerodynamic coupling between the stator and the downstream front frame struts. The two fat service struts in the fan bypass duct are found to produce significant spatial variations in the fan stator flow field, with localized choking occurring in the high Mach number regions of the annulus. A flow-induced aerodynamic instability is initiated in these high Mach number regions, with interactions between the passage shock and the downstream separation zone leading to large amplitude periodic unsteadiness that is the driver for the NSV problem.

Problem Background

The fan module that experienced the stator NSV problem is shown in Fig. 1. The fan stage features a moderately swept 22 blade shroudless fan rotor, 53 full-span swept and bowed composite fan stator vanes, and a front frame assembly featuring eight struts in both the core and bypass streams. Of the eight struts in the downstream front frame assembly, two fat service struts are located at top dead center (TDC) and bottom dead center (BDC) in the bypass duct with a single fat strut in the core duct at BDC. Notice that the front frame struts are in very close proximity to the fan stator vanes, with the closely coupled stator-strut system being one of many contributing factors that drive the NSV instability.

Figure 2 displays the bypass shroud static pressure measurements from a subscale fan rig taken at the fan stator leading edge plane for the 90% corrected speed peak efficiency operating point. Note that this corrected speed corresponds to the operating point at which the vibration problem was encountered along the nominal fan operating line during the engine tests. The two fat bypass struts located at TDC and BDC are seen to produce a significant static pressure variation (±4% of the fan inlet total pressure) around the annulus of the stator. Thus, the struts locally backpressure the bypass region of the fan stage, with the low static pressure regions of the fan stator operating on choke-side of the characteristic and the high static pressure regions operating on the stall-side. Keep in mind that for any given operating point the fan stator assembly will exhibit nominal, choke-side, and stall-side regions due to these downstream strut effects, with the fan stator assembly as a whole operating on the average axisymmetric design intent characteristic.

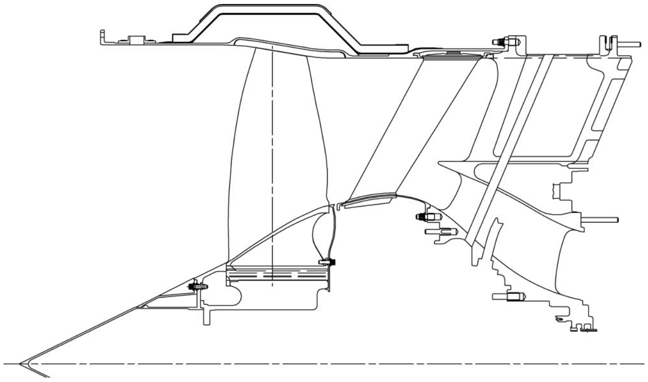

Fig. 1 Fan stage cross section

To address the source of the NSV problem, extensive development engine testing was conducted with strain gages sensitive to the first bending mode positioned on selected vanes at various locations around the annulus. As more data became available it became obvious that the highest responding vanes primarily occurred in the vicinity of low static pressure (high Mach number) regions of the fan stator assembly. Figure 3 shows typical strain-gage time histories for the fan stator vanes as an acceleration was performed along the nominal fan operating line. For this particular engine test, strain gages were located on vanes 10, 16, 26, and 43. The circumferential locations of these instrumented vanes correspond to both the low and high static pressure sectors of the fan stator assembly as shown schematically in Fig. 2. Analysis of the strain gage data indicated that the response was nonsynchronous, with the peak hold frequency spectrum for this time interval shown in Fig. 4. Also notice that the vibration occurs at a distinct frequency approximately 25% below the fundamental mode frequency.

Extensive bench testing was performed to characterize the structural dynamics of the fan stator assembly to help explain the vibration frequency observed in the strain gage data. Figure 5 displays the results of acoustic ring signature (ARS) testing for a typical fan stator vane mounted in the assembly. ARS data was acquired for all 53 vanes in the stator assembly, with the mean frequency 435 Hz with a 10.6 Hz standard deviation. Based on the data, the $\pm 3\sigma$ vanes have frequencies of 405 Hz and 470 Hz, respectively. Also note that very distinct modes are present in the ARS spectrum, with even the -3σ vanes well above the vibration frequency observed in the strain gage data. Similar results were obtained from both shaker table and holography tests.

In addition, several attempts at eliminating the NSV problem through vane composite fiber modulus and assembly boundary condition changes aimed at raising the fundamental mode frequency were also met with limited success. In fact, rigidly fixing both the shroud and hub boundary conditions resulted in only a modest improvement in the onset of the NSV instability (~7.5% in corrected fan speed along the nominal operating line) even though the fundamental mode frequency was increased nearly 75%. This indicated that frequency, and, hence, reduced frequency, were not strong drivers for this particular vibration prob-

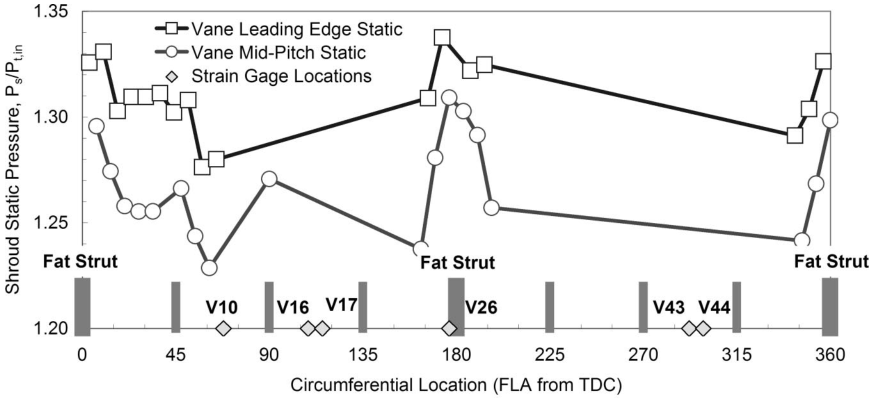

Fig. 2 Fan stator shroud static pressure wave form at 90% corrected speed peak efficiency operating point

lem. In addition, engine testing with a hub stiffening ring to raise the assembly frequency verified that it was not a system mode of the vane-shroud-hub assembly that was being excited.

A variable exhaust nozzle (VEN) was also used to back-pressure the fan and map out the NSV boundary, with the onset of the NSV response found to be a strong function of the fan operating point. During this testing the VEN was adjusted to set the fan operating line at the desired condition and then an acceleration was performed until either high vibratory strains were encountered or the engine interstage turbine temperature limit was reached, at which point the speed sweep was terminated. This process was repeated until the entire fan map had been explored with sufficient detail to map the location of the NSV boundary. Since the vibratory strains rose very rapidly as the instability boundary was penetrated, the onset of the NSV instability was defined as the fan speed at which the vibratory strain first exceeded 200 μin/in p-p for any of the strain gages. This strain level was chosen because it was a strain level that exhibited both a high signal-to-noise ratio and at the same time was low enough to characterize incipient instability conditions. Figure 6 shows the results of the VEN testing, with both choke- and stall-side instability zones present that converge toward the nominal operating line and prevent operation above approximately 90% corrected fan speed.

Additional fan stator strain gage instrumentation was also included in the VEN test to gather information to better understand the fan stator vibratory response characteristics. This included mode 1 (first bending) and mode 2 (first torsion) dynamic strain gages on vanes 10, 16, 26, and 43. Static strain gages capable of measuring the mean and alternating strain were also positioned on vanes 17 and 44 at the same location as the mode 1 dynamic gages. These additional strain gages were used to provide information about the phasing of the vibratory response once the NSV instability was encountered. Figure 7 shows the strain gage time histories for vanes 43 and 44 during the instability for a typical speed sweep during the VEN test, with the response amplitude highly random. Figure 8 shows a windowed time interval in which it is seen that vanes 43 and 44 are vibrating approximately 180 degrees out of phase. Several other time intervals during the NSV instability were also examined, and this 180 degree phase relationship was always present. Review of the vane 16 and 17 strain gage data also revealed the same 180 degree phasing.

Initially it was thought that the low material-to-air density ratio (mass ratio) of the composite fan stator vanes may have been leading to coupled bending-torsion mode type flutter common to aircraft wings and composite prop fans. However, examination of

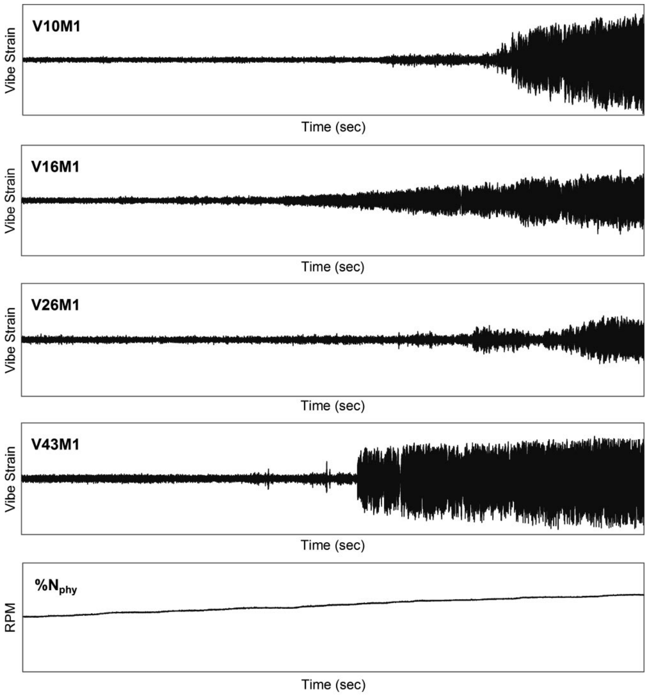

Fig. 3 Fan stator strain gage time histories for acceleration along nominal operating line

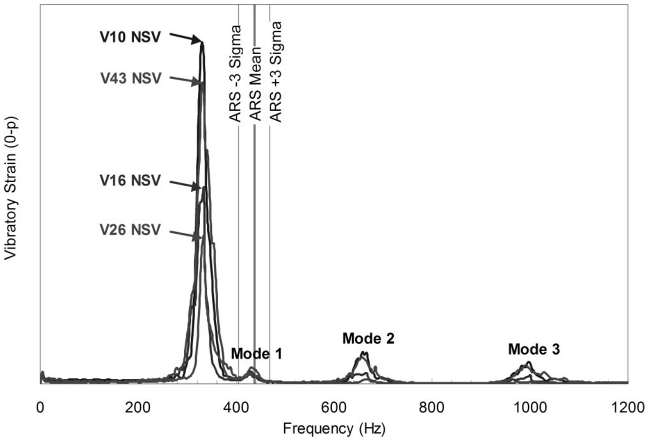

Fig. 4 Fan stator vane peak hold frequency spectrum during NSV instability

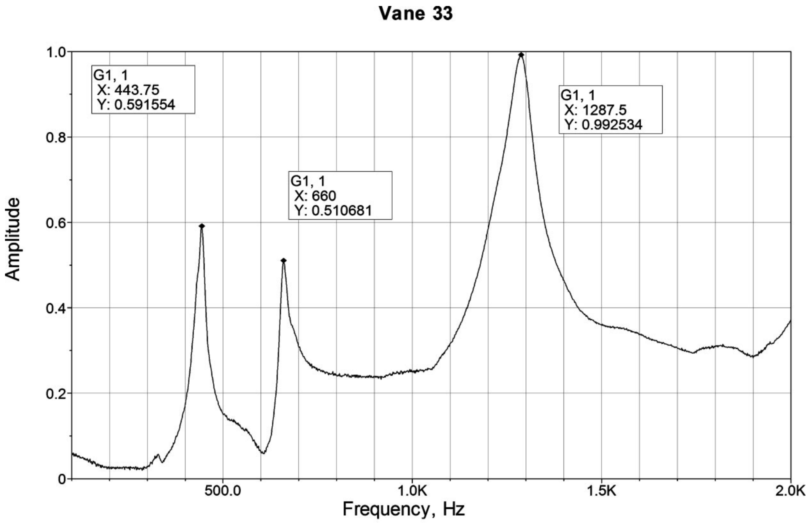

Fig. 5 ARS spectrum for a typical fan stator vane

the mode 1 and mode 2 dynamic strain gage data gave no indication of frequency coalescence for any of the speed sweeps, i.e., the mode 2 frequency did not drop with speed or the mode 1 frequency rise such that the two coalesced into a coupled mode response. Thus, coupled flutter was ruled out as the root cause of the NSV problem.

Following the VEN test it became apparent that further attempts at eliminating the NSV problem should focus on identifying the aerodynamic driver. Figure 9 displays results of an engine flow visualization test at 87.5% corrected fan speed along the nominal fan operating line just prior to the onset of the NSV instability. For this test, yellow Fuller's earth was injected from a tube mounted on the inlet bellmouth screen at the engine centerline approximately 14 in. upstream of the fan spinner. Note that a horseshoe vortex forms at the airfoil leading edge near the junction of the vane and the hub grommet. The vortex follows the grommet in the forward portion of the passage where the favorable suction surface pressure gradient in the leading edge region forces it to remain close to the airfoil surface. Once the suction surface pressure gradient becomes adverse, the vortex begins to spiral up the trailing edge of the vane. This very strong secondary flow pattern is not typical of most fan stator designs and is thought to be contributing to the onset of the NSV instability. It will be shown in the next section that these flow structures are captured by the unsteady CFD predictions.

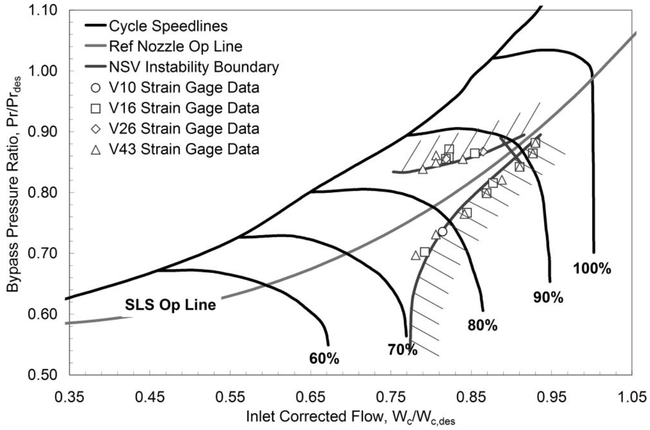

Fig. 6 VEN test fan stator NSV instability boundary

Analysis Results

To identify the flow physics driving the NSV problem, unsteady three-dimensional viscous CFD simulations of the fan stator were performed using TURBO-AE v4.1 with a CMOTT k-ε turbulence model [11]. This code is a time-accurate three-dimensional Euler/Navier-Stokes flow solver for axial-flow turbomachinery under development at Mississippi State University and NASA Glenn Research Center. A single blade passage was modeled in the unsteady analysis, with periodic phase-lag boundary conditions used to simulate the desired interblade phase angle for nonzero nodal diameter patterns. This same analysis has been used very successfully in the past to predict the onset of stall flutter in advanced fan blisk designs [12]. Further details of the code can be found in Bakhle et al. [13,14], Chen and Whitfield [15], and Srivastava et al. [16].

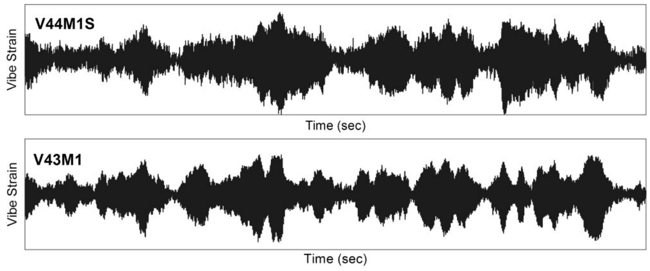

Fig. 7 Fan stator strain gage time histories for vanes 43 and 44 during a typical VEN speed sweep

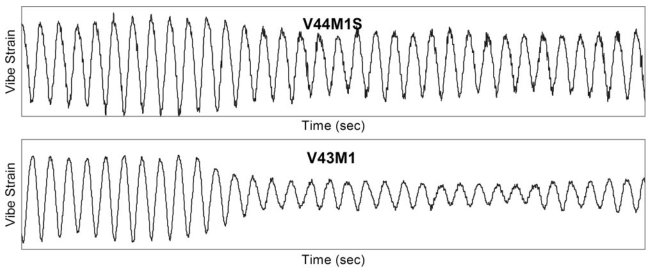

Fig. 8 Windowed fan stator strain gage time histories displaying 180 degrees phasing

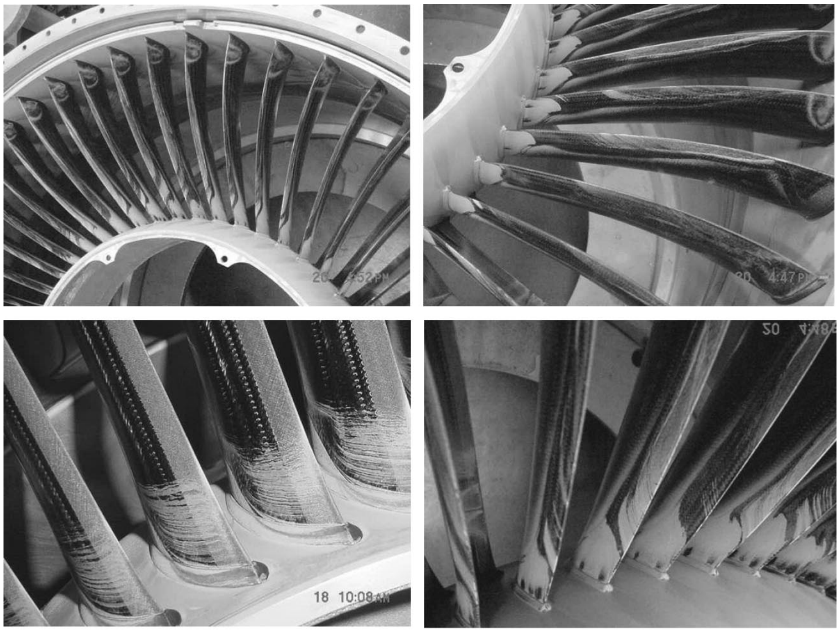

Fig. 9 Engine flow visualization test of fan stator just prior to onset of NSV instability

The grid used for the fan stator simulations was a single block smoothed H mesh with 122 points in the streamwise, 39 points in the blade-to-blade, and 51 points in the spanwise direction, Fig. 10. The inlet and exit radial profiles to the stator were specified as boundary conditions for the TURBO-AE simulations, with these profiles determined from steady ADPAC three-dimensional viscous mixing plane solutions [17] of the fan rotor-stator-strut-splitter geometry. These multiblade row solutions were readily available because they had been performed as part of the fan stage aerodynamic design. Figure 10 displays an example of the stator exit static pressure profile determined from the ADPAC solution of the fan stage at the aerodynamic design point. Also displayed in this figure is the static pressure profile determined from a radial equilibrium solution of the fan stator using a cylindrical duct downstream of the stator exit. The effect of the downstream splitter is very pronounced, with the radial profiles from the ADPAC simulations providing a more realistic exit boundary condition to the fan stator when compared to the radial equilibrium solution.

The operating conditions analyzed using TURBO-AE included the nominal operating line as well as both choke- and stall-side operating points at 90% corrected fan speed as shown in Fig. 11. The intent here was to analyze operating conditions that were tested and shown to be either stable or unstable in order to identify and understand the phenomena driving the NSV problem. For each operating point, the fan stator inlet and exit radial profiles were extracted from the multiblade row ADPAC solutions and applied as boundary conditions to the isolated vane row TURBO-AE simulations. As both the inlet and exit boundary conditions were fixed in the TURBO-AE simulations, a small amount of shifting in the exit static pressure profile was required to match the flow rates of the two CFD analyses. This was necessary because the two CFD codes featured different turbulence models (Baldwin-Lomax for ADPAC and k-ϵ for TURBO-AE), with the predicted fan stator loss and, hence, flow rate for a fixed exit static pressure slightly different for the two codes.

Figure 12 displays the mass flow rate through the fan stator as

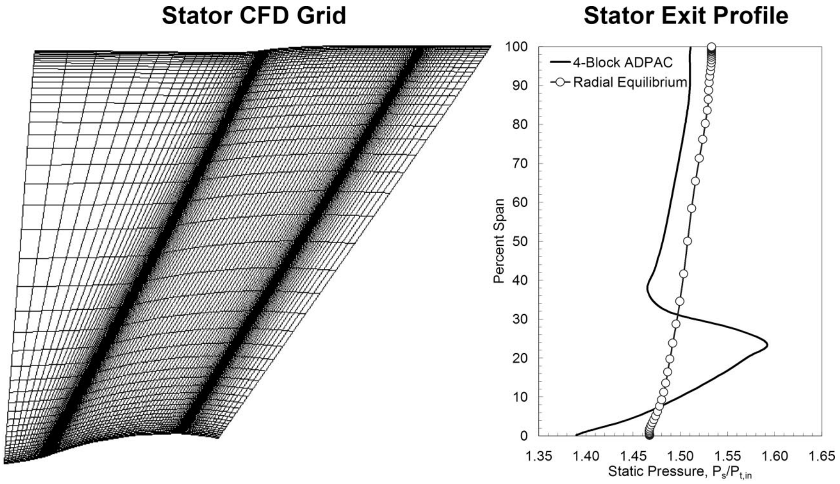

Fig. 10 Fan-stator CFD grid and exit profile

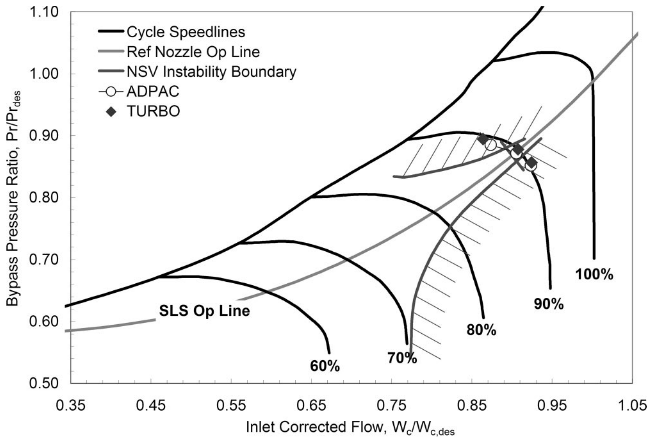

Fig. 11 Fan stator CFD analyses points

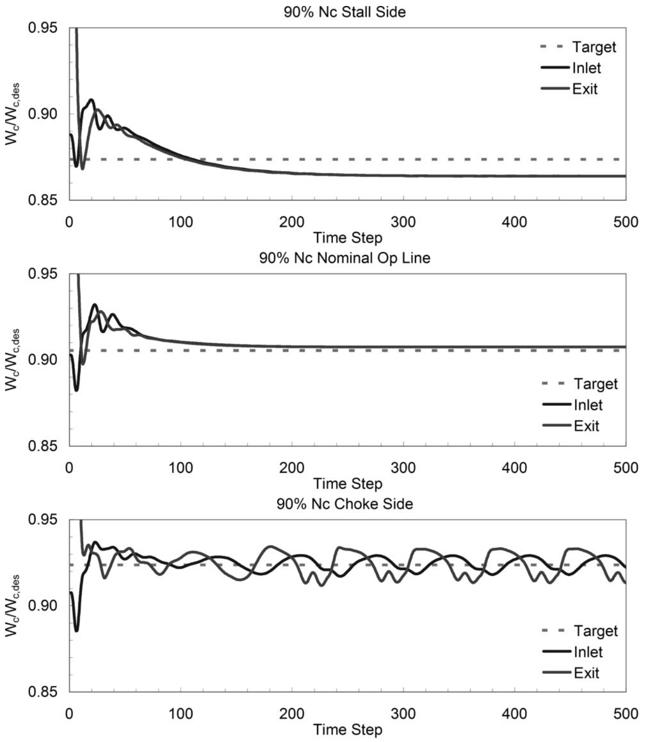

Fig. 13 Steady mass flow convergence histories for the stall-side, nominal, and choke-side operating points

a function of the static pressure adder for the choke-side operating point. Note that shifting the exit static pressure profile simply alters the flow rate and, hence, inlet Mach number to the stator because the inlet flow angle is fixed as a boundary condition. Also shown in this figure is a second-order least-squares curve fit of the CFD predictions, with the flow rate seen to asymptote slightly above the target flow rate. This behavior indicates that the flow through the vane passage is on the verge of choking for this operating point, with matching the flow rate to the target value critical because the flow field in the hub region is transonic. Also notice that both the ADPAC and TURBO-AE analyses nearly fall on top of the cycle speedline for all three operating points depicted in Fig. 11, indicating that both CFD analyses accurately predict the one-dimensional performance of the fan stage. Although not presented here, it was found that the TURBO-AE inlet Mach number profiles agreed very well with the ADPAC predictions once the inlet flow rate was matched in the manner just described.

Figure 13 shows the steady mass flow convergence histories for the stall-side, nominal, and choke-side operating points depicted in Fig. 11. The nominal operating line and stall-side steady convergence histories are flat while the choke-side solution exhibits significant mass flow oscillations about a mean value. It was also found that there was a critical back-pressure at which the instability was initiated for the choke-side solutions depicted in Fig. 12. Specifically, as the exit static pressure profile was shifted to match the target mass flow rate, the flow field was stable up until this critical back-pressure was reached, with large amplitude flow-induced oscillations developing with any further reductions in back-pressure. Additionally, the mass flow through the fan stator passage remained nearly constant once the critical back-pressure was reached, indicating that the fan stator was choked at this operating condition. For both Figs. 11 and 12, the mean value of the mass flow rate over the final cycle was used whenever oscillatory behavior was observed in the mass flow convergence histories.

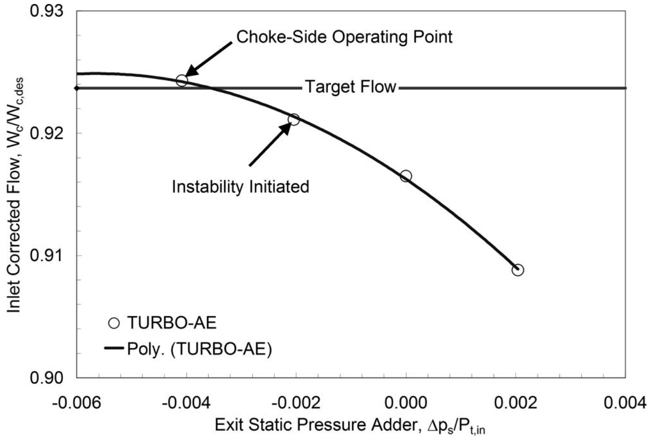

Fig. 12 Effect of static pressure adder on flow rate

To investigate the source of the flow-induced oscillations, the steady solutions were time-accurately marched forward and the flow fields allowed to evolve at their own time scale while the vanes were held rigidly fixed, i.e., the vibratory deflection was set equal to zero in the unsteady simulations. Figure 14 shows the unsteady mass flow convergence histories for all three operating points using periodic boundary conditions, i.e., an interblade phase angle of zero. Note that for the case of rigid vanes, the interblade phase angle simply specifies the periodicity of the flow field at the tangential boundaries of the grid because there is no airfoil motion. For the nominal operating line and stall-side simulations the flow fields remain steady as the solution is marched forward in time. In contrast, a flow-induced instability develops for the choke-side operating point.

It should be noted that the only difference between the steady and unsteady TURBO-AE simulations is in the time stepping algorithm employed, with local time stepping used in the steady solution and global time stepping used in the unsteady. In fact, the steady solution is simply obtained by marching the unsteady equations forward in time until a converged asymptotic solution is obtained, with the time step locally different at each grid cell to accelerate convergence. In the unsteady solution, the time step is fixed at the same constant value for each grid cell based on the CFL number and the flow field marched forward in time until the solution becomes periodic, at which point it is deemed converged. The oscillations in the steady convergence history are thus an indication that unsteady phenomena will be present in the time-accurate simulations.

Figure 15 displays the unsteady static pressure convergence history near mid-chord on the vane suction surface in the hub, mid-

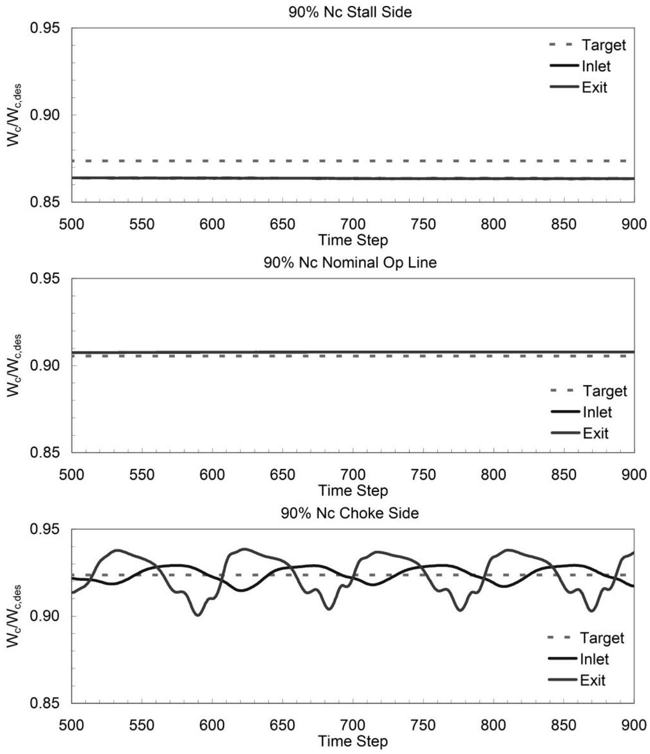

Fig. 14 Unsteady mass flow convergence histories for the stall-side, nominal, and choke-side operating points

span, and tip region of the fan stator for the choke-side operating point. The unsteadiness is largest in the hub region of the vane and diminishes as the tip is approached, with the pressure fluctuations nearly sinusoidal in character and of significant magnitude (nearly 30% of the inlet total pressure in the hub region at mid-chord). Additionally, the frequency of the unsteadiness is 260 Hz, which is in reasonable agreement with the vibration frequency (330 Hz) measured in the engine strain gage tests.

Figure 16 displays the unsteady pressure envelopes for the fan stator choke-side operating point for eight equally spaced time instants over one periodic cycle for airfoil sections at 15%, 50%, and 85% span. Also displayed in this figure by the bold line is the time-average of these eight time instants. The amplitude of the unsteady pressure fluctuations are very significant in the hub and mid-span regions of the airfoil, with the peak-to-peak pressure fluctuations as large as 40% of the fan inlet total pressure on the airfoil suction surface. It will be shown that these pressure fluctuations are generated by dynamic stalling phenomena triggered by periodic shock-boundary layer interaction in the stator hub region where the flow is transonic.

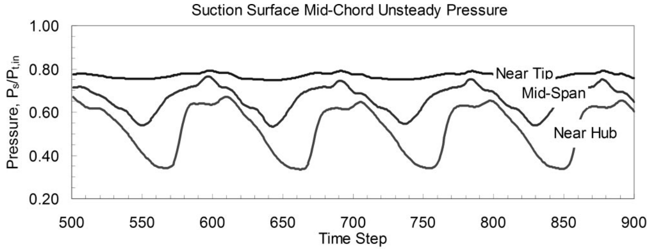

Fig. 15 Unsteady suction surface static pressure convergence history for the choke-side operating point

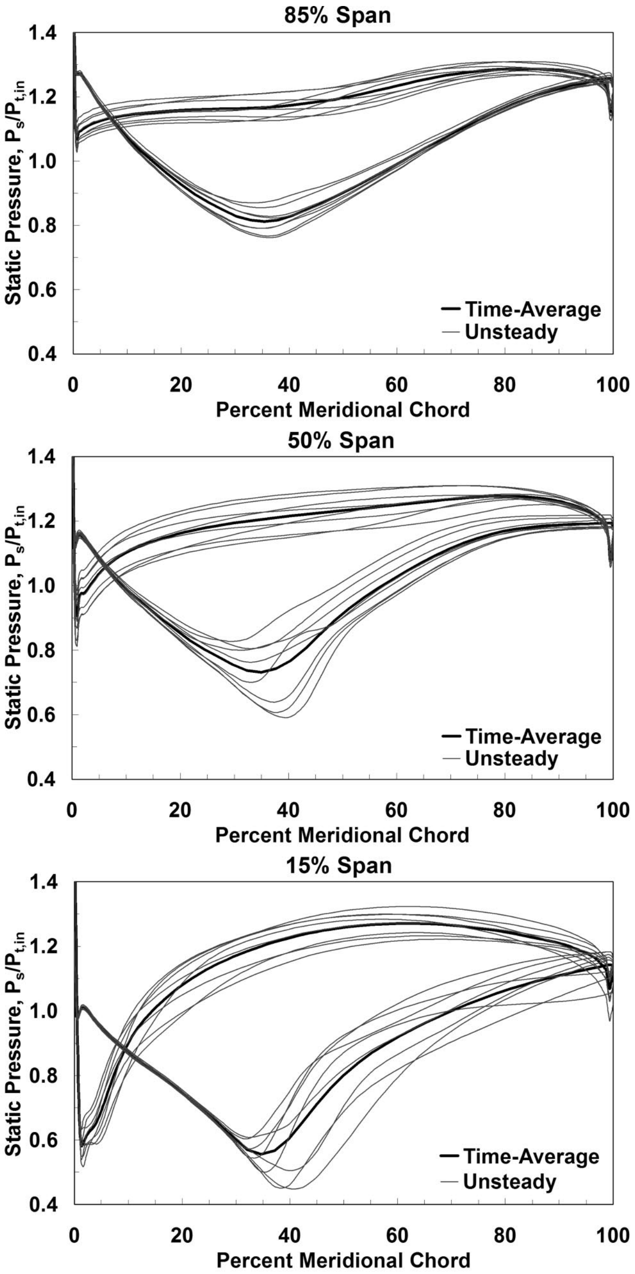

Fig. 16 Fan stator unsteady pressure envelopes for the choke-side operating point

Figures 17 and 18 display the instantaneous suction surface streaklines and static pressure contours at four equally spaced time instants over one periodic cycle of the flow-induced unsteadiness for the choke-side operating point. A vortical separated flow structure is clearly visible in the hub region of the vane aft of the suction surface shock at the second and third time instants, with the low momentum fluid in this separation zone being swept up the trailing edge of the vane. As time progresses the separation zone decreases in size as the low momentum fluid is swept downstream. As the size of the separation zone decreases, the shock strength increases and the shock moves aft as the boundary layer reattaches. The shock strength continues to grow as the cycle progresses until the boundary layer can no longer sustain the adverse pressure gradient, at which point separation is again initiated. As the separation zone grows in size, it pushes the shock forward along the suction surface and the shock strength decreases. As the shock strength decreases, the boundary layer starts to reattach and the cycle repeats, with these dynamic stall events periodically repeating at a frequency of 260 Hz. These CFD snap-

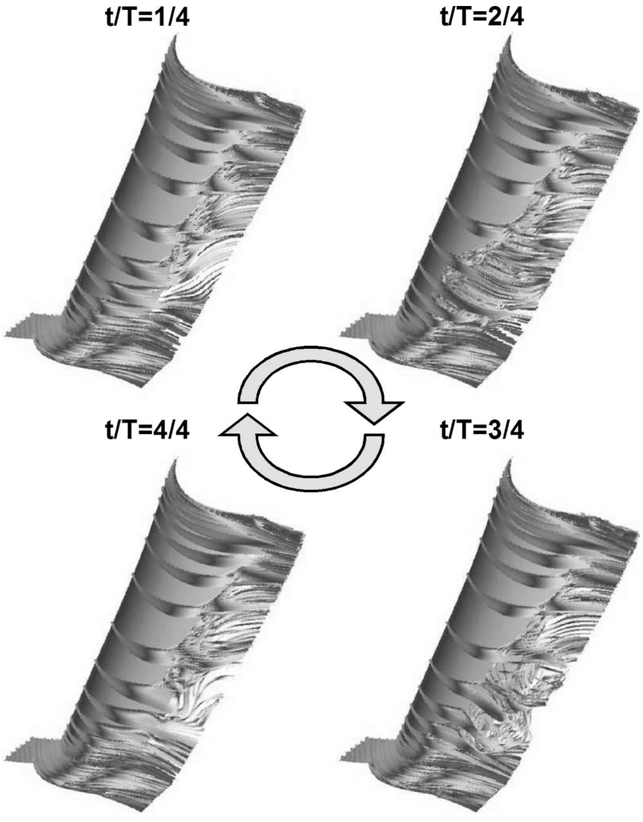

Fig. 17 Instantaneous suction surface streaklines over one periodic cycle for the choke-side operating point

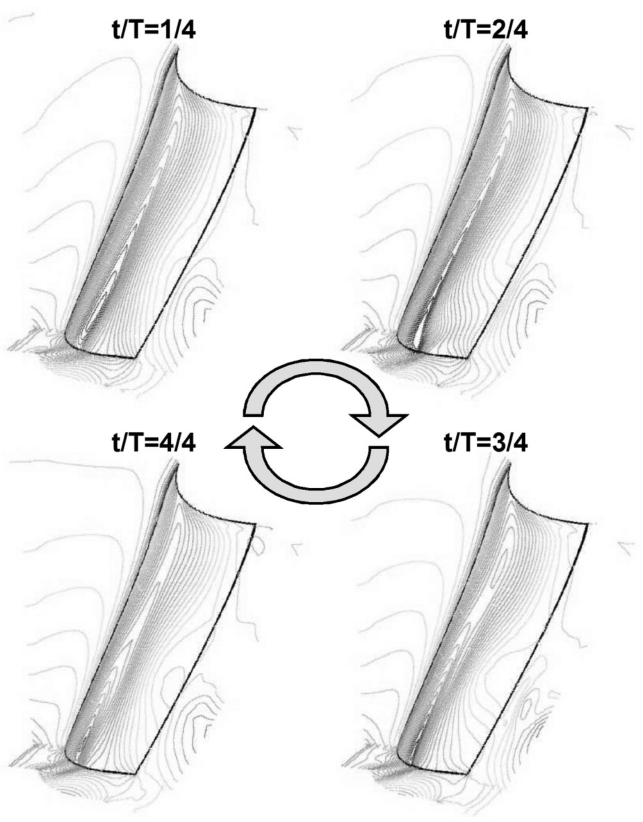

Fig. 18 Instantaneous suction surface static pressure over one periodic cycle for the choke-side operating point

shots of the instantaneous flow field correlate very well with the engine test flow visualization patterns shown in Fig. 9 acquired just prior to the onset of the NSV instability at 87.5% corrected fan speed. Specifically, note the vortical flow structure in the hub region of the airfoil suction surface predicted by the CFD analysis is very similar to that measured during the engine flow visualization tests.

Note that vane motion is not required to initiate the NSV instability because the vanes are rigidly fixed in the CFD simulations. Rather, the instability is inherent to the flow field, with the flow-induced unsteadiness driving the vane vibratory response at the flow field frequency. Recall that the frequency of the flow-induced unsteadiness is predicted to be significantly lower than the vane natural frequency, with the predicted instability frequency 260 Hz and the vane natural frequency 435 Hz. Most structures have well defined resonant peaks in which case the flow field will lock-on to one of the structural natural frequencies. The present fan stator assembly, however, does not exhibit typical structural dynamics characteristics due to the flexible nature of the composite vanes and the manner in which they are mounted in the rubber grommets. Here it is postulated that the fan stator natural frequency drops and locks-on to the flow field frequency once the vibratory response becomes large enough to overcome the static friction between the fan stator vanes and grommets due to a softening of the boundary conditions. This seems like a plausible scenario given the highly nonlinear characteristics of the fan-stator assembly and that fact that the predicted pressure fluctuations are more than sufficient to produce structural failure of the fan stator based on one-dimensional modal force calculations.

Also recall that the strain gage data indicated that the interblade phasing of the vibratory response was 180 degrees, but that the CFD simulations correspond to an interblade phase angle of zero. Although not presented here, additional unsteady TURBO-AE simulations were performed for an interblade phase angle of +176.6 degrees (26 nodal diameter pattern) using phase-lag boundary conditions. However, when analyzing nonzero interblade phase angles, an iterative process was required to predict the frequency of the flow-induced unsteadiness. Specifically, the frequency of the unsteadiness had to be assumed, with this frequency, and the specified interblade phase angle used to calculate a time shift correction to the boundary conditions at the periodic boundaries of the grid. If the predicted frequency of the flow-induced unsteadiness differed from the assumed frequency, then the time shift used for the phase-lag analysis was incorrect and the analysis had to be repeated until the predicted and assumed frequencies matched one another within reasonable accuracy. As the operating point on the fan map at which the flow-induced instability was encountered were identical for both the periodic and phase-lag simulations, the zero interblade phase angle periodic boundary condition analysis was adopted in the redesign effort because it did not require an iterative approach.

Although not demonstrated in these CFD simulations, one possible reason why the flow-induced instability locks-on to the 180 degree interblade phasing observed in the engine test may be due to fluid-structure interaction effects. In particular, for large deflection amplitudes a 180 degree interblade phase angle will result in the smallest throat area across a given vane passage over the course of one vibration cycle. Since localized choking of the fan stator passages drives the flow-induced instability, this out-of-phase vibration may develop once the fan stator vanes begin to respond to the aerodynamic excitation. Thus, future work using a fluid-structure interaction simulation will more than likely be needed to explain the 180 degree phasing observed in the strain gage test data. However, for design applications the intent is to simply avoid the instability altogether. Therefore, if it can be stopped from developing in the first place, there is no need to predict the nodal diameter pattern that it develops into. In fact, the

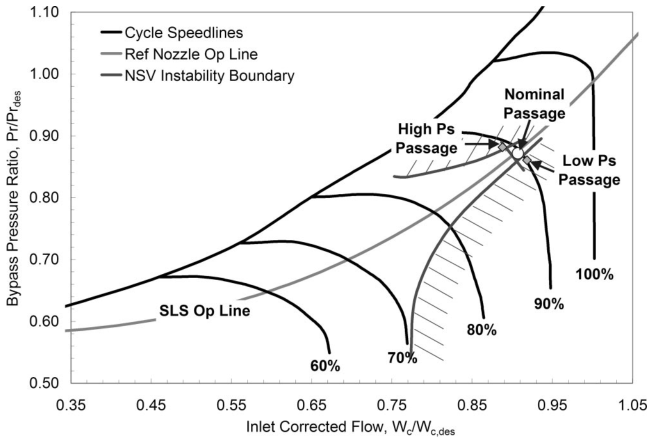

Fig. 19 Parallel compressor analogy of downstream strut effects on fan stage performance

approach outlined in this paper was successfully used to redesign the fan stator and eliminate the source of the NSV problem using the present CFD analysis.

Up until now no mention has been made as to how the downstream struts impact the onset of the flow-induced oscillations because the test data indicated these effects were significant. One way to look at this is to draw the analogy with the early parallel compressor theories used to assess inlet distortion effects on stall margin [18]. In these theories the compressor is divided into two or more parallel compressors in which each compressor operates with a different inlet total pressure, but discharges to the same exit static pressure. A similar analogy can be applied to model the circumferentially nonuniform exit static pressure variation generated by the downstream struts. Because the inlet total pressure to the fan rotor is constant, the exit static pressure variation due to the struts results in the fan stage locally operating on both the choke- and stall-sides of the characteristic, depending on the circumferential location of the individual stator passages.

Recall from Fig. 2 that the two fat bypass struts impose a ±4% variation in the static pressure around the annulus of the fan stator. Figure 19 displays an estimate of how this ±4% variation in the bypass exit static pressure will locally throttle the fan stage ADPAC solutions along the characteristic. Using the parallel compressor analogy it is seen that the low static pressure regions of the fan stator are the first passages to choke and, hence, experience the flow-induced instability. By applying the appropriate inlet and exit boundary conditions to the computational domain, the localized effects of the struts on the fan stator flow field can be modeled in a relative simple fashion using only a single passage in the unsteady simulation. A more rigorous approach would be to perform a full annulus simulation of the fan stator in which all 53 vane passages are modeled along with the downstream struts. However, the computational expense of such a detailed analysis was deemed beyond the scope of the current investigation.

Additionally, the CFD analysis did not predict the onset of the stall-side instability, with no indications of the stall-side solutions exhibiting the same periodic flow-induced oscillations predicted for the choke-side operating point. Attempts were made at marching the steady solutions further toward the stall boundary, but numerical convergence difficulties were encountered for all of these higher back-pressure operating conditions. Also note that the CFD simulations failed to predict the occurrence of the suction surface corner tip separation evident in the engine test flow visualization pictures of Fig. 9. Perhaps the stall-side instability is driven by the dynamic characteristics of this tip separation zone, which the CFD analysis fails to predict. Future work is thus needed to identify the fundamental driver for the stall-side instability.

Summary and Conclusions

A new type of nonsynchronous vibration (NSV) problem has been observed in the development of an advanced design composite fan stator for an aircraft engine application. Extensive development engine testing was conducted using strain gages to determine the characteristics of the vibratory response. Analysis of the strain gage data indicated that the response was nonsynchronous and occurred at a frequency approximately 25% below the fundamental bending mode frequency. A variable exhaust nozzle was used to back-pressure the fan, with both choke- and stall-side instability zones identified that converged toward the nominal operating line placing a high-speed limit on the fan stage. Analysis of strain gage data acquired on adjacent stator vanes during this test indicated that the interblade phasing of the vibratory response was approximately 180 degrees, with the response amplitude varying in a highly random manner with time once the NSV instability was encountered.

Time-accurate three-dimensional viscous CFD simulations were performed at stable and unstable operating points on the fan map. For the choke-side operating points corresponding to unstable operating conditions, a flow-induced aerodynamic instability was identified that generated large amplitude unsteadiness of sufficient magnitude to explain the high vibratory strains. Note that vane motion was not required to initiate the onset of this instability since the simulations were performed for rigid airfoils. Rather, a flow-induced aerodynamic instability evolved at its own time scale as the time-accurate simulations were marched forward in time eventually reaching a periodic limit cycle oscillation, with the predicted instability frequency in reasonable agreement with the strain gage data. The flow-induced aerodynamic instability shared many characteristics similar to dynamic stall, with periodic shock oscillations generating large amplitude unsteadiness due the periodic growth and collapse of a separation zone in the hub region of the fan stator. Furthermore, the instability was only initiated once the flow through the vane passage was on the verge of choking, with any further reductions in back-pressure resulting in large amplitude flow-induced oscillations.

An explanation of why the downstream struts exasperated the onset of the flow-induced instability was given through the use of a parallel compressor analogy similar to that used for inlet distortion problems. Specifically, the fan stage exit static pressure variation around the annulus generated by the two fat service struts in the downstream bypass duct caused the fan stage to operate on the choke-side of the characteristic in the low static pressure regions and on the stall-side for the high static pressure regions of the annulus. This explained why the low static pressure sectors of the fan stator assembly were the ones that experienced the highest vibratory strains, with these sectors of the fan stage becoming the first to choke. On a similar note, the nominal (design intent) passages were not predicted to exhibit the flow-induced instability because they had an adequate choke margin.

In summary, a new analysis procedure has been presented in which an unsteady CFD solver originally developed for flutter and forced response applications has been used to predict the onset of a flow-induced aerodynamic instability driving an NSV problem. Unfortunately, the CFD analysis was not capable of predicting the onset of the stall-side instability observed in the development engine test, with future work needed to understand the driving flow physics in this flow regime. Nevertheless, the CFD simulations presented in this paper highlight how high-fidelity CFD simulations can be used to predict a new class of turbomachinery vibration problem. Although results were not presented in this paper, this new analysis capability has been used to successfully redesign the fan stator to eliminate the source of the NSV problem, which only confirms the hypothesis set forward in this paper regarding the driving flow physics.

Acknowledgments

The author would like to thank Honeywell Engines, Systems and Services for permission to publish this paper. He would also like to acknowledge the contributions of several colleagues at Honeywell who assisted in various phases of this work, in particular Dan Clemmons, Jeff Hayes, Darrell James, Russ Repp, Dr. Joe Panovsky, Dr. Mahmoud Mansour, Brandy Goodell, Malcolm Fleming, Dr. Khaled Hassan, and Dr. Jong Liu. Special thanks is also given to T. K. Kallenbach, Vice President of Engineering, for taking a personal interest in the work described in this paper.

References

[1] Schlichting, H., 1987, *Boundary-Layer Theory*, Seventh Edition, McGraw-Hill, New York, Chap. 2.

[2] Skop, R. A., and Griffin, O. M., 1973, ‘‘A Model for the Vortex-Excited Resonant Response of Bluff Cylinders,’’ J. Sound Vib., **27**(2), pp. 225–233.

[3] Blevins, R. D., and Burton, T. E., 1976, ‘‘Fluid Forces Induced by Vortex Shedding,’’ ASME J. Fluids Eng., **98**(2), pp. 19–26.

[4] Zaman, K. B. M. Q., McKinzie, D. J., and Rumsey, C. L., 1989, ‘‘A Natural Low-Frequency Oscillation of the Flow Over an Airfoil Near Stalling Conditions,’’ J. Fluid Mech., **202**, pp. 403–442.

[5] Rumsey, C. L., Thomas, J. L., Warren, G. P., and Liu, G. C., 1986, ‘‘Upwind Navier-Stokes Solutions for Separated Periodic Flows,’’ AIAA Paper No. 86-0247.

[6] Rumsey, C. L., 1987, ‘‘A Computational Analysis of Flow Separation Over Five Different Airfoil Geometries at High Angles-of-Attack,’’ AIAA Paper No. 87-0188.

[7] Camp, T. R., 1999, ‘‘A Study of Acoustic Resonance in a Low-Speed Multistage Compressor,’’ ASME J. Turbomach., **121**(1), pp. 36–43.

[8] Mailach, R., Sauer, H., and Vogeler, K., 2001, ‘‘The Periodical Interaction of the Tip Clearance Flow in the Blade Rows of Axial Compressors,’’ ASME Paper No. 2001-GT-0299.

[9] Lenglin, G., and Tan, C. S., 2002, ‘‘Characteristics of Wake- and Tip-Vortex-Induced Unsteady Blade Response in Multistage Compressor Environment,’’ 7th National Turbine Engine High Cycle Fatigue (HCF) Conference, W. Palm Beach, FL, May 2002.

[10] Kielb, R. E., Thomas, J. P., Barter, J. W., and Hall, K. C., 2003, ‘‘Blade Excitation by Aerodynamic Instabilities – A Compressor Blade Study,’’ ASME Paper No. GT2003-38634.

[11] Shabbir, A., and Zhu, J., 1996, ‘‘Assessment of Three Turbulence Models in a Compressor Rotor,’’ ASME Paper No. 96-GT-198.

[12] Sanders, A. J., Hassan, K. K., and Rabe, D. C., 2004, ‘‘An Experimental and Numerical Study of Stall Flutter in a Transonic Low-Aspect Ratio Fan Blisk,’’ ASME J. Turbomach **126**(1), pp. 166–174.

[13] Bakhle, M. A., Srivastava, R., and Keith, Jr., T. G., 1997, ‘‘A 3D Euler/Navier-Stokes Aeroelastic Code for Propulsion Applications,’’ AIAA Paper No. 97-2749.

[14] Bakhle, M. A., Srivastava, R., and Keith Jr., T. G., 1998, ‘‘Aeroelastic Calculations Based on Three-Dimensional Euler Analysis,’’ AIAA Paper No. 98-3295.

[15] Chen, J. P., and Whitfield, D. L., 1993, ‘‘Navier-Stokes Calculations for the Unsteady Flowfield of Turbomachinery,’’ AIAA Paper No. 93-0676.

[16] Srivastava, R., Bakhle, M. A., and Keith, Jr., T. G., 1999, ‘‘Phase-Lagged Boundary Condition Methods for Aeroelastic Analysis of Turbomachines—A Comparative Study,’’ ASME Paper No. 99-GT-19.

[17] Hall, E. J., and Delaney, R. A., 1995, *Investigation of Advanced Counterrotation Blade Configuration Concepts for High Speed Turboprop Systems: Task VII—ADPAC Users Manual*, NASA CR 195472.

[18] Cumpsty, N. A., 1989, *Compressor Aerodynamics*, Longman Group, UK, Chap. 9.